Mémoire en vue d'obtenir le diplôme

d'Habilitation à Diriger des Recherches

de l'Université Paris 7, D. Diderot

Séismes d'hier et d'aujourd'hui
Des clefs pour comprendre les séismes de demain ?

Yann Klinger

Equipe de Tectonique

Institut de Physique du Globe de Paris

Soutenue le 19 Juin 2007 devant le jury composé de

P. Tapponnier	IPGP
M. Campillo	LGIT
S. Wesnousky	Univ. Reno, Nevada
R. Armijo	IPGP
D. Pantosti	INGV
P. Bernard	IPGP

1 Préambule

« Et alors, les séismes on peut toujours pas les prévoir ? Mais à quoi vous servez ! »

Cette question relève presque de la brève de comptoir et pourtant peu de géologues et encore moins de sismologues y ont échappé au cours de leur carrière. Alors, ne peut-on vraiment rien dire ? Au cours des 20 dernières années, la sismotectonique et la néotectonique sont venues bouleverser notre savoir en matière de failles actives et de séismes et, profitant des progrès technologiques, de nouvelles méthodes ont été inventées qui nous ont permis de cartographier les failles, d'estimer les vitesses de glissement et de comprendre les sources sismiques avec toujours plus de précision. A un certain niveau, cela nous permet déjà de faire beaucoup de prévisions ; par exemple, les séismes d'Izmit et Düzce en 1999 avaient été prédits et le séisme qui se produira dans la Mer de Marmara d'ici la fin de ce siècle est prédit. De la même façon, cela n'est pas forcément s'avancer beaucoup que de prédire qu'un grand séisme se produira sur la partie sud de la faille de San Andreas dans les 100 ans à venir. Cependant on le sent bien, ces prédictions ne sont pas suffisantes, notamment face à la demande sociétale, car elles ne sont pas assez précises et ne permettent pas d'anticiper les séismes à court terme. Le rêve de tout un chacun serait naturellement de pouvoir disposer d'un bulletin sismologique comme l'on dispose d'un bulletin météorologique.

Ce qui me semble clair, c'est qu'avec les seuls outils de la sismotectonique et de la néotectonique on ne pourra pas répondre à cette question et qu'il est nécessaire de développer de nouvelles techniques qui nous permettent d'acquérir les données pertinentes pour comprendre comment s'organise l'activité sismique au cours du temps et de l'espace, de façon détaillée. Brièvement il s'agit de savoir si le cycle sismique existe et, dans l'affirmative, de savoir comment il s'organise, premier pas vers une possible prédiction à plus court terme.
La majeure partie du travail présenté dans ce mémoire est tournée vers cet objectif. D'une part, directement aux travers d'études paléosismologiques qui nous permettent de mieux comprendre l'activité sismique passée de certaines failles en particulier. D'autre part, au travers de l'étude d'un très grand séisme instrumental qui nous permet de mieux comprendre les processus mis en jeu lors d'un séisme, processus dont nous n'avons forcément qu'une vue très partielle quand il s'agit d'étudier les séismes anciens.

Ce manuscrit est organisé en trois parties. Dans une première partie je fais un rapide inventaire des principaux modèles de cycle sismique qui ont été proposés ainsi que des principales hypothèses et conditions qui sont derrières. Je rappelle aussi quelques observations clefs qui ont marquées les études sur le cycle sismique et les séismes anciens. La deuxième partie est directement consacrée à mes propres travaux dans cette thématique. Dans une troisième partie j'indique quelques pistes que j'envisage de suivre pour prolonger ce travail, certaines étant déjà engagées et d'autres simplement à l'état de projet.

2 Cycle sismique : modèles et données existants

2.1 De la néotectonique au cycle sismique, une transition naturelle

La fin des années 70, au sortir de l'ébullition créée par l'avènement nouveau de la tectonique des plaques, est l'époque d'une compréhension nouvelle des grands systèmes tectoniques actifs, comme par exemple la Méditerranée ou l'Asie [Tapponnier, 1977; Molnar and Tapponnier, 1978; Garfunkel*, et al.*, 1981]. En effet, à cette époque, avec le développement permanent des réseaux de sismomètres, notamment le réseau WWSSN, le nombre de mécanismes au foyer disponibles augmente rapidement, qui permettent de différentier les séismes suivant le type de déformation qu'ils accommodent et de les interpréter dans un schéma cohérent de déformation à l'échelle continentale [McKenzie, 1972; Jackson and McKenzie, 1984]. Parallèlement des progrès considérables sont fait dans l'utilisation nouvelle de l'imagerie satellitaire qui permet de ne plus se concentrer uniquement sur un petit bout d'affleurement spécifique mais d'embrasser les structures géologiques dans leur ensemble. Ces images, et notamment les images satellites Landsat, permettaient, grâce à cette vue d'ensemble, de percevoir la cohérence du système tectonique et du même coup d'en comprendre le fonctionnement mécanique [Tapponnier and Molnar, 1977; Armijo*, et al.*, 1986]. Cette appropriation de ce nouvel outil par des disciplines qui étaient elle-même en train de naître, la néotectonique et la sismotectonique, était en soit une révolution et a permis des avancées majeures. La limitation principale de ce travail était la très grande difficulté de dater précisément les structures Quaternaires récentes affectées par ces failles nouvellement identifiées, afin de déterminer les taux de déformation récents. La seule possibilité était d'utiliser, dans le cas par exemple d'un décrochement, l'age géologique des formations décalées par les failles, ce qui ne donnait accès le plus souvent qu'à une borne inférieure du taux de déformation, au mieux à moyen terme, le plus souvent à long terme [Quennell, 1958; Freund*, et al.*, 1968].

La deuxième révolution de la néotectonique s'est déroulée au début des années 90. Elle concerne les progrès important en matière de datation des formations géologiques Quaternaires récentes. D'une part, les datations ^{14}C furent considérablement améliorées grâce aux mesures faites avec des accélérateurs de particules et à la calibration des ages ^{14}C [Bard*, et al.*, 1990]. D'autre part, les années 90 ont vu l'apparition d'autres méthodes de datation qui utilisent les isotopes cosmogéniques ^{10}Be, ^{26}Al et ^{36}Cl pour mesurer le temps d'exposition au bombardement par des particules α d'échantillons collectés sur les surfaces que l'on souhaite dater [Gosse and Phillips, 2001]. Ces méthodes non seulement permettent de dater des formations ne contenant pas de restes organiques, éléments nécessaires pour le ^{14}C, mais elles permettent aussi de dépasser largement la limite des 45000 ans à 50000 ans qui est intrinsèquement liée aux datations ^{14}C. L'application de ces méthodes de datation, associée à une utilisation intensive de l'imagerie satellitaire, a permis, grâce aussi à une meilleure compréhension des processus de morphogenèse, de déterminer le taux de glissement Quaternaire pour de nombreuses failles actives de la planète, notamment en Asie [Lasserre*, et al.*, 2002; Van Der Woerd*, et al.*, 2002; Ritz*, et al.*, 2003; Chevalier*, et al.*, 2005; Meriaux*, et al.*, 2005], en domaine méditerranéen [Klinger*, et al.*, 2000a; Benedetti*, et al.*, 2002; Daëron*, et al.*, 2004; Palumbo*, et al.*, 2004] ou en Amérique du Nord [Matmon*, et al.*, 2005; Matmon*, et al.*, 2006; Van der Woerd*, et al.*, 2006].

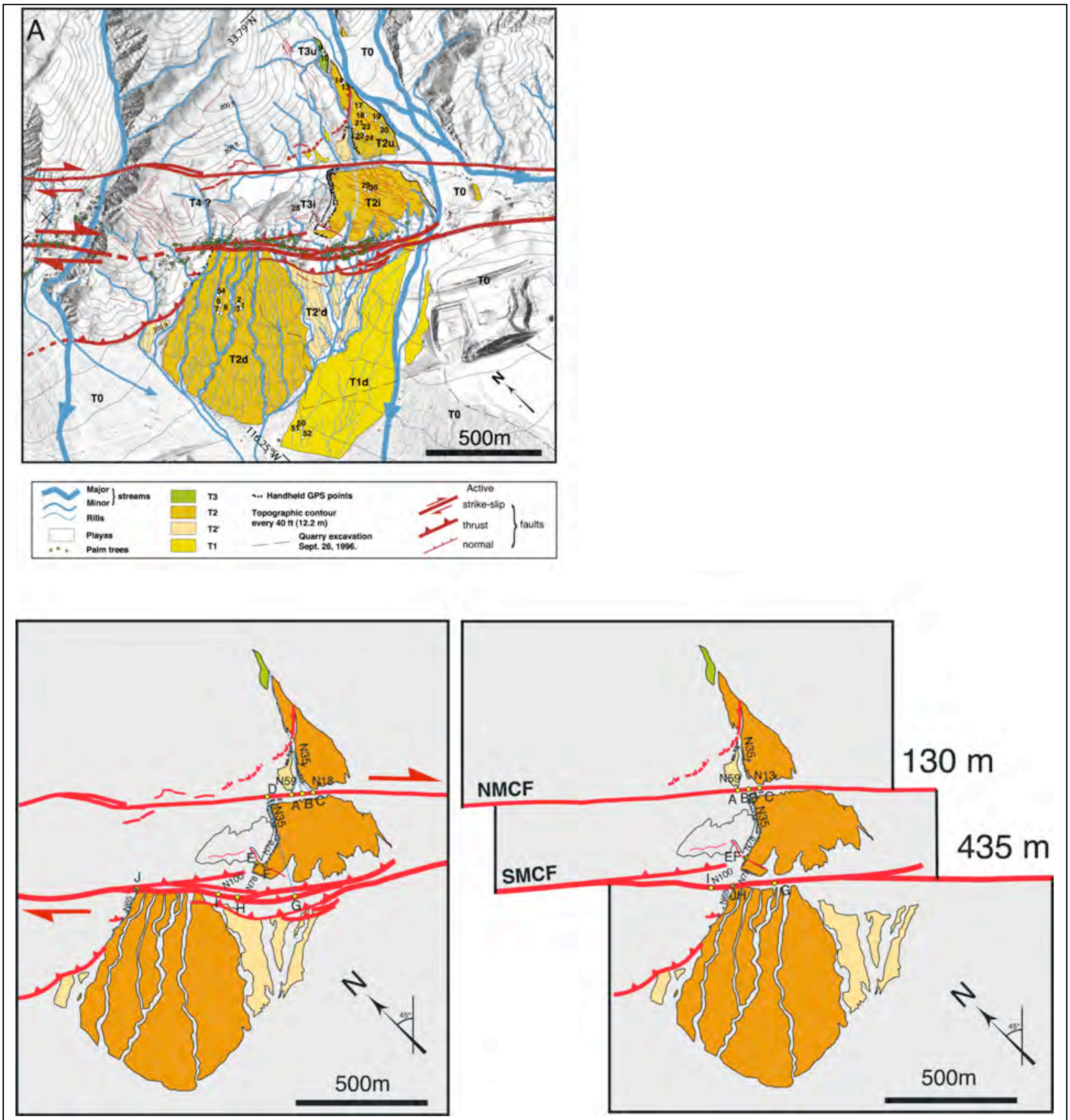

Figure 1 : reconstruction de la géométrie initiale du cône alluvial d'Indio. La vignette du haut montre la géométrie actuelle, avec les branches actives de la faille de San Andreas ainsi que les différentes surfaces de dépôt qui sont identifiables. Les vignettes du bas montrent une reconstruction possible de la surface T2 dans sa géométrie de dépôt. La datation de la surface T2 nous a permis d'estimer une vitesse moyennée sur ~36ka de 16mm/an pour cette branche de la faille de San Andreas. D'après [Van der Woerd*, et al.*, 2006].

La figure 1 illustre le principe d'une telle mesure dans le cas d'une faille décrochante. Elle illustre aussi certaines difficultés qui sont associées à ce type de mesure : La géométrie de la faille peut être complexe et rendre impossible une reconstruction univoque de la forme initiale de l'objet décalé. L'identification de surfaces alluviales d'âge identique de part et d'autre de la faille peut être difficile du fait d'une érosion différente des surfaces. Enfin les stratégies d'échantillonnage et l'interprétation même des âges d'exposition restent encore âprement discutés [Brown, *et al.*, 2005; Chevalier, *et al.*, 2005].

Parallèlement aux progrès très importants de la géochronologie, une autre façon de mesurer le déplacement en travers des failles s'est très largement répandue au cours des années 90 avec le développement de la géodésie spatiale. Deux techniques importantes ont émergé qui sont l'interférométrie radar (l'INSAR) et les mesures GPS (Global Positioning System). Contrairement aux taux de déformation donnés par la néotectonique, qui sont des taux intégrés au minimum sur quelques milliers d'années, les taux de déformation mesurés grâce à ces techniques sont des taux instantanés. Jusqu'à récemment les applications INSAR concernaient essentiellement les déformations ayant une amplitude importante sur un temps court, typiquement les déformations co- et post-sismiques ou les subsidences rapides. Le manque d'archive et les différents problèmes liés à la perte de cohérence entre deux scènes avec le temps limitaient la mesure de déformation intersismique. Des résultats récents [Burgmann, *et al.*, 1998; Peltzer, *et al.*, 2001; Wright, *et al.*, 2001] montrent qu'avec l'accumulation des données et les progrès importants réalisés dans le traitement de l'image une part de ces difficultés peut être contournée, et qu'il devient possible de mesurer la déformation intersismique sur un intervalle de temps de quelques années. Le principe du GPS est de mesurer régulièrement la géométrie d'un réseau géodésique qui se déforme, par exemple à cause d'une faille active. La couverture spatiale est bien évidement beaucoup plus faible qu'avec l'INSAR mais par contre le problème de perte de cohérence du signal entre deux campagnes de mesure n'existe pas. Une difficulté importante de la mesure GPS est de trouver des points qui soient stables sur de longues périodes de temps. La différence entre les différentes campagnes de mesures permet de connaître la déformation d'un réseau GPS avec une très grande précision. Tout comme pour l'INSAR la différence de temps entre les différentes campagnes ne peut pas excéder la durée de vie de la technique, soit une dizaine d'années à l'heure actuelle. De très nombreuses mesures ont été effectuées au cours des 15 dernières années et des vitesses instantanées de déformation ont été déterminées pour de nombreuses structures tectoniques actives [Bennett, *et al.*, 1996; Vernant, *et al.*, 2004; Socquet, *et al.*, 2006]. La figure 2 montre un profil typique de déplacement en travers d'une faille entre deux campagnes de mesures GPS espacées de 5ans.

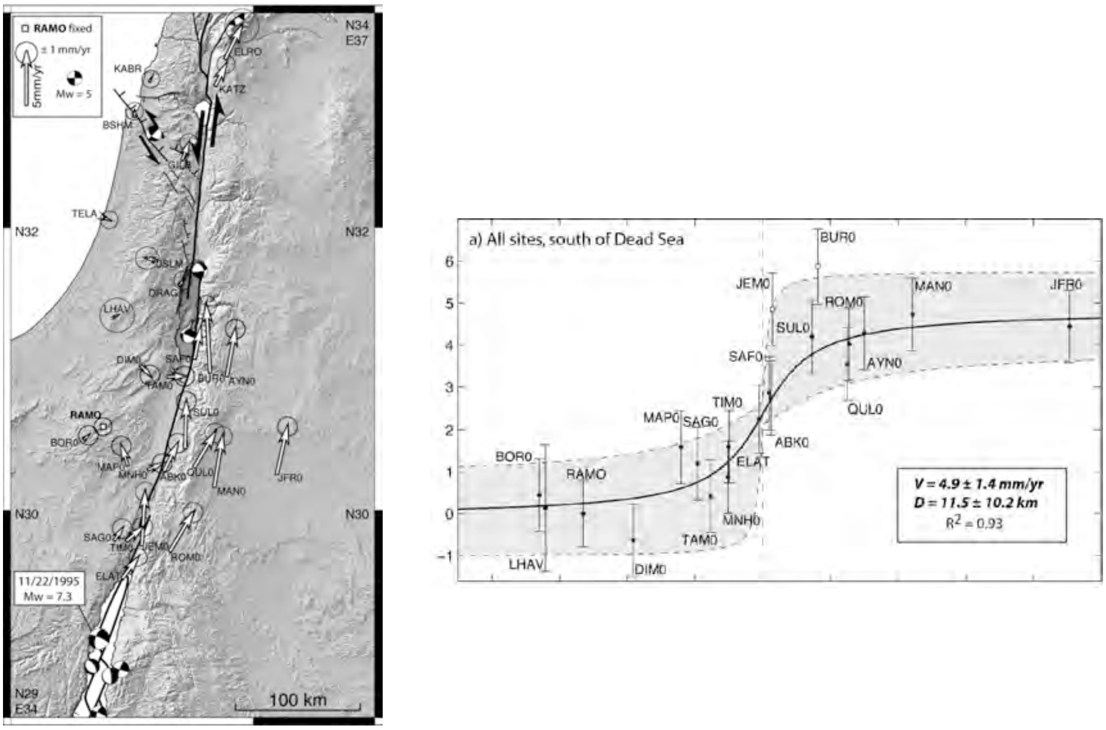

Figure 2 : mesures GPS en travers de la faille du Levant. Les données de campagne permettent de retrouver une courbe en arctangente typique d'une faille en phase de chargement intersismique dans un milieu élastique. D'après [Lebeon*, et al.*, 2006]

La multiplication des mesures de vitesse de déformation en travers des failles, dans des contextes géologiques variés et sur des échelles de temps très différentes, a rapidement posé de nouvelles questions. En effet, il est apparu que les vitesses mesurées par différentes méthodes au travers de mêmes structures pouvaient être très différentes, comme par exemple le long de la faille de l'Altyn Tag où la vitesse déterminée à partir de mesures géomorphologiques est de ~17.8 mm/an alors que la vitesse mesurée à partir de données GPS est de ~9 mm/an [Bendick*, et al.*, 2000; Meriaux*, et al.*, 2005]. Probablement à cause d'un aspect instrumental faussement rassurant, les mesures GPS ont largement bénéficié d'un a priori favorable face aux mesures néotectoniques, sous le prétexte que l'analyse géologique d'un site impliquerait de l'opérateur une part plus importante de subjectivité que le traitement de données GPS. Quiconque s'est déjà essayé à la mise en place d'un réseau GPS, aux mesures proprement dites, puis à leur analyse détaillée sait que cette vision est en grande partie inexacte. La mesure et l'interprétation de données GPS, comme pour toutes autres données, comprend sa part de « bricolage » et de subjectivité dans le choix des stratégies de mesure puis de calcul des résultats.

Malgré tout, devant la persistance insolente de variations importantes entre les vitesses mesurées par différentes méthodes pour les mêmes sites, l'idée a fait son chemin que cette différence pourrait être réelle et significative [Chery and Vernant, 2006] + Perfettini et Avouac. Il est en fait possible qu'il y ait là un message sur le fonctionnement des failles à moyen et long terme et la façon dont la déformation est accommodée au cours du cycle sismique. Dans la perspective de pouvoir un jour prédire les séismes, les phases transitoires pré-sismiques sont de première importance et essayer de décrypter ce message est un objectif de premier ordre pour la communauté des sciences de la Terre.

Pour pouvoir avancer sur cette question il est nécessaire de mieux comprendre ce que représente la notion de cycle sismique. En effet, cette notion est souvent utilisée dans des contextes très différents et pour des échelles de temps et d'espace variées. Si l'on veut pouvoir comprendre comment s'organise l'activité sismique au sein d'un système tectonique, il est nécessaire de hiérarchiser les structures afin de pouvoir emboîter les échelles.

Le segment de faille peut être compris comme l'élément de base de cette hiérarchie. Il est donc nécessaire de bien comprendre quel est son rôle dans le fonctionnement de la faille ; D'une part, il s'agit d'estimer jusqu'à quel point la déformation co-sismique est localisée sur le segment, et éventuellement si une part de déformation asismique y est aussi accommodée. D'autre part, il est important d'interroger la manière dont les séismes se répètent, ou non, sur un segment en particulier. En fait il est essentiel de bien identifier la relation structurelle qui le lie avec la faille lithosphérique plus profonde dont il est l'image en surface.

Au niveau supérieur, on retrouve la faille, constituée par un ensemble de segments. Parmi les points clefs que l'on peut identifier si l'on s'intéresse aux séismes, et plus généralement au cycle sismique, il y a la géométrie dans laquelle s'enchaînent les segments pour former une faille. Savoir jusqu'à quel point cette géométrie a un sens, sur quelles échelles de temps elle peut être considérée comme stable et comment elle peut influer sur le déclenchement, la propagation et l'arrêt d'une rupture sismique sont autant de questions critiques pour la compréhension de l'histoire sismique de la faille [King and Nabelek, 1985; Sibson, 1985; Wesnousky, 2006]. Par ailleurs, parce que c'est justement cette histoire sismique de la faille qui va nous intéresser pour essayer de comprendre le cycle sismique, il est important d'accumuler le plus d'information possible sur l'histoire sismologique présente et passée de la faille dans son ensemble. Clairement, si une faille est constituée de segments, il est très probable que ces segments interagissent au cours du temps pour former une séquence sismique qui accommode la déformation en champs lointain appliquée le long de l'ensemble de la faille [Stein*, et al.*, 1997]. Cette échelle est typiquement l'échelle qui intéressera la communauté travaillant sur les problèmes liés au risque sismique.

Enfin une faille est rarement unique sur une terre infinie et homogène. Elle fait généralement partie d'un système tectonique plus ou moins complexe, comme par exemple l'East California Shear Zone ou le Tibet. A cette échelle, certaines failles se propagent et d'autres sont abandonnées ; la question de l'échelle de temps pertinente se pose à nouveau. Par ailleurs, parce que le système tectonique est formé par un ensemble de failles qui interagissent, le taux de déformation de chaque structure individuelle n'est pas indépendant, en tous cas pas à toutes les échelles de temps, de ce qui se passe dans le reste du système. Pour la même raison, on peut penser qu'il existe une certaine organisation de l'activité sismique au sein du système. Il ne s'agit donc plus de collecter seulement les informations les plus précises quant à l'histoire sismique d'une faille particulière mais plutôt l'information concernant chaque faille formant le système. Il n'y a qu'en passant par cette étape très longue et ardue que l'on pourra espérer, peut-être, avoir une vue globale du fonctionnement mécanique d'un système tectonique.

Au cours de mon travail, j'ai largement utilisé certaines des techniques de la néotectonique décrites précédemment, notamment au Proche-Orient, le long de la faille du Levant [Klinger*, et al.*, 2000a; Klinger*, et al.*, 2003a; Lebeon*, et al.*, 2006], et de façon plus ponctuelle le long de la faille de San Andreas, [Van der Woerd*, et al.*, 2006]. Une partie du travail de thèse de Maryline Lebéon (2004-2007) repose d'ailleurs sur l'analyse conjointe de données géologiques et géodésiques pour un site donné. Ce n'est cependant pas l'objet particulier de ce mémoire et ces travaux ne sont donc pas décrits plus avant ici. La suite de ce mémoire est plus spécifiquement consacrée à des études récentes concernant le cycle sismique et la segmentation des failles.

2.2 Cycle sismique, de nombreux modèles

Depuis que l'on observe des séismes, un des objectifs est la prédiction. Si la communauté scientifique n'a pas encore atteint ce but, et rien ne permet aujourd'hui de garantir qu'elle y arrivera un jour, elle n'a de cesse d'essayer. Dans ce cadre, plusieurs modèles conceptuels de cycle sismique ont été développés que je vais rappeler brièvement dans les paragraphes qui suivent. Comme dans toute discipline, la validation des modèles passe par la confrontation avec des données réelles. Dans le cas des séismes, comme je vais le montrer, cela n'est pas facile car les données sont encore (trop) rares.

Les modèles de cycle sismique ne peuvent pas tous être comparés les uns aux autres. En fait on peut distinguer deux classes de modèles : d'une part les modèles qui considèrent la faille comme une entité mécanique gouvernée par les contraintes dans la croûte, dont on regarde essentiellement le comportement au cours du temps et éventuellement l'interaction avec les failles voisines, sans vraiment se préoccuper du détail du glissement le long de la faille. D'autre part, les modèles qui, au contraire, regardent plus en détail ce qui se passe le long de la faille, et plus précisément le long des segments de cette faille, quand des séismes successifs se produisent. Les données pour contraindre ces modèles ne sont donc pas tout à fait les mêmes ; dans le premier cas l'important est surtout de disposer de longues séries temporelles, les dates des séismes. Dans le second cas, en plus de l'aspect temporel, il est non seulement crucial d'avoir une vision la plus précise possible de la distribution de glissement et de la taille des séismes anciens, mais aussi une information détaillée quant à la géométrie de la rupture.

2.2.1 Le modèle périodique et ses variations

La figure 3 montre le modèle le plus simple auquel on puisse penser en terme de comportement mécanique, le modèle purement périodique, ainsi que deux variations à partir de ce modèle, le modèle prédictible en temps et le modèle prédictible en déplacement [Shimazaki and Nakata, 1980].

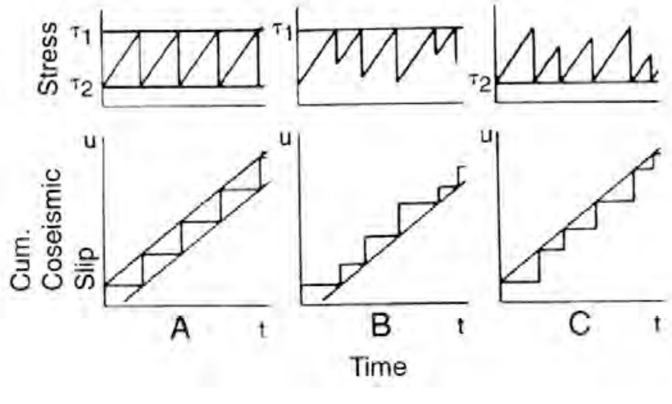

Figure 3 : modèles de cycle sismique (A) purement périodique, (B) prédictible en temps et (C) prédictible en déplacement. D'après [Scholz, 1990]

Le modèle purement périodique postule que la croûte terrestre, dans des conditions normales, se déforme élastiquement quand elle est soumise à des contraintes extérieures, par exemple celles résultant du mouvement à grande échelle des plaques tectoniques. La déformation élastique de la croûte est cependant limitée et au-delà d'un certain seuil la croûte atteint une limite maximale de chargement et rompt, relâchant au cours d'un séisme tout ou une partie de la contrainte accumulée. Dans le cadre du modèle périodique, la chute de contrainte associée aux grands séismes est constante, et donc on peut déterminer un niveau inférieur de contrainte dans lequel se retrouve la croûte terrestre juste après un séisme. Une fois définie la limite supérieure et inférieure des variations du niveau de contrainte au niveau de la faille, en faisant l'hypothèse que le taux de chargement en contrainte du système tectonique est constant à l'échelle de temps qui nous intéresse (c'est-à-dire que le mouvement des plaques varie peu, ou pas du tout, pendant la période d'observation), il est alors possible de prédire le temps de récurrence des grands séismes sur la faille. Il apparaît clairement qu'avec un tel modèle on génère toujours des séismes de la même magnitude. Sauf à considérer que les propriétés de la croûte varient grandement suivant le segment de faille que l'on considère à l'intérieur d'un même système tectonique, ce qui semble peu probable, il est donc difficile de générer une sismicité qui respecterait une distribution de Gutenberg-Richter avec un tel modèle. Il y a donc là une contradiction flagrante entre modèle et observations.

Le modèle prédictible en temps correspond à une variation du modèle précédent. Dans ce cas, on ne fixe qu'une borne supérieure qui est la contrainte maximale que peut supporter la croûte élastique avant de rompre. Aucune hypothèse n'est faite sur la chute de contrainte associée au séisme. Par ailleurs, comme précédemment on considère que le taux de chargement du système tectonique est constant au cours du temps. Dans ce cas, si l'on connaît le déplacement associé au dernier séisme, on peut alors prédire combien de temps il est nécessaire d'attendre avant que le tremblement de terre suivant ne se produise.

Le modèle prédictible en déplacement, à l'inverse, utilise la borne inférieure qui correspond au niveau inférieur acceptable pour la contrainte sur la faille. Dans ce cas, chaque séisme a pour effet de redescendre le niveau de contrainte sur la faille à ce niveau plancher. Comme précédemment, en utilisant l'hypothèse d'un taux de chargement élastique constant, lié aux conditions aux limites lointaines, on peut alors prédire l'ampleur du déplacement attendu lors du prochain séisme en fonction du temps qui s'est écoulé depuis le précédent.

Contrairement au modèle purement périodique, les modèles prédictibles en temps ou en déplacement permettent de générer une large gamme de magnitude qui respecte la distribution de Gutenberg-Richter, classiquement observée pour les grands systèmes tectoniques.

Ces trois modèles reposent sur une hypothèse forte qui n'est cependant que rarement explicitée, à savoir que le chargement en contrainte de la faille est constant au cours du temps. Si tel n'est pas le cas, aucun de ces 3 modèles ne fonctionne. La véracité d'une telle hypothèse reste à démontrer. Il est possible que loin des frontières de plaque la vitesse des plaques tectoniques soit constante sur de longues périodes de temps. Mais la différence entre les vitesses mesurées à différentes échelles de temps au niveau des failles elles-mêmes pourrait bien nous indiquer qu'au niveau des failles cela n'est pas vrai, et que la vitesse peut changer au cours du cycle sismique [Perfettini, *et al.*, 2005]. Continuer à mesurer ces vitesses, à toutes les échelles de temps, est donc crucial car non seulement cela nous renseignera sur le déroulement du cycle sismique en général mais cela pourrait aussi nous permettre de savoir où nous nous positionnons dans le cycle sismique, pour une faille donnée, ce qui est de première importance en terme de prévision des séismes.

Existe-t-il des données qui puissent être confrontées à ces modèles ? La répétition de plusieurs séismes sur une même faille au cours de la période dite instrumentale (~1 siècle), si l'on ne considère que les séismes d'une taille significative, magnitude ≥ ~6, reste exceptionnelle. Le meilleur exemple connu à ce jour reste l'exemple de la série de séismes qui se sont produits à Parkfield, le long de la faille de San Andréas (Figure 4).

Sur ce site 6 séismes se sont produits entre 1857 et 1966, avec un temps de récurrence de ~22ans. La magnitude de ces différents séismes était comparable, autour de 6. Cette série a été présentée comme l'exemple type prouvant qu'un modèle prédictible en temps pouvait fonctionner [Bakun and Lindh, 1985]. Le 7ème séisme, prédit pour 1988 ± 5ans, ne s'est produit que bien plus tard, en 2004, remettant en cause la validité de ce modèle [Murray and Segall, 2002]. Il est intéressant de noter que bien que ce type de modèle ait failli face aux observations, il reste encore de nos jours à la base de nombreux modèles probabilistes d'aléa sismique pour des zones où le risque sismique est très grand, comme par exemple la Californie [Working Group for California Earthquake Probabilities, 1995; Cramer*, et al.*, 2000].

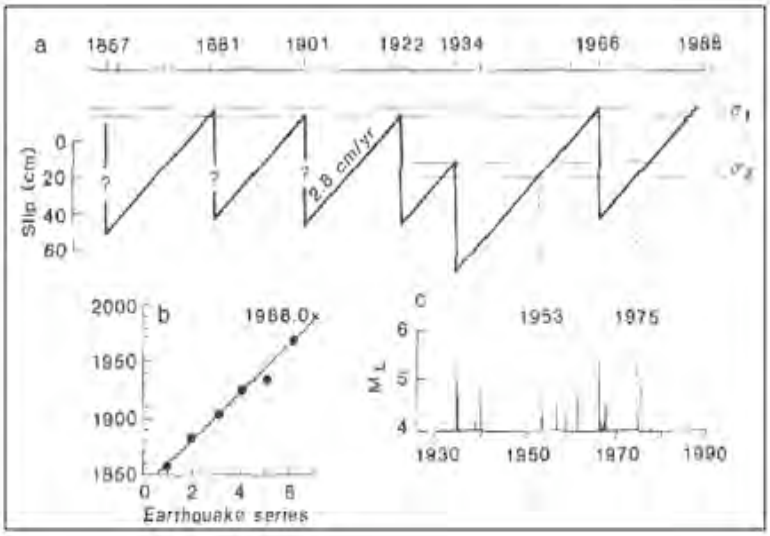

Figure 4 : la série des séismes de Parkfield constitue l'une des plus belles séquences sismiques connue à ce jour. Le dernier séisme qui s'est produit en 2004 (pas représenté sur cette figure) vient cependant contredire l'hypothèse que ce système puisse être simplement prédictible en temps. D'après [Bakun and Lindh, 1985]

2.2.2 sismique et géométrie de la faille

Une deuxième classe de modèle aborde le problème du cycle sismique différemment. Cette fois-ci il ne s'agit plus de considérer la faille comme un objet ponctuel cassant plus ou moins régulièrement en fonction de la contrainte qui est appliquée aux limites du système, mais de considérer ce qui se passe en chaque point le long de la faille. C'est une approche plus locale dont l'intérêt est évident en ce qui concerne l'évaluation du risque sismique en un point donné. La figure 5 illustre les 3 principaux modèles que l'on peut regrouper dans cette catégorie.

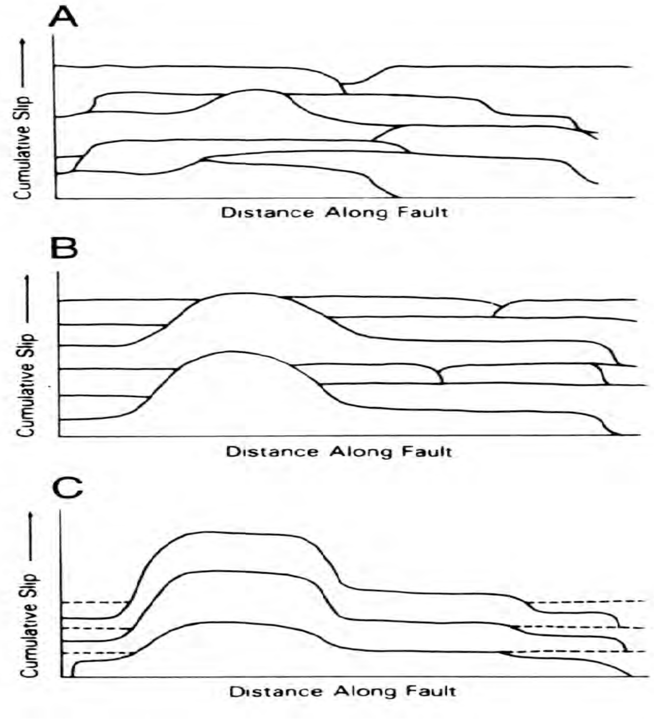

Figure 5 : distribution du glissement le long d'un faille pour des séismes successifs dans le cas (A) ou le glissement est purement aléatoire lors de chaque séisme, dans le cas (B) d'un modèle de glissement caractéristique et dans le cas (C) d'un modèle de séisme caractéristique. D'après [Sieh, 1978b; Schwartz and Coppersmith, 1984]

Le premier modèle est un modèle complètement aléatoire. Dans une certaine mesure ce modèle n'est pas typique de cette catégorie et pourrait aussi être rattaché aux modèles décrits précédemment. Nous l'incluons dans cette catégorie car la façon dont on le décrit ici permet une comparaison directe avec les autres modèles. Dans ce modèle, des séismes de toutes magnitudes se produisent le long de la faille (on entend ici pour faille un ensemble de plusieurs segments, par exemple la faille Nord Anatolienne ou la faille de San Andréas), qui affectent différentes sections de la faille. Le déplacement co-sismique en un point particulier de la rupture, ainsi que l'extension latérale de la rupture, sont aléatoires. Les seules limites imposées à un tel modèle sont les grandes lois d'échelle liant longueur de rupture, dislocation et moment sismique associé [Wells and Coppersmith, 1994]. Un tel modèle, s'il sonne le glas de toute cohérence interne dans le fonctionnement du système tectonique, ne peut cependant pas être rejeté, du moins pour le moment, car il peut reproduire deux observations importantes, à savoir une distribution de sismicité conforme à la loi de Gutenberg-Richter, et un taux de glissement qui, en moyenne, est constant tout au long de la faille. Seul un plus grand nombre de données concernant la distribution temporelle des séismes sur les failles pourrait permettre de tester réellement ce modèle.

Le deuxième modèle est appelé modèle de séisme caractéristique. Présenté pour la première fois en 1981 puis repris et développé en 1984, il est construit à partir d'observations faites sur les failles normales du front des Wasatch, à l'est du Basin and Range dans l'ouest des Etats-Unis [Schwartz and Coppersmith, 1984]. Utilisant des données collectées dans des tranchées paléosismologiques creusées en travers de plusieurs segments de failles normales qui forment le front des Wasatch, [Schwartz and Coppersmith, 1984] ont montré que les ruptures historiques, et préhistoriques, étaient identiques d'un séisme à l'autre : chaque partie de la faille rompait toujours de la même façon, lors d'un séisme de magnitude prévisible, en provoquant un glissement prévisible. La question de la récurrence temporelle n'est pas réellement abordée dans ce modèle. Naturellement, du point de vue de l'estimation du risque sismique, ce modèle est très intéressant car il permet de contraindre des paramètres importants de la rupture, notamment l'amplitude de la dislocation co-sismique attendue en un point donné. Ce modèle se heurte cependant à deux difficultés : d'une part un tel modèle ne permet pas de retrouver une distribution de sismicité conforme à la loi de Gutenberg-Richter. Ce point est évoqué dès les premières lignes du papier présentant le modèle de séisme caractéristique et les auteurs montrent que si l'on extrapole brutalement le nombre de séismes de faible magnitude vers les grandes magnitudes, on sous-estime grandement le nombre de séismes de grandes magnitudes par rapport à ce qui est observé dans les tranchées, sous-estimant par là même le risque associé [Schwartz and Coppersmith, 1984]. La difficulté ici est de savoir comment l'on définit la zone sur laquelle on établit la distribution de sismicité, la relation de Gutenberg-Richter étant censée s'appliquer sur un système tectonique alors que le modèle de séisme caractéristique ne concerne qu'une portion de faille donnée. L'autre difficulté, de taille, de ce modèle est qu'il implique que le taux de déformation le long de la faille ne soit pas constant. Il est clair sur la figure 5 qu'au cours du temps certaines régions vont accumuler plus de déplacement que d'autres, ce qui ne semble pas viable à l'échelle des temps géologiques. Les auteurs du modèle, conscients de cette difficulté, proposent que la variabilité du taux de déformation ne soit qu'apparente et qu'elle doive être directement reliée à la complexité de la zone de faille : Là où la faille se complexifie, le taux de déformation pour une branche donnée de la faille décroît en proportion de la quantité de déformation accommodée par les structures secondaires. Cette vision est clairement inspirée par les travaux sur les failles normales du front des Wasatch. En effet, le long du front, comme souvent dans les contextes de failles normales, les segments de faille sont discontinus et les terminaisons des différents segments peuvent dédoubler localement la faille, ce qui permettrait éventuellement un taux de déformation uniforme.

De façon indépendante, et à peu près en même temps qu'était développé le modèle de séisme caractéristique, a été proposé un modèle dit « modèle de glissement caractéristique » [Sieh, 1981]. Sous un vocable qui peut paraître semblable au premier abord, ce modèle est en fait fondamentalement différent. Alors que le modèle de séisme caractéristique est construit à partir d'observations faites le long de failles normales, ce modèle-ci s'appuie essentiellement sur des observations faites le long de la faille de San Andréas, en contexte décrochant. Dans ce modèle, l'idée de segments caractéristiques n'existe pas, peut être en partie parce que cette segmentation est moins évidente sur le terrain le long de la faille de San Andréas que le long des grandes facettes triangulaires du front des Wasatch. L'observation qui domine ici est le fait que localement la dislocation co-sismique est similaire d'un séisme à l'autre. L'existence de segments implique en revanche que ces segments peuvent s'associer de façon différente lors de séismes successifs, provocant des événements de magnitudes différentes. Parce que la géométrie de la rupture n'est pas figée, il est tout à fait possible dans un tel modèle d'avoir des zones avec des glissements co-sismiques différents le long d'une même rupture, la différence de glissement entre les zones étant compensée par un nombre de séismes plus important dans les zones où le glissement par séisme est plus faible. Ce modèle permet donc non seulement de retrouver une distribution de sismicité qui est conforme à la distribution de Gutenberg-Richter, mais aussi d'obtenir un taux moyen de déformation uniforme le long de la faille (figure 5).

Comme on le voit, différents modèles de cycle sismique existent. Se font-ils concurrence pour autant ? Cela n'est pas évident. Ces modèles ont généralement été établis dans des contextes tectoniques particuliers dont ils gardent la marque de fabrique. L'existence même d'un seul modèle qui permettrait d'expliquer l'ensemble des observations pour toutes les failles n'a d'ailleurs pas forcément de raison d'être. Bien au contraire, il est probable qu'une zone de subduction ne fonctionne pas comme une zone de cisaillement continentale. Les géométries de ruptures sont différentes, les interactions entre segments de faille aussi, pourquoi donc le fonctionnement d'ensemble devrait-il être identique ?

La problématique actuelle réside essentiellement dans la capacité à tester ces différents modèles. En effet, ce n'est pas de modèles dont nous manquons à l'heure actuelle mais de données réellement discriminantes. D'autre part, le pas entre la collecte des données et leur intégration dans des modèles de cycle sismique est souvent difficile à franchir et chacun, le plus souvent, préfère rester cantonné dans sa propre spécialité.

2.3 Cycle sismique, de trop rares données

Comme cela a déjà été mentionné auparavant, les données disponibles pour tester et calibrer les modèles de cycle sismique sont rares. Quelques pistes ont cependant été explorées, souvent de façon opportuniste, qui sont brièvement rappelées dans les paragraphes qui suivent.

2.3.1 Données instrumentales

Les données instrumentales disponibles sont très peu nombreuses. En effet, il existe extrêmement peu de failles pour lesquelles on dispose d'un jeu de données bien documenté décrivant plusieurs séismes successifs sur la même faille. De plus, même pour ce petit jeu de données, une partie importante correspond à des séismes qui se produisent en zone de subduction, où la déformation ne peut être mesurée que de façon indirecte. Les zones de Parkfield et d'Imperial Valley, le long de la faille de San Andréas, sont probablement les seules zones continentales pour lesquelles il existe des données sismologiques pour au moins deux séismes successifs. Nous rappelons ici brièvement l'observation clef que constitue la séquence sismique d'Impérial Valley, la séquence de Parkfield ayant déjà été décrite précédemment.

Le segment de faille d'Impérial Valley correspond à l'extrémité sud de la partie californienne de la faille de San Andréas, à la frontière mexicaine. Deux séismes se sont produits sur ce segment, en 1940 et en 1979, de magnitude respective 7,1 et 6,6, qui ont en partie rompu la même zone de faille. Ces deux séismes, accompagnés de ruptures de surface, ont été documentés rapidement après les séismes, ce qui permit de construire des courbes de glissement précises pour chacun des séismes. Ceci est en soit remarquable car ce n'est malheureusement qu'assez récemment que la communauté des sciences de la terre a pleinement réalisé l'importance de ce type de relevé. La figure 6 montre les deux distributions de glissements. Ce qu'il faut remarquer ici, au-delà de la différence de longueur des ruptures, c'est la similitude des distributions de glissement pour la partie commune aux deux ruptures.

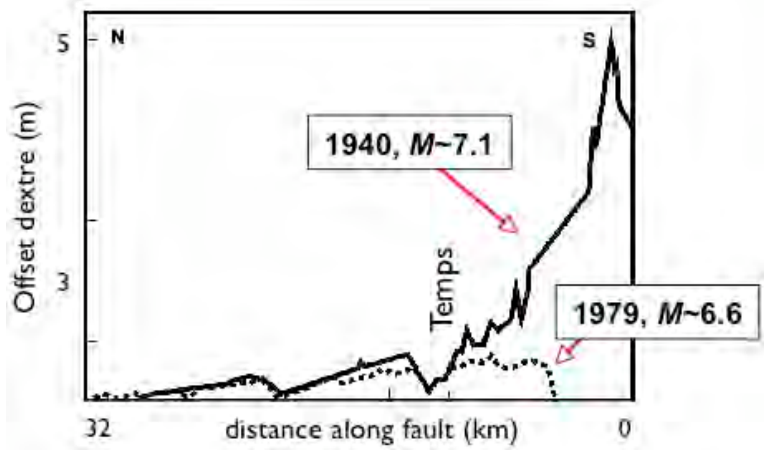

Figure 6 : distribution du déplacement en fonction de la distance le long de la faille pour les séismes de 1940 et 1979 le long d'Imperial Fault. Sur la section qui a rompu lors des deux séismes, la similitude des distributions de glissement est frappante. D'après [Ward, 1997]

De façon évidente, la partie nord de la faille, qui a rompu en 1940 et en 1979, a rompu exactement de la même façon les deux fois. Si l'on interprète cette observation à l'aune du modèle de glissement caractéristique (Fig. 7), on peut alors suggérer que cette partie de la faille est constituée de deux segments qui rompent ensemble de temps à autre. La partie nord ayant un glissement co-sismique plus faible, elle glisse aussi de façon additionnelle, indépendamment du segment sud, ce qui permet sur le long terme de combler le déficit de glissement de cette partie de la faille. La figure 7 montre une modélisation de ce comportement avec un catalogue de sismicité synthétique de 2000 ans qui reproduit ce schéma de fonctionnement [Ward, 1997].

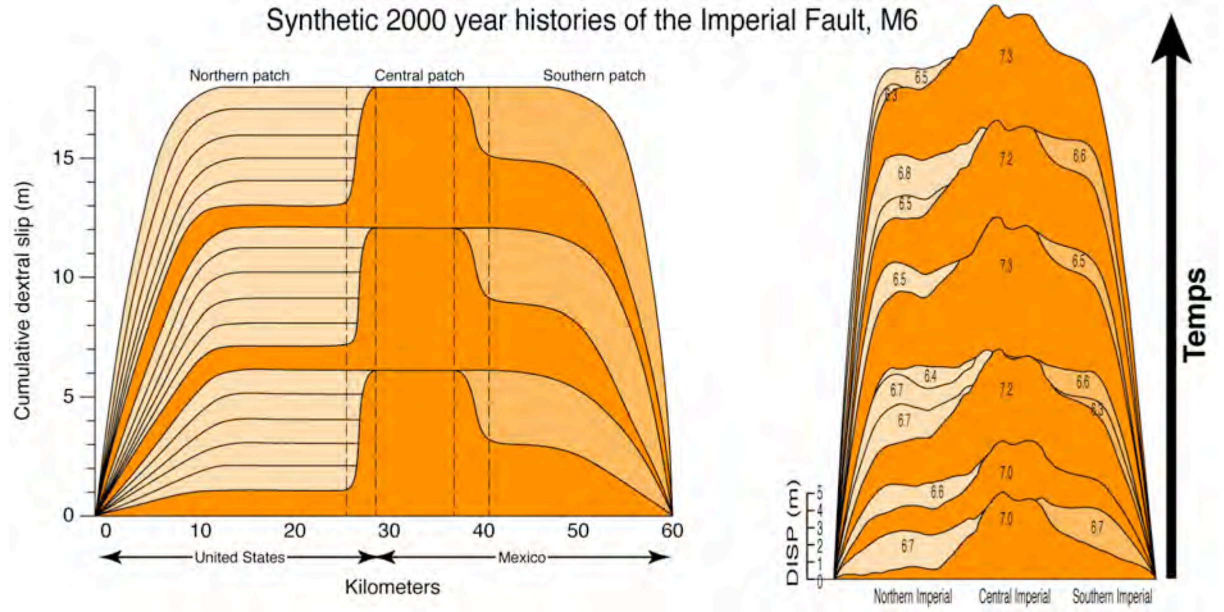

Figure 7 : schématisation de la séquence sismique d'Imperial Valley d'après [Sieh, 1996] et catalogue synthétique reproduisant les caractéristiques de cette séquence, d'après [Ward, 1997].

2.3.2 Données sismologiques historiques

Les données sismologiques historiques sont difficiles à utiliser pour plusieurs raisons.

D'une part, les régions du monde où l'on conserve des documents historiques assez anciens pour que cela soit compatible avec le temps de retour des séismes sont rares. L'exemple caricatural d'une telle difficulté est la Californie, pour laquelle les temps de retour des grands séismes sont évalués à ~250 à 300 ans, donc assez courts, mais pour laquelle on ne possède pas réellement de documents plus vieux que ~150ans. De façon intéressante, mais qui reste anecdotique, une corrélation a pu être établie entre des récits oraux d'amérindiens de la côte nord-ouest et l'occurrence de séismes dans la zone des Cascades (C. Goldfinger, com. pers.). Les zones les plus favorables pour ce qui est de l'exploitation des données historiques sont le bassin méditerranéen au sens large et une partie de l'Asie, notamment la Chine et le Japon.

D'autre part, la nature même de ces données complique leur interprétation. En effet, les textes historiques qui mentionnent des séismes ne le font quasiment jamais dans une perspective d'étude scientifique mais plutôt en décrivant les effets secondaires des séismes, qui touchent plus directement la vie quotidienne (nombre de victimes, destructions, trouble de l'ordre public...). Dans certains cas, les documents peuvent contenir des descriptifs détaillés de destructions qui permettent de reconstruire à posteriori des cartes d'isoséistes comme pour les séismes historiques en Turquie ou en Perse [Ambraseys and Finkel, 1987; Ambraseys*, et al.*, 1994]. Plus rarement, ils permettent d'identifier des ruptures co-sismiques comme dans le cas du séisme de Calabre en 1783 [Dolomieu, 1784]. Malheureusement, ce type de donnée reste souvent sujet à caution et de nombreux désaccords subsistent entre les différents auteurs sur la traduction et l'interprétation des textes anciens pour un même événement, limitant par là même leur utilisation.

Dans tous les cas, même si le bassin méditerranéen n'est pas équivalent à la côte ouest américaine, les possibilités de retour dans le temps restent limitées. La figure 8 montre les limites de l'exercice sur un exemple au Proche-Orient. Dans ce cas grâce aux nombreux textes historiques disponibles, qui couvrent environ 2000ans, nous avons pu compléter les données paléosismologiques que nous avions acquises dans le bassin de Yammoûneh pour associer de façon univoque les différents séismes historiques aux différentes failles. Les données historiques ont notamment été cruciales pour localiser le séisme d'AD551 sur les chevauchements localisés en mer, au large de Beyrouth [Elias*, et al.*, accepted]. Par contre, étant donné les temps de retour longs de ces séismes, ~1000ans sur la faille de Yammoûneh [Daëron*, et al.*, in-press], les données historiques ne permettent que très difficilement de remonter au delà de la dernière séquence sismique.

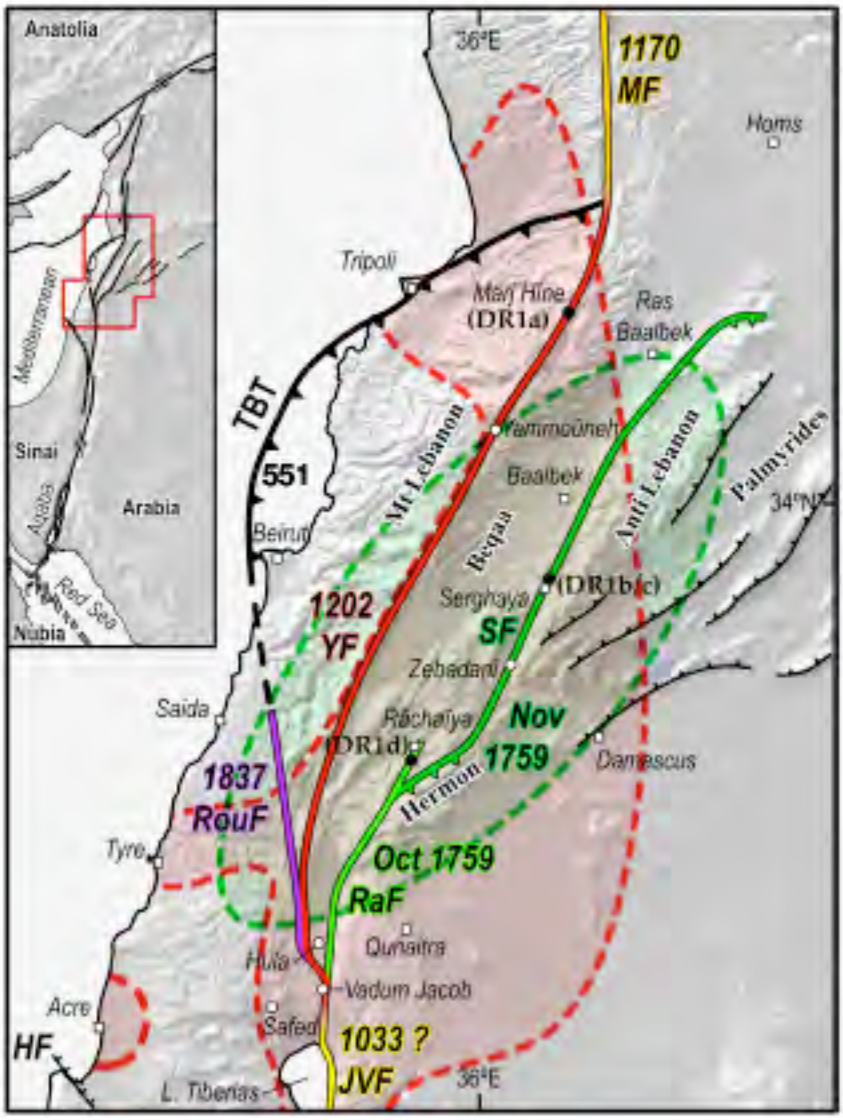

Figure 8 : sismicité historique de la faille du Levant au niveau du coude libanais. Un travail sur les textes historiques décrivant les dégâts occasionnés par les différents séismes, associé à des études géomorphologiques et paléosismologiques détaillées, permet d'assigner sans ambiguïté une faille source à chacun des grands séismes historiques connus dans la région. D'après [Daëron*, et al.*, 2005] et [Elias*, et al.*, accepted].

2.3.3 Données géomorphologiques et paléosismologiques

Dans certaines conditions, une observation fine des formes géologiques Quaternaires et des dépôts qui y sont associés permet de retrouver les cicatrices laissées par des séismes anciens. Utiliser ces indices pour établir la chronologie de ces séismes passés est probablement l'une des méthodes les plus efficaces à ce jour pour tester les différents modèles de cycle sismique car c'est la seule façon d'obtenir de relativement longues séries temporelles, avec dans quelques cas une estimation du déplacement associé à chaque événement. Ces études sont généralement regroupées sous le vocable de géomorphologie et paléosismologie. Laissant la paléosismologie proprement dite de coté, car elle est plus largement abordée dans la seconde partie de ce mémoire, je décrirai rapidement ci-dessous trois observations, une en domaine continental et deux en domaine marin mer, faites ces dernières années qui me semblent significatives, tant en regard de la technique, que de notre compréhension des processus liés au cycle sismique.

En domaine continental, le séisme de Superstition Hill (Mw6.6, 1987), Californie, est probablement l'un des premiers exemples où il a été possible d'établir un lien clair entre la dernière rupture co-sismique et des déplacements plus anciens (figure 9). Lors de la cartographie de la rupture faite sur le terrain, les observateurs ont remarqué que non seulement il était possible de mesurer le décalage horizontal dû au dernier séisme, mais qu'en plus il était possible de mesurer des décalages cumulés plus grands. En ordonnant l'ensemble des mesures, il est apparu que les valeurs de décalage cumulé correspondaient à des multiples de la valeur unitaire mesurée à l'occasion du dernier séisme [Lindvall*, et al.*, 1989], montrant que localement la dislocation co-sismique se répète d'un séisme à l'autre, comme cela est proposé dans le modèle de glissement caractéristique [Sieh, 1981, 1996]. Bien que ce type d'observation ne soit pas totalement unique [Klinger*, et al.*, 2000b; Kondo*, et al.*, 2005; Li*, et al.*, 2005], c'est la première fois que l'on dispose réellement d'une rupture « fraîche » permettant de calibrer l'ensemble des observations, avec un nombre d'observations important tant en ce qui concerne la dernière rupture que les ruptures passées..

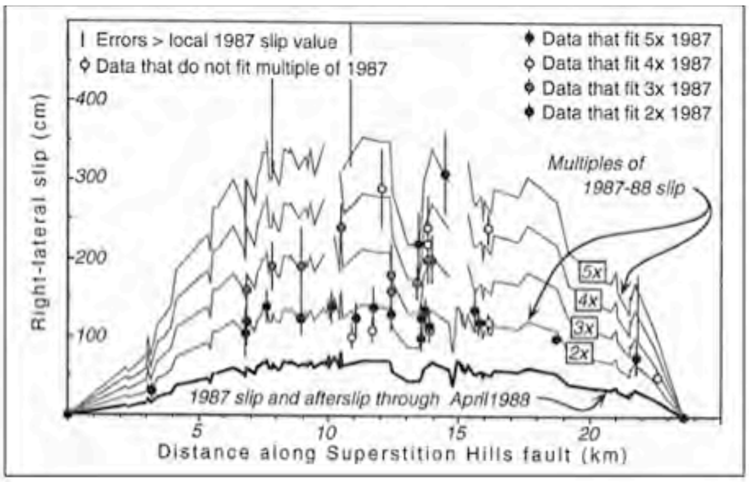

Figure 9 : mesures des déplacements dus au séisme de Superstition Hill, en 1987. La mesure de décalages cumulés montre que les séismes précédents avaient une distribution de glissement semblable au séisme de 1987. D'après [Lindvall*, et al.*, 1989]

En domaine marin, les zones de subduction sont intéressantes quand on s'intéresse au cycle sismique car les vitesses de glissement peuvent être très rapides (jusqu'à 8 cm/an) avec des temps de récurrence plus courts, permettant de fait d'avoir des séries temporelles de séisme plus longues. Par contre, les zones de subduction, du point de vue de la déformation co-sismique, sont particulièrement difficiles à étudier car une grande partie de la zone où se déroule la déformation se trouve sous l'eau. Autant l'utilisation de méthodes géodésiques (radar et GPS) permettent en partie de circonvenir ce problème pour ce qui est des séismes modernes, autant ce n'est pas le cas pour les séismes anciens. Deux zones ont été plus spécialement étudiées en ce qui concerne les séismes anciens, la zone des Cascades le long de la cote ouest américaine et la subduction de Sumatra, le long de l'arc indonésien.

L'idée que l'on puisse reconstruire l'histoire sismologique de la zone des Cascades n'est pas récente. Des 1987, [Atwater, 1987] identifient une première série de 6 paléoséismes à partir de l'empilement des paléosols visibles dans des carottages faits dans les estuaires de rivières côtières. En effet, chaque grand séisme de subduction provoque une subsidence de certaines zones côtières qui sont brutalement envahies par l'eau de mer, tuant du même coup toute la végétation. Si en plus un tsunami est associé au séisme, une couche de sable très caractéristique se dépose dans ces zones nouvellement submergées. Avec le temps, de nouveaux dépôts d'estuaires vont se déposer qui enfouiront la surface précédente et petit à petit une nouvelle plateforme côtière, émergée, se remettra en place avec un nouveau couvert végétal, jusqu'au séisme suivant. Plus récemment, pour prolonger cette série [Goldfinger*, et al.*, 2003] ont analysé des effondrements turbiditiques provoqués dans les canyons sous-marins de la côte lorsqu'un grand séisme se produit. A partir d'une centaine de carottes environs, il a été possible de montrer que dans la région des Cascades les dépôts turbiditiques majeurs étaient corrélés temporellement, et ce sur plus de 200km de côte, excluant de facto les tempêtes comme possible élément déclenchant pour les glissements sous-marin. Utilisant la signature sédimentaire de ces turbidites, ainsi que quelques points de repère temporels indépendants (datations ^{14}C), 18 séismes ont pu être identifiés pour les derniers ~10000 ans. L'analyse préliminaire de cette série temporelle montre que l'activité sismique semble structurée avec une variation du temps de retour entre deux séismes qui respecte une séquence (2 ou 3 événements séparés par un temps plutôt court, suivis d'un séisme avec un temps de retour beaucoup plus long) se répètant trois fois dans la série des séismes documentés (figure 10). En faisant une hypothèse sur la surface rompue par chaque séisme à partir des corrélations entre carottes puis sur le déplacement moyen à partir des lois d'échelles reliant la taille de la surface cassée au déplacement, C. Goldfinger a pu montrer qu'en première approximation cette série de séismes semblait respecter un modèle de type prédictible en temps (C. Goldfinfer, séminaire IPGP, 2006).

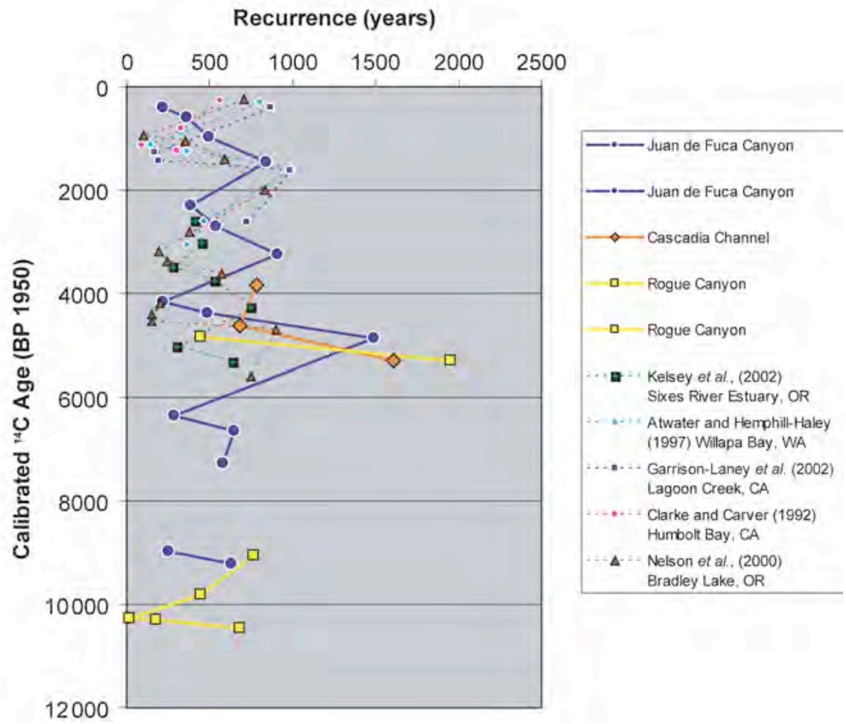

Figure 10 : évolution de la durée entre deux séismes successifs pour la série d'événements identifiés dans la zone de subduction des Cascades (lignes pleines). Les données en pointillée correspondent aux données recueillies à terre. Bien que les deux ensembles de données soient un peu décalés dans le temps, on identifie clairement une structure temporelle qui se répète. D'après [Goldfinger*, et al.*, 2003]

Un deuxième travail important concernant les séismes anciens en zone de subduction doit être mentionné ici, qui concerne la zone de subduction indonésienne. Dans ce cas, ce ne sont pas les dépôts turbiditiques qui ont été exploités, mais la croissance de massifs coralliens localisés sur la plaque chevauchante. En effet, certains types de coraux sont très sensibles à la profondeur et ne peuvent se développer que dans une épaisseur d'eau très précise. En utilisant cette particularité et le fait que les coraux croissent de façon concentrique, de la même façon qu'un arbre, il est donc possible de déterminer la variation du niveau de l'eau au cours du temps avec une grande précision. A condition de tenir compte des variations eustatiques d'origine climatique, les coraux enregistrent donc directement les épisodes successifs de submergence et d'émergence liés à l'activité de la subduction (Figure 11a).

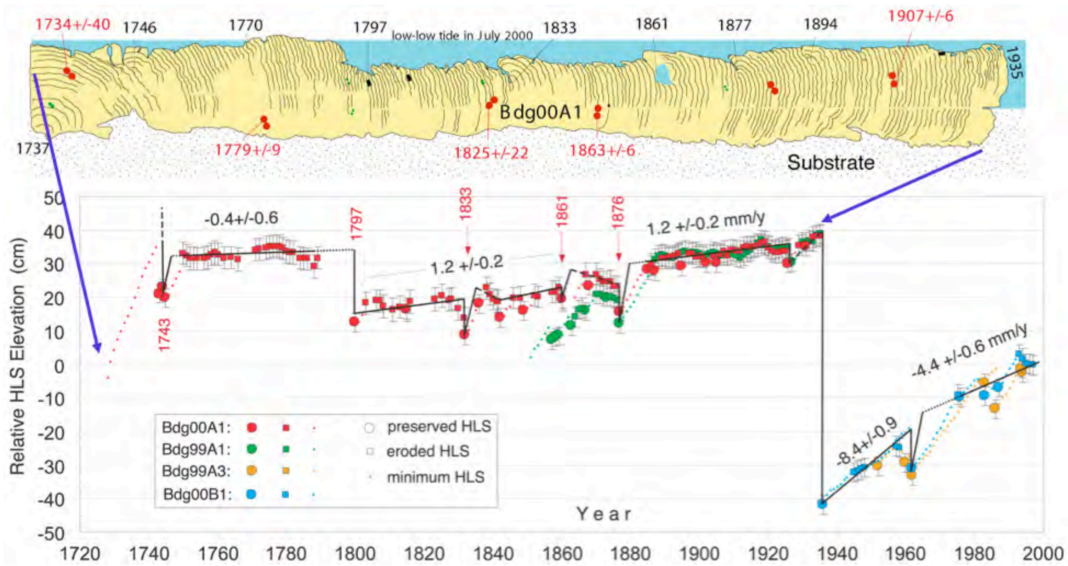

Figure 11a : la vignette du haut montre une tranche de corail. Les points rouges correspondent à des datations U/Th absolues qui sont utilisées pour caler le calendrier formé par les bandes concentriques annuelles du corail. Le corail ne pouvant se développer que dans une hauteur d'eau très spécifique, les variations de la géométrie du corail nous renseignent directement sur les hauteurs d'eau (vignette du bas), variation que l'on peut associer à l'activité de la subduction, une fois corrigée des variations d'eustatime. D'après (Sieh, séminaire IPGP 2005)

En échantillonnant de nombreux massifs coralliens le long de la côte, il a ainsi été possible de reconstruire l'histoire sismique des derniers siècles, montrant d'une part que certaines sections de la subduction pouvaient rompre lors de séismes importants très proches dans le temps et, d'autre part, que des glissements asismiques de grande amplitude se produisent sur certaines sections de la subduction. Par ailleurs, ces mesures montrent que le taux de déformation au niveau de la subduction est très variable dans le temps et peut s'écarter de façon considérable du taux moyen mesuré loin de la fosse [Natawidjaja*, et al.*, 2004; Natawidjaja*, et al.*, 2006]. De façon intéressante, de nouvelles données acquises au niveau de l'île de Pagai dans la zone sud de la subduction, celle qui a rompu en 1833, permettent de montrer que des séismes importants s'y seraient aussi produits en 1346 et 1592. En utilisant la quantité de déformation verticale associée à ces deux événements mesurée à partir des coraux et le temps écoulé entre les séismes, il semble que l'on puisse mettre en avant un comportement de type prédictible en temps, avec un temps de retour de l'ordre de 240ans (Fig. 11b).

Une telle observation, si elle est confirmée par les études en cours sur les massifs coralliens des îles voisines, serait primordiale. En effet, il serait alors tentant de rapprocher cette observation des observations faites pour la zone des Cascades, et aussi dans une moindre mesure dans les zones de subduction de Nankai (Japon) [Kumagai, 1996] et des Aléoutiennes (Russies) [Wyss and Wiemer, 1999], où les données recueillies semblent aussi compatibles avec un modèle prédictible en temps, et de s'interroger sur de possibles raisons mécaniques qui amèneraient les systèmes en subduction à suivre un tel comportement.

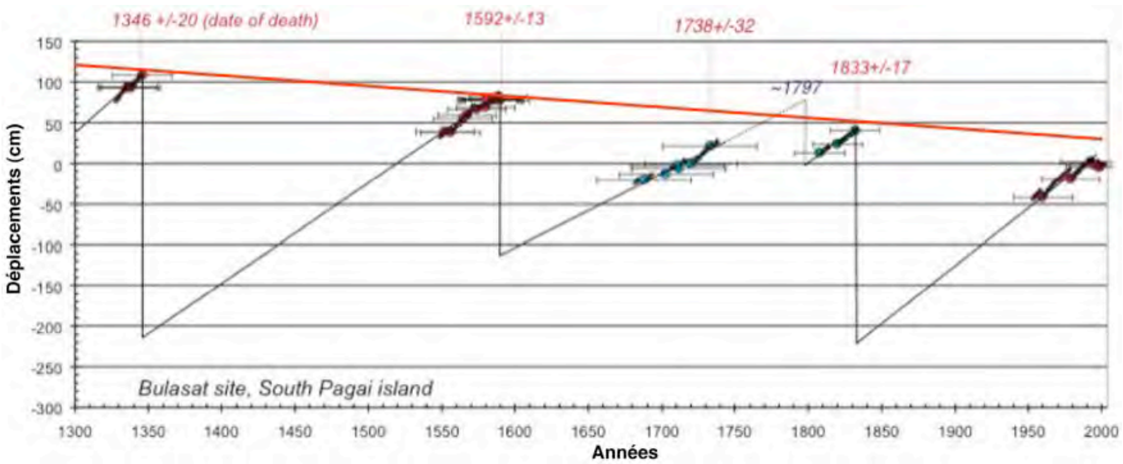

Figure 11b : Ensemble des données disponibles pour le site de Bulasaf sur l'île de Pagai, Indonésie. On voit très clairement les différents épisodes de surrection des massifs coralliens qui s'interrompent brutalement à chaque fois qu'un séisme se produit. On a l'impression de voir deux cycles de ~240ans. (D'après Sieh, séminaire IPGP 2005).

3 Résumé de quelques travaux personnels récents concernant la problématique du cycle sismique

Le rapide panorama brossé au fil des paragraphes précédents présente les différents modèles de cycle sismique qui ont été proposés au cours des dernières décennies, ainsi que quelques études marquantes en ce qui concerne l'acquisition de données pertinentes pour progresser dans ce domaine. Il montre surtout très largement les limites actuelles de l'exercice, du fait d'un manque flagrant de données. Une large partie de mon travail, au cours des 6 dernières années, a donc été tournée vers la collecte et l'analyse de ces données manquantes afin d'essayer de progresser dans la compréhension du cycle sismique. En marge de ce travail, j'ai bien sur continué à travailler sur des problèmes relatifs aux taux de glissement des failles à différentes échelles de temps, et dans différents contextes géologiques, mais cela n'est pas présent dans ce mémoire.

L'objectif principal, comme j'ai tenté de le montrer précédemment, c'est de pouvoir reconstruire des séries temporelles de séismes et, si possible, de quantifier la déformation qui est associée à chaque séisme. Il est évident que plus on cherche à remonter dans le temps, plus il est difficile de décrypter les informations géologiques. Pour essayer de palier à cette difficulté, il est essentiel, parallèlement à la quête des séismes anciens, de s'intéresser aux ruptures modernes. Parce que tout y est plus évident, que rien n'est encore estompé par le temps, ces ruptures constituent une sorte d'alphabet de la déformation co-sismique qui nous aide par la suite à déchiffrer les fragments de textes anciens que sont les séismes préhistoriques.

De nombreuses techniques peuvent permettre de quantifier les déformations co-sismiques pour des tremblements de terre modernes ou anciens. Je me suis personnellement investi plus spécifiquement dans l'utilisation de deux techniques, la paléosismologie et l'imagerie spatiale, avec lesquelles j'ai obtenu quelques résultats qui sont présentés dans les paragraphes qui suivent. Certains articles correspondant à ces résultats sont joints dans la dernière partie du mémoire. La présentation de mes travaux récents s'ordonne de la façon suivante : la première partie est consacrée à l'étude des paléoséismes, d'une part pour l'aspect série temporelle et d'autre part pour l'aspect déplacement par évènement. La seconde partie est consacrée à l'étude de divers aspects de la rupture co-sismique moderne, notamment en utilisant de nouveaux outils d'imagerie spatiale, dans le cas du séisme en décrochement de Kokoxili, de magnitude 7.8.

L'ensemble de ces travaux concerne des zones géographiques assez variées. Sans nier que cela soit dû en partie au contexte professionnel dans lequel je me trouvais au moment où ces études ont été réalisées, cela souligne aussi l'importance qu'il y a à aller chercher les données pertinentes où qu'elles se trouvent, pour pouvoir réellement s'atteler à l'étude des processus physiques mis en jeu, au-delà du cadre ponctuel d'une étude particulière.

3.1 Séismes anciens

La paléosismologie s'intéresse à la recherche des séismes préhistoriques. Cette discipline a commencé à se développer au cours des années 70.

En utilisant le principe de la diffusion des particules sur une pente comme processus d'érosion, il a été possible d'estimer l'âge d'escarpements sismiques préhistoriques [Wallace, 1977]. La précision des âges obtenus reste cependant limitée et la technique devient difficile à mettre en oeuvre quand les escarpements ne représentent non plus un seul événement, mais la déformation cumulée due à de nombreux séismes.

C'est aussi à cette période que furent réalisés les premiers travaux importants de tranchées qui permirent un regard nouveau sur l'activité sismique au cours du temps, grâce à l'allongement des catalogues de sismicité [Sieh, 1978a; Schwartz and Coppersmith, 1984]. Les progrès réalisés en matière de datation du ^{14}C au cours des années 90, qui nous permettent de dater des échantillons toujours plus petits, notamment grâce aux mesures en accélérateur, ont permis un développement récent important des études paléosismologiques en augmentant considérablement le champ des investigations possibles.

Les travaux sur les séismes anciens présentés ici s'appuient essentiellement sur l'étude de tranchées creusées en travers et parallèlement à la faille, afin de cartographier les perturbations des dépôts sédimentaires dues aux ruptures sismiques. Le principe, très simple, est illustré par la figure 12. La difficulté majeure de mise en oeuvre de cette technique réside dans le choix d'un site favorable. En effet tout repose sur un enregistrement sédimentaire le plus complet possible, avec une granulométrie adaptée, qui permette d'identifier les ruptures successives. C'est souvent au choix pertinent du site que l'on reconnaît un bon trancheur. Une autre difficulté, sur laquelle l'opérateur a moins de prise, est la possibilité, ou non, de dater les dépôts mis à jour dans la tranchée. La méthode de datations utilisant le ^{14}C étant la méthode principale utilisée, le potentiel de datation est très dépendant de la quantité de débris organiques que l'on peut trouver dans la tranchée. Les différentes études présentées ci-dessous illustrent ces difficultés.

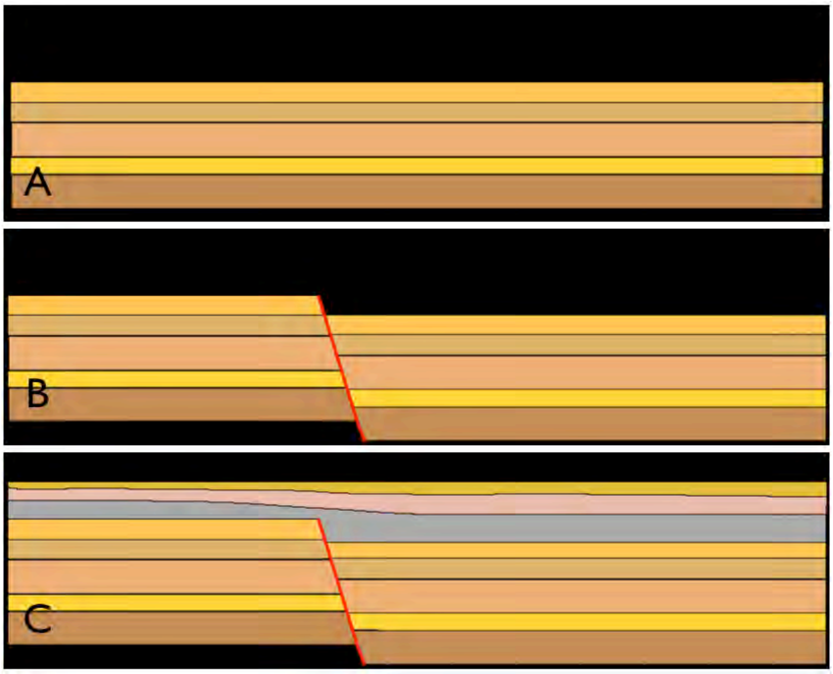

Figure 12 : principe de base de paléosismologie. A) Les unités sédimentaires se déposent à plat, formant une série de couches parallèles. B) Une rupture sismique se produit et décale verticalement un compartiment par rapport à l'autre. C) Les sédiments continuent à se déposer, comblant d'abord l'espace supplémentaire crée puis revenant progressivement à des dépôts complètement plats. Si plusieurs séismes se produisent, la même séquence va se répéter, les unités anciennes présentant un décalage cumulé de plus en plus important.

3.1.1 Séries temporelles

Les deux études résumées ici ont comme objectif commun d'établir des séries temporelles pour des grandes failles décrochantes continentales. La première étude concerne la faille d'Haiyuan, en Chine, et la seconde la faille de Yammouneh, au Liban.

3.1.1.1 Paléosismicité de la faille de Haiyuan, Chine

La faille d'Haiyuan est l'une des grandes failles décrochantes senestres qui participent à l'extrusion du Tibet vers l'Est. La vitesse de glissement estimée sur la faille varie de 4 à 12 mm/an suivant les auteurs, avec un décalage cumulé estimé entre 20 et 100km. La faille d'Haiyuan, qui passe à environ 150km des villes de Lanzouh et Xining (toutes deux dépassent le million d'habitants, avec de nombreux immeubles élevés), a connu deux séismes importants au cours des derniers 100 ans. Un premier séisme de magnitude M~8.5 a rompu l'est de la faille en 1920. Un deuxième séisme a rompu une autre partie du système de faille en 1927, beaucoup plus à l'Ouest, lors d'un séisme de magnitude M~8. Entre les deux se trouve une section de la faille d'environ 200km, une lacune, pour laquelle on ne connaît pas de rupture historique. Au-delà de l'aspect purement fondamental, l'enjeu pour l'évaluation du risque sismique est donc important, la région étant fortement peuplée.

La région est en grande partie couverte d'épaisses unités de lœss largement dépourvues de stratigraphie. Notre choix pour le site de tranchée s'est porté sur un petit bassin en pull-apart, dans lequel les traces de la faille sont bien visibles, et pour lequel on pouvait espérer une stratigraphie correcte du fait du réseau de drainage aboutissant dans le bassin. Cela s'est effectivement vérifié dans les deux tranchées creusée. Dans la tranchée sud, la plus éloignée du front montagneux, les dépôts sont majoritairement loessiques. Cependant, une alternance bien marquée de couleurs, due au degré de formation du sol lors du dépôt de chaque nouvel horizon, permet d'avoir une description stratigraphique détaillée des murs de chaque tranchée. Les déformations co-sismiques y sont bien visibles (figure 13). La deuxième tranchée, au nord, à la base du relief, est caractérisée par des alternances de dépôts silteux et de dépôts comprenant des galets. A titre illustratif, il est intéressant de noter qu'une autre tranchée ouverte à quelques kilomètres de là, dans un contexte de dépôt moins favorable, ne nous a même pas permis de localiser la faille en coupe, du fait de l'homogénéité absolue des sédiments de loess, alors que son expression en surface était toute aussi claire.

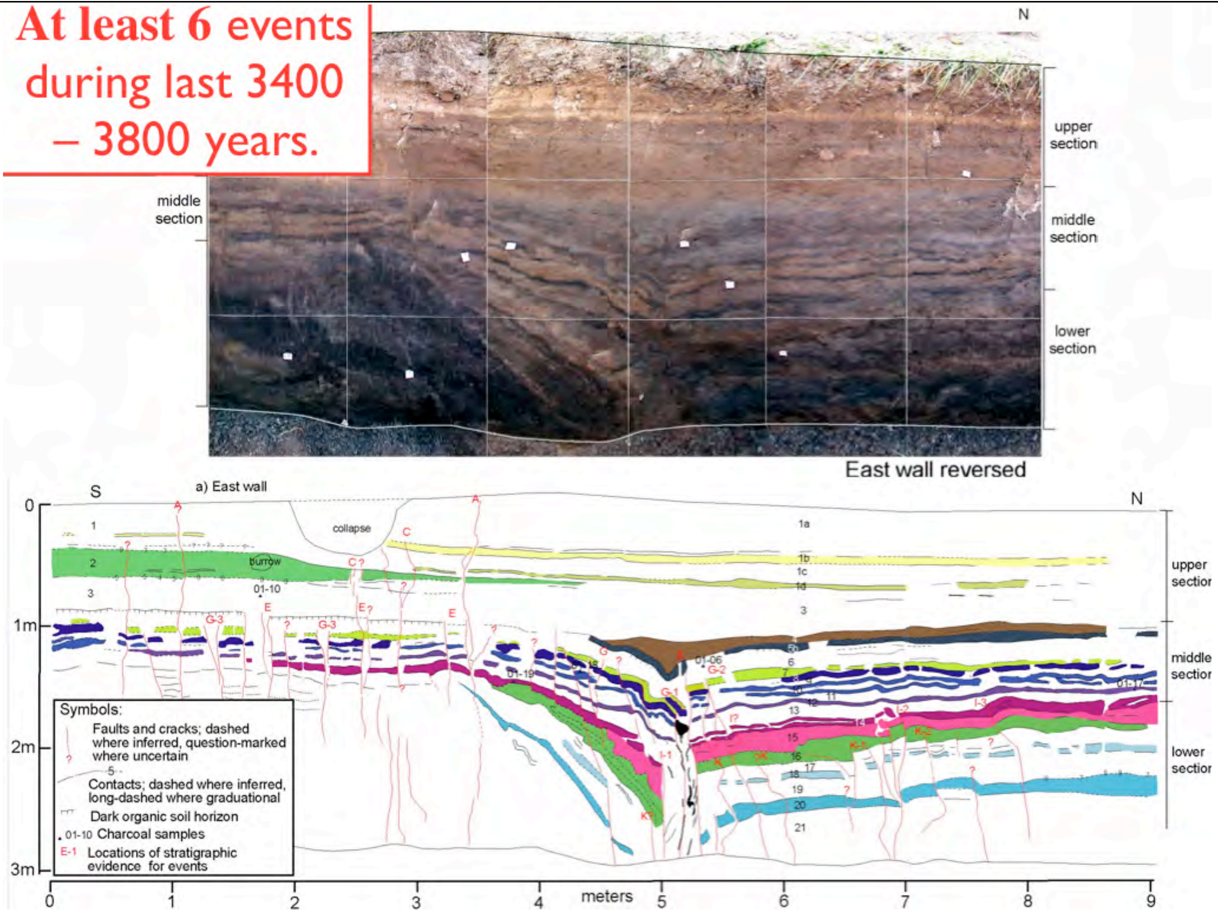

Figure 13 : tranchée d'Haiyuan. La vignette du haut montre une mosaïque photo d'un des murs de la tranchée. Les différentes unités sont bien visibles. La vignette du bas montre le log interprété associé à ce mur, qui permet de séparer les différents événements. D'après [Liu-Zeng, *et al.*, 2007]

Ces tranchées nous ont permis d'identifier 6 paléoséismes dont 4, au vue des déformations verticales visibles dans les tranchées, semblent avoir été des événements de forte magnitude. Les deux autres se manifestent uniquement par de petites fissures et doivent avoir été des séismes de magnitude faible à modérée. C'est notamment le cas du séisme le plus récent. Nous pensons que nous voyons dans la tranchée le séisme de magnitude Mw5.8 qui s'est produit en 1990. Cela n'est possible que parce que notre tranchée est localisée quasiment à l'épicentre, d'après les données instrumentales, et donne une idée assez précise du niveau de détection, M~6, que l'on peut espérer des études paléosismologiques.

La matière organique est abondante dans la région et les drainages qui aboutissent dans le bassin sont très courts. Cela a permis de dater 13 échantillons de ^{14}C sans rencontrer de difficulté majeure liée à des échantillons anormalement vieux, du fait de transports multiples. On a pu ainsi montrer que les 6 événements se sont produits en 3500ans à 3900ans. Si l'on laisse de coté les deux séismes les plus récents qui semblent clairement plus petits que les 4 autres, cela nous conduit à un temps de récurrence de ~1000 ans. Naturellement, nous ne pouvons pas exclure que d'autres séismes du type 1990 se soient produits entre temps, que nous n'aurions pas identifié dans nos tranchées car masqués par des séismes postérieurs plus importants. Cependant leur impact dans le bilan de déformation resterait faible et n'affecte donc pas grandement la vision générale que l'on peut avoir de la façon dont la déformation est accommodée le long de la faille d'Haiyuan. La chronologie des séismes établie dans cette étude indique que pour ce qui est des séismes majeurs, le dernier séisme sur cette section de la faille correspond au séisme historique de AD 1092. Le taux de récurrence étant de ~1000ans, il est donc très probable que cette section de la faille soit proche de la rupture.

3.1.1.2 Paléosismicité de la faille de Yammouneh, Liban

La faille de Yammouneh est l'une des branches de la faille du Levant, au niveau du coude transpressif libanais. La faille du Levant, longue d'environ 1200km, est une faille décrochante senestre, qui accommode le mouvement différentiel entre la plaque Arabie, à l'est, et une petite plaque aux limites mal identifiées, la plaque Sinaï, à l'ouest. La vitesse de glissement est estimée entre 5mm/an et 7mm/an. Cette faille, qui connecte la zone extensive de la mer Rouge, au sud, à la zone décrochante compressive du Taurus, au nord, est globalement orientée N-S. Cependant, au niveau du Liban, sur environ 150km, la faille fait un coude significatif vers l'est, de ~20°, transformant une partie du mouvement horizontal en déformation verticale, à l'origine des monts Liban et Antiliban. Il apparaît que la déformation est bien partitionnée entre mouvement vertical, essentiellement accommodé par des chevauchements localisés off-shore Liban, et mouvement horizontal, accommodé par deux failles, la faille principale de Yammouneh, et une faille secondaire, la faille de Serghaya (figure 14). Toute cette région est densément peuplée, les villes de Beyrouth et Damas se trouvant à moins de 50km des structures majeures. Encore une fois, il y a donc ici un enjeu humain important qui se superpose aux enjeux de recherche fondamentale.

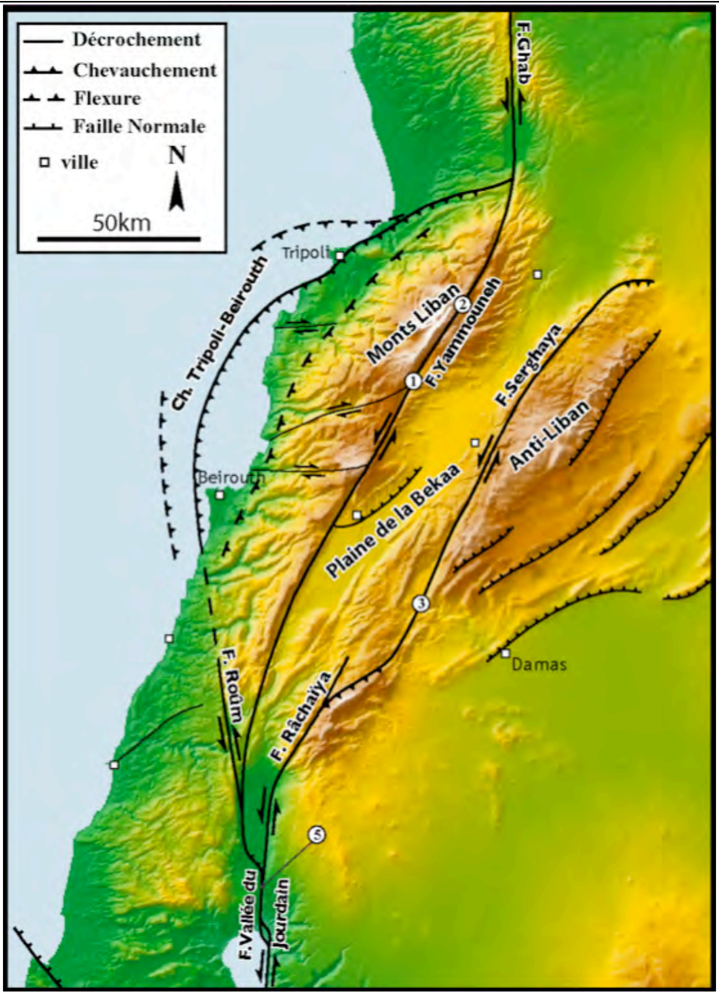

Figure 14 : carte des structures actives au niveau du coude libanais de la faille du Levant. Le site de Yammouneh est indiqué par le numéro 1. D'après [Daëron*, et al.*, 2004]

Le Liban, comme une large partie du bassin méditerranéen, peut s'enorgueillir d'une histoire particulièrement longue et riche, qui constitue une mine de renseignements en ce qui concerne l'histoire des séismes anciens. Pour la zone libanaise, plusieurs séismes très importants sont rapportés dans les écrits historiques, en 551 AD, en 1202 AD et en novembre 1759. Ces séismes ont provoqué des destructions majeures et ont été ressentis dans une large part du bassin est méditerranéen. Cependant, jusqu'aux travaux présentés ici, il avait été impossible d'assigner clairement ces séismes à des structures spécifiques, les descriptions n'étant pas assez précises. Tout au plus, les descriptions du séisme de 551 AD laissaient pressentir que ce séisme avait été plutôt côtier, ce qui a depuis été confirmé dans le cadre des travaux de thèse d'A. Elias (IPGP, 2006). Le travail sur la faille de Yammouneh visait donc d'une part à identifier la faille responsable de chaque événement, et si possible, à construire une série temporelle longue pour pouvoir dire quelque chose sur le temps de retour des séismes sur la faille de Yammouneh.

Le site retenu est situé dans un ancien lac asséché en 1930. Le site du lac correspond en fait à un ancien bassin en pull-apart qui est maintenant court-circuité par la faille qui le traverse en diagonale. La faille recoupe une série composée de sédiments lacustres finement laminés qui fournissent un enregistrement sédimentaire d'une qualité exceptionnelle (figure 15a). Par ailleurs, l'environnement s'est avéré particulièrement favorable en ce qui concerne le stockage de débris organiques, permettant des datations ^{14}C nombreuses et de qualité.

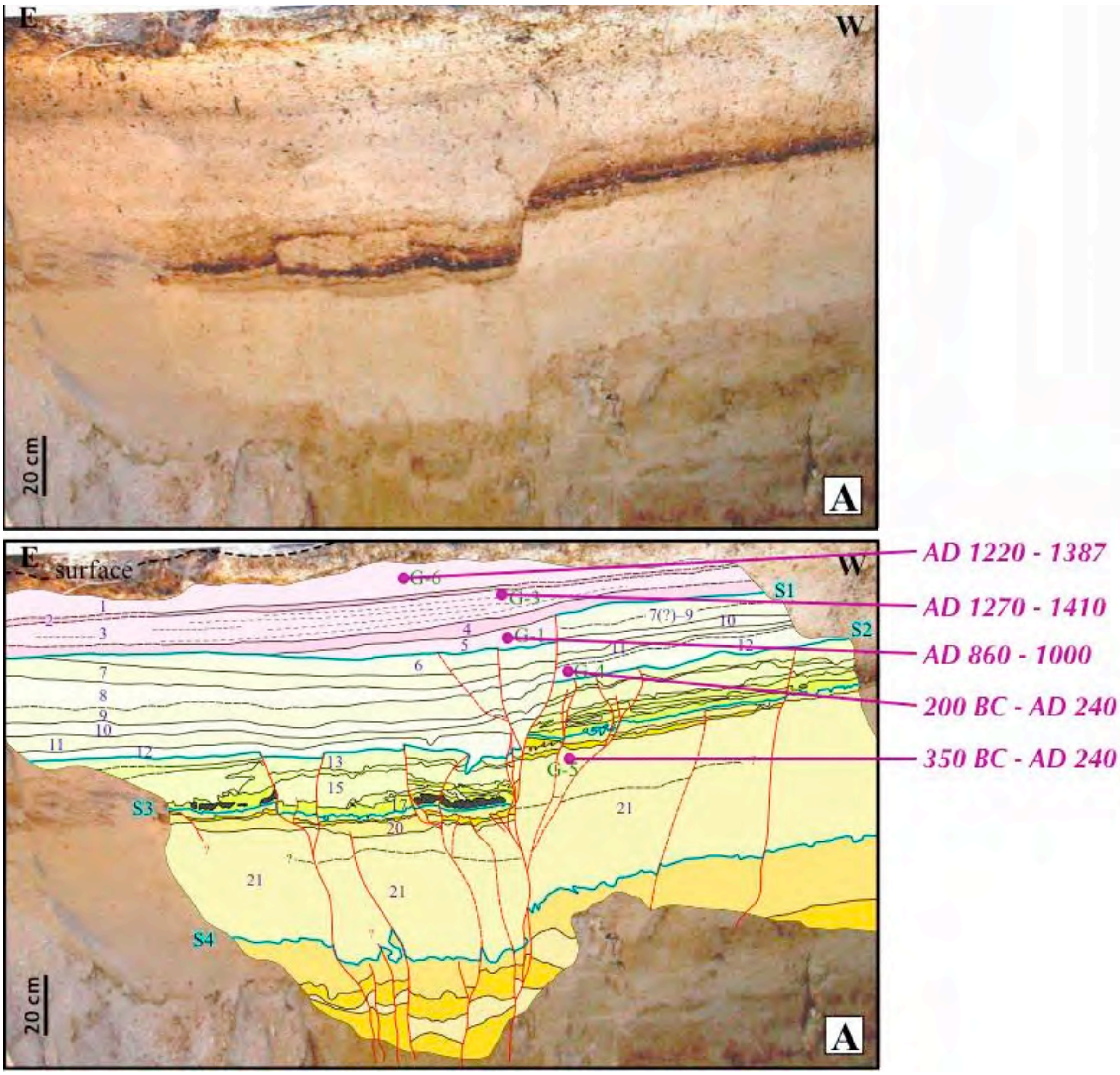

Figure 15a : tranchée dans le bassin de Yammouneh. La tranchée est creusée dans le fond d'un ancien lac asséché, mettant à jour une stratigraphie très détaillée qui permet de bien différencier les événements succéssifs. L'abondance des carbones permet d'avoir une bonne contrainte d'age pour un certain nombre des événements identifiés. D'après [Daëron, *et al.*, 2005]

Une cartographie précise de plusieurs murs dans plusieurs tranchées nous a permis de constater que l'ensemble de la déformation co-sismique récente se concentre dans une bande de ~2m de large. Au-delà les unités sédimentaires sont déposées de façon parfaitement horizontale ou très légèrement pentées à proximité de la zone de faille. La succession rapide des unités sédimentaires caractérisées par de petites variations de couleur permet de déterminer avec précision où se propagent et s'arrêtent les différents cracks qui correspondent aux séismes successifs. Au final, il nous a été possible d'identifier 10 à 14 séismes (une incertitude sur quelques séismes explique cette fourchette), dont 7 événements avec une contrainte d'age acceptable, sur un laps de temps total de 12000ans (Figure 15b). L'ampleur des déformations de surface visible dans les tranchées, si on les compare aux déformations de surface pour des séismes contemporains, indique que ces séismes sont des séismes de forte magnitude, M ≥ 7.

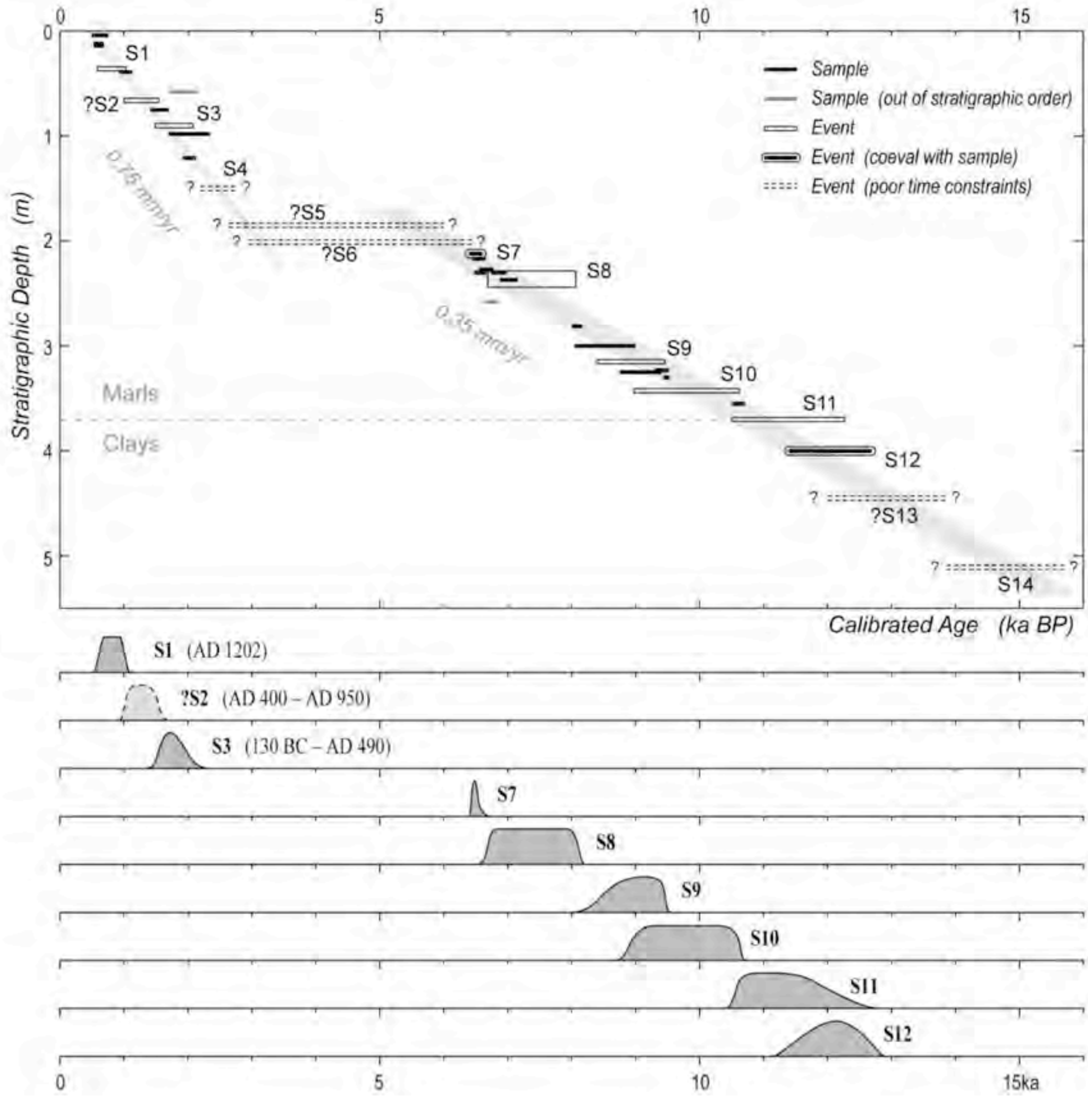

Figure 15b : Récapitulatif des séismes historiques identifiés dans les tranchées paléosismologiques du bassin de Yammoûneh. Les événements sont représentés différemment selon le degré de confiance que l'on attribue à l'existence du séisme. Les échantillons utilisés pour la datation sont aussi indiqués, indiquant le niveau de contrainte temporelle pour chaque séisme. Les vitesses indiquées correspondent au taux de sédimentation, qui n'est pas constant à l'échelle de 15 ka. Le diagramme du bas, qui représente juste la distribution temporelle des séismes, montre le peu de variation du temps de retour entre deux événements. D'après [Daëron, *et al.*, in-press].

Nous avons pu établir sans ambiguïté que le dernier séisme qui s'est produit sur la faille de Yammouneh est le séisme de 1202, ce qui, *de facto*, localise le séisme de novembre 1759 sur la faille de Serghaya. Par ailleurs, en se fondant sur quelques documents historiques, il est aussi possible d'associer le pénultième séisme sur la faille de Yammouneh avec le séisme historique de 350 AD. Enfin, en utilisant l'information temporelle sur l'ensemble de la série documentée, il semble possible de proposer un temps de retour pour les séismes de la faille de Yammouneh de l'ordre de 1000ans. Le dernier séisme sur la faille de Yammouneh ayant eu lieu en 1202, la faille de Yammouneh n'est donc probablement plus très loin de son seuil de rupture. L'intégration de l'ensemble des données paléosismologiques le long de la faille du Levant pourrait apporter un élément supplémentaire dans ce sens, bien que plus spéculatif. En effet, si l'on considère les grands séismes sur la faille du Levant, il semble que l'ensemble de la faille rompe dans un laps de temps assez court, de un à deux siècles, encadré par des périodes de quiescence sismique de l'ordre du millénaire. Le dernier épisode sismique ayant mobilisé l'ensemble de la faille du Levant serait donc autour du XI^{ème} – XII^{ème} siècle, avec notamment le séisme de 1202 en fin de séquence, il y a presque 1000ans. Dans ce contexte, le séisme de magnitude 7.3 qui s'est produit dans le Golfe d'Aqaba en 1995, à l'extrémité sud de la faille du Levant, pourrait être le signe d'une prochaine reprise de l'activité sismique le long de cette faille au cours des un à deux siècles à venir.

3.1.2 Déplacement co-sismique pour les paléoséismes

Contrairement aux deux études présentées ci-dessus, où l'objectif principal était clairement de déterminer quand avait eu lieu le dernier séisme sur ces failles et ce que l'on pouvait dire sur la série temporelle, les deux études présentées dans les paragraphes qui suivent ont pour but principal de comparer le glissement co-sismique, en un endroit donné, pour des séismes successifs.

3.1.2.1 La faille Nord Anatolienne et le séisme d'Izmit, Turquie

En 1999 se sont produits coup sur coup, en Août puis en Novembre, deux séismes de magnitude supérieure à 7 dans la région d'Izmit, à proximité d'Istanbul. Ces séismes ont rompu deux sections voisines de la faille Nord Anatolienne. Cette structure, bien identifiée, accommode le déplacement de la micro-plaque Anatolie vers l'Ouest par rapport à l'Eurasie fixe. Suivant les méthodes et les échelles de temps considérées, la vitesse de glissement estimée varie entre 18 mm/an et 24 mm/an. La faille Nord Anatolienne, du point de vue sismotectonique, présente une particularité remarquable du fait qu'elle a rompu sur presque l'entièreté de sa longueur, soit environ 1000km, au cours des derniers 100ans. De la même façon, bien que les dates soient un peu moins certaines, il semblerait que la faille Nord Anatolienne ait déjà rompu entièrement en l'espace d'une centaine d'année au cours du

XVIIIème siècle. Cette faille serait donc l'archétype de la faille décrochante qui rompt par saccades, séparées par des périodes sans activité sismique notable.

De notre point de vue, le séisme d'Izmit nous donnait l'opportunité de pouvoir ouvrir une tranchée paléosismologique tout en connaissant la déformation due au dernier événement sismique, que l'on peut du coup utiliser comme calibration. Nous avons donc sélectionné un site le long de la rupture de 1999, au niveau du segment de Gölcük. Ce segment est orienté un peu différemment du reste de la rupture, ce qui se traduit localement par une déformation quasi-purement verticale avec une très faible composante en décrochement. Au niveau du site choisi, le rejet vertical co-sismique associé au séisme de 1999 est de 1.6m. La topographie indique clairement qu'un escarpement cumulé existait déjà avant 1999, dont la hauteur avoisine au minimum les 4m, qui atteste de l'activité sismique de ce site au moins sur quelques cycles sismiques.

Deux tranchées ont été ouvertes en travers de l'escarpement vertical. Dans les deux cas, elles montrent une déformation très localisée sur une zone de faille large de 10cm à 20cm, avec un pendage de ~70° vers le NE. Les unités stratigraphiques sont bien différenciées, avec des unités de graviers et de sables plus ou moins grossiers alternant pour former un environnement typique de cône alluvial avec des faciès alluviaux (figure 16). Les mêmes unités sédimentaires ne se retrouvent pas de part et d'autre de la zone de faille, indiquant que le rejet cumulé réel est considérable, et dans tous les cas est supérieur à 4m. Le milieu est riche en matière organique et 16 échantillons ont été datés au ^{14}C.

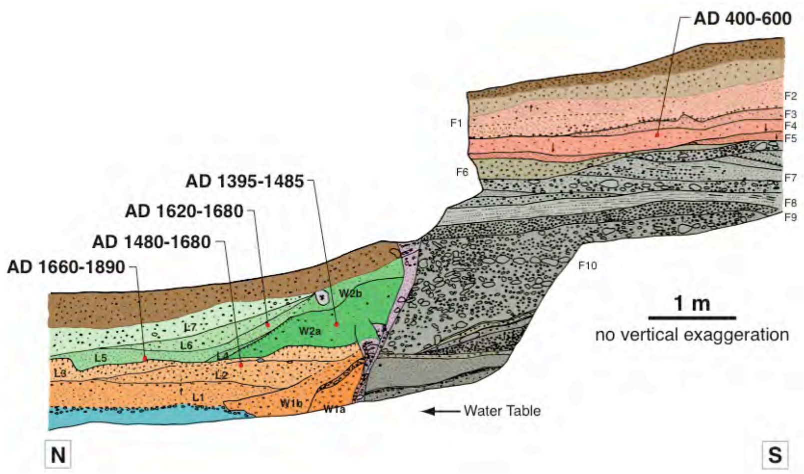

Figure 16 : trenchlog de la tranchée faite en travers de l'escarpement co-sismique associé au séisme de 1999. La superposition de séries typiquement fluviales, intercroisées avec des sédiments plus fins, permet d'identifier deux wedges colluviaux caractéristiques de séismes anciens. D'après [Klinger, *et al.*, 2003b]

L'observation principale dans ces tranchées est l'existence de deux coins formés par des colluvions (par la suite appelés « wedges »), témoins de ruptures anciennes. Ces wedges apparaissent clairement en carte (figure 16), avec des limites définies par un changement brutal de faciès traduisant bien leur mode de mise en place, qui débute par des effondrements au pied de l'escarpement, juste après le séisme. Dans un modèle de formation de wedge, une fois cette première phase rapide d'effondrement partielle de l'escarpement due à la gravité finie, une phase plus longue de diffusion des sédiments le long de la pente de l'escarpement va se mettre en place, lissant l'escarpement (figure 17). En utilisant ce modèle, extrêmement simpliste naturellement, qui reproduit les observations au premier ordre, on peut alors faire une hypothèse sur la taille totale de la dislocation co-sismique en ne mesurant que la partie inférieure du wedge, qui est enfouie au fur et à mesure que les séismes se répètent. Dans le cas de nos tranchées à Gölcük, chacun des deux wedges, si on les prolonge jusqu'à la faille, fait ~80cm de coté, ce qui d'après notre modèle correspond à un rejet vertical de ~1.6m, tout à fait comparable au rejet vertical du séisme de 1999.

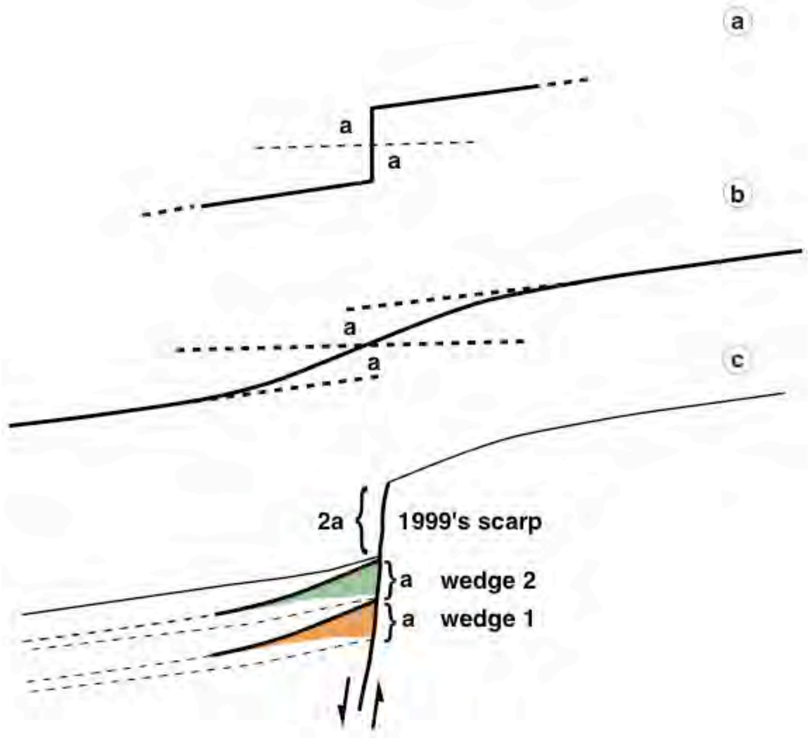

Figure 17 : schéma de formation des wedges colluviaux observés en Turquie. A) Formation de l'escarpement co-sismique. B) Après une phase courte d'éboulement gravitaire de l'escarpement, les processus de diffusions vont lisser l'escarpement. C) En renouvelant ce processus trois fois, on se retrouve dans la configuration observée en Turquie. D'après [Klinger, *et al.*, 2003b]

Dans le cas du séisme d'Izmit, tout au moins sur le segment de Gölcük, on peut donc mettre en évidence trois séismes consécutifs qui présentent un rejet co-sismique, vertical dans ce cas, quasi-identique. Cette observation vient s'ajouter au corpus de données qui appuie le modèle de glissement caractéristique dans le cadre des failles décrochantes. Par ailleurs, à partir des datations obtenues, on peut très probablement associer les deux paléoséismes identifiés aux deux séismes documentés historiquement que sont les séismes de 1509 et 1719. Cette corrélation semble en bon accord avec les autres données paléosismologiques disponibles le long des segments ouest de la faille Nord Anatolienne. Dans ce cas, le temps de retour pour ces deux séismes serait respectivement de 210ans et 280ans, des durées quasi-identiques, aux barres d'erreur près, ce qui ferait de la faille Nord Anatolienne une faille très régulière, du moins au cours des derniers cycles sismiques.

3.1.2.2 Glissement caractéristique sur la faille de San Andreas, Californie

La faille de San Andreas (SAF) est probablement l'une des failles décrochantes les plus étudiées au monde. Elle marque la bordure ouest de la plaque Amérique. Bien que sa vitesse fasse l'objet de quelques discussions, d'une manière générale la communauté scientifique s'accorde sur une vitesse de décrochement dextre de ~34mm/an, en accord avec les mesures géodésiques instantanées et avec les mesures morphologiques qui couvrent quelques milliers d'années. Dans sa partie centrale, comprise entre le Big Bend juste au nord de Los Angeles et la partie en fluage à Parkfield, la SAF présente une géométrie particulièrement simple. Elle est constituée de segments très linéaires séparés par quelques relais qui se traduisent le plus souvent par de petits bassins en pull-apart. Par ailleurs, le long de cette section, contrairement à la partie sud de la SAF, il n'existe pas d'autres failles importantes, parallèles à la SAF, pour compliquer les séquences sismiques, du fait d'interactions encore mal comprises entre les différents segments.

Le site choisi est caractérisé par un segment de faille unique et très linéaire (figure 18). Celui-ci est traversé par une série de rivières qui sont en eau de façon éphémère, lors des grosses précipitations qui se produisent quelques fois par décennie. A cette occasion, il arrive que ces rivières se transforment en torrents de boue très violents, capables d'incision et/ou de dépôts importants et rapides. Un des intérêt du site choisi est d'être fortement asymétrique par rapport à la faille ; la surface située à l'est de la faille (appelée partie amont par la suite) est soulevée et concentre l'eau ruisselant en surface dans de petits réseaux drainants très incisés qui débouchent au niveau de l'escarpement de faille. Au niveau de l'escarpement de faille, suivant le régime de la rivière et sa capacité de transport des sédiments, soit un petit cône alluvial se met en place, situation peu intéressante pour nous, soit la rivière est capable de continuer à inciser son lit dans la surface localisée à l'ouest de la faille (appelée partie avale par la suite). L'idée exploitée dans cette étude est que lors de séismes décrochants de forte magnitude, le décalage horizontal co-sismique est suffisamment important pour déconnecter la partie amont de la partie avale du chenal. A partir de ce moment, l'alimentation en eau des chenaux étant concentrée dans quelques drainages distants de plusieurs dizaines de mètres (fig. site), la partie avale du chenal devient complètement passive et finie par être comblée en surface par les sédiments fins transportés par le lessivage de surface ou le vent. En face de la partie amont, d'où débouche le chenal actif, un nouveau chenal sera incisé lors de la précipitation importante suivante. Comme cela est bien visible sur la figure 18, un tel mécanisme permet de mettre en place, puis de préserver, toute une série de chenaux qui sont successivement abandonnés au fur et à mesure du fonctionnement de la faille.

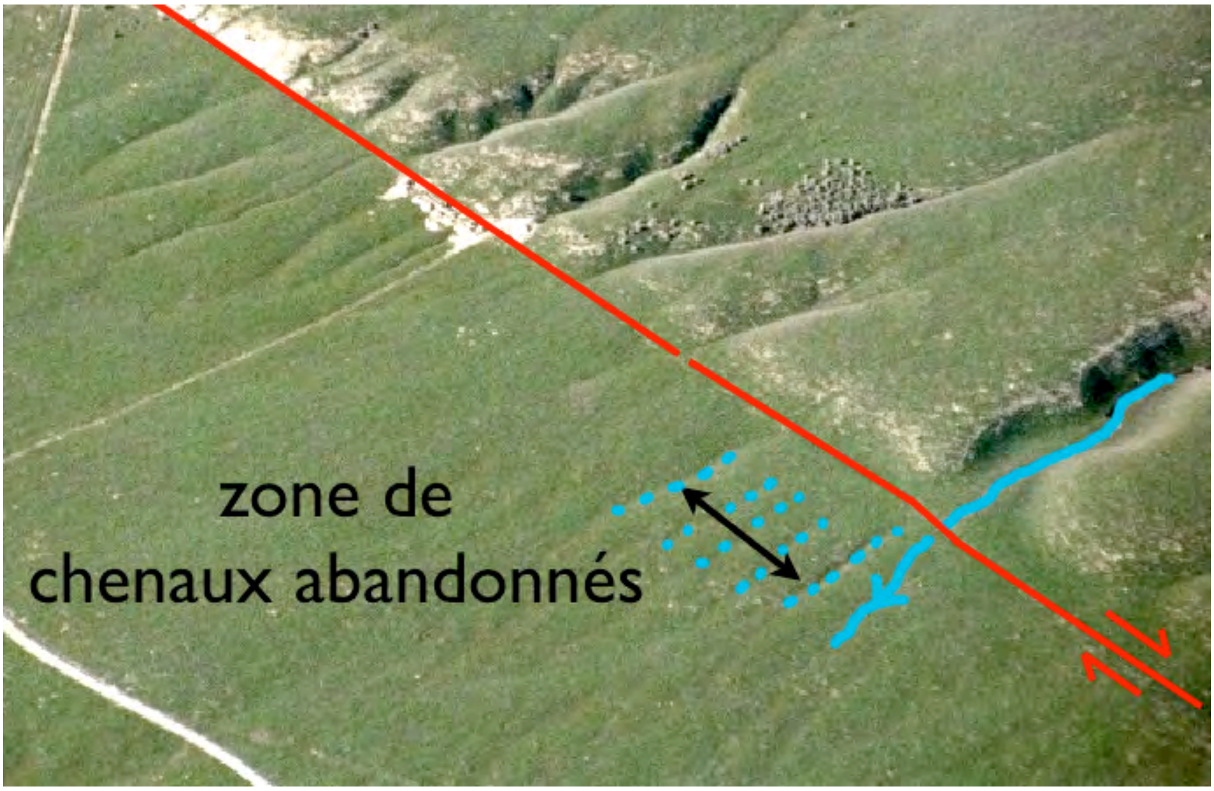

Figure 18 : dans la partie amont de la rivière le court est concentré dans une petite vallée. Dans la partie avale, au fur et à mesure que les séismes se produisent le lit du chenal est déconnecté de son alimentation et abandonné, le chenal actif creusant un nouveau lit en face du débouché amont.

La technique utilisée ici, pompeusement appelée paléosismologie 3D, est un peu différente de ce qui a été présenté précédemment et est résumé dans la figure 19.

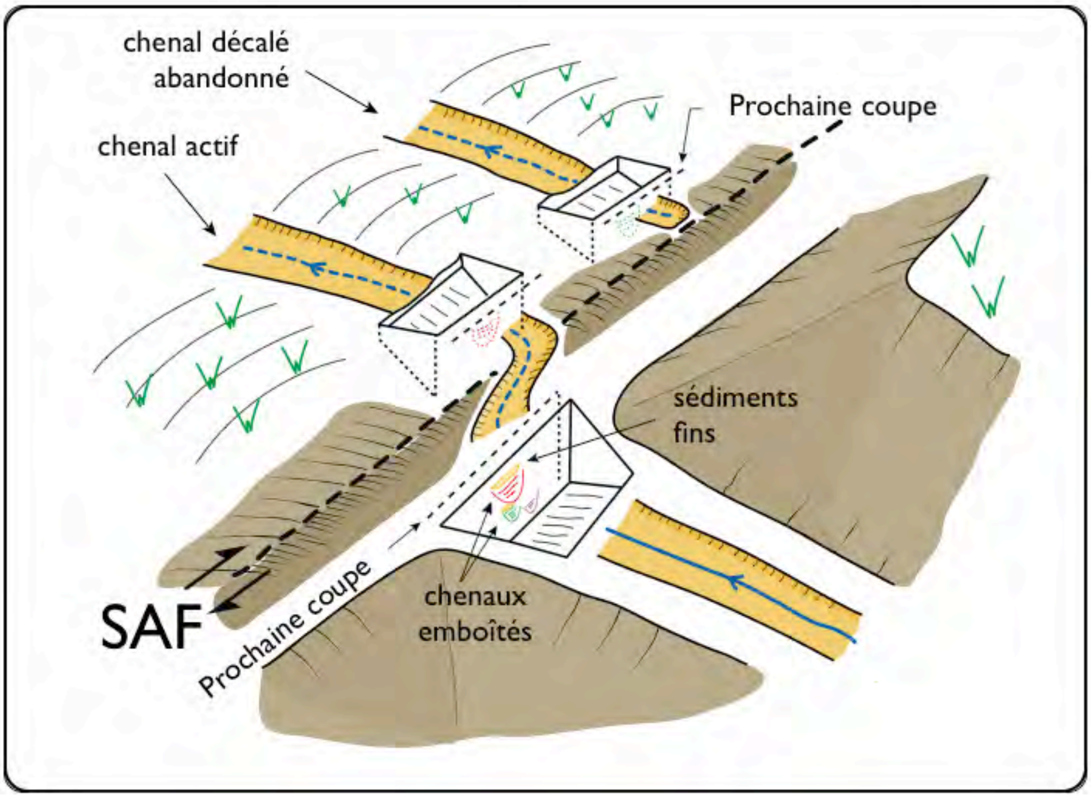

Figure 19 : schéma de principe de la tranchée 3D qui montre la position des différents chenaux actifs et abandonnés, ainsi que la position des différentes tranchées.

L'idée n'est plus de déterminer où est la faille et quand se sont produits les derniers séismes, mais d'estimer le décalage horizontal dû à chaque séisme de façon aussi précise que possible. Pour cela des tranchées sont ouvertes de part et d'autre de la faille, parallèles à la faille, à environs 5m de la faille. Ces tranchées permettent de voir les chenaux en coupe. Typiquement, dans la tranchée amont (Figure 20) on voit une série de chenaux emboîtés qui correspondent aux épisodes d'incision successifs. On remarque aussi de grandes lentilles d'un matériau plus fin, présentant par endroits de fines lamines. Ces lentilles se forment après un séisme, quand le déplacement co-sismique a barré le drainage et que la rivière, pas assez puissante, n'a pas encore réussi à réinciser la partie avale. A ce moment, l'eau débouchant du chenal se retrouve piégée et stagne, déposant les sédiments fins qu'elle transporte. La base de ces lentilles constitue donc un excellent marqueur de l'instant où s'est produit le séisme. De la même façon, du coté aval une longue tranchée parallèle à la faille est ouverte à quelques mètres de la faille. Cette tranchée, dont la lecture est beaucoup plus simple, montre une série de chenaux caractérisés par un remplissage alluvial, assez rythmé, comprenant des faciès sableux et de graviers plus ou moins roulés (figure 20). Ces chenaux sont incisés dans un substratum Pléistocène induré, très distinct.

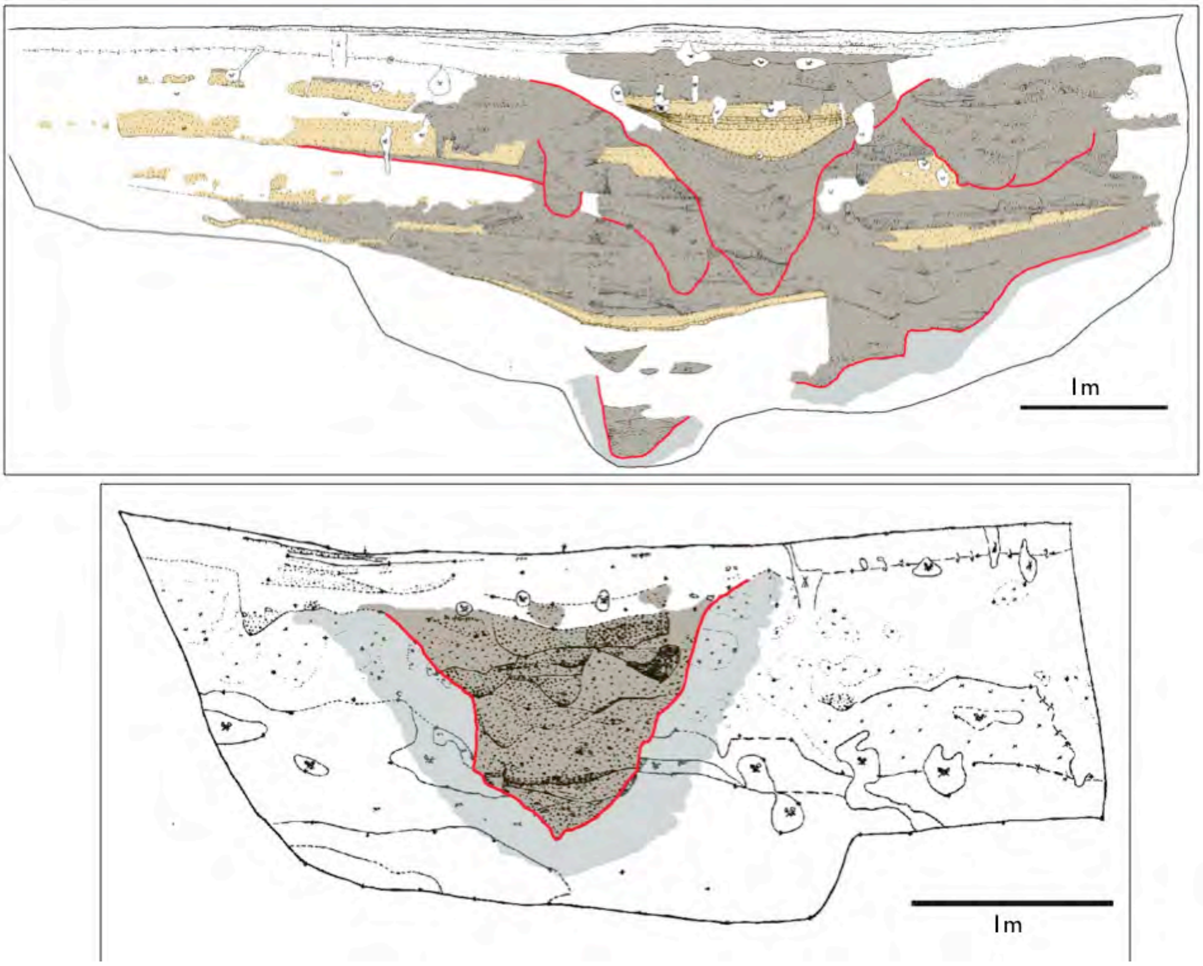

Figure 20 : exemple de cartographie pour les murs amonts (en haut) et avals (en bas). On voit clairement sur ces deux exemples que le chenal amont présente une complexité importante reflétant l'histoire des incisions et des remplissages successifs du chenal, en fonction des modifications morphologiques dues au jeu de la faille.

Par la suite, ces tranchées, des deux cotés de la faille, sont progressivement étendues par coupe successive dont l'épaisseur varie entre 30cm et 60cm, jusqu'à intercepter la faille. Ces coupes sériées nous ont permis de reconstruire avec une très grande précision la géométrie exacte des différents chenaux, et notamment leur point d'intersection avec la zone de faille. Par ailleurs, du coté amont, la multiplication des cartes nous permet de compenser les épisodes successifs de remplissages et d'incisions qui ont pu localement oblitérer une partie de l'enregistrement sédimentaire. L'association des parties avale et amont des chenaux, nécessaire pour la mesure du décalage co-sismique, s'est faite sur quelques critères simples assez robustes : la position relative des chenaux, les continuités de forme et de stratigraphie au travers de la faille, et quand cela a été possible, quelques datations ^{14}C. Finalement, nous avons été capable d'identifier sans ambiguïté 6 paires de chenaux pour lesquelles nous avons pu mesurer le décalage horizontal et vertical avec une très grande précision (figure 21). Le décalage vertical cumulé est nul pour ces 6 événements. Le décalage horizontal par contre présente une distribution assez particulière, qui avait déjà été subodorée à partir des observations de morphologie de surface : Sur les 6 événements clairement identifiés pour lesquels nous sommes capables de mesurer le décalage horizontal, 3 présentent un décalage de l'ordre de 7.5m à 8m, c'est-à-dire quasiment identique. Pour le dernier événement de la série, du fait de la géométrie particulière du chenal, nous n'avons pu déterminer qu'un décalage minimal de 5.4m mais il nous semble très probable que le décalage total pour ce chenal puisse aussi être de l'ordre de 7.5m à 8m. Deux chenaux, au milieu de la série, présentent des décalages nettement plus petits, respectivement de 5.2m et 1.4m, qui sont associés à des séismes distincts. Il est cependant remarquable que la somme de ces deux événements nous ramène à un décalage de l'ordre de 7m, compatible avec les décalages mesurés pour les autres événements. La possibilité que ces deux chenaux correspondent en fait à un seul séisme qui aurait une relation rupture / distribution de chenal plus compliquée que les autres, même si elle ne peut être totalement exclue, semble cependant peu probable au vu de la bonne corrélation que l'on peut établir entre les séismes identifiés sur ce site et ceux identifiés dans d'autres tranchées, sur des sites très voisins. Au premier ordre, nous avons donc une série de séismes présentant un décalage horizontal très similaire de 7.5m à 8m, plus deux séismes dont le décalage cumulé est lui aussi proche de la valeur de 7.5m à 8m. Sans être une preuve définitive, ces données appuient clairement une description de type « glissement caractéristique » pour ce segment de faille.

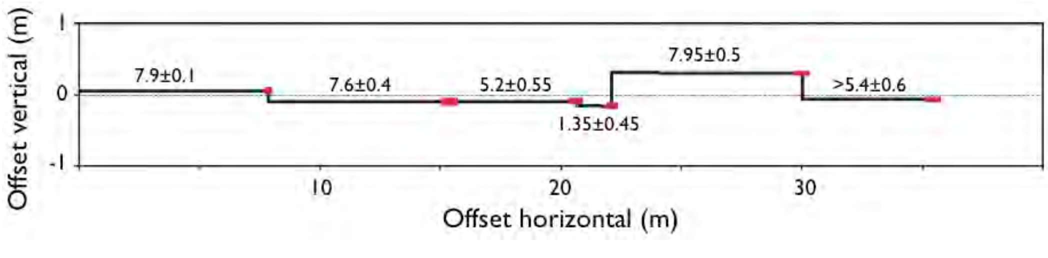

Figure 21 : offset horizontal et vertical pour chaque séisme identifié sur le site de Carrizo Plain. En moyenne l'offset vertical est nul. Le décalage horizontal montre que trois séismes ont une valeur très proche de 8m, valeur qui semble caractéristique pour le site. D'après [Liu, *et al.*, 2004]

En ce qui concerne les aspects temporels, cette étude illustre bien le type de difficultés que l'on peut rencontrer dans les études paléosismologiques. Globalement les échantillons de matière organique que nous avons pu collecter sont très petits, souvent à la limite des capacités instrumentales actuelles. De plus, après datation, il s'est avéré qu'une partie importante des échantillons correspond à des échantillons remobilisés, dont l'ordre stratigraphique et chronologique n'était pas cohérent, rendant inexploitable ces datations. Au final, en utilisant les quelques dates qui nous paraissaient avoir un sens et les corrélations que l'on peut établir avec les sites voisins, il est possible de proposer la série de dates suivantes pour les 6 événements identifiés, du plus récent au plus ancien : 1857, 1540, 1360, (?), 1240 et (?), le signe (?) dénotant l'impossibilité de donner une date raisonnablement contrainte. En utilisant cette chronologie et les valeurs de décalage obtenues, nous avons pu proposer le scénario représenté sur la figure 22 qui illustre bien l'idée de « glissement caractéristique » appliquée au segment de faille de Carrizo Plain.

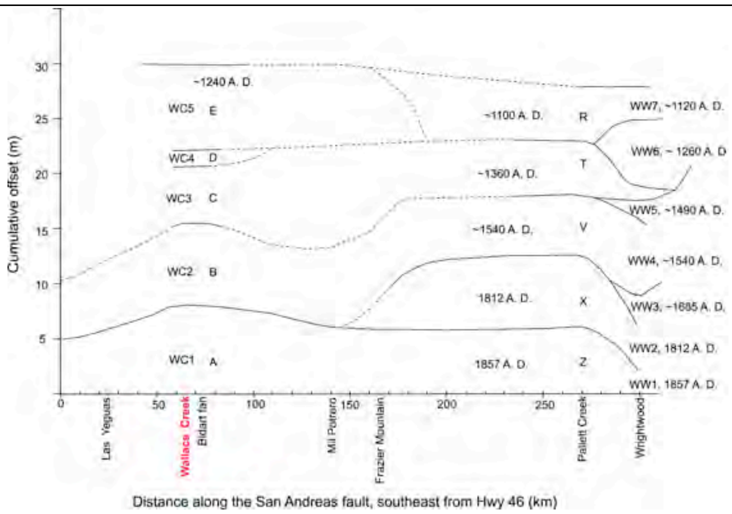

Figure 22 : scénario de rupture le long de la faille de San Andreas construit a partir des données paléosismologiques disponibles. D'après [Liu-Zeng*, et al.*, 2006]

3.2 Séismes récents

Au cours de mon activité de recherche, j'ai eu de nombreuses occasions d'observer des ruptures co-sismiques, plus ou moins longtemps après que le séisme se soit produit. J'ai notamment eu la chance de travailler sur trois séismes contemporains de façon plus détaillée, le séisme d'Aqaba (Mw7.3, 1995), le séisme d'Izmit (Mw7.4, 1999) et le séisme de Kokoxili (Mw7.8, 2001). Dans les trois cas, il s'agit de séismes en décrochement. Cela m'a convaincu que les problématiques liées aux séismes anciens et aux séismes récents étaient très proche et que travailler sur les deux échelles de temps en parallèle est en fait très naturel, même si les méthodes utilisées ne sont pas toujours exactement les mêmes. Dans la partie qui suit, je présenterai une partie des études réalisées sur le séisme de Kokoxili, qui est représentative de mon activité la plus récente dans ce domaine.

L'étude d'un séisme peut s'envisager à plusieurs échelles. On peut proposer une vision locale très détaillée de la rupture qui permet d'appréhender les différents modes de déformation et de faire la relation entre la dernière rupture et ce qui a pu se passer avant. En utilisant la masse de donnée amassée lors de cette première étape, on peut prendre un peu de recul et voir ce qui se passe au niveau d'un segment de la rupture. Dans le cas du séisme de Kokoxili, la partie centrale de la rupture présente un fonctionnement mécanique un peu particulier de partitionnement, qui peut être modélisé. Enfin, une vision plus générale de la rupture permet de voir comment les différentes parties de la rupture s'organisent et à quel point la géométrie est prépondérante dans le déroulement de la rupture, ce qui permet, *in fine*, de proposer un modèle de structuration de la faille que nous pensons pérenne sur plusieurs cycles sismiques.

3.2.1 Le séisme de Kokoxili, une rupture majeure pour un séisme majeur

Le séisme de Kokoxili s'est produit sur la terminaison ouest de la faille du Kunlun, au nord du plateau tibétain. Cette grande faille décrochante fait partie d'un système tectonique à grande échelle qui permet l'extrusion du plateau tibétain sous la pression de l'Inde qui remonte vers le nord, en emboutissant l'Eurasie. La vitesse de glissement le long de la faille du Kunlun est de ~1cm/an, quelles que soient les méthodes et les durées de temps que l'on considère. Une des particularités de la faille du Kunlun par rapport aux autres grandes failles de ce système, qui la rend spécialement intéressante dans le cadre de ma thématique de recherche, est qu'elle a presque rompu sur l'entièreté de sa longueur au cours du dernier siècle. A ce titre, elle fait partie de ces quelques rares failles décrochantes pour lesquelles on peut essayer de dire quelque chose sur les possibles interactions entre différents segments d'une même faille et pour lesquelles on possède une base de séismes instrumentaux (plus ou moins bien documentés) auxquels comparer les données paléosismologiques.

Le séisme de Kokoxili s'est produit sur la section ouest de la faille, le long d'une zone pour laquelle l'on n'a pas d'informations sur l'activité sismique passée. Ce séisme, de magnitude 7.8, fait partie des plus grands séismes continentaux connus à ce jour, et à ce titre méritait une étude approfondie des mécanismes mis en jeu. La rupture de surface fait 450km de long, dans un environnement peu accueillant. L'altitude moyenne à laquelle se trouve la rupture est de 4000m, avec plusieurs sections au dessus de 4500m. Il n'existe qu'une route qui croise la rupture, proche de son extrémité est, mais aucun cheminement facile le long de la rupture (figure 23).

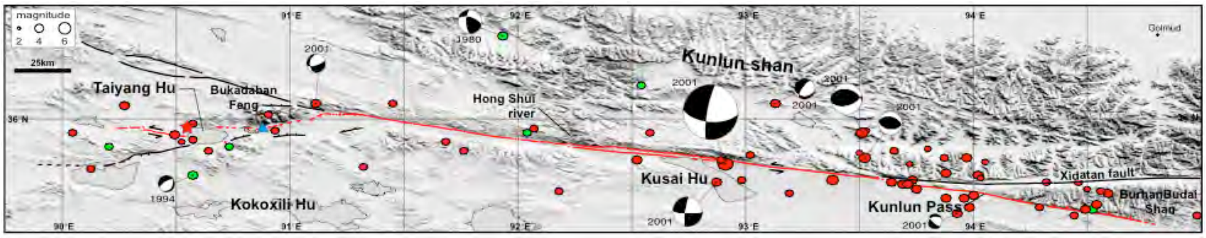

Figure 23 : cartographie d'ensemble de la rupture du séisme de Kokoxili, Mw7.8, 2001. Sont aussi représentés le centroid et les principales répliques (en rouge). D'après [Klinger*, et al.*, 2005]

Cartographier l'ensemble de la rupture sur le terrain est donc très difficile et demanderait un investissement en temps trop important pour être réaliste. Nous avons donc développé une stratégie un peu différente afin de réussir quand même à avoir une idée aussi précise que possible des différents aspects de la rupture : deux campagnes de terrain ont été menées, à chaque fois d'environ ~15j, permettant d'observer et de faire des mesures sur un ensemble de points clefs de la rupture. En complément de ces mesures ponctuelles, nous avons saisi l'opportunité offerte par les nouvelles images satellitaires optiques à haute résolution qui commençaient tout juste à être disponibles à ce moment là. Ces images, d'une résolution légèrement inférieure ou égale au mètre, se sont révélées être un outil extraordinaire pour cartographier la rupture avec un très grand degré de détail, sur de grandes distances (figure 24). Au total, à l'aide de cet outil nous avons été capables de cartographier environ 1/3 de la rupture.

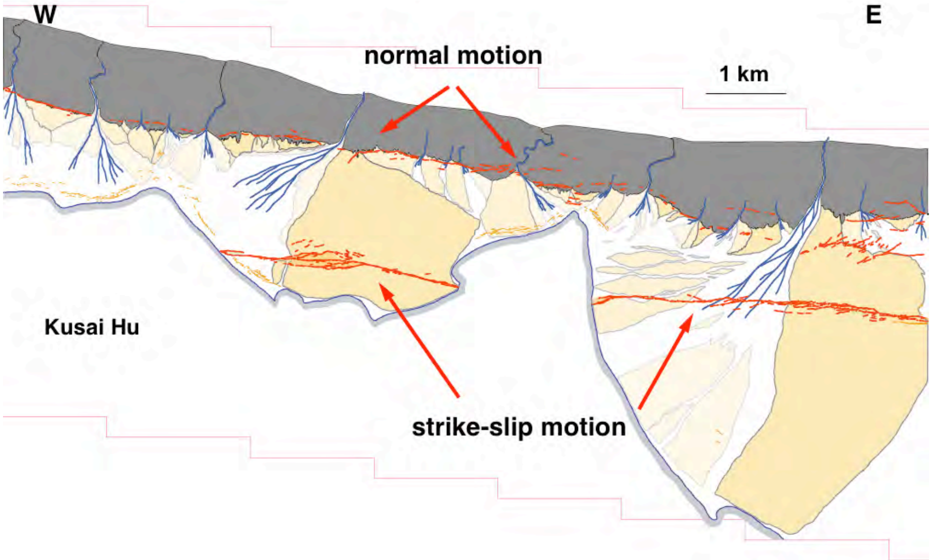

Figure 24 : exemple de cartographie détaillée de la rupture. Des terrasses d'age différent sont identifiées ainsi que les différents segments de la rupture. Le long de cette section on peut clairement voir deux branches de la rupture, l'une accommodant uniquement le déplacement horizontal et l'autre seulement le déplacement vertical. C'est le partitionnement de la rupture.

Au niveau des résultats principaux, cela a permis d'établir clairement où se terminait la rupture à l'Ouest, et de quelle ampleur était les déplacements dans cette zone peu propice aux autres techniques d'imagerie. De la même façon, nous avons clairement identifié et documenté la terminaison est de la rupture pour laquelle la composante compressive, en plus du décrochement, devient importante, sinon dominante. Une des conséquences directes de cette compression est la surrection du massif directement situé au nord de cette terminaison est de la faille. Cette composante compressive est liée au changement d'azimut de la rupture, au niveau de la terminaison est de la section centrale, où la rupture, au lieu de continuer vers l'est le long de la trace principale de la faille du Kunlun, oblique vers le sud-est le long de la faille dite « du Kunlun Pass ». Ce branchement vers le Sud, le long d'un segment à première vue secondaire, ne correspond pas forcément à ce que l'on aurait prédit à priori et apporte donc un éclairage intéressant sur la façon dont les ruptures s'enchaînent le long de la faille du Kunlun. Notamment, il semble que des aspects liés à la dynamique de la rupture soient en jeu au niveau de ce branchement, sur lesquels nous sommes encore en train de travailler en collaboration avec le groupe de dynamique de la rupture de J. Rice (Harvard Univ.). Nos études ont aussi porté sur le couloir extensif qui se situe directement à l'est de l'épicentre (figure 23). Là encore, les techniques classiques d'imagerie n'ont pas pu donner de résultats très satisfaisant. Les études sismologiques indiquent clairement une composante extensive mais elles ne peuvent la quantifier précisément car l'énergie correspondant à cette partie de la source est en grande partie masquée par le reste de la rupture. Nous avons pu visiter et cartographier une grande partie de cette zone et montrer que pour une bonne partie, la rupture ne semble pas arriver en surface. Si c'est le cas, elle est alors très distribuée et peu visible sur le terrain, même si de grandes facettes triangulaires attestent d'une activité extensive à long terme le long de cette section. Enfin, le long de la section centrale, sur un site où la rupture est d'une extrême simplicité, il a été possible de mesurer sur le terrain et sur les images de nombreux décalages co-sismiques associés sans ambiguïté au séisme de 2001. Il a aussi été possible de mesurer des chenaux décalés montrant des décalages cumulés résultant de plusieurs séismes. La comparaison de ces deux jeux de données montre que les décalages cumulés correspondent à des multiples du dernier décalage co-sismique, en 2001, appuyant de fait le schéma de « glissement caractéristique », au moins pour cette portion de faille.

3.2.2 De la cartographie à la mécanique

Documenter dans le détail une rupture sismique et produire une carte précise constituent les briques de base dans l'étude d'un séisme. Il est cependant essentiel de ne pas s'arrêter là. Dans le cas du séisme de Kokoxili, le travail de terrain, associé à l'utilisation extensive des images haute résolution, nous a permis de mettre en évidence un comportement mécanique original de la rupture sur la partie centrale de la rupture. En effet, le long de cette section la rupture se scinde en deux branches qui restent quasiment parallèles sur ~80km, avant de se rejoindre pour continuer le long d'une trace unique. La distance qui sépare les deux branches n'excède jamais 2km. L'étude détaillée de cette section de la rupture révèle que chaque branche accommode uniquement un seul type de déformation, au nord le mouvement vertical en faille normale, au sud le mouvement décrochant. Ce comportement est appelé partitionnement de la rupture. En regardant les variations d'azimut moyen de la rupture, on s'aperçoit qu'il est associé à une déflection de l'azimut de la rupture de ~3°, qui localement provoque un peu d'extension. Si le partitionnement de la déformation avait déjà été observé, notamment au niveau de la déformation cumulée ou, dans un tout autre contexte, dans certaines zones de subduction, il n'avait cependant jamais été mis en évidence lors d'une rupture sismique, montrant que les deux types de déformation peuvent se propager en même temps.

L'utilisation des données cartographiques nous a permis de construire un modèle cinématique de la déformation dans lequel on peut ajuster deux paramètres afin de reproduire la géométrie observée (figure 25). Ce modèle prédit pour chaque point de la grille quel est le type de déformation le plus probable en fonction de la déformation que l'on se donne à une certaine profondeur. Le premier paramètre du modèle correspond à la profondeur à laquelle l'on passe d'un déplacement sur un plan de faille unique, où sont combinés les composantes horizontales et verticales, à une déformation partitionnée entre deux zones de rupture distinctes. Bien que l'on puisse imaginer d'autres possibilités, la raison qui apparaît comme la plus probable pour une telle transition est le passage de la rupture du socle vers les sédiments plus meubles de la surface. Cette interprétation est cohérente avec le fait que le comportement en partitionnement implique une propagation en profondeur de la rupture plus rapide qu'en surface. Le second paramètre du modèle correspond au rapport d'amplitude entre la composante verticale et horizontale du glissement. En réalité ce deuxième paramètre est largement contraint par les observations de terrain, ne laissant comme paramètre réellement libre que la profondeur de transition. La figure 25 montre bien qu'avec un tel modèle d'une grande simplicité nous sommes capable de reproduire la géométrie des ruptures de surface, y compris pour la zone située entre les deux branches principales où de petites ruptures normales, obliques à la branche en décrochement sont observées avec la direction prédite par le modèle. L'observation de la morphologie le long de cette section, avec de grandes facettes triangulaires typiques de failles normales et des déplacements horizontaux cumulés indique clairement que ces deux branches parallèles de la faille sont régulièrement activées et que le partitionnement observé pendant le séisme de Kokoxili est probablement plutôt la règle que l'exception.

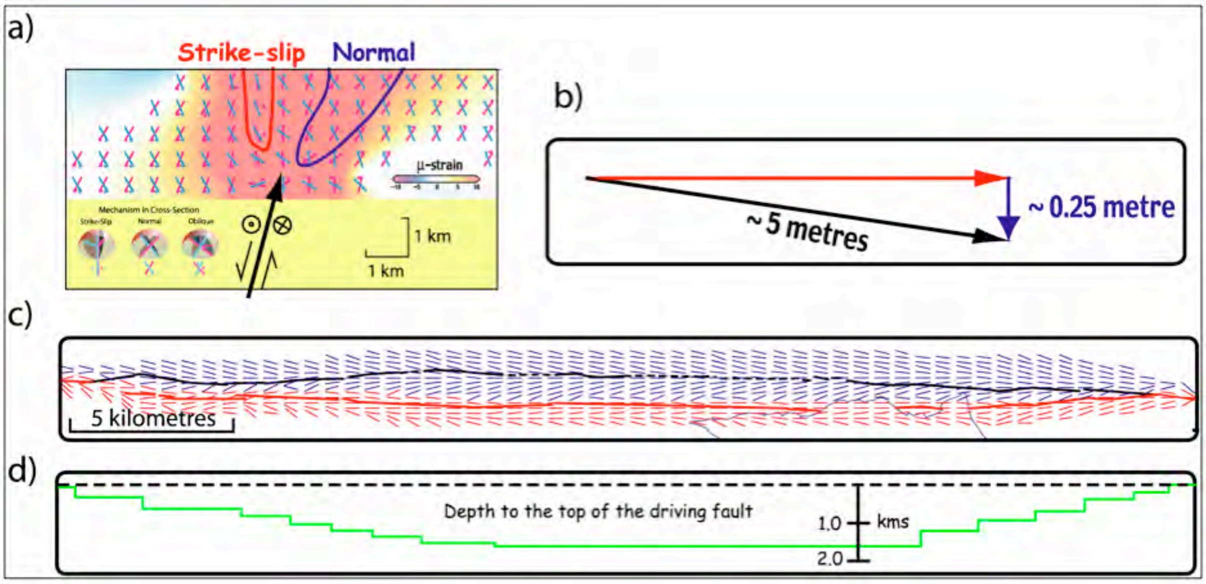

Figure 25 : modèle de partitionnement de la rupture pour le séisme de Kokoxili. (A) Principe du modèle avec un glissement oblique en profondeur dont les deux composantes, horizontale et verticale, se séparent à une certaine profondeur. (B) Rapport d'amplitude des deux composantes, déterminé a partir d'observation de terrain. (C) Observation et direction modélisée des ruptures (décrochement en rouge et déplacement vertical en bleu). (D) Profondeur de l'interface glissement oblique / glissement partitionné. D'après [King, *et al.*, 2005]

3.2.3 Segmentation de la rupture

Regarder ce qui se passe au niveau d'un segment en particulier, comme cela a été fait dans le paragraphe précédent, induit implicitement que l'on considère que la rupture peut être discrétisée en segments individuels. Dans le cas de la rupture de Kokoxili, nous avons pu montrer sans ambiguïté l'existence de cette segmentation. La technique utilisée, complémentaire de l'imagerie radar classique, fait appel à des images satellitaires optiques acquises avant et après la rupture. En corrélant les deux images, si l'on est capable de prendre en compte un certain nombre de paramètres concernant l'image (géométrie des capteurs, trajectoire des capteurs, correction de topographie, etc...), il devient possible de mesurer le déplacement des pixels correspondant au même « objet » entre les deux images, et cela même si le gradient de déformation est très grand. L'un des intérêt de cette méthode est qu'en utilisant des images acquises avec une visée très proche de la verticale, il est possible de mesurer les deux composantes du déplacement horizontal, ce qui n'est généralement pas le cas pour l'Insar, et qui est critique dans le cas de séismes en décrochement. Typiquement, le seuil de détection en déplacement pour ce type de méthode est de l'ordre du 1/10$^{\text{ème}}$ de pixel.

Dans notre cas, nous avons utilisé des images acquises par la famille de satellites Spot qui ont une résolution de 10m, ce qui nous a permis d'abaisser notre seuil de détection des déplacements à 1m.

A partir des cartes du déplacement parallèle et perpendiculaire à la faille, en faisant des profils en travers de la faille il est possible de mesurer la distribution de glissement co-sismique suivant les deux composantes avec une grande densité de mesure. Dans le cas de Kokoxili, nous avons sommé les profils dans des boites d'un kilomètre de coté afin de réduire le bruit sur la mesure pour les ~300km où la corrélation donnait des résultats acceptables, ce qui nous donne un jeu de 300 mesures de glissement indépendantes réparties uniformément. Les données montrent un bon accord avec les mesures faites par d'autres méthodes (Insar ou terrain), validant ainsi cette méthode qui était utilisée ici pour la première fois dans un exercice d'une telle ampleur.

L'observation de la distribution du glissement pour la composante parallèle à la faille montre une oscillation avec des minima de glissement, typiquement tous les ~15km. La densité exceptionnelle des mesures nous permet d'écarter sans aucun doute tout effet dû à un problème d'échantillonnage irrégulier. La mise en relation de la distribution de glissement avec les observations morphologiques de terrain montre que chacun de ces minima de la courbe de glissement peut être associé sur le terrain à une irrégularité géométrique, par exemple une zone de relais, un changement d'azimut, ou le branchement d'une faille secondaire (figure 26). Il existe donc clairement une relation entre distribution du glissement et géométrie de la rupture. Si l'on considère la distribution du glissement sur la composante perpendiculaire à la faille, qui est nulle en moyenne, on constate qu'elle est anti-corrélée avec la distribution de glissement parallèle à la faille. Ceci montre que les minima de glissement ne correspondent pas à un déficit du glissement mais plutôt à un transfert du glissement d'une composante parallèle bien localisée vers un mode de déformation plus diffus qui peut comporter une part de déformation verticale importante, par exemple dans les zones de relais, déformation qui est imagée sur la composante transverse. Dans le cas du séisme de Kokoxili, ces irrégularités géométriques, que l'on peut aussi nommer barrières, sont bien marquées. La longueur des segments que l'on peut ainsi définir est de ~15km, une longueur qui nous renvoie typiquement à l'épaisseur de la croûte sismogénique.

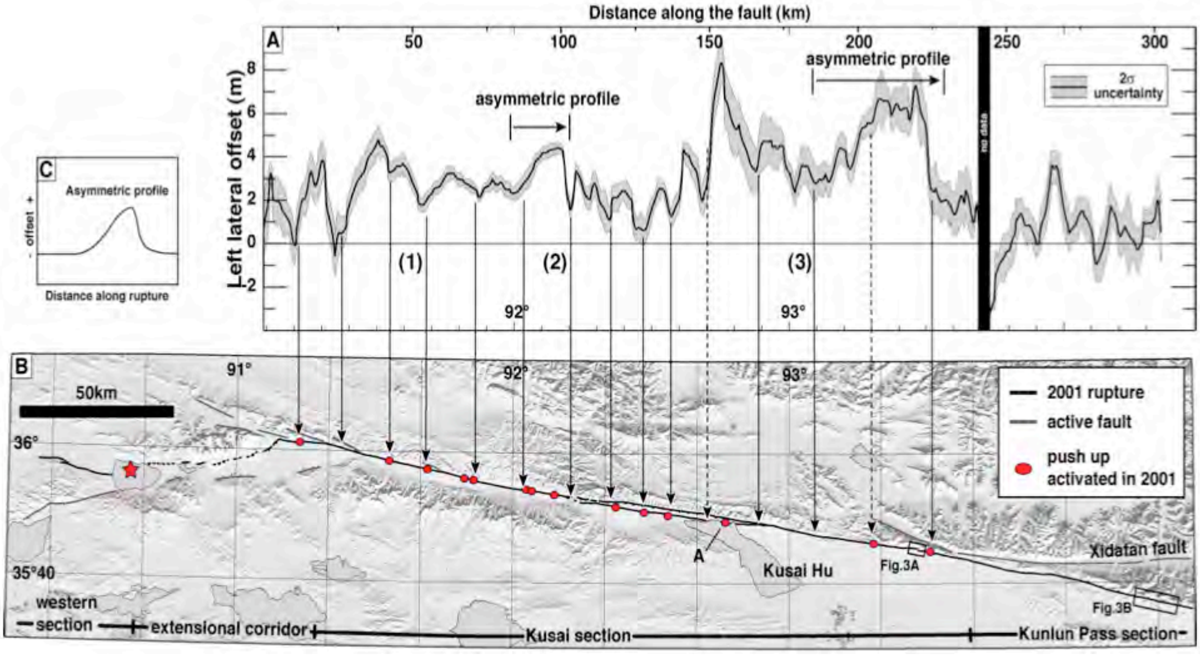

Figure 26 : distribution détaillée de la courbe de glissement liée au séisme de Kokoxili pour la composante parallèle à la faille, déduite de la corrélation d'images satellitaires optiques. L'association d'un minimum local de glissement à une aspérité géométrique de la rupture est systématique. D'après [Klinger*, et al.*, 2006]

4 Discussion et Perspectives

Les quelques études présentées dans les paragraphes précédents donnent une idée des directions dans lesquelles j'ai essayé de progresser au cours de ces dernières années. Il me semble qu'elles illustrent bien le fait que sans données de qualité il n'y aura pas de progrès possible dans le domaine du cycle sismique, mais que ces données ne sont pas faciles à acquérir. Comme j'ai essayé de le montrer dans la première partie de ce mémoire, en ce qui concerne le type de données que l'on peut utiliser, rien n'est écrit et il sera nécessaire de faire preuve d'inventivité pour essayer de tirer parti au maximum de chaque contexte particulier.

Etude du cycle sismique et paléosismologie. Un point qui reste essentiel à mes yeux est d'accumuler plus de données car cela reste la limitation majeure à toute avancée conceptuelle significative. En effet, dans chacun des cas présenté, nous avons eu la chance de travailler sur un site qui nous a permis d'obtenir un enregistrement paléosismologique de très bonne qualité, voir exceptionnel dans le cas du bassin de Yammoûneh (Liban) ou de Carrizo Plain (Californie). Peut-on pour autant considérer que les données acquises sont contraignantes par rapport aux questions initialement posées qui sont où et à quelle fréquence se produisent les séismes ? Oui, jusqu'à un certain niveau ces données sont contraignantes car elles montrent bien qu'à l'échelle de quelques milliers d'années le déroulement temporel des séismes n'apparaît pas comme aléatoire (Liban, Turquie, Chine) et elles semblent donc exclure un modèle de cycle sismique purement chaotique. De la même façon, la manière dont la déformation est accommodée par les séismes successifs semble être organisée avec la répétition d'un motif de déformation spécifique pour un endroit donné de la faille, au moins dans un contexte de faille décrochante (Turquie, Californie), qui nous renvoie directement au modèle de glissement caractéristique. Il semble donc au vue de ces travaux que tout n'est plus possible en terme de modèle.

Les données acquises ne sont cependant pas suffisantes. Il nous est toujours très difficile, ne serait ce que pour un seul système de faille sur la planète, de décrire précisément le déroulement de l'histoire sismologique passé et de dire quelque chose de solide quant à son activité future. En effet, pour la majorité des failles le nombre de sites d'étude reste trop faible et la qualité même des sites étudiés ne permet pas toujours de remonter loin dans le passé. Il reste donc difficile d'avoir une vision d'ensemble de ce qui se passe pour une faille. Partant de cette constatation, mais sachant au vu de mes travaux précédents que cela n'est pas irrémédiable, je souhaite donc poursuivre un travail de paléosismologie intensif. Chaque nouvelle tranchée est l'occasion de prolonger un peu plus les séries temporelles, de compléter l'histoire de l'extension latérale des ruptures le long de la faille et donc de comprendre sa segmentation et enfin, quand cela est possible, d'en savoir plus sur les mouvements co-sismiques passés. La clef de voûte de ce travail est la continuation du programme de paléosismologie que j'ai engagé depuis trois ans sur les grandes failles du plateau tibetain et qui commence à donner ses premiers résultats. L'objectif à terme est non seulement de pouvoir décrire l'histoire sismologique de l'ensemble de ces failles, au moins pour le passé récent mais aussi de pouvoir comprendre comment ces différentes failles interagissent au niveau de l'ensemble du système tectonique. En effet, comme l'a montré [Rockwell*, et al.*, 2000] dans un travail du même type sur les failles du désert de Mojave, Californie, quand on dispose de l'information temporelle sur la sismicité d'un ensemble tectonique, on s'aperçoit alors qu'il peut exister un niveau d'organisation supérieur qui structure l'activité sismique à l'échelle du système entier (figure 27). Il me semble qu'il s'agit là d'une piste de recherche importante qui consiste à faire sauter le concept de cycle sismique du niveau de la faille au niveau du système tectonique tout entier, et dont le corollaire directe est qu'il faut acquérir des données dans le système entier et non plus sur une seule faille.

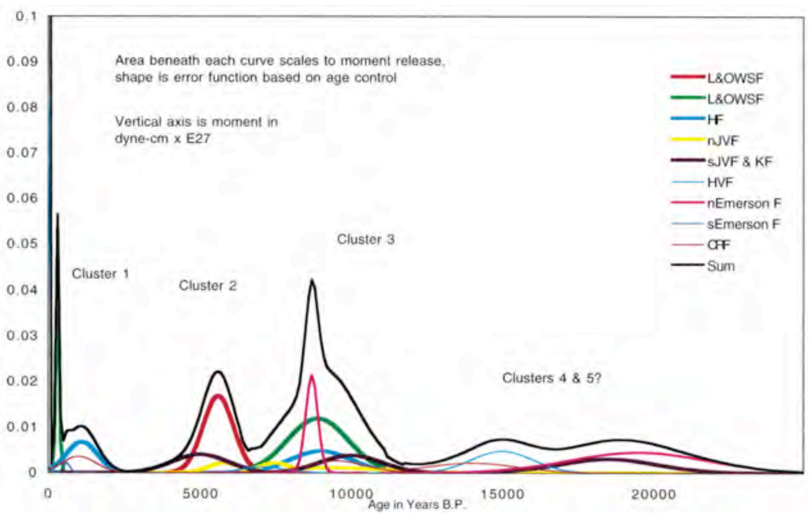

Figure 27 : Chaque courbe de couleur représente l'estimation de l'énergie libérée par les paléoséismes identifiés sur les différentes failles de l'ouest du désert de Mojave, Californie, en fonction du temps. La courbe noire représente la somme. On voit clairement qu'il existe une structure temporelle à l'échelle du système entier avec des périodes d'activité séparées par des périodes de quiescence, et que l'approche considérant uniquement les failles de façon individuelle n'est probablement pas pertinente. D'après [Rockwell*, et al.*, 2000].

Bien que dans un futur proche, ce programme de paléosismologie sur les grandes failles du Tibet reste prioritaire car ces failles représentent un système tectonique exemplaire, je ne conçois cependant pas ce travail comme géographiquement exclusif et je souhaite bien saisir toutes les opportunités de collecter de bonnes données pour faire avancer cette réflexion, où que cela se présente, et notamment au Proche-Orient dès que cela sera à nouveau possible.

Segmentation des failles et géométrie. Comme je l'ai décrit dans les paragraphes précédents, notre méconnaissance de l'histoire sismologique ancienne des failles tient en grande partie au fait que le long des failles le nombre de sites d'étude reste réduit, nous donnant de fait qu'une vision limitée de ce qui se passe latéralement. Cependant, même si un effort important doit être fourni pour augmenter le nombre de sites, d'une part cela n'est pas toujours possible car il n'existe pas de sites appropriés partout, et d'autre part, quand bien même cela est possible cela ne permet pas forcement de lever toute les ambiguïtés sur l'extension latérale des paléoséismes. Parallèlement aux investigations paléosismologiques il est donc nécessaire de réfléchir à d'autres indicateurs pouvant nous guider dans la compréhension de la façon dont se localisent dans le temps et l'espace les séismes sur un système donné de failles. La géométrie même du système tectonique et des différentes failles qui le compose me semble être l'un de ces indicateurs. Typiquement, dans le cas de la partie sud de la faille de San Andreas (illustré par la figure 28), si l'on est capable d'identifier avec précision les différents segments qui composent la faille, de montrer que ces segments ont une durée de vie au moins égale à quelques cycles sismiques, et qu'ils ont une réelle influence sur le déroulement des ruptures sismiques (en terme d'initiation et d'arrêt de la rupture), il est alors possible de choisir entre les scénarios A et B de la figure 28. Cela est un pas important en terme de compréhension de l'organisation des séismes sur ce système car le scénario A implique une certaine organisation de la sismicité avec une alternance des séismes sur les segments sud et nord alors que le scénario B ne montre aucune cohérence. Ils sont donc diamétralement opposés et pouvoir montrer que c'est le scénario A qui s'applique aurait des conséquences directes non seulement sur la compréhension fondamentale des mécanismes régissant la sismicité mais aussi pour tous ce qui concerne les aspects d'évaluation du risque sismique, notamment les approches probabilistes.

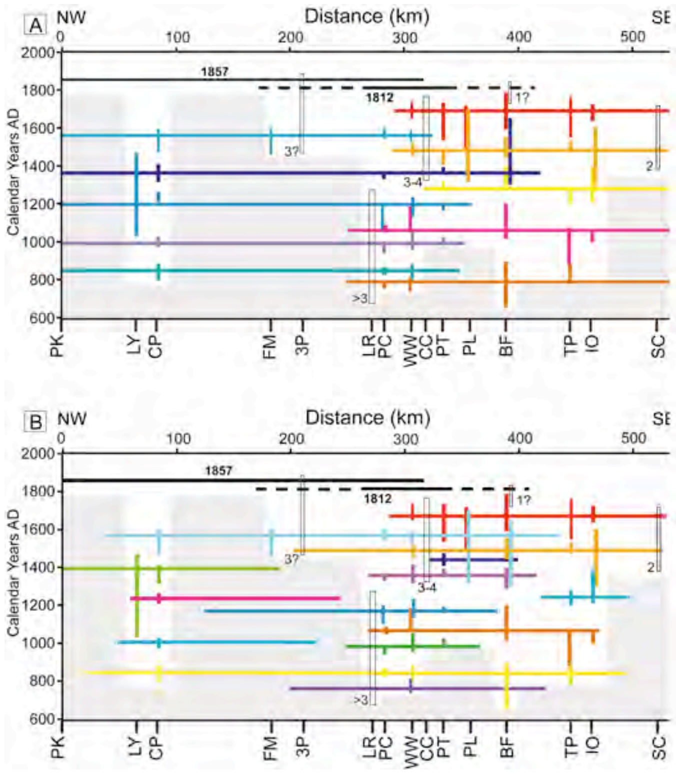

Figure 28 : Ces deux figures montrent pour le sud de la faille de San Andreas les dates possibles de séismes (la longueur des barrettes verticales est proportionnelle à l'incertitude sur les âges) reconnus sur les différents sites paléosismologiques (en abscisse). Les barres colorées horizontales correspondent à de possibles corrélations latérales entre les sites, indiquant l'extension latérale de la rupture quand on pense qu'il s'agit du même séisme observé à plusieurs endroits, basé sur les datations. Dans le scénario A, les observations paléosismologiques ont été corrélées en utilisant aussi ce que l'on sait sur la segmentation de premier ordre de la faille. Le scénario B montre une autre corrélation possible des observations, sans tenir compte des connaissances *a priori* sur la géométrie de la faille. D'après [Weldon*, et al.*, 2004].

Travailler sur ces aspects concernant la géométrie des failles et le rôle qu'elle peut avoir dans la propagation des ruptures est donc aussi l'un de mes objectifs. Faire ce travail sur les séismes anciens est extrêmement difficile car en règle générale nous ne savons rien sur les aspects liés à la propagation de la paléorupture. L'étude des séismes instrumentaux pour lesquels nous avons ces informations est donc assez naturelle et j'espère à terme obtenir un degré de compréhension suffisant de la relation géométrie/propagation pour ces séismes afin de pouvoir repasser aux séismes anciens et proposer des scénarios de propagation à partir de la géométrie observée aujourd'hui. Cette étape est essentielle pour pouvoir comprendre les interactions possibles entre les différentes failles composant un système tectonique et le déroulement de séquences sismiques dans ce système.

J'ai donc débuté un travail de collecte et d'analyse des données décrivant des ruptures sismiques, pour essayer de déterminer s'il existe quelques paramètres génériques importants, indépendants des particularismes de chaque rupture, qui puissent nous permettre de comprendre comment la faille se structure à différentes échelles de temps et d'espace. Les premiers résultats pour les failles décrochantes montrent que cela semble être le cas, et qu'en ce qui concerne la segmentation spatiale, la taille des segments semble être assez comparable d'une rupture à l'autre, et ce indépendamment du contexte tectonique, avec une longueur moyenne oscillant autour de 20 km (figure 29), ce qui nous renvoie directement à l'épaisseur de la croûte sismogénique comme élément de contrôle de la géométrie de la faille.

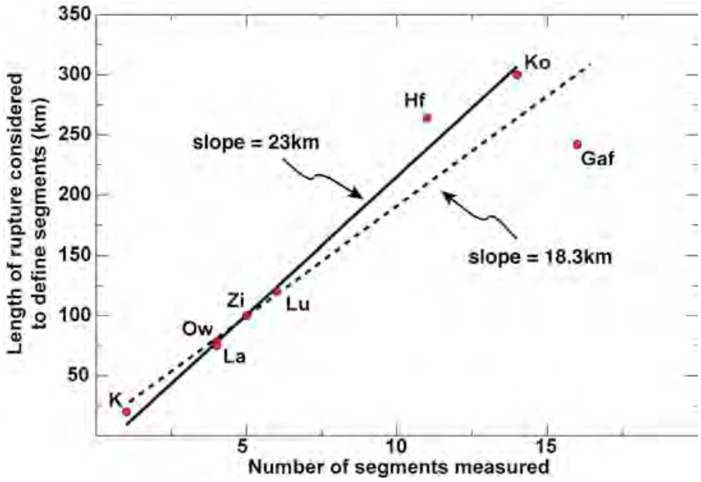

Figure 29 : Pour 7 séismes décrochants de magnitude ≥ 6.6 pour lesquels on peut avoir une carte détaillée de la rupture de surface, on représente le nombre de segments que l'on peut individualiser en fonction de la longueur de la rupture. Les segments sont définis avec des arguments géométriques très simples tels qu'un coude ou un saut de la rupture. Les observations peuvent être approximées de façon satisfaisante par une droite, ce qui indique que la longueur moyenne des segments (donnée par la pente) est la même dans tous les cas. Cela indique clairement que la structuration en segment est indépendante, au premier ordre, du contexte tectonique, et est contrôlée par un facteur extérieur que je suggère être l'épaisseur de la croûte sismogénique. Ko : Kokoxili 2001, Gaf : Gobi Altay 1957, Hf : Haiyuan 1920, Lu : Luzon 1990, Zi : Zirkuh 1997, Ow : Owens valley 1872, La : Landers 1992, Korizan 1979.

Le nombre d'événement pouvant servir à ce type d'analyse reste cependant restreint à ce jour et je vois plusieurs pistes pour essayer de l'augmenter. D'une part en faisant preuve d'une réactivité forte, sur un mode opportuniste, quand un grand séisme se produit pour pouvoir récolter un maximum de données concernant la rupture, et cela grâce à toutes les méthodes dont nous pouvons disposer, comme nous l'avons fait pour le séisme de Kokoxili par exemple. D'autre part, pour compléter ces données Il est nécessaire de mener un inventaire systématique des archives d'images satellitaires car il existe un certain nombre de séismes pour lesquels les techniques de corrélation d'images pourraient être utilisées pour obtenir des distributions de glissement précises et denses supplémentaires. J'ai d'ailleurs déjà engagé ce travail sur les deux derniers séismes de Californie du sud, Landers et Hector Mines, à partir de photographies aériennes. Les résultats préliminaires montrent que cette méthode de mesure nous permet de résoudre le glissement avec une grande finesse et notamment d'étudier les variations du glissement avec la géométrie de la rupture. Enfin, il est aussi possible, grâce à l'utilisation de l'imagerie optique haute résolution, quand les conditions climatiques sont favorables, de retrouver la trace de séismes anciens. Cela mérite une exploration plus approfondie afin de pouvoir reconstruire le plus grand nombre possible de cartes de rupture, et quand cela est possible la distribution du glissement associé. A titre de test j'ai entamé cette exploration sur le cas du séisme historique du Fuyun (M~8, Chine, 1931) et là encore les premiers résultats sont encourageant, montrant qu'il est possible de cartographier des ruptures avec une grande finesse, plus de 70 ans après l'événement.

Au final, l'ensemble de ces données doit me permettre de construire un corpus de données plus étendu et mieux résolu que ce qui existe à l'heure actuelle. Cela constituera une base solide permettant ensuite de faire le lien entre ces observations et les modèles théoriques de croissance de failles, et de ruptures sismiques, qui sont développés par les mécaniciens de la fracture, piste que j'ai commencé à explorer au travers d'une collaboration avec le groupe de mécanique de la rupture de Harvard, dirigé par J. Rice.

Cycle sismique et signaux transitoires pour un décrochement, approche instrumentale. A l'exception du segment de Parkfield, le long de la faille de San Andreas, la majeure partie de l'effort fourni pour étudier le cycle sismique de façon instrumental a été concentrée sur l'étude des zones de subduction. En effet, d'une part ces zones représentent la majorité des très grandes failles actives et d'autre part, pour un certain nombre, elles accommodent une déformation très rapide, pluri-centimétrique, qui assure un temps de retour des grands séismes relativement court. Ces zones présentent cependant deux inconvénients majeurs : la structure active n'est pas directement visible car elle arrive en surface au fond de la mer. On doit donc toujours se limiter à une vision indirecte de la faille. D'autre part, à quelques exceptions près quand il existe des îles sur la plaque subductante, l'étude de ces failles reste pour le moment asymétrique avec l'impossibilité d'instrumenter la partie marine de la subduction. Les failles décrochantes continentales ne présentent pas ces inconvénients. Elles sont bien visibles et l'on peut instrumenter les deux cotés de la structure. Nous avons donc entamé un programme de recherche instrumental consistant à déployer un réseau dense de GPS en travers du segment de Xidatan, le long de la faille décrochante du Kunlun. Notre choix s'est porté sur ce segment car c'est le dernier segment de cette grande faille à n'avoir pas rompu au cours du dernier siècle. Il représente donc une lacune sismique évidente. Nos objectifs sont multiples : bien sur nous allons pouvoir déterminer avec précision le taux de glissement de ce segment de faille, ce qui apportera de l'eau au moulin de la controverse actuelle sur le mode de déformation du Tibet. Cependant avec le type de réseau que nous sommes en train de déployer, une station environ tous les 12km, nous espérons surtout pouvoir directement mesurer les déformations liées aux différentes phases du cycle sismique, notamment d'éventuels signes précurseurs d'un séisme de grande magnitude que l'on est en droit d'attendre le long de ce segment de faille. Dans l'hypothèse où ce séisme se produirait dans un laps de temps compatible avec la durée de vie de notre réseau, nous avons configuré notre réseau (fréquence d'échantillonnage et géométrie) de telle sorte qu'il puisse « voir » le déroulement temporel de la rupture, de la même façon qu'un sismomètre large-bande mais sans les problèmes de saturation. Enfin, la configuration de ce réseau a aussi été pensée de façon à pouvoir détecter d'éventuels signaux transitoires de déformation liés à des séismes lents ou silencieux, similaires à ceux identifiés dans les zones de subduction. L'existence de tels processus dans les zones de décrochement continentaux n'est pas encore totalement avérée pour le moment, mais de fortes présomptions existent, fondée sur des observations le long de la faille de San Andreas [Nadeau and McEvilly, 2004]. La mise en place de ce réseau, le premier réseau GPS permanent installé en Chine par une équipe étrangère, représente un volume de travail important.

5 Bibliographie relative aux parties 1 à 4

Ambraseys, N., et al. (1994), *The seismicity of Egypt, Arabia and the Red Sea*, Cambridge Univ. Press.

Ambraseys, N. N., and C. F. Finkel (1987), Seismicity of Turkey and neighbouring regions, 1899-1915, *Annales Geophysicae*, *5B*, 701-726.

Armijo, R., et al. (1986), Quaternary extension in Southern Tibet: field observations and tectonic implications, *J.Geophys.Res.*, *91*, 13,803-813,872.

Atwater, B. (1987), Evidence for great Holocene earthquakes along the outer coast of Washington state, *Science*, *236*, 942-944.

Bakun, W. H., and A. Lindh (1985), The Parkfield, California, earthquake prediction experiment, *Science*, *229*, 619-624.

Bard, E., et al. (1990), Calibration of the ^{14}C timescale over the past 30,000 years using mass spectrometic U-Th ages from Barbados., *Nature*, 405-410.

Bendick, R., et al. (2000), Geodetic evidence for a low slip rate in the Altyn Tagh fault system, *Nature*, *404*, 69-72.

Benedetti, L., et al. (2002), Post-glacial slip history of the Sparta fault (Greece) determined by Cl-36 cosmogenic dating: Evidence for non-periodic earthquakes, *Geophys. Res. Lett.*, *29*.

Bennett, R. A., et al. (1996), Global Positioning System constraints on fault slip rates in southern California and northern Baja, Mexico, *J. Geophys. Res.*, *101*, 21943 - 21960.

Brown, E. T., et al. (2005), Comment on "Slip-rate measurements on the Karakorum fault may imply secular variation in fault motion", *Science*, *309*.

Burgmann, R., et al. (1998), Slip along the Hayward fault, California, estimated from space-based synthetic aperture radar interferometry, *Geology*, *26*, 559 - 562.

Chery, J., and P. Vernant (2006), Lithospheric elasticity promotes episodic fault activity, *Earth Planet. Sci. Lett.*, *243*, 211-217.

Chevalier, M. L., et al. (2005), Slip-rate measurements on the Karakorum Fault may imply secular variations in fault motion, *Science*, *307*, 411-414.

Cramer, C., et al. (2000), A time-dependent probabilistic seismic-hazard model for California, *Bulletin of the Seismological Society of America*, *90*, 1-21.

Daëron, M., et al. (2004), Constraints on the post ~25-ka slip rate of the Yammouneh fault (Lebanon) using in-situ cosmogenic Cl^{36} dating of offset limetsone-clast fans, *Earth Planet. Sci. Lett.*, *227*, 105-119.

Daëron, M., et al. (2005), Sources of the large AD1202 and 1759 Near East earthquakes, *Geology*, *33*, 529-532.

Daëron, M., et al. (in-press), 12,000-year-long record of up to 14 paleo-earthquakes on the Yammoûneh fault (Levant fault system), *Bulletin of the Seismological Society of America*.

Dolomieu, D. (1784), *Mémoire sur les tremblements de terre de la Calabre pendant l'année 1783.*, Fulgoni, Rome.

Elias, A., et al. (accepted), Active thrusting offfshore Mount Lebanon: source of the tsunamigenic, 551 AD Beirut-Tripoli earthquake, *Geology*.

Freund, R., et al. (1968), Age and rate of the sinistral movement along the Dead Sea Rift, *Nature*, *220*, 527-538.

Garfunkel, Z., et al. (1981), Active Faulting in the Dead Sea Rift, *Tectonophysics*, *80*, 1-26.

Goldfinger, C., et al. (2003), Deep-water turbidites as Holocene earthquake proxies: the Cascadia subduction zone and Northern San Andreas fault systems, *Annals of Geophysics*, *46*, 1169-1193.

Gosse, J. C., and F. M. Phillips (2001), Terrestrial in situ cosmogenic nuclides: Theory and application, *Quaternary Science Review*, *20*, 1475-1560.
Jackson, J., and D. McKenzie (1984), Active tectonics of the Alpine-Himalayan Belt between western Turkey and Pakistan, *Geophysical Journal of the Royal Astronomical Society*, *77*, 185-264.
King, G., et al. (2005), Slip partitioned surface breaks for the 2001 Kokoxili earthquake, China (Mw 7.8), *Bull. Seis. Soc. Am.*, *95*, 731 - 738.
King, G. C., and J. Nabelek (1985), The role of fault bends in faults in the initiation and termination of earthquake rupture, *Science*, *283*, 984-987.
Klinger, Y., et al. (2003a), Alluvial deposition and lake-level fluctuations forced by Late Quaternary climate change: the Dead Sea case example, *Sedimentary geology*, *162*, 119-139.
Klinger, Y., et al. (2000a), Slip rate on the Dead Sea transform fault in northern Araba Valley (Jordan), *Geophys. J. Int.*, *142*, 755-768.
Klinger, Y., et al. (2000b), Seismic behaviour of the Dead Sea Fault along Araba Valley, Jordan, *Geophys. J. Int.*, *142*, 769-782.
Klinger, Y., et al. (2006), Evidence for an earthquake barrier model from Mw similar to 7.8 Kokoxili (Tibet) earthquake slip-distribution, *Earth Planet. Sci. Lett.*, *242*, 354-364.
Klinger, Y., et al. (2003b), Paleoseismic Evidence of Characteristic Slip on the Western Segment of the North Anatolian Fault, Turkey, *Bull. Seis. Soc. Am.*, *93*, 2317-2332.
Klinger, Y., et al. (2005), High-resolution satellite imagery mapping of the surface rupture and slip distribution of the MW 7.8, 14 November 2001 Kokoxili Earthquake, Kunlun Fault, northern Tibet, China, *Bull. Seis. Soc. Am.*, *95*, 1970-1987.
Kondo, H., et al. (2005), Slip distribution, fault geometry, and fault segmenation of the 1944 Bolu-Gerede earthquake rupture, North Anatolian Fault, Turkey, *Bulletin of the Seismological Society of America*, *95*, 1234-1249.
Kumagai, H. (1996), Time sequence and the reccurence models for larges earthquakes along the Nankai through revisited, *Geophys. Res. Lett.*, *23*, 1139 -1142.
Lasserre, C., et al. (2002), Fast late Pleistocene slip rate on the Leng Long Ling segment of the Haiyuan fault, Qinghai, China, *Journal of Geophysical Research-Solid Earth*, *107*.
Lebeon, M., et al. (2006), Geodetic versus geologic slip rate along the Dead Sea fault, paper presented at SSA Annual Meeting, San Francisco, USA.
Li, H. B., et al. (2005), Slip rate on the Kunlun fault at Hongshui Gou, and recurrence time of great events comparable to the 14/11/2001, Mw similar to 7.9 Kokoxili earthquake, *Earth Planet. Sci. Lett.*, *237*, 285-299.
Lindvall, S., et al. (1989), Evidence for prehistoric earthquakes on the Superstition Hills fault from offset geomorphic features, *Bull. Seismol. Soc. Am.*, *79*, 342-361.
Liu, J., et al. (2004), Six similar sequential ruptures of the San Andreas fault, Carrizo Plain, California, *Geology*, *32*, 649-652.
Liu-Zeng, J., et al. (2006), Serial ruptures of the San Andreas fault, Carrizo Plain, California, revealed by three-dimensional excavations, *J. Geophys. Res.*, *111*.
Liu-Zeng, J., et al. (2007), Millenial recurrence of large earthquakes on the Haiyuan fault near Songshan, Gansu province, China, *Bulletin of the Seismological Society of America*, *97*.
Matmon, A., et al. (2005), Dating offset fans along the Mojave section of the San Andreas fault using cosmogenic 26Al and 10Be, *Geological Society of America Bulletin*, *117*, 795-807.
Matmon, A., et al. (2006), Denali fault slip rates and Holocene-late Pleistocene kinematics of central Alaska, *Geology*, *34*, 645-648.
McKenzie, D. P. (1972), Active tectonics of the Mediterranean region, *Geophys. J. R. Astron. Soc.*, *30*, 109-185.

Meriaux, A. S., et al. (2005), The Aksay segment of the northern Altyn Tagh fault: Tectonic geomorphology, landscape evolution, and Holocene slip-rate, *J. Geophys. Res.*, *110*, B04404.
Molnar, P., and P. Tapponnier (1978), Active tectonics of Tibet, *J.Geophys.Res.*, *83*, 5361-5375.
Murray, J., and P. Segall (2002), Testing time-predictable earthquake recurrence by direct measurement of strain accumulation and release, *Nature*, *419*, 287-291.
Nadeau, R. M., and T. V. McEvilly (2004), Periodic pulsing of characteristic microearthquakes on the San Andreas Fault, *Science*, *303*, 220-222.
Natawidjaja, D., et al. (2006), Source parameters of the great Sumatran megathrust earthquakes of 1797 and 1833 inferred from coral microatolls, *J. Geophys. Res.*, *111*, B06403.
Natawidjaja, D., et al. (2004), Paleogeodetic records of seismic and aseismic subduction from central Sumatran microatolls, Indonesia, *J. Geophys. Res.*, *109*, B04306.
Palumbo, L., et al. (2004), Slip history of the Magnola fault (Apennines, Central Italy) from 36Cl surface exposure dating: evidence for strong earthquakes over the Holocene, *Earth Planet. Sci. Lett.*, *225*, 163-176.
Peltzer, G., et al. (2001), Transient strain accumulation and fault interaction in the eastern California Shear zone, *Geology*, *29*, 975 - 978.
Perfettini, H., et al. (2005), Geodetic displacement and aftershocks following the 2001Mw=8.4 Peru earthquake: implications for the mechanics of the earthquake cycle along subducction zones, *J. Geophys. Res.*, *110*.
Quennell, A. M. (1958), The Structural and Geomorphic Evolution of the Dead Sea Rift, *Quaterly Journal of the Geological Society of London*, *114*, 1-24.
Ritz, J. F., et al. (2003), Late Pleistocene to Holocene slip rates for the Gurvan Bulag thrust fault (Gobi-Altay, Mongolia) estimated with Be-10 dates, *Journal of Geophysical Research-Solid Earth*, *108*.
Rockwell, T., et al. (2000), Paleoseismology of the Johnson Valley, Kikapoo, and Homestead Valley fault: Clustering of earthquakes in the eastern California shear zone, *Bulletin of the Seismological Society of America*, *90*, 1200 - 1236.
Scholz, C. (1990), *The Mechanics of Earthquakes and Faulting*, 439 pp., Cambridge University Press, New York.
Schwartz, D. P., and K. J. Coppersmith (1984), Fault behavior and characteristic earthquakes: examples from the Wasatch and San Andreas fault zones, *J. Geophys. Res.*, *89*, 5681-5698.
Shimazaki, K., and T. Nakata (1980), Time-predictable recurrence model for large earthquakes, *Geophys. Res. Lett.*, *7*, 279-282.
Sibson, R. (1985), Stopping of earthquake ruptures at dilational fault jogs, *Nature*, *316*, 248-251.
Sieh, K. (1978a), Pre-historic large earthquakes produced by slip on the San Andreas fault at Pallett Creek, California, *J. Geophys. Res.*, *83*, 3907-3939.
Sieh, K. (1978b), Slip along the San Andreas fault associated with the great 1857 earthquake, *Seismol. Soc. Am. Bull.*, *68*, 1421-1428.
Sieh, K. (1981), A review of geological evidence for recurrence times of large earthquakes, in *Earthquake Prediction -- An International Review*, edited, pp. 181-207.
Sieh, K. (1996), The repetition of large-earthquake ruptures, paper presented at Proc.Natl.Acad.Sci.
Socquet, A., et al. (2006), India and Sunda plates motion and deformation along their boundary in Myanmar determined by GPS, *J. Geophys. Res.*, *111*.
Stein, R., et al. (1997), Progressive failure on the North Anatolian fault since 1939 by earthquake stress triggering, *Geophys. J. Int.*, *128*, 594-604.

Tapponnier, P. (1977), Evolution tectonique du systeme alpin en Méditerranée: poinçonnement et ecrasement rigide-plastique., *Bull. Soc. Geol. France*, *19*, 437-460.
Tapponnier, P., and P. Molnar (1977), Active faulting and tectonics in China, *J. Geophys. Res.*, *82*, 2905-2930.
Van der Woerd, J., et al. (2006), Long-term slip rate of the southern San Andreas Fault from Be-10-Al-26 surface exposure dating of an offset alluvial fan, *J. Geophys. Res.*, *111*.
Van Der Woerd, J., et al. (2002), Uniform postglacial slip-rate along the central 600 km of the Kunlun Fault (Tibet), from Al-26, Be-10, and C-14 dating of riser offsets, and climatic origin of the regional morphology, *Geophys. J. Int.*, *148*, 356-388.
Vernant, P., et al. (2004), Present-day crustal deformation and plate kinematics in the Middle East constrained by GPS measurements in Iran and nothern Oman, *Geophys. J. Int.*, *157*, 381-398.
Wallace, R. E. (1977), Profiles and ages of young fault scarps, north-central Nevada, *Geol.Soc.Am.Bull.*, *88*, 1267-1281.
Ward, S. (1997), Dogtails versus rainbows: Synthetic earthquake rupture models as an aid in interpreting geological data, *Bulletin of the Seismological Society of America*, *87*, 1422-1441.
Weldon, R., et al. (2004), Wrightwood and the earthquake cycle: what a long recurrence record tells us about how faults work, *GSA Today*, *14*, 4 - 10.
Wells, D. L., and K. J. Coppersmith (1994), New Empirical Relationships Among Magnitude, Rupture Length, Rupture Width, Rupture Area, and Surface Displacement, *Bulletin of the Seismological Society of America*, *84*, 974-1002.
Wesnousky, S. (2006), Predicting the endpoints of earthquake ruptures, *Nature*, *444*, 358-360.
Working Group for California Earthquake Probabilities (1995), Seismic hazard in Southern California: probable earthquakes, 1994 to 2024., *Bulletin of the Seismological Society of America*, *85*, 379-439.
Wright, T., et al. (2001), Measurements of interseismic strain accumulation across the North Anatolia fault by satellite radar interferometry, *Geophys. Res. Lett.*, *28*, 2117 - 2120.
Wyss, M., and S. Wiemer (1999), How can one test the seismic gap hypothesis? The case of repeated ruptures in the Aleutians, *Pure and Applied Geophysics*, *155*, 259 -278.

6 Renseignements administratifs

6.1 Curriculum Vitae

Nom et Prénom : Klinger Yann
Date et lieu de naissance : 30 mars 1970, Strasbourg
Nationalité : français
Situation familiale : concubin, 2 enfants.

Obligations militaires : Service national effectué comme scientifique du contingent au Laboratoire de Géophysique du C.E.A., à Bruyères le Châtel, durant l'année 1995.

Adresse professionnelle
Equipe de Tectonique - UMR 7154
Boite 89
Institut de Physique du Globe
4, Place Jussieu
75252 Paris cedex 05, France

tel : 01 44 27 24 37
fax : 01 44 27 24 40
email : klinger@ipgp.jussieu.fr

Cursus:

• Depuis Octobre 2001, chargé de recherche au CNRS, dans le laboratoire de tectonique de l'IPG de Paris.

• Octobre 1999 – Septembre 2001, Chercheur post-doctorant au laboratoire de sismologie du California Institute of Technology, Pasadena, USA

• Février 1999 – Septembre 1999, Chercheur contractuel à l'IPG de Strasbourg.

• Janvier 1999, Doctorat en sismo-tectonique sur la faille du Levant à l'Institut de Physique du Globe de Strasbourg sous la responsabilité de L. Dorbath et J.P. Avouac (LDG/CEA).

• Décembre 1994, Diplôme d'Ingénieur géophysicien de l'Ecole et Observatoire de Physique du Globe, Université Louis Pasteur, Strasbourg.

• Juin 1994, Diplôme d'Etude Approfondies en sciences de la terre, mention bien. Ecole et Observatoire de Physique du Globe, Université Louis Pasteur, Strasbourg.

Distinction :

2004, Prix Pierre Cardin catégorie Sciences dans le cadre des années France-Chine.

Gestion de projets :

2003 - 2004 : Responsable du projet « Mesures des ruptures sismiques à l'aide d'images satellites haute résolution et mesures hyperspectrales : sismologie et paleosismologie satellitaire » centré sur le séisme de Kokoxili (Chine) qui s'est produit en Nov. 2001, de magnitude 7.8. Ce projet est financé par l'ACI Observation de la Terre.

2004 – 2005 : Responsable français pour le Projet de Recherche Avancé financé par l'Association Franco-Chinoise pour la Recherche Scientifique et Technique : Paléosismologie des grandes failles du Tibet (Altyn Tagh, Kunlun, et Haiyuan) en collaboration avec le Dr. X. Xu.

2004 – 2005 : Responsable du projet « Fonctionnement de la frontière de plaque Arabie/Afrique – Faille du Levant – Mer Morte » financé par le programme Dyeti 2004

2005 – 2007 : Responsable du projet « Faille du Levant – Mer Morte : de la géodynamique à l'aléa sismique » financé par l'ACI Aléas et changements globaux.

2006 Responsable du projet « paléosismologie spatiale » financé par le PNTS

2006 – 2008 : Co-responsable du projet « Lacune » financé par l'ANR catastrophe tellurique.

Responsabilité collectives :

2004 – présent : Membre de la CS du programme Artemis (datation C14).
2005 – 2006: Membre de la CS de l'ANR Catell.
2006 – présent : Secrétaire de la CS du PNTS, responsable du volet Imagerie Très Haute Résolution.
2007 – présent : Membre de la Commission Spécialisée des Sciences de la Terre, INSU.

2005 – présent : Membre du conseil de direction élargi de l'IPGP.

2007 – 2009 : Membre de l'éditorial Board de Geology

6.2 Enseignements et encadrements de recherche

Enseignement :

Depuis 2006 participe au module de niveau M1/M2 intitulé « Failles et séismes ». En 2007 ma participation représente la moitié du module en terme d'heures enseignées.

Encadrement des étudiants :

2001 – 2005 : Participation active à l'encadrement du travail de thèse de Mathieu Daëron intitulé : Rôle, cinématique et comportement sismique à long terme de la faille de Yammoûneh.

2004 : Responsable pour le financement et l'encadrement de Mlle Jing Liu en stage post-doctoral au laboratoire de tectonique de L'IPGP (Financement sur bourse Chateaubriand puis CNRS).

2004 : Encadrement du stage de DEA d'Anatole Lorne : traitement d'image appliqué à la mesure de déformation pour le séisme d'Hector Mine.

2004 : Encadrement du stage de DEA de Maryline Lebéon : paléosismologie de la faille du Levant au Liban.

2005 – présent : encadrement de la thèse de Maryline LeBéon : Détermination des vitesses à court et long terme de la faille du Levant.

2007 : Encadrement du stage de DEA de Marie Etchebes : Paléosismologie spatiale, application au séisme de Fuyun.

6.3 Liste complète des références (Mars 2007)

Thèse :

Klinger Y., 1999. Sismotectonique de la faille du Levant. Université Louis Pasteur, Strasbourg, France. 238 pp.

Congrès Internationaux :

Van der Woerd J., Li H., Tapponnier P., **Klinger** Y., Xu X., Meriaux A.S., Ryerson F.J. From coseismic to cumulative offsets : linking the earthquakes to the long term slip rate along the Kunlun fault (Tibet). Abstract, AGU fall meeting, San Francisco, December 11-15, 2006.

Lebeon, M., **Klinger**, Y., Agnon, A., Dorbath, L., Baer, G., Meriaux, A-S., Ruegg, J-C., Charade, O., Finkel, R. and Ryerson, F., Geodetic versus geologic slip rate along the Dead Sea Fault, Abstract, SSA Annual Meeting, San Francisco, USA, April 18-22 2006.

Van der Woerd J., **Klinger** Y., Sieh K., Tapponnier P., Ryerson F., Meriaux A.S. Long-term slip rate of the southern San Andreas Fault, from 10Be-26Al surface exposure dating of an offset alluvial fan., Geophys. Res. Abstract, 8, 07786, EGU, Vienna, Austria., April 2006.

Klinger Y., Michel R., King G.C.P., Tapponnier P., Evidence for an earthquake barrier model from Mw7.8 Kokoxili (Tibet) earthquake slip-distribution. Eos Trans. AGU, 86(52), Fall Meet. Suppl., Abstract T23B-03, 2005.

Bhat H.S., Dmowska R., King G.C.P., **Klinger** Y., Rice J.R., Supershear Slip Pulse and off-fault Damage. Eos Trans. AGU, 86(52), Fall Meet. Suppl., Abstract S34A-06, 2005.

Liu, J., **Klinger**, Y., Xu, X., Lasserre, C., Chen, G., Chen, W., and Tapponnier, P., Eight-hundred-year recurrence of large earthquakes on the Haiyuan fault near Songhan, Gansu province, China. 20th Himalysa-Karakoram-Tibet Workshop. March 29- April 1, 2005, Aussois, France.

Lorne A., **Klinger** Y., Binet R., Michel R., Horizontal displacement of the Hector Mine earthquake, (California, 16/10/99, Mw 7.1), derived from aerial photography

intercorrelation. AGU 2004 Fall meeting, abstract T31C-1322. December 13-17, 2004, San Francisco, USA.

Daëron M., Elias A., **Klinger** Y., Tapponnier P., Jacques E., Sursock A., Sources of the AD 551, 1202 and 1759 earthquakes (Lebanon and Syria). AGU 2004 Fall meeting, abstract T41F-1294. December 13-17, 2004, San Francisco, USA.

Klinger Y., Michel R., Van der Woerd J., Xu X., Tapponnier P., Slip-distribution and rupture pattern of the 14 November 2001, Mw 7.8 Kokoxili earthquake (China). AGU 2004 Fall meeting, abstract T31E-06. December 13-17, 2004, San Francisco, USA.

Liu, J., **Klinger**, Y., Xu, X., Lasserre, C., Chen, G., Chen, W., and Tapponnier, P., Paleoseismological evidence of large pre-historical earthquakes on the western Haiyuan fault near Tianzhu, Gansu province, China. AGU 2004 Fall meeting, abstract T11C-1268. December 13-17, 2004, San Francisco, USA.

Klinger Y., Michel R., Lasserre C., Xu X., Tapponnier P., Van der Woerd J., Peltzer G., Surface rupture of the Nov., 14th, 2001 Kokoxili earthquake (Mw 7.8) imaged from space. 4th International symposium on the Tibetan Plateau, Lhasa, China, August 2004.

Liu J., **Klinger** Y., Xu X., Lasserre C., Chen G., Chen W., Tapponnier P., Paleosismological evidence of large pre-historical earthquakes on the western Haiyuan Fault near Tianzhu, Gansu Province, China. 4th International symposium on the Tibetan Plateau, Lhasa, China, August 2004.

Klinger Y., Michel R., Lasserre C., Xu X., Tapponnier P., Van der Woerd J., Peltzer G., Surface rupture of the Nov., 14th, 2001 Kokoxili earthquake (Mw 7.8) imaged from space. 3rd International conference on continental earthquakes. Beijing, China, July 2004

Van der Woerd J., **Klinger Y**., Xu X., Tapponnier P., Li H., Chen W., Ma W., Coseismic and cumulative deformation along the 14 November 2001 Mw=7.9 Kokoxili earthquake (northern Tibet). *EGU meeting (abstract)*, Nice, France, April 2004.

Bowman D., King G., **Klinger Y**., Tapponnier P., Slip partitioning and the regional stress field. *AGU meeting (abstract*), San Francisco, USA, December 2003

Simonetto E., Michel R., **Klinger Y.,** Atmospheric Correction in Differential SAR Interferometry: Application to the Interseismic Deformation along the Levantine Fault. *IGARSS (abstract),* Toulouse, France, 21-25 July 2003.

Xu, X.W. ; Chen, W.B.; Ma, W.T.; Van der Woerd, J.; **Klinger, Y**.; Tapponnier, P.; King, G.; Zhao, R.B.; Li, J., Re-Evaluation of Co-Seismic Strike-Slip and Surface Rupture Length of the 2001 Kunlunshan Earthquake, Northern Tibetan Plateau, China. *EGS-AGU-EUG (abstract)*, Nice, France, April 2003.

King, G. ; **Klinger, Y**., Bowman, D.; Tapponnier, P., Slip Partitioned Surface Breaks for the 14 November 2001, Mw 7.8 Kokoxili Earthquake. *EGS-AGU-EUG (abstract)*, Nice, France, April 2003.

Klinger, Y. ; Van der Woerd, J.; Tapponnier, P.; Xu, X.W.; King, G.; Chen, W.B.; Ma, W.T.;

Peltzer, G.; Bowman, D., Detailed strip map of the Kokoxili earthquake rupture (Mw 7.8, 14/11/01) from space. *EGS-AGU-EUG (abstract)*, Nice, France, April 2003.

Li, H. ; Qi, X.; Zhu, Y.; Yang, J.; **Klinger, Y**.; Tapponnier, P.; Van der Woerd, J., Coseismic ruptures of the 14/11/2001, Mw=7.8 Kokoxili earthquake near Hongshui Gou. *EGS-AGU-EUG (abstract)*, Nice, France, April 2003.

Lasserre, C. ; Peltzer, G.; Van der Woerd, J.; **Klinger, Y**.; Tapponnier, P., Coseismic deformation from the Mw=7.8 Kokoxili, Tibet earthquake, from ERS InSAR data. *EGS-AGU-EUG (abstract)*, Nice, France, April 2003.

Rivera, L. ; van der Woerd, J.; Tocheport, A.; **Klinger, Y**.; Lasserre, C., The Kokoxili, November 14, 2001, earthquake: history and geometry of the rupture from teleseismic data and field observations. *EGS-AGU-EUG (abstract)*, Nice, France, April 2003.

Daeron M., **Klinger Y**., Tapponnier P., Elias A., Gasse F., Sursock A., Brax M., Jacques E., Nemer T., Lake beds in the Yammouneh basin (Lebanon) record more than 12000 Yr of seismic history on the Levant Fault. *EGS-AGU-EUG (abstract)*, Nice, France, April 2003.

Elias A., Tapponnier P., Jacques E., Daeron M., **Klinger Y**., Sursock A., Quaternary deformation associated with the Tripoli-Roum thrust, and the rise of the Lebanese coast. *EGS-AGU-EUG (abstract)*, Nice, France, April 2003.

Rockwell T., Aksoy E., Ferry M., **Klinger Y**., Langridge R., Meghraoui M., Meltzner A., Ragona D., Seitz G., Ucarkus G., Paleoseismic record of surface ruptures of the western third of the north anatolian fault :implications for fault segmentation models. *EGS-AGU-EUG (abstract)*, Nice, France, April 2003.

Van der Woerd, J. ; **Klinger, Y**.; Tapponnier, P.; Xu, X.; Chen, W.; Ma, W.; King, G., Coseismic offsets and style of surface ruptures of the14 November 2001 mw=7.8 Kokoxili earthquake (northern Tibet). *EGS-AGU-EUG (abstract)*, Nice, France, April 2003.

Lassere C., Pelzer G., Van der Woerd J., **Klinger Y**., Coseismic deformation from the Mw=7.8 Kokoxili, Tibet earthquake, from ERS InSAR data. *EOS (abstract) AGU 2002*

Liu J., **Klinger** Y., Sieh K., Rubin C., Seitz G., Earthquake recurrence models : new constraints from a 3-D paleoseismic investigation across the San Andreas fault. *EOS (abstract) AGU 2002*

Friedrich A., **Klinger** Y., What controls the regular surface geometry of diffusely deforming continental regions? GSA 2002

Klinger Y., Van der Woerd J., Sieh K., Tapponnier P., Ryerson F.J., First long term slip rate along the San Andreas fault based on 10Be-26Al surface exposure dating : The Biskra Palm site, 23mm/yr for the last 30,000 yrs. EGS (abstract), Nice, Avril 2002

Van der Woerd J., Meriaux A.S., **Klinger** Y., Tapponnier P., Ryerson F.J., Gaudemer Y., The 14th november 2001 Mw 7.8 Kokoxili earthquake in northern Tibet (Qinghai, China), EGS (abstract), Nice, avril 2002

Van der Woerd J., **Klinger** Y., Sieh K., Tapponnier P., Ryerson F.J., First long term slip rate along the San Andreas fault based on 10Be-26Al surface exposure dating : The Biskra Palm site, 23mm/yr for the last 30,000 yrs. *EOS (abstract),* AGU 2001

Klinger Y., Liu J., Sieh K., Rubin C., Slip behavior of the San Andreas Fault through several earthquakes, EUG 11 (abstract), Strasbourg, 2001

Rockwell, T.K., B. Akbalik, A. Akoglu, E. Aksoy, A. Barka, D. Dier, M. Ferry, Y. **Klinger**, R. Langridge, M. Meghaoroui, A. Meltzner, D. Ragona, D. Satir, G. Seitz, and G. Ucarkus. Results of Paleoseismic Studies After the 1999 Izmit Earthquake: Implications for Seismic Hazard to Istanbul. EUG 11 (abstract), Strasbourg, 2001

Rockwell T., Lindvall S., Dawson T., Langridge R., Lettis W., **Klinger** Y., Lateral Offsets on Surveyed Cultural Features Resulting From the 1999 Izmit and Duzce Earthquakes, Turkey. *Seis. Soc. Am*. (abstract), 2000

Rockwell, T K; Barka, A; Seitz, Gordon; Ragona, Daniel; Aksoy, E; **Klinger**, Y; Meltzner, Aron; Meghaoroui, M; Dier, D; Langridge, R; Ukarcus, G; Akoglu, A; Ferry, M; Akbalik, A; Satir, D. Paleoseismology of the North Anatolian Fault east and west of the Marmara Sea; implications for seismic hazard to Istanbul. *Geol. Soc. Am*. (Abstract), vol.33, no.3, pp.80, April 2000

Klinger Y., Dawson T., Akoglu A., Gonzales T., Meltzner A., Sieh K., Rockwell T., Barka A., Langridge R., Ragona D., Altunel E. Paleoseismic Evidence for prior ruptures similar to the August 1999 event on the North Anatolian Fault. *EOS (abstract)*, AGU, 81, 48, 2000.

Punongbayan J., **Klinger** Y. et Dorbath L. The rupture process of the 1990 Baguio Earthquake (*M*w7.8) based on broad-band body wave inversion. EUG10, Strasbourg, France, 28 March – 1 April, 1999.

Klinger Y., Avouac J.P., Bourles D., Bowman D., Reyss J.L., Tisnerat N. Late quaternary alluvial deposition and lake-level variations around the Dead Sea. EUG10, Strasbourg, France, 28 March – 1 April, 1999.

Dorbath L., Hoffstetter R., Rivera L., Shamir G. et **Klinger** Y. Microseismicity, focal mechanism and stress tensor along the Levantine fault. ESC 98, Tel-Aviv, Israël, 23-28 August 1998, 1998.

Klinger Y, Michel R., Avouac J.P. and Dorbath L. Investigation of the *M*w=7.3 Aqaba earthquake of Nov. 22, 1995 from seismology and interferometry. EGS 98, Nice, France, 20-24 April 1998, 1998.

Klinger Y., Avouac J.P. and Abou Karaki N. Sismotectonics of Wadi Araba Fault (Jordan). EGS 97, Vienna, Austria, 21-25 April, 1997.

Klinger Y., Rivera L., and Maurin J.C. The Gulf of Aqaba Earthquake of November 22, 1995 : Bodywave inversion, aftershocks and field observations. EUG 9, Strasbourg, France, 23-27 March, 1997.

Publications dans des revues à comité de lecture :

21/ Liu J., **Klinger** Y., Xu X., Lasserre C., Chen G., Chen W., Tapponnier P., Zhang B., Millenial recurrence of large earthquakes on the Haiyuan fault near Songshan, Gansu province, China. *Bull. Seis. Soc. Am.*, 97, 1B, 14 – 34, 2007.

20/ Hofstetter R., **Klinger** Y., Abdel-Qader A., Rivera L., Dorbath L., Stress tensor and focal mechanisms along the Dead Sea Fault and related structural elements based on seismological data. *Tectonophysics,* **429***,* 165-181, 2007

19/ Xu X., Yu G., **Klinger** Y., Tapponnier P., Van der Woerd J., Re-evaluation of surface rupture parameters and faulting segmentation of the 2001 Kunlunshan earthquake (Mw 7.8), northern tibet plateau, China. *J. Geophys. Res.,* **111***,* B05316, doi :10.1029/2004JB003488, 2006.

18/ Van der Woerd J., **Klinger** Y., Sieh K., Tapponnier P., Ryerson F.J. and Mériaux A.S., Long-term slip rate of the southern San Andreas fault, from 10Be-26Al surface exposure dating of an offset alluvial fan. *J. Geophys. Res. ,* **111**, B04407, doi :10.1029/2004JB003559. 2006.

17/ **Klinger** Y., Michel R., King G.C.P., Evidence for a barrier model from Mw7.8 Kokoxili (Tibet) earthquake slip-distribution. *EPSL*, **242**, 354-364, 2006.

16/ Liu-Zeng, J., Y. **Klinger**, K. Sieh, C. Rubin, and G. Seitz, Serial ruptures of the San Andreas fault, Carrizo Plain, California, revealed by three-dimensional excavations, *J. Geophys. Res*., **111**, B02306, doi:10.1029/2004JB003601, 2006.

15/ Lasserre C., Peltzer G., Crampé F., **Klinger** Y., Van der Woerd J., Tapponnier P., Co-seismic deformation of the Mw =7.8 Kokoxili earthquake in Tibet, measured by SAR interferometry. *J. Geophys. R*es., **110** (B12), B12408, doi:10.1029/2004JB003500, 2005.

14/ **Klinger** Y., Xu X., Tapponnier P., Van der Woerd J., Lasserre C., King G. High-resolution satellite imagery mapping of the surface rupture and slip distribution of the Mw ~7.8, 14 november 2001 Kokoxili earthquake, Kunlun fault, northern Tibet, China. *Bull. Seis. Soc. Am.*, **95** (5),1970-1987, 2005.

13/ Li H., Van der Woerd J., Tapponnier P., **Klinger** Y., Qi X., Yang J., Zhu Y. Slip rate on the Kunlun fault at Hongshui Gou, and reccurence time of great events comparable to the 14/11/2001, Mw~7.9 Kokoxili earthquake. *EPSL*, **237**, 285-299, 2005.

12/ Daëron M., **Klinger** Y., Tapponnier P., Elias A., Jacques E., Sursock A. Sources of the large AD 1202 and 1759 near east earthquakes. *Geology*, **33**, 529-532, 2005.

11/ King G., **Klinger** Y., Bowman D., Tapponnier P., Slip-partitioned surface breaks for the Mw 7.8, 2001, Kokoxili earthquake, China. *Bull. Seis. Soc. Am.*, **95**, 731-738, 2005.

10/ Closson D., Abou Karaki N., **Klinger** Y., Hussein M.J., Subsidence and sinkhole hazard assessment in the southern Dead Sea area, Jordan. *Pageoph*, **162**, 221-248, 2005.

9/ Liu J., **Klinger** Y., Sieh K., Rubin C. Six similar, sequencial ruptures of the San Andreas Fault, Carrizo Plain, California. *Geology*, **32**, 649-652, 2004.

8/ **Klinger** Y., Sieh K., Altunel E., Akoglu A., Barka A., Dawson T., Gonzales T., Meltzner A., Rockwell T., Paleoseismic evidence of characteristic slip on the western segment of the North Anatolian fault, Turkey. *Bull. Seis. Soc. Am*., **93**, 2317 – 2332, 2003.

7/ **Klinger Y**., Avouac J.P., Bourles D., Tisnerat N., Alluvial deposition and lake-level fluctuations forced by Late Quaternary climate change: the Dead-Sea case example. *Sedimentary Geology*, **162**, 119-139, 2003.

6/ Rockwell T., Lindvall S., Dawson T., Langridge R., Lettis W., **Klinger** Y., Lateral offsets on surveyed cultural features resulting from the 1999 Izmit and Duzce earthquakes,Turkey. *Bull. Seis. Soc. Am*., **92**, 79-94, 2002.

5/ Van der Woerd J., Meriaux A.S., **Klinger** Y., Tapponnier P., Ryerson F.J., Gaudermer Y., The 14 november 2001, Mw 7.8 Kokoxili earthquake in northern Tibet (Qinghai Province, China). *Seis. Res. Lett*., **73**, 125-135, 2002.

4/ **Klinger** Y., Avouac J.P., Dorbath L., Abou Karaki N., Bourles D., Reyss J.L. Slip-rate on the Dead Sea transform fault in northern Araba valley (Jordan). *Geophy. J. Int*., **142**, 755-768, 2000.

3/ **Klinger** Y., Avouac J.P., Dorbath L., Abou Karaki N., Tisnerat N. Seismic behavior of the Dead Sea fault along Araba valley (Jordan). *Geophys. J. Int*., **142**, 769-782, 2000.

2/ **Klinger** Y., Michel R., Avouac J.P. Co-seismic deformation during the *Mw* 7.3 Aqaba earthquake (1995) from ERS-SAR interferometry. *Geophys. Res. Lett*., **27**, 3651-3654, 2000.

1/ **Klinger** Y., Rivera L., Haessler H. et Maurin J.C. Active faulting in the gulf of Aqaba : New knowledge from the *M*w 7.3 earthquake of 22 November 1995. *Bull. Seis. Soc. Am*., **89**, 1025-1036, 1999.

Publications acceptées dans une revue à comité de lecture :

Bhat H., Dmowska R., King G., **Klinger** Y., Rice J., Off-fault damage patterns due to supershear ruptures with application to the 2001 Mw 8.1 Kokoxili (Kunlun) Tibet earthquake. Sous-press *JGR*, 2006.

Daëron M., **Klinger** Y., Tapponnier P., Elias A., Jacques E., Sursock A., 12,000-year-long record of up to 14 paleo-earthquakes on the Yammoûneh fault (Levant fault system). Sous presse *BSSA*, parution prévue printemps 2007.

Elias A., Tapponnier P., Singh S., King G.C.P., Briais A., Daëron M., Carton H., Sursock A., Jacques E., Jomaa R., **Klinger** Y. Active thrusting offshore Mount Lebanon : source of the tsunamigenic, 551 AD Beirut-Tripoli earthquake. Accepté *Geology,* Mars 2007.

Autres publications

Klinger Y., Tapponnier P., La traque des anciens séismes. Dossier Pour la Science « Les éléments en furie », n°51, avril 2006.

Cansi Y. and **Klinger** Y. An automated data processing method for mini-arrays. *CSEM/EMSC Newsletter*, 11, 2-4, 1997.

7 Publications illustrant les travaux les plus importants

Sont présenté dans l'ordre du manuscrit une sélection d'articles illustrant les différents aspects de mon travail qui sont développés dans ce manuscrit.

Séismes anciens :

Séries temporelles :

Liu J., **Klinger** Y., Xu X., Lasserre C., Chen G., Chen W., Tapponnier P., Zhang B., Millenial recurrence of large earthquakes on the Haiyuan fault near Songshan, Gansu province, China. *Bull. Seis. Soc. Am.*, 97, 1B, 14 – 34, 2007.

Daëron M., **Klinger** Y., Tapponnier P., Elias A., Jacques E., Sursock A. Sources of the large AD 1202 and 1759 near east earthquakes. *Geology*, **33**, 529-532, 2005.

Daëron M., **Klinger** Y., Tapponnier P., Elias A., Jacques E., Sursock A., 12,000-year-long record of up to 14 paleo-earthquakes on the Yammoûneh fault (Levant fault system). Sous presse *BSSA*, parution prévue printemps 2007.

Déplacement co-sismiques pour les paléoséismes :

Klinger Y., Sieh K., Altunel E., Akoglu A., Barka A., Dawson T., Gonzales T., Meltzner A., Rockwell T., Paleoseismic evidence of characteristic slip on the western segment of the North Anatolian fault, Turkey. *Bull. Seis. Soc. Am.*, **93**, 2317 – 2332, 2003.

Liu-Zeng, J., Y. **Klinger**, K. Sieh, C. Rubin, and G. Seitz, Serial ruptures of the San Andreas fault, Carrizo Plain, California, revealed by three-dimensional excavations, *J. Geophys. Res.*, **111**, B02306, doi:10.1029/2004JB003601, 2006

Séismes récents :

Klinger Y., Xu X., Tapponnier P., Van der Woerd J., Lasserre C., King G. High-resolution satellite imagery mapping of the surface rupture and slip distribution of the Mw ~7.8, 14 november 2001 Kokoxili earthquake, Kunlun fault, northern Tibet, China. *Bull. Seis. Soc. Am.*, **95** (5),1970-1987, 2005.

King G., **Klinger** Y., Bowman D., Tapponnier P., Slip-partitioned surface breaks for the Mw 7.8, 2001, Kokoxili earthquake, China. *Bull. Seis. Soc. Am.*, **95**, 731-738, 2005.

Klinger Y., Michel R., King G.C.P., Evidence for a barrier model from Mw7.8 Kokoxili (Tibet) earthquake slip-distribution. *EPSL*, **242**, 354-364, 2006.

Bulletin of the Seismological Society of America, Vol. 97, No. 1B, pp. 14–34, February 2007, doi: 10.1785/0120050118

Ⓔ

Millennial Recurrence of Large Earthquakes on the Haiyuan Fault near Songshan, Gansu Province, China

by Jing Liu-Zeng, Yann Klinger, Xiwei Xu, Cécile Lasserre, Guihua Chen, Wenbing Chen, Paul Tapponnier, and Biao Zhang

Abstract The Haiyuan fault is a major active left-lateral fault along the northeast edge of the Tibet-Qinghai Plateau. Studying this fault is important in understanding current deformation of the plateau and the mechanics of continental deformation in general. Previous studies have mostly focused on the slip rate of the fault. Paleoseismic investigations on the fault are sparse, and have been targeted mostly at the stretch of the fault that ruptured in the 1920 $M \sim 8.6$ earthquake in Ningxia Province. To investigate the millennial seismic history of the western Haiyuan fault, we opened two trenches in a small pull-apart basin near Songshan, in Gansu Province. The excavation exposes sedimentary layers of alternating colors: dark brown silty to clayey deposit and light yellowish brown layers of coarser-grained sandy deposit. The main fault zone is readily recognizable by the disruption and tilting of the layers. Six paleoseismic events are identified and named SS1 through SS6, from youngest to oldest. Charcoal is abundant, yet generally tiny in the shallowest parts of the trench exposures. Thirteen samples were dated to constrain the ages of paleoseismic events. All six events have occurred during the past 3500–3900 years. The horizontal offsets associated with these events are poorly known. However, events SS3 to SS6 appear to be large ones, judging from comparison of vertical separations and widths of fault zones. The youngest event SS1 instead seems to be a minor one, probably the 1990 M_w 5.8 earthquake. Thus, four large events in 3500–3900 years would imply a recurrence interval of about 1000 years. Three events SS2 to SS4 prior to 1990 occurred sometime during 1440–1640 A.D., shortly after 890–1000 A.D. and 0–410 A.D., respectively. We tentatively associate them with the 1514 A.D., 1092 A.D., and 143 or 374 A.D. historical earthquakes. Taking 10 ± 2 m of slip for large events (SS3 and SS4), comparable to the 1920 $M > 8$ Haiyuan earthquake, their occurrence times would be consistent with the long-term 12 ± 4 mm/yr estimate of Lasserre *et al.* (1999). However, a more realistic evaluation of slip rate and its possible change with time requires a more rigorous determination of coseismic slip amounts of past earthquakes.

Online material: Trench photos with interpretation.

Introduction

The Haiyuan, Altyn Tagh, and Kunlun faults are three large, active left-lateral strike-slip faults in northern Tibet (Fig. 1a, inset). How fast these faults move is a diagnostic test of modes of deformation of the Tibet Plateau (e.g., England and Houseman, 1986; Peltzer and Tapponnier, 1988; Avouac and Tapponnier, 1993; Houseman and England, 1993; Tapponnier *et al.*, 2001). Therefore much effort has been devoted to the determination of geological slip rates during the late Pleistocene-Holocene (e.g., Zhang *et al.*, 1988; Working group on the Altyn Tagh active fault, 1992; He *et al.*, 1994, 1996; Gaudemer *et al.*, 1995; Yuan *et al.*, 1998; Lasserre *et al.*, 1999, 2002; van der Woerd *et al.*, 2000, 2002; Mériaux *et al.*, 2004, 2005) and of current Global Positioning System (GPS) geodetic rates (e.g., Bendick *et al.*, 2000; Shen *et al.*, 2001; Wang *et al.*, 2001; Chen *et al.*, 2004; Zhang *et al.*, 2004; Wallace *et al.*, 2005).

GPS-derived rates are not systematically consistent with geologic rates. For example, the 6–9 mm/yr GPS rates (Bendick *et al.*, 2000; Shen *et al.*, 2001; Zhang *et al.*, 2004; Wallace *et al.*, 2005) and the 18–27 mm/yr geologic rates

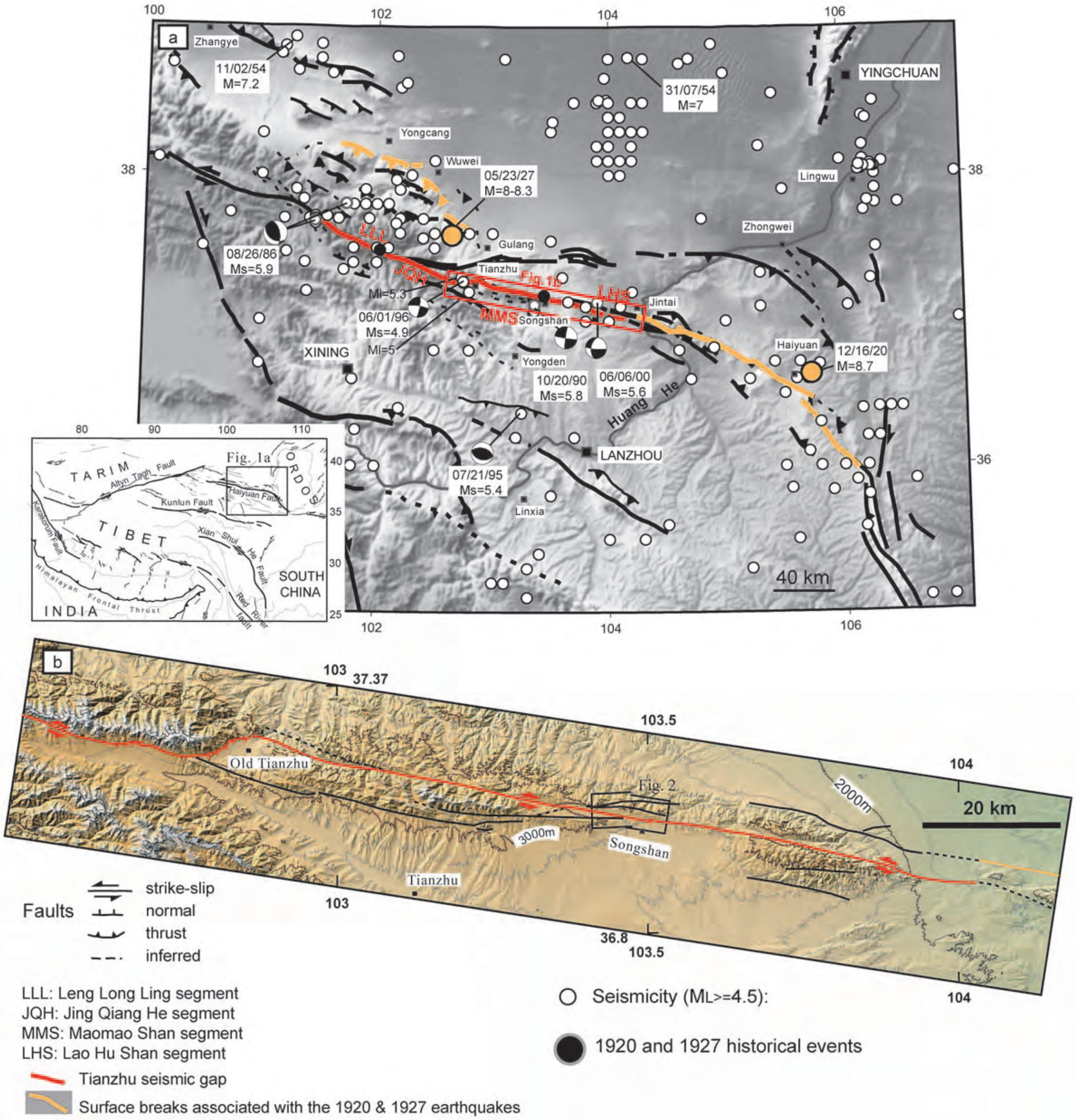

Figure 1. Tectonic setting of the Haiyuan fault. (a) Major active faults and historical earthquakes ($M_L \geq 4.5$) in the region adjacent to the Haiyuan fault. Surface ruptures associated with the 1920 and 1927 earthquakes are shown in orange. Tianzhu seismic gap is highlighted in red (after Lasserre *et al.*, 2001). (b) Surface traces of the Haiyuan fault system near Tianzhu and Songshan, superimposed on Shuttle Radar Topography Mission (SRTM) Digital Elevation Models (DEMs). Elevation contour interval is 250 m.

(Mériaux *et al.*, 2004, 2005) determined near 90° E along the Altyn Tagh fault differ by a factor of two. The GPS and Holocene rates of the Kunlun fault (11 ± 2 mm/yr), on the other hand, are now consistent within uncertainties (van der Woerd *et al.*, 2000, 2002; Wang *et al.*, 2001; Chen *et al.*, 2004; Zhang *et al.*, 2004). No definitive GPS results across the Haiyuan fault are available yet; GPS points from large-scale GPS studies in Tibet (e.g., Wang *et al.*, 2001; Zhang *et al.*, 2004) are too sparse to adequately constrain the present rate. Preliminary results from two campaign GPS profiles east and west of Songshan (Lasserre, 2000) seem to indicate a lower rate than the 8–16 mm/yr Holocene rate determined by Gaudemer *et al.* (1995) and Lasserre *et al.* (1999, 2002).

Discrepancies between GPS and geomorphic rates on active faults are not unique to Tibet. They are also found, for instance, on the Blackwater fault in southern California, the geodetic rate being four times higher than geologic rates (Dokka and Travis, 1990; Miller *et al.*, 2001; Peltzer *et al.*, 2001; Oskin and Iriondo, 2004). Understanding the relationship between GPS and geological rates is a fundamental issue. Possible reasons for such discrepancy could be incompleteness of the paleoseismologic/geologic record or assumptions about rheologic properties of the crust and fault geometry used to model GPS data. However, the most probable reason for discrepancy may be the difference in the duration of the observational period. Present GPS measurements record motions for at most a couple of decades of elastic strain accumulation, a period much shorter than the seismic cycle, whereas Quaternary geologic rates derived from dated geomorphic offset markers yield values averaged over periods of thousands of years (10–100 ka). How short-term elastic deformation is converted with time into long-term permanent unrecoverable strain is not fully understood. Short-term fault-loading rates may vary with time because of interaction between conjugate or adjacent faults (Peltzer *et al.*, 2001; Hubert-Ferrari *et al.*, 2003), prior fault-rupture history and postseismic relaxation (Stein *et al.*, 1997; Dixon *et al.*, 2000, 2003), or the rheology of the crust and mantle below the seismogenic zone (e.g., Segall, 2002; Perfettini and Avouac, 2004). Without quantitative knowledge of multiple deformation cycles, it remains difficult to understand the present-day motions and recent tectonic evolutions of most fault systems.

Because paleoseismology addresses the issue of how frequently large earthquakes occur on a fault, it provides information on repeated fault motion during several earthquake cycles, in time windows of hundreds to thousand of years. Thus, it has adequate temporal resolution to fill the gap between current GPS measurements and geomorphic studies of active faults. For this reason, we have started a multiyear project to systematically investigate the paleoseismic behavior of active faults in Tibet. As a step toward this goal, this article presents our initial effort on the Haiyuan fault.

Seismotectonic Setting

Together with the Altyn Tagh, Kunlun, and Xianshuihe faults, the ~1000-km-long, active left-lateral Haiyuan fault accommodates part of the eastward component of movement of Tibet relative to the Gobi-Ala Shan platform to the north (e.g., Peltzer *et al.*, 1988). It branches off the Altyn Tagh fault in the Qilian Shan mountain range, and continues eastward, striking about N110°. It then veers to a N140° strike east of the Yellow River, and to a ~north–south strike along the edges of the Liupan Shan, and resumes a N100° strike again before merging with the northern boundary of the Qinling Shan. By dating offset lateral moraines at a site near 101.85° E, Lasserre *et al.* (2002) determined that the Late Pleistocene average slip rate on the westernmost Haiyuan fault is 19 ± 5 mm/yr. This rate decreases to 12 ± 4 mm/yr, constrained by dated offset alluvial terraces, east of the junction between the Haiyuan and Gulang faults, with the latter probably accommodating about 4 mm/yr (Gaudemer *et al.*, 1995; Lasserre *et al.*, 1999). In less well-circulated Chinese literature, however, the left-slip rate between 102° E and 104° E is estimated to be less than 5 mm/yr using offset river terraces (He *et al.*, 1994, 1996; Yuan *et al.*, 1998). This estimate, however, is not constrained by the dating of individual offset terraces, but by using inferred ages based on regional correlation of terraces and climatic events. East of the Yellow river, Zhang *et al.* (1988) derived a rate of 8 ± 2 mm/yr, a value intermediate between those mentioned previously. Though, strictly speaking, only lower bounds of the rate were constrained at various sites, Zhang *et al.* (1988) concluded that 8 ± 2 mm/yr likely represented the possible range of the slip rate.

No consensus exists on the total offset and inception age of the Haiyuan fault. The Yellow River has an apparent left-lateral deflection of ~90 km where it crosses the fault (Fig. 1a). This has been inferred to represent the total left-lateral displacement on the fault since ~8 Ma (Gaudemer *et al.*, 1989, 1995). Based on geologic mapping along a 60-km stretch of the fault, Burchfiel *et al.* (1991) derived a total displacement of only 10.5–15.5 km and inferred that the left-lateral slip began near the end of Pliocene time (1.8 ± 0.3 Ma). Ding *et al.* (2004) used the development of pull-apart basins along the fault to argue for a total offset of ~60 km since 10 Ma.

During the past century the Haiyuan fault system (*sensu lato*) has produced two great earthquakes: the *M* 8.6 Haiyuan earthquake in 1920, along the eastern Haiyuan fault, and the *M* 8–8.3 Gulang earthquake in 1927, likely on a thrust-fault system north of the western Haiyuan fault (Fig. 1). The earthquake of 16 December 1920 produced a 237-km-long rupture, now well mapped, with a maximum left-lateral slip of 10–11 m, and claimed over 220,000 lives (Deng *et al.*, 1986; Zhang *et al.*, 1987; Institute of Geology, China Earthquake Administration and Ninxia Bureau of China Earthquake Administration, 1990). The rupture, spanning several fault segments, extended along the eastern part of the fault east of the Yellow River. The western end of the rupture was located just south of Jingtai, west of the bend of the Yellow River (Fig. 1). The mainshock was followed a week later, on 25 December 1920, by an aftershock with magnitude ~7 located less than 50 km east of the epicenter of the mainshock (Institute of Geology, China Earthquake Administration and Ninxia Bureau of China Earthquake Administration, 1990). The slip curve of this earthquake is bell shaped, with the maximum slip in the center, decreasing toward either end (Institute of Geology, China Earthquake Administration and Ninxia Bureau of China Earthquake Administration, 1990). Seven years later, the earthquake of 23 May 1927 occurred north of the Haiyuan fault, between 102° and 103°. It activated a south-dipping thrust, inferred to branch off from the Haiyuan fault at depth (Fig. 1a) (Gaudemer *et al.*, 1995; Lasserre *et al.*, 2001).

Several paleoseismic studies have been undertaken along the 1920 rupture (Zhang *et al.*, 1988; Institute of Geology, China Earthquake Administration and Ninxia Bureau of China Earthquake Administration, 1990; Ran *et al.*, 1997; Xiang *et al.*, 1998; Min *et al.*, 2000) to better assess the long-term hazard related to the occurrence of such a destructive earthquake. The earthquake history of the Haiyuan fault west of Jingtai has raised much less interest.

The 260-km-long stretch of the Haiyuan fault (marked red in Fig. 1b) is composed of four segments. Despite clear evidence of Holocene activity in the field, this section of the fault bears no historical record of a large earthquake in the past several centuries. It has therefore been considered a major seismic gap (the "Tianzhu gap") with rather high potential seismic hazard (Gaudemer *et al.*, 1995). The 1920–1927 sequence of great earthquakes has lead to speculation that the Tianzhu gap would be the next section to break, in view of growing evidence for temporal clustering of earthquakes, in domino-type occurrence on single faults or fault systems (e.g., Sykes *et al.*, 1981; Barka *et al.*, 1992, Stein *et al.*, 1997). Moreover, the pattern of modern seismicity along this part of the fault is suggestive of concentrated loading along this gap (Lasserre *et al.*, 2001), and thus heightened seismic hazard. Figure 1a shows that after 1985, *M* 5–6 earthquakes cluster near the two ends of the gap region, and in the middle (Tianzhu pull-apart basin, the largest geometrical complexity on this stretch of the fault). This pattern is in sharp contrast with the diffuse and random modern seismicity along the section that broke in 1920, where crustal stress was likely relaxed for many decades after the great earthquake.

Site Description

To better assess the seismic hazard along the Tianzhu gap, and to investigate the frequency of large-earthquake occurrence on this fault, we have conducted paleoseismic investigations at a site near 103.5° E, in a small pull-apart basin, a few kilometers north of the village of Songshan (Figs. 2 and 3). Near the Songshan site, the fault cuts through a landscape of subdued topography, mantled by loess (Fig. 3). Because of the spectacular fault trace, clear geomorphic records of cumulative offsets and the easy access, the area had been targeted by Gaudemer *et al.* (1995) and Lasserre *et al.* (1999) to determine the Holocene slip rate of the fault. A detailed description of the geologic and geomorphic setting of the site is given in Gaudemer *et al.* (1995).

The excavation site selected is located at the eastern end of a left-stepping extensional jog, along the main fault trace. Figure 3 shows a photo looking south toward the basin and trench locations. The two fault strands that bound the basin are clear in the field. The northern strand, in particular, truncates alluvial fans, forming a south-facing scarp of up to 1 m locally. At the base of the scarp, a spring currently supplies water to a 3-m-deep river channel at the southeast corner of the basin. Toward the west, however, the northern strand disappears, possibly because it is covered by fast-depositing fans, or due to diminished fault slip, or both. The southern fault strand, associated with an upslope-facing scarp up to 0.5 m in places (Figs. 3 and 4), is geomorphically clearer than the northern strand and can be continuously traced toward the west.

Deposition in the basin originates from several small catchments on the northern slope. These small drainages build fans with toes extending into the basin. Although the basin is currently drained by a stream, it could have once been closed, judging from the smooth and flat basin floor and vegetation characteristics.

Stratigraphy

We opened two trenches across the two bounding fault strands. Trench 1, ~25 m long, 4 m wide, and 3 m deep, was excavated across the southern strand. Trench 2, dug across the northern strand, provided only limited exposure due to the shallower depth of the water table, ~2.2 m below ground surface. Each wall was systematically cleaned, gridded in squares of 1 m by 1 m using a total station, and photographed. The detailed field mapping of trench exposures was performed on printouts of photos of individual grid cells.

Figures 5a and 5b show an overview of the stratigraphy exposed in trenches 1 and 2, respectively. The sediments in trench 1 are mostly composed of fine-grained sand, silt, and clay indicating a low-energy depositional facies. Pebbles and coarser clasts are uncommon, likely because of the distal position of the trench relative to feeding catchments. Based on the similarity of facies, texture, and color, we divide the stratigraphy into three sections: lower, middle, and upper sections (Fig. 5).

The upper section, about 1 m thick, mainly consists of massive homogeneous sandy silt, interpreted as loess or reworked loess (Table 1). A couple of organic-rich soil horizons have developed. Bioturbation is extensive in this section, as indicated by large burrows and deep-penetrating roots of dry-land plants.

The middle section is mainly composed of two types of layers: light yellowish brown sandy deposits and thin dark-brown to black peatlike layers (Table 1). The preservation of fine layers (5–10 cm) and the presence of dark layers suggest that, at the time the middle section was emplaced, the water table was close to the surface, preventing strong bioturbation from burrowing and growth of dry-ground vegetation.

In contrast with the middle section, the lower section is darker; alternation of dark- and light-color layers is less common. It consists of clayrich, fine deposits, and is thus more coherent. The deposits may represent continuous marsh deposits, as exposed by trenching in similar environments, which often show massive deposits of dark-gray clay with few stratigraphic markers (Rockwell *et al.*, 1986).

Figure 5c is a composite stratigraphic section illustrating the representative thickness of individual units and stratigraphic locations of charcoal samples discussed later in the text. We did not illustrate the grain size and texture of individual layers because most of the deposits are homogenous sand and silt. Color contrast is the most significant difference. Most units, from 1 through 14, are laterally continuous and can be mapped across the fault zone with confidence.

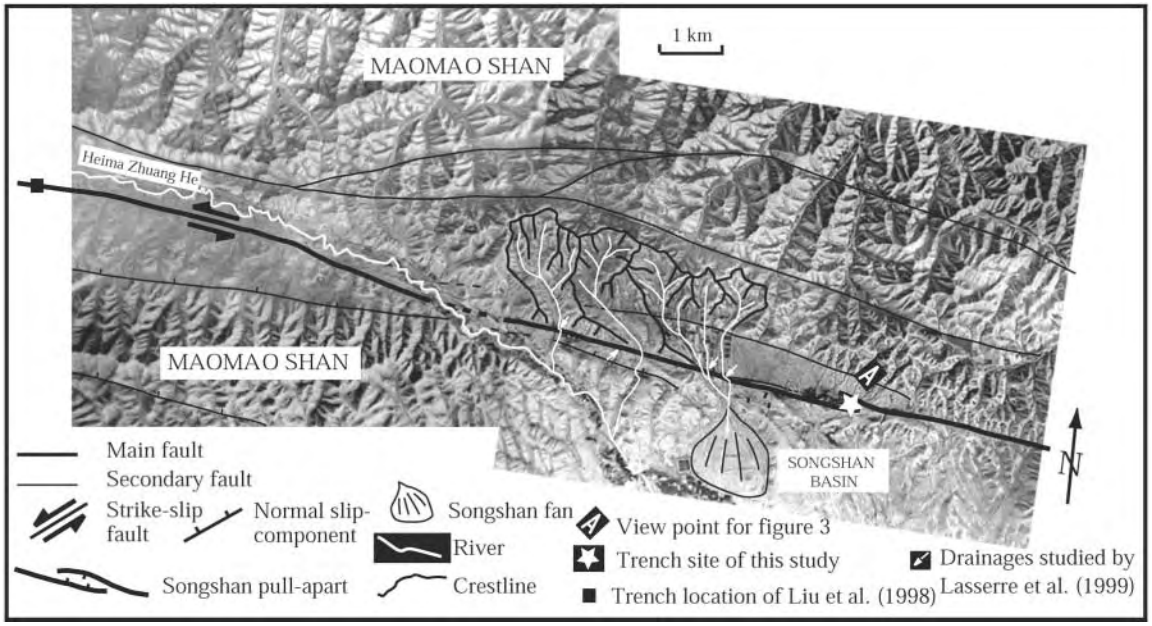

Figure 2. Map of the Haiyuan fault near Songshan, superimposed on aerial photos (modified from Lasserre *et al.*, 1999). Thick black line in the middle indicates the trace of the Haiyuan fault. Paleoseismic site described in this study (shown as a star) is located in the pull-apart basin north of Songshan village. Small drainages north of Songshan are highlighted in white, as is the Heimazhuang river, the major perennial river in this area. The locations of Lasserre *et al.*'s (1999) slip-rate determinations are indicated by white arrows. The location of a previous paleoseismic investigation site by Liu *et al.* (1998) is shown by a square, just outside the map area on the left.

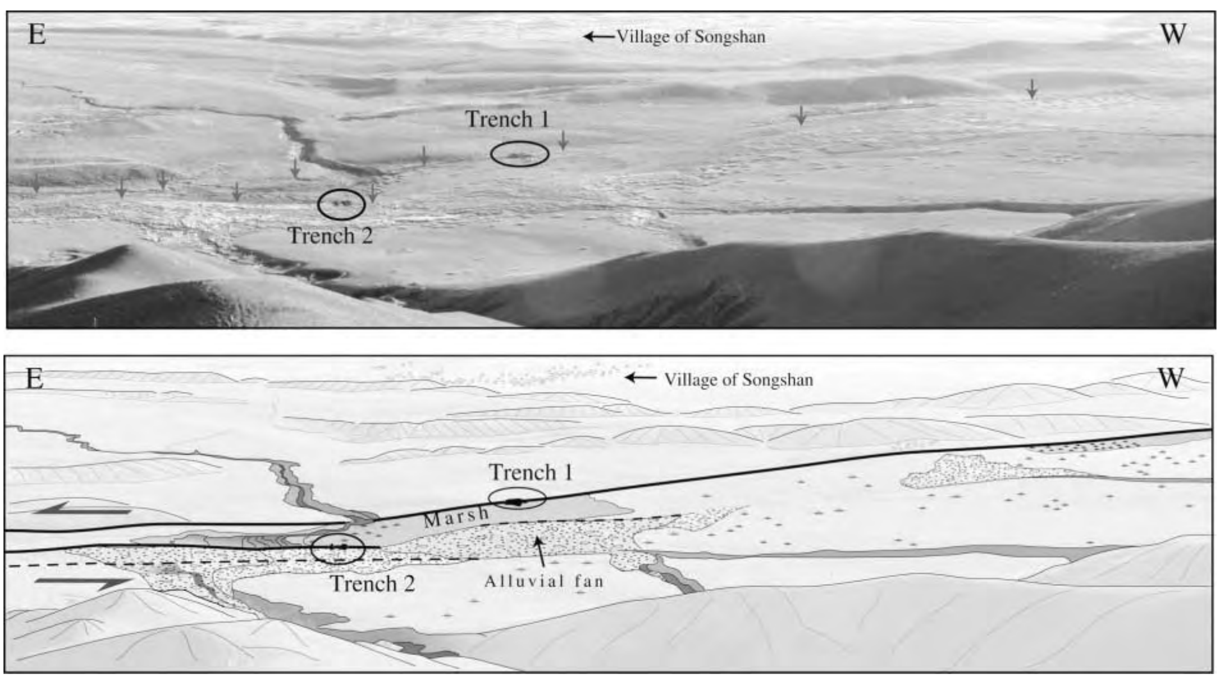

Figure 3. Mosaic of south-looking photos of the Haiyuan fault north of Songshan village and corresponding geomorphic interpretations. Locations of fault traces are indicated by red arrows. The southern strand coincides with a vegetation transition line. Trench 1 is located across the southern fault branch, and trench 2 is across the northern fault branch.

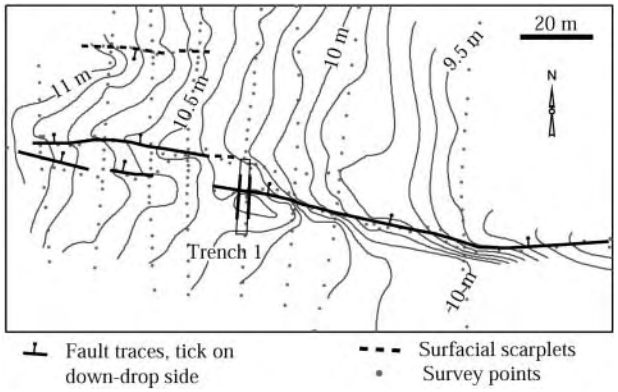

Figure 4. Topographic map derived from total station survey points (dots) near trench 1. The location of trench 1 is indicated by the rectangle in the middle. Logged portions of exposures are indicated by bold lines. In the vicinity of trench 1, the fault forms a north-facing scarp, about 0.5 m high in the east and decreasing westward. At the location of trench 1, the scarp is only about 10–15 cm high. Contour interval is 10 cm.

Correlation of units from trench 1 to trench 2 is primarily based on the identification of the three main sedimentary packages (Fig. 5c and Table 1). The transition between the top and the middle section is sharp, denoting a dramatic change from wet to dry climatic or hydrologic conditions at this location. In trench 2, the stratigraphic transition from the upper to the middle section is as sharp as in trench 1, confirming that the change from wet to dry was recorded basinwide. The one-to-one correlation of individual units is more difficult. Only the correlation of unit 2 is constrained by charcoal samples of similar age. Other unit correlations are based on qualitative observations. We reason that major gravel layers in trench 2, representing flooding periods, must be correlated with the main lighter-colored layers in trench 1. Thus, equivalents of units 5, 7, and 15 are determined. Such correlation is probable, because alternation of black-and-white thin layers between units 7 and 15 would be in the same stratigraphic position in both trenches.

Evidence of Faulting Events

In this section, we present and discuss stratigraphic evidence for six paleoearthquakes at the site. We name these events SS1 through SS6 from the youngest to the oldest.

Among various indicators for recognizing paleoearthquakes in unconsolidated sediments in a strike-slip fault setting, the best and clearest evidence of fault rupturing of the ground surface includes scarp formation, scarp-derived colluvium, in-filled and void fissures, and sand blows (e.g., Sieh, 1978; Weldon *et al.*, 1996; Fumal *et al.*, 2002). Upward fault terminations are most effective in identifying the most recent faulting event, but may not be as reliable for older events because subsequent ruptures sometimes follow the same plane and may overprint the evidence of previous events (Weldon *et al.*, 1996).

Most Recent Event (SS1)

Event SS1 appears to be a minor cracking event that probably ruptured the present ground surface (Figs. 6 and 7).

Multiple cracks on both walls of trench 1 can be traced confidently up to about 20 cm below the ground surface. The actual level of termination of these cracks, however, remains ambiguous because of loose loam near the surface. These cracks are not roots. They are not as straight and continuous as plant roots, but instead resemble *en echelon* cracks in a vertical plane. Voids at corners (Fig. 7), where the cracks change orientation, and visible clean shearing planes devoid of roots also argue for a tectonic origin. These cracks, however, show no offset in the underlying sedimentary layers. This suggests that the event corresponds to a small-magnitude earthquake, or was near the rupture termination of a somewhat larger one.

Analysis of the recent, local seismicity supports a tectonic origin for the cracks. Probably they are associated with the 20 October 1990 M_w 5.8 earthquake, whose reported epicenter was located at ~37.1° N and 103.5° E (Gansu Bureau of China Earthquake Administration, 1990; Committee for Chinese Earthquake Bulletin, 1990). This earthquake was the biggest event in Gansu province since the 1954 Shandan earthquake (M_s ~7.3). It caused severe damage (intensity VIII) in villages along a 27-km-long stretch of the Haiyuan fault, from the Heima Zhuang river (Fig. 2) eastward. The long axis of the intensity distribution had the same orientation as that of the Haiyuan fault, as did one plane of the focal mechanism (Gansu Bureau of China Earthquake Administration, 1990). Surface *en echelon* tensional cracks with up to 10 cm of opening were reported in the highest-damage area (intensity VIII), 7 km to the southeast of our paleoseismic site (Fig. 8). No exhaustive investigation was carried out to trace the extent of cracks shortly after the earthquake. Although ground fissures were observed in many places, only those in the maximum-intensity region (intensity VIII) were believed to be of tectonic origin. In the village of Songshan, which is quite close to the epicenter, there were many accounts of building damage; pillars or columns moved counterclockwise relative to the ground, most likely indicating near-field ground motion rather than far-field oscillation. The walls of the small ancient fortified city (Songshan), erected sometime during the Ming Dynasty (1368–1644 A.D.), which were mostly standing intact before this earthquake, partially collapsed (Gansu Bureau of China Earthquake Administration, 1990; Gaudemer *et al.*, 1995).

Together, the consistent reports suggest that the October 1990 earthquake may have been large enough to produce ground rupture extending several kilometers away from the epicenter. As our excavation site is located closer to the instrumental epicenter than the reported tectonic cracks, it

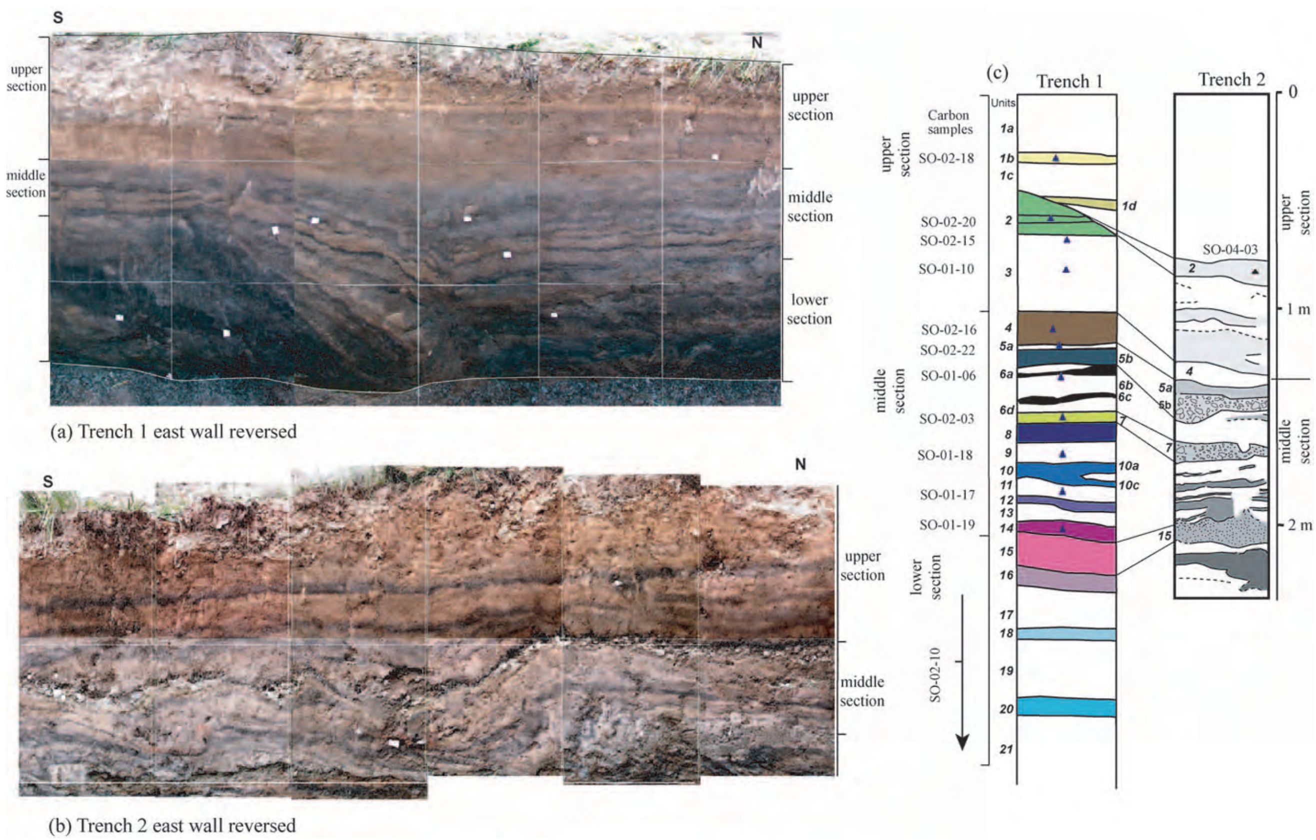

Figure 5. Photo mosaic of central section of the eastern walls of trench 1 (a) and trench 2 (b) showing the general characteristics of the stratigraphy and the tilting and warping of strata due to deformation. Stratigraphy is divided into upper, middle, and lower sections. Photos were reversed as if looking toward the west. (c) Generalized stratigraphic column of sedimentary deposits in trenches 1 and 2, and proposed correlation between the two trenches. We label units in trench 1 from 1 to 21, from top to bottom. Color coding corresponds to Figures 6 and 10. Stratigraphic position of radiocarbon samples are shown by triangles.

Table 1

Unit Descriptions from Trench 1 and 2 Exposures

	Unit No.	Trench 1	Trench 2
Upper section	1	Bioturbated silty loess and reworked loess. Subunit 1b is a distinctive thin layer, better sorted and lighter in color than units above and below. Subunit 1d is a darker organic-rich layer.	Massive bioturbated light yellowish brown sand and silt.
	2	Gray organic-rich sand and silt, containing a discontinuous carbonate layer.	Dark-gray organic-rich sand and silt.
	3	Massive yellow to brownish yellow sand and silt.	Massive yellow to brownish yellow sand and silt, with multiple dark organic-rich soil horizons.
Middle section	4	Wedge-shaped deposit of gray clayey sand and silt	
	5	5a: A thin layer of silt, on the up-thrown side of the fault. 5b: Pale-yellow silty sand, on the down-thrown side of the fault.	Clast-supported gravel layer of angular to subangular pebbles.
	6	Brownish sandy silt, locally containing dark organic-rich layers.	
	7	Pale-yellow silty sand.	Clast-supported pebbly to granular gravel in coarse sand matrix.
	8–14	Alternating dark peatlike layers (units 8, 10, 12, and 14) and light yellowish brown coarser-grained silty sand (units 9, 11, and 13).	Alternating thin, dark organic-rich layers and white to light-gray clayey silt.
Lower section	15	Gray sand and silt.	Relatively well-sorted coarse and medium sand.
	16–21	Alternating brown clayey sand and silt (units 16–20) and dark gray finer-grained clay (units 17, 19, and 21).	

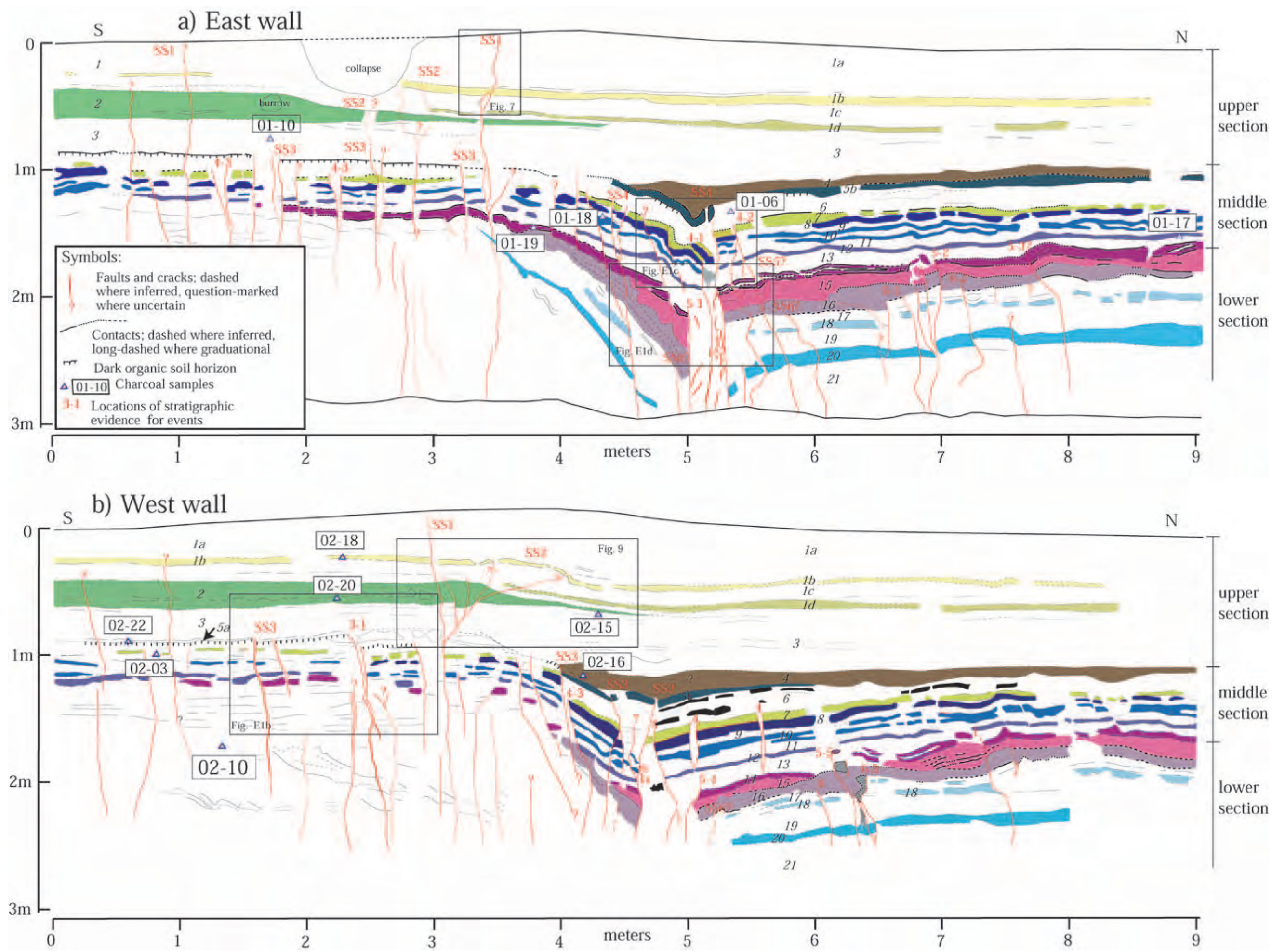

Figure 6. Logs of portions of the east (a) and west (b) walls of trench 1. Sedimentary units are indicated by different colors and are labeled numerically. Ruptures associated with six events are identified and named SS1, SS2, SS3, SS4, SS5, and SS6, from the youngest to oldest. See text for description of evidence of individual events.

seems likely that the cracks observed in the trench walls are indeed tectonic cracks due to the 1990 event.

Penultimate Event (SS2)

Evidence for Event SS2 in Trench 1. The next youngest deformation event we identify prior to event SS1 occurred when unit 1b was at or near the surface. The clearest evidence for event SS2 in trench 1 is the convex-upward, bulging out of unit 1b in the fault zone, between meters 3 and 4 in the western wall (Figs. 6b and 9). Unit 1b is a distinctive 5-cm-thick layer of silty fine sand that is continuously traceable on both walls of trench 1. It is lighter in color and better sorted than the sediment layers below and above. It is likely an aeolian deposit, or less likely a flood deposit. The convex-upward shape of unit 1b near meter 4 is probably an indication of folding. Below unit 1b, faults exhibit a flowerlike structure offsetting both the upper and lower surfaces of unit 2 and possibly unit 1d as well. The offset is not large, no more than a couple of centimeters in a vertical plane. The underlying layers (i.e., unit 5 and those below) also do not display large vertical separation. This pattern is typical of *en echelon* ground ruptures forming small pressure ridges at the surface with only strike-slip motion at depth (e.g., Yeats *et al.*, 1997; Barka *et al.*, 2002).

Unfortunately, we cannot be sure that the bulging of unit 1b is an indication of coseismic deformation because of the bulging is quite small and subtle. Alternatively, unit 1b may have been deposited after event SS2 and mantled the scarp. In the eastern wall exposure, a few cracks seem to extend through layer 1b, which would support the former interpretation. But this is not conclusive because plants can take advantage of pre-existing cracks. The key area in the east wall was accidentally destroyed during excavation (Fig. 6a).

Evidence for SS2 in Trench 2. Stronger stratigraphic evidence for SS2 is found in trench 2 (Fig. 10 and Ⓔ Fig. E1a in the online edition of BSSA). Fissures cut through unit 2,

Figure 7. Enlarged photo of eastern wall of trench 1 showing that the crack associated with the youngest event SS1 (outlined by black arrows) appears to extend to the ground surface. We believe this event is the 1990 M_w 5.8 earthquake. See location in Figure 6.

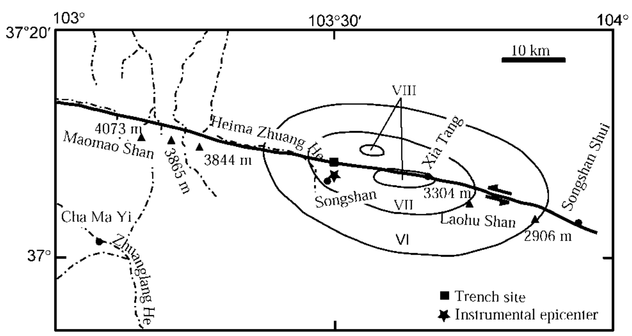

Figure 8. Map of intensity associated with the 1990 M_w 5.8 earthquake. Adapted from Gansu Bureau of China Earthquake Administration (1990).

down-drop blocks from unit 2, and fissure fills are clearly associated with this event. The organic-rich layer, unit 2, is disrupted with a few centimeters of vertical separation. Sediments from this layer form part of the colluvium that fell into the fault zone. A cobble, about 6–7 cm in diameter, located in the fault zone, does not correspond to any fine-grain-sized unit characteristic of the upper section in trench 2, and has probably been dragged into the fault zone. The fissure is filled with sediments lighter in color, most likely from layers above unit 2. The fissure fill and colluvium suggest that the event horizon is slightly above unit 2. There is also indication of strike-slip motion along the fault in trench 2. The thickness of unit 2 changes across the fault zone, being thicker on the northern side than on the southern side (Fig. 10).

Event SS3

Evidence for Event SS3 in Trench 1. Unlike events SS1 and SS2, event SS3 is associated with a wide zone of deformation, 4 to 5 m in total, which suggests that event SS3 probably had larger offset than SS1 and SS2. Figure 6 shows that event SS3 involves both shearing on the main fault zone and offsets on multiple secondary faults between meters 1 and 4. Some of the best evidence for event SS3 is preserved along the southern half of trench 1, outside the main fault zone (denoted "3-1" on the west wall, Fig. 6b Ⓔ and Fig. E1b in the online edition of BSSA). Unit 5a buries a dark organic soil horizon on top of unit 6. The soil horizon is easily traced in both the east and west walls. Unit 5a, together with the soil horizon beneath it, is sharply offset by three secondary fissures, with about 7 cm of vertical separation. Material from unit 3, a massive loess layer, usually fills these fissures, delineating open cracks up to 1 m deep. At approximately meter 2.5 on the west wall (Fig. 6b and Ⓔ Fig. E1b in the online edition of BSSA), a secondary fault limits chunky deposits that appear to be broken pieces of the underlying layers. These blocks are probably coseismic colluvium, transported here from locations out of the section plane. They are separated by infilling of unit 3 sediments.

Combining the deformation on the main fault and secondary faults, the overall effect of event SS3 is a down-drop of the block located north of the main fault zone, together with northward tilting and dragging of unit 5b and of all the units below, most prominently south of the main fault. The event horizon should be slightly above unit 5a because units 5a and 5b are disrupted. Unit 4, a wedge-shaped deposit of light-gray clayey sand and silt north of the main fault zone, which thickens above it, is likely the postevent in-fill of the depression produced by event SS3.

Evidence for Event SS3 in Trench 2. Evidence for event SS3 in trench 2 is different from the cracks exposed in trench 1. The stratigraphy shows strong ductile-style folding (Fig. 10). This style of deformation would be consistent with strong ground shaking in water-saturated deposits during an earthquake. Unit 5, a gravel layer, is the top most deformed layer. Layers located above are much less contorted and clearly drape unit 5. Hence, the event horizon associated with event SS3 is probably at, or slightly above, unit 5. It would be ambiguous to locate the position of ground surface if units 1 through 5 were subaqueous soft sediments when the earthquake occurred (e.g., Weldon *et al.*, 1996). This is not the case at the Songshan site, because units 1 through 4 consist of subaerial deposits. They are loess and reworked loess with multiple soil horizons developed subaerially.

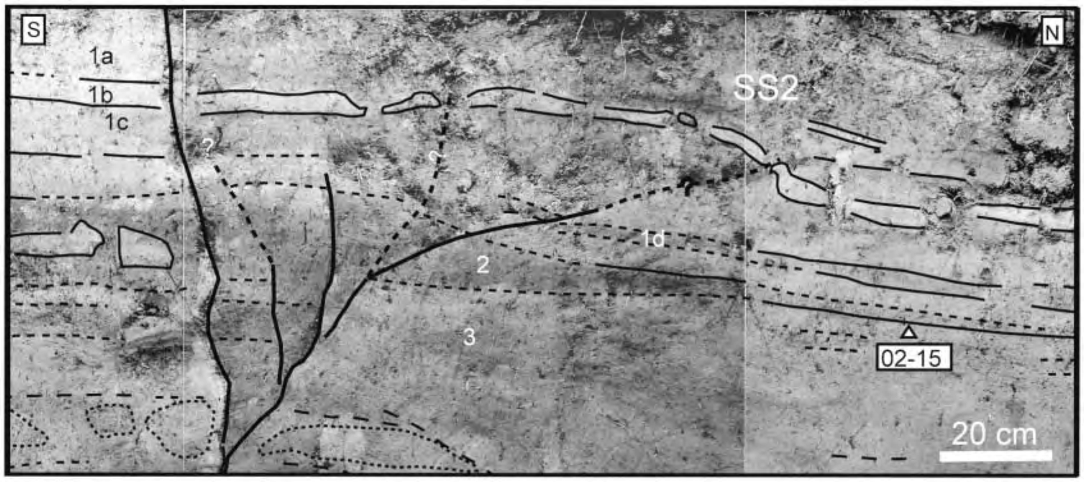

Figure 9. Photo mosaic and interpretations of a portion of the western wall of trench 1 showing the evidence for event SS2. See location in Figure 7.

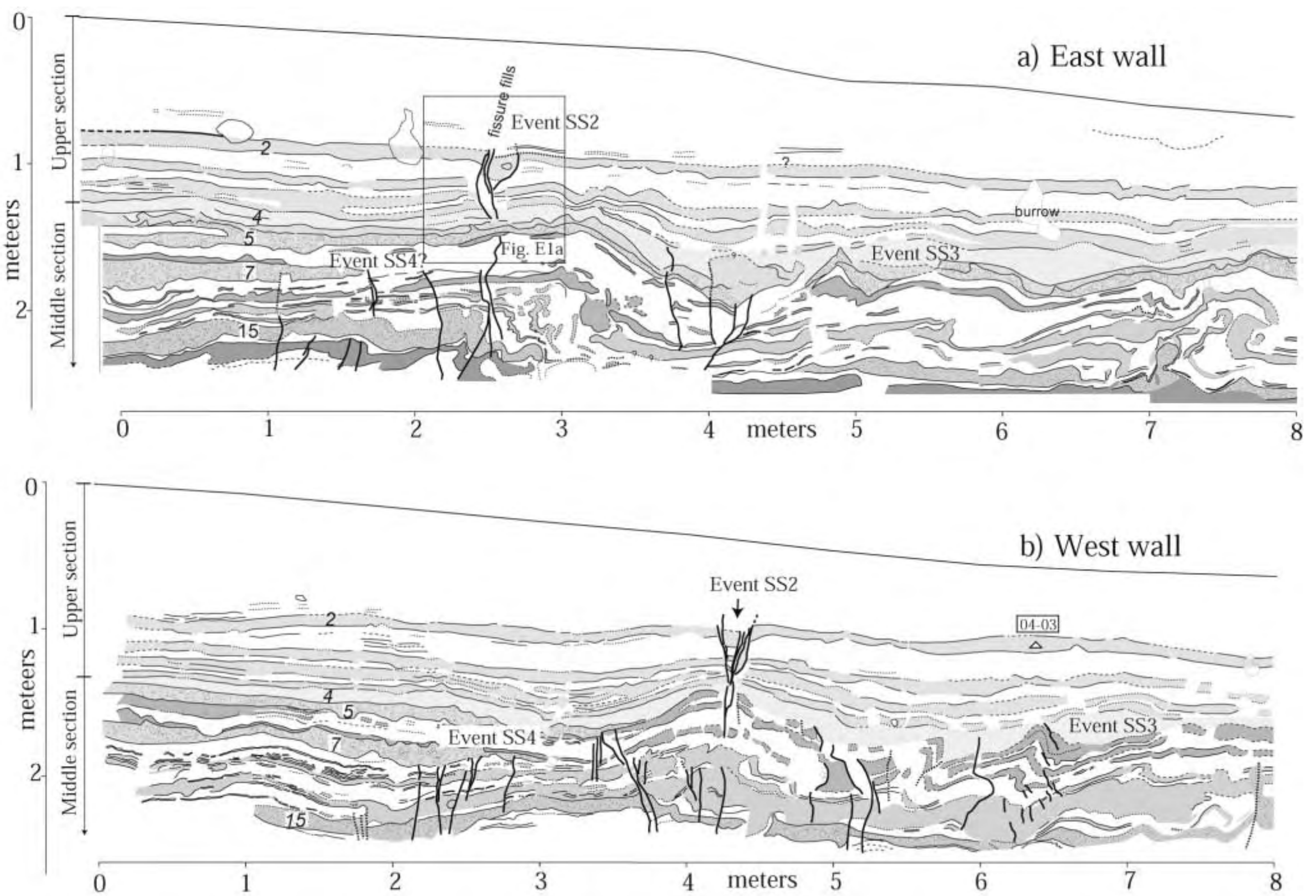

Figure 10. Logs of the east (a) and west (b) walls of trench 2 depicting the stratigraphy and deformation associated with events SS2, SS3, and SS4. See legend in Figure 6 for explanation of symbols.

Coarser grain size, the lack of clay in the sediments, and deeply penetrating plant roots corroborate this subaerial interpretation.

Event SS4

Fault breaks associated with event SS4 disrupt the upper surface of unit 7 over a width of several meters and terminate within unit 6 of trench 1 (Fig. 6). Multiple strands terminate at this stratigraphic position. The strongest evidence for the event is within the fault zone on the east wall, at meter 5, where a major shear plane separates the coherent strata of units 7 to 12 to the left from a mélange of sheared material to the right (designated "4-1" on Fig. 6a and Ⓔ Fig. E1c in the online edition). The fault is capped by a small duplex of units 7 and 8, thrust on top of one another, which suggests that this layer was at or very near the ground surface when rupture occurred. Additional evidence includes a fault strand north of the main fault (designated "4-2" in Fig. 6a and Ⓔ Fig. E1c in the online edition) offsetting unit 7 by a few centimeters; and at least two open cracks south of the main fault (designated "4-3" in Fig. 6a) terminating in the same stratigraphic position.

Although events SS3 and SS4 are only separated by unit 5 and 6 deposits with only about 40 cm in total thickness, multiple lines of evidence suggest that they are distinctly separate events. First, at locations 4-1 and 4-2, unit 7 and underlying units are warped more and thus deformed more than the overlying unit 5. This difference between unit 5 and underlying unit 7 requires an event horizon after the deposition of unit 7. Second, at location 4-3, the stratigraphic contacts show clearly that the open cracks of event SS4 terminate below the sharp soil horizon developed in the top of unit 6, whereas fault strands associated with event SS3 offset this horizon. Inside the cracks, fissure fills of event SS4 consist of material of unit 6, darker than those in the cracks of event SS3. Third, the change in thickness of unit 6 across the fault on the west wall is consistent with a pre-existing scarp, presumably due to event SS4 (Fig. 6b). Also, unit 6 is thickest near the main fault zone. It thins out northward away from the main fault zone on the down-thrown north side. Southward, it stops abruptly against the southern-bounding fault and cannot be traced farther away from the fault on the up-thrown side. Thus the wedge-shaped thickness of unit 6 suggests it filled a sag created by a north-facing fault scarp. The subsequently deposited unit 5 has similar variation in thickness, but it is less conspicuous because of the more subdued scarp relief after filling by unit 6 on the north side.

Like event SS3, event SS4 in trench 2 manifests itself by sediment warping and folding in both walls. The event horizon of SS4 is less clear in trench 2 because of the superposition of deformation due to event SS3. Event SS4 probably occurred after unit 7 was deposited, because the layers below unit 7 are more deformed than units above.

Event SS5

Evidence for event SS5 is manifested in several places in trench 1. Fault traces from event SS5 break unit 14 (Fig. 6). On the east wall, a fault separates unit 14 and underlying units on the south side from the heterogeneous shear-zone fabric on the north side ("5-1" on Fig. 6a and Ⓔ Fig. E1d in the online edition). The small fissures cracking unit 12 and higher do not seem to connect to the main crack-breaking unit 14 at location 5-1. Hence the fault ending at 5-1 seems to be capped by unit 12. Outside the main fault zone, a few minor faults, which terminate above the upper surface of unit 14 ("5-2" and "5-3"), provide additional evidence for event SS5 on the eastern wall. Evidence for event SS5 is also visible on the west wall, both within the main fault zone ("5-4") and beyond ("5-5"). The event horizon associated with event SS5 is probably at or above unit 14.

Event SS6

Evidence for event SS6 is best preserved at the northern end of trench 1. On the east wall, several minor faults break unit 16 ("6-1" and "6-2" on Fig. 6a), producing a south-facing scarp and the greater thickness of unit 15 between this scarp and the main fault zone. On the western wall, unit 16 also displays evidence of event SS6. A mound delineated by the thickness variation of unit 16 ("6-3" on Fig. 6b) probably represents a pressure ridge. Undisturbed unit 15 lies above unit 16, smoothing out the irregular topography after event SS6. The event horizon of SS6 is clearly unit 16.

Evidence for event SS6 at the main fault zone is less straightforward because of the large amount of shear due to later events. However, the angular unconformity between units 14 and 16 suggests that motion in the main fault zone caused these units to tilt during event SS6. As will be discussed later, reconstruction of the stratigraphy before and after event SS6 helps to elucidate this effect.

Radiocarbon Dating of Earthquakes

Numerous charcoal fragments were found in both trenches, yet most were small. Thirteen samples were sent for accelerometer mass spectrometer (AMS) dating at Universiteit Utrecht in the Netherlands and Laboratoire de Mesure du Carbone 14 (LMC 14) in France. Radiocarbon dates are summarized in Table 2 and Figure 11. The stratigraphic positions of the samples are shown in Figures 5, 6, and 10.

Figure 11a plots the ages of charcoal samples in trench 1 in stratigraphic order. Most samples yielded ages younger than 3000 years B.P. Two samples, SO-01-19 and SO-02-18 (Table 2 and Figs. 5 and 6), collected 0.3 m and 2.0 m below the surface yielded ages of 7080–7480 B.C. and 5840–6170 B.C., respectively. They are excessively older than the rest of samples and are most probably reworked charcoal fragments. Therefore we choose to not use them for age control. Two samples, SO-02-22 and SO-02-20, appear to be several

Table 2
Radiocarbon Samples

Sample	Laboratory No.	$\delta^{13}C$ (p. mil)*	Radiocarbon Age (Years B.P. $\pm$ σ)	Calendar Years[†] (cal B.P.) 1 σ	Calendar Years[†] (cal B.P.) 2 σ	Mass (mg)	Description	Unit Sampled
SO-01-06	12963[‡]	−32.6	1752 ± 44	230–350 A.D.	130–160 A.D.	0.260	small piece of charcoal	6b, trench 1
				360–390 A.D.	170–200 A.D.			
					210–410 A.D.			
SO-01-10	12964[‡]	−28.6	1180 ± 50	770–900 A.D.	710–750 A.D.	0.39	angular charcoal fragment, solid	3, trench 1
				920–940 A.D.	760–990 A.D.			
SO-01-17	12965[‡]	−26.3	2841 ± 38	1050–920 B.C.	1130–900 B.C.	0.380	charcoal	11, trench 1
SO-01-18	12966[‡]	−22.2	2674 ± 38	970–950 B.C.	1000–820 B.C.	2.23	charcoal	9, trench 1
				930–890 B.C.				
				880–830 B.C.				
SO-01-19	12967[‡]	−26	8258 ± 45	7450–7390 B.C.	7480–7130 B.C.	1.56	charcoal	14, trench 1
				7380–7290 B.C.	7100–7080 B.C.			
				7270–7180 B.C.				
SO-02-03	001603[§]	−24.3	1915 ± 45	20–140 A.D.	0–230 A.D.		charcoal	7, trench 1
SO-02-10	001602[§]	−27.4	3410 ± 45	1860–1840 B.C.	1880–1790 B.C.		charcoal	below unit 16, trench 1
				1770–1620 B.C.	1780–1600 B.C.			
					1570–1530 B.C.			
SO-02-15	12968*	−21.4	989 ± 35	990–1040 A.D.	980–1160 A.D.	1.140	small pieces of broken charcoal grain	3, trench 1
				1090–1120 A.D.				
				1140–1160 A.D.				
SO-02-16	12969[‡]	−23.3	1338 ± 49	650–720 A.D.	600–780 A.D.	0.180	tiny piece of charcoal, treated only with acid	4, trench 1
				740–770 A.D.				
SO-02-18	12970[‡]	−22.9	7150 ± 60	6160–6150 B.C.	6170–6130 B.C.	2.26	large piece of charcoal, solid	1b, trench 1
				6080–5980 B.C.	6110–5880 B.C.			
				5950–5920 B.C.	5860–5840 B.C.			
SO-02-20	12971[‡]	−22.1	393 ± 36	1440–1520 A.D.	1430–1530 A.D.	0.610	charcoal	2, trench 1
				1590–1620 A.D.	1550–1640 A.D.			
SO-02-22	12972[‡]	−23.2	1102 ± 28	895–925 A.D.	890–1000 A.D.	0.690	charcoal	5, trench 1
				940–985 A.D.				
SO-04-03	12973[‡]	−23.4	723 ± 38	1260–1300 A.D.	1220–1310 A.D.	2.30	charcoal	2, trench 2
				1370–1380 A.D.	1350–1390 A.D.			

*$\delta^{13}C$ (ppm), ratio of $^{13}C/^{12}C$ with respect to PDB reference.
[†]Calculated using OxCal program Version 3.5 (Ramsey, 2000), atmospheric data from Stuiver *et al.* (1998).
[‡]Universiteit Utrecht, Accelerator Mass Spectrometry facility, Utrecht, Netherlands. All samples were pretreated using AAA (acid-alkali/acid) method, except SO-02-16, which was treated only with acid.
[§]Laboratoire du Mesure du Carbone (LMC) 14, France.

hundred years younger than implied by stratigraphic ordering. In particular, sample SO-02-22 has an inverse stratigraphic age compared to two samples in overlying sediments. We have no reason to doubt the validity of this sample's age, a larger (0.6 mg) sample than the two preceding and retrieved from a well-defined sedimentary layer. Because of the detrital nature of our samples, the most plausible explanation is that older overlying samples may be reworked fragments. Discordant or stratigraphic inverse ages of detrital charcoal are common (e.g., Blong and Gillespie, 1978; Nelson, 1992; Grant and Sieh, 1993, 1994; Rubin and Sieh, 1997; Vaughan *et al.*, 1999; Rockwell *et al.*, 2000; Fumal *et al.*, 2002; Liu-Zeng *et al.*, 2006).

In Figure 11b, stratigraphic positions of event horizons are shown as filled rectangles. The horizontal dimensions of the rectangles indicate the age ranges of the events. They are loosely bracketed by the dates of samples from immediately older and younger units.

As previously discussed, we interpret event SS1 to be the 1990 M_w 5.8 earthquake. Event SS2 occurred after the deposition of sample SO-02-20, which has a calibrated age of 1430–1640 A.D. (2σ). We can further infer that event SS2

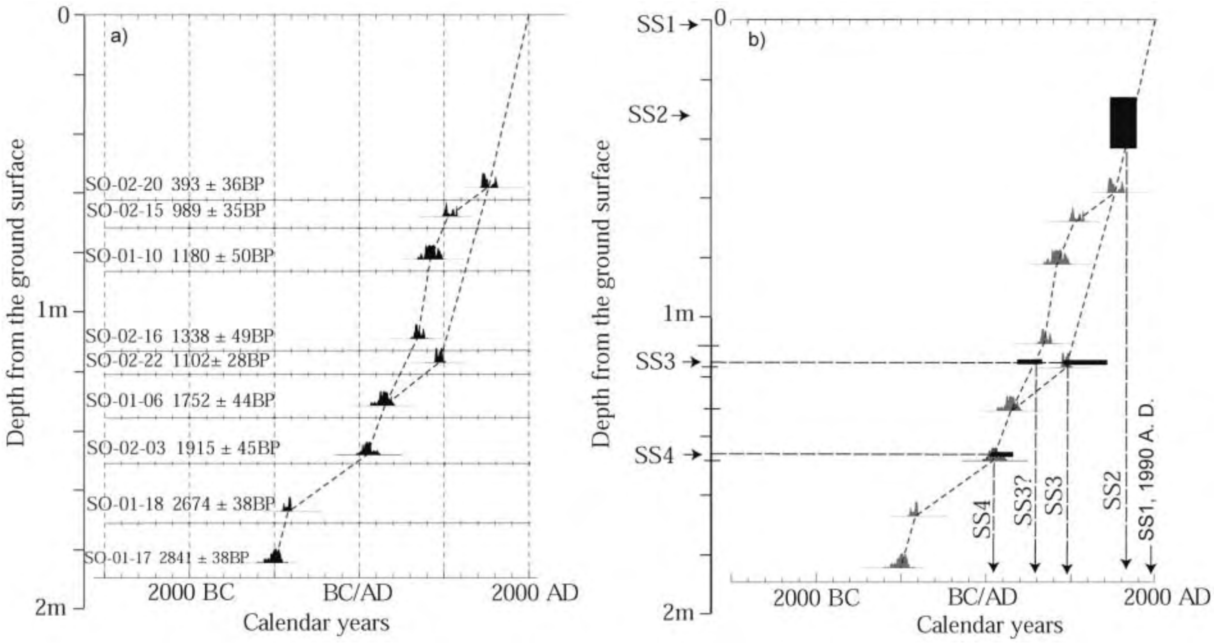

Figure 11. (a) Radiocarbon date ranges of samples from upper 2 m of sediments in trench 1, plotted in stratigraphic order. Two anomalously old samples, SO-01-19 and SO-02-18, probably due to reworking, are not included. Apparent stratigraphic age inversion of samples at about 1 m depth is probably due to reworked samples. (b) Constrained and inferred ages of four youngest events. Arrows and letters mark the stratigraphic levels of events. Horizontal bars indicate the bounds of event ages. The thickness of the box for event SS2 indicates uncertainty in the event horizon.

probably occurred before the Ming fortified city in Songshan was built, because the city walls were intact until the 1990 earthquake (Gansu Bureau of China Earthquake Administration, 1990; Gaudemer *et al.*, 1995). Because sample SO-02-20 has an age range almost the same as the duration of the Ming dynasty (1368–1644 A.D.), this age range probably includes the time of event SS2. Two interpretations of age for event SS3 are possible (Fig. 11b). Our preferred one is that the age of event SS3 is loosely bound by samples SO-02-22 and SO-02-20. It occurred some time after 890–1000 A.D. and before 1430–1640 A.D., but probably shortly after the deposition of unit 5a. Because unit 5a is thin, 2–4 cm, and the average sedimentation rate is rather fast (0.5–1 mm/yr as indicated by Fig. 11), event SS3 probably occurred in the eleventh or twelfth century. Another possibility for the age of event SS3, though not our preferred interpretation, is between the age bounds provided by samples SO-01-06 and SO-02-16. In keeping with this scenario, event SS3 would have occurred sometime after 130–410 A.D. and before 600–780 A.D. Using the OxCal program (Ramsey, 2000), we can infer a 2-σ range of 370–650 A.D. The timing of event SS4 is relatively well constrained by samples SO-02-03 and SO-01-06. In other words, it occurred sometime after 0–230 A.D., and before 130–410 A.D. Therefore, a conservative estimate of the age range for event SS4 is 0–410 A.D.

Sample SO-02-10, not shown in Figure 11, provides bounds on the ages of older events. It is located in an indistinctive unit on the up-thrown side of the fault, about 0.6 m below unit 14 (Fig. 6b). Its relation with units 15 though 21, however, is unclear because the stratigraphy on the up-thrown side is not well preserved enough to correlate individual layers with confidence. The 0.6-m depth of sample SO-02-10 below unit 14, if one assumes a similar sedimentation rate on both sides of the fault, suggests that the sample would date unit 19. This assumption is unlikely, however. The sedimentation rate is rather lower on the southern side, making the sample correlative to a deeper unit. In any case, sample SO-02-10 is located in sediments deformed by SS6 and therefore provides the lower-bounding age of our oldest event SS6. Its event horizon is unit 16, which has a 2-σ age range of 1530–1880 B.C. Thus, we conclude that all six events occurred during the past 3500–3900 years.

Discussion and Conclusions

Excavations at the Songshan pull-apart site expose stratigraphic evidence for six events during the past 3500–3900 years. Of these events, the four oldest are probably associated with large horizontal offsets, based on comparison of vertical separations and fault-zone widths. Event SS1 appears instead to be the minor, historical, 1990 M_w 5.8 earthquake. Thus, the four large events within 3500–3900 years would imply a recurrence interval of about 1000 years. Note that events with minor disturbance, such as event SS1 and perhaps SS2, could have occurred, but corresponding evidence cannot be retrieved because of overprinting of larger events. Thus, only the most recent of such events are recognizable. Therefore, we do not consider these smaller events in our estimate of earthquake recurrence. Charcoal samples within the uppermost 2 m of sediments indicate that, in addition to the 1990 earthquake and SS2, two large events occurred after 0–230 A.D. This is consistent with an average recurrence interval of about 1000 years.

Offsets of Events at the Site

Our trenching program at Songshan was not designed to determine the horizontal offsets of specific events. Nevertheless, based on vertical offsets, amounts of disruption and widths of deformation zones associated with each event, we may infer qualitatively the relative sizes of events.

Four of the events, SS3, SS4, SS5, and SS6, appear to be large surface-rupture earthquakes. The vertical offsets are best determined for these events through restoration of strata before and after each event (Fig. 12). For event SS6, we restore the stratigraphy in the east wall of trench 1. For events SS3 to SS5, we perform similar restoration of the stratigraphy mostly in the west wall, because the deformation shown in this wall includes less warping than in the east wall, and thus requires less "subjective" judgment in the reconstruction. Two assumptions are used in the restoration. First, the ground surface before each event was almost flat. Second, the blocks between fault strands mostly underwent translation (offset) and rigid-body rotation. Although nonbrittle warping is not explicitly considered, its existence would be indicated by the residual nonflat shape in the restored strata.

Restoration of the stratigraphy indicates that SS6 caused about 10 cm of down-dropping on the northern side of the fault, and 35 cm at the main fault zone. Shown in Fig. 12b, the triangular block between two faults near meter 5 is down-dropped and tilted clockwise. This produces a top wedge at the main fault zone, which is subsequently filled up by unit 15. The transgressive unit 14 covers the entire fault zone and further smoothes the topography. Reconstruction of the upper surface of unit 14 before and after event SS5 (Fig. 12d) indicates that the rupture produced a graben at the main fault zone that was down-dropped about 27 cm. The graben was filled later by unit 13. The reconstruction of the top of unit 7 before and after event SS4 (Fig. 12e and f) indicates that the fault breaks of this event have overall normal components of slip, with the north side down by 17 cm. The deformation is mainly in the form of abrupt offsets at faults, because the strata do not show obvious tilting or warping. The comparison between panels g and h of the upper surface of unit 5 shows that the northern side down-dropped another 45 cm due to event SS3. Unlike during event SS4, however, the strata in the vicinity of the main fault zone were deformed by rotation and warping, suggesting that event SS3 was likely bigger than SS4.

Figure 13 further summarizes the difference in amounts of offset during events SS3 and SS4 using a common marker line. Initially, the top of unit 7 was flat, then it was deformed incrementally as it experienced more earthquakes. Overall, event SS3 has a 2.5 times larger vertical offset at the fault than SS4, although there is a similar amount of down-dropping on the north side in the "far field."

Comparison with Previous Paleoseismic Investigations

As described earlier, a paleoseismic investigation was previously conducted at a site ~13 km west of our Songshan site (Fig. 2). Only four events were found to have occurred during the Holocene period, two events between 1675 ± 45 to 1696 ± 50 years B.P. and 4578 ± 60 to 4800 ± 400 years B.P., and another two events between 4578 ±60 to 4800 ± 400 and 9098 ± 76 years B.P., respectively (uncalibrated ages; Liu *et al.*, 1998). Based on the evidence described by Liu *et al.* (1998), it is likely that they uncovered evidence for only a minimum number of earthquakes. Their excavation was located across a cumulative pressure ridge on the lowest terrace of the Heima Zhuang He (Fig. 2), about 4 m above the river bed where little sedimentation occurred between events. Instead, they relied on thin layers of colluvium to separate events because there had been no substantial fluvial deposition since the abandonment of the terrace, probably a few thousand years ago. Depositional hiatus will be cause for events not being recorded or recognized in paleoseismic trenches. In addition, using solely colluvial wedges to differentiate events is problematic in a strike-slip setting (Weldon *et al.*, 1996), especially along a "mole track" type of surface break, with small and variable scarp heights. Thus, it is plausible that several of the recent events we see in the past 3500–3900 years at the current study site were not recognized by Liu *et al.* (1998). We cannot completely rule out the possibility that their site is on one of the two branches (Figs. 1 and 2), thus may miss the rupture on the southern branch. Regardless, it is also possible that the two events they identified between 1675 ± 45 to 1696 ± 50 years B.P. and 4578 ± 60 to 4800 ± 400 years B.P. correspond to either our events SS4 and SS5 or SS5 and SS6, but data are insufficient to prove or disprove this.

Comparison with Historical Seismicity in the Region

The region, which was called Liangzhou before the 1900s, encompasses a variably large territory of western Gansu and eastern Qinghai provinces. Wuwei (Fig. 1), the capital of Liangzhou, is about 120 km northwest of our trench site. The first record of an earthquake dates back to 193 B.C. Table 3 summarizes known historical earthquakes in the broad region since 0 A.D. (Working Group on Historical Earthquake Compilation, Academic Sinica, 1965; Gu *et al.*, 1989).

Searching for accurate dates of our older surface-faulting earthquakes in regional historical accounts may be

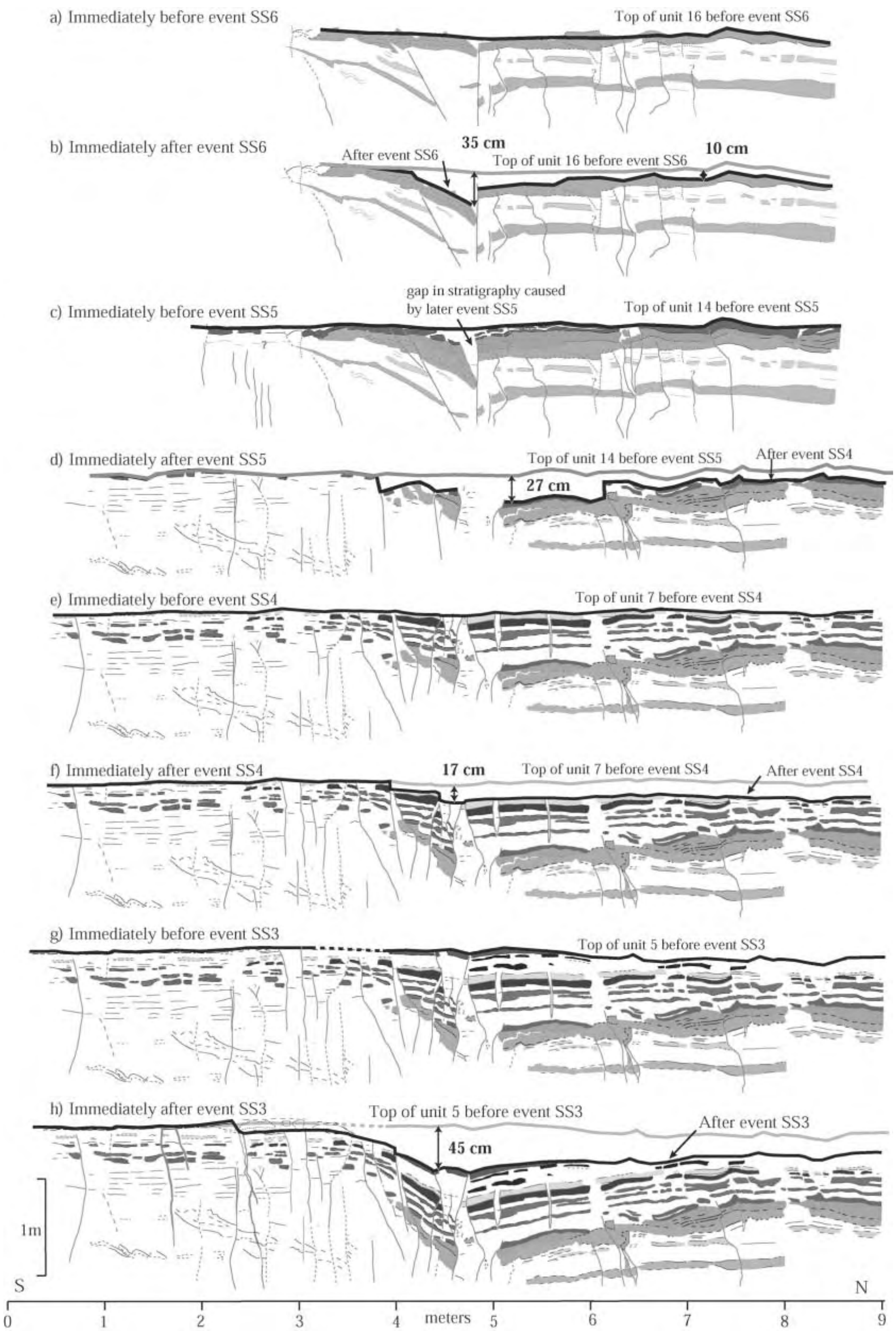

Figure 12. Possible restoration of stratigraphy in trench 1 showing deformation associated with events SS6 to SS3. Panels are arranged to show proposed stratigraphy and ground surface immediately before and after each earthquake is shown. Fault strands activated during each event are highlighted in red. Color coding is according to Figure 6. Panels a to c show the restoration of stratigraphy in the east wall, whereas panels d through h show that in the west wall.

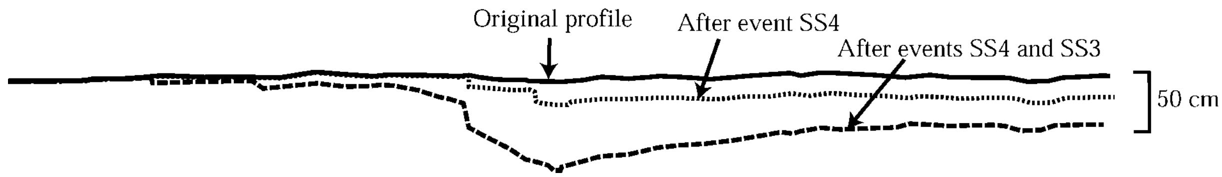

Figure 13. Comparison of amounts of vertical deformation associated with events SS3 and SS4, using the top profile of unit 7 in west wall as the reference line. Event SS3 produced more tilting and warping of strata in the vicinity of the main fault zone than SS4 did.

Table 3
Historical Earthquakes Felt or Caused Damages in Liangzhou (Wuwei)*

Dates of Earthquakes (A.D.)†	Descriptions	Significance of the Earthquake
July 161	Earthquake in Liangzhou	
October 143	Felt in large area including Wuwei, Lingwu (~280 km east of Wuwei), west to Zhangye, south to Wudu (~550 km south-southeast of Wuwei). Mountains rip apart, cities wrecked, people killed; 180 shocks happened from October to the next January.	Large area affected, epicenter uncertain
September 361	Earthquake in Liangzhou.	
26 May 362	Earthquake in Liangzhou.	
March 366	Earthquake in Liangzhou, spring emerged.	
8 August 374 (reports of 371 A.D. may be erroneous)	In Liangzhou: earthquakes continuously occurred in multiple years. Landslides; springs emerged. In Xining: rocks cascade the mountain in Tulou (northwest of Xining city). Ten shocks occurred in 50 days. Gu *et al.* (1989) thought that the quake reported in Liangzhou and Xining should be the same earthquake.	Could be on the western Haiyuan fault
30 August 506	A thundering earthquake struck Liangzhou (Wuwei); city gate collapsed.	
14 January 575 (could be reported as in 573 or January 574)	Earthquakes continuously occurred in Liangzhou in multiple years. City wall destroyed. The ground cracked and springs emerged.	A 1927 Gulang earthquake-type thrust event?
27 November 756	Zhangye and Jiuquan were worst hit. Ground sank or cracked. Audible sound could be heard in Liangzhou.	Distant earthquake, west of Wuwei
Winter 1092 (1 November 1092)	Earth shocked violently, towers tilted. Also felt in Lanzhou.	Could be 1920 $M > 8$ Haiyuan earthquake type on the Haiyuan fault
18 December 1380	Earthquake in Hezhou (Linxia) and Liangzhou (vague)	
28 January 1381 and 21 April 1381	Earthquake in Liangzhou	
21 September 1471 and 21 October 1471	Earthquake with thunders in Liangzhou	
13 May 1477	Yingchuan earthquake	Distant earthquake to the northeast in the Yingchuan graben
7 December 1514	Earthquake at Wuwei, Yongcang (~65 km northwest of Wuwei) and Yongdeng (~140 km southeast of Wuwei) with thunders.	Earthquake on the Haiyuan fault, local to our site?
7 January 1558	Earthquake and thunders in Wuwei and other places	
9 October 1587	Yongcang (~65 km northwest of Wuwei) earthquake, sound heard in Wuwei.	
1665	Top of a temple in western Wuwei fell.	On a thrust fault northwest of our site?
14 October 1709	Giant earthquake, worst hit in Zhongwei. Many accounts of damage in large area, felt in towns 900 km east of Zhongwei.	Earthquake occurred on the Tianjin Shan thrust fault north of the Haiyuan fault

*See locations of most towns in Figure 1.

†Earthquakes that may correlate with surface-faulting events on the Haiyuan fault exposed at the Songshan trench site are shown in **bold** and discussed further in the text.

Data sources: Working group on historical earthquake compilation, Academic Sinica (1965), and Gu *et al.* (1989).

biased for several reasons (see also Gaudemer *et al.*, 1995). First, accounts of earthquakes are in general brief, especially in the early history of the area (e.g., before 1600 A.D.). For example, the 1125 A.D., $M > 7$, Lanzhou earthquake (a population center larger than or comparable to Wuwei), is described in less than 50 words. Such brief earthquake accounts in such a vast region make it hard to determine which fault might be responsible for a specific event. Second, for a long time this region was located at the frontier of Han culture, with northwest nomadic tribes making it more unstable than the interior of the Han empires, which certainly affected the completeness of the historical record. Third, population centers in the region (e.g., Wuwei) are often located on alluvial plains outside the high mountain ranges, thus at some distance from active faults with high slip rates (Fig. 1). Even the shaking effect from a great earthquake on the Haiyuan fault might be damped considerably because of the large distance. In short, historical accounts in such a sparsely populated region will not permit us to distinguish moderate local earthquakes from large distant ones. In addition, the uncertainty in ages of paleoseismic events in the Songshan trench using bounds on ^{14}C samples in the stratigraphy further compounds the problem. For example, given the 0–410 A.D. range of our trench event SS4, multiple possible matches occur, including July 161 A.D., October 143 A.D., September 361 A.D., May 362 A.D., March 366 A.D., and 8 August 374 A.D (Table 3). The brief historical account of each of these earthquakes makes it impossible to be sure which among them correlates with event SS4.

Despite such difficulties, one may still make plausible attempts at reconciling historical accounts (Table 2) with our paleoseismic events. We reason that a large earthquake on the Haiyuan fault would be felt in a large area. The largest towns in the region besides Wuwei, in ancient times as well as now, are Xining and Lanzhou located to the south of the Haiyuan fault (Fig. 1). Xining and Lanzhou are located 80 km and 90 km, respectively, from the nearest approach to the fault. For both cities, this is the closest and most active seismogenic fault. An earthquake felt in both Wuwei and Xining or Lanzhou would thus be a good candidate for one of our paleoseismic events.

In keeping with this line of reasoning, the best candidates for event SS4, which occurred during 0–410 A.D., are the October 143 A.D. and 8 August 374 A.D. earthquakes. If event SS3 occurred shortly after 890–1000 A.D., it could be the winter 1092 A.D. earthquake. This earthquake was felt both in Lanzhou and Wuwei, and hence was a large event. Furthermore, one paleoseismic investigation (Ran *et al.*, 1997), at a site 130 km east of Songshan (Fig. 14), concluded that the penultimate event prior to the 1920 great earthquake occurred sometime after 540 $\pm$ 65 B.P. (^{14}C) and before 1470 $\pm$ 120 yr (TL dating). It could be correlated with event SS3 and the 1092 A.D. historical earthquake. For event SS2, which occurred sometime during 1440–1640 A.D., the best candidate would be the 7 December 1514 earthquake. This earthquake was felt in Wuwei, Yongcang, and Yundeng, cities close to the Haiyuan fault, but not in places farther away. Therefore, it was probably a relatively local event. This is supported by trench evidence that event SS2 caused smaller disturbance and offset than events SS3 through SS6.

Based on the preceding discussion, we show a preliminary scenario of earthquake ruptures for the four youngest events exposed in the Songshan trenches (Fig. 14). Events SS4 and SS3 would have been large earthquakes, with rupture lengths over 200 km, comparable to the 1920 Haiyuan (M 8) earthquake. If event SS2 had a rupture of about 60 km, then it could be a M 7+ event (Wells and Coppersmith, 1994), either on the Maomaoshan segment of the Haiyuan fault, or possibly on the South Maomaoshan branch of the Haiyuan fault (Gaudemer *et al.*, 1995). This portion of the fault has the required length between the Tianzhu pull-apart basin and the Songshan junction. Figure 14 also depicts the ruptures of three large historical earthquakes in 1709, 1920, and 1927 in the region.

Implications for the Slip Rate on the Western Haiyuan Fault

Lasserre *et al.* (1999) inferred that the range of slip per event was between 8 and 16 m and suggested that 10 m was the smallest small-scale geomorphic offset recognizable in this reach of the fault. Event SS2 is characterized by only minor fractures and fissures with little or no vertical offset, but we cannot exclude that it might have had a horizontal offset of up to a few tens of centimeters ($\leq$1 m). For example, the over-100-km-long rupture of the $M \sim 7.5$ earthquake that occurred on 8 December 1812 A.D. along the San Andreas fault (Jacoby *et al.*, 1988) was manifested in trenches at the Wrightwood site by only open fissures and an unconformity (Fumal *et al.*, 1993, 2002). Yet, at this site it had more than one meter of horizontal offset (Weldon *et al.*, 2004). Thus, by comparison, event SS2 at the Songshan site could represent a significant earthquake ($M \sim 7$?). It seems possible that the 10-m smallest geomorphic offset estimate of Lasserre *et al.* (1999) may represent a combination of event SS2 and a previous larger-offset event. Event SS3 most likely represents a large, several-meter-offset earthquake. If we further assume that event SS2 had an offset of <1 m, then event SS3 might have had an offset of about 10 m. Event SS3 might have had a greater horizontal offset than event SS4, given the larger vertical offset visible in the trench. Both events SS3 and SS4 might have had offsets similar to the 1920 Haiyuan earthquake (maximum slip, 10–11 m) (Zhang *et al.*, 1987), and therefore comparable magnitudes (M 8) (see also rupture lengths on Figs. 1 and 14).

Inferring the horizontal offsets of events SS3 and SS4 to be 10 $\pm$ 2 m, a crude slip-time diagram would be more consistent with the slip rate of 8–16 mm/yr found by Lasserre *et al.* (1999) and Gaudemer *et al.* (1995) during the past 2000 years (Fig. 15), than with that of 5 mm/yr inferred by He *et al.* (1994, 1996) and Yuan *et al.* (1998). An ide-

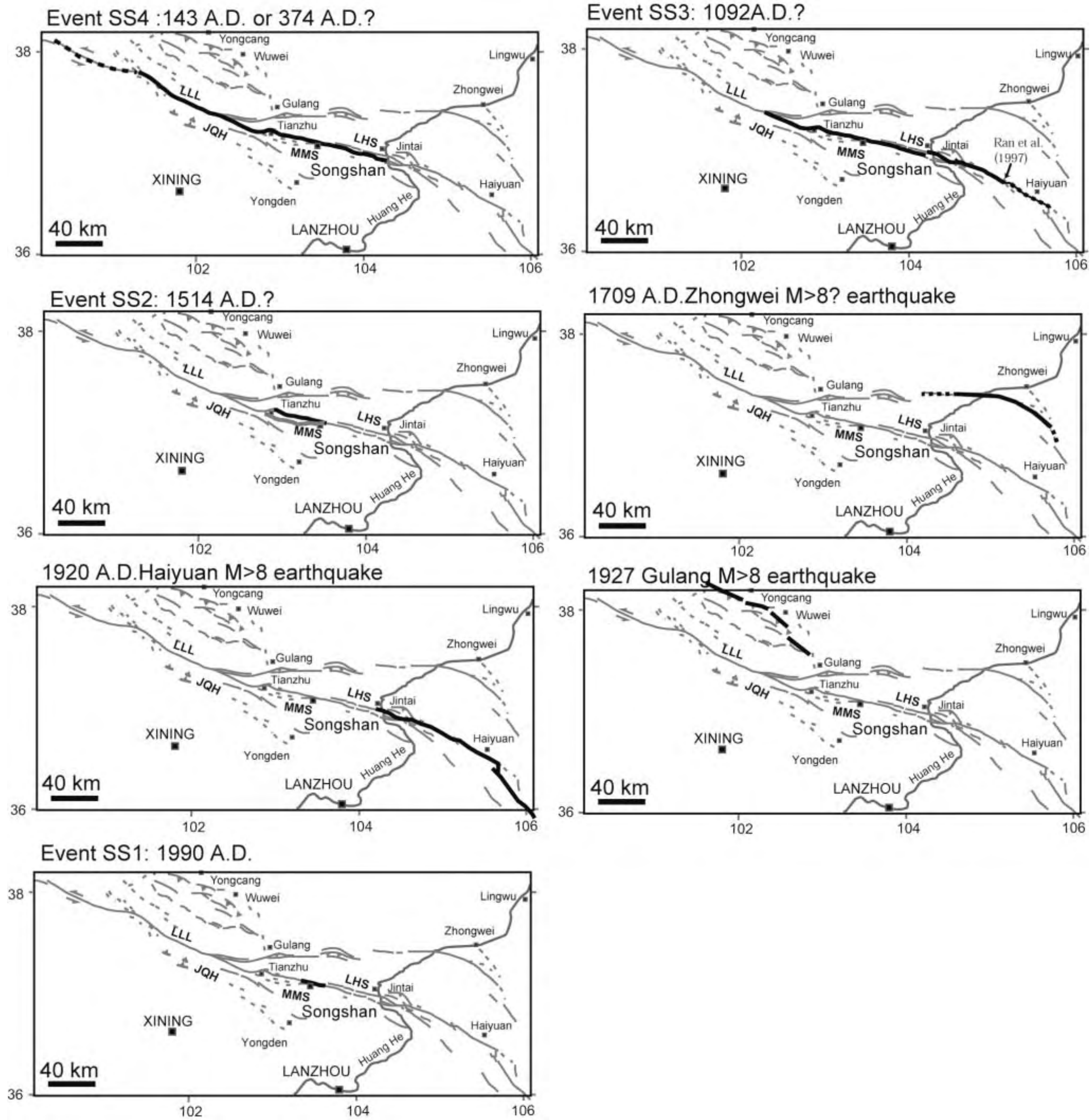

Figure 14. Hypothesized rupture extents (bold dark lines) of the youngest four events exposed at the Songshan site. Events SS3 and SS4 were likely large events similar to the 1920 $M > 8$ Haiyuan earthquake. The smaller event SS2 was located either on the main trace of Haiyuan fault, or the continuation from a secondary branch to the south (shown as a bold-gray line). Also shown are the ruptures associated with three large regional historical earthquakes in 1709, 1920, and 1927.

alized projection of the occurrence times of events SS3 and SS4 also implies that an earthquake may be pending, and now this stretch of the fault is close to the end of a seismic cycle. If the preliminary low GPS rate on the Haiyuan fault is real, the long time since the last large event seems to lend support to the suggestion that geodetic measurements might underestimate slip rate if the fault is late in its earthquake cycle (Chevalier *et al.*, 2005).

Clearly, however, without rigorous measurements of slip per event for the earthquakes exposed in the Songshan trenches, the slip-rate estimation shown in Figure 15 should be considered, at best, not contradictory with the slip rate

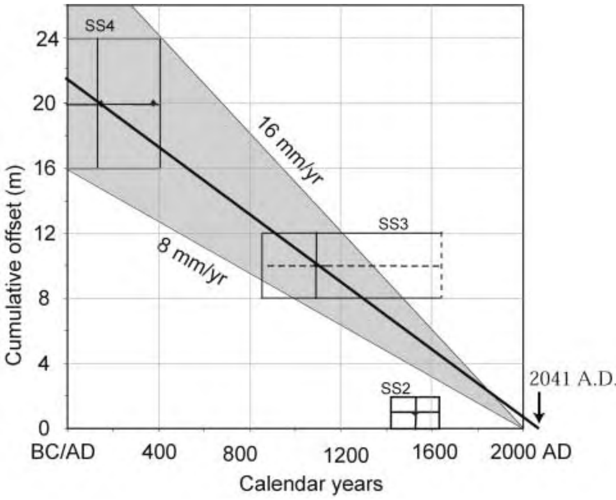

Figure 15. Slip-time function during the past 2000 years. Events SS4 and SS3 are assumed to have 10 ± 2 m offsets. The best fit gives the apparent slip rate of 8–16 mm/yr. The dimensions of boxes designate the errors in age and offset estimates.

inferred from cumulative horizontal offsets at dated terrace sites. Our study is merely a first step toward understanding the long-term seismic behavior of the western Haiyuan fault. As pointed out by Weldon *et al.* (1996) and demonstrated (Liu *et al.*, 2004; Liu-Zeng *et al.*, 2006), a site adequate for dating paleoearthquakes may not be an ideal site for measuring slip per events, and vice versa. Future work to determine the slip associated with each event at sites nearby will provide much needed critical information about the earthquake history on this section of the Haiyuan fault.

Summary

Two trenches were excavated at a stepover on the Haiyuan fault, north of Songshan (37.1° N, 103.5° E). They exposed stratigraphic evidence for six paleoearthquakes, events SS1, SS2, SS3, SS4, SS5, and SS6 from youngest to oldest, in the upper 3 m of sediments. Based on charcoal samples, the earthquakes occurred after 1530–1888 B.C. or in the past 3500–3900 years. Samples within the uppermost 2 m of sediments further constrain the youngest four events to have occurred in the past ~2000 years since 0–230 A.D. The youngest event (SS1) ruptured the ground surface with only one or two tensile crack in one trench. It is likely correlated with the local 1990 M_w 5.8 earthquake. Events SS2, SS3, and SS4 occurred sometime during the periods 1440–1640 A.D., shortly after 890–1000 A.D., and 0–410 A.D., respectively. The trenches do not provide information about horizontal slip during these events. However, events SS3 to SS6, which caused a few tens of centimeters of vertical offset and prominent tilting of depositional layers, appear to be larger events. We tentatively associate events SS2, SS3, and SS4, respectively, to the 1514 A.D., 1092 A.D., and 143 or 374 A.D. historical earthquakes in the region. If we take the estimation of 10 ± 2 m of slip per large event (Lasserre *et al.*, 1999), the millennial recurrence time of large events does not contradict the 12 ± 14 mm/yr average slip rate found by Gaudemer *et al.* (1995) and Lasserre *et al.* (1999). Clearly, a more robust slip-rate estimate depends on more rigorous determination of slip per individual earthquake.

Acknowledgments

This collaborative work was partly funded by Association Franco-Chinoise pour la Recherché Scientifique et Technique (Y.K. and X.X.), by the French Embassy in China, the Chinese National Science Foundation (Project no. 4047 4037), and a Chateaubriand Fellowship from the French Foreign Affair Ministry (J.L.-Z.). Part of the AMS ^{14}C dating was processed at the French National Laboratory LMC14. We thank staff at Lanzhou Institute of Seismology, China Earthquake Administration, and two drivers (Xianglong Wang and Cheng Fu) for logistic arrangements and A.-C. Morillon for Figure 3. S. Olig and M. Hemphill-Haley provided us with a very helpful review that improved this manuscript. This is IPGP contribution no. 2152.

References

Avouac, J., and P. Tapponnier (1993). Kinematic model of active deformation in central Asia, *Geophys. Res. Lett.* **20,** 895–898.

Barka, A., H. S. Akyuz, E. Altunel, G. Sunal, Z. Cakir, A. Dikbas, B. Yerli, R. Armijo, B. Meyer, J. B. de Chabalier, T. Rockwell, J. R. Dolan, R. Hartleb, T. Dawson, S. Christofferson, A. Tucker, T. Fumal, R. Langridge, H. Stenner, W. Lettis, J. Bachhuber, and W. Page (2002). The surface rupture and slip distribution of the 17 August 1999 Izmit earthquake (M 7.4), North Anatolian fault, *Bull. Seism. Soc. Am.* **92,** 43–60.

Barka, A. A., R. C. Buckman, and P. L. Hancock (1992). The North Anatolian fault zone, *Ann. Tecton.* **6** (Suppl.), 164–195.

Bendick, R., R. Bilham, J. T. Freymueller, K. Larson, and G. Yin (2000). Geodetic evidence for a low slip rate in the Altyn Tagh fault, *Nature* **404,** 69–72.

Blong, R. J., and R. Gillespie (1978). Fluvially trasported charcoal gives erroneous ^{14}C ages for recent deposits, *Nature* **271,** 739–741.

Burchfiel, B. C., Z. Peizhen, W. Yipeng, Z. Weiqi, S. Fangmin, D. Qidong, P. Molnar, and L. Royden (1991). Geology of the Haiyuan Zone, Ningxia-Hui Autonomous Region, China, and its relation to the evolution of the northeastern margin of the Tibetan Plateau, *Tectonics* **10,** 1091–1110.

Chen, Q., J. Freymueller, Q. Wang, Z. Yang, C. Xu, and J. Liu (2004). A deforming block model for the present-day tectonics of Tibet, *J. Geophys. Res.* **109,** B01403, doi 01410.01029/02002JB002151.

Chevalier, M. L., F. J. Ryerson, P. Tapponnier, R. C. Finkel, J. v. d. Woerd, H. Li, and Q. Liu (2005). Slip-rate measurements on the Karakorum fault may imply secular variations in fault motion, *Science* **307,** 411–414.

Committee for Chinese Earthquake Bulletin (1990). The October 20, 1990 Ms 6.2 Tianzhu—Jintai, Gansu earthquake, in *Chinese Earthquake Yearly Bulletin, 1990*, Seismological Publishing House, Beijing, 167–171.

Deng, Q., F. Song, S. Zhu, Y. Wang, W. Zhang, D. Jiao, B. C. Burchfiel, P. Molnar, L. Royden, and P. Zhang (1986). Variations in the geometry and amount of slip on the Haiyuan (Nanxihaushan) fault zone, China, and the surface rupture of the 1920 Haiyuan earthquake, in *Earthquake Source Mechanics*, S. Das, J. Boatwright, and C. H. Scholz (Editors), American Geophysical Monograph 37, 169–182.

Ding, G., J. Chen, Q. Tian, X. Shen, C. Xing, and K. Wei (2004). Active faults and magnitudes of left-lateral displacement along the northern margin of the Tibetan Plateau, *Tectonophysics* **380,** 243–260.

Dixon, T. H., M. M. Miller, F. Farina, H. Wang, and D. Johnson (2000). Present-day motion of the Sierra Nevada block and some tectonic implications for the Basin and Range province, North America Cordillera, *Tectonics* **19,** 1–24.

Dixon, T. H., E. Norabuena, and L. Hotaling (2003). Paleoseismology and Global Positioning System: earthquake-cycle effects and geodetic versus geologic fault slip rates in the Eastern California shear zone, *Geology* **31,** 55–58.

Dokka, R. K., and C. J. Travis (1990). Late Cenozoic strike-slip faulting in the Mojave Desert, California, *Tectonics* **9,** 311–340.

England, P., and G. Houseman (1986). Finite strain calculations of continental deformation, 2. Comparison with the India-Asia collision zone, *J. Geophys. Res.* **91,** 3664–3676.

Fumal, T. E., S. K. Pezzopane, R. J. Weldon, and D. P. Schwartz (1993). A 100-year average recurrence interval for the San Andreas fault at Wrightwood, California, *Science* **259,** 199–203.

Fumal, T. E., R. J. Weldon, G. P. Biasi, T. E. Dawson, G. G. Seitz, W. T. Frost, and D. P. Schwartz (2002). Evidence for large earthquakes on the San Andreas fault at the Wrightwood, California paleoseismic site: A.D. 500 to present, *Bull. Seism. Soc. Am.* **92,** 2726–2760.

Gansu Bureau of China Earthquake Administration and Lanzhou Institute of Seismology, China Earthquake Administration (1990). Field report of the 1990 Tianzhu-Jintai earthquake, Gansu Province.

Gaudemer, Y., P. Tapponnier, B. Meyer, G. Peltzer, S. Guo, Z. Chen, H. Dai, and I. Cifuentes (1995). Partitioning crustal slip between linked, active faults in the eastern Qilian Shan, and evidence for a major seismic gap, the "Tianzhu Gap", on the western Haiyuan Fault, Gansu (China), *Geophys. J. Int.* **120,** 599–645.

Gaudemer, Y., P. Tapponnier, and D. Turcotte (1989). River offsets across active strike-slip faults, *Ann. Tecton.* **3,** 55–76.

Grant, L. B., and K. Sieh (1993). Stratigraphic evidence for seven meters of dextral slip on the San Andreas Fault during the 1857 earthquake in the Carrizo Plain, *Bull. Seism. Soc. Am.* **83,** 619–635.

Grant, L. B., and K. Sieh (1994). Paleoseismic evidence of clustered earthquakes on the San Andreas Fault in the Carrizo Plain, California, *J. Geophys. Res.* **99,** 6819–6841.

Gu, G., T. Lin, and Z. Shi (1989). *Catalogue of Chinese earthquakes (1831 BC–1969 AD)*, Science Press, Beijing, China, 872 pp.

He, W., B. Liu, T. Lu, D. Yuan, and X. Liu (1996). The late Quaternary activity of the Maomaoshan fault zone, in *Research on Active Fault Series 5*, Q. Deng, Y. Wang, and P. Zhang (Editors), Seismological Press, Beijing, China, 63–77 (in Chinese with English abstract).

He, W., B. Liu, T. Lu, D. Yuan, J. Liu, and X. Liu (1994). Study on the segmentation of Laohushan fault zone, *Northwestern Seism. J.* **16,** 66–72 (in Chinese with English abstract).

Houseman, G., and P. England (1993). Crustal thickening versus lateral expulsion in the Indian—Asian continental collision, *J. Geophys. Res.* **98,** 12,233–12,249.

Hubert-Ferrari, A., G. King, I. Manighetti, R. Armijo, B. Meyer, and P. Tapponnier (2003). Long-term elasticity in the continental lithosphere; modeling the Aden Ridge propagation and the Anatolian extrusion process, *Geophys. J. Int.* **153,** 111–132.

Institute of Geology, China Earthquake Administration and Ninxia Bureau of China Earthquake Administration (1990). *Active Haiyuan Fault Zone Monograph*, Special Publications on Active Fault Studies in China, Seismological Publishing House, Beijing, 286 pp.

Jacoby, G. C., P. R. Sheppard, and K. E. Sieh (1988). Irregular recurrence of large earthquakes along the San Andreas Fault; evidence from trees, *Science* **241,** 196–199.

Lasserre, C. (2000). Fonctionnement sismique, cinématique et histoire géologique de la faille d'Haiyuan, *Ph.D. Thesis*, Université Paris **7,** 244 pp.

Lasserre, C., P. H. Morel, Y. Gaudemer, P. Tapponnier, F. J. Ryerson, G. C. P. King, F. Metivier, M. Kasser, M. Kashgarian, B. Liu, T. Lu, and D. Yuan (1999). Postglacial left slip rate and past occurrence of M > or = 8 earthquakes on the western Haiyuan Fault, Gansu, China, *J. Geophys. Res.* **104,** 17,633–17,652.

Lasserre, C., B. Bukchin, P. Bernard, P. Tapponnier, Y. Gaudemer, A. Mostinsky, and D. Rong (2001). Source parameters and tectonic origin of the 1996 June 1 Tianzhu (M (sub w) = 5.2) and 1995 July 21 Yongden (M (sub w) = 5.6) earthquakes near the Haiyuan Fault (Gansu, China), *Geophys. J. Int.* **144,** 206–220.

Lasserre, C., Y. Gaudemer, P. Tapponnier, A. S. Meriaux, J. Van der Woerd, D. Yuan, F. J. Ryerson, R. C. Finkel, and M. W. Caffee (2002). Fast late Pleistocene slip rate on the Leng Long Ling Segment of the Haiyuan Fault, Qinghai, China, *J. Geophys. Res.* **107,** B11, 2276, doi 10.1029/2000JB000060.

Liu, B., W. He, X. Liu, and D. Yuan (1998). Study on the trench of paleoearthquake in compressive ridge, in *Research on Active Fault Series 6*, Q. Deng, Y. Wang, and P. Zhang (Editors), Seismological Press, Beijing, China, 56–65 (in Chinese with English abstract).

Liu, J., Y. Klinger, K. Sieh, and C. Rubin (2004). Six similar sequential ruptures of the San Andreas fault, Carrizo Plain, California, *Geology* **32,** 649–652, doi 10.1130/G20478.1.

Liu-Zeng, J., Y. Klinger, K. Sieh, C. Rubin, and G. Seitz (2006). Serial ruptures of the San Andreas Fault, Carrizo Plain, California, revealed by three-dimensional excavations, *J. Geophys. Res.* **111,** B02306, doi 10.1029/2004JB003601.

Mériaux, A.-S., F. J. Ryerson, P. Tapponnier, J. Van der Woerd, R. C. Finkel, X. Xu, Z. Xu, and M. W. Caffee (2004). Rapid slip along the central Altyn Tagh fault: morphochronologic evidence from Cherchen He and Sulamu Tagh, *J. Geophys. Res.* **109,** B06401, doi 06410.01029/02003JB002558.

Mériaux, A.-S., P. Tapponnier, F. J. Ryerson, X. Xu, G. King, J. V. d. Woerd, R. C. Finkel, H. Li, M. W. Caffee, Z. Xu, and W. Chen (2005). The Aksay segment of the northern Altyn Tagh fault: tectonic geomorphology, landscape evolution, and Holocene slip rate, *J. Geophys. Res.* **110,** B04404 doi 04410.01029/02004JB003210.

Miller, M. M., D. J. Johnson, T. H. Dixon, and R. K. Dokka (2001). Refined kinematics of the Eastern California shear zone from GPS observations, *J. Geophys. Res. B Solid Earth Planets* **106,** 2245–2264.

Min, W., P. Zhang, and Q. Deng (2000). Preliminary study of regional paleoseismic behavior, *Acta Seism. Sinica* **22,** 163–170 (in Chinese with English abstract).

Nelson, A. R. (1992). Discordant ^{14}C ages buried tidal-marsh soils in the Cascadia subduction zone, southern Oregon coast, *Quat. Res.* **38,** 74–90.

Oskin, M., and A. Iriondo (2004). Large-magnitude transient strain accumulation on the Blackwater Fault, Eastern California shear zone, *Geology* **32,** 313–316.

Peltzer, G., and P. Tapponnier (1988). Formation and evolution of strike-slip faults, rifts, and basins during the India-Asia collision: an experimental approach, *J. Geophys. Res.* **93,** 15,085–15,117.

Peltzer, G., F. Crampé, S. Hensley, and P. Rosen (2001). Transient strain accumulation and fault interaction in the Eastern California shear zone, *Geology* **29,** 975–978.

Peltzer, G., P. Tapponnier, Y. Gaudemer, B. Meyer, S. Guo, K. Yin, Z. Chen, and H. Dai (1988). Offsets of late Quaternary morphology, rate of slip, and recurrence of large earthquakes on the Chang Ma Fault (Gansu, China), *J. Geophys. Res.* **93,** 7793–7812.

Perfettini, H., and J. P. Avouac (2004). Stress transfer and strain rate variations during the seismic cycle, *J. Geophys. Res.* **109,** B06402, doi 06410.01029/02003JB002917.

Ramsey, C. B. (2000). OxCal Program Ver. 3.5, Radiocarbon Accelerator4 Unit, University of Oxford, U.K., http://www.rlaha.ox.ac.uk/ (last accessed December 2006).

Ran, R., R. Duan, Q. Deng, D. Jiao, and W. Min (1997). 3-D trench excavation and paleoseismology at Gaowanzi of the Haiyuan fault, *Seism. Geol.* **19,** 97–107 (in Chinese with English abstract).

Rockwell, T. K., D. L. Lamar, R. S. McElwain, and D. E. Millman (1986). Recurrent late Holocene faulting on the Glen Ivy North Strand of the Elsinore fault at Glen Ivy Marsh, in *Neotectonics and Faulting in Southern California*, P. Ehlig (Editor), Geol. Soc. Am. Fieldtrip

Guidebook for the Cordilleran Section Meeting in Los Angeles, 167–176.

Rockwell, T. K., S. Lindvall, M. Herzberg, D. Murbach, T. Dawson, and G. Berger (2000). Paleoseismology of the Johnson Valley, Kickapoo, and Homestead Valley faults; clustering of earthquakes in the eastern California shear zone, *Bull. Seism. Soc. Am.* **90,** 1200–1236.

Rubin, C. M., and K. Sieh (1997). Long dormancy, low slip rate, and similar slip-per-event for the Emerson Fault, eastern California shear zone, *J. Geophys. Res. B Solid Earth Planets* **102,** 319–315.

Segall, P. (2002). Integrating geologic and geodetic estimates of slip rate on the San Andreas fault system, *Int. Geol. Rev.* **44,** 62–82.

Shen, Z.-K., M. Wang, Y. Li, D. D. Jackson, A. Yin, D. Dong, and P. Fang (2001). Crustal deformation along the Altyn Tagh Fault system, western from GPS, *J. Geophys. Res., B Solid Earth Planets* **106,** 30,607–30,621.

Sieh, K. (1978). Prehistoric large earthquakes produced by slip on the San Andreas fault at Pallett Creek, California, *J. Geophys. Res. B Solid Earth Planets* **83,** 3907–3939.

Stein, R., A. Barka, and J. H. Dieterich (1997). Progressive failure on the North Anatolian fault since 1939 by earthquake stress triggering, *Geophys. J. Int.* **128,** 594–604.

Stuiver, M., P. J. Reimer, E. Bard, J. W. Beck, G. S. Burr, K. A. Hughen, B. Kromer, G. McCormac, J. van der Plicht, and M. Spurk (1998). INTCAL98 radiocarbon age calibration, 24,000-0 cal BP, *Radiocarbon* **40,** 1041–1083.

Sykes, L. R., J. B. Kisslinger, L. S. House, J. N. Davies, and K. H. Jacob (1981). Rupture zones and repeat times of great earthquakes along the Alaska-Aleutian Arc, 1784–1980, in *Earthquake Prediction: An International Review, Maurice Ewing Series 4*, D. W. Simpson and P. G. Richards (Editors), America Geophysical Union, Washington, D.C., 73–79.

Tapponnier, P., X. Zhiqin, F. Roger, B. Meyer, N. Arnaud, G. Wittlinger, and Y. Jingsui (2001). Oblique stepwise rise and growth of the Tibet plateau, *Science* **294,** 1671–1677.

Van der Woerd, J., F. J. Ryerson, P. Tapponnier, A. S. Meriaux, Y. Gaudemer, B. Meyer, R. C. Finkel, M. W. Caffee, G. Zhao, and Z. Xu (2000). Uniform slip-rate along the Kunlun Fault; implications for seismic behaviour and large-scale tectonics, *Geophys. Res. Lett.* **27,** 2353–2356.

Van der Woerd, J., P. Tapponnier, F. J. Ryerson, A.-S. Meriaux, B. Meyer, Y. Gaudemer, R. C. Finkel, M. W. Caffee, G. Zhao, and Z. Xu (2002). Uniform postglacial slip-rate along the central 600 km of the Kunlun Fault (Tibet), from (super 26) Al, (super 10) Be, (super 14) C dating of riser offsets, and climatic origin of the regional morphology, *Geophys. J. Int.* **148,** 356–388.

Vaughan, P. R., K. M. Thorup, and T. K. Rockwell (1999). Paleoseismology of the Elsinore Fault at Agua Tibia Mountain, southern California, *Bull. Seism. Soc. Am.* **89,** 1447–1457.

Wallace, K., G. Yin, and R. Bilham (2005). Inescapable low slip on the Altyn Tagh fault, *Geophys. Res. Lett.* **31,** L09613, doi 10.1029/2004GL019724.

Wang, Q., P. Z. Zhang, J. T. Freymueller, R. Bilhan, K. M. Larson, X. Lai, X. Z. You, Z. J. Niu, J. C. Wu, Y. X. Li, J. N. Liu, Z. Q. Yang, and Q. Z. Chen (2001). Present-day crustal deformation in China constrained by global positioning system measurements, *Science* **294,** 574–577.

Weldon, R., P. McCalpin, and T. K. Rockwell (1996). Paleoseismology of strike-slip tectonic environments, in *Paleoseismology*, J. McCalpin (Editor), Academic Press, San Diego, 271–329.

Weldon, R., K. Scharer, T. Fumal, and G. Biasi (2004). Wrightwood and the earthquake cycle; what a long recurrence record tells us about how faults work, *GSA Today* **14,** 4–10.

Wells, D. L., and K. J. Coppersmith (1994). New empirical relationships among magnitude, rupture length, rupture width, rupture area, and surface displacement, *Bull. Seism. Soc. Am.* **84,** 974–1002.

Working group on the Altyn Tagh active fault (1992). *Active Altun Fault Zone Monograph*, Special Publications on Active Fault Studies in China, Seismological Publishing House, Beijing, 319 pp.

Working group on historical earthquake compilation, Academic Sinica (1956). Catalogue of earthquake accounts in Gansu Province, in *Catalogue of Chinese Earthquakes*, Science Press, Beijing, 440–562.

Xiang, H., S. Guo, B. Zhang, W. Zhang, Y. Ikeda, and H. He (1998). Active features of the eastern Liupanshan piedmont reverse fault zone since late Quaternary, *Seism. Geol.* **20,** 321–327 (in Chinese with English abstract).

Yeats, R., K. Sieh, and C. Allen (1997). *The Geology of Earthquakes*, Oxford University Press, New York, 568 pp.

Yuan, D., B. Liu, T. Lu, W. He, X. Liu, and W. Gan (1998). Study on the segmentation in east segment of the northern Qilianshan fault zone, *Northwestern Seism. J.* **20,** 27–34 (in Chinese with English abstract).

Zhang, P., P. Molnar, B. C. Burchfiel, L. Royden, Y. Wang, Q. Deng, S. Fangmin, Z. Weiqi, J. Decheng, F. Song, W. Zhang, and D. Jiao (1988). Bounds on the Holocene slip rate of the Haiyuan Fault, north-central China, *Quat. Res.* **30,** 151–164.

Zhang, P., P. Molnar, W. Zhang, Q. Deng, Y. Wang, B. C. Burchfiel, F. Song, L. H. Royden, and D. Jiao (1988). Bounds on the average recurrence interval of major earthquakes along the Haiyuan fault in north-central China, *Seism. Res. Lett.* **59,** 81–89.

Zhang, P., Z. Shen, M. Wang, W. Gan, R. Buergmann, P. Molnar, Q. Wang, Z. Niu, J. Sun, J. Wu, H. Sun, and X. You (2004). Continuous deformation of the Tibetan Plateau from Global Positioning System data, *Geology* **32,** 809–812.

Zhang, W., D. Jiao, P. Zhang, P. Molnar, B. C. Burchfiel, Q. Deng, Y. Wang, and F. Song (1987). Displacement along the Haiyuan fault associated with the great 1920 Haiyuan, China, earthquake, *Bull. Seism. Soc. Am.* **77,** 117–131.

Laboratoire de Tectonique
Institut de Physique du Globe de Paris
BP89, 4 place Jussieu
75005 Paris, France
(J.L.-Z., Y.K., P.T.)

Institute of Tibetan Plateau Research
Chinese Academy of Sciences
P.O. Box 2871, 18 Shuang Qing Road
Beijing 100085, China
(J.L.-Z.)

Insitute of Geology
China Earthquake Administration
Beijing 100029, China
(X.X., G.C., W.C.)

Laboratoire de Géologie
Ecole Normale Supérieure
24 Rue Lhomond
75231 Paris Cedex 05, France
(C.L.)

Tianzhu Bureau of Earthquake Administration
92 Tuanjie Road Tianzhu County
Gansu Province 733200, China
(B.Z.)

Manuscript received 9 June 2005.

Sources of the large A.D. 1202 and 1759 Near East earthquakes

M. Daëron* Institut de Physique du Globe de Paris, UMR 7578, 4 place Jussieu, Boîte 89, 75252 Paris, France
Y. Klinger*
P. Tapponnier* Institut de Physique du Globe de Paris, UMR 7578, 4 place Jussieu, Boîte 89, 75252 Paris, France
A. Elias* Institut de Physique du Globe de Paris, UMR 7578, 4 place Jussieu, Boîte 89, 75252 Paris, France, and National Council for Scientific Research, P.O. Box 165432, Ashrafieh, 1100-2040 Beirut, Lebanon
E. Jacques* Ecole et Observatoire des Sciences de la Terre de Strasbourg, 5 rue René Descartes, F-67084 Strasbourg, France
A. Sursock* National Council for Scientific Research, P.O. Box 11-8281, Riad El-Solh, 1107 2260 Beirut, Lebanon

ABSTRACT

The sources of the May 1202 and November 1759, M 7.5 Near East earthquakes remain controversial, because their macroseismal areas coincide, straddling subparallel active faults in the Lebanese restraining bend. Paleoseismic trenching in the Yammoûneh basin yields unambiguous evidence both for slip on the Yammoûneh fault in the twelfth–thirteenth centuries and for the lack of a posterior event. This conclusion is supported by comparing the freshest visible fault scarps, which imply more recent slip on the Râchaïya-Serghaya system than on the Yammoûneh fault. Our results suggest that the recurrence of an A.D. 1202–type earthquake might be due this century, as part of a sequence similar to that of A.D. 1033–1202, possibly heralded by the occurrence of the 1995 Mw 7.3 Aqaba earthquake. The seismic behavior of the Levant fault might thus be characterized by millennial periods of quiescence, separated by clusters of large earthquakes.

Keywords: Lebanon, Levant fault, historical earthquakes, paleoseismology, event clustering.

INTRODUCTION

The 1000-km-long, left-lateral Levant fault (e.g., Dubertret, 1932; Quennell, 1959; Freund et al., 1968; Garfunkel et al., 1981) marks the boundary between the Arabian plate and the Sinai-Levantine block (Courtillot et al., 1987; Salamon et al., 2003). Since Biblical time, it has generated large (M > 7) earthquakes (e.g., Poirier and Taher, 1980; Ben-Menahem, 1991; Abou Karaki, 1987; Guidoboni et al., 2004b). However, the sources of most historical events in the Near East remain unclear. This is particularly true between 33°N and 34.5°N, where the plate-boundary fault system is divided (Dubertret, 1955), owing to transpression within the Lebanese restraining bend (Freund et al., 1970; Griffiths et al., 2000). Recent offshore seismic studies (Carton et al., 2004; Elias et al., 2004) suggest that the strike-perpendicular and strike-parallel components of motion are accommodated by discrete features east and west of Mount Lebanon (3090 m): the offshore Tripoli-Beirut thrust (Tapponnier et al., 2001), and the Yammoûneh and Râchaïya-Serghaya faults, respectively (Fig. 1). The latter strike-slip fault, which follows the Anti Lebanon Range (2630 m) east of the Beqaa Plain (1000 m), merges with the former at the southern tip of the Hula basin. By linking the Jordan Valley fault with the Missyaf fault, the Yammoûneh fault ensures the continuity of the plate boundary across Lebanon.

Seismic hazard evaluation in this region depends on a better understanding of the seismic potential of the various strands and segments of the Levant fault system. On the basis of new paleoseismic data and geomorphic observations, we propose a reassessment of the sources of arguably the two strongest historical earthquakes (A.D. 1202 and 1759) that devastated the Beqaa Plain and surrounding areas. The Yammoûneh fault has usually been believed responsible for both the May 1202 and November 1759 earthquakes (e.g., Ambraseys and Barazangi, 1989; Ben-Menahem, 1991). Our results indicate instead that the paired October and November 1759 events ruptured the Râchaïya-Serghaya system rather than the Yammoûneh fault. Although historical data alone are inconclusive, paleoseismic dating and comparison of geomorphic observations remove the ambiguity.

MACROSEISMIC CONSTRAINTS ON THE 1202 AND 1759 EVENTS

The effects of the 1202 and 1759 earthquakes were assessed by Ambraseys and Melville (1988) and Ambraseys and Barazangi (1989), respectively, using first-hand accounts. The 20 May 1202 earthquake shook western Syria and the Crusader states, toppling 31 columns of the Jupiter temple in the city of Baalbek (Ben-Menahem, 1991), which was destroyed. The cities of Nablus, Acre, Safed, Tyre, Tripoli, and Hamah, among others, were severely damaged (Fig. 1). Rock falls in Mount Lebanon killed 200 people. Shaking was felt throughout the Mediterranean and Middle East, as much as 1200 km away.

The seismic sequence of 1759 affected roughly the same region (Ambraseys and Barazangi, 1989). The smaller 30 October shock ruined Safed, Qunaitra, and many villages nearby, killed 2000 people, and triggered a seismic wave in Lake Tiberias (Ben-Menahem, 1979). The second, larger shock on 25 November destroyed all villages in the Beqaa. Baalbek was ruined. Three of the last nine columns of the Jupiter temple (Ben-Menahem, 1991) and three columns of the Bacchus temple collapsed. Safed, Ras Baalbek, and Damascus were damaged, and the earthquake was felt as far as Egypt and Anatolia, 1100 km away.

The areas of maximum destruction of the 1202 and November 1759 events overlap, covering an elongated, 150–200-km-long, south-southwest–trending zone centered on the Beqaa plain (Fig. 1). Historical accounts of damage thus imply that the events originated on the Yammoûneh or Serghaya fault. Macroseismic isoseismal contours tend to be biased toward populated areas: here, the fertile Beqaa Plain. It is therefore impossible to use such data alone to discriminate between the two faults.

SURFACE FAULTING

The identification and localization of surface faulting associated with the 1202 and 1759 events provides additional clues to determine the faults involved. Archeological and paleoseismic investigation (Ellenblum et al., 1998) showed that the 1202 earthquake caused 1.6 m of left-lateral displacement of fortification walls at Vadum Jacob (Fig. 1). A later 0.5 m offset may correspond either to the October 1759 event or to the last large regional event of 1 January 1837 (Ambraseys, 1997). The castle at Vadum Jacob is located south of the junction between the Yammoûneh and Râchaïya-Serghaya faults, so the question of which fault took up slip to the north during either event remains open. On the Serghaya fault, in the southern Zebadani valley in Syria,

*E-mails: daeron@ipgp.jussieu.fr; klinger@ipgp.jussieu.fr; tappon@ipgp.jussieu.fr; elias@ipgp.jussieu.fr; eric.jacques@eost.u-strasbg.fr; asursock@cnrs.edu.lb.

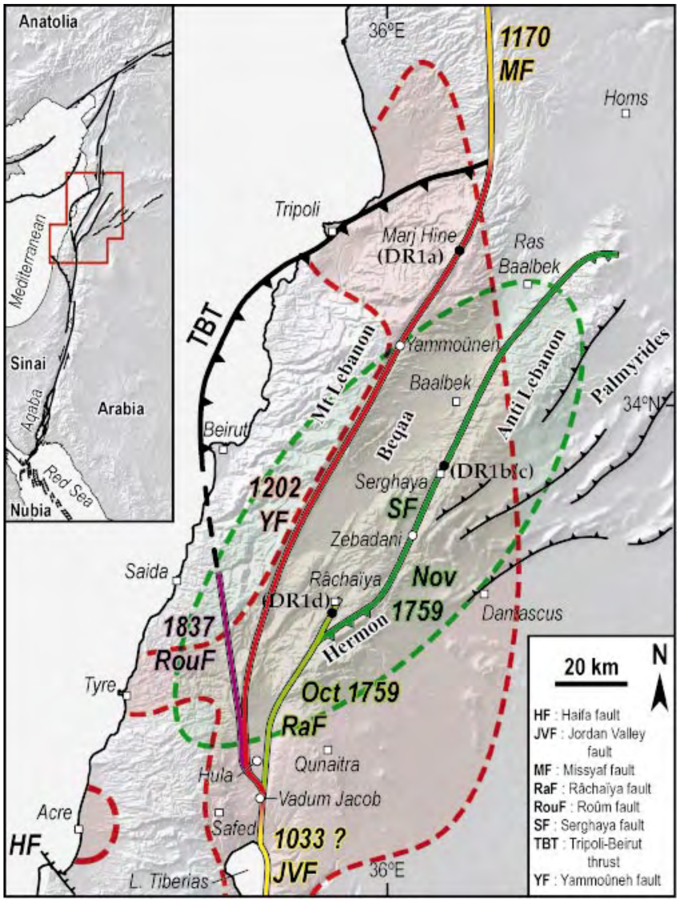

Figure 1. Schematic map of main active faults of Lebanese restraining bend: bold colored lines show maximum rupture lengths of large historical earthquakes in past 1000 yr, deduced from this study and historical documents (see discussion in text). Bold dashed lines enclose areas where intensities ≥VIII were reported in A.D. 1202 (red) and November 1759 (green) according to Ambraseys and Melville (1988) and Ambraseys and Barazangi (1989). Open symbols show location of cities (squares) and sites (circles) cited in text. Black dots mark location of field photographs shown in Figure DR1 (see footnote 1). (Inset: Levant transform plate boundary.)

Gomez et al. (2001) described evidence of recent faulting in the form of a persistent free face 0.5 m high on a scarp cutting soft lacustrine sediments. Trenching in this area, Gomez et al. (2003) exposed a colluvial wedge with modern ^{14}C ages, implying that the latest seismic event postdates A.D. 1650. They interpreted this event to be one of two eighteenth century earthquakes (A.D. 1705 or 1759), but could not discriminate between the two.

Historical sources concerning surface disruption witnessed at the time of the earthquakes are ambiguous. The 1202 Mount Lebanon rock falls might hint at stronger shaking on the west side of the Beqaa, hence on the Yammoûneh fault, but comparable shaking to the east might have gone unreported. Ambraseys and Barazangi (1989, p. 4010) mentioned 100-km-long surface ruptures in the Beqaa in November 1759, but stated that ''the exact location and attitude of (these ruptures) is [sic] not possible to ascertain today.'' Nevertheless, they inferred the Yammoûneh fault to be the most likely candidate. Building on this inference, Ellenblum et al. (1998) referred to Ambraseys and Barazangi (1989) as quoting a description of ground breaks on the Yammoûneh fault by the French ambassador in Beirut. Our own investigation of the French sources cited by Ambraseys and Barazangi (1989, p. 4010) yielded only a second-hand account by the French consul in Saida: ''One claims that [. . .] on the Baalbek side (or possibly: near Baalbek) pulling toward the plain the earth cracked open by more than [~6 m] and that this crack extends for over twenty leagues (~80 km)'' (Archives Nationales, Paris, B1/1032/1959-60). The wording suggests that this rupture took place on one side of the Beqaa, and the mention of Baalbek points to the east side, thus to the Serghaya fault.

The inference that the 1759 earthquakes might be due to slip on the Râchaïya-Serghaya fault and the 1202 event on the Yammoûneh fault is qualitatively supported by comparing the preservation of scarps and mole tracks along the two faults. Data Repository Figure DR1[1] shows the freshest seismic surface breaks we studied in the field. On the east side of the Marj Hîne basin, the Yammoûneh fault juxtaposes Cretaceous limestones with Quaternary colluvial limestone fanglomerates. The surface trace of the fault is marked by a classic coseismic scarplet (fault ribbon: e.g., Armijo et al., 1992; Piccardi et al., 1999) that is fairly weathered (Fig. DR1A; see footnote 1). North of Serghaya, one strand of the Serghaya fault shows a scarplet of comparable origin, between limestone and limestone colluvium, but with a relatively unaltered surface and lighter color (Fig. DR1B; see footnote 1). This scarplet marks the base of a prominent slope break many kilometers long, at places only tens of meters above the valley floor, hence not due to landsliding. On the Râchaïya fault, we found fresh mole tracks in unconsolidated limestone scree (Fig. DR1D; see footnote 1), while none are preserved on the Yammoûneh fault. The fault ribbon north of Serghaya, which testifies to down-to-the-west normal faulting, fits well the French consul's description. Such evidence complements that of Gomez et al. (2001) at Zebadani, implying that the latest earthquakes on the Râchaïya-Serghaya fault are younger than on the Yammoûneh fault (Tapponnier et al., 2001).

PALEOSEISMIC EVIDENCE

To test the inference that the 1202 earthquake is the latest event to have ruptured the Yammoûneh fault, we investigated the paleoseismic record of this fault by trenching lacustrine deposits in the Yammoûneh basin, on the eastern flank of Mount Lebanon (Figs. 1 and DR2 [see footnote 1]). The floor of that closed pull-apart basin used to be flooded each year by meltwater from karstic resurgences (Besançon, 1968). The lake was artificially dried 70 yr ago, and is now a cultivated plain. Aerial photographs and high-resolution satellite images show that the trace of the active strike-slip fault shortcuts the pull-apart (Fig. DR2; see footnote 1). This geometry is clear from changes in soil color and vegetation, as well as inflections or offsets of gullies. Trenching on the east side of the paleolake (Fig. DR2; see footnote 1) confirmed the location of the main fault, which cuts a finely stratified, subtabular sequence of lake beds (Fig. 2). Here, we summarize information relevant to the 1759 and 1202 events in the shallowest part of one trench (Kazzâb trench).

Beneath the 25-cm-thick cultivated soil, the upper 2–3 m of the sequence consists mostly of compact, homogeneous, white calcareous marls, with buff to brown layers, 5–200 mm thick, richer in silts and clays. Some of the lighter colored layers contain small (1–4 mm diameter) freshwater shells. A few of the layers are contorted and cloudy owing to liquefaction of probable seismic origin. Several layers contain abundant charcoal fragments (0.5–3 mm), of which 30 of 200 have already been dated. The 75-m-long trench exposes spectacular faulting within a rather narrow (<2 m wide) zone. Figure 2 shows two north-facing trench walls, <1 m apart. Owing to minor dip slip, the lake beds are sharply cut and vertically offset by fault splays, with local tilt and/or thickness changes. The effects of two seismic events are visible

[1]GSA Data Repository item 2005110, Figures DR1 and DR2 and Table DR1, field photographs of the Yammoûneh, Serghaya, and Râchaïya faults, satellite image of Yammoûneh paleolake and fault, and accelerator mass spectrometer radiocarbon data, is available online at www.geosociety.org/pubs/ft2005.htm, or on request from editing@geosociety.org or Documents Secretary, GSA, P.O. Box 9140, Boulder, CO 80301-9140, USA.

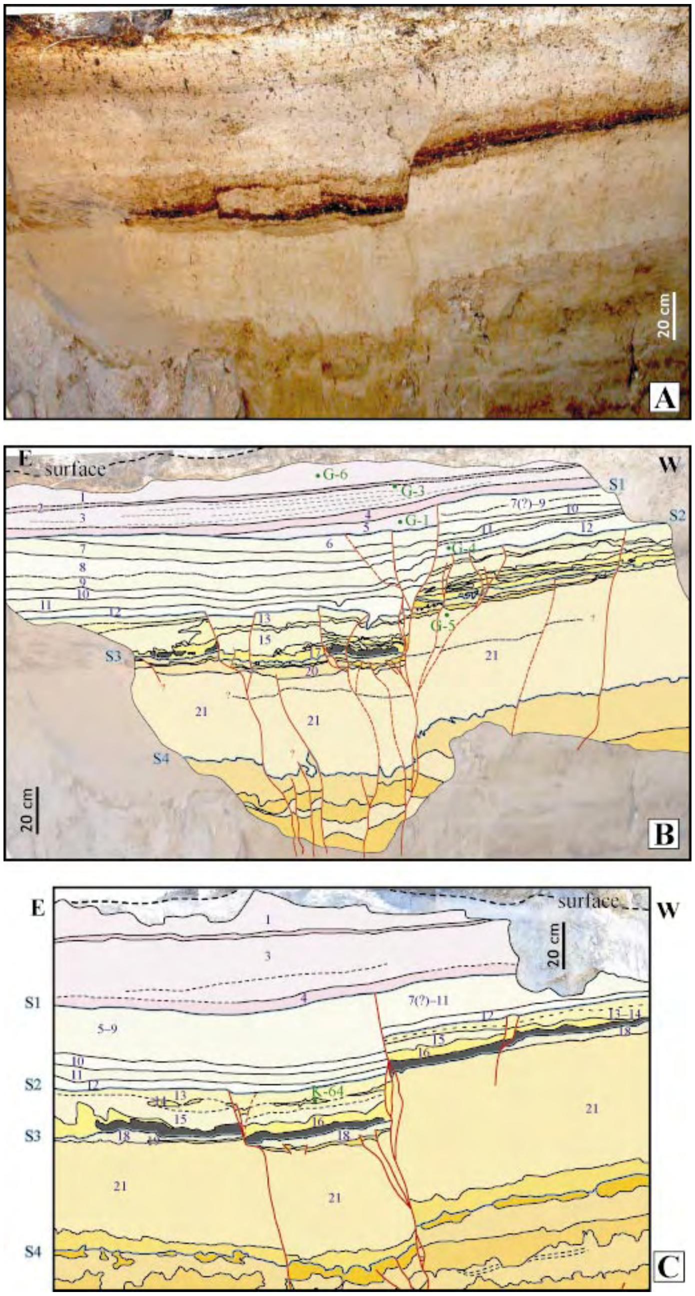

Figure 2. Photograph (A) and log (B) of wall of shallow Kazzâb-2002 trench, and log (C) of Kazzâb-2001 trench. K23, K24, and K29 were sampled on part of Kazzâb-2001 wall outside area shown here.

on both walls, in the uppermost 80 cm. The latest one (S1), marked by a subvertical principal splay, occurred after deposition of layer 6 and before that of layer 4. Layer 6, which is clearly visible on one wall, is preserved only east of the fault, suggesting it was eroded to the west after coseismic uplift. Unit 5, which tapers rapidly eastward, is most likely a type of subaquatic colluvial wedge (redistributed lake mud) emplaced shortly after S1. The penultimate event was recorded as multiple splays (S2) cutting layers 13–16 over a width of 1 m and terminating at the base of layer 12. Layer 11 shows no disruption. Hence we interpret S2 to have occurred between the emplacement of layers 12 and 11. Older events, e.g., S3 and S4, will be discussed elsewhere.

The timing of S1 is constrained by accelerator mass spectrometry radiocarbon dating of samples K23, G3, G1, and K24 (Fig. 2 and Table DR1 [see footnote 1]). Samples K23 (A.D. 1295–1410) and G3 (A.D. 1272–1412) clearly postdate the event. Sample K24 (A.D. 780–1001), from a paleochannel that is clearly capped by layer 4 (and likely by layer 6) to the east, predates the event. Sample G1 (A.D. 864–1002) comes from postseismic wedge 5, which likely contains samples from redistributed layers predating the event. Thus, the latest ground-breaking earthquake occurred between A.D. 864–1001 and 1295–1410. The only possible candidate for this event is the 1202 earthquake, since macroseismic damage for other large Near East events near that time was clearly located either well south (A.D. 1033) or well north (A.D. 1157 and 1170) of the Beqaa (e.g., Ben-Menahem, 1991; Meghraoui et al., 2003; Guidoboni et al., 2004a, 2004b). Any event postdating A.D. 1400 would have disrupted layer 2, and can be safely ruled out.

SUMMARY AND DISCUSSION

Our results put to rest the inference that the Yammoûneh fault might not be the main active branch of the Levant fault system in Lebanon (Butler et al., 1997). They provide evidence of coseismic slip on the Yammoûneh fault in A.D. 1202, and show that this segment of the fault has remained locked since then. Because the size of the November 1759 event implies that it ruptured the surface, our data preclude that it took place on the Yammoûneh fault. Because the 1759 earthquake sequence comprised two large events and because of the new evidence we found—in the form of well-preserved mole tracks—of a recent, large event south of Râchaïya, the only other large fault system adjacent to the Beqaa (Râchaïya-Serghaya) is the most plausible source. We propose that the 30 October 1759 earthquake was caused by slip on the shorter (<50 km) Râchaïya fault, and the larger-magnitude 25 November event was caused by slip on the longer (<130 km) Serghaya fault, in keeping with the evidence of recent movement on both (Tapponnier et al., 2001), and the French consul's letter. Our results thus build on those of Gomez et al. (2003) by lifting the ambiguity between the 1705 and 1759 shocks.

We interpret the occurrence of two events in 1759 and the month-long delay between them as a classic earthquake triggering example. Such triggered delayed rupture may be due to the presence of the Mount Hermon asymmetric push-up jog, a geometric irregularity that prevented immediate rupture propagation along the entire Râchaïya-Serghaya fault system. Though not unique, this scenario is in keeping with scaling laws (Wells and Coppersmith, 1994; Ambraseys and Jackson, 1998) that predict (2-sigma) magnitudes of 6.4–7.3 and 7.0–8.0 respectively, compatible with those derived from historical accounts (6.6 and 7.4; Ambraseys and Barazangi, 1989) and from the ~2 m stream channel offset attributed to the last event on the Serghaya fault at Zebadani (7.0–7.2 for the November 1759 event; Gomez et al., 2003).

With its fine lacustrine sequence, midway along the Yammoûneh fault, the Yammoûneh basin is particularly useful for understanding the timing of ancient Lebanese earthquakes. We have investigated this sequence down to 11 m depth: 2–3 m beneath the topsoil is a major stratigraphic transition, of probable climatic origin, from the calcareous marls to an ~8-m-thick clay unit. We have identified and mapped 10 event horizons down to this transition, which we dated as 11 ka (onset of the early Holocene climatic optimum).

Our results have critical implications for the assessment of seismic hazard in the area. On the Missyaf segment of the Ghab fault (Fig. 1), there is paleoseismological and archaeological evidence for three earthquakes since A.D. 70 (Meghraoui et al., 2003), the A.D. 1170 event being the latest. In Lebanon, the classic inference of a ~550 yr recurrence time for large events on the Yammoûneh fault (A.D. 1202 to 1759) must be revisited. The penultimate ground-breaking event (S2) in the Kazzâb trench postdates A.D. 261–537 (Table DR1; see footnote 1), such that the quiescence interval prior to 1202 lasted 800 ± 140 yr at most. This is to be compared with the time elapsed since then

(803 yr), and with our preliminary finding of an ~1 k.y. average recurrence time for previous events since 13 ka. The earthquake sequence of the eleventh to twelfth centuries (e.g., Poirier and Taher, 1980; Ben-Menahem, 1991; Abou Karaki, 1987; Guidoboni et al., 2004a, 2004b; Ambraseys, 2004), which ended with the 1202 event, might thus represent a concatenation of successively triggered earthquakes, analogous to those observed on the North Anatolian and Kunlun faults in the past 100 yr. Likewise, the Levant fault might exhibit millennial periods of quiescence separated by clusters of events rupturing its entire length in a couple of centuries. One might speculate that the 1995 Mw 7.3 Aqaba earthquake (Klinger et al., 1999) heralds the onset of such a clustered sequence.

Therefore, we should be prepared for the occurrence of a large destructive event similar to that of 1202 during the coming century in Lebanon. Given the rate of 5.1 $\pm$ 1.3 mm/yr derived from cosmogenic dating of offset fans along the Yammoûneh fault (Daëron et al., 2004), such an earthquake could produce 3–5 m of coseismic slip, and untold damage in areas vastly more populated today than in medieval times.

ACKNOWLEDGMENTS

We thank the National Council for Scientific Research (Lebanon), the Institut National des Sciences de l'Univers (Centre National de la Recherche Scientifique, France), and the French Ministère des Affaires Etrangères for support. Without additional funding by the Coopération pour l'Evaluation et le Développement de la Recherche (Ministère des Affaires Etrangères) and by the Institut de Physique du Globe de Paris, this work could not have been accomplished. We also thank G. Seitz and M. Kashgarian, from the Center for Accelerator Mass Spectrometry (AMS) (Lawrence Livermore National Laboratory, USA), for ^{14}C sample processing and AMS dating, A. Charbel and R. Jomaa for logistical help in the field, and two anonymous reviewers for constructive criticism. This is International Geological Correlation Programme contribution 2030.

REFERENCES CITED

Abou Karaki, N., 1987, Synthèse et carte sismotectonique des pays de la bordure orientale de la Méditerranée: Sismicité du système de failles du Jourdain–Mer Morte [Ph.D. thesis]: Strasbourg, Université Louis Pasteur de Strasbourg.

Ambraseys, N.N., 1997, The earthquake of 1 January 1837 in southern Lebanon and northern Israel: Annali di Geofisica, v. XL, p. 923–935.

Ambraseys, N.N., 2004, The 12th century seismic paroxysm in the Middle East: A historical perspective: Annals of Geophysics, v. 47, p. 733–758.

Ambraseys, N.N., and Barazangi, M., 1989, The 1759 earthquake in the Bekaa valley: Implications for earthquake hazard assessment in the Eastern Mediterranean region: Journal of Geophysical Research, v. 94, p. 4007–4013.

Ambraseys, N.N., and Jackson, J.A., 1998, Faulting associated with historical and recent earthquakes in the Eastern Mediterranean region: Geophysical Journal International, v. 133, p. 390–406.

Ambraseys, N.N., and Melville, C.P., 1988, An analysis of the eastern Mediterranean earthquake of 20 May 1202, *in* Lee, W.K.H., et al., eds., History of seismography and earthquakes of the world: San Diego, Academic Press, p. 181–200.

Armijo, R., Lyon-Caen, H., and Papanastassiou, D., 1992, East-west extension and Holocene normal-fault scarps in the Hellenic arc: Geology, v. 20, p. 491–494.

Ben-Menahem, A., 1979, Earthquake catalogue for the Middle East (92 B.C.–1980 A.D.): Bollettino di Geofisica Teorica ed Applicata, v. 21, p. 245–310.

Ben-Menahem, A., 1991, Four thousand years of seismicity along the Dead Sea rift: Journal of Geophysical Research, v. 96, p. 20,195–20,216.

Besançon, J., 1968, Le poljé de Yammoûné: Hannon, v. 3, p. 3–62.

Butler, R.W.H., Spencer, S., and Griffiths, H.M., 1997, Transcurrent fault activity on the Dead Sea Transform in Lebanon and its implications for plate tectonics and seismic hazard: Geological Society [London] Journal, v. 154, p. 757–760.

Carton, H., Singh, S.C., Elias, A., Tapponnier, P., Briais, A., Sursock, A., Jomaa, R., Daëron, M., King, G., and Jacques, E., 2004, Miocene to Quaternary folding and thrusting offshore Lebanon from SHALIMAR seismic profiles: Eos (Transactions, American Geophysical Union), v. 85, abs. T53B-0488.

Courtillot, V., Armijo, R., and Tapponnier, P., 1987, The Sinai triple junction revisited: Tectonophysics, v. 141, p. 181–190.

Daëron, M., Benedetti, L., Tapponnier, P., Sursock, A., and Finkel, R.C., 2004, Constraints on the post ~25-ka slip rate of the Yammoûneh fault (Lebanon) using in situ cosmogenic ^{36}Cl dating of offset limestone-clast fans: Earth and Planetary Science Letters, v. 227, p. 105–119.

Dubertret, L., 1932, Les formes structurales de la Syrie et de la Palestine: Paris, Académie des Sciences Comptes Rendus, v. 195.

Dubertret, L., 1955, Note explicative de la carte géologique du Liban au 1/200 000, Beirut.

Elias, A., Tapponnier, P., King, G., Singh, S.C., Sursock, A., Briais, A., Carton, H., Jacques, E., Daëron, M., and Jomaa, R., 2004, Fresh submarine seismic breaks due to historical thrust earthquakes offshore Lebanon: Eos (Transactions, American Geophysical Union), v. 85, abs. T13C-1382.

Ellenblum, R., Marco, S., Agnon, A., Rockwell, T., and Boas, A., 1998, Crusader castle torn apart by earthquake at dawn, 20 May 1202: Geology, v. 26, p. 303–306.

Freund, R., Zak, I., and Garfunkel, Z., 1968, Age and rate of the sinistral movement along the Dead Sea rift: Nature, v. 220, p. 253–255.

Freund, R., Garfunkel, Z., Zak, I., Goldberg, I., Weisbrod, T., and Derin, B., 1970, The shear along the Dead Sea rift: Royal Society of London Philosophical Transactions, v. 267, p. 107–130.

Garfunkel, Z., Zak, I., and Freund, R., 1981, Active faulting in the Dead Sea rift: Tectonophysics, v. 80, p. 1–26.

Gomez, F., Meghraoui, M., Darkal, A.N., Sbeinati, R., Darawcheh, R., Tabet, C., Khawlie, M., Charabe, M., Khair, K., and Barazangi, M., 2001, Coseismic displacements along the Serghaya Fault: An active branch of the Dead Sea fault system in Syria and Lebanon: Geological Society [London] Journal, v. 158, p. 405–408.

Gomez, F., Meghraoui, M., Darkal, A.N., Hijazi, F., Mouty, M., Souleiman, Y., Sbeinati, R., Darawcheh, R., Al-Ghazzi, R., and Barazangi, M., 2003, Holocene faulting and earthquake recurrence along the Serghaya branch of the Dead Sea fault system in Syria and Lebanon: Geophysical Journal International, v. 153, p. 658–674.

Griffiths, H.M., Clark, R.A., Thorp, K.M., and Spencer, S., 2000, Strain accommodation at the lateral margin of an active transpressive zone: Geological and seismological evidence from the Lebanese restraining bend: Geological Society [London] Journal, v. 157, p. 289–302.

Guidoboni, E., Bernardini, F., and Comastri, A., 2004a, The 1138–1139 and 1156–1159 destructive seismic crises in Syria, south-eastern Turkey and northern Lebanon: Journal of Seismology, v. 8, p. 105–127.

Guidoboni, E., Bernardini, F., Comastri, A., and Boschi, E., 2004b, The large earthquake on 29 June 1170 (Syria, Lebanon, and central southern Turkey): Journal of Geophysical Research, v. 109, no. B07304.

Klinger, Y., Rivera, L., Haessler, H., and Maurin, J.-C., 1999, Active faulting in the Gulf of Aqaba: New knowledge from the Mw 7.3 earthquake of 22 November 1995: Seismological Society of America Bulletin, v. 89, p. 1025–1036.

Meghraoui, M., Gomez, F., Sbeinati, R., Van der Woerd, J., Mouty, M., Darkal, A.N., Radwan, Y., Layyous, I., Al Najjar, H., Darawcheh, R., Hijazi, F., Al-Ghazzi, R., and Barazangi, M., 2003, Evidence for 830 years of seismic quiescence from palaeoseismology, archaeology and historical seismicity along the Dead Sea fault in Syria: Earth and Planetary Science Letters, v. 210, p. 35–52.

Piccardi, L., Gaudemer, Y., Tapponnier, P., and Boccaletti, M., 1999, Active oblique extension in the central Apennines (Italy): Evidence from the Fucino region: Geophysical Journal International, v. 139, p. 499–530.

Poirier, J.P., and Taher, M.A., 1980, Historical seismicity in the Near and Middle East, North Africa, and Spain from Arabic documents (VIIth–XVIIIth century): Seismological Society of America Bulletin, v. 70, p. 2185–2201.

Quennell, A.M., 1959, Tectonics of the Dead Sea rift: Proceedings, International Geological Congress, 20th, Mexico, p. 385–403.

Salamon, A., Hofstetter, A., Garfunkel, Z., and Ron, H., 2003, Seismotectonics of the Sinai subplate—The eastern Mediterranean region: Geophysical Journal International, v. 155, p. 149–173.

Tapponnier, P., Daëron, M., King, G., Jacques, E., Sursock, A., and Elias, A., 2001, Active faulting and seismic hazard in Lebanon: Journal of Conference Abstracts, v. 6 (EUG XI).

Wells, D.L., and Coppersmith, K.J., 1994, New empirical relationships among magnitude, rupture length, rupture width, rupture area, and surface displacement: Seismological Society of America Bulletin, v. 84, p. 974–1002.

Manuscript received 5 November 2004
Revised manuscript received 26 January 2005
Manuscript accepted 5 February 2005

Printed in USA

12,000-year-long record of 10 to 13 paleo-earthquakes on the Yammoûneh fault (Levant fault system, Lebanon)

Mathieu DAËRON (daeron@gps.caltech.edu)
Institut de Physique du Globe de Paris, France
Yann KLINGER (klinger@ipgp.jussieu.fr)
Institut de Physique du Globe de Paris, France
Paul TAPPONNIER (tappon@ipgp.jussieu.fr)
Institut de Physique du Globe de Paris, France
Ata ELIAS (elias@ipgp.jussieu.fr)
National Council for Scientific Research, Lebanon,
& Institut de Physique du Globe de Paris, France
Eric JACQUES (jacques@ipgp.jussieu.fr)
Institut de Physique du Globe de Paris, France
Alexandre SURSOCK (asursock@cnrs.edu.lb)
National Council for Scientific Research, Lebanon

Abstract

We present results of the first paleoseismic study of the Yammoûneh fault, the main on-land segment of the Levant fault system within the Lebanese restraining bend. A trench was excavated in the Yammoûneh paleo-lake, where the fault cuts through finely laminated sequences of marls and clays. First-order variations throughout this outstanding stratigraphic record appear to reflect climate change at centennial and millennial scales. The lake beds are offset and deformed in a 2-m-wide zone coinciding with the mapped fault trace. 10 to 13 events are identified, extending back more than ~12 kyr. Reliable age bounds on 7 of these events constrain the mean seismic return time to 1127±135 yr between ~12 ka and ~6.4 ka, implying that this fault slips in infrequent but large (M~7.5) earthquakes. Our results also provide conclusive evidence that the latest event at this site was the great AD 1202 historical earthquake, and suggest that the Yammoûneh fault might have been the source of a less well-known event circa AD 350. These findings, combined with previous paleoseismic data from the Zebadani valley, imply that the parallel faults bounding the Beqaa release strain in events with comparable recurrence intervals but significantly different magnitudes. Our results contribute to document the clustering of large events on the Levant fault into centennial episodes, such as that during the 11^{th}-12^{th} centuries, separated by millennial periods of quiescence, and raise the possibility of a M>7 event occurring on the Yammoûneh fault in the coming century. Such a scenario should be taken into account in regional seismic hazard assessments, and planned for accordingly.

1 Introduction

Understanding fault behavior over the span of many seismic cycles is key to answering several unresolved questions. How irregularly do earthquakes occur? What governs the time-clustering of large events on a fault system? How do faults interact mechanically at centennial and millennial time scales? How should the timing, magnitudes and sources of past earthquakes be taken into account to assess future events? Documenting long-term fault activity is not straightforward, however, due to the requirement of exhaustive historical and/or paleoseismological data sets. Currently, there are relatively few examples of long time-series of events on a fault segment [e.g., Sieh, 1984; Liu-Zeng *et al.*, 2006; Biasi *et al.*, 2002; Weldon *et al.*, 2004] or of well-documented time/space-series of historical earthquakes along strike-slip faults [e.g., Barka and Kadinskycade, 1988; Hubert-Ferrari *et al.*, 2000; Stein *et al.*, 1997].

The Levant fault system (LFS), along the eastern coast of the Mediterranean, offers a good opportunity for such work, thanks to a very long historic record spanning more than two millennia. Recently, a number of archeo- and paleoseismic studies have offered evidence linking historical earthquakes to specific fault segments [Ellenblum *et al.*, 1998; Klinger *et al.*, 2000b; Gomez *et al.*, 2003; Meghraoui *et al.*, 2003; Marco *et al.*, 2005; Daëron *et al.*, 2005]. Here we present new paleoseismic data that provide a particularly long record of earthquakes on the main "Lebanese" segment of the LFS.

2 Seismotectonic setting

2.1 The Levant fault system

The northward motion of Arabia away from Africa, corresponding to the opening of the Red Sea and Gulf of Aden [e.g., McKenzie *et al.*, 1970; Courtillot *et al.*, 1987], started in the Early Miocene (20–25 Ma) [e.g., Manighetti *et al.*, 1998; Bosworth *et al.*, 2005]. Along the Levantine coast of the eastern Mediterranean, this motion is taken up by a 1000-km-long transform fault, the Levant fault system (or "Dead Sea transform"), which connects the Red Sea ridge to the southwest segment of the East Anatolian fault system (fig. 1a). The Quaternary rate of slip on the LFS is poorly constrained, with current estimates ranging from 2 to 8 mm/yr [Chu and Gordon, 1998; Klinger *et al.*, 2000a; Niemi *et al.*, 2001; McClusky *et al.*, 2003; Meghraoui *et al.*, 2003; Gomez *et al.*, 2003; Wdowinski *et al.*, 2004; Daëron *et al.*, 2004; Daëron, 2005; Mahmoud *et al.*, 2005].

A rich body of historical sources and archaeological data, extending back more than 26 centuries, testifies to the occurrence of numerous strong (M>7), destructive earthquakes along this plate boundary [e.g., Poirier and Taher, 1980; Abou Karaki, 1987; Ben-Menahem, 1991; Guidoboni *et al.*, 1994; Guidoboni and Comastri, 2005; Ambraseys *et al.*, 1994]. Nevertheless, there are few constraints on the return times of such events or on their possible time-clustering at the scale of several centuries. The magnitudes of these large historical earthquakes contrast sharply with the relative quiescence of the fault system during most of the instrumental period. Between AD 1837 and 1995, the strongest event on the Levant fault was the M~6.2 Jericho earthquake [e.g., Plassard, 1956; Ben-Menahem and Aboodi, 1981; Avni *et al.*, 2002]. In 1995, the southernmost section of the LFS produced a Mw~7.3 earthquake in the Gulf of Aqaba [e.g., Klinger *et al.*, 1999; Al-Tarazi, 2000; Hofstetter, 2003]. This event calls attention again to the long-term potential for large earthquakes along the plate boundary, highlighting the risk of other strong events during the coming decades in this densely populated region. To address this scientific and practical issue requires extending and refining the historical record using paleoseismic data from various segments of the fault system. We discuss below the first such study of the Yammoûneh fault, within the Lebanese restraining bend.

2.2 The Lebanese restraining bend

Along most of its length, especially south of Lake Tiberias, the surface trace of the Levant fault is composed of en-echelon strike-slip segments separated by large pull-aparts or smaller push-ups [Garfunkel *et al.*, 1981]. In the area of Lebanon, however, the Levant fault's trace curves to the right, forming the 160-km-long "Lebanese" restraining bend (LRB). The resulting strike-perpendicular strain has long been held responsible for crustal shortening and uplift [e.g., Quennell, 1959; Freund *et al.*, 1970]. Within the restraining bend, deformation is partitioned between north-northeast-trending thrusts and strike-slip faults, which bound areas of active mountain building in the Lebanon and Anti-Lebanon ranges (fig. 1b) [Daëron *et al.*, 2004; Daëron, 2005; Elias, 2006; Carton, 2005]. The Yammoûneh fault appears to be the most active of these strike-slip segments. It connects the Jordan Valley fault, in the south, to the northern Levant fault, and forms the sharp topographic and structural eastern boundary of Mount Lebanon. The slip rate on this fault was constrained to be 3.8–6.4 mm/yr using cosmogenic dating of offset alluvial fans [Daëron *et al.*, 2004], accounting for much of the Levant fault's overall slip at this latitude.

Historical studies of earthquakes in the area of the LRB [e.g., fig. 5 in Ben-Menahem, 1991] have generally assumed that the Yammoûneh fault was the source of the three known M>7 events of the past 15 centuries, in AD 551, 1202 and November 1759 (table 2). If this were the case, the historical mean return time of strong earthquakes on this fault would be ~6 centuries, suggesting that we are currently halfway through the seismic cycle. Because the active fault strands of the LRB are sub-parallel and closely spaced, however, discriminating between potential fault sources requires combining historical data with direct geomorphic and paleoseismic evidence [Gomez *et al.*, 2003; Daëron *et al.*, 2005]. Here we describe and discuss new paleoseismic data from the Yammoûneh basin, along the eponymous Yammoûneh fault (fig. 1b).

3 Trench setting: the Yammoûneh basin

The Yammoûneh basin is located 1400 m a.s.l., on the eastern flank of Mount Lebanon (fig. 1b and 2a). It is the largest (1.5×6 km) of several fault-controlled troughs that disrupt the linearity of the Yammoûneh fault. The basin's long axis strikes NNE, roughly parallel to the fault's trace. It is inset between thick sub-tabular sequences of karstified Cenomanian limestone (fig. 2c). To the west, the Jabal Mnaïtra karstic plateau rises abruptly to 2100 m (fig. 2b). To the east, the basin is separated from the Beqaa by gently sloping hills (Jabal el-Qalaa, ~1500 m).

North and south of the basin, we mapped the trace of the Yammoûneh fault in detail. To the south, it follows the western flank of a north-trending limestone ridge, merging with the basin's SE margin (fig. 3a). To the north, Dubertret [1975, Baalbek sheet] mapped the fault as following the Aïnata river (see location in fig. 4a). From our own observations, however, the active trace lies above and west of the Aïnata river bed, cutting across the limestone flank of the Jabal Mnaïtra (fig. 3b). In map view, the basin thus clearly lies within a left step-over of the fault (fig. 2a). Along with the basin's rhomboidal shape, this implies that it originally formed as a pull-apart, as proposed by Garfunkel *et al.* [1981].

The study of high-resolution satellite images and 50-year-old air photographs, however, shows that there is now a direct connection between the northern and southern faults, cross-cutting through the basin sedimentary infill. Within the basin, the surface trace of this connection is marked by subtle soil color and vegetation changes, and by deviated or offset gullies. Rather than continuing along the flank of Jabal Mnaïtra, the northern fault segment bends to the south as it approaches the basin. Before entering the basin's flat floor, it cuts and offsets two alluvial fans by a few tens of meters [Daëron *et al.*, 2004]. Our mapping of the fault across the basin's southern half (fig. 4) is consistent with resistivity data, interpreted by Besançon [1968] as evidence that the fault cuts through the basin and vertically offsets the underlying bedrock. The available observations thus imply that, although the basin initially formed as a pull-apart, this releasing step-over evolved toward a simpler, smoother geometry, with a new fault cutting across the basin. Such a geometry has often been observed along other strike-slip faults [e.g., Deng *et al.*, 1986; Pelzer *et al.*, 1989; Armijo *et al.*, 2005]. On both sides of the basin, where young, clastic sediments abut the surrounding limestone units, we find no evidence of recent strike-slip motion, which suggests that all or most of the horizontal slip on the Yammoûneh fault is taken up by the mid-basin strand.

The basin's floor comprises two types of Quaternary sediments (fig. 2b). In its larger, northern part, limestone fanglomerates and red-brown clays (fig. 4a), mostly fed by the Aïnata river, overlie the Cenomanian limestone bedrock. They are locally covered by debris flow and colluvial fans at the base of the steep slope of Jabal Mnaïtra. In the southern third of the basin, a 700×1800 m patch of whitish deposits contrasts with the clastic alluvium. The deposits are calcareous lacustrine marls, containing abundant freshwater gastropod shells.

The white marls accumulated in the lowest part of the basin due to its peculiar hydrographic setting. The Mnaïtra plateau remains completely snow-covered almost 4 months a year [Service météorologique du Liban, 1971]. Beneath the plateau, subterranean karstic networks collect melt-water, feeding a dozen springs along the western edge of the basin. In times of slow discharge, the water follows sinuous channels that drain into karstic sinkholes near the opposite eastern border. Since at least Roman times, in seasons of stronger discharge (March to June) due to melting of the snow atop the plateau, the water filled a lake which used to persist for a few months[1] [Besançon, 1968]. This seasonal lake was drained in the early 1930's following construction of an underground duct designed to collect water from the main Yammoûneh sinkhole (el-Baloua, cf fig. 4b) in order to irrigate the Beqaa plain. Today, the former area of the paleo-lake corresponds to the most fertile, cultivated part of Yammoûneh basin (fig. 4b).

The distinctive tectonic and hydrographic characteristics of the basin offer an excellent opportunity to study the long-term seismic record of the Yammoûneh fault. The tectonic setting, in which the active fault trace cuts through finely stratified lake beds, provides good conditions for trenching. This was confirmed by a 5-m-deep exploratory pit near el-Baloua (fig. 4b), away from the fault, which exposed a thinly laminated sequence of marls and clays, with multiple peat layers (fig. 5a). Finally, in this lacustrine setting, excavating was greatly facilitated by the recent lowering of the water table following the drying-up of the lake.

We trenched across the inferred fault trace, ~80 m west of the eastern paleo-shoreline, on the bank of a semi-permanent stream, the Nahr el-Kazzâb (fig. 4b). In order to test our mapping of the fault trace, we started excavating well west of the expected intersection between the fault and the Kazzâb channel. The resulting "Kazzâb" trench was 4 m wide, ~75 m long and 3–5 m deep. The sub-horizontal lacustrine marls and clays thus exposed were found to be undisturbed except in one 2-m-wide zone at the inferred location of the fault. Plate 1 and figure 7 show the central 8 m of the southern wall of the Kazzâb trench ("wall K"). In order to further constrain the latest recorded events, a secondary, shallower trench was later excavated, parallel to wall K and ~1 m south of it ("wall G", fig. 8).

4 Stratigraphy

4.1 Main stratigraphic sequences

In keeping with the surface facies of the basin infill, the trench sediments comprise two distinct units: compact calcareous marls overlying red-brown clays. The distinctive clay/marl transition (fig. 5b), about 3–3.5 m below the surface, is remarkably horizontal away from the fault zone, as are most of the exposed layers. Although shallow dips perpendicular to the trench would be difficult to observe, one would expect the lake beds to dip west, if at all, away from the eastern paleo-shoreline. We observe no such dips in the trench, and conclude that most beds were deposited horizontally in the shallow water environment.

The lacustrine sediments have a rather homogeneous texture, apart from first-order variations such as the clay/marl transition. The various units' colors, by contrast, vary distinctively from

[1] Etymologically, "Yammoûneh" can be translated as "little sea" in Arabic, which might refer to the lake.

one layer to another. These color transitions generally occur abruptly (in depth), which likely reflect correspondingly abrupt (in time) sedimentary changes, and/or short-term perturbations of the sedimentary regime allowing for slight alteration of the top-most deposits. In this setting, most individual layers can be followed over long distances (at least tens of meters). We characterized and correlated the units based on sequence patterns of color and thickness[1] (fig. 6, 7 and 8). The main sequences are briefly described below. Table 3 provides a layer-by-layer description of units.

The upper 3.7 m of the exposed stratigraphic column (sequences I–IV) are silty, white-gray to beige-brown, calcareous marls. They exhibit color and texture variations at different scales, from thin laminae to homogeneous beds up to 40 cm thick. Under the modern, tilled surface lies a 150-cm-thick sequence, ("**sequence I**") of whitish, gray and light beige marls (layers L1 to L10). Within this section, at a stratigraphic depth of 90 cm, a beige marl subsequence (L6–8) becomes distinctively darker near the fault zone (L7a). Underlying sequence I, **sequence II** (L11 to L21) is a 65-cm-thick series of beige and light-brown layers (L11–16) displaying liquefaction patterns, and beige to dark brown units (L17–21) affected by local erosion. **Sequence III** (L22–30) is a 100-cm-thick package of beige marl beds, each 10–15 cm thick. **Sequence IV** (L31–35) is a 55-cm-thick set of very distinctive units, corresponding to the base of the overall marl series. Near its top, layer L34 displays evidence of pervasive bioturbation. The deepest unit in sequence IV comprises thinly laminated gray/green marls (L35), with a relatively high clay content.

The brown-to-red clay units at the bottom of the trench (sequences V–VII) are smoothly stratified, with typical thicknesses ranging from ~1 mm to more than 20 cm. **Sequence V** (50 cm thick) is topped by a distinctive, thin bed of light blue clay (L36), directly overlying mottled yellow-brown beds. The base of the sequence is marked by a very distinctive, red-brown double bed (L47). The clay beds of **sequence VI** (L48–54, 90 cm thick) are of similar aspect to that of the sequence above, except for the pervasive presence of 5-to-50-mm-wide calcareous concretions (fig. 5c), which we interpret as nodules which crystallized around sand grains or gravels. The deepest clay section, **sequence VII**, comprises relatively uniform clays, with no nodules. Only two darker layers (thin beds L55 and L58), are distinctive enough to be used as stratigraphic markers.

4.2 Age constraints

Time constraints were derived from AMS radiocarbon dating of mostly detrital charcoal and a few wood fragments sampled in various layers. Radiocarbon dating of gastropods shells from the upper marl series was also attempted, but the resulting apparent ages came out systematically older than 8 ka, even within centimeters of the surface. We interpret this as a reservoir effect resulting from the karstic origin of the paleo-lake waters.

Due to practical issues and a tight field schedule, samples from wall K were collected along broad stretches of the wall on both sides of the fault. Many samples were thus collected outside of the area shown in figure 7. However, taking advantage of the remarkably continuous and color-distinctive stratigraphy, we were able to trace the sampled layers laterally and identify them with specific logged units near the fault zone. We discarded samples for which the lateral correlation appeared to be unreliable. The stratigraphic positions of all "reliable" samples are reported in figure 6, and the corresponding radiocarbon ages in table 4.

The tree-ring calibrated ages of our samples follow a generally monotonic function of stratigraphic depth (fig. 6). Near the surface (sequence I), the dates are consistent with a sedimentation rate of 0.6 to 0.75 mm/yr. Within sequence III, the age distribution reflects a slower rate of ~0.4 mm/yr. We do not use samples from sequences V and below to estimate the latter value, because there is ample evidence of bioturbation in sequence IV, implying a different depositional setting than in sequence III.

[1] e.g., *"shell-rich, thick, white marl overlying thin, brown marl"*

Due to a lack of samples between sequences I and III, the age-depth function for sequence II is unknown. Assuming that the stratigraphic record is continuous and sedimentation rates constant within each sequence would yield an approximate rate of 0.2 mm/yr in this sequence. We suspect, however, that a more likely explanation is that part of the stratigraphic record is missing. Although there is little evidence of widespread pedogenesis, as would be expected if sedimentation had stopped altogether for a significant amount of time, layers L(17/18)b to L21 are angularly truncated and capped, west of the fault zone, by layer L16 (fig. 7). Based on this observation, we favor the hypothesis that part of the sedimentary record has been removed through erosion, possibly by eolian processes or transient channels, due to complete or partial drying-up of the lake. Testing this inference will require direct dating of sequence II, and investigating the overall paleoclimatic record in the basin.

Whatever the origin of the age-data gap within sequence II, the ages of units L11 to L21 are for now loosely constrained between 2025±102 and 6420±137 cal yr BP.

5 Paleoseismic events

5.1 Evidence for paleoseismic deformation

The 2-m-wide zone of faulted, warped and offset lake beds observed on wall K (plate 1, fig. 7) coincides not only with our initial surface mapping, but also with the fault location previously deduced from resistivity data [Besançon, 1968]. This is the only significant deformation zone observed along the entire length (75 m) of the trench. Subsequent trenches across much of the width of the paleo-lake exposed no additional fault zone. Although we cannot rule out minor active faulting elsewhere in the basin, particularly along the eastern paleo-shoreline, all the available evidence suggests that the fault zone observed in the Kazzâb trench is the current locus of most, if not all, of the strike-slip motion along the Yammoûneh fault at this location.

On vertical cross-sections of a strike-slip fault, such as shown in figures 7 and 8, offsets appearing as “vertical” can result from a small component of dip-slip, and/or from the horizontal motion of beds with a fault-parallel dip component. Overall, the lake beds, which are horizontal away from the fault zone, progressively bend down within ~5 m of the fault. The upper marl sequence is ~90 cm thicker east of the fault than west of it, corresponding to a cumulative “vertical” downthrow of the clay/marl transition (plate 1, fig. 7). Certain darker layers (e.g., L7a and L19/21), are only observed locally, in sags produced by flexure of the beds near the fault. The fault zone is composed of branches that for the most part merge downwards at various depths. However, certain layers (e.g., L4-10, L15-23, L34-45) are cut and offset by smaller faults and cracks that cannot be traced down to the central fault zone.

Below is a detailed description of the observed coseismic deformations. Overall, we interpret these observations as evidence for up to 13 paleo-earthquakes down to a stratigraphic depth of ~5 m. We discuss these events from youngest to oldest, and label them accordingly from S1 to S13. Evidence for some of these events is somewhat ambiguous, as denoted by the label “?S”, and will need to be further investigated.

Event S1:

On wall K, layer L3c is cut by a sub-vertical break F1 which uplifted L3d/f by 10 or 15 cm, depending on whether L3d/f is the western continuation of L3d or L3f (fig. 7). The corresponding change in L3c thickness, from 25 cm east of the fault, to 15 cm west of it, implies erosion of the upper section of western L3c. This is consistent with the observation on wall G (fig. 8) of a wedge of lighter marl (L3b2) which we interpret as a colluvial deposit resulting from erosion of a coseismic scarplet where F1 pierced the surface. After emplacement of L3b2, the darker layer L3b1 sealed F1. This event, S1, must predate L3b1 but postdate L3c, and the colluvial wedge L3b2 is expected to contain material re-worked from L3c.

Event ?S2:

Two other breaks, F2 and F3 (fig. 7 and 8), cut and offset the dark layer L7a by 5 cm about 50 cm to the east and west of F1. F3 can be traced upwards to the base of L3d/f, but mapping its upward continuation is impossible due to poor exposure of the sediments near the modern surface. F2 can be precisely mapped up to L3f. While this could be interpreted as evidence of an event ?S2 roughly coeval with L3e-f, layers L3e to L3c are systematically warped above F2, consistent with the observed offset of L7a. This is observed on both walls K and G. On the latter, the base of L3b1 is similarly warped, making this layer thicker to the west of F2. Since the base of L3b1 marks the S1 event horizon, we favor the interpretation that F2 and F3 formed during S1, propagating above L3f in a slightly less localized fashion, and forming a 70-cm-wide, 10-to-20-cm-deep graben at the surface. Such surface deformation is typical of en-echelon features ("mole tracks") commonly observed along strike-slip ruptures [e.g., Klinger *et al.*, 2005; Emre *et al.*, 2003]. If distinct from S1, however, ?S2 could be argued to postdate L4a and predate L3e.

Event S3:

In the middle of the down-thrown block between F1 and F2, the base of L7a is sharp, linear and undisturbed. By contrast, just beneath this continuous marker, L9 is disrupted by several oblique breaks with apparent thrust components (fig. 7, 8). The two westernmost breaks merge with the downward continuation of the main fault (F1). The corresponding event (S3) must postdate L9 and predate L7a.

Event S4:

Directly adjacent to F1, the base of L10 is warped upwards over a width of ~20 cm, above two breaks which splay off from F1 and cut layers L12 to L16. East of the fault zone, L10 tapers eastwards over a few meters. By contrast, the western section of L10 displays no thickness change, in keeping with the general geometry of the lake beds.

We interpret this tapering as a result of fault-ward tilting and deformation of the top of L11 due to event S4, and of subsequent deposition of L10 over the west-dipping top of L11, restoring a horizontal surface. While small-scale warping of L11-12 can be interpreted as direct coseismic deformation, the larger-scale tilting of L11 may be related to liquefaction within underlying layers. Indeed, directly below the tapering section of L10, layers L12 to L15 exhibit irregular, convoluted features, reminiscent of fluid mixing, probably due to thixotropy within the superficial, water-saturated lake beds during S4. In support of this interpretation, a sand-blow/mud fountain was observed at the base of L10, about 40 m west of the fault zone. The S4 horizon would thus correspond to the top of L11. Note that the contorted shapes of the thixotropic sediments make it difficult to trace the downward continuation of F2, even though it postdates liquefaction.

Event ?S5:

From minor breaks that cut L16 just east of F1 and terminate upwards into fissures filled with L15 deposits, and from small, coeval faults that offset L21-16 west of F1 and reach the base of L15, we infer the existence of event ?S5. This tentative event would therefore postdate L16 and predate the end of deposition of L15. An alternative interpretation would be that these breaks formed during S4, with liquefied marl from L15 flowing into the cracks during the shaking.

Event ?S6:

L17a is offset vertically by 5 cm across the sub-vertical fault F4. Although the break is sharp and clear in L17a, it does not appear to offset the top of L16, in contrast with the filled-in cracks observed at the top of L16 (see above, ?S5). There is no discernible evidence that F4 connects upwards with F2 across layers L15-12. This lack of evidence cannot result directly from liquefaction , since F2 clearly postdates S4. At most, the convoluted shapes of L15-12, predating F2, could make it less easy to observe a connection. Thus, based on the sharpness of F4 in L17a and its disappearance within the well-preserved layer L16, we conclude that it might result from a tentative event (?S6) postdating L17a and possibly coeval with L16.

Event S7:

Between F1 and F4, the base of L22 is offset by a sub-vertical break F5. About 20 cm to the west, L22 disappears altogether, as L23 is brought up in contact with L17a by another fault, F6. Whether F6 offsets the base of L17a is debatable, but there is no doubt that L17a seals the top of F5. Thus an event (S7), distinct from ?S6, must have occurred between deposition of L22 and that of L17a.

About 1 m east of F4, units L18a and L19/21 accumulated locally in a shallow trough. These dark, clay-rich beds were likely deposited locally in sags resulting from coseismic ground rupture. L7a, which is observed only within ~1 m of the fault, capping the S3 horizon, likely has a similar origin. Thus, in the absence of a direct dating of L17a, we propose that S7 is roughly coeval with L19b.

Event S8:

East of F1, layers L26-28 have been eroded by L23 and L24-25 due to strong folding of L26-29. This deformation results from 30–40 cm of thrust motion on a 45° west-dipping fault, F7. We interpret such thrusting as an example of local shortening caused by surface rupture irregularities, in this case an en-echelon pressure ridge. On top of this ridge, L26 has been completely removed and only part of L27 remains. It is likely that the sub-vertical faults just east of F4, which terminate abruptly where they reach the base of L23, formed during the same event (S8), which postdates L26. L24-25, which exists only east of F7, is likely derived from material eroded from the folded and uplifted layers L26-27. Thus the oldest layer which unambiguously postdates the event is L23.

Event S9:

Numerous breaks affect layers L31-34, terminating within or at the top of L31 (see close-up in fig. 9c). This event (S9) clearly postdates L31, and predates deposition of the top of L30. Faulting associated with S9 is broadly distributed, mostly within a couple of meters east of F1. This distributed rupture pattern might be related to mechanical coupling between the thin L34-35 marl cover and the clay sequence underneath.

Additionally, within ~1 m of the fault zone, the white marl of L34 displays widespread evidence of plastic flow, beautifully highlighted by the facies of L34 (fig. 9c). Such flow is particularly spectacular in the fault zone, where a large, east-facing, recumbent fold deforms the preexisting, sub-vertical bioturbation marks. This pattern can be observed up to ~1 m farther east, in the form of asymmetric folding of the lower part of L34. We propose that thixotropy and/or water saturation allowed the marls of L34 to flow east, probably due to uplifting of the western block.

The relationship between the flow and bioturbation marks implies that L33 was already in place and L34 bioturbated at the time of liquefaction. Although we cannot rule out that S9 triggered the flow, there is little evidence for coseismic uplift of the block west of the fault, which should have produced observable vertical separation. Moreover, since S9 disrupted the dark soil layer L32-33 in many places, one might expect that sand-blows of white marl (L34) would have erupted at the surface, above L31, which is not observed.

An alternative interpretation is that liquefaction was caused by S8. The vertical motion associated with this event can be traced along F7 down to L33, and its downward continuation corresponds to the locus of strongest flow. The ~30 cm of uplift associated with S8 (reflected by the abrupt thickening of layers L22–30) would be consistent with gravity-driven eastward flow of L34.

Event S10:

On both sides of the fault zone, the clay/marl interface is cut by several distinctive cracks (C1 to C5 in fig. 7, C6 in fig. 9). These fissures are 40 to 50 cm deep, up to ~15 cm wide, and rather regularly spaced (~1.5 m) near the fault zone. Away from the fault, they become smaller and wider spaced. They are all topped by L34 and taper rapidly through the uppermost clay beds, down to L44-45. White marl from L34 systematically fills these fissures, with no discernible stratification. Most of the cracks exhibit a peculiar "bayonet" shape (fig. 9a-b), with an upper part systematically offset to the east relative to the bottom tip.

The concentration of cracks within ~10 m on both sides of the fault zone, the absence of colluvial sub-units within the fissures, and the rather uniform facies of the marly infill imply that the cracks formed as a result of sudden coseismic deformation rather than desiccation, and that the corresponding event (S10) postdates the deposition of L34. Mechanically, they could result from flexure and broad down-warping of the plastic clay beds. They might also correspond to broadly distributed surface shear related to upward propagation of a seismic rupture. For instance, after the Mw~7.8 Kokoxili earthquake of 2001 in Northern Tibet, Klinger *et al.* [2005] interpreted distributed surface cracking as damage features shortly preceding the main, strike-slip surface break.

It is less straightforward to explain the bayonet geometry. Locally, the lateral offset of each crack results from bedding-parallel slip within the upper, finely laminated L35, but the exact level of décollement varies from one fissure to another. Although the upper parts of the cracks located west of the fault might have slid downslope, thus eastwards, this explanation does not hold for cracks located east of the fault. Alternatively, in order to explain the asymmetry, one might invoke very shallow block rotations about vertical axes, consistent with left-lateral slip, but we found no independent evidence in support of this explanation.

As mentioned above, the rather uniform filling of the cracks implies that L34 was present at the time of S10 and flowed rapidly in the fissures. By contrast, within the cracks farthest from the fault zone (e.g., C6, in fig. 9a-b), the dark, sub-vertical bioturbation marks in the upper part of L34, as well as the level at the base of L32-33, display no perturbation whatsoever above the fissure. The development of soil and vegetation in L32-33 thus postdates S10.

Event S11:

In several places (just east of C3, between F4 and F5, and in the area shown in fig. 9a), the uppermost clay layers are offset by several fault breaks. Each of the breaks offsets the thin blue clay unit L36, and some of them affect the lowermost part of overlying L35. At most, the vertical offset of L36 is 8 cm (between F4 and F5). The breaks can be traced downwards for a few tens of centimeters, at most down to L46. We interpret these faults to flatten out above L47, some of them accommodating dip-slip motion only, because of downward flexing of the clay beds near the fault zone. The corresponding event, S11, should be roughly coeval with the lower part of L35.

Event S12:

The dark red-brown double layer L47 is down-thrown and completely disrupted in the eastern half of the deep part of the fault zone. Only discontinuous fragments of this layer are recognizable near the bottom of a 90-cm-wide, ~25-cm-deep half-graben. Recognition of L47 in this half-graben is unambiguous because of its distinctive appearance. Clay lenses with a peculiar, brick-red color, observed nowhere else in the trench, are inter-stratified in the half-graben fill, mostly between L41 and L47. This is suggestive of local collapse, accounting for the poor state of preservation of layers L42-47 within the half-graben. The western half of the graben might be missing due to posterior strike-slip (i.e. wall-perpendicular) motion on the fault. Layers younger than L47 are difficult to recognize within the half-graben, although clear thickening is evident below the unaffected layer L41, which smoothly overlies the trough. The corresponding event, S12, thus predates L41 and postdates L47. Unfortunately, the degraded stratigraphic sequence within the graben precludes a more precise assessment.

Event S13:

L55 is vertically offset, by up to 5 cm, across numerous small breaks on both sides of the main fault zone. Some, such as F9 or F10, can be traced down to L58-60. These breaks all terminate upwards about 5–10 cm above L55. At this level, between L55 and L53, the thickness of L54 changes abruptly across the main fault zone from 30–36 cm (W) to 42–46 cm (E). This is the deepest observed evidence of coseismic deformation in this trench. The corresponding event, S13, predates L53 and postdates the top of L54.

5.2 Timing of events

Table 5 summarizes the stratigraphic constraints relevant to each event described above. S1, ?S2 and S3 are well-constrained by 6 radiocarbon dates from sequence I (fig. 10). K23 and G3 were sampled in units unambiguously postdating S1. We interpret L3b2 as a post-seismic colluvial wedge derived from L3c material, implying that G1 predates S1. Event ?S2, in turn, predates G1 and postdates K64. Sample G4 is clearly out of sequence, being older than K64 and similar in age to G5, which are located 16 and 40 cm below it, respectively (cf table 4 and fig. 6). Event S3 predates K64 and postdates both samples G5 and K29. Figure 10 displays the output of an OxCal Bayesian model for this sequence:

$$\mathrm{K29} > \mathrm{G5} > \mathbf{S3} > \mathrm{K64} > \mathbf{{}^{?}S2} > \mathrm{G1} > \mathbf{S1} > \mathrm{G3} > \mathrm{K23}\ ,$$

where the $>$ sign denotes “is older than”. The age bounds predicted by the model are listed in table 5.

The events recorded between layers L10 and L19b can only be very loosely constrained to have occurred between 2.0 and 6.4 cal kyr BP, due to the scarcity of radiocarbon data. Until the sedimentary history of sequence II is elucidated, one cannot assume that our record of events is complete in this section of the trench. Moreover, the ambiguous evidence for ?S5 and ?S6 further detracts from an estimate of the total number of events between 6.4 and 2.0 ka. Since the sedimentary sequence between L10 and L11 appears to be continuous, one could argue that a reasonable age estimate for S4 can be obtained from extrapolating the sedimentation rate in sequence I to the base of L10 (cf fig. 6). Doing so would place S4 some time around 2.5–3.0 ka.

The timing of the events recorded in sequences III–V, by contrast, is constrained by numerous dated samples. Excluding samples K43 and K120, which are out of stratigraphic order (cf fig. 6), the stratigraphic relationships between event horizons and radiocarbon samples can be summarized as:

$$\mathbf{S12} \approx \mathrm{K93} > \mathbf{S11} > \begin{pmatrix} \mathrm{K20} \\ \mathrm{K129} \end{pmatrix} > \begin{pmatrix} \mathbf{S10} \\ \mathrm{K3} \end{pmatrix} > \begin{pmatrix} \mathrm{K50} \\ \mathrm{K50b} \end{pmatrix} > \mathbf{S9} > \mathrm{K49} \cdots$$

$$\cdots \mathrm{K49} > \begin{pmatrix} \mathrm{K83} \\ \mathrm{K80c} \\ \mathrm{K80b} \\ \mathrm{K82} \end{pmatrix} > \begin{pmatrix} \mathbf{S8} \\ \\ \mathrm{K78} > \begin{pmatrix} \mathrm{K35} \\ \mathrm{K35b} \end{pmatrix} \end{pmatrix} > \mathrm{K16b} > \mathrm{K76} > \begin{pmatrix} \mathrm{K111} \\ \mathrm{K13a} \\ \mathrm{K13b} \end{pmatrix} \approx \mathbf{S7}$$

where parenthesized groups represent phases (unordered sets of dates) and the $\approx$ symbol denotes similar ages. As noted above, we interpret S7 to be roughly coeval with layer L19b, where samples K111, K13a and K13a were collected. Similarly, the stratigraphic position of sample K93 corresponds roughly to that of the S12 horizon. In the absence of an older sample which would allow for a more robust dating of S12, we use the age of K93 as our best estimate of the timing of S12. The corresponding OxCal model is displayed in figure 11, and resulting age bounds are reported in table 5.

Finally, the S13 horizon lies more than 1 m below the oldest dated sample, K93, and as a result its timing can only be constrained to be significantly older than ~12 ka.

6 Discussion

6.1 Paleoclimatic interpretation

The age-vs-depth calibration of the Kazzâb sediments (fig. 6) supports the inference that first-order stratigraphic divisions of the lacustrine sequence reflect regional climatic change. The fact that the clay/marl transition is a lake-wide feature, systematically observed not only in the Kazzâb trench, but also in other trenches not discussed here, implies that it reflects external environmental forcing. The age of this transition can be estimated by interpolating between the ages of K129 and K93, which yields a date of 11271±400 cal yr BP, coeval with the ~11.5 ka end of the Younger Dryas, as recorded by speleothems in the Soreq Cave, 300 km south of Yammoûneh [Bar-Matthews *et al.*, 2003].

Similarly, the marls of sequence III form a distinctive, 1-m-thick package of thick beds (L22–30), whose ages range from 8692±309 to 6550±102 cal yr BP. Again, this closely fits the bounds of the Early Holocene Climatic Optimum, constrained by the Soreq data to the period between 8.5 and 7 ka [Bar-Matthews *et al.*, 2003]. The alternating light and dark beige beds within this Early Holocene marl sequence may reflect roughly bicentennial cycles linked to solar forcing, as detected during MIS 2 in the Lisan lake beds by Prasad *et al.* [2004].

More specific interpretations in terms of past climates will require a thorough paleoclimatic study of the Yammoûneh sediments, currently underway. Preliminary sedimentological and palynological analyses [*F. Gasse*, personal communication] suggest that the clays of sequences V–VII were deposited in an ephemeral swamp under relatively dry and cool conditions, and that the calcareous marls reflect wetter (and presumably warmer) conditions.

Several factors might have triggered the sedimentary change from clays to marls. In the northern part of the basin, channel mapping based on surface shades in the fanglomerate infill show a south-diverging fan pattern, implying that the Aïnata river once filled the basin with a prograding delta. By contrast, calcareous marls are only observed in the southern third of the basin, in the area located directly between the Jabal Mnaïtra karstic springs, and the Jabal el-Qalaa sinkholes (fig. 4). Such disparity suggests that the two types of sediments have different origins. The abrupt transition from clays to marls, around the end of the Younger Dryas, could have resulted from climate-driven damming of the Aïnata river by transverse debris-flow fans (fig. 4a), greatly reducing the supply of clay-rich detrital sediments.

Preliminary investigation from a nearby trench reveals that the Holocene marls comprise mostly authigenic carbonate [*F. Gasse*, personal communication]. The dearth of detrital material suggests that the supply by local runoff was then small, in keeping with the modern basin's limited watershed and with the predominantly karstic origin of its water.

A purely paleoclimatic interpretation of some of the dark horizons that stand out in the uppermost light-colored marls is less straightforward. L7a, which is particularly dark in the central section of wall K, tapers and lightens away from the fault zone. L19/21, at the base of sequence II, is thickest in a sag located 1 m east of the fault, and tapers eastwards. Such horizons appear to be related to ground deformation in the fault zone, due to ponding resulting from coseismic warping of the underlying layers, and therefore may be unrelated to regional climate.

Finally, regional paleoclimate records offer insight into the paleo-environment of sequence II. There is reliable evidence for a regional episode of great aridity circa 4 ka [e.g., Cullen *et al.*, 2000], which correlates with the largest Holocene drops in the level of the Dead Sea [e.g., Bookman *et al.*, 2004; Klinger *et al.*, 2003] and of Lake Tiberias [e.g., Hazan *et al.*, 2005]. An arid paleo-environment at Yammoûneh around 4 ka would be consistent with partial erosion of sequence II, either due to meandering channels in a low-water setting, or to eolian erosion of the dried-up lake. It might also account in part for the lack of organic material in sequence II.

6.2 Historical identification of events

Overall, the Kazzâb record displays evidence for at least 10 and at most 13 paleo-earthquakes, over a period extending back more than 12 kyr. Within this time span, we have good time constraints on two plurimillennial intervals, a "historical" sequence from 178 BC–AD 26 to the early 20^{th} century, and a "prehistoric" sequence from 12047 ± 658 to 6445 ± 121 cal yr BP.

The occurrence of the latest event recorded at this site, S1, is constrained to the 10^{th}-14^{th} centuries AD (fig. 10). During that interval, the most prominent regional historical earthquake was the Ms$\sim$7.6, AD 1202 event (table 2). Its area of strongest damage was centered around the Beqaa [Ambraseys and Melville, 1988] and it is known to have offset the walls of a Crusader fortification by 1.6 m [Ellenblum *et al.*, 1998], just south of the Lebanese restraining bend ("Vadum Jacob", fig. 1b). Although other, smaller events have been reported locally in the area of the restraining bend during that period (AD 991, near Damascus and Baalbek; AD 1063, near Tripoli; Ben-Menahem [1991]; Guidoboni *et al.* [1994]; Abou Karaki [1987]), their strongest effects were reported tens of kilometers away from the Yammoûneh fault, which points to other active faults as the sources of these events. Our data thus imply that S1 was the 1202 earthquake, in keeping with previous historical inferences. For a more detailed discussion of this event, including qualitative geomorphic evidence and a reinterpretation of historical reports, see Daëron *et al.* [2005].

As noted above, we favor the interpretation that the breaks tentatively attributed to $^?$S2 were in fact produced by S1. The large estimated magnitude of the AD 1202 earthquake is consistent with a zone of surface deformation ("mole tracks") broader than the single, localized break F1 (fig. 7-8 and plate 1). If $^?$S2 were a distinct event, it would have occurred between AD 405 and 945 (fig. 10). One might be tempted to correlate it with the historical AD 551 earthquake (table 2), but there is growing support for the offshore Mount Lebanon thrust system to be the source of this event [*Elias et al.*, submitted, Elias, 2006; Morhange *et al.*, 2006]. Thus we conclude that if an earthquake did occur between AD 405 and 945 on the Yammoûneh fault, the historical record fails to provide an obvious corresponding event.

The occurrence of S3 is constrained to 30 BC–AD 469 (fig. 10). This event might correspond to a poorly documented earthquake reported to have damaged Beirut in AD 348/349 [Plassard, 1968; Abou Karaki, 1987; Ben-Menahem, 1991; Guidoboni *et al.*, 1994]. Roman temples within ~10 km of the Yammoûneh fault (Niha, Afqa) show evidence of strong shaking such as toppled walls and columns, although the date of the corresponding destructive event remains unknown. A mid-fourth century earthquake might also account for the sudden termination of construction work on the Baalbek temples, more conventionally interpreted as a result of the Roman empire's official conversion to Christianity [Alouf, 1998; Jidejian, 1998].

The overall interpretation of the S1–3 "historical" sequence depends on whether ?S2 is distinct from S1. If it is not, the two latest earthquakes were S1 (AD 1202) and S3 (30 BC–AD 469), and the corresponding interseismic period lasted 733–1230 yr (fig. 12). If, on the other hand, ?S2 was a distinct event, the "historical" mean return time of would be only half as long (366–615 yr).

6.3 Prehistoric sequence of events

The stratigraphic units which record the prehistoric sequence of events (S7–12) are among the most distinctive, with many unambiguous and continuous markers and no evidence of a sedimentary gap. It is thus likely that this sequence represents a locally complete record of paleo-earthquakes. 5635$\pm$675 yr elapsed between S12 and S7, which yields a mean return time ("MRT") of 1127$\pm$135 yr over this period (fig. 12). We must stress that the error bar of this value reflects the uncertainty in the dating of S7 and S12, rather than the statistical variance in the successive interseismic time intervals. Unfortunately, the available constraints on individual events are too broad to address the issue of the regularity or irregularity of earthquake occurrence at this site.

6.4 Re-assessment of seismic hazard related to the Yammoûneh fault

The time probability distribution of the "long-term" MRT from ~12 ka to ~6.4 ka is not statistically different from that of the time elapsed between S3 and S1 (fig. 12), which suggests that the average frequency of events might not have varied significantly since ~6.4 ka. If indeed this is the case, previous assessments of seismic hazard in the Lebanese restraining bend would need to be radically revised. It has generally been inferred that the Yammoûneh fault was the source of both the May 1202 and November 1759 events [e.g., Ambraseys and Barazangi, 1989], which implies a return time on the order of 560 yr [e.g., Harajli *et al.*, 2002]. The Yammoûneh fault would thus presently be far from the end of its seismic cycle.

Instead, our results establish that the 1202 event was the last one to rupture the fault [Daëron *et al.*, 2005]. In figure 12 we compare the 804 yr elapsed since AD 1202 with the time probability distribution of six of the intervals elapsed between the Kazzâb events, and with the "prehistoric" MRT. Such a span of 8 centuries is statistically similar to all individual intervals, including the most tightly constrained one, between S3 and S1. It should be stressed that although 804 yr lie outside the error bar of the "prehistoric" *mean* return time, this does not imply that an earthquake is unlikely to occur in the coming ~100 yr, because, as noted above, this MRT error bar tells us nothing about the variability of individual seismic cycle durations.

Based on the average ~1100-yr-long loading time of the Yammoûneh fault and on the post-glacial slip rate (~5 mm/yr), estimated from the offsets of ^{36}Cl-dated fans [Daëron *et al.*, 2004], a characteristic coseismic slip on the order of 5.5 m is expected. Using macroseismic scaling laws [Wells and Coppersmith, 1994; Ambraseys and Jackson, 1998], this would correspond to magnitudes of 7.3–7.5, similar to estimates derived from historical reports for the AD 1202 event (table 2). Assuming a slip-predictable fault behavior, if an earthquake occurred today it would still be expected to produce a magnitude larger than 7. Were it to occur, such an event would likely have a devastating impact on the whole of Lebanon, whose territory lies entirely within 30 km of the Yammoûneh fault. The seismic hazard from this fault thus presents an immediate safety concern which should rapidly be addressed, at a time when many Lebanese population centers are being rebuilt.

6.5 Regional seismic hazard from paleo- and historical seismicity

How does the Kazzâb record compare with historical, archaeological and paleoseismic data from adjacent strands of the Levant fault? In the southern Zebadani valley (fig. 1b), Gomez *et al.* [2003] have documented the paleoseismic record of the Serghaya fault since 6.5 ka. They identified five events, the latest having occurred in the 18th century (fig. 13). It is extremely likely that this 18th century event is the M_s~7.4 earthquake of November 1759 (table 2), as discussed by Daëron *et al.* [2005] based on the combined assessment of historical sources, geomorphic observations and the paleoseismic data detailed here. All the older Zebadani events occurred during the poorly constrained time interval of the Kazzâb record (2.0–6.4 ka). The corresponding MRT was ~1300 yr, with average coseismic slip amounts of ~2 m.

For now, unfortunately, it is difficult to compare these two data sets, although testing the time-correlation of large events on these two parallel strike-slip faults, which lie only 25–30 km apart, would be of great interest. Because of elastic interaction, coseismic slip on one of these faults is expected to significantly unload the other, providing a good opportunity to document short-range fault interaction from combined paleoseismic records. For instance, one might speculate that the occurrence of the 1202 event is responsible for the longer than average quiescence period prior to 1759 on the Serghaya fault (~1800 yr versus 1300 yr).

On the Yammoûneh fault, slip appears to be released in slightly more frequent and significantly larger earthquakes (~5.5 m every ~1100 yr on average). This suggests that the similar mean return times on the two faults are driven by regional stress loading, while the size of individual earthquakes is more directly related to fault geometry, in particular segment length. The faster slip rate on the Yammoûneh fault (5.1±1.3 mm/yr) than on the Serghaya fault (1.4±0.2 mm/yr [Gomez *et al.*, 2003]) might thus primarily result from a longer seismic rupture length (~190 km versus ~115 km).

North of the restraining bend, Meghraoui *et al.* [2003] have described evidence for the last three events on the Missyaf segment of the Ghab fault, in Western Syria (fig. 1). The latest one is the large AD 1170 earthquake, historically well described by Guidoboni *et al.* [2004]. The two preceding events occurred around AD 100–450 (event X) and AD 700–1030 (event Y). South of the restraining bend, a number of studies suggest that the Jordan Valley fault system (fig. 1) slipped during the earthquakes of 31 BC, AD 363, 749, 1033 and 1546 [Ben-Menahem, 1991; Guidoboni *et al.*, 1994; Ambraseys *et al.*, 1994; Abou Karaki, 1987; Reches and Hoexter, 1981; Marco *et al.*, 2003; Ambraseys and Karcz, 1992]. Figure 13 summarizes these records along with the most recent Kazzâb events.

The only well-dated medieval earthquakes on the Yammoûneh and Ghab faults took place during a period of unusually high seismic activity along the Levant fault, spanning the 11th and 12th centuries. From AD 1033 to 1202, it appears that the whole length of the fault system slipped in a series of at least five M>7 events [e.g., Ben-Menahem, 1991; Guidoboni *et al.*, 1994; Ambraseys *et al.*, 1994]. The records of the North Anatolian and Kunlun fault systems [e.g. Ambraseys and Melville, 1982; Van der Woerd *et al.*, 2002], which typically release strain during ~100-yr-long sequences of large earthquakes, suggest that this behavior might be characteristic of strike-slip systems at this scale. If this were the case, the large (Mw~7.3) earthquake which ruptured the southernmost section of the Levant fault system in AD 1995 might herald such a centennial sequence, contrasting with the relative quiescence of 20th-century Levantine seismicity.

Testing this hypothesis will require tighter age constraints on early medieval and older events on the Yammoûneh and Ghab faults. For instance, if event S3 in the Kazzâb record were indeed the mid-fourth-century earthquake which damaged Beirut, it could be correlated with the well-known AD 363 earthquake on the Jordan Valley fault [Ben-Menahem, 1991; Guidoboni *et al.*, 1994]. Moreover, the exact sources of these ancient events must be systematically sorted out, taking into account the surface complexity of the fault system. Resolving these issues requires combining paleoseismic and archaeological data to reach beyond the scope of this study. The Levant area, with its exceptional historical and archaeological records, in a mostly arid environment, offers a unique opportunity to document the behavior of fault systems at millennial time scales.

Acknowledgments

Many thanks to everyone at the National Center for Geophysical Research in Bhannes, Lebanon, for their invaluable help in the field. This work has been supported by the National Council for Scientific Research of Lebanon, the Institut National des Sciences de l'Univers of France, and the French Ministère des Affaires Etrangères. Additional funding was provided by the Institut de Physique du Globe de Paris. We wish to thank NCSR General Secretary M. Hamze, for his long-term support; G. Seitz and M. Kashgarian, for help and advice about radiocarbon sample processing and AMS; and F. Gasse, for sharing her early paleoclimatic and palynological results. This paper benefitted greatly from thorough reviews by T. Niemi and G. Biasi. This is Institut de Physique du Globe de Paris contribution #2190.

Tables and Figures

Table 1: Notations used in this study.

Table 2: Summary of the effects of the strongest historical earthquakes of the Lebanese restraining bend. Based on re-assessed historical sources, geomorphic observations and paleoseismic evidence further discussed in this study, we previously argued that the sources of the 1202 and Nov. 1759 events were the Yammoûneh and Serghaya faults, respectively [Daëron *et al.*, 2005].

Table 3: Detailed stratigraphic units. Corresponding stratigraphic log is shown in fig. 6.

Table 4: Radiocarbon dates. Samples K29 and K82 are partly carbonized wood fragments. K13b, K76 and K49, are crushed charcoal, locally mixed with marly sediments. All other samples are detrital charcoal fragments. "K" samples were processed at Lawrence Livermore National Laboratory's Center for AMS, and "G" samples at the Van de Graaff laboratory of the University of Utrecht. For all "K" samples, $\delta^{13}C$ was assumed to be -25‰. C-14 ages were converted to calendar years using OxCal 4β3 [Bronk Ramsey, 1995, 2001] with terrestrial calibration curve IntCal04 [Reimer *et al.*, 2005]. Only 4 samples, marked *, appear to be out of stratigraphic order.

Table 5: Stratigraphic and chronological constraints on event ages. Stratigraphic models used to estimate the 95% age bounds are discussed in the text and displayed in fig. 10-11.

Figure 1: Regional tectonic setting. (a) Map of the Levant fault system. (b) Active faults of the Lebanese restraining bend.

Figure 2: Overview of the Yammoûneh basin. (a) Satellite image of the basin, between the Mnaïtra plateau and the Qalaa hills. The white arrow indicates the viewpoint of (b), and the red line marks the active trace of the Yammoûneh fault. The location of the town of Aïnata is marked by a white circle. (b) WSW-looking, oblique aerial photograph of the basin. (c) Simplified geological cross-section, modified from Dubertret [1975, Baalbek sheet].

Figure 3: Active fault trace south and north from the Yammoûneh basin. (a) S-looking view of the paleo-lake (darker infill area). The active trace of the fault (white arrows) runs along the W flank of a limestone ridge aligned with the E margin of the basin. (b) S-looking view of the Yammoûneh fault above the village of Aïnata. Cumulative slip has formed several asymmetric, scarp-bounded, limestone shutter ridges (white arrows). Distance between the arrows is 400 m.

Figure 4: Maps of the Yammoûneh basin. (a) Quaternary geology of the basin. (b) The trench (black rectangle) parallels the channel of the Nahr el-Kazzâb stream (thin dashed line) where it crosses the fault (solid white line). A white star marks the location of the main karstic sinkhole (el-Baloua), where the exploratory pit of fig. 5a was excavated.

Figure 5: Sediments exposed in the Yammoûneh paleo-lake. (a) Peat laminae in the Baloua pit (location in fig. 4b). Marl/clay interface (b) and calcareous nodules (c) exposed in the Kazzâb trench.

Figure 6: Stratigraphic log of the Kazzâb sediments, east (E) and west (W) of the fault zone, with vertical positions of dated samples and event horizons. The main sedimentary sequences (I–VII) are shown left of the stratigraphic columns, as well as a plot of the calibrated ages of radiocarbon samples versus depth (cf table 4).

Figure 7: Log of wall K. The corresponding photo-mosaic is shown in plate 1. White labels indicate the stratigraphic levels of event horizons. White corners in the deeper fault zone correspond to the outline of fig. 9c. White star marks the location of similar star in plate 1 and fig. 9ab.

Figure 8: Wall G. (a) Photograph of trench wall G. (b) Corresponding log, with labels marking the stratigraphic levels of event horizons. The shaded area in the lower part of the log corresponds to backfill and rough parts of the wall.

Figure 9: Examples of coseismic deformation. (a, b) One of several bayonet-shaped cracks which systematically open in L35, taper down to L44-45, and are filled with L34 (see discussion in text). Note the shallow décollement in L35a. The dark bioturbation marks in L34 appear to be unaffected by the crack. The white star shows the location of the similar stars in plate 1 and fig. 7. (c) Preexisting bioturbation marks record E-directed flow of whitish marl (L34) in the fault zone. The outline of this photograph is shown as white corners in fig. 7.

Figure 10: "Historical" series of events. Time probability distributions (TPD) in light gray are calibrated using terrestrial curve IntCal04 [Reimer *et al.*, 2005]. Dark gray TPD are modeled using OxCal 4β3 [Bronk Ramsey, 1995, 2001], according to the Bayesian model discussed in the text, and the resulting TPD of events S1–3 are plotted in black. Horizontal bars correspond to 95.4% confidence limits.

Figure 11: "Prehistoric" series of events. Time probability distributions (TPD) in light gray are calibrated using terrestrial curve IntCal04 [Reimer *et al.*, 2005]. Dark gray TPD are modeled using OxCal 4β3 [Bronk Ramsey, 1995, 2001], according to the Bayesian model discussed in the text, with sub-sequences displayed as rectangles, and phases (unordered groups) as rounded boxes. The resulting TPD of events S7–12 are plotted in black. Horizontal bars correspond to 95.4% confidence limits.

Figure 12: Seismic return intervals. Time probability distributions (TPD) of the various intervals elapsed between consecutive events in the Kazzâb record are plotted in gray. The narrower, black TPD is that of the mean return time at this site between ~12 and ~6.4 ka. The uncertainty on this *mean* return time does not reflect variability in the length of individual seismic cycles. Horizontal bars correspond to 95.4% confidence limits. Dashed line indicates the 804 yr currently elapsed since the latest event (AD 1202).

Figure 13: Compared paleoseismic records of faults in the LRB area, based on data from this study, Meghraoui *et al.* [2003], Gomez *et al.* [2003], Reches and Hoexter [1981], Marco *et al.* [2003], and historical catalogs (references in text).

Plate 1: North-facing wall of the Kazzâb trench, across the left-lateral Yammoûneh fault ("wall K"). Calcareous, whitish to light brown, lacustrine marl beds overlie red-brown clays of likely palustrine origin. The generally continuous units exposed here have recorded 10 to 13 events, which resulted in a 2-m-wide zone of splaying fault breaks and distributed deformation. The log of this wall is shown in fig. 7. The white star marks the location of the similar symbols in fig. 7 and 9ab.

References

Abou Karaki, N. (1987). *Synthèse et carte sismotectonique des pays de la bordure orientale de la Méditerranée : sismicité du système de failles du Jourdain - Mer Morte*, Ph.D. thesis, Université Louis Pasteur de Strasbourg.

Al-Tarazi, E. (2000). The major Gulf of Aqaba earthquake, 22 November 1995 – maximum intensity distribution, *Natural Hazards* **22**, 17–27.

Alouf, M. (1998). *History of Baalbek*, Book Tree.

Ambraseys, N., and M. Barazangi (1989). The 1759 earthquake in the Bekaa valley: implications for earthquake hazard assessment in the Eastern Mediterranean region, *Journal of Geophysical Research* **94**, no. B4, 4007–4013.

Ambraseys, N., and J. Jackson (1998). Faulting associated with historical and recent earthquakes in the Eastern Mediterranean region, *Geophysical Journal International* **133**, 390–406.

Ambraseys, N., and I. Karcz (1992). The earthquake of 1546 in the Holy Land, *Terra Nova* **4**, no. 2, 254–263.

Ambraseys, N., and C. Melville (1982). *A history of Persian earthquakes*, Cambridge University Press.

Ambraseys, N., and C. Melville (1988). An analysis of the eastern Mediterranean earthquake of 20 May 1202, in *History of Seismography and Earthquakes of the World*, W. Lee, H. Meyers, and K. Shimazaki, editors, Academic Press, San Diego, CA, pp. 181–200.

Ambraseys, N., C. Melville, and R. Adams (1994). *The Seismicity of Egypt, Arabia and the Red Sea - a historical review*, Cambridge University Press.

Armijo, R., N. Pondard, B. Meyer, G. Ucarkus, B. de Lepinay, J. Malavieille, S. Dominguez, M. Gustcher, S. Schmidt, C. Beck, N. Cagatay, Z. Cakir, C. Imren, K. Eris, B. Natalin, S. Ozalaybey, L. Tolun, I. Lefevre, L. Seeber, L. Gasperini, C. Rangin, O. Emre, and K. Sarikavak (2005). Submarine fault scarps in the Sea of Marmara pull-apart (North Anatolian Fault): implications for seismic hazard in Istanbul, *Geochemistry Geophysics Geosystems* **6**, Q06009.

Avni, R., D. Bowman, A. Shapira, and A. Nur (2002). Erroneous interpretation of historical documents related to the epicenter of the 1927 Jericho earthquake in the Holy Land, *Journal of Seismology* **6**, 469–476.

Bar-Matthews, M., A. Ayalon, M. Gilmour, A. Matthews, and C. Hawkesworth (2003). Sea-land oxygen isotopic relationships from planktonic foraminifera and speleothems in the Eastern Mediterranean region and their implication for paleorainfall during interglacial intervals, *Geochimica et Cosmochimica Acta* **67**, no. 17, 3181–3199.

Barka, A., and K. Kadinskycade (1988). Strike-slip-fault geometry in Turkey and its influence on earthquake activity, *Tectonics* **7**, no. 3, 663–684.

Ben-Menahem, A. (1991). Four thousand years of seismicity along the Dead Sea rift, *Journal of Geophysical Research* **96**, no. B12, 20195–20216.

Ben-Menahem, A., and E. Aboodi (1981). Micro- and macro-seismicity of the dead sea rift and off-coast eastern mediterranean, *Tectonophysics* **80**, no. 1–4, 199–233.

Besançon, J. (1968). Le poljé de Yammoûné, *Hannon (revue libanaise de géographie)* **3**, 3–62.

Biasi, G., R. Weldon, T. Fumal, and G. Seitz (2002). Paleoseismic event dating and the conditional probability of large earthquakes on the southern San Andreas fault, California, *Bulletin of the Seismological Society of America* **92**, no. 7, 2761–2781.

Bookman, R., Y. Enzel, A. Agnon, and M. Stein (2004). Late Holocene lake levels of the Dead Sea, *Geological Society of America Bulletin* **116**, no. 5-6, 555–571.

Bosworth, W., P. Huchon, and K. McClay (2005). The Red Sea and Gulf of Aden basins, *Journal of African Earth Sciences* **43**, 334–378.

Bronk Ramsey, C. (1995). Radiocarbon calibration and analysis of stratigraphy: the OxCal program, *Radiocarbon* **37**, no. 2, 425–430.

Bronk Ramsey, C. (2001). Development of the radiocarbon program OxCal, *Radiocarbon* **43**, no. 2A, 355–363.

Carton, H. (2005). *Etudes tectoniques en Me?diterranne?e orientale par analyse de donne?es de sismique reflexion : Mer de Marmara (Bassin de Cinarcik) et marge du Liban*, Ph.D. thesis, Institut de Physique du Globe de Paris.

Chu, D., and R. Gordon (1998). Current plate motions across the Red Sea, *Geophysical Journal International* **135**, 313–328.

Courtillot, V., R. Armijo, and P. Tapponnier (1987). The Sinai triple junction revisited, *Tectonophysics* **141**, 181–190.

Cullen, H., P. deMenocal, S. Hemming, G. Hemming, F. Brown, T. Guilderson, and F. Sirocko (2000). Climate change and the collapse of the Akkadian empire: evidence from the deep sea, *Geology* **28**, no. 4, 379–382.

Daëron, M. (2005). *Rôle, cinématique et comportement sismique à long terme de la faille de Yammoûneh, principale branche décrochante du coude transpressif libanais*, Ph.D. thesis, Institut de Physique du Globe de Paris, (http://www.whooshingsounds.net/tecto/public/daeron-phd-2005.pdf).

Daëron, M., L. Benedetti, P. Tapponnier, A. Sursock, and R. Finkel (2004). Constraints on the post ~25-ka slip rate of the Yammoûneh fault (Lebanon) using *in situ* cosmogenic ^{36}Cl dating of offset limestone-clast fans, *Earth and Planetary Science Letters* **227**, 105–119.

Daëron, M., Y. Klinger, P. Tapponnier, A. Elias, E. Jacques, and A. Sursock (2005). Sources of the large A.D. 1202 and 1759 Near East earthquakes, *Geology* **33**, no. 7, 529–532, doi:10.1130/G21352.1.

Darawcheh, R., M. Sbeinati, C. Margottini, and S. Paolini (2000). The 9 July 551 AD Beirut earthquake, Eastern Mediterranean region, *Journal of Earthquake Engineering* **4**, no. 4, 403–414.

Deng, Q., S. Chen, F. Song, S. Zhu, Y. Wang, W. Zhang, B. Burchfiel, P. Molnar, L. Royden, and P. Zhang (1986). Variations in the geometry and amount of slip on the Haiyuan fault zone, China and the surface rupture of the 1920 Haiyuan earthquake, *Earthquake Source Mechanics, Geophysical Monograph* **3**, 169–182.

Dubertret, L. (1975). Carte géologique du Liban au 1/50 000.

Elias, A. (2006). *Le chevauchement de Tripoli-Saïda : Croissance du Mont-Liban et risque sismique*, Ph.D. thesis, Institut de Physique du Globe de Paris.

Ellenblum, R., S. Marco, A. Agnon, T. Rockwell, and A. Boas (1998). Crusader castle torn apart by earthquake at dawn, 20 May 1202, *Geology* **26**, 303–306.

Emre, Ö., Y. Awata, and T. Duman (Editors) (2003). *Surface rupture associated with the August 17, 1999 Izmit earthquake*, volume 1, MTA Ankara, Special publication series.
Freund, R., Z. Garfunkel, I. Zak, I. Goldberg, T. Weisbrod, and B. Derin (1970). The shear along the Dead Sea rift, *Philos. Transactions of the Royal Society of London* **267**, 107–130.
Garfunkel, Z., I. Zak, and R. Freund (1981). Active faulting in the Dead Sea rift, *Tectonophysics* **80**, 1–26.
Gomez, F., M. Meghraoui, A. Darkal, F. Hijazi, M. Mouty, Y. Souleiman, R. Sbeinati, R. Darawcheh, R. Al-Ghazzi, and M. Barazangi (2003). Holocene faulting and earthquake recurrence along the Serghaya branch of the Dead Sea fault system in Syria and Lebanon, *Geophysical Journal International* **153**, 658–674.
Guidoboni, E., F. Bernardini, A. Comastri, and E. Boschi (2004). The large earthquake on 29 June 1170 (Syria, Lebanon, and central southern Turkey), *Journal of Geophysical Research* **109**, no. B07304.
Guidoboni, E., and A. Comastri (2005). *Catalogue of earthquakes and tsunamis in the Mediterranean area from the 11th to 15th century*, Bologna, INGV-SGA.
Guidoboni, E., A. Comastri, and G. Traina (1994). *Catalogue of ancient earthquakes in the Mediterranean area up to the 10th century*, Instituto Nazionale di Geofisica.
Harajli, M., S. Sadek, and R. Asbahan (2002). Evaluation of the seismic hazard of Lebanon, *Journal of Seismology* **6**, 257–277.
Hazan, N., M. Stein, A. Agnon, S. Marco, D. Nadel, J. Negendank, M. Schwab, and D. Neev (2005). The late quaternary limnological history of Lake Kinneret (Sea of Galilee), Israel, *Quaternary Research* **63**, no. 1, 60–77.
Hofstetter, A. (2003). Seismic observations of the 22/11/1995 Gulf of Aqaba earthquake sequence, *Tectonophysics* **369**, 21–36.
Hubert-Ferrari, A., A. Barka, E. Jacques, S. Nalbant, B. Meyer, R. Armijo, P. Tapponnier, and G. King (2000). Seismic hazard in the Marmara Sea region following the 17 August 1999 Izmit earthquake, *Nature* **404**, 269–273.
Jidejian, N. (1998). *Baalbek-Héliopolis, "cité du soleil"*, Librairie Orientale, Beyrouth.
Klinger, Y., J. Avouac, D. Bourlès, and N. Tisnerat (2003). Alluvial deposition and lake-level fluctuations forced by Late Quaternary climate change: the Dead Sea case example, *Sedimentary Geology* **162**, no. 1-2, 119–139.
Klinger, Y., J.-P. Avouac, N. Abou Karaki, L. Dorbath, D. Bourlès, and J.-L. Reyss (2000a). Slip rate on the Dead Sea transform fault in northern Araba valley Jordan, *Geophysical Journal International* **142**, 755–768.
Klinger, Y., J.-P. Avouac, L. Dorbath, N. Abou Karaki, and N. Tisnerat (2000b). Sesimic behaviour of the Dead Sea fault along the Araba valley, Jordan, *Geophysical Journal International* **142**, 769–782.
Klinger, Y., L. Rivera, H. Haessler, and J.-C. Maurin (1999). Active faulting in the Gulf of Aqaba: New knowledge from the Mw 7.3 earthquake of 22 November 1995, *Bulletin of the Seismological Society of America* **89**, no. 4.
Klinger, Y., X. Xu, P. Tapponnier, J. Van der Woerd, C. Lasserre, and G. King (2005). High-resolution satellite imagery mapping of the surface rupture and slip distribution of the Mw~7.8, 14 November 2001 Kokoxili earthquake, Kunlun fault, northern Tibet, China, *Bulletin of the Seismological Society of America* **95**, no. 5, 1970–1987.
Liu-Zeng, J., Y. Klinger, K. Sieh, C. Rubin, and G. Seitz (2006). Serial ruptures of the San Andreas fault, Carrizo Plain, California, revealed by three-dimensional excavations, *Journal of Geophysical Research* **111**, no. B2, B02306.
Mahmoud, S., R. Reilinger, S. McClusky, P. Vernant, and A. Tealeb (2005). Gps evidence for northward motion of the Sinai Block: implications for E. Mediterranean tectonics, *Earth and Planetary Science Letters* **238**, 217–224.
Manighetti, I., P. Tapponnier, P.-Y. Gillot, E. Jacques, V. Courtillot, R. Armijo, J.-C. Ruegg, and G. King (1998). Propagation of rifting along the Arabia-Somalia plate boundary: Into Afar, *Journal of Geophysical Research* **103**, no. B3, 4947–4974.
Marco, S., M. Hartal, N. Hazan, L. Lev, and M. Stein (2003). Archaeology, history and geology of the a.d. 749 earthquake, Dead Sea transform, *Geology* **31**, 665–668.
Marco, S., T. Rockwell, A. Heimann, U. Frieslander, and A. Agnon (2005). Late Holocene activity of the Dead Sea Transform revealed in 3D palaeoseismic trenches on the Jordan Gorge segment, *Earth and Planetary Science Letters* **234**, no. 1–2, 189–205.
McClusky, S., R. Reilinger, S. Mahmoud, D. Ben Sari, and A. Tealeb (2003). Gps constraints on Africa (Nubia) and Arabia plate motions, *Geophysical Journal International* **155**, 126–138.
McKenzie, D., D. Davies, and P. Molnar (1970). Plate tectonics of the Red Sea and East Africa, *Nature* **226**, no. 5242, 243–248.
Meghraoui, M., F. Gomez, R. Sbeinati, J. Van der Woerd, M. Mouty, A. Darkal, Y. Radwan, I. Layyous, H. Al Najjar, R. Darawcheh, F. Hijazi, R. Al-Ghazzi, and M. Barazangi (2003). Evidence for 830 years of seismic quiescence from palaeoseismology, archaeology and historical seismicity along the Dead Sea fault in Syria, *Earth and Planetary Science Letters* **210**, 35–52.
Morhange, C., P. Pirazzoli, N. Marriner, L. Montaggioni, and T. Nammour (2006). Late Holocene relative sea-level changes in Lebanon, Eastern Mediterranean, *Marine Geology* **230**, no. 1-2, 99–114.
Niemi, T., H. Zhang, M. Atallah, and J. Harrison (2001). Late Pleistocene and Holocene slip rate of the Northern Wadi Araba fault, Dead Sea Transform, Jordan, *Journal of Seismology* **5**, no. 3, 449–474.
Pelzer, G., P. Tapponnier, and R. Armijo (1989). Magnitude of Late Quaternary left-ateral displacements along the North edge of Tibet, *Science* **246**, 1285–1289.
Plassard, J. (1956). Annales séismologiques de l'observatoire de Ksara, (Beirut).
Plassard, J. (1968). Crise séismique au Liban du IVe au VIe siècel, *Mélanges de l'Université Saint-Joseph* **XLIV**, no. 2, 9–20.
Poirier, J., and M. Taher (1980). Historical seismicity in the Near and Middle East, North Africa, and Spain from Arabic documents (VIIth-XVIIIth century), *Bulletin of the Seismological Society of America* **70**, no. 6, 2185–2201.
Prasad, S., H. Vos, J. Negendank, N. Waldmann, S. Goldstein, and M. Stein (2004). Evidence from Lake Lisan of solar influence on decadal- to centennial-scale climate variability during marine oxygen isotope stage 2, *Geology* **32**, no. 7, 581–584, doi:10.1130/G20553.1.

Quennell, A. (1959). Tectonics of the Dead Sea rift, in *Proceedings of the 20th International Geological Congress, Mexico*, pp. 385–403.

Reches, Z., and D. Hoexter (1981). Holocene seismic and tectonic activity in the Dead Sea area, *Tectonophysics* **80**, 235–254.

Reimer, P. J., M. G. Baillie, E. Bard, A. Bayliss, W. W. Beck, C. J. Bertrand, P. G. Blackwell, C. E. Buck, G. S. Burr, K. B. Cutler, P. E. Damon, L. L. Edwards, R. G. Fairbanks, M. Friedrich, T. P. Guilderson, A. G. Hogg, K. A. Hughen, B. Kromer, G. Mccormac, S. Manning, C. B. Ramsey, R. W. Reimer, S. Remmele, J. R. Southon, M. Stuiver, S. Talamo, F. Taylor, J. v. d. van der Plicht, and C. E. Weyhenmeyer (2005). IntCal04 terrestrial radiocarbon age calibration, 0–26 cal kyr BP, *Radiocarbon* **46**, no. 3, 1029–1058.

Service météorologique du Liban (1971). Atlas climatique du Liban.

Sieh, K. (1984). Lateral offsets and revised dates of large prehistoric earthquakes at Pallett Creek, Southern California, *Journal of Geophysical Research* **89**, no. B9, 7641–7670.

Stein, R. S., A. A. Barka, and J. Dieterich (1997). Progressive failure on the North Anatolian fault since 1939 by earthquake stress triggering, *Geophysical Journal International* **128**, no. 3, 594–604.

Van der Woerd, J., P. Tapponnier, F. Ryerson, A.-S. Mériaux, B. Meyer, Y. Gaudemer, R. Finkel, M. Caffee, Z. Guoguang, and X. Zhiqin (2002). Uniform postglacial slip-rate along the central 600 km of the Kunlun Fault (Tibet), from ^{26}Al, ^{10}Be, and ^{14}C dating of riser offsets, and climatic origin of the regional morphology, *Geophysical Journal International* **148**, 356–388.

Wdowinski, S., Y. Bock, G. Baer, L. Prawirodirdjo, S. Bechor, S. Naaman, R. Knafo, Y. Forrai, and Y. Melzer (2004). GPS measurements of current crustal movements along the Dead Sea Fault, *Journal of Geophysical Research* **109**, B05403.

Weldon, R., T. Fumal, and G. Biasi (2004). Wrightwood and the earthquake cycle: what a long recurrence record tells us about how faults work, *Geological Society of America Today* **14**, no. 9, 4–10.

Wells, D., and K. Coppersmith (1994). New empirical relationships among magnitude, rupture length, rupture width, rupture area, and surface displacement, *Bulletin of the Seismological Society of America* **84**, 974–1002.

L	*Stratigraphic layers*
K	*Samples from wall K*
G	*Samples from wall G*
F	*Fault breaks observed in the trenches*
C	*Bayonet-shaped cracks (see text)*
S	*Paleoseismic events*
?S	*Ambiguous paleoseismic events*

Table 1

Date & main references	Known macroseismic effects
AD 551 (July 9th) Plassard [1968] Darawcheh *et al.* [2000] Guidoboni *et al.* [1994]	Shaking and a powerful sea wave caused severe damage all along the Phoenician coast (destruction of Berytus, Tripolis, Sidon, Byblus, Botrys, Tyre, and 101 towns in that area), with many casualties. In Berytus (Beirut), which suffered the worst ("30 000" casualties, widespread collapse of buildings), the sea retreated two miles before returning. The coast north of Laodicea and south of Tyre appears to have been comparatively spared. This event was felt strongly in Antioch, Alexandria, and felt in Phoenicia, Syria, Palestine, Arabia and Mesopotamia. Estimated magnitudes: M_L~7.8 [Ben-Menahem, 1991], M_S~7.2 [Darawcheh *et al.*, 2000].
AD 1202 (May 20th) Ambraseys and Melville [1988]	Heavy destruction in western Syria and the Crusader states. At the Jupiter temple of Baalbek (Beqaa), 31 out of 40 monumental columns were toppled. The cities of Nablus, Acre, Safed, Tyre, Tripoli and Hamah, among others, suffered severe damage. Rock falls in Mount Lebanon killed ~200 people. Shaking was felt throughout the Mediterranean and Middle East, up to 1200 km away, and aftershocks were reported for at least four days in Hamah, Damascus and Cairo. There is archaeological and paleoseismic evidence for 1.6 m of left-lateral offset recorded by the walls of the Vadum Jacob castle, just north of Lake Tiberias [Ellenblum *et al.*, 1998]. Estimated magnitude: M_S~7.6 [Ambraseys and Melville, 1988].
AD 1759 (November 25th) Ambraseys and Barazangi [1989]	Near-complete destruction of the villages in a 120-km-long narrow zone extending NNE from the Beqaa plain to the upper reaches of the Orontes. Safed, Hasbaya, Serghaya, Baalbek were almost completely destroyed, and heavy damage extended to Ras-Baalbek. At the Jupiter temple of Baalbek (Beqaa), 3 out of the 9 remaining columns were toppled. Ambraseys and Barazangi [1989] mention reports of ground ruptures over 100 km long in the Beqaa. The earthquake caused heavy but repairable damage in Damascus, and was strongly felt in Antioch, Aleppo, Ladhikiya, Gaza, Al-Arish and Tarba. A seismic wave was reported as far south as the Nile delta. Estimated magnitude: M_S~7.4 [Ambraseys and Barazangi, 1989]. This event was preceded, on Oct. 30, by a M_S~6.6 earthquake to the south of it.

Table 2

Sequence	Unit	Notes
I	1	*Whitish calcareous marl with sub-modern, mm-thick roots, and freshwater gastropod shells (1–4 mm) similar to those observed in the active channels of the modern basin.*
	2	*Darker gray marl, with small fragments of charcoal.*
	3a	*Similar to L1, but with ∼2-cm-thick sub-layers and much fewer roots.*
	3b1	*Gray marl. Although parallel to L3c west of the fault zone, L3b1 appears to truncate L3b2 and possibly L3c east of the fault zone.*
	3b2, 3c	*Light gray marl.*
	3d, e, f	*Alternating layers of whitish and beige marl.*
	4a	*Light brown marl.*
	4b	*Darker brown unit, locally chocolate-colored, with detrital charcoal and organic matter.*
	4c, 5	*Similar to L4a.*
	6a, b, c	*Darker beige marl.*
	7a	*Dark brown, clay-rich marl, observed only near the fault zone.*
	8	*Lighter brown marl.*
	9	*Dark brown marl, observed only near the fault zone.*
	10	*Rather homogeneous, 50-cm-thick bed of beige marl, with brownish, sub-vertical streaks.*
II	11–15	*50-cm-thick succession of beige and light-brown units, locally disturbed by liquefaction, particularly near the fault zone, resulting in contorted outlines. Some beds (L12, L14) are locally interrupted by injections from contiguous units.*
	16	*Brown bed with a contorted top and a smoother base. E of the fault zone, it caps and truncates L17a. In the W block, its base truncates angularly L17–21 and the top of L23. Since the top of L16 remains parallel to the overlying beds, the thickness of this unit increases significantly toward the fault above the eroded section.*
	17a [East]	*Slightly darker brown bed, unaffected by liquefaction. It rests in a ∼2-m-wide sag.*
	18a, 19/21 [East]	*Darker, clay-rich marl, coating the bottom of the sag.*
	(17/18)b [West]	*Light brown marl, angularly truncated by the base L16.*
	19 [West]	*Thin, distinctive bed of brown marl, angularly truncated by the base L16.*
	20 [West]	*Beige marl, angularly truncated by the base L16.*
	21 [West]	*Thin, distinctive bed of brown marl, angularly truncated by the base L16.*
III	23–30	*Package of alternating lighter and darker beige marl beds, each 10 to 15 cm thick. This sequence is ∼40 cm thicker east than west of the fault zone. Facies comparisons across the fault suggest that the units missing in the western block are L24–26 and the upper part of L27, although this interpretation is not unique.*
IV	31	*3-cm-thick whitish marl bed, topped by a characteristic, ocher horizon.*
	32-33	*Gray marl beds with irregular thickness (10 cm on average), darkest at the base. The sediments of L33 exhibit darker patches rich in organic matter, and the base of this unit forms an irregularly contorted surface.*
	34	*25-cm-thick bed of whitish/light gray marl. This unit displays evidence of pervasive bioturbation, probably by roots or by burrowing organisms, in the form of sub-vertical gray streaks of variable lengths that extends downwards from the base of L33. It also displays evidence of plastic flow/liquefaction, outlined by the folding of the bioturbation marks, chiefly localized within a few meters of the fault zone.*
	35	*20-cm-thick bed of gray-to-light-green marls with a relatively high clay content, with thin laminae of alternating green and whitish colors. The base of L35 is generally lighter than its top.*
V	36	*∼3-cm-thick bed of light blue clay.*
	37	*Mottled yellow-brown, poorly defined clay beds.*
	37-46	*Relatively uniform succession of clay beds.*
	38	*Distinctive, 10mm-thick dark lamina.*
	41	*Distinctive, 5-mm-thick dark lamina.*
	47	*Very distinctive, dark red-brown double layer, comprising a 30–35-mm-thick bed overlying a 5-mm-thick laminae of similar color and texture. L47 is very uniform across the whole trench.*
VI	48–54	*Less than 10 cm below the base of L47 begins a level with abundant calcareous nodules. It is difficult to map individual beds within this nodular unit, in part because the concretions prevent proper smoothing of the trench wall. One can nevertheless map two darker layers, L51 (1 cm thick) and L53 (5 cm), which are clear enough to act as deformation markers*
VII	55–59	*Immediately beneath the nodular level, the dark-brown bed L55 is the deepest distinctive clay bed recognizable on both sides of the fault zone. A lower layer L58 can be mapped in the western block, ∼20 cm below L55, but it lies deeper than the base of wall G east of the fault.*

Table 3

Sample	**Layer**	**Depth** (cm)	**Lab Ref.**	δ^{13}**C** (‰)	**Fraction Modern** (‰)	δ^{14}**C** (‰)	^{14}**C Age** (yr BP)	**Calibrated Age Range** (2σ, yr BP)
G6*	1	4	12237	-29.3			718 ± 35	566–727
K23	2	12	85982	-25	927.1 ± 5.1	-72.9 ± 5.1	610 ± 45	540–662
G3	(top) 03a	14	12234	-28.5			650 ± 60	539–684
G1	03b	39	12233	-25.3			1115 ± 35	935–1125
G4*	03f	58	12235	-21			1980 ± 90	1711–2153
K64	04b	74	86069	-25	815.5 ± 4.3	-184.5 ± 4.3	1640 ± 45	1411–1691
G5	(top) 10	98	12236	-32.6			2000 ± 100	1714–2301
K29	10	121	85984	-25	774.1 ± 3.5	-225.9 ± 3.5	2055 ± 40	1924–2127
K111	19b	212	86077	-25	497.3 ± 3.7	-502.7 ± 3.7	5610 ± 70	6283–6556
K13a	19b	212	85977	-25	495.6 ± 2.8	-504.4 ± 2.8	5640 ± 50	6305–6533
K13b	19b	212	85978	-25	486.3 ± 2.5	-513.7 ± 2.5	5790 ± 45	6478–6719
K76	22	217	86070	-25	488.8 ± 2.3	-511.2 ± 2.3	5750 ± 40	6449–6652
K16b	(bottom) 23	227	85979	-25	482.5 ± 2.2	-517.5 ± 2.2	5855 ± 40	6557–6778
K35	(top) 24	230	85987	-25	487.6 ± 2.3	-512.4 ± 2.3	5770 ± 40	6473–6667
K35b	(top) 24	230	85988	-25	472.4 ± 2.1	-527.6 ± 2.1	6025 ± 40	6750–6976
K78	24	237	86071	-25	467.5 ± 2.1	-532.5 ± 2.1	6105 ± 40	6885–7158
K43*	(top) 27	258	85993	-25	480.1 ± 2.1	-519.9 ± 2.1	5895 ± 40	6637–6831
K83	28	281	86075	-25	406.8 ± 2	-593.2 ± 2	7225 ± 40	7966–8161
K80c	28	281	86093	-25	406.7 ± 2.1	-593.3 ± 2.1	7230 ± 45	7968–8163
K80b	28	281	86072	-25	401.2 ± 2	-598.8 ± 2	7335 ± 45	8018–8302
K82	28	281	86074	-25	397 ± 4.5	-603 ± 4.5	7420 ± 100	8025–8400
K49	(top) 30	300	85994	-25	386 ± 8.6	-614 ± 8.6	7650 ± 180	8158–8993
K120*	32	323	86078	-25	351.3 ± 1.4	-648.7 ± 1.4	8405 ± 35	9308–9519
K50b	(top) 33	325	86066	-25	367.2 ± 1.9	-632.8 ± 1.9	8045 ± 45	8768–9032
K50	(top) 33	325	85995	-25	358 ± 1.6	-642 ± 1.6	8250 ± 40	9090–9403
K3	(bottom) 33	330	85976	-25	348.6 ± 1.6	-651.4 ± 1.6	8465 ± 40	9436–9533
K20	(top) 35	355	85981	-25	312.8 ± 1.6	-687.2 ± 1.6	9335 ± 45	10414–10683
K129	(top) 35	355	86080	-25	306.3 ± 2.5	-693.7 ± 2.5	9510 ± 70	10587–11100
K93	(top) 44	400	86076	-25	277.9 ± 6.2	-722.1 ± 6.2	10290 ± 190	11389–12705

Table 4

Event	Stratigraphic constraints	Age bounds (95.4%)	
		(AD/BC)	(BP)
S1	post L3c, pre L3b1	AD 926 – 1381	569 – 1024
?S2	post L4a, pre L3e	AD 405 – 945	1005 – 1545
S3	post L9, pre L7a	30 BC – AD 469	1481 – 1979
S4	post L11, pre L10	–	2115 – 6288*
?S5	post L16, pre L14	–	2115 – 6288*
?S6	post L17a, pre L15	–	2115 – 6288*
S7	coeval L19b	–	6324 – 6565
S8	post L28, pre L23	–	6645 – 7990
S9	post L31, pre L30	–	8384 – 9001
S10	post L35, pre L32	–	9231 – 10546
S11	post L37, pre top L35	–	10726 – 12268
S12	post L47, pre L41	–	11389 – 12705*
S13	post L55, pre top L54	–	$> 12047 \pm 658$

** (see text)*

Table 5

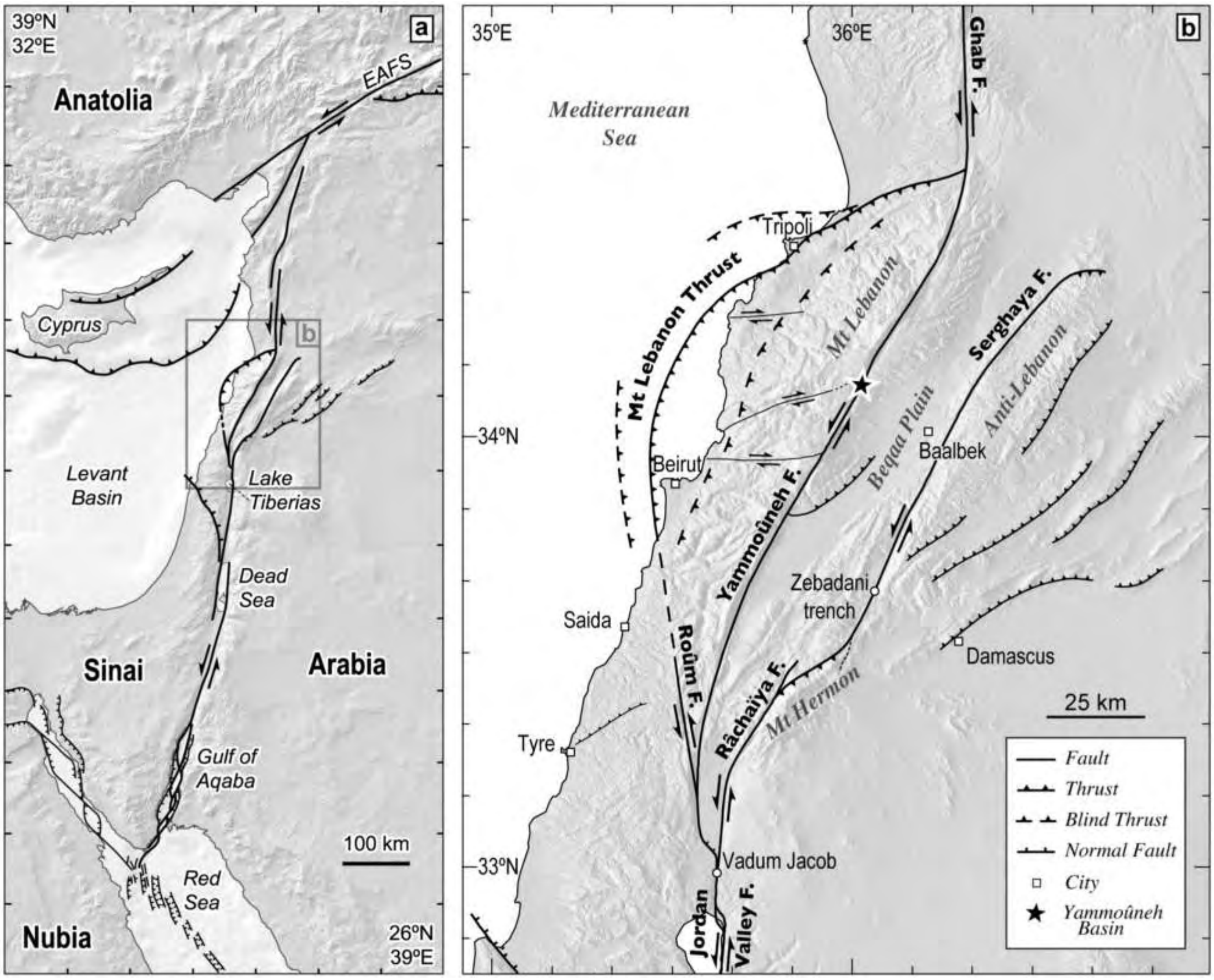
a
39ºN
32ºE
Anatolia
EAFS
Cyprus
b
Levant Basin
Lake Tiberias
Dead Sea
Sinai
Arabia
Gulf of Aqaba
100 km
Red Sea
Nubia
26ºN
39ºE
b
35ºE
36ºE
Ghab F.
Mediterranean Sea
Tripoli
Mt Lebanon Thrust
Mt Lebanon
Serghaya F.
Anti-Lebanon
34ºN
Beirut
Baalbek
Beqaa Plain
Yammoûneh F.
Zebadani trench
Saida
Roûm F.
Damascus
25 km
Râchaïya F.
Mt Hermon
Tyre
Fault
Thrust
Blind Thrust
Normal Fault
City
Yammoûneh Basin
33ºN
Vadum Jacob
Jordan
Valley F.

Figure 1

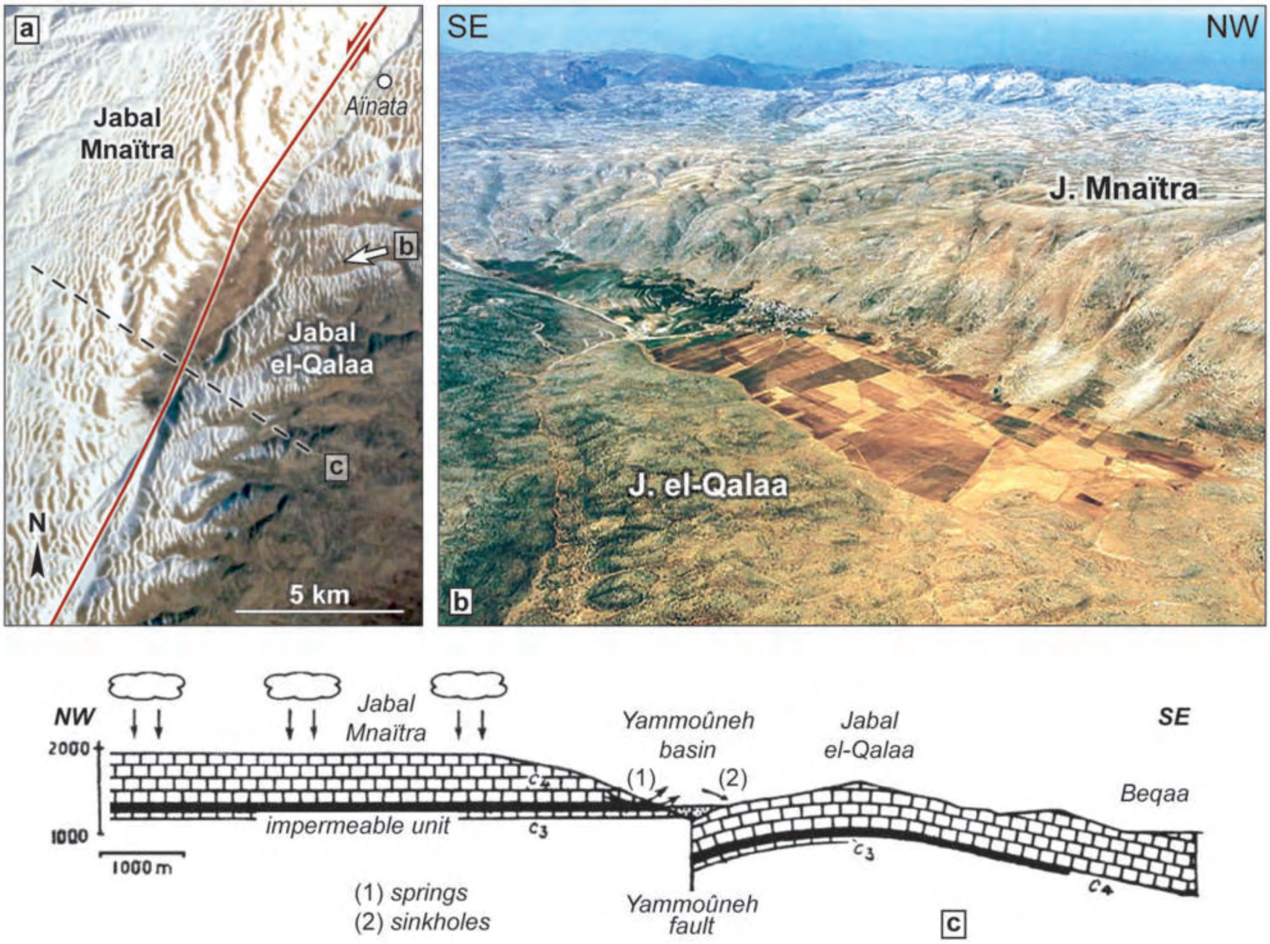
a
Jabal Mnaïtra
Aïnata
b
Jabal el-Qalaa
c
N
5 km
SE
NW
J. Mnaïtra
J. el-Qalaa
b
NW
Jabal Mnaïtra
Yammoûneh basin
Jabal el-Qalaa
SE
2000
1000
1000 m
(1)
(2)
Beqaa
impermeable unit
c4
c3
(1) springs
(2) sinkholes
Yammoûneh fault
c

Figure 2

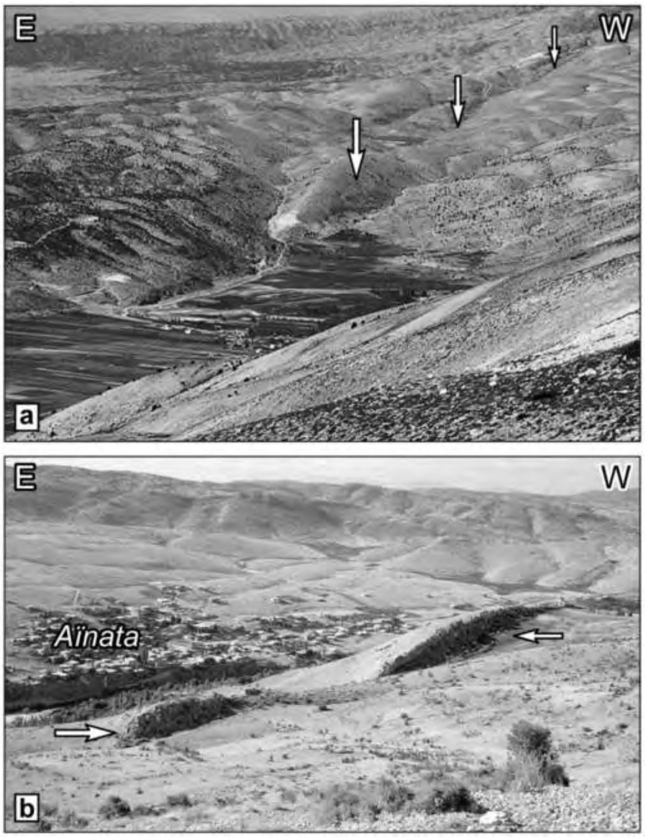

Figure 3

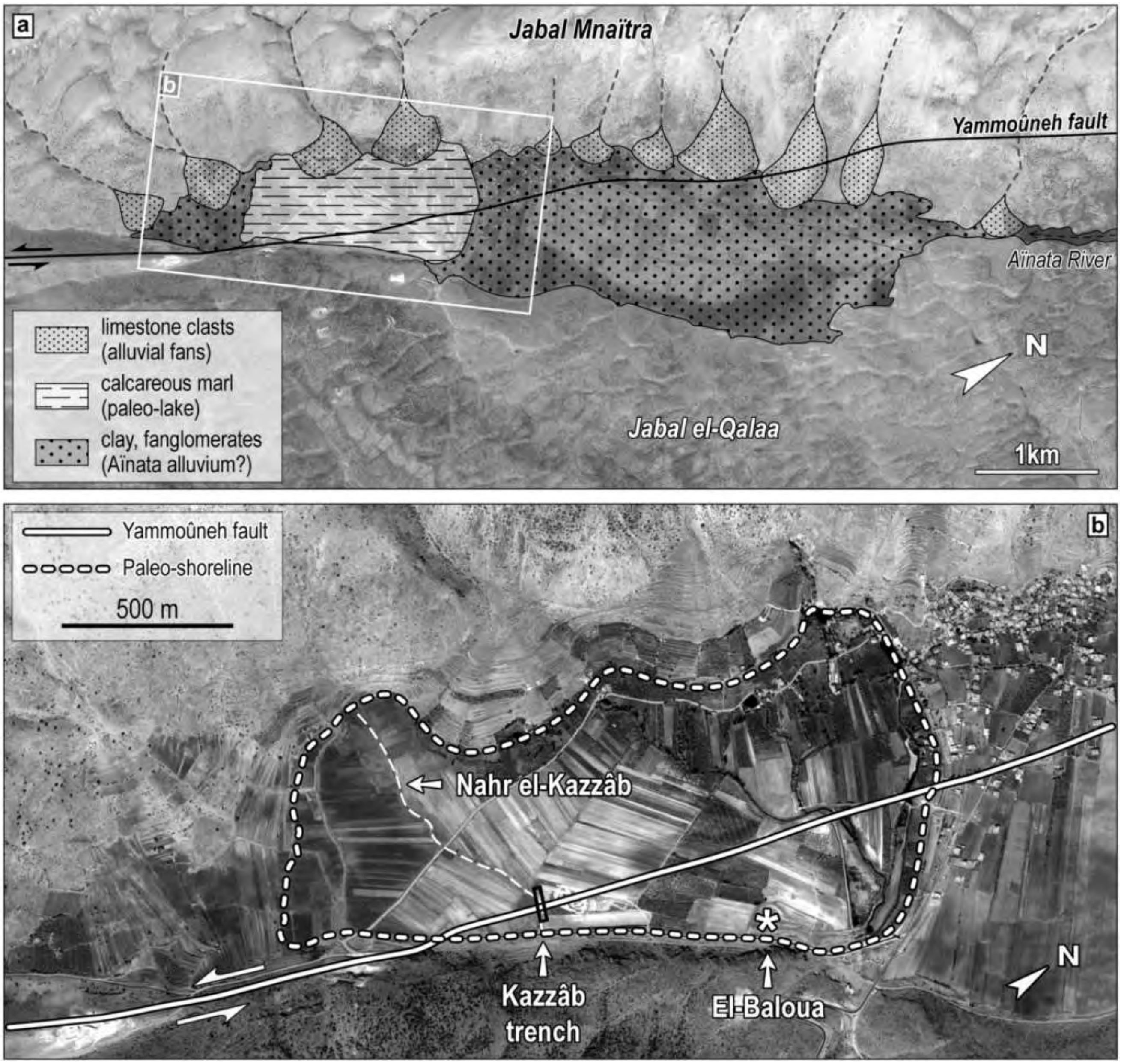
a
Jabal Mnaïtra
b
Yammoûneh fault
Aïnata River
limestone clasts
(alluvial fans)
calcareous marl
(paleo-lake)
clay, fanglomerates
(Aïnata alluvium?)
N
Jabal el-Qalaa
1km
Yammoûneh fault
Paleo-shoreline
500 m
b
Nahr el-Kazzâb
Kazzâb
trench
El-Baloua
N

Figure 4

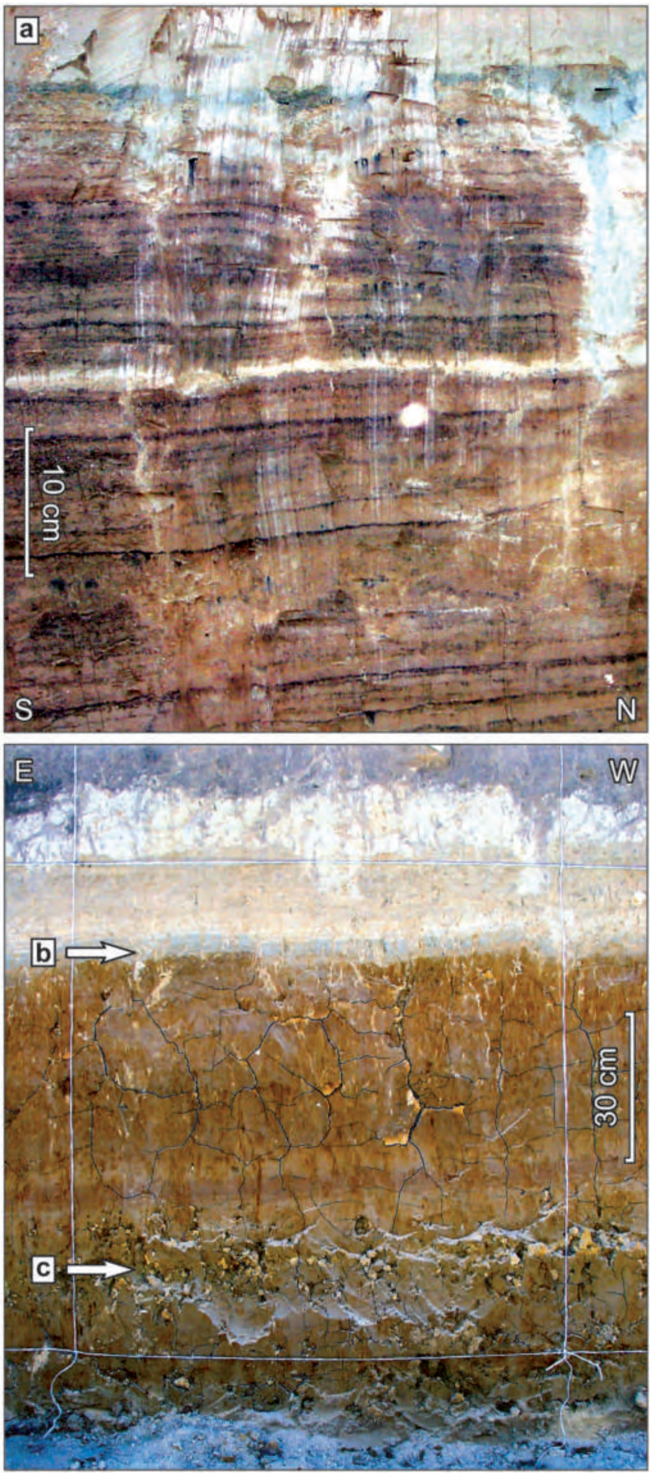

Figure 5

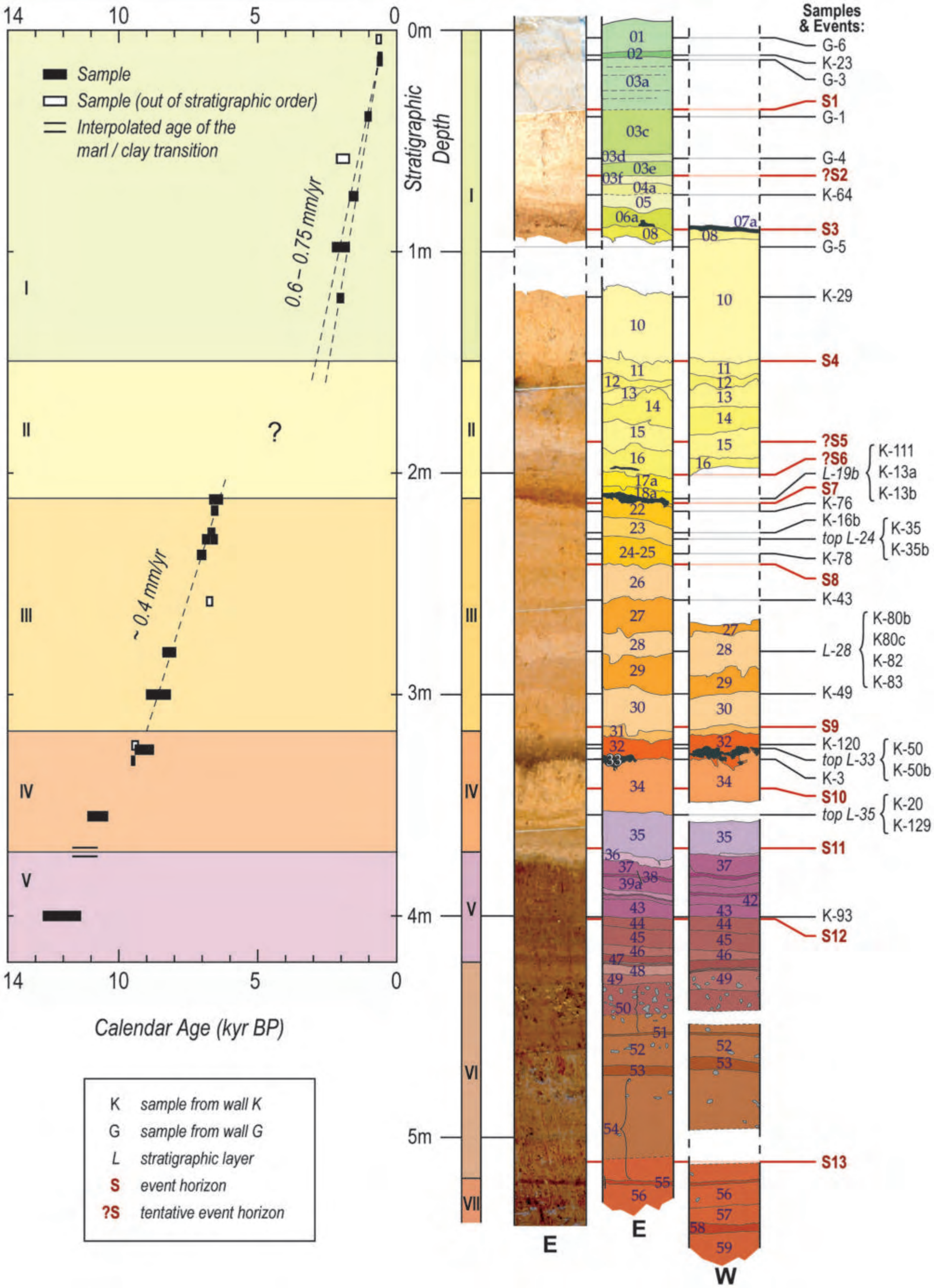
Sample
Sample (out of stratigraphic order)
Interpolated age of the marl / clay transition
0.6 – 0.75 mm/yr
~ 0.4 mm/yr
Calendar Age (kyr BP)
Stratigraphic Depth
Samples & Events:
K sample from wall K
G sample from wall G
L stratigraphic layer
S event horizon
?S tentative event horizon
E
E
W

Figure 6

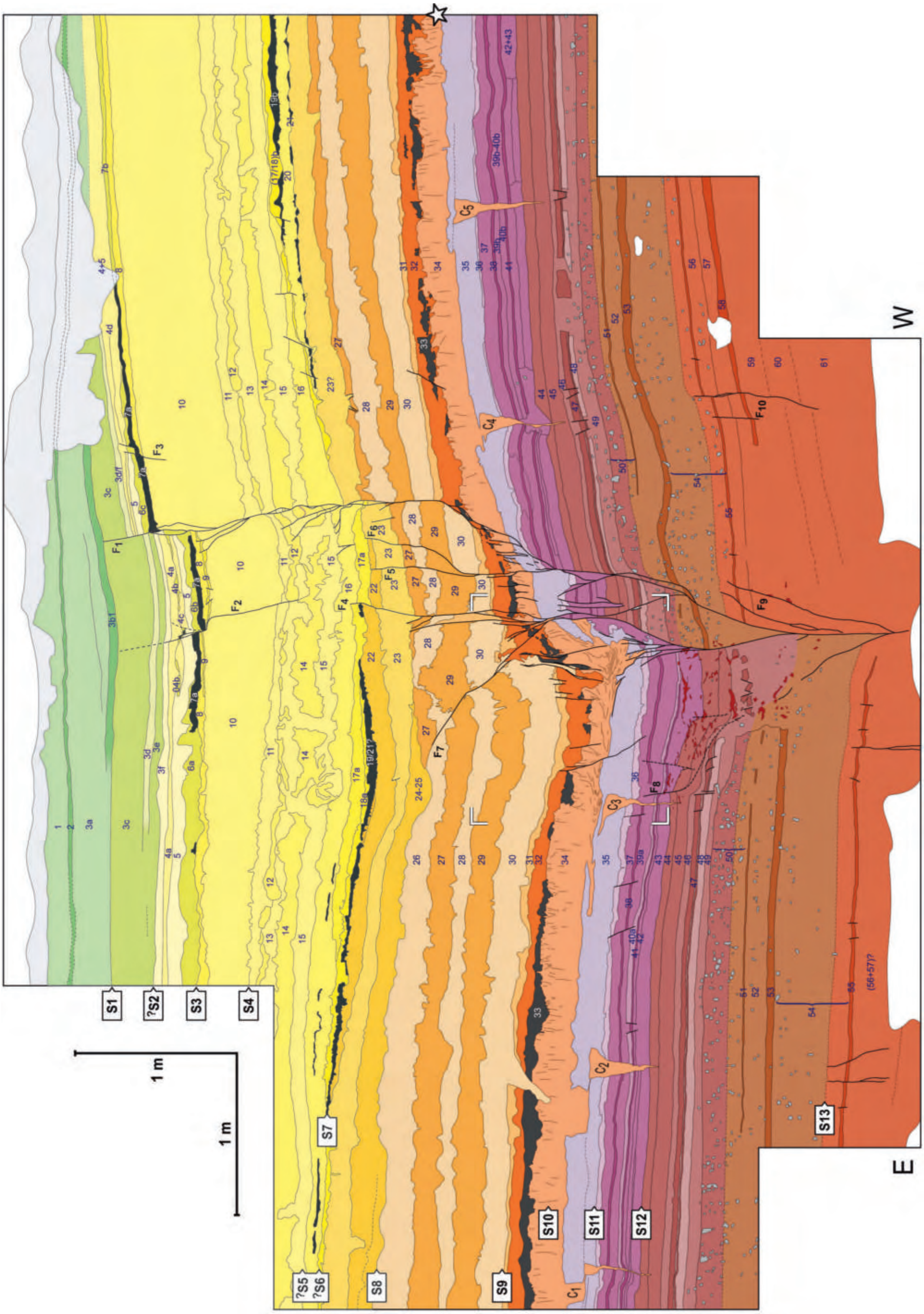
1 m
1 m
S1
?S2
S3
S4
?S5
?S6
S7
S8
S9
S10
S11
S12
S13
E
W
F1
F2
F3
F4
F5
F6
F7
F8
F9
F10
C1
C2
C3
C4
C5

Figure 7

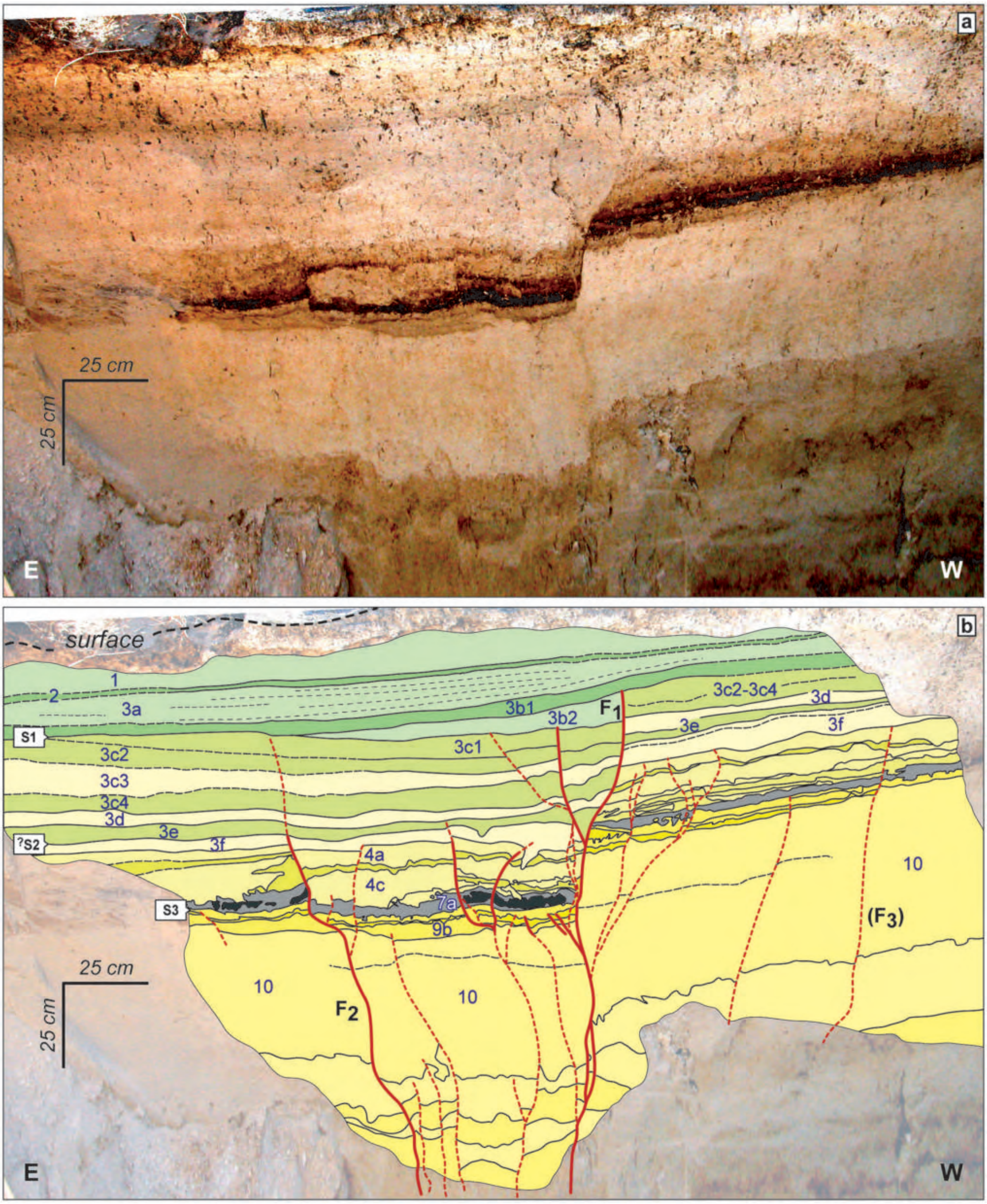

a
25 cm
25 cm
E
W
b
surface
1
2
3a
3b1
3b2
F1
3c2-3c4
3d
3e
3f
S1
3c1
3c2
3c3
3c4
3d
3e
3f
?S2
4a
4c
7a
S3
9b
10
(F3)
25 cm
25 cm
10
F2
10
E
W

Figure 8

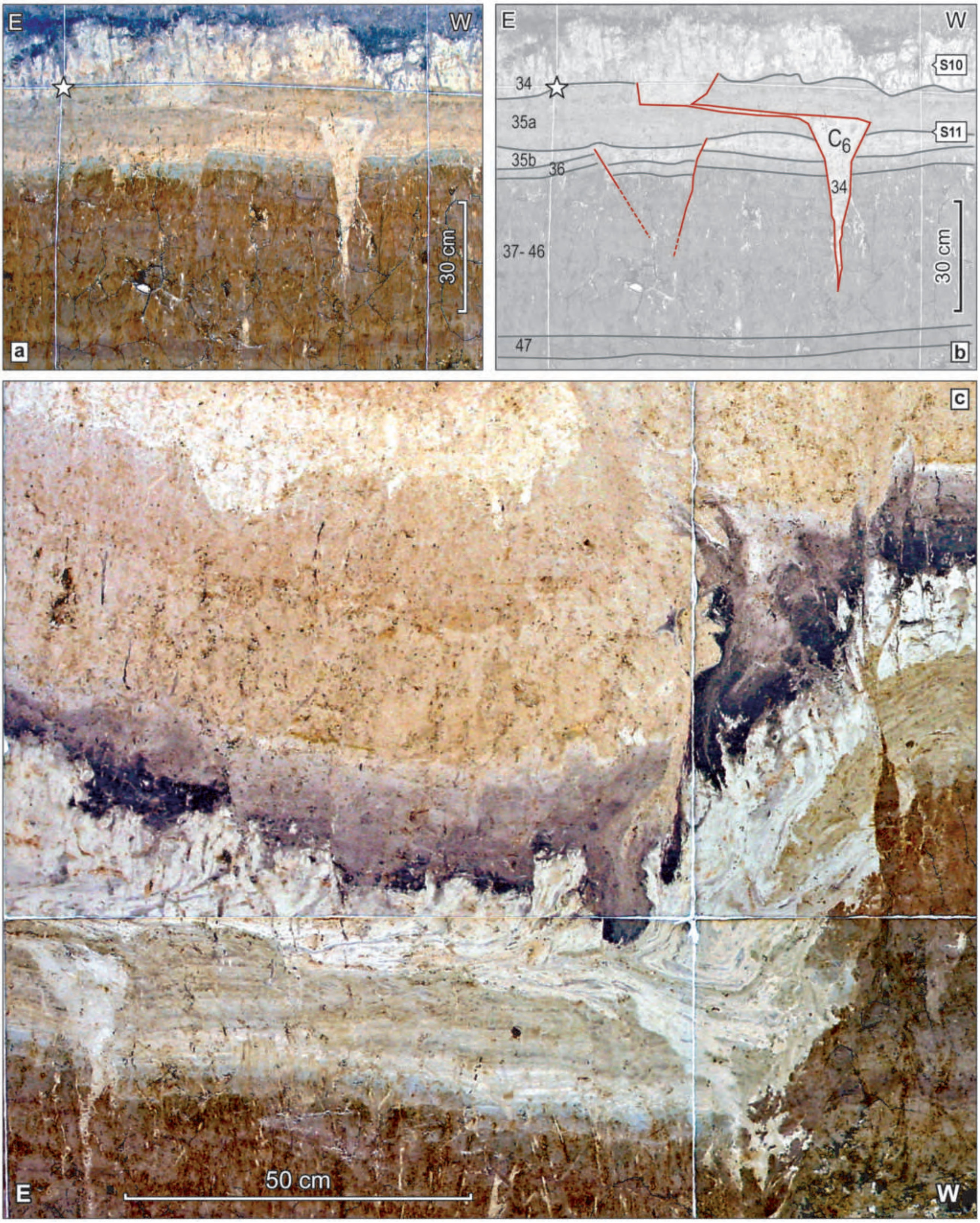

Figure 9

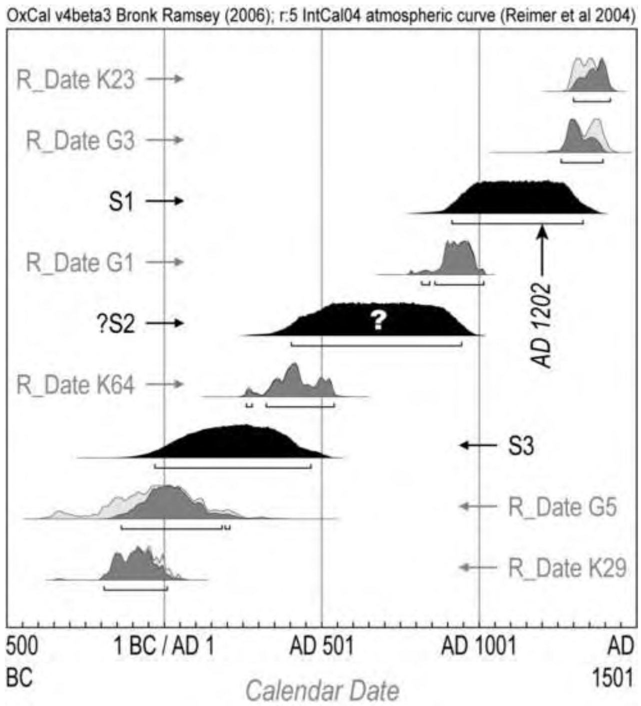
OxCal v4beta3 Bronk Ramsey (2006); r:5 IntCal04 atmospheric curve (Reimer et al 2004)
R_Date K23
R_Date G3
S1
R_Date G1
?S2
?
AD 1202
R_Date K64
S3
R_Date G5
R_Date K29
500 BC
1 BC / AD 1
AD 501
AD 1001
AD 1501
Calendar Date

Figure 10

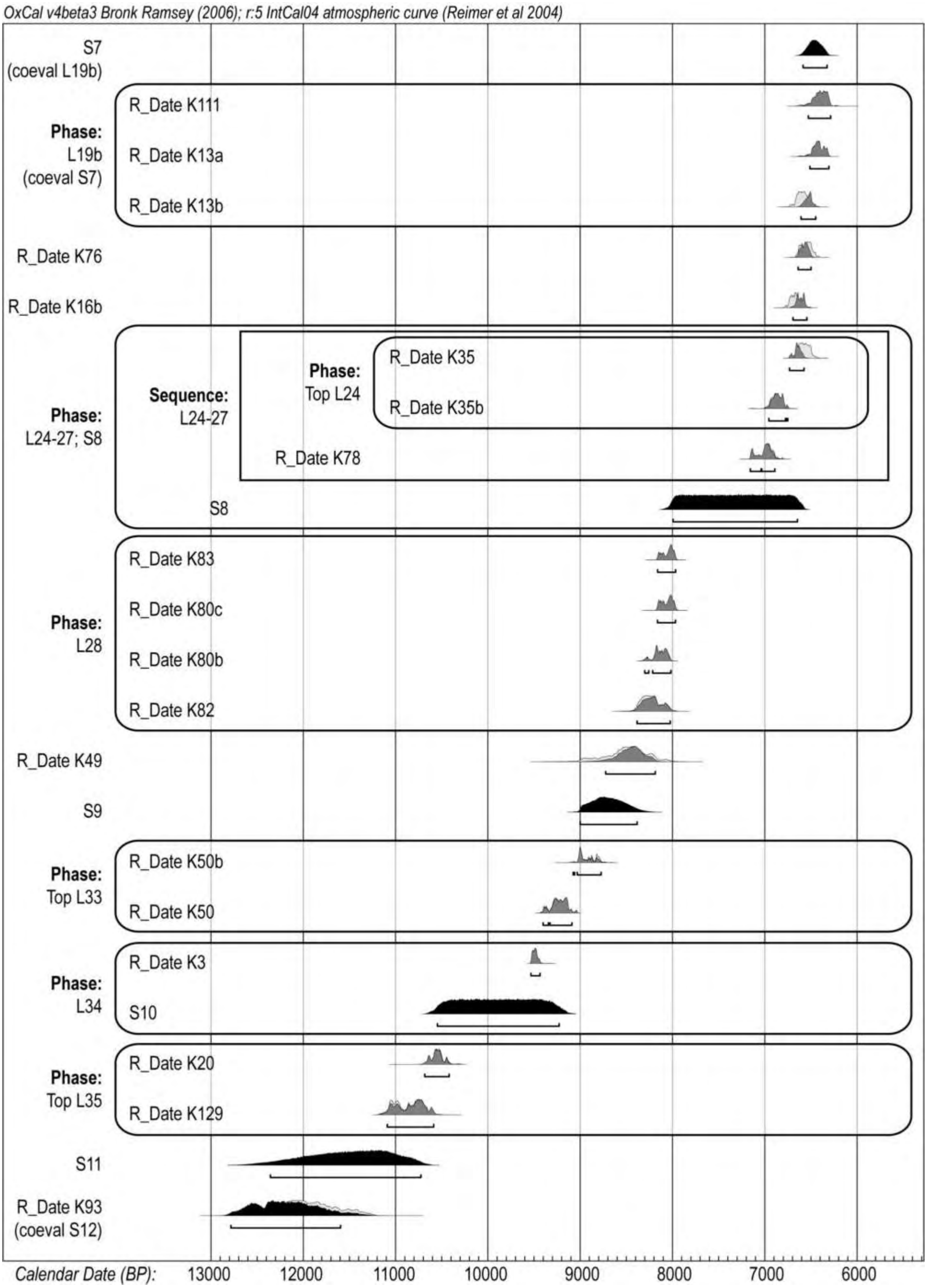

OxCal v4beta3 Bronk Ramsey (2006); r:5 IntCal04 atmospheric curve (Reimer et al 2004)
S7
(coeval L19b)
Phase:
L19b
(coeval S7)
R_Date K111
R_Date K13a
R_Date K13b
R_Date K76
R_Date K16b
Phase:
L24-27; S8
Sequence:
L24-27
Phase:
Top L24
R_Date K35
R_Date K35b
R_Date K78
S8
Phase:
L28
R_Date K83
R_Date K80c
R_Date K80b
R_Date K82
R_Date K49
S9
Phase:
Top L33
R_Date K50b
R_Date K50
Phase:
L34
R_Date K3
S10
Phase:
Top L35
R_Date K20
R_Date K129
S11
R_Date K93
(coeval S12)
Calendar Date (BP):
13000
12000
11000
10000
9000
8000
7000
6000

Figure 11

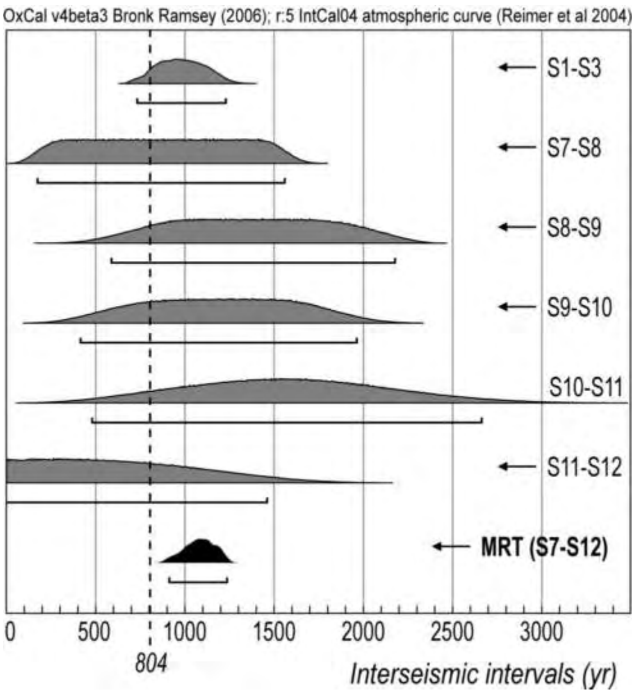
OxCal v4beta3 Bronk Ramsey (2006); r:5 IntCal04 atmospheric curve (Reimer et al 2004)
S1-S3
S7-S8
S8-S9
S9-S10
S10-S11
S11-S12
MRT (S7-S12)
0
500
1000
1500
2000
2500
3000
804
Interseismic intervals (yr)

Figure 12

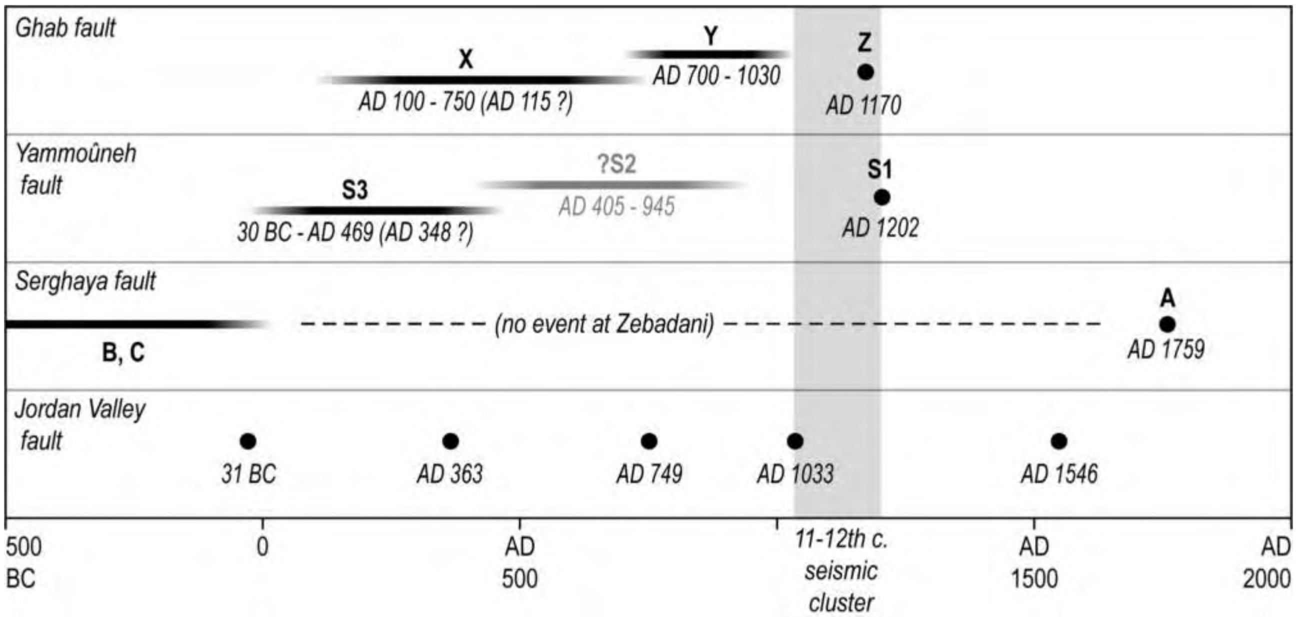

Ghab fault
X
AD 100 - 750 (AD 115 ?)
Y
AD 700 - 1030
Z
AD 1170
Yammoûneh fault
?S2
AD 405 - 945
S3
30 BC - AD 469 (AD 348 ?)
S1
AD 1202
Serghaya fault
(no event at Zebadani)
B, C
A
AD 1759
Jordan Valley fault
31 BC
AD 363
AD 749
AD 1033
AD 1546
500 BC
0
AD 500
11-12th c. seismic cluster
AD 1500
AD 2000

Figure 13

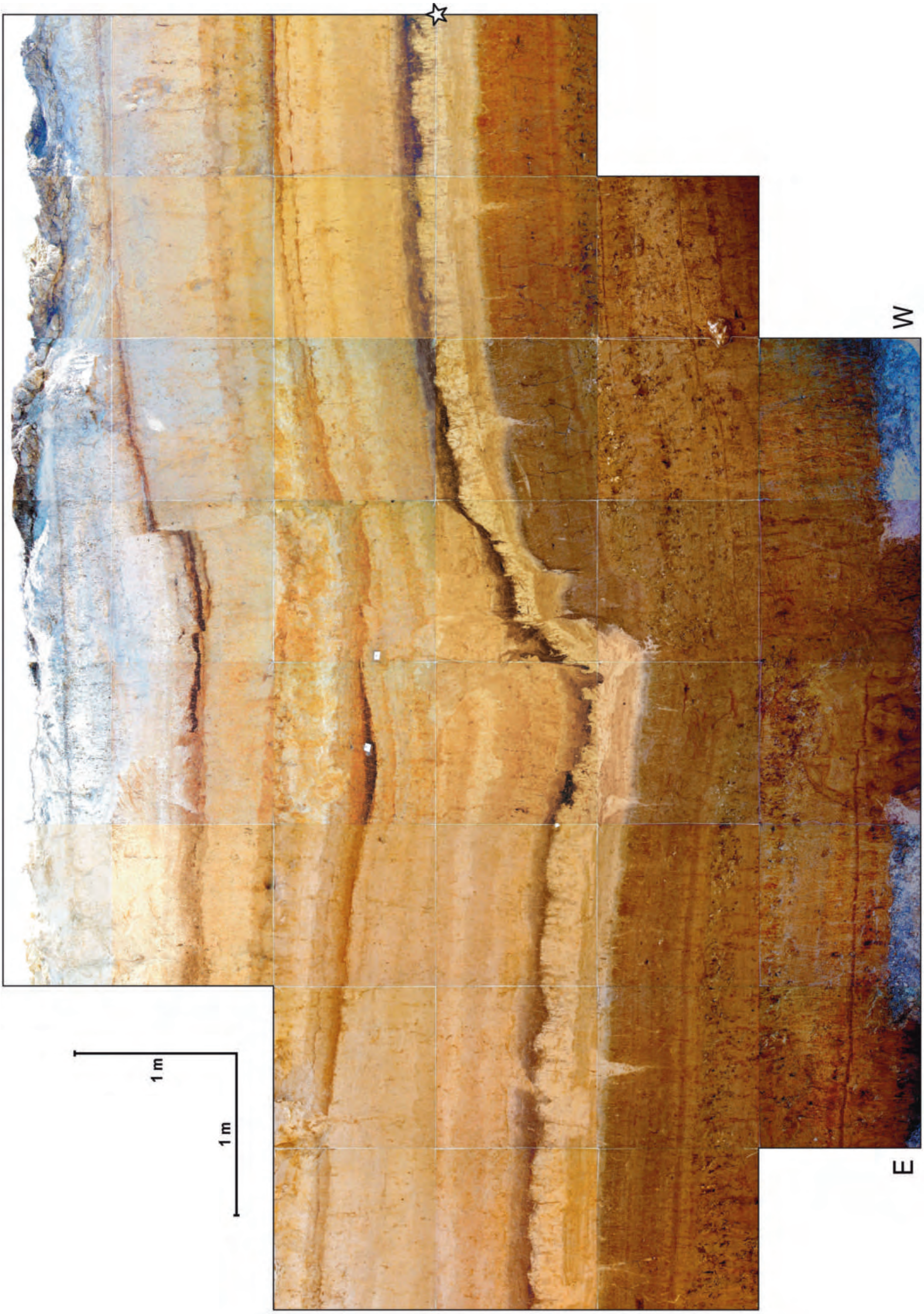

Plate 1

Bulletin of the Seismological Society of America, Vol. 93, No. 6, pp. 2317–2332, December 2003

Paleoseismic Evidence of Characteristic Slip on the Western Segment of the North Anatolian Fault, Turkey

by Y. Klinger,* K. Sieh, E. Altunel, A. Akoglu, A. Barka, T. Dawson, T. Gonzalez, A. Meltzner, and T. Rockwell

Abstract We have conducted a paleoseismic investigation of serial fault rupture at one site along the 110-km rupture of the North Anatolian fault that produced the M_w 7.4 earthquake of 17 August 1999. The benefit of using a recent rupture to compare serial ruptures lies in the fact that the location, magnitude, and slip vector of the most recent event are all very well documented. We wished to determine whether or not the previous few ruptures of the fault were similar to the recent one. We chose a site at a step-over between two major strike-slip traces, where the principal fault is a normal fault. Our two excavations across the 1999 rupture reveal fluvial sands and gravels with two colluvial wedges related to previous earthquakes. Each wedge is about 0.8 m thick. Considering the processes of collapse and subsequent diffusion that are responsible for the formation of a colluvial wedge, we suggest that the two paleoscarps were similar in height to the 1999 scarp. This similarity supports the concept of characteristic slip, at least for this location along the fault. Accelerator mass spectrometry (AMS) radiocarbon dates of 16 charcoal samples are consistent with the interpretation that these two paleoscarps formed during large historical events in 1509 and 1719. If this is correct, the most recent three ruptures at the site have occurred at 210- and 280-year intervals.

Motivation

Over the past several years, evidence has accumulated in support of the hypothesis that the magnitude of fault slip at a particular site along a fault does not vary greatly from event to event (Sieh, 1996). However, data are still too scant to determine how universal these observations are and under which conditions faults produce similar serial ruptures and under which conditions they do not.

The M_w 7.4 Izmit, Turkey, earthquake of 17 August 1999 was produced by more than 100 km of right-lateral rupture along the North Anatolian fault (Fig. 1). Detailed documentation of the fresh rupture (Armijo *et al.*, 2000; Lettis *et al.*, 2000; Barka *et al.*, 2002; Langridge *et al.*, 2002) combined with a centuries-long historical record of prior large earthquakes (Ambraseys and Finkel, 1995; Ambraseys, 2002) provide an unusual opportunity to investigate the nature of sequential fault rupture. Since prior historical ruptures are known only from records of shaking, paleoseismic work is necessary to characterize the nature and amount of slip from one event to the next.

*Present address: Institut de Physique du Globe, Paris, France.

Tectonic Setting of the North Anatolian Fault and the 1999 Earthquake Sequence

The arcuate, right-lateral North Anatolian fault system forms the northern margin of the Anatolian block, a minor crustal plate that is extruding westward, out of the collision zone between Eurasia and Arabia (Fig. 1). Along its eastern 1000 km, the structure consists primarily of one fault (Barka, 1992). Farther west, the fault system divides into southern, central, and northern strands. The northern branch, part of which broke in 1999, appears to carry most of the long-term slip. From Global Positioning System measurements, the dextral slip rate on the North Anatolian fault has been estimated to be 24 $\pm$ 1 mm/yr, the rate of motion between the Anatolian block and Eurasian blocks (McClusky *et al.*, 2000). A slip rate of 17 mm/yr, averaged over the past 5 My, has been derived for the northern strand of the fault (Armijo *et al.*, 1999). Thus, the central and southern strands may have a combined rate of about 7 mm/yr.

During the past 500 years the North Anatolian fault has produced many large, destructive earthquakes. Historical accounts of shaking and damage suggest that most of the fault ruptured in each of two major seismic episodes during the sixteenth and the eighteenth centuries (Ambraseys and Finkel, 1991, 1995; Ambraseys, 2002). Furthermore, most of the fault system reruptured between 1912 and 1999 (Stein *et al.*, 1997; Ambraseys and Jackson, 2000). Along the northern branch, only the 160-km-long section of the fault beneath the Sea of Marmara has not ruptured in the past century (Barka, 1996, 1999).

The rupture of August 1999 consists of four distinct segments. From east to west, these are the Karadere, Sakarya, Izmit–Sapança, and Gölcük segments (Fig. 2) (e.g., Barka *et al.*, 2002). Each segment is delimited by step-overs or bends. The Izmit–Sapança and Gölcük segments are separated by a right step about 2 km wide. A northwest-striking, northeast-side-down, normal fault about 3.2 km long, which we here call the Gölcük fault, is the principal structure that occupies the step-over. Detailed description of the rupture associated with the 1999 Izmit earthquake is beyond the scope of this article, and the reader should refer to the special issue of the *Bulletin* edited by Toksöz (2002).

Paleoseismic Investigations along the Gölcük Segment

Trench Site

The Gölcük fault traverses a large alluvial fan delta built by the northward-flowing Hisar River (Fig. 3), with the Kazikle River contributing to the building of the western side of the fan. This Quaternary fan delta is composed mostly of alluvium derived from the Triassic rocks of the mountain range that bounds the Gulf of Izmit on the south. Along much of the step-over fault, a scarp, clearly delineated in the topography, existed prior to 1999. The current height of the scarp varies along strike from about 1 to 6 m, with the maximum slip associated to the 1999 Izmit earthquake being located where the cumulative scarp is the highest (Barka *et al.*, 2002). Since this is up to 4 times the height of the scarp that formed in 1999, it is reasonable to suspect that the older scarp formed as a result of several prior ruptures.

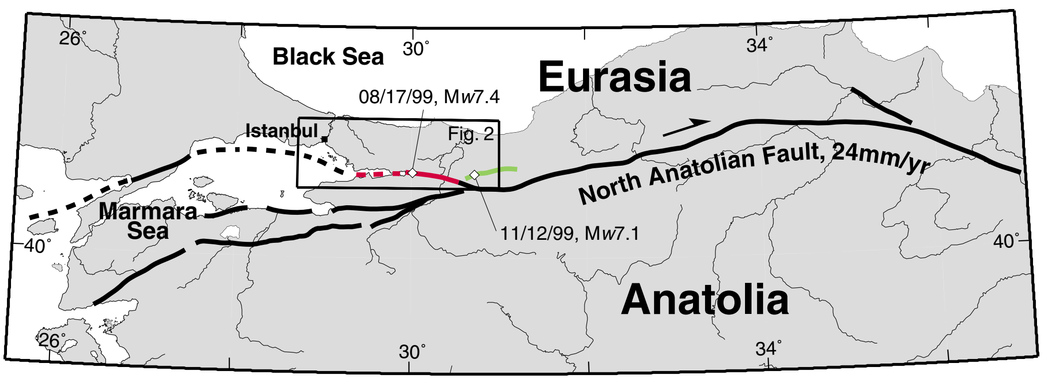

Figure 1. The highly segmented North Anatolian fault has ruptured repeatedly in the past 500 years of historical record. The rupture of several segments in August (red) and November 1999 (green) afforded an unusual opportunity to compare the slip of sequential ruptures.

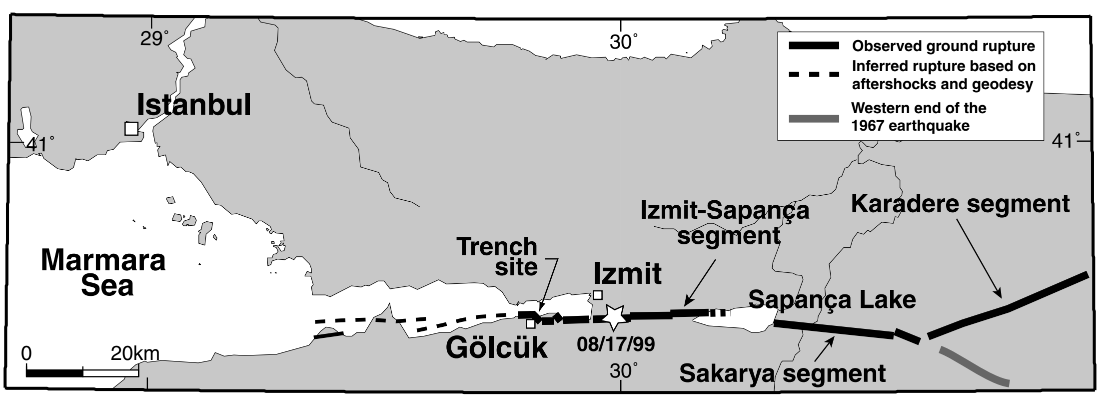

Figure 2. The August 1999 earthquake was caused by rupture of four different segments: the Gölcük segment, the Izmit segment, the Sakarya segment, and the Karadere segment. Right-lateral slip of several meters was predominant along most of the rupture (Barka *et al.*, 2002). Secondary ruptures (lighter lines) with significant vertical slip occurred very locally (Gonzalez *et al.*, 2000; Walls *et al.*, 2001).

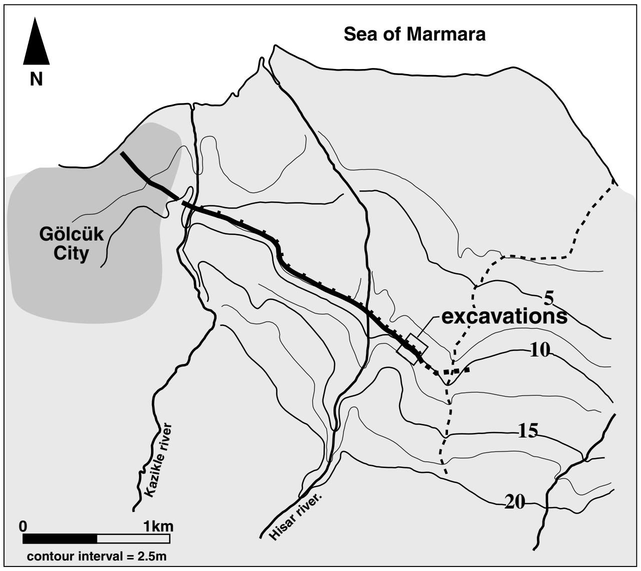

Figure 3. In the vicinity of our paleoseismic site, on the delta of the Hisar River, the Gölcük segment exhibits a 2-km-wide extensional step-over. Our excavations were across the step-over fault, which exhibited more than 1 m of nearly pure normal slip. The topographic contours show the existence of a pre-existing scarp associated with activity prior to 1999.

The Hisar River has incised the part of the fan on the upthrown block south of the fault. The material that has been eroded from the block south of the scarp has been redeposited just north of the scarp, forming a small alluvial fan upon the larger Hisar delta fan (Fig. 3). The shape of the younger fan shows that, in the course of its formation, the river has swept across the entire fan, at times flowing along the fault scarp and depositing sediments at its base.

The entire length of the Gölcük fault was mapped in detail soon after the earthquake (Gonzalez *et al.*, 2000; B. Meyer, *et al.*, personal comm., 2000; Barka *et al.*, 2002). Slip on the Gölcük fault was almost purely normal. Measurable components of right-lateral slip occurred primarily in association with local deviations in strike. The vertical component of slip averaged about 1.5 m, with a maximum value of 2.3 m. The lateral component reached a maximum of about 1 m but was commonly much less.

The Paleoseismic Site

Our paleoseismic site is located east of the Hisar River (Fig. 3), where the 1999 rupture is unusually simple. Here the 1999 scarp was 1.6 m high and nearly uneroded at the time of our excavations. We opened two trenches along the 1999 rupture, the first in November 1999, just after the earthquake. The second was cut in July 2000 to investigate further the relationships seen in the first excavation and to retrieve additional datable material. When the second trench was opened, in July 2000, the scarp had already begun to degrade and collapsing material from the free face had formed an incipient colluvial wedge along parts of the scarp (Fig. 4).

Figure 5a shows the topography of the site, including the pre- and post-1999 scarps and colluvial wedges. Profile AB (Fig. 5b) shows that the total apparent offset across the scarp is about 3.8 m, about 2 m greater than the height of the 1999 scarp. The actual height of the scarp is somewhat greater, because the profile does not extend across the crest of the scarp.

The Excavations

The two trenches expose similar faulted late Holocene fluvial and colluvial deposits. We could not inspect the lowest part of each trench, because of high groundwater. Pumping of the groundwater limited flooding of the trench but also encouraged collapse of portions of the walls.

Trench 1. Figure 6 depicts the strata and fault zone that were exposed in trench 1. This excavation was made in November 1999, 3 months after the earthquake (Gonzalez *et al.*, 2000). At that time, the 1999 scarp had sustained no erosional collapse, as evidenced by the pristine nature of the fault scarp and by the presence of a pre-earthquake grassy mat that continued up to the fault scarp on the down-thrown block. The scarp free face, however, was cut back by about 30 cm during the excavation.

Other than the 20- to 60-cm-thick organic soil at the ground surface, none of the units exposed in trench 1 appeared on both sides of the fault zone, making the total vertical offset across the fault larger than the thickness of the exposed downstream deposits plus the height of the scarp.

Southwest of the fault, strata on the up-thrown block consist of a sequence of well-sorted planar and lenticular sand and gravel beds overlain by a sequence of finer-grained sandy beds. The contact between the coarser and finer beds (F6/F7) is a shallow eastward-dipping angular unconformity. Beneath the unconformity, the sandy, well-sorted, massive gravels are heterolithologic and clasts are subangular to subrounded (units F7, F9, and F10). Lenses and planar beds of sand below and between the gravel beds are also well sorted, and some exhibit planar lamination or cross-bedding (F8). We interpret the coarser beds to have formed during periods of high stream discharge and the sandy beds to have formed during less energetic flow.

The nature of the younger sandy beds is consistent with deposition in a fluvial overbank setting. These constitute the upper meter or so of the section southwest of the fault (F1–F4) and are less well sorted. The finer-grained beds probably formed by settling of suspended load, whereas those with coarser sandy components probably were emplaced as bed load. The youngest bed beneath the modern soil layer, for example, grades upward from medium to coarse sand to clayey, fine to medium sand. This is consistent with initial emplacement as bed load and later deposition as suspended load.

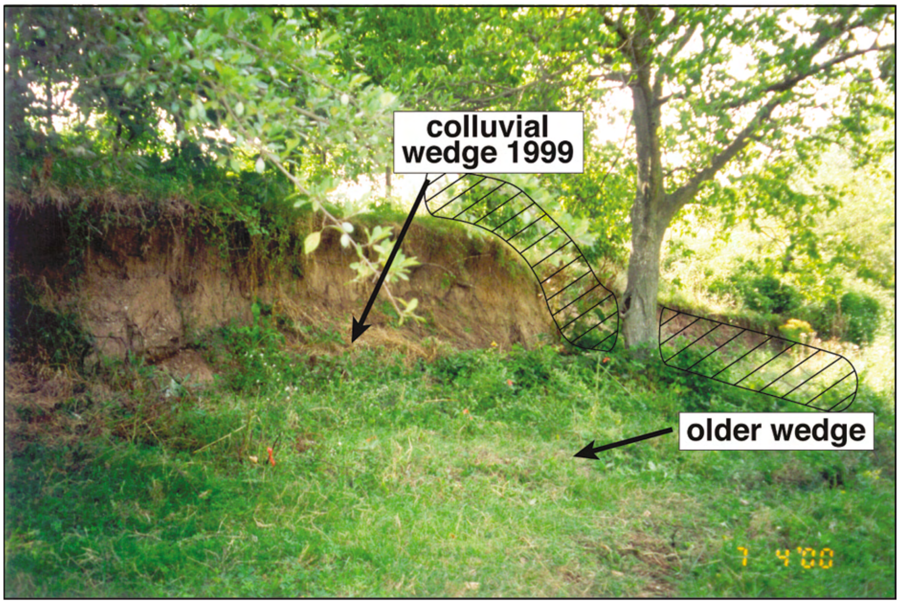

Figure 4. The scarp of the August 1999 rupture was 1.6 m high at the excavation. Some parts of the scarp had already collapsed to form a colluvial wedge by the time the photo was taken in July 2000. An older colluvial wedge, formed by earlier collapse of previous scarps, appears in the foreground. The hatched band in the background indicates the rough location of trench 1.

The sediments exposed southwest of the fault appear to have been deposited during the middle of the first millennium A.D. or earlier. Detrital charcoal from a bed about a meter below the ground surface, above the angular unconformity, yielded a calibrated radiocarbon age of A.D. 400–600 (Table 1). Tiles found in coarse fluvial channel sediments in a similar position farther below the surface of the up-thrown block, in an excavation, about 900 m to the northwest, are similar in age to this sample, as they appear to be early Byzantine in age (A.D. 500–600) (Gonzalez *et al.*, 2000).

The lowest unit exposed on the down-thrown block (G0) consists of well-sorted pebbles. Above unit G0 are two poorly sorted triangular beds that thicken toward the fault. These beds, W1 and W2, intercalate with sandy lenses that pinch out toward the fault (L1–L7) (Fig. 6). W1 and W2 appear to be of colluvial origin. Like the gravely deposits across the fault, the rounding and sorting of G0 indicate deposition in a high-energy fluvial environment. Auxiliary pits dug next to the trench showed, however, that this bed forms a narrow deposit that parallels the fault (Gonzalez *et al.*, 2000). This geometry indicates that it formed in a channel that ran parallel to and on the northeast side of the fault, possibly along a pre-existing scarp.

The sequence of deposits that overlie the gravel appears to be colluvial wedges. W1 consists of a block of older sediment, nearest the fault zone (W1a) and overlying debris (W1b). W1a consists of material that is nearly identical in color and composition to sandy clay bed, F6, across the fault and just above the unconformity, draped by a thin gravel lens. The younger portion of the lower wedge, W1b, is massive clayey, silty sand. The color and grains that form this part of the wedge are similar to those in F1–F5 across the fault. Thus, it seems plausible, at first glance, that this part of the wedge formed by progressive, piecemeal erosion of these beds.

Three sandy lenses (L1, L2, and L3) overlie wedge W1. Each of these lenses thins toward the fault scarp and onto the wedge. The lowest lens is composed of silty sand grading upward into silty clay. We interpret this as a suspended-load deposit, formed in a very shallow pool of quiet water on the down-thrown block. L2 consists of massive silty sand to clayey sand. The upper surface of this unit is nearly horizontal, with the distal end sloping gently away from the fault. We interpret L2 to be a suspended-load deposit, but we cannot totally discard the possibility that it is a colluvial deposit, formed by the slow erosion of the fault scarp. L3 consists of massive sandy clay. The upper surface of this deposit is highly irregular, probably due to bioturbation during the years it formed the ground surface. In general, however, the surface slopes away from the fault. The upper few centimeters are darkened by organic material and display slight bioturbation. These characteristics indicate a soil-forming interval before deposition of the overlying units. We infer this deposit to be scarp-derived colluvial wedge. The soil indicates a period of stability following deposition of L3. One sample of detrital charcoal within L2 (Table 1, sample 14C-4) indicates that the younger portions of the wedge (W1b) formed within or somewhat before the range A.D. 1480–1680. This interpretation is reinforced by the dates

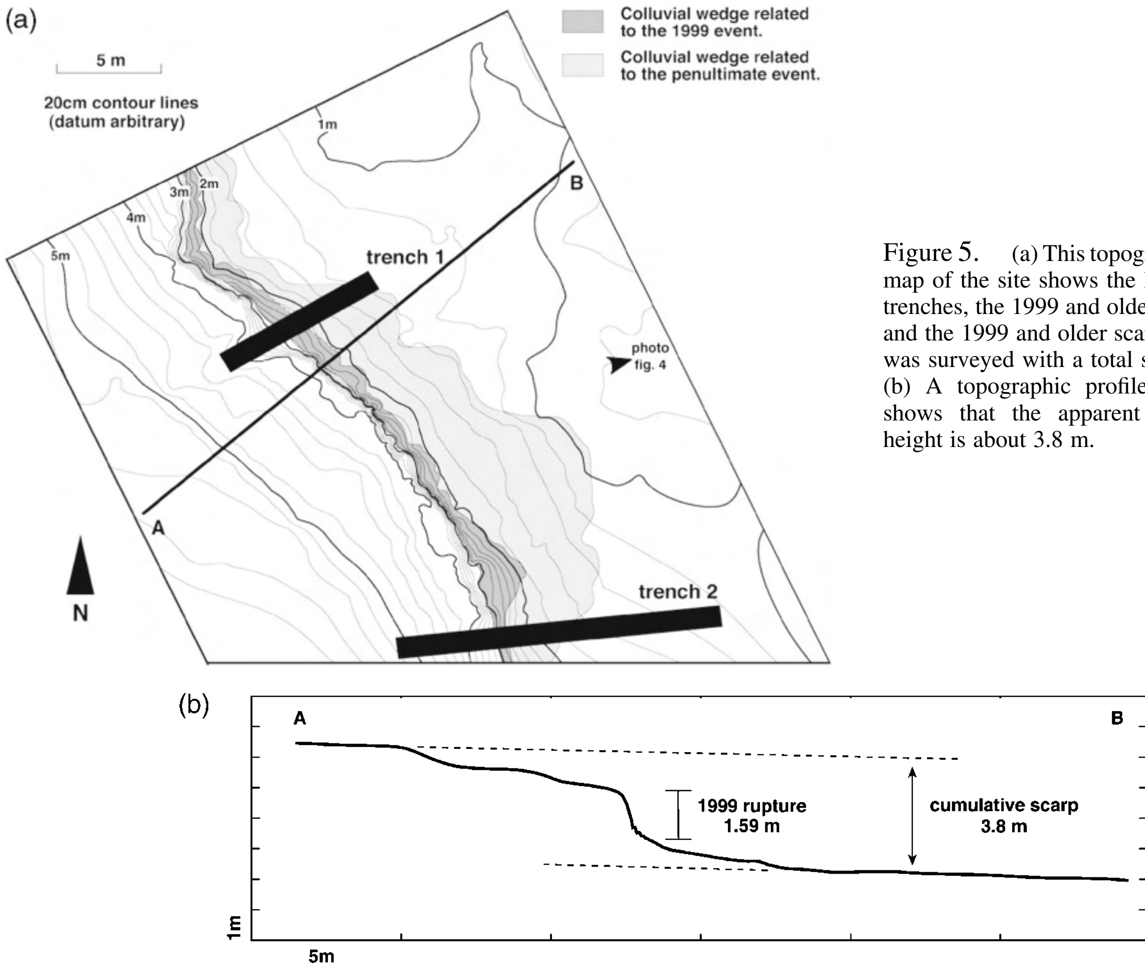

Figure 5. (a) This topographic and geologic map of the site shows the location of the two trenches, the 1999 and older colluvial wedges, and the 1999 and older scarp. The topography was surveyed with a total station (July 2000). (b) A topographic profile across the scarp shows that the apparent cumulative scarp height is about 3.8 m.

from the units corresponding to W1 in trench 2 (see next section).

A second sequence of colluvial wedges and lenses overlies L3. Wedge W2 consists of two parts. The lower part (W2a) consists of poorly sorted sand and silt, similar to the exposed nonpebbly portion of the up-thrown block, that is, units F1–F6. The upper part of wedge 2 (W2b) is formed of sandier material. The upper surface of the toe of wedge W2 is slightly darker. This indicates that enough time elapsed between the deposition of wedge 2 and the overlying lenses to allow the formation of a weak organic soil.

Units L4–L7 overlie the toe of wedge W2 and slope away from the fault. Their position, composition, and shape indicate that they are the result of gradual erosion of the scarp, after initial collapse of the scarp to form wedge W2. Units L4 and L5 consist of sandy material that could be derived from the raveling of sandy units of the up-thrown block exposed during faulting. Alternatively, considering the small volume of L4, the lens L4 may have formed by remobilization of material from W2b. Units L6 and L7 consist of pebbly sand, indicating that at least part of these colluvial units must be derived from different units than lenses L4 and L5.

From similarities of facies between some units forming the colluvial wedges and units in the up-thrown block, it is tempting to try to make correlations to constrain the temporal framework for the emplacement of the wedges. For example W1a is similar in composition to F6, and the overlying gravel drape is similar to unit F7. Thus, it might be suggested that W1a is an intact block that fell from F6 and then was mantled by gravels that fell from F7 after these units were exposed by fault slip. We do, in fact, interpret W1a to be a coherent block that fell off the fault scarp, followed by fall of a little gravel, but it cannot have fallen from unit F6. None of the units F1–F7 appear to have suffered any erosion at the scarp face, at least until our backhoe took a chunk out of the scarp. Thus, an origin of block W1a from any of these units is untenable. The base of W1a must be restored to a position at least as high as the current ground surface on the up-thrown block, and the block forming W1a has to come from a unit located above the present ground surface that is no longer present on the up-thrown block. (We will show this reconstruction later.) The source units on the up-thrown block are missing due to erosion, in large part due to intense man-made grading of the surface for agricultural purposes.

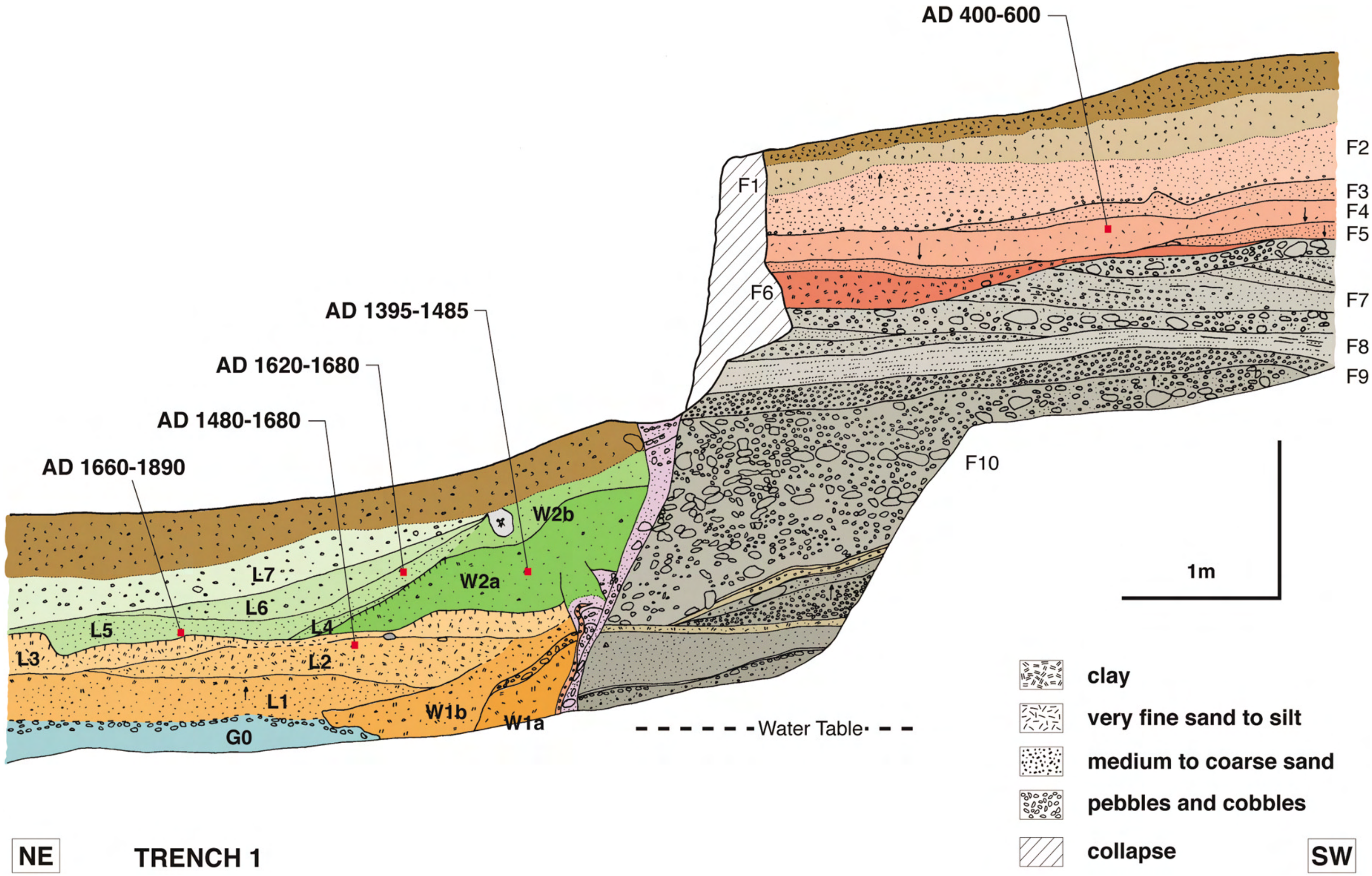

Figure 6. Map of the southern wall of trench 1. The up-thrown block consists of coarse and fine fluvial sands and gravel. The down-thrown block consists of two scarp-derived colluvial wedges and interfingering fluvial sand and gravel. The dates indicate the 2σ calendric age range for each sample, based upon AMS radiocarbon analyses (Table 1). The step in the ground surface of the up-thrown block (also visible in trench 2) results from man-made grading of the surface for agricultural purposes.

Table 1
Radiocarbon Dates for Trench 1

Sample Number	Laboratory Number	Sampled Unit (Fig. 6)	$^{13}C/^{12}C$ Ratio	^{14}C Age (^{13}C corrected) B.P.	Calibrated Age A.D. (2σ)
14C-1	Beta-135,199	W2a	−25.9	490 ± 40	1395–1485
14C-2	Beta-135,200	L5	−26.1	260 ± 30	1520–1570 (14%)
					1620–1680 (61%)
					1770–1810 (17%)
14C-3	Beta-135,201	L5	−29.4	190 ± 40	1660–1890
14C-4	Beta-135,202	L2	−22.5	280 ± 40	1480–1680
14C-5	Beta-135,203	F4	−26.6	1590 ± 40	400–600

All samples were pretreated with standard acid and base wash. Calib 3.0 software (Stuiver and Reimer, 1993) was used for calibration.

In trench 1 the fault zone is 10–20 cm wide. Sediments have been reoriented to align with the shear direction. At the base of the fault zone some pebbles are tilted toward the northeast, in good agreement with normal motion on the fault. Two small faults branch off the main fault zone and end in colluvial wedge W2a. This indicates that they formed after the formation of the wedge. Sediments (mapped in purple), trapped between those faults and the main fault zone, have been highly sheared and cannot be associated confidently to any of the units outside the fault zone.

The stratigraphy and structural relationships in trench 1 suggest the occurrence of at least two faulting events: colluvial wedge W1 resulted from the collapse of a scarp, later mantled by suspended-load units L2 and L3 and the formation of an organic soil on unit L3. It is worth noting that this soil is thinner and less mature than the soil exposed at the present ground surface. This difference might be due to the intense plowing of the present surface. Later, the scarp was refreshed by faulting and colluvial wedge W2 and units L4–L7 were deposited. Finally, following a new period of modest soil formation, faulting in 1999 once again refreshed the scarp.

The date of the faulting event that led to the formation of colluvial wedge W2 is constrained by three radiocarbon dates (Table 1). Two samples of detrital charcoal in unit L5 yielded AMS calibrated radiocarbon age ranges of A.D. 1520–1810, with the most probable date ranges being A.D. 1620–1680 and 1660–1890 (Table 1, samples 14C-2 and 14C-3). A third sample (Table 1, 14C-1), from the middle of wedge W2, yielded an accelerator mass spectrometry (AMS) calibrated radiocarbon age of A.D. 1395–1485. Based on the consistency of the other dates from the two trenches, this last date very probably is from a chunk of detrital charcoal that antedates the stratum. The three other dates provide a maximum limiting age for the faulting event, since detrital charcoal often antedates the age of the stratum in which it occurs (Nelson *et al.*, 2000). Thus, the youngest of the three dates, A.D. 1660–1890, gives the closest maximum limiting date range for the faulting event that led to the formation of wedge W2.

Trench 2. Trench 2 was excavated about 15 m southeast of trench 1 to explore the relationship between the older, and deeper, units on the down-thrown side of the fault. The flooding that resulted from this attempt to expose older layers led to partial collapse of the walls of the trench, which thwarted our attempts to map a complete exposure of the wall. Instead, we had to map an inset into the main exposure separately from the principal exposure (Fig. 7). Also, the principal exposure had to be benched to prevent additional collapse.

Trench 2 exposed stratigraphic units similar to those in trench 1. As in trench 1, only the uppermost soil occurs on both sides of the fault. The up-thrown block consists of beds of fine to coarse sandy cobble gravel, overlain by beds of coarse sand to silt. Grain size and distribution, erosional scours, and cross-bedding all indicate deposition on a braided riverbed. As in trench 1, the grain size and grading of the finer-grained units on the upper part of the up-thrown block are indicative of overbank deposition.

Detrital charcoal from a silty bed near the base of the oldest exposed sediment yielded an AMS calibrated radiocarbon age of A.D. 995–1162. This is about 500 years younger than the age of the detrital sample from the overlying beds in trench 1. We suspect that this indicates that the sample from trench 1 is several hundred years older than the age of the enclosing stratum. The simplest interpretation of this discrepancy is that the A.D. 995–1162 age from trench 2 is a better estimate of the age of the coarse fluvial section in both trenches.

Despite the poor condition of the wall of trench 2 on the down-thrown block, we were able to map the relationships exposed. The exposure reveals the same two colluvial sequences that appeared in trench 1. In addition, trench 2 provided a good exposure of the units underlying wedge W1 (Figs. 7 and 8) and allowed a better understanding of the basic relationship between the units and the fault zone. Unlike the exposure in trench 1, however, the fault zone in trench 2 is complicated by warping of the down-thrown block adjacent to the fault.

Trench 2 more clearly exposes the fluvial deposits (G0) that were only partially exposed at the bottom of trench 1 (Figs. 7 and 8). This fluvial unit is dominated by a thick, massive pebble gravel lens. Thin silty sand beds (units P1–P3) overlie and underlie the gravel away from the fault. The

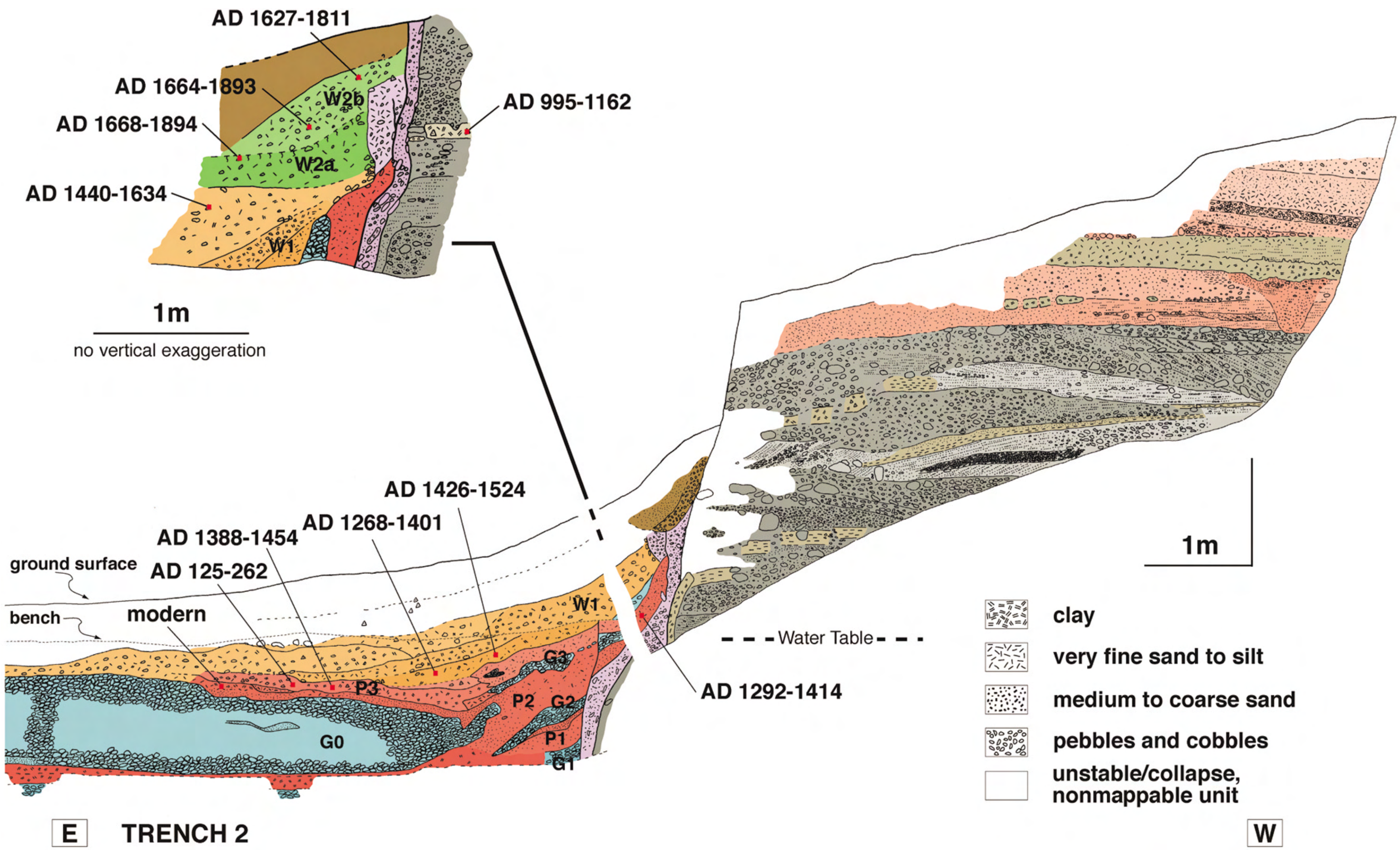

Figure 7. Map of the southern wall of trench 2. Color coding reflects our correlations of units with those in trench 1 (Fig. 6). The uncolored areas collapsed before we could map them. The inset figure is a map of part of the down-thrown block, in a small cut about 1 m south of the principal mapped cut. Both colluvial wedges exposed in trench 1 appear in this trench as well, although the form and composition of the wedges differ between the two trenches.

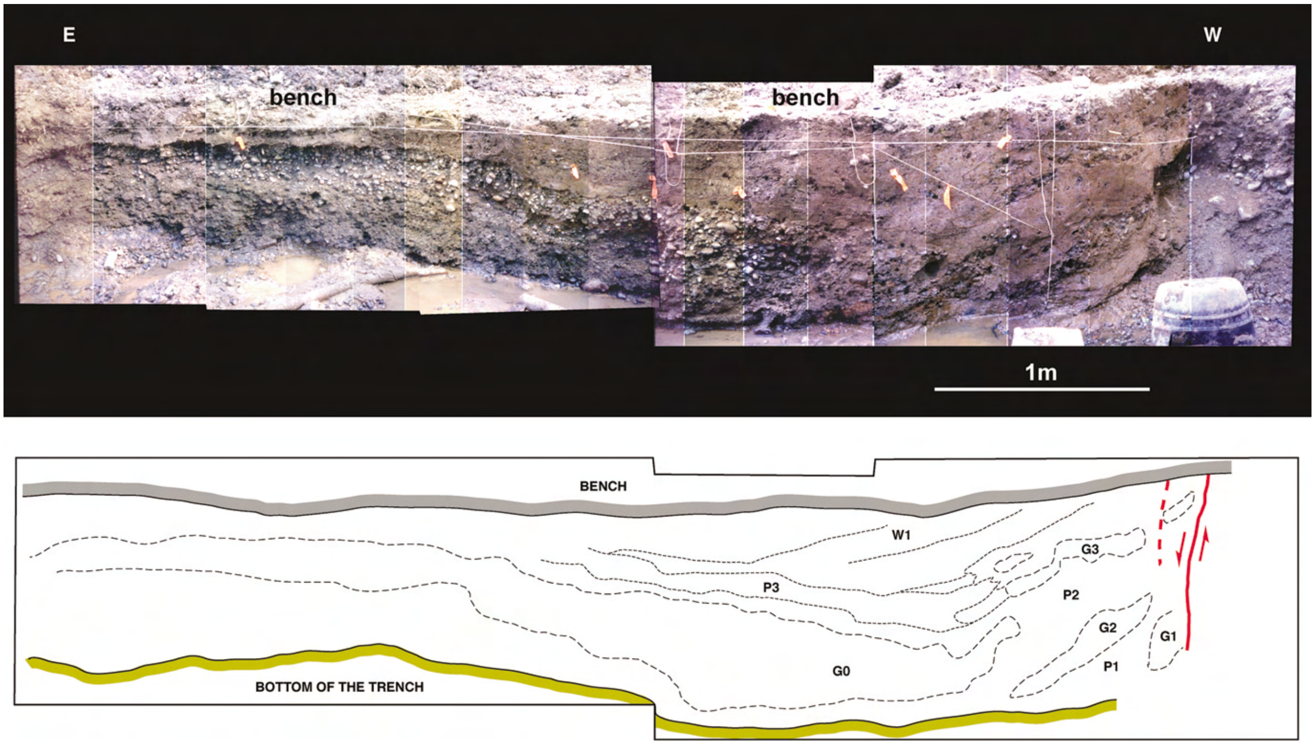

Figure 8. The upper panel shows a photo mosaic of the lowest exposed part of the down-thrown block in trench 2. The fluvial gravel bed and its warping near the fault are clearly visible. The fine sandy and silty units that warp up along the fault and are intercalated with the coarse fluvial gravel are also clearly visible. The lower panel outlines the main units of the lower part of the trench 2, with labeling referring to Figure 7.

thick gravel bed G0 pinches out before intersecting the fault. It also pinches out about 12 m east of the fault, but this part of the trench is not shown in Figure 7. Within 1 m of the fault, the lower unit consists of several small lenses of pebble gravel, G1–G3, surrounded by fine sand to silt, P1–P3. The long axes of both the large and the small lenses are parallel to the trend of the fault scarp. This indicates that the gravel beds were deposited by a stream flowing parallel to and next to the scarp. Units P3 and below exhibit eastward tilt within 1 m of the fault zone (Fig. 7).

Detrital charcoal from near the top of the lowest unit yielded an AMS calibrated radiocarbon age of A.D. 1292–1414 (Table 2, For-14). This date range provides a maximum limiting age for the stratum. Note that this age range is at least a century or two younger than the maximum limiting age of the coarse gravels on the up-thrown side of the fault. This is consistent with redeposition of materials from the up-thrown block at the base of the fault scarp.

Colluvial wedge W1 caps the lowest unit (Fig. 7). As in trench 1, this wedge consists of poorly sorted silt, sand, and pebbles. The shape of the unit indicates that it was formed by deposition of materials eroded from the fault scarp. The shape of colluvial wedge W1 differs from that in trench 1, because in trench 2 the portion of the wedge nearer the fault rests on tilted underlying sediment (top of unit P3). Thus, the thickest part of the wedge is not at the fault but 1 m away.

Several samples of detrital charcoal constrain the age of this colluvial wedge. AMS radiocarbon ages of samples from this deposits range widely, from about the first century A.D. to the present (Table 2). The modern sample must represent a root that was interpreted in error to be detrital charcoal. The 2000-year-old sample must surely be a piece of charcoal that was eroded from an older stratum and redeposited twice, first in the fluvial units of the up-thrown block and then re-eroded and deposited in the colluvial wedge. The remaining four AMS radiocarbon ages more closely approximate the time of deposition of the wedge. The three age ranges from strata near the bottom of the wedge are A.D. 1388–1454, 1268–1401, and 1426–1524 (Table 2; Fig. 7). The youngest of these, A.D. 1426–1524, provides a maximum limit to the age of the stratum, as it, too, could have been reworked from soil that rested on the up-thrown side of the fault. This suggests that the wedge began to form during or after the fifteenth century. The age range for a sample near the top of the wedge is A.D. 1440–1634. This is not appreciably younger than the age range for a sample at the base of the wedge. This age range is indistinguishable from the age range determined on charcoal from the younger part of the wedge in trench 1, A.D. 1480–1680 (Table 1, 14C-4).

Table 2
Radiocarbon Dates for Trench 2

Sample Number	Laboratory Number	Sampled Unit (Fig. 7)	^{14}C Age (^{13}C corrected) B.P.	Calibrated Age A.D. (2σ)
Gol-04	CAMS-70739	Up-thrown block	970 ± 40	995–1162
For-14	CAMS-70740	P2	610 ± 50	1292–1414
Gol-15	CAMS-70741	P2	Modern	Modern
Gol-01	CAMS-70742	P3	1810 ± 40	125–262
Gol-16	CAMS-70743	P3	510 ± 40	1388–1454
Gol-08	CAMS-70744	W1	670 ± 50	1268–1401
Gol-09	CAMS-70745	W1	410 ± 40	1426–1524
Gol-11	CAMS-70746	W1	380 ± 40	1440–1634
Gol-12	CAMS-70747	W2	140 ± 40	1668–1894
Gol-20	CAMS-70748	W2	150 ± 50	1664–1893
Gol-19	CAMS-70749	W2	230 ± 40	1627–1811

All samples where processed at the Lawrence Livermore National Laboratory AMS facility. Samples were pretreated with standard acid and base wash. $\delta^{13}C$ is assumed to be -25. Calib 4.3 software (Stuiver and Reimer, 1993) was used for calibration.

The upper colluvial wedge W2 in trench 2 is quite similar to the upper wedge exposed in trench 1. Wall collapse prevented us from mapping this wedge as completely as we did in trench 1. Nonetheless, we were able to clearly define the two units (W2a and W2b) that represent the initial collapse of the fault scarp. These units are composed mostly of unsorted silt and gravel. As in trench 1, the contact between W2a and W2b is characterized by a darker color. This more organic horizon indicates a short period of soil formation prior to emplacement of the remainder of the wedge.

AMS radiocarbon ages from three detrital charcoal samples constrain the period of accumulation of colluvial wedge W2. These age ranges, A.D. 1668–1894, 1664–1893, and 1627–1811, (Table 2) are indistinguishable from one another and in agreement with the ages in trench 1. They indicate that the wedge formed after about A.D. 1668.

As in trench 1, the fault zone is quite simple in trench 2. The main fault zone is about 20 cm wide, with many pebbles tilted by shear. Some of the fine units from the upthrown block have also been dragged into the fault zone, but identifying the original location of the dragged chunk would require more intensive dating of each fine unit of the upthrown block than we did. As in trench 1, one secondary fault branches off the main fault zone, cutting lower units P2 and P3. This minor fault appears to terminate upward in the bottom of unit W1.

Summary of the Evidence for Paleoseismic Events

Both trenches clearly expose the Gölcük fault, directly below the scarp that formed in 1999. In trench 1 it is a 10- to 20-cm-wide zone of normal faulting that dips 70° northeastward. In trench 2 the fault consists of both a discrete, narrow fault plane and a meter-wide zone of warping just northeast of the fault. Both exposures reveal two colluvial wedges on the down-thrown block at the foot of the fault scarp. The youngest wedge, W2, is of similar size and form in the two exposures. Trench 1 exposed the late-stage deposits that form the upper, more distal part of the wedge. In both trenches a dark organic soil developed on the top of the lower unit W2a. This suggests that a short period of time separated the formation of the lower and upper portions of the wedge. AMS calibrated radiocarbon dates, which represent maximum ages for the deposition of wedge W2, are consistent between the two trenches (Table 1 and 2) and indicate that the wedge formed sometime after about A.D. 1660.

In trench 1 two small faults that splay off of the main fault plane disrupt the base of colluvial wedge 2. These faults might be associated with the formation of the upper part of the wedge 2 (W2b) separated from the lower part of the wedge (W2a) by the weak organic soil. In that case these small faults suggest that wedge 2 might represent two events. These secondary faults, however, may also have been caused by the 1999 earthquake.

Both excavations expose an earlier colluvial wedge, W1. In trench 1, the oldest part of wedge W1a is a block of debris that fell intact from the scarp. Another short prism of debris, W1b, overlies it. Between these two initial collapse deposits and the upper colluvial deposits of the wedge is a suspended-load bed, L1. The stratigraphy of the wedge exposed in trench 2 is consistent in general with that in trench 1, but it is also complicated by additional warping. The unstable nature of trench 2, however, obscured much of the stratigraphic relationships. The radiocarbon ages from samples within wedge W1 indicate that it formed sometime during or after the period A.D. 1426–1524 (Tables 1 and 2).

The near-fault warping of the layers beneath wedge W1 is not evidence for a still-earlier episode of deformation. This warping appears to be quite localized, since we do not see it in trench 1. Some warping may also have occurred in trench 1 that has not been exposed, but in any case it would be smaller. Nonetheless, the warping is quite useful, because it is independent evidence for the faulting that led to deposition of wedge W1. If a fold or fault scarp formed in association with this warping, we would expect the concomitant deposition of debris eroded from the scarp directly atop the warped beds. Since wedge 1 lies directly upon the warped beds, that wedge is the result of faulting that accompanied the warping.

Offsets during the Paleoearthquakes

We have documented evidence for three scarp-forming episodes at this site along the Gölcük fault. The earliest led to the formation of wedge 1. The second resulted in the formation of wedge 2. And the most recent was associated with the M_w 7.4 Izmit earthquake of August 1999. The height of the scarp associated with the 1999 event is 1.6 m at trench 1 and 1.1 m at trench 2. The height of the scarps associated with the earlier events must be inferred from the height of the two buried wedges and the cumulative height of the fault scarp.

In estimating the offset of the two paleoseismic scarps, an evaluation of the cumulative scarp offset is a good place to start. From the extrapolation of slopes on both sides of the fault, the apparent cumulative scarp is about 3.8 m high (Fig. 5b). If we subtract the 1.6 m of vertical slip that occurred at trench 1 in 1999, we estimate that the total offset that produced the pre-1999 scarp was about 2.2 m. If the surfaces on both sides of the fault scarp were the same age, we would conclude that this is the amount of offset across the fault since the date of formation of the disarticulated surface. In this case, however, the two surfaces are not correlative. The up-thrown surface is the top of the sandy overbank deposits that must have been deposited after about A.D. 1000 (sample Gol-4, trench 2). The down-thrown surface is approximately the top of the sand and gravel sequence that underlies wedge 1. Its age must be younger than the age of the youngest beds on the up-thrown block, that is, an age between about A.D. 1000 and the age of wedge 1, perhaps A.D. 1500.

Another complication in using the cumulative scarp height to estimate the magnitude of earlier offsets is the fact that the up-thrown block next to the fault has been modified by agricultural activities and road building. The best we can do with the cumulative scarp height is to say this: since deposition of the lower gravel and sand unit on the down-thrown block, the vertical offset has been at least 2.2 m in addition to the 1.6 m that accumulated in 1999.

The shape and size of the two colluvial wedges at the base of the fault scarp are far more useful in determining the offsets associated with the two prior episodes of scarp formation. Since Wallace's (1977) seminal paper on the nature of fault scarps in granular materials, many have investigated colluvial wedges that form at the base of fault scarps. Many paleoseismic studies of normal faults have used the presence of eroded scarp debris as evidence for paleoearthquakes (e.g., Schwartz and Coppersmith, 1984; Schwartz and Crone, 1985; McCalpin and Nishenko, 1996). Others have used physical models based upon diffusion equations to understand the processes of erosion and deposition that follow the formation of a fault scarp (e.g., Nash, 1980; Avouac and Peltzer, 1993; Hanks, 2000). Observations demonstrate that once a scarp has been created, the first stage in the process of modification involves gravity-induced collapse. The length of this period depends upon the cohesion of the faulted material, the regional slope, and the climatic conditions (Arrowsmith and Rhodes, 1994). Diffusive processes predominate later. These are controlled by the erosion of material from the upper half of the scarp and deposition downslope. This process tends to smooth the profile across the former fault scarp. Typically, if the regional slope is not too steep, the steady state is achieved when the elevation of the inflection point between the convex (up-thrown block) and the concave (down-thrown block) part of the slope reaches about half of the total height of the initial free scarp (Fig. 9).

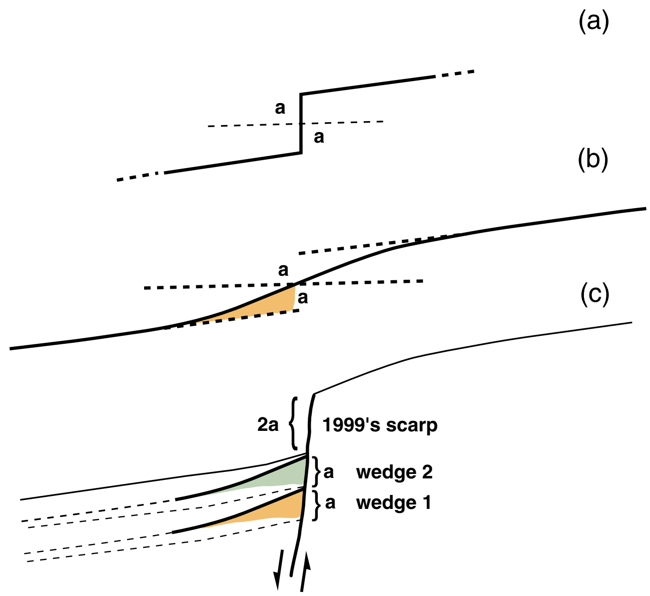

Figure 9. An idealized representation of the formation of the scarp and colluvial wedges during three successive ruptures. The height of the scarp formed during both earthquakes equals twice the thickness, *a*, of the colluvial wedge that forms subsequently on the downthrown block. (a) First sudden dislocation of the fluvial surface results in a scarp of height 2*a*. (b) After the first dislocation, the scarp degrades to form a colluvial wedge of thickness, *a*. In this idealization, the volume of material eroded from the scarp equals the volume of material emplaced at the toe of the scarp. The dislocation and erosion depicted in (a) and (b) repeat one more time before the dislocation of 1999. (c) The configuration of scarp and colluvial wedges at the Gölcük trench site immediately following the 1999 rupture. The 1999 scarp has a height of 2*a* (1.6 m) and the height, *a*, of each colluvial wedge is about 0.8. The fact that the 1999 scarp is about twice as high as the colluvial wedges are thick suggests that the past three ruptures have been of the same magnitude, about 1.6 m.

In the case of a normal fault, the colluvial wedge underlies the concave-upward, lower half of the slope, which is buried during the formation of the colluvial wedge related to the next earthquake. The height of the colluvial wedge should therefore give us a net indication of the local size of the coseismic slip.

In trench 1, if we extend the base of wedge W1 to the scarp, assuming no dramatic geometric change in the unexposed part of the wedge, the thickness of W1 at the fault is 0.8 ± 0.3 m (Fig. 6). Later faulting of colluvial wedge 1 obscures this measurement somewhat, which leads to the large error indicated. The thickness of colluvial wedge 2, also measured at the fault in trench 1, is 0.7 ± 0.1 m (Fig. 6) if we consider only W2a and 0.9 ± 0.1 m if we consider the entire wedge, W2.

The restoration of the surfaces through the earthquake series (Fig. 10) shows the relation between the height of individual wedges and the total fault offset during each earthquake, assuming the model discussed previously (Fig. 9). It is obvious from this reconstruction that the units from the downstream block could not originate from the unit we have exposed in the up-thrown block.

The height of the two colluvial wedges W1 and W2 are quite similar; in fact they are indistinguishable. The height of the 1999 scarp at the trench location is 1.6 ± 0.1 m (Fig. 5b), about twice the height of the older colluvial wedges. This suggests that the scarps associated with the paleoseismic colluvial wedges 1 and 2 were similar in size to the fault scarp created in 1999. This would mean that at this location slip during the past three episodes has been identical, or nearly so. This similarity supports the hypothesis that faults tend to produce offsets of similar size during serial ruptures.

Insights from Historical Accounts

Written history for the region surrounding the Sea of Marmara extends more than two millennia into the past. This is because Istanbul (formerly Constantinople) has long been a center of trade and political activity. Several earthquake catalogs have been compiled for the region. Ambraseys and Finkel (1995) and Ambraseys (2002) have provided the most recent review of these records. Because radiocarbon analyses constrain the fault ruptures we have identified in our excavations to the historical period, we may well be able to assign specific dates to these events. The oldest episode of rupture exposed in the excavations occurred sometime after about A.D. 1425. The second episode occurred sometime after about A.D. 1660, and it may represent two distinct events. According to Ambraseys and Finkel (1991, 1995), no large destructive earthquakes occurred in the region between an event on 25 October 989 and the great Marmara earthquake of 10 September 1509. Thus the oldest date we could assign to our oldest event is A.D. 1509. The next large earthquake after this is the destructive earthquake of 25 May 1719. This is also the first large event after the maximum limiting age for the second wedge, A.D. 1660. Thus 1509 and 1719 are good candidates for the events that resulted in the formation of wedges 1 and 2.

However, several other large events occurred later in the eighteenth century: one in A.D. 1754 and two in 1766. An additional large event occurred in the region in 1894. Thus our second episode of faulting can plausibly be associated with any of these five earthquakes.

The 1509 earthquake was felt throughout the eastern Mediterranean basin, as far as the Nile delta, and caused heavy damage around the Sea of Marmara. Istanbul was severely damaged. It is reported that this earthquake was responsible for the death of 4000–5000 people (Ambraseys and Finkel, 1990). Since there are no reports of faulting during the event, the lateral extent of the rupture is largely a matter of speculation. Based upon interpretation of the levels of shaking experienced at various locations, Ambraseys and Jackson (2000), Ambraseys (2001), and Parsons *et al.* (2000) considered whether or not this earthquake involved rupture of the fault throughout the entire length of the Sea of Marmara and beyond. The historical data are not sufficient for resolving this issue; most of the reported damage occurred west of Istanbul, but some eastern cities, including Izmit, were also severely damaged (Ambraseys and Finkel, 1995). Our data suggest that the Golcük segment did break during the 1509 earthquake, and the dislocation at our site was of the same sense and magnitude as that in 1999.

Assigning a precise date to the second event identified in the trenches is more difficult. The AMS radiocarbon dates indicate that this earthquake occurred after about A.D. 1660. Five large earthquakes occurred between that date and 1999. The two large events in 1766 have intensity patterns that limit their source ruptures to the Sea of Marmara and the Gelibolu peninsula, well west of our site. But felt reports (Ambraseys and Finkel, 1995) for the events of A.D. 1719, 1754, and 1894 indicate severe damage in the region of Izmit.

The earthquake of 25 May 1719 destroyed most of the towns on the coasts of the Bay of Izmit, from Yalova, 64 km west of our excavations, to Düzce, 100 km to the east (Ambraseys and Finkel, 1991). The number of casualties in this event may have been as large as 6000.

The earthquake of 2 September 1754 also destroyed many villages around the Bay of Izmit, but the city of Izmit itself is not specifically mentioned as having been severely damaged. So it may be, as proposed by Ambraseys (2002), that the earthquake was not produced by rupture of any faults close to the town of Izmit but further west in the gulf, or even in the Sea of Marmara. The magnitude of this earthquake appears from the extent and severity of the felt reports to have been smaller than the magnitude of either the 1719 or 1894 earthquakes (Ambraseys and Finkel, 1995).

The earthquake of 10 July 1894 strongly affected the region of Izmit and the southwestern coastline of the Gulf of Izmit. Some ground failures also occurred east of Izmit, in the area of the Lake Sapanca. Ambraseys's (2002) reassessment of the distribution of the destruction places this

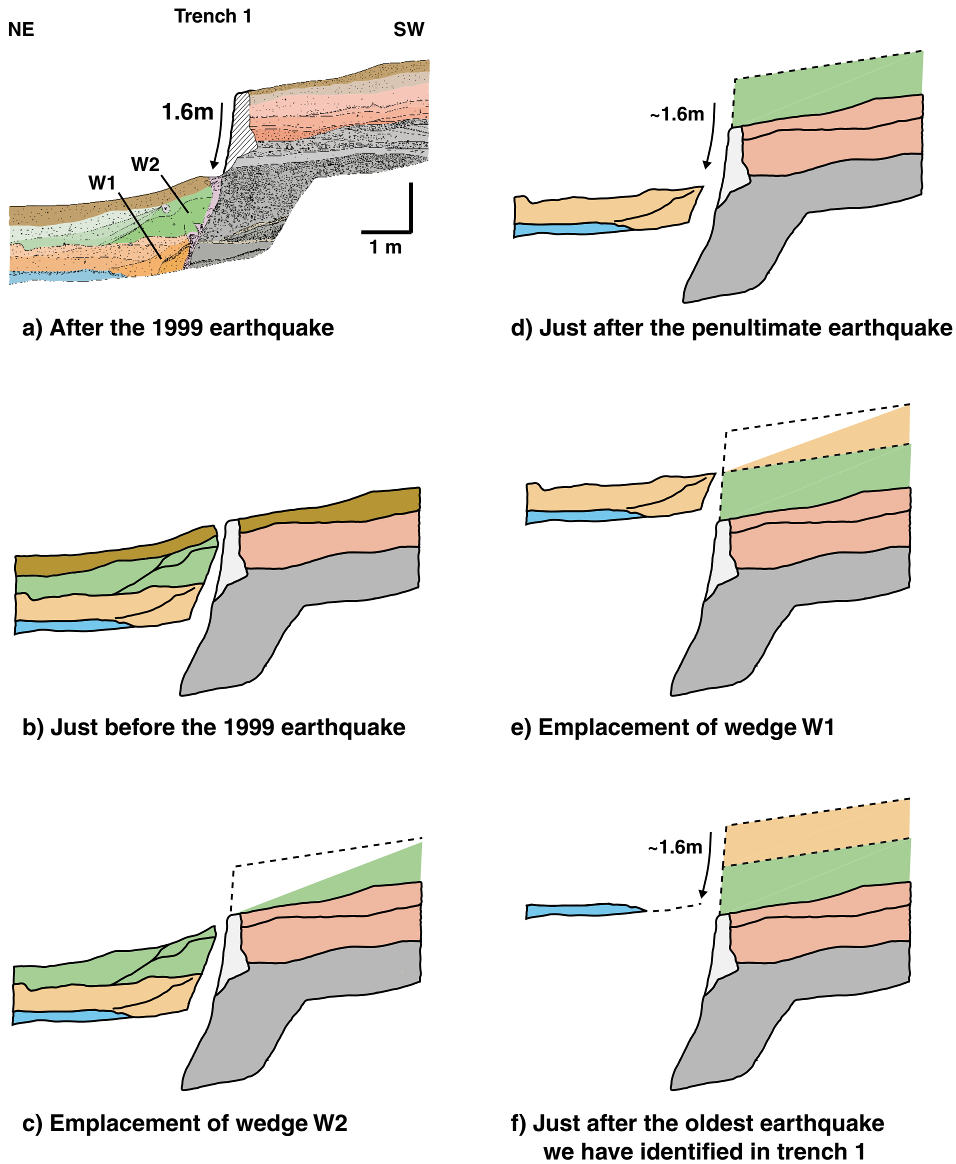

Figure 10. Possible restoration of trench 1 following the model described in Figure 9. (a) The present situation. (b) Restoration of the ground surface to its position prior to the 1999 event. The trench log has been simplified for more clarity. (c) Restoration of the scarp when the diffusive processes have reached a state of equilibrium. Some bed-load lenses have draped the toe of the wedge at its northeast end. The soil at the present ground surface does not exist yet. (d) The penultimate earthquake has just happened. Wedge W2 does not exist yet and the fault scarp is about 1.6 m high. (e) Formation of wedge W1 from the oldest earthquake we can identify in trench 1, similar to (c). (f) Geometry of the different units when the oldest event has just happened. W1 has not formed yet.

event on the southern coast of the Gulf of Izmit. However, the intensities derived from the description of the damage seem generally lower than the intensities derived for the same places during the 1719 event (Parsons *et al.*, 2000) or the 1999 event (USGS, 2000). Therefore we can assume that this event was smaller in size than the 1719 and 1999 earthquakes.

From this set of observations, we suggest that the second event we have identified in the trenches is associated with the earthquake of 25 May 1719. Ambraseys and Jackson (2000) have estimated a magnitude of M_s 7.4 for this event, identical to the magnitude of the 1999 earthquake. Moreover, our interpretation is in good agreement with Parsons *et al.* (2000), who assigned historical events to fault segments using a probabilistic method (Bakun and Wentworth, 1997) applied to the macroseismic data. In their analysis of the felt reports of the 1509, 1719, 1754, and 1894 events, only the 1719 earthquake involved rupture of the Golcük segment for both minimal and maximal rupture scenarios.

Discussion

The 17 August 1999 earthquake rupture along the North Anatolian fault provides a rare opportunity to study the repeatability of fault displacement at a specific location through several earthquakes. We have selected a site along the Gölcük fault where the fault trace is unusually simple and shows a topographic scarp height about twice the height of the 1999 scarp.

The two trenches we have opened show consistent stratigraphy with clear evidence for two previous earthquakes. The oldest earthquake, event 1, can be clearly identified from the lowest colluvial wedge, W1, which is nicely exposed in the two trenches. Radiocarbon dates and historical accounts are consistent with this rupture being associated with the great earthquake of 1509.

The upper wedge, W2, is also clearly expressed, and radiocarbon dates and historical records suggest that it formed at the base of a scarp associated with the 1719 earthquake. However, the presence of a weak soil within this wedge and the occurrence of lesser earthquakes in the region in 1754 and 1894 give credence to the possibility that this wedge is a composite of more than one event. Since only a weak soil formed atop the collapse debris before deposition of the wash debris, we might doubt a multiple-event origin for this second wedge. Nonetheless, the presence of two small secondary faults within the lower part of the second wedge suggests independently the composite nature of the second wedge. Hence, we favor the interpretation that the second wedge formed in association with both the 1719 and 1894 earthquakes. This is supported by recent analyses of the historical catalogs (Ambraseys, 2000; Ambraseys and Jackson, 2000). We cannot exclude the possibility that minor rupture of the base of wedge 2 also occurred during the 1754 earthquake. However, the relatively small intensities at Izmit in 1754 and 1894 argue against this.

Figure 11 displays the history of vertical offset at the site, assuming that we have interpreted the two paleoseismic colluvial wedges correctly. Between 989 and 1509, the historical record (Ambraseys, 2002) suggests that the fault was quiescent, although we have no data from the site to either confirm or deny this. In 1509, an offset about double the thickness of wedge 1 (about 1.6 m) occurred. The offset of 1719, quite possibly in combination with offsets in 1754 or 1894, was about twice the height of wedge 2 (also about 1.6 m). And, most recently, the 1999 event added another 1.6 m to the height of the scarp.

Although some uncertainties remain, this history of three serial ruptures suggests a tendency toward both similar magnitude of offset at a site and nearly periodic rupture. However, the possible involvement of two increments of faulting in the eighteenth century (1719 and 1754) or another in 1894 creates significant ambiguity. And the apparent five-century hiatus in activity during the first half of the millennium also argues that any short-term periodicity does not hold for the long term. A hitherto unrecognized earthquake in the middle of the thirteenth century would erase this irregularity quite effectively, but the historical record appears to be complete for the first half of the millennium (Ambraseys, 2002).

This study of a single paleoseismic site does not answer all of the current questions about the nature of serial rupture of active faults. For example, we still do not know how the lengths of the 1509, 1719, and 1999 ruptures compare. Different interpretations of macroseismic data (Ambraseys and Finkel, 1995; Ambraseys and Jackson, 2000; Parsons *et al.*, 2000; Ambraseys, 2002) and paleoseismological data (Rockwell *et al.*, 2001) do not agree, but do show that rupture lengths were not similar for these events. Thus, we can reject the characteristic-earthquake hypothesis (Schwartz and Coppersmith, 1984) in this case. If the eighteenth-century event in our sequence is only one event, then a slip-patch model (Sieh, 1996) may work. In this concept, the displacement is similar for each slip patch from event to event, although the number of adjacent slip patches that fail

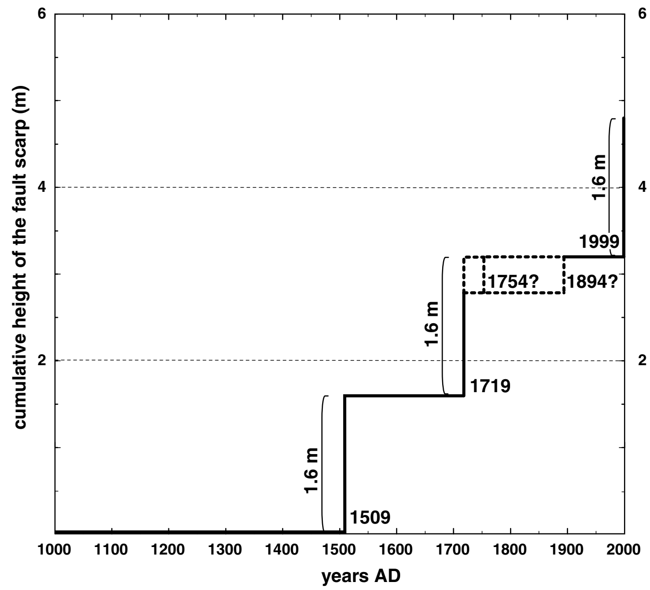

Figure 11. Tentative vertical offset across the fault through time from paleoseismic and historical data, following the assumption that the height of the colluvial wedge is indicative of the total height of the coseismic scarp. The 1509 and 1999 earthquakes have a very similar displacement. The dashed lines illustrate different scenarios for the middle event that conform with the data associated with the formation of wedge 2. Either only one large earthquake with an offset of 1.6 m occurred in 1719, or two smaller earthquakes occurred in 1719 and 1754 or 1894. The possibility of having three earthquakes seems very unlikely from the trench exposure.

in each event may vary. This number could vary from one earthquake to the other, producing earthquakes of different magnitude. But if the eighteenth-century scarp formed during both the 1719 and 1754 or 1894 earthquakes, then even this hypothesis would be deficient.

Despite its limitations, this site along the 1999 North Anatolian rupture contributes significant data to an important debate about the repetition of fault rupture.

Acknowledgments

The authors wish to thank the Ford Otosan for its support during this work. Some of the maps have been prepared using the Generic Mapping Tool free software. We thank R. Langridge and D. Ragona for their help during the field work. J. Liu, R. Armijo, and B. Meyer helped to improve this manuscript by their comments. We thank M. Meghraoui and an anonymous reviewer for very helpful reviews that significantly improved our analysis of the data. In memoriam of A. Barka, who died tragically while the article was in review. This is Caltech Contribution Number 8989 and IPGP Contribution Number 1936.

References

Ambraseys, N. N. (2001). The earthquake of 1509 in the Sea of Marmara, Turkey, revisited, *Bull. Seism. Soc. Am.* **91,** 1397–1416.

Ambraseys, N. N. (2002). The seismic activity of the Marmara Sea region over the last 2000 years, *Bull. Seism. Soc. Am.* **92,** 1–18.

Ambraseys, N. N., and C. F. Finkel (1990). The Marmara Sea earthquake of 1509, *Terra Nova* **2,** 167–174.

Ambraseys, N. N., and C. F. Finkel (1991). Long-term seismicity of Istanbul and of the Marmara Sea region, *Terra Nova* **3,** 527–539.

Ambraseys, N. N., and C. F. Finkel (1995). The seismicity of Turkey and adjacent areas, a historical review, 1500–1800, Eren, Istanbul.

Ambraseys, N. N., and J. A. Jackson (2000). Seismicity of the Sea of Marmara (Turkey) since 1500, *Geophys. J. Int.* **141,** F1–F6.

Armijo, R., B. Meyer, A. Barka, J. B. De Chabalier, and A. Hubert-Ferrari (2000). The fault breaks of the 1999 earthquakes in Turkey and the tectonics evolution of the sea of Marmara: a summary, in *The 1999 Izmit and Ducze Earthquakes: Preliminary Results*, A. Barka, O. Kozaci, S. Akayuz, and E. Altunel (Editors), Istanbul Technical University, Istanbul.

Armijo, R., B. Meyer, A. Hubert, and A. Barka (1999). Westward propagation of the North Anatolian fault into the northern Aegean: timing and kinematics, *Geology* **27,** no. 3, 267–270.

Arrowsmith, J. R., and D. D. Rhodes (1994). Original forms and initial modifications of the Galway Lake road scarp formed along the Emerson fault during the 28 June 1992 Landers, California, earthquake, *Bull. Seism. Soc. Am.* **84,** no. 3, 511–527.

Avouac, J.-P., and G. Peltzer (1993). Active tectonics in southern Zinjiang, China: analysis of terrace riser and normal fault scarp degradation along the Hotan–Qira fault system, *J. Geophys. Res.* **98,** no. B12, 773–807.

Bakun, W. H., and C. M. Wentworth (1997). Estimating earthquake location and magnitude from seismic intensity data, *Bull. Seism. Soc. Am.* **87,** no. 6, 1502–1521.

Barka, A. (1992). The North Anatolian fault zone, *Ann. Tectonicae* **6,** 164–195.

Barka, A. (1996). Slip distribution along the North Anatolian fault associated with the large earthquakes of the period 1939 to 1967, *Bull. Seism. Soc. Am.* **86,** 1238–1254.

Barka A. (1999). The 17 August 1999 Izmit earthquake, *Science* **285,** 1858–1859.

Barka, A., S. Akyuz, E. Altunel, G. Sunal, Z. Cakir, A. Dikbas, B. Yerli, R. Armijo, B. Meyer, J. B. Chabalier, T. Rockwell, J. Dolan, R. Hartleb, T. Dawson, S. Christofferson, A. Tucker, T. Fumal, R. Langridge, H. Stenner, W. Lettis, W. Page, and J. Bachhuber (2002). The surface rupture and slip distribution of the 17 August 1999 Izmit earthquake (*M* 7.4), North Anatolian fault, *Bull. Seism. Soc. Am.* **92,** 43–60.

Gonzalez, T., K. Sieh, T. Dawson, E. Altunel, and A. Barka (2000). Faulting and ground subsidence at the Ford–Otosan Plant near Gölcük, Turkey as a result of the August 17, 1999 Kocaeli earthquake, *Am. Assoc. Petrol. Geol. Bull.* **84,** no. 6, 870.

Hanks, T. C. (2000). The age of scarplike landforms from diffusion-equation analysis, in *Quartenary Geochronology: Methods and Applications* J. S. Nollet, J. M. Sower, and W. R. Lettis (Editors), AGU, Washington, D.C.

Langridge, R. M., H. D. Stenner, T. Fumal, S. Christofferson, T. Rockwell, R. Hartleb, J. Bachhuber, and A. Barka (2002). Geometry, slip distribution, and kinematics of surface rupture on the Sakarya fault segment during the 17 August 1999 Izmit, Turkey earthquake, *Bull. Seism. Soc. Am.* **92,** 107–125.

Lettis, W., J. Bachhuber, A. Barka, R. Witter, and C. Brankman (2000). Surface fault rupture and segmentation during the Kocaeli earthquake, in *The 1999 Izmit and Ducze Earthquakes: Preliminary Results*, A. Barka, O. Kozaci, S. Akayuz, and E. Altunel (Editors), Istanbul Technical University, Istanbul.

McCalpin, J., and S. Nishenko (1996). Holocene paleoseismicity, temporal clustering, and probabilities of future large ($M > 7$) earthquakes on the Wasatch fault zone, Utah, *J. Geophys. Res.* **101,** 6233–6253.

McClusky, S., S. Balassanian, A. Barka, C. Demir, S. Ergintav, I. Georgiev, O. Gurkan, M. Hamburger, K. Hurst, H. Kahle, K. Kastens, G. Kekelidze, R. King, V. Kotzev, O. Lenk, S. Mahmoud, A. Mishin, M. Nadariya, A. Ouzounis, D. Paradissis, Y. Peter, M. Prilepin, R. Reilinger, I. Sanli, H. Seeger, A. Tealeb, M. N. Toksoz, and G. Veis (2000). Global positioning system constraints on plate kinematics and dynamics in the eastern Mediterranean and Caucasus, *J. Geophys. Res.* **105,** no. 3, 5695–5719.

Nash, D. B. (1980). Morphologic dating of degraded normal fault scarps, *J. Geol.* **88,** 353–360.

Nelson, A. R., S. F. Personius, R. E. Rimando, R. S. Punongbayan, N. Tungol, H. Mirabueno, and A. Rasdas (2000). Multiple large earthquakes in the past 1500 years on a fault in metropolitan Manila, the Philippines, *Bull. Seism. Soc. Am.* **90,** no. 1, 73–85.

Parsons, T., S. Toda, R. Stein, A. Barka, and J. H. Dieterich (2000). Heightened odds of large earthquakes near Istanbul: an interaction-based probability calculation, *Science* **288,** 661–665.

Rockwell T., A. Barka, T. Dawson, S. Akyuz, and K. Thorup (2001). Paleoseismology of the Gazikoy–Saros segment of the North Anatolia fault, northwestern Turkey: comparaison of the historical and paleoseismic records, implications of regional seismic hazard, and models of earthquake recurrence, *J. Seism.* **5,** 433–448.

Schwartz, D. P., and K. J. Coppersmith (1984). Fault behavior and characteristic earthquakes: examples from the Wasatch and San Andreas fault zones, *J. Geophys. Res.* **89,** 5681–5698.

Schwartz, D., and A. Crone (1985). The 1983 Borah Peak earthquake: a calibration event for quantifying earthquake reccurence and fault behavior on Great Basin normal faults, *U.S. Geol. Surv. Open-File Rept. 85–290*, 153–160.

Sieh, K. (1996). The repetition of large-earthquake ruptures, *Proc. Natl. Acad. Sci.* **93,** 3764–3771.

Stein, R., A. Barka, and J. Dieterich (1997). Progressive failure on the North Anatolian fault since 1939 by earthquake stress triggering, *Geophys. J. Int.* **128,** 594–604.

Stuiver, M., and P. J. Reimer (1993). Extended ^{14}C data base and revised CALIB 3.0 ^{14}C age calibration program, *Radiocarbon* **35,** no. 1, 215–230.

Toksöz, M. N. (Editor) (2002). Issue dedicated to the Izmit, Turkey, earthquake of 17 August 1999, *Bull. Seism. Soc. Am.* **92,** 526 pp.

U.S. Geological Survey (USGS) (2000). Implication for earthquake risk reduction in the United States from the Kocaeli, Turkey, earthquake of August 17, 1999, *U.S. Geol. Surv. Circ. 1193.*

Wallace, R. E. (1977). Profiles and ages of young fault scarps, north-central Nevada, *Geol. Soc. Am. Bull.* **88,** 1267–1281.

Walls, C., K. Sieh, Y. Klinger, A. Barka, S. Akyuz, and E. Altunel (2001). Geomorphology, paleoseismology, and effects of the *M* 7.4 August 17, 1999 Izmit earthquake on auxiliary strands of the Yalova fault (abstract). Presented at European Union Geosciences 11, 8–12 April, Strasbourg, France, 293.

Seismolab
California Institute of Technology
Pasadena, California 91125
(Y.K., K.S.)

Osmangazi University
Bademlik-Eskesehir, Turkey
(E.A.)

Istanbul Technical University
Istanbul, Turkey
(A.A., A.B.)

U.S. Geological Survey
Menlo Park, California 94025
(T.D.)

Earth Consultant International
Orange, California 92867
(T.G.)

San Diego State University
San Diego, California 92182
(A.M., T.R.)

Manuscript received 23 October 2001.

Serial ruptures of the San Andreas fault, Carrizo Plain, California, revealed by three-dimensional excavations

Jing Liu-Zeng,[1,2,3] Yann Klinger,[1,2] Kerry Sieh,[1] Charles Rubin,[4] and Gordon Seitz,[5]

Received 27 December 2004; revised 15 August 2005; accepted 21 September 2005; published 28 February 2006.

[1] It is poorly known if fault slip repeats regularly through many earthquake cycles. Well-documented measurements of successive slips rarely span more than three earthquake cycles. In this paper, we present evidence of six sequential offsets across the San Andreas fault at a site in the Carrizo Plain, using stream channels as piercing lines. We opened a latticework of trenches across the offset channels on both sides of the fault to expose their subsurface stratigraphy. We can correlate the channels across the fault on the basis of their elevations, shapes, stratigraphy, and ages. The three-dimensional excavations allow us to locate accurately the offset channel pairs and to determine the amounts of motion for each pair. We find that the dextral slips associated with the six events in the last millennium are, from oldest to youngest, ≥5.4 ± 0.6, 8.0 ± 0.5, 1.4 ± 0.5, 5.2 ± 0.6, 7.6 ± 0.4 and 7.9 ± 0.1 m. In this series, three and possibly four of the six offset values are between 7 and 8 m. The common occurrence of 7–8 m offsets suggests remarkably regular, but not strictly uniform, slip behavior. Age constraints for these events at our site, combined with previous paleoseismic investigations within a few kilometers, allow a construction of offset history and a preliminary evaluation of slip- and time-predictable models. The average slip rate over the span of the past five events (between A.D. 1210 and A.D. 1857.) has been 34 mm/yr, not resolvably different from the previously determined late Holocene slip rate and the modern geodetic strain accumulation rate. We find that the slip-predictable model is a better fit than the time-predictable model. In general, earthquake slip is positively correlated with the time interval preceding the event. Smaller offsets coincide with shorter prior intervals and larger offset with longer prior intervals.

Citation: Liu-Zeng, J., Y. Klinger, K. Sieh, C. Rubin, and G. Seitz (2006), Serial ruptures of the San Andreas fault, Carrizo Plain, California, revealed by three-dimensional excavations, *J. Geophys. Res.*, *111*, B02306, doi:10.1029/2004JB003601.

1. Introduction

[2] Forecast of large earthquakes might be possible if theorists could constrain the range of plausible physical models with precise reconstructions of prior rupture histories, that is, the variations in timing and rupture magnitude of past events. Our understanding of the nature of earthquake repetition is hampered by a lack of long records of relevant high-quality data bearing on the behavior of past large ruptures. A myriad of models have been proposed to describe earthquake recurrence. Some models predict highly regular sequences [e.g., *Reid*, 1910; *Schwartz and Coppersmith*, 1984; *Sieh*, 1981, 1996; *Stuart*, 1986; *Tse and Rice*, 1986; *Ward and Goes*, 1993; *Rice*, 1993; *Rice and Ben-Zion*, 1996; *Lapusta et al.*, 2000], whereas others predict highly irregular behavior [e.g., *Bak and Tang*, 1989; *Carlson and Langer*, 1989; *Ito and Matsuzaki*, 1990; *Huang et al.*, 1992; *Shaw*, 1995; *Ben-Zion*, 1996; *Cochard and Madariaga*, 1996; *Ward*, 1997; *Lyakhovsky et al.*, 2001; *Shaw and Rice*, 2000]. The lack of determinative data makes it difficult to narrow down the list of feasible models.

[3] Our limited understanding of earthquake recurrence also influences the practice of seismic hazard analysis. The characteristic earthquake model was considered such a simple yet reasonable idealization that it was extensively applied in seismic hazard assessment [e.g., *Working Group of California Earthquake Probabilities*, 1988, 1995]. However, one should be aware of our reliance on tenuous assumptions of source recurrence in these approaches. For example, it was believed that seismicity on a fault could be represented realistically by a repeating characteristic rupture and that slip patterns along large historical ruptures reflect along-strike differences in fault friction [e.g., *Stuart*, 1986; *Rundle*, 1988; *Ward and Goes*, 1993]. In reality, we have only very sparse data to

[1]Division of Geological and Planetary Sciences, California Institute of Technology, Pasadena, California, USA.
[2]Laboratoire de Tectonique, Institut de Physique du Globe Paris, Paris, France.
[3]Now at the Institute of Tibetan Plateau Research, Chinese Academy of Sciences, Beijing, China.
[4]Department of Geological Sciences, Central Washington University, Ellensburg, Washington, USA.
[5]Department of Geological Sciences, San Diego State University, San Diego, California, USA.

0148-0227/06/2004JB003601$09.00

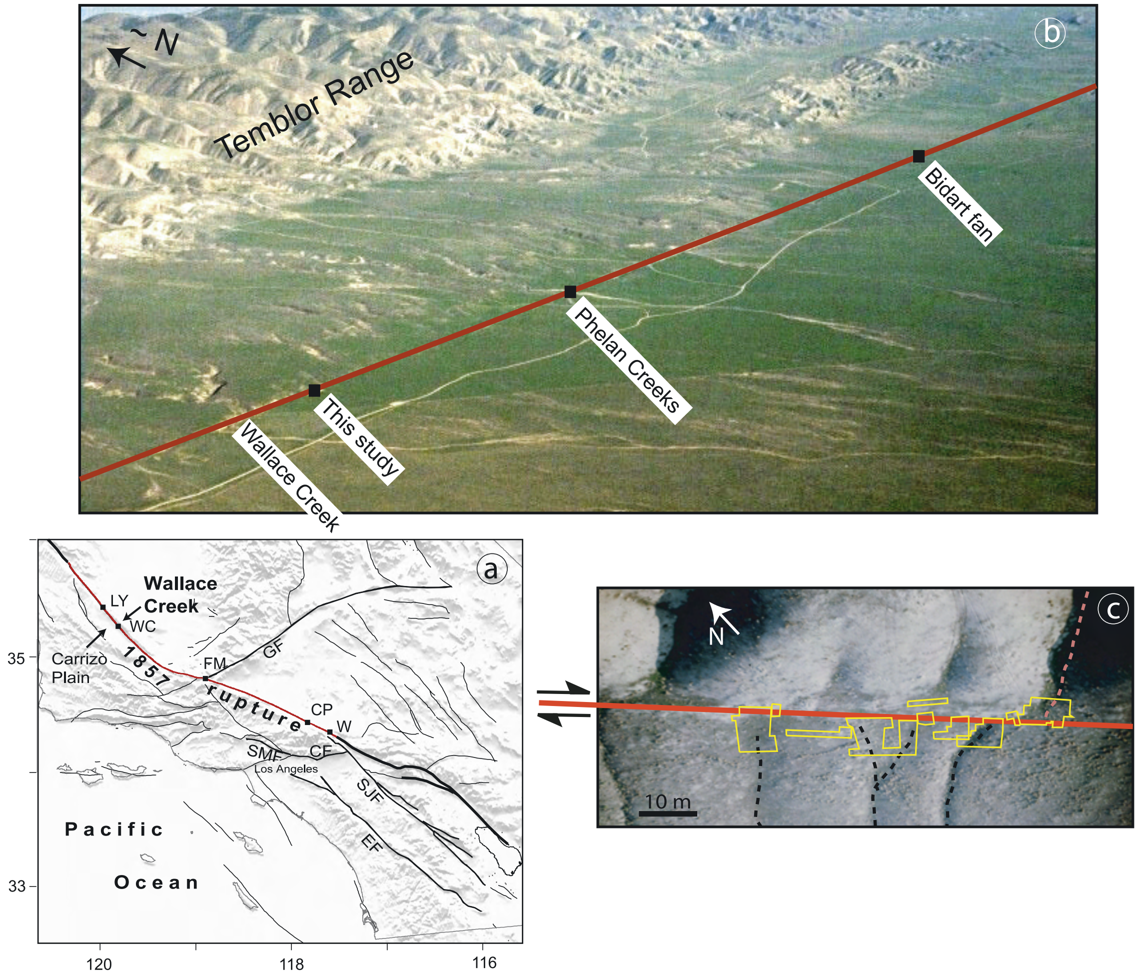

Figure 1. Location of the Wallace Creek trench site. (a) Active faults in California, with 1857 earthquake rupture on the San Andreas fault highlighted in red. Abbreviations of some paleoseismic investigation sites along the San Andreas fault: LY, Las Yeguas; WC, Wallace Creek; FM, Frasier Mountain; CP, Pallett Creek; W, Wrightwood. Abbreviations of faults: GF, Garlock fault; SMF, Sierra Madre fault; CF, Sierra Madre-Cucamonga fault; SJF, San Jacinto fault and EF, Elsinore fault. (b) Oblique aerial photo of the San Andreas fault near the Wallace Creek site showing locations of two previous investigations. Photo by T. Rockwell. (c) Close-up aerial oblique photo of the trench site. Thin dashed lines indicate geomorphic stream channels. Polygons in yellow denote locations of excavation volumes. A narrow excavation on the upstream side is placed in front of a secondary channel. The exposures in this trench show that the incision is minor and not enough to be a source channel.

support this idea [*Lindvall et al.*, 1989; *Sharp et al.*, 1982].

[4] Paleoseismology has contributed to understanding serial fault ruptures by documenting the history of earthquakes at specific locations along faults worldwide [e.g., *McCalpin*, 1996; *Yeats et al.*, 1997]. However, most paleoseismic investigations uncovered only the times of paleoearthquakes. Well-documented examples of slip measurements for these earthquakes are still rare. High-quality data rarely span more than two earthquake cycles [*Sieh*, 1996, and references therein]. Longer records of paleoearthquake slips [e.g., *Schwartz and Coppersmith*, 1984; *Sieh*, 1984; *Pantosti et al.*, 1996; *Ran et al.*, 1997; *Weldon et al.*, 2002] are, however, inaccurate or mostly based on indirect evidence; for example, the similar displacement of paleoseismic events on the Wasatch fault was inferred from the heights of colluvial wedges caused by these events.

[5] Thus our goal in this study is to document details of several sequential offsets from a single site on the Carrizo section of the San Andreas fault (Figure 1). We have recently summarized this work [*Liu et al.*, 2004]. Here we present a more complete documentation of our results, including efforts to date the offsets and speculate about the slip history. At the site, a feeder channel cuts a late Pleistocene alluvial fan on the upstream side of the fault. On the downstream side, several small channels have been offset dextrally from the feeder channel and sequentially abandoned. We have conducted three-dimensional excavations across these channels. Using offset channels as piercing lines, we have recovered an accurate record of offsets for six sequential ruptures. Sparse reliable radiometric dates

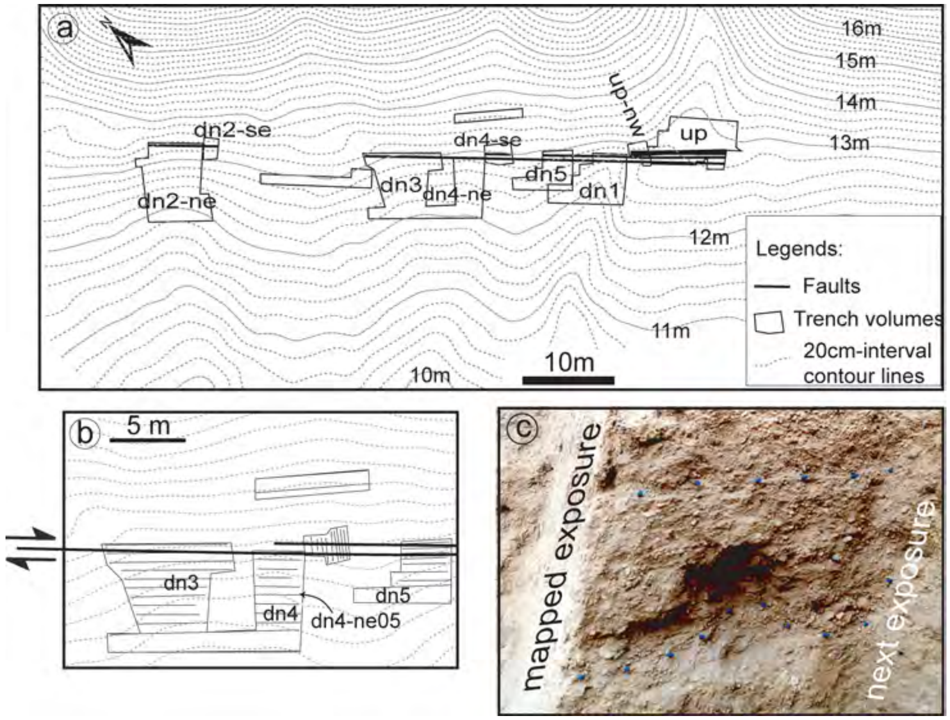

Figure 2. Map of excavations at the site. (a) Map of the 11 separate volumes that were excavated. The seven that exposed channels are labeled "up" or "dn," depending on their location upstream or downstream from the fault. The suffixes "ne" and "se" indicate the direction of serial cuts within the excavation. (b) An example of the arrangement of mapped exposures within the excavated volumes. (c) Photo showing the procedure that we use channel stratigraphy to check for evidence of a fault between two consecutive cuts.

do not allow us to determine accurately their dates from this site alone. However, previous paleoseismic studies at sites within several kilometers, the Phelan Creeks and the Bidart fan sites, have yielded tighter constraints on the occurrence times, but not the offsets of paleoruptures (Figure 1b) [*Prentice and Sieh*, 1989; *Grant and Sieh*, 1994; *Sims*, 1994; J. D. Sims et al., unpublished manuscript, 1994]. A combination of these studies improves the slip time sequence.

[6] We organize the paper into 10 sections: Sections 1, 2, and 3 set forth the nature of the study, the background, previous work and methodology. Section 4 is a lengthy detailed description of the stratigraphy and morphology of channels exposed in the excavations. Section 5 gives the evidence for correlation of 6 upstream and downstream pairs of offset channels. In section 6 we calculate the offset values. In section 7 we derive the rupture sequence and address the question of whether each offset is a single rupture event. Section 8 provides radiocarbon constraints on the offset events. Then, in section 9 we proceed to create an offset history on the basis of the sequence of offsets and our best estimates of the dates of events. Finally, in section 10 we discuss the implications of the sequence of offsets at the site. We suggest that the casual readers of this paper focus their attention on the figures in the sections 2, 3, 4, 7, and 8, and focus on sections 5, 6, 9, and 10.

2. Site Description

[7] The Carrizo Plain is an arid to semiarid intermontane closed basin about 80 km northeast of the California coastline. Ephemeral streams, dry except during local cloudbursts in the dry season or during large Pacific storms in the wetter winter months, incise the flanks the Temblor Range on the northeast. In the vicinity of Wallace Creek (Figure 1b), the main surface is an apron of late Pleistocene alluvial fans derived principally from Miocene marine deposits of the Temblor Range [*Dibblee*, 1973]. The fans were aggrading through the period from 33 ka to at least 19 ka [*Sieh and Jahns*, 1984]. This surface became inactive about 13,250 years B.P. Entrenchment of the late Pleistocene surface by active streams has continued throughout the Holocene epoch. At Wallace Creek the vertical component of motion on the San Andreas fault has been northeast side up, resulting in the present south facing 8- to 9-m-high scarp. This section of the San Andreas fault ruptured during the latest large earthquake in 1857 with several meters of right-lateral offset [*Agnew and Sieh*, 1978; *Sieh*, 1978].

[8] The Carrizo section of the San Andreas fault is an ideal place to determine whether or not a fault segment can experience similar amounts of slip through many earthquake cycles. First of all, along much of this segment the fault trace is geometrically simple and well expressed. Secondly, beheaded channels indicating various amounts of offset are common. Thirdly, the potential to discriminate individual offsets has been known [*Wallace*, 1968; *Sieh*, 1978; *Sieh and Jahns*, 1984].

[9] We refer to our excavation site as the "Wallace Creek paleoseismic site," because it is just a few hundred meters southeast of Wallace Creek (Figure 1b), where *Sieh and Jahns* [1984] made the first determination of a slip rate

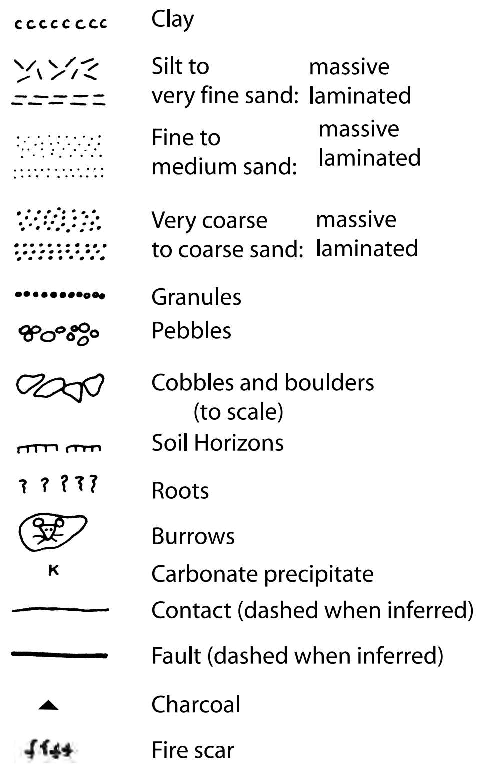

Figure 3. Lithologic and other symbols used in documenting the exposures. Modified from *Grant and Sieh* [1994].

along the San Andreas fault, ~34 mm/yr. The site is at the outlet of one of several small gullies that cut the late Pleistocene alluvial fan but extend only a hundred meters or so upstream. The particular small drainage that we chose was first studied by *Wallace* [1968] and then by *Sieh* [1978] (site 25, 35°16′10″ 119°49′05″). *Sieh* [1978] measured the offsets of the beheaded channels to be 8.7 ± 1.4 m, 24.1 ± 1.4 m, 32.0 ± 2.0 m and 56.4 ± 2.9 m, from the youngest to the oldest.

[10] However, these purely geomorphic estimations of channel offsets are plagued with ambiguities. First, colluviation at the base of the scarp has buried these small downstream gullies partially, so their precise geometry near the fault is obscure. Thus geomorphic measurements of offsets are imprecise. Another source of uncertainty in the interpretation of geomorphic measurements is the possibility of channel piracy. Strike-slip motion along a fault can bring a downstream channel, whose source is far away, into alignment with a different upstream channel [*Wallace*, 1968; *Gaudemer et al.*, 1989; *Huang*, 1993; *Schumm et al.*, 2000]. If unrecognized, such piracy can lead to mismatching of offset channels and incorrect measurements of offset.

3. Methods

[11] Guided by the geomorphic observations, we conducted three-dimensional excavations on either side of the San Andreas fault and matched channels based on the similarity in subsurface channel morphology and stratigraphy. Basically, we have explored 11 volumes: three on the upstream side of the fault, and eight on the downstream side (Figure 2a). The excavated volumes downstream from the fault exposed relationships along a 50-m length parallel to the fault and northwest of the source channel. They were placed to reveal all downstream channel segments within the 50-m fault-parallel length of the channel outlet.

[12] Most of the volumes were excavated progressively. That is, we began by excavating a narrow trench by hand, 4–5 m from and parallel to the fault, astride a gully. After mapping both walls of these initial trenches, we cut into the wall closest to the fault, creating another exposure closer to the fault. After mapping this new face, we once again cut a new exposure, still closer to the fault. Subsequent faces were cut closer and closer to the fault by increments of 50 to 60 cm. Near the fault, the increments were commonly only about 20 cm (Figure 2b). In places where channels flowed nearly parallel to the fault zone, trench cuts would be oriented fault-normal. Between parallel cuts near the fault zone, we would cut a ~50-cm-wide notch and use channel stratigraphy to check for faults between the faces (Figure 2c). In this manner, we carefully followed each potential piercing line into the fault zone. Although making series of successive cuts was time consuming, it greatly reduced the uncertainty in interpreting channel stratigraphy. Contacts that were ambiguous in one wall would often be clear in the next.

[13] Our choice of 60- to 20-cm increments represented a compromise between the demands of rigor and logistics. These increments were small enough to reveal the continuation of channel stratigraphy between cuts. Using smaller increment would undoubtedly have revealed more detail in channel variation, but would also have increased the time and effort required. Instead of mapping cuts at smaller increments, we chose to inspect important channel contacts (e.g., channel thalwegs and sharp edges) as we dug from one cut to the next.

[14] The fault-parallel orientation of progressive cuts is optimal for reconstruction of channel stratigraphy and offset markers. Yet, fault-perpendicular cuts are optimal for mapping the geometry of the fault zone. Although most of our excavations were fault-parallel, auxiliary fault-perpendicular trenches in areas away from the channels revealed the location of important faults.

[15] The name of each exposure reflects the name of the volume it belonged to, when in the sequence it was cut, and the direction of cutting. For example, exposure dn4-ne05 was the fifth cut within downstream volume 4, and it was on the northeastern wall of the volume. Exposures were cleaned, surveyed with a Total Station, using the same reference frame, and mapped at 1:15 scale (except 1:20 scale for trench dn1). Symbols used in mapping appear in Figure 3. Strata within the channels were correlated from one exposure to the next based on lithologic similarity, stratigraphic position and elevation of the upper and lower contacts. We later reconstructed the three-dimensional geometry of channels and faults from dense survey data. High-precision channel geometry and location thus gave greatly refined slip measurements.

4. Channel Stratigraphy and Morphology

[16] We assign the downstream channels letter names (from a to l, Figure 4), where a is closest to the mouth of source channel and l is farthest. Upstream channels are named numerically from 1 to 9, from youngest to oldest.

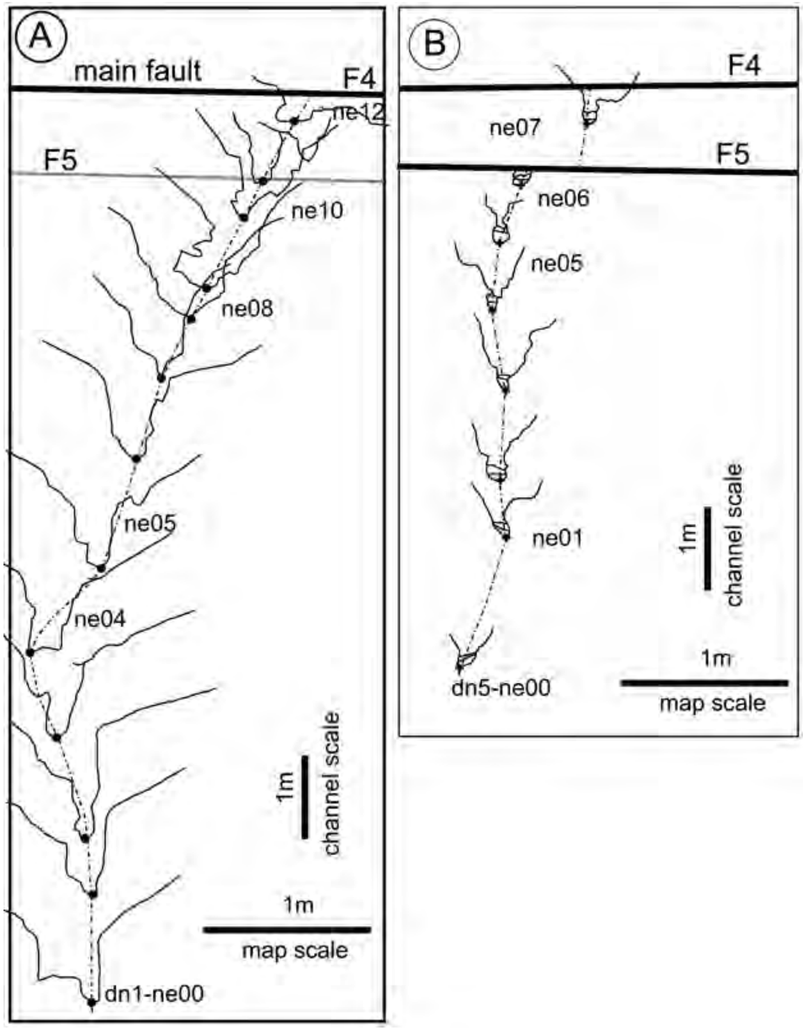

Figure 4. Summary of the results of excavations of all channels. (f) Locations of the channels and excavated volumes in map view. Downstream channels are assigned letters, from a to l, southeast to northwest. Upstream channels are numbered from 1 to 9, from youngest to oldest. Major fault strands F1 through F6 are correlated from exposure to exposure on the basis of the projection of strikes, relative position, and the spacing between them. Gray polygons indicate the perimeters of excavated volumes. (a)–(e) Detailed maps of the deepest thalwegs of downstream channels and their meanders. The cross sections appear on the plan view map to illustrate the change in channel shape that occurs along the stream profile. The viewing direction in each cross section is toward upstream, and the deepest thalweg of the channel in each exposure appears as a dot in its correct geographic location. (g) Thalwegs of upstream channels in map view. Symbols connected with dashed lines indicate the position of the thalwegs in each mapped exposure. Simplified cross sections of downstream channels from each mapped exposure show the variability in channel shape and stratigraphy. Numbers at the base of Figure 4g indicate the horizontal offsets of channels 1 through 6 across fault F1 and F2. The shading between F1 and F2 indicates that F2 is a shallow branch of F1.

The stratigraphic sequence of the channels generally revealed a complex history of cuts and fills. Major units were defined by their textures and the prominence of their lower contacts, which were generally major erosional surfaces. Each major unit contained multiple subunits. Because of limited space, we have put the maps and descriptions of channel stratigraphy of most channels as in the auxiliary material[1] (Figures S1–S15).

[1]Auxiliary material is available at ftp://ftp.agu.org/apend/jb/2004JB003601.

4.1. Downstream Channels

[17] The substrate underlying all the downstream channels was a massive indurated and matrix-supported pebbly sand and silt, interbedded with sorted gravelly and sandy lenses. A more than 1-m-thick pedogenic carbonate horizon (B_k) developed within this unit and had penetrated into the matrix, consistent with its late Pleistocene age [*Sieh and Jahns*, 1984].

[18] The distinction between the late Pleistocene fan and recent channel deposits manifests itself in three ways:

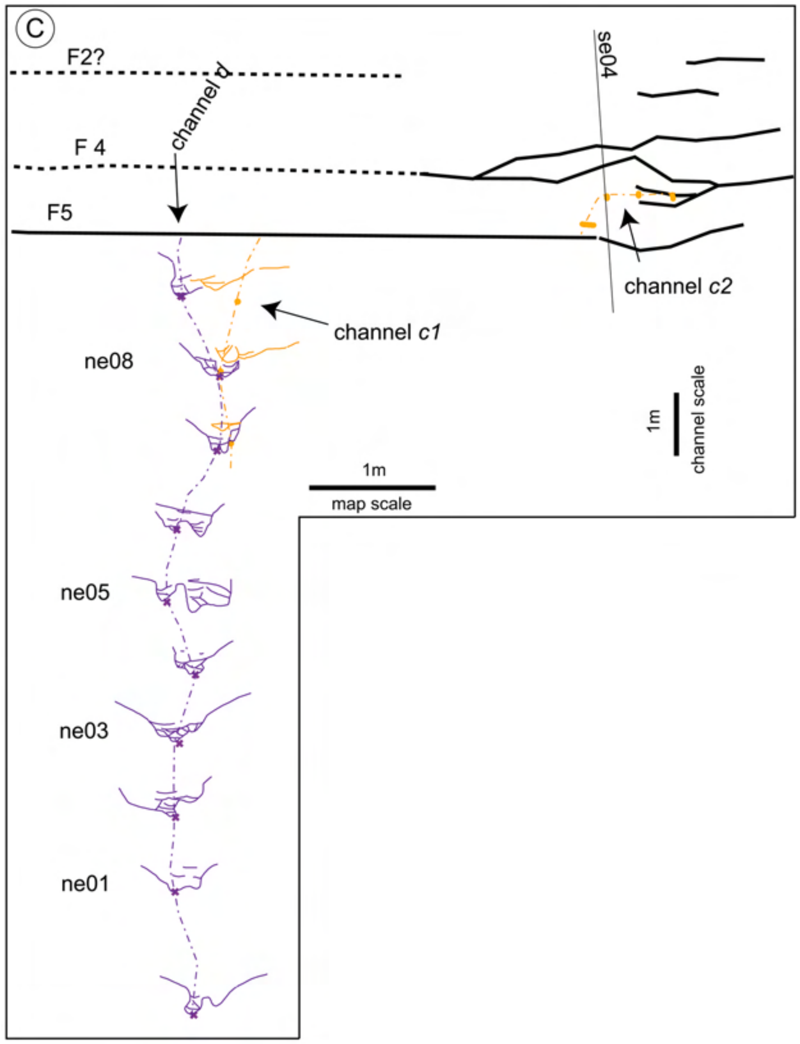

Figure 4. (continued)

[19] 1. The colors of the two units differ. The channel deposits are usually darker than the older underlying unit.

[20] 2. The edges of the channels, especially in the lower part, are generally clear. However, finding the channel walls was sometimes tricky, especially in the upper part of the channel, where deposits filling the channel were commonly colluvium, derived from collapse of the upper channel wall and thus compositionally similar to the substrate material.

[21] 3. Lenses of well-sorted sand and gravel within the younger channels are traceable from cut to cut. These well-sorted sand and gravel layers within the channels, when they can be traced over several meters in the channels, provided good markers for stratigraphic correlation from cut to cut in each trench.

4.1.1. Channel a

[22] Channel a was the southernmost channel on the downstream side of the fault (Figure 4f). In map view (Figure 4a), the deepest thalweg of channel a curved right as one views it looking toward the fault. It had a prominent right step in the middle of its course, between exposure ne04 and ne05. This step was demonstrably not an offset across a minor fault. A large cobble, 25 cm long and 3–10 cm thick, blocked the channel in exposure ne04 (Figure S2). The thalweg skirted the blockage on the left. Figure 4a also shows the simplified cross-sectional outlines of channel a derived from our mapping of sequential channel walls. Although channel a cut into the landscape only about 0.5 m, its deepest thalweg (the deepest part of the channel) was 1.5 m or so deeper.

4.1.2. Channel b

[23] Channel b appeared in the excavation volume 5–6 m northwest of channel a (Figure 4f). Any geomorphic evidence for this channel was lost following the incision of channel a. Its presence was only hinted at by the asymmetry of the banks of channel a near the fault, and the slight bending of a couple of topographic contour lines near the fault.

[24] Channel b was distinctly different than channel a. In all exposures, it was narrow, with a bottleneck in the channel walls some centimeters up from the thalweg (Figure 4b). The thalweg of channel b ran straight into the fault. Its lack of curvature is additional evidence that the bend in younger channel a was not tectonic in origin. Secondary fault F5 cut through exposure ne06 (Figure 4b). In this exposure, the fault dipped into the exposure such that the channel was missing above the fault. This secondary

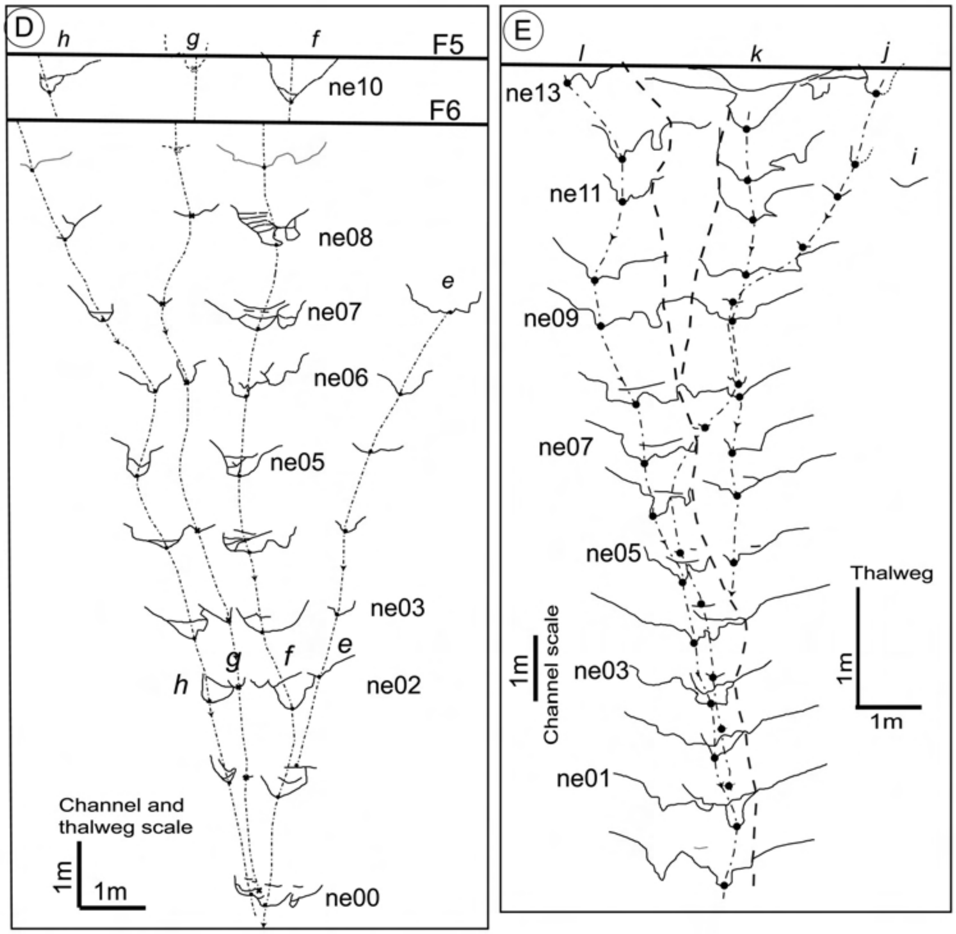

Figure 4. (continued)

fault did not disrupt younger channel a and thus was active only between filling of channel b and cutting of channel a.

4.1.3. Channels c and d

[25] We found a set of two channels, c and d, 5 to 11 m northwest of channel b (Figures 4c and 4f). In plan view, channel d was nearly perpendicular to and ran straight into fault F5. Channel d was 1 to 1.2 m deep and generally W-shaped, which was the result of two major phases of scour and fill (Figure 5). The second major down-cutting event widened channel d, mostly by scouring the southern bank. This cutting extended as deep as the first incision, thus forming a second thalweg less than a meter southeast of the first.

[26] Channel c was more complicated. It consisted of two segments, c1 and c2, on either side of fault F5. In plan view, channel c1 diverged from the path of channel d in a right-lateral sense within a meter of the fault (Figure 4c). In cross sections, channel c1 cut the channel d in the upper right corner. Best exposed in ne08, channel c1 consisted of a semicircular erosion surface filled with gravel and sand (labeled "c-10" in Figure 5). The deposits within the channel were thickest near the fault and diminished quickly to zero farther downstream (Figure 4c). Channel c2, was a 1.5-m-long channel segment within in the fault zone and to the southeast of c1. It had a cylindrical shape and was about 40–50 cm wide in cross sections perpendicular to the fault zone (e.g., dn4-se04; Figure 6). The bottom 30 cm of the channel was covered with loose, massive clast-supported pebbly sand and granules.

[27] Channel c1 correlates with channel c2. Together, they constituted a single right-deflecting channel that post-dated channel d. Our correlation is based on their lithologic similarity, their stratigraphic position and the similar elevations of their upper and lower contacts. Other evidence includes (1) the arrangement of and imbrications in the pebbly gravels in c1 were consistent with a right-curving channel course (Figure 5), as indicated by its thalweg (Figure 4c); and (2) it was consistent with the asymmetric widening of channel d on the right.

[28] Could the fault-bounded segment c2 be a channel fragment that was much older than c1 and just lodged within the fault zone near channel c1? In other words, are we correlating channel segments of different ages? We think this possibility is very remote. First, the outline of the channel and the deposits within it were still coherent, which suggests a relatively young age. Second, as will be shown later, the shapes and deposits of older channels to the northwest do not make them better candidates than c1 to be the downstream correlative of c2. In support of this correlation, it is worth reiterating that channel c merged with d right after it departed the fault zone. This proximity of the right deflection of channel c to the fault zone suggests that when channel c was incised, channel d was nearly connected with its former upstream segment. Perhaps, the

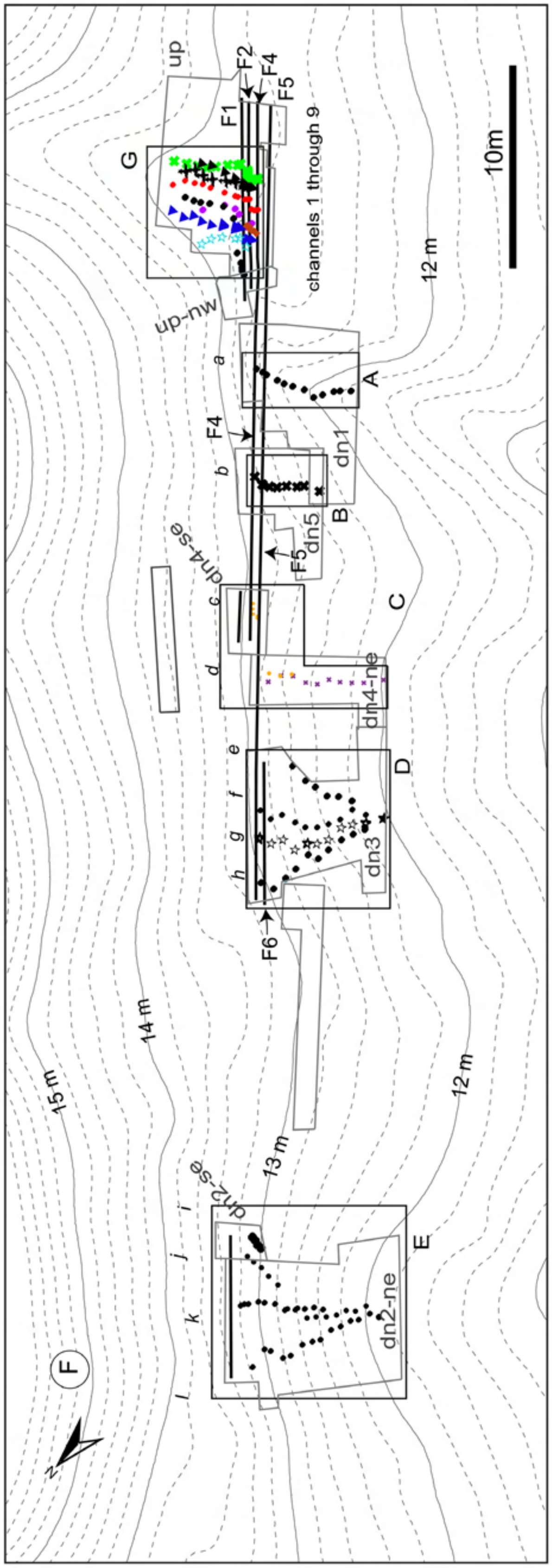

Figure 4. (continued)

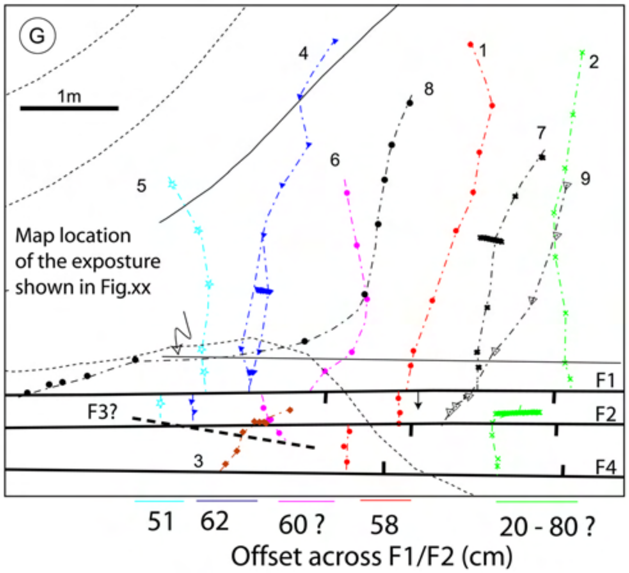

Figure 4. (continued)

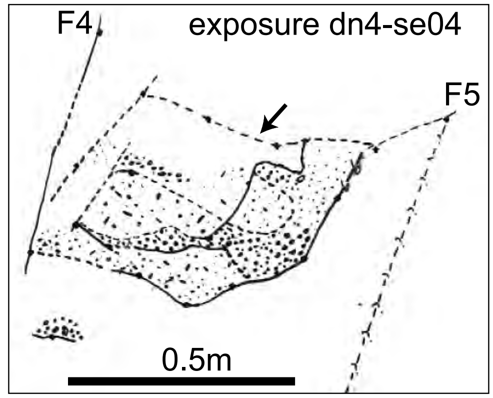

Figure 6. Map of exposure dn4-se04 shows the stratigraphy in channel c2.

rupture that immediately postdated formation of channel d offset the channel only a small amount, enabling a new channel connection to form between the upstream and downstream channels. If, for example, the offset were merely half the width of the channel, it would be relatively easy for water in the upstream channel find its way into the slightly offset downstream channel and to erode that portion of the fault zone between the channels. However, if the offset of channel d was much larger than the width of the channel, the connection would be more difficult to reestablish.

4.1.4. Channels e, f, g, and h

[29] The excavated volume 30 to 36 m northwest of the upstream source channel contained four channels, e, f, g and h, that fanned out upstream toward the fault zone (Figure 4f). Channels f and g trended roughly at right angles to the fault, whereas channels e and h merged from the right and left, respectively (Figure 4d). All four channels merged into a single channel 6 to 7 m downstream from the fault.

[30] Channel f was the deepest and widest of the four (Figure 4d). Its cross-sectional shape was roughly U-shaped. Locally, it had a secondary thalweg to the southeast, most likely the remnant of an earlier phase of downcutting. Channel h, another deep channel, had variable cross-sectional shape and stratigraphy. The cross-sectional shape of channel h changed dramatically from cut to cut. Note that in exposure ne10, immediately adjacent to the principal fault (F5), channel h had a steep northern bank and reclining southern bank. The asymmetry in channel shape suggests that channel h made a sharp turn to the southwest as it departed the fault zone. Such a turn would be consistent with the trace of its thalweg indicated by the plot of thalwegs in cuts ne06 through ne09 in Figure 4d. Channel g was a shallow, less conspicuous channel between channels f and h. In cross section, it was narrow and contained channel sand and gravel of varying thickness at near its base. Channel e was also shallow. Channel e was still recognizable in exposure ne02, but it disappeared downstream, in ne01 and ne00. Channel e could not be traced with confidence upstream of ne07, closer than 2 to 3 m of the fault zone. One possibility is that bioturbation had obliterated the trace of channel e near the fault. Although we cannot rule out this possibility, it seems unlikely as no other channels, including much older ones, had been completely erased by bioturbation. Another possibility is that the headward limit of channel e was near exposure ne07 and that the channel was formed by headward erosion and that the channel did not reach or cross the fault zone. The longitudinal profile of channel e supports this hypothesis (Figure 7). From exposures ne07 to ne06, the profile exhibited a sharp drop in elevation and the width of the channel narrows (Figure 4d). Thus ne07 might slice across the knickpoint of channel e.

[31] Traces of thalwegs alone also suggested that channel f was the oldest of the four channels. Of the four channels, channel f occurred in the middle and perpendicular to the fault, flanked by channels h and e from left and right, respectively. Channels g and h were younger than f even though they appeared to be offset more than f from the source. The rationale behind the above speculation is that the upstream channels in this stretch of the San Andreas fault meet the fault almost orthogonally. This implies that downstream channels should also depart the fault perpendicularly, unless the microtopography near the fault (for example, an older downstream channel in close vicinity) favored a deflected channel course, e.g., channel h. Cross-

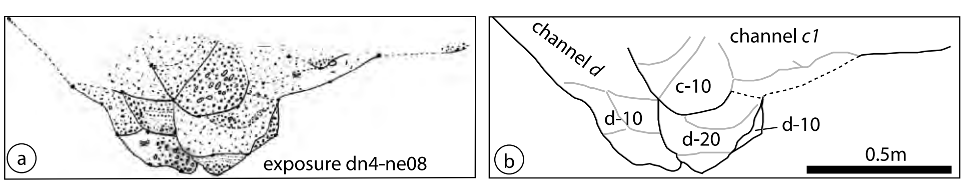

Figure 5. Stratigraphic units of channels d and c1, illustrated using exposure dn4-ne08.

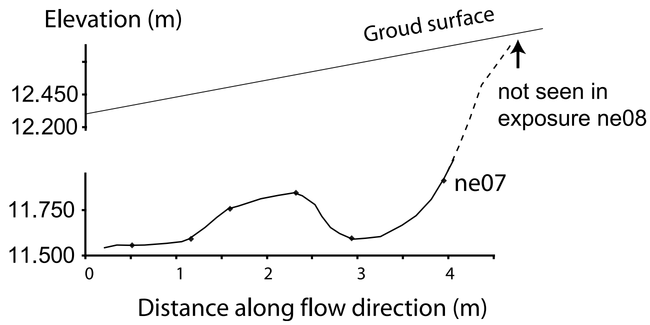

Figure 7. Longitudinal profile of the thalweg of channel e. The hollow in the profile just downstream from exposure ne07 suggests that channel e was eroding a plunge pool at this location and may not have eroded headward across the fault. If this is true, the channel cannot be used as an offset piercing line.

cutting relationships provided information about the relative ages of the channels (see Figure S3). Channel f was older than channel h, which was in turn older than channel g. The age of channel e relative to the ages of channels g and h was indeterminate, because channel e did not have direct contact with channels g or h. This left us with this temporal ordering: f > h > g and f > e.

4.1.5. Channels i, j, k, and l

[32] Another group of 4 channels existed farther northwest channel h (Figure 4f). An unnamed trench cut parallel to the fault confirmed that no channels existed downstream from the fault between this group of four channels and channel h.

[33] Channel k was the largest and deepest channel in the volume and intersected the fault at nearly a right angle (Figures 4e and 4f). Channel l, another deep channel, exited the fault zone at an acute angle and snaked

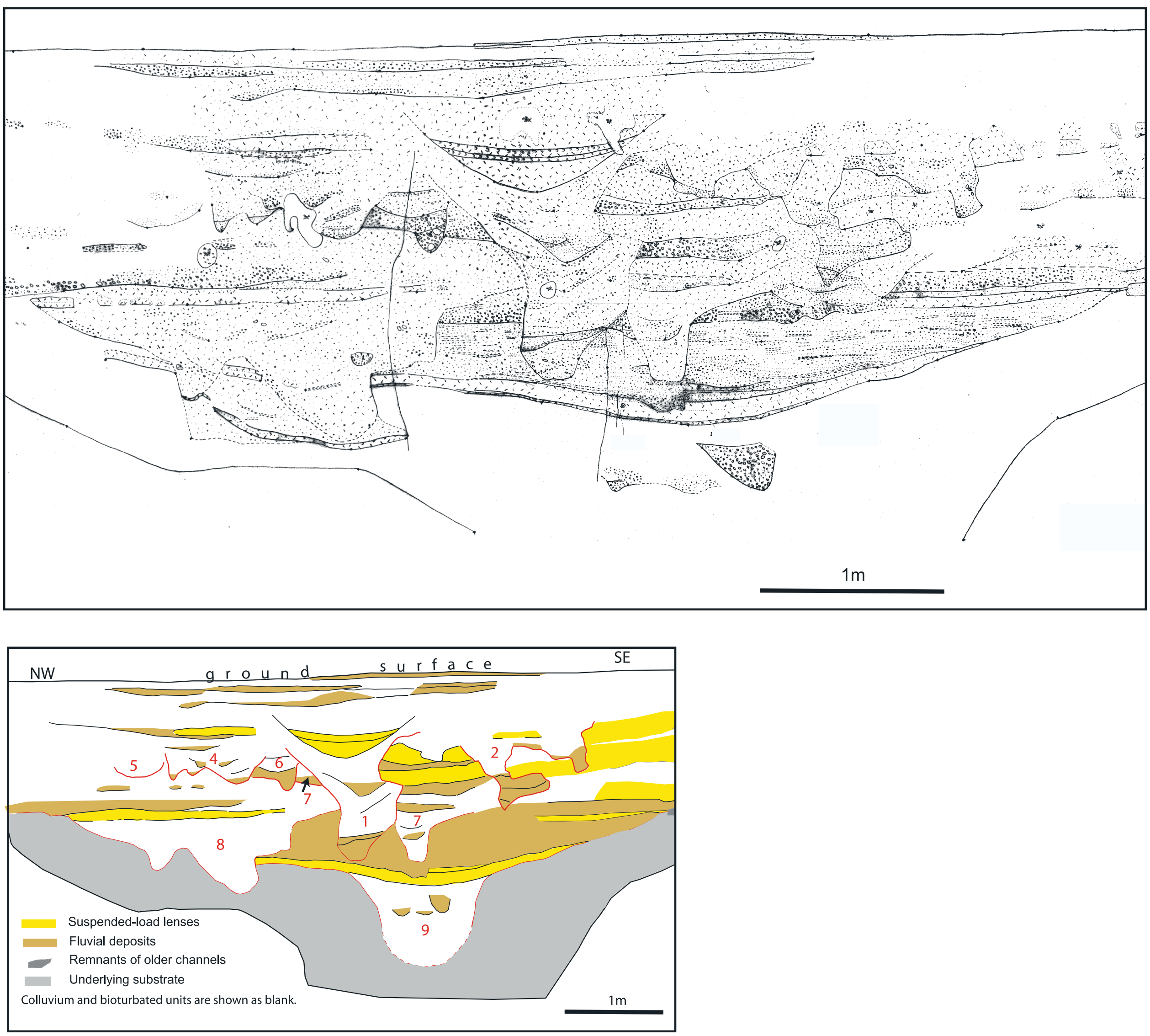

Figure 8. (a) Map and (b) simplified map of the wall of an excavation upstream from the fault show eight of the nine nested upstream channels. Suspended load silts (in yellow) testify to the temporary ponding of the drainages behind shutter ridges. Channel margins and names are in red. View is upstream.

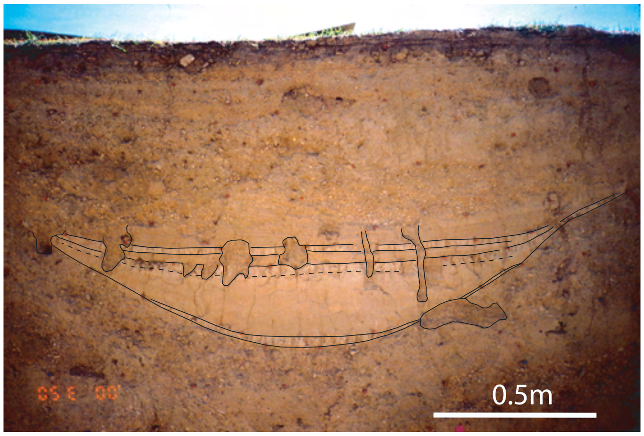

Figure 9. Photograph of the suspended load lens in channel 1. Note that the lens has a gently curved top and deeply curved base and consists of multiple individual lenses. Each of the lenses is thickest in the middle and thins to feather edges on their margins. The lenses consist of fines deposited out of suspension in a muddy puddle just upstream from the fault and straddling the middle of the channel. The photo is flipped so that the viewing direction is upstream.

downstream (Figure 4e). It had an irregular channel floor with multiple thalwegs, separated by lateral ridges. The configurations of channels k and l suggested that k was older than l. Channel k left the fault at nearly a right angle and continued downstream in a nearly straight path. Furthermore, the channel thalweg run immediately below the lowest point in the topographically visible channel (Figure 4f). Channel l, by contrast, flowed in the center of the topographic channel only in its lower reaches and entered the topographic channel from a position well up on the northwestern flank of the topographic channel. This suggests that it was diverted left-laterally into the channel. Thus channel geometries suggests that channel l postdated channel k. Our exposures of stratigraphic relationships confirmed this relationship. Figure 4e (also see Figure S4) shows that channel l truncated the northern bank of channel k in exposure ne08 and its thalweg a few meters farther downstream, between ne05 and ne04. Downstream from ne04, channel k was completely absent, having been completely obliterated by channel l. Thus channel k was reoccupied and erased by the younger channel l at this juncture.

[34] Channel j intersected the fault zone at a 45° angle (Figure 4f). It flowed westward, away from the fault zone and merged with channel l about 7 m downstream. The channel was well expressed up to a few tens of centimeters from the fault, typically marked by a thin lens of sandy gravel. Farther downstream, channel j cut into the upper colluvial fill of channel k, and then it continued northwestward and merged with channel l. This correlation implies that channel j was younger than both channels k and l. Channel i lay just a meter or so south of and run almost parallel to channel j (Figure 4e). In the southernmost exposure of channel i (ne11), it was well defined as a 60-cm-wide lens of sand and fine gravel [*Liu*, 2003]. Further downstream, channel i was not visible, probably due to a lack of coarse fluvial channel fill. The relative age of channels i and j was indeterminate, because no direct crosscutting relationship was exposed.

4.2. Upstream Channels

[35] The subsurface stratigraphy of the outlet of this drainage, just upstream from the San Andreas fault, differed greatly from that downstream. Whereas 12 downstream channels string out separately along a 55-m length of the fault, 9 upstream channels nested at the outlet of the drainage (Figure 4f) This nesting represents repeated cuts and fills in roughly the same place.

[36] Figure 8 illustrates the basic nature of the nested upstream channels, using the map of exposure up-sw06, whose map position is indicated on Figure 4g. Eight of the 9 upstream channels were visible in this cut. The base of the deposit of these young channels was easy to recognize, because the underlying late Pleistocene deposits were massive and featureless fine-grained sand and silt with sparse gravel lenses. Bioturbation had homogenized the late Pleistocene substrate, and pedogenic carbonate precipitation had given it a pale hue and induration that contrasted sharply with the richer shades and looser consolidation of the recent channel deposits. In general, the boundaries of individual channels were also easy to recognize.

[37] A prominent feature of many of the channels was a distinctive lens of well-sorted fine sand to silt. These beds are highlighted in yellow in Figure 8. Such beds were absent from any of the downstream channels. Figure 9 is a photograph of one of the lenses. The lenses consisted of fines deposited from suspension in a

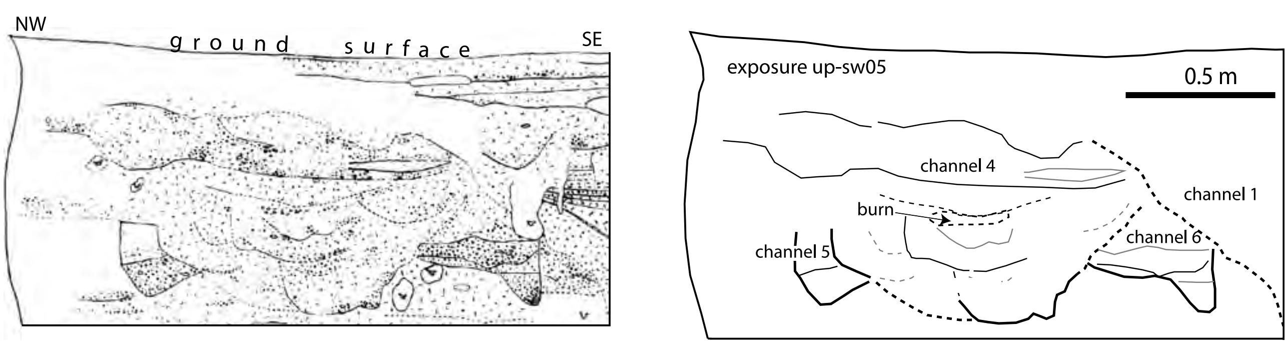

Figure 10. Stratigraphic units of channels 4, 5, and 6, illustrated using exposure up-sw06. The stratigraphy in channel 4 was grouped into five major units.

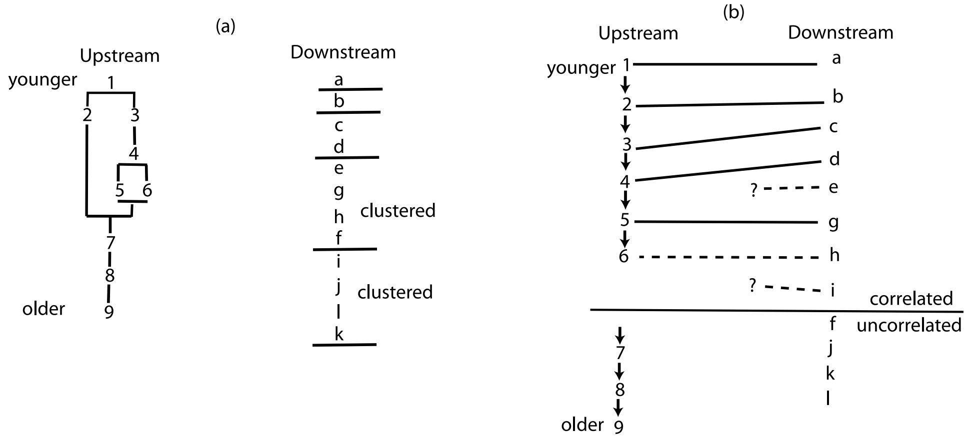

Figure 11. (a) Relative ages of upstream and downstream channels. The sequence of the upstream channels is based on crosscutting relationships. Ambiguities appear as bifurcations. On the downstream side, age is assumed to increase with the distance from the upstream trench, with a couple of exceptions that are constrained by stratigraphic relationships. (b) Correlation of upstream and downstream channels. Solid lines designate confident correlations. Dashed lines indicate uncertainty.

muddy puddle just upstream from the fault and straddling the middle of the channel. They appeared to be the result of blockage of the channel by a shutter ridge, emplaced by large dextral offset along the fault. Thus the silty lenses likely are direct evidence of occasional large ruptures of the fault.

[38] Crosscutting relationships among the channels revealed the sequence of their formation, from 1 to 9, from the youngest to oldest. Some of these relationships were ambiguous in Figure 8. For instance, the relationship between channels 5 and 6 was ambiguous, because the two channels had no direct contact. In such cases, to determine relative ages used other evidence, which we discuss in the following sections.

4.2.1. Channels 1 and 2

[39] Channel 1 sat in the middle of the exposures and was 1.8 m deep (Figure 8). Channel 2 rested a meter or so southeast of channel 1. The principal characteristic of channel 2 was its narrowness. In many of the exposures, it was more than a meter deep but only ten or twenty centimeters wide. The channel geometry was complicated by a second, higher side channel, which merged with the main channel before the channel entered the fault zone. In plan view (Figure 4g), both channels intersected the fault zone at a high angle. They were completely cut off by F4. Crossing F4, we immediately ran into a wall of indurated pebbly sand and silt with a pedogenic carbonate horizon (B_k), similar to the substrate exposed in all downstream trenches.

4.2.2. Channels 3, 4, 5, and 6

[40] Channels 3, 4, 5, and 6 appeared in the northwestern part of the excavated upstream volume. All four were shallow channels at a depth of 1 to 1.2 m below the ground surface (Figures 8 and 10).

[41] Channel 3 was unlike the other channels upstream from the fault, in that it did not exist upstream from the fault zone. It was only about a meter long, existed only within the fault zone and trended westward, rather than southwestward (Figure 4g). If it extended farther upstream, it had been eroded away by the younger channel 1. Channel 3 was demonstrably younger than channels 4, 5 and 6, because it was not offset by fault F3, and because it cut channels 4 and 6 in exposures up-sw08, up-sw09, and up-sw10 (Figure S8). Channel 4 had a W-shaped to nearly square-shaped cross section. It was due to two major phases of down-cutting that reached to similar depths (Figure 10). Channel 5 was a small channel whose upper section was eroded away by scouring of channel 4. It was narrow with a semicircular floor in most exposures. The preserved portion of channel 5 commonly contained two packets of fluvial sediments. In up-sw06 (Figure 10), the lower of the two beds was massive and coarser-grained, composed of pebbles in a matrix of granules to coarse sand. The upper bed was finer-grained, well-sorted coarse to medium sand. The sorting of both of these beds indicates they were fluvial deposits. Channel 6 was truncated by channel 4 on the northwest and by channel 1 on the southeast. Only the lowest 40 cm of the channel was preserved. The surviving portion of channel 6 was preserved best in exposure up-sw05 (Figure 10). There it was filled with two well-sorted fluvial beds separated by a thin layer of poorly sorted granule-rich silty sand. The lower fluvial layer consisted of loose pebbly granule-rich sand that fined upward slightly. The upper fluvial bed was coarser-grained, and it was deposited when the channel floor was flat and wider.

[42] In plan view (Figure 4g), channels 4, 5, and 6 were subparallel and moderately sinuous. They were sharply offset a similar amount by fault F1. Also, they disappeared about 0.5 m north of the main strand F4. Because of this disappearance before the main fault strand, we suspected that they were offset by another strand, F3. In the reach between F1 and F3, channels 4 and 5 remained straight, whereas channel 6 flowed southward.

4.2.3. Channels 7, 8, and 9

[43] In a typical upstream cut, channels 7, 8, and 9 occupied the lower two thirds of the exposure (Figure 8). The stratigraphy of all three channels was easily correlated from exposure to exposure. Commonly in channels 7, 8 and 9, the silty fine sand lenses that represented the

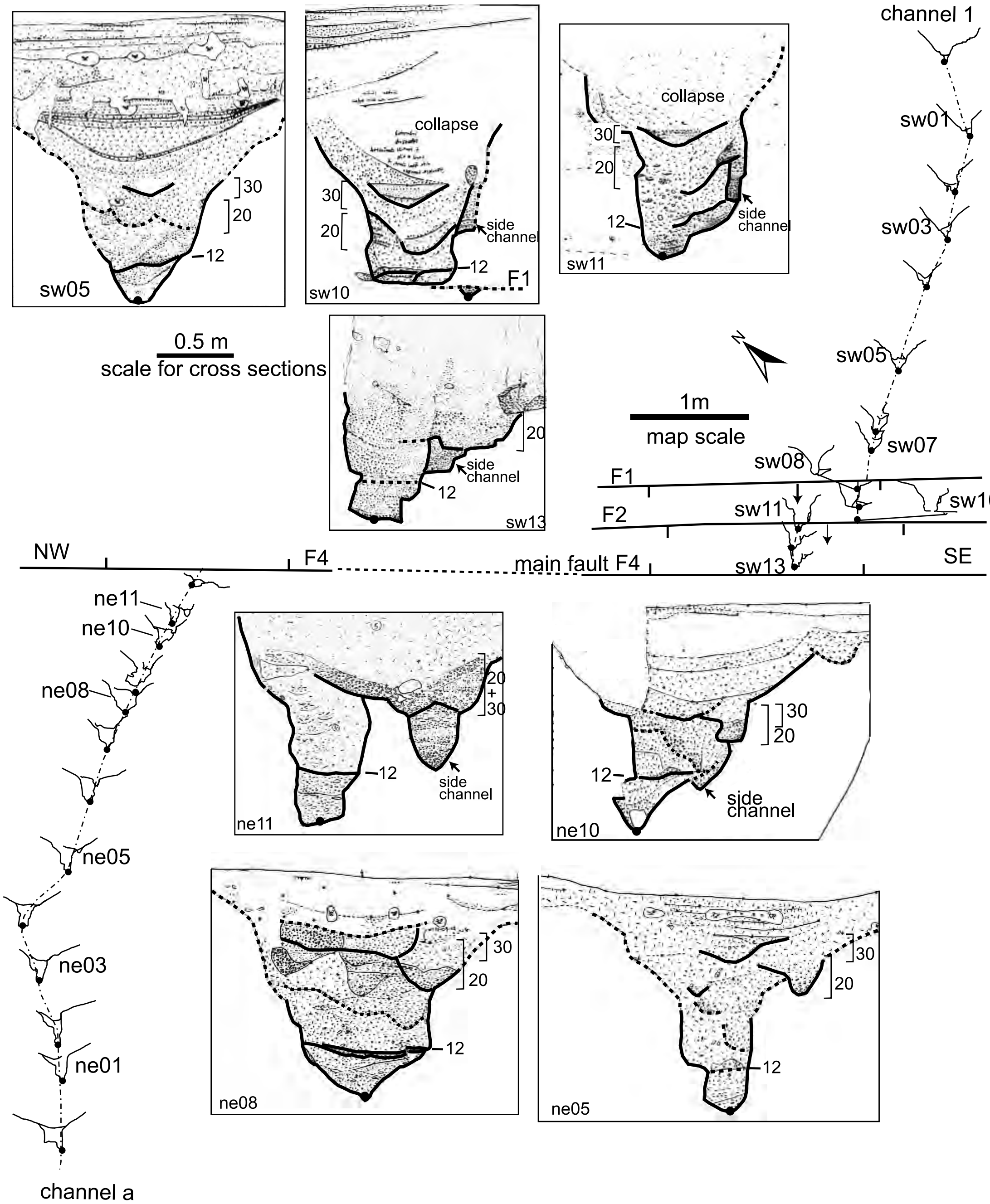

Figure 12. Correlation of channel 1-a based on the similarity of stratigraphy and morphology in channels 1 and a. The eight vertical exposures show examples of the stratigraphic details within the channels. In map view, the dots indicate the geographic position of the deepest channel thalweg. Outlines of the channel shape and key internal contacts allow viewing the changes in the features along the trend of the channel. Note that the scale of the detailed cross sections is larger than that of the map.

behind-the-shutter-ridge deposits were broader than in younger channels. Two suspended load beds that topped channel 7 were the widest. These beds overlaid the central channel and extended over prechannel 7 colluvial apron up to 5 m farther southeast. They might have also extended to the northwest, but if so, they had been removed by erosion during the creation of younger channels. The width and height of these beds suggested that the shutter ridge was high at the time of the deposition of the lenses. This could either be due to a considerable amount of vertical motion along the fault with downstream side moving up, or a juxtaposition of a broad topographic high downstream with channel 7, or a combination of the two. Detailed descriptions of the strata in channels 7, 8 and 9 were given by *Liu* [2003] (chapter 2, section 2.3.3.6).

[44] In plan view (Figure 4g), channels 7 and 9 met the fault zone at a high angle. The path of channel 8 is different. It veered sharply to the northwest, less than a meter upstream from the fault. It then flowed parallel to the fault

before being truncated by fault F1 at the northwestern edge of the excavated volume.

5. Channel Correlation

5.1. General Criteria for Channel Correlation

[45] Multiple criteria were available for assessing correlations. Channel morphology and stratigraphy described in the section above are important information to match channels across the fault. In addition, three other considerations are important in making bona fide correlations. These are (1) the relative ages of channels on each side of the fault, (2) the similarity of the angles at which channels enter and exit the fault, and (3) age constraints from ^{14}C dates on charcoal extracted from channel strata. We use all five criteria in proposing correlations, below.

[46] We begin by ordering the relative ages of channels on each side of the fault (Figure 11a). On the upstream side of the fault, the relative ages of many of the channels were clear from their crosscutting relationships. On the downstream side of the fault, the order of formation of the channels may be inferred from their distance from the nearest upstream channel and, where available, their crosscutting relationships. This criterion would, of course, be inappropriate for any channel that originated from upstream channels farther to the southeast. Furthermore, in matching of upstream and downstream channels, it is a necessary but not a sufficient condition that these relative ages be obeyed. Figure 11a illustrates a problem that arises immediately upon showing this hypothetical ordering of upstream and downstream channels: the downstream side had three more channels than the upstream side. Plausible explanations for this mismatch include that upstream channels had been obliterated by the incision of younger channels, or the downstream sequence contains channels that did not originate from the upstream channel, or both.

5.2. Channel 1-a

[47] Three lines of evidence support the correlation of channel 1-a. First, channel 1 was the youngest channel on the upstream side, and channel a was the closest of all the downstream channels to the upstream channel.

[48] Second, the shapes of the channels were similar. However, in considering the match of channel shapes across the fault, we must first evaluate how similar channel shapes need to be in order to be plausibly correlated across the fault. Generally, the variations in channel shape along profile were large. Only the principal characteristics of the channel continued from one exposure to the next. These were the basic V-shaped geometry of the channel and its depth. Second-order features, such as overhangs and other details of the channel walls, commonly were not continuous from exposure to exposure. Thus we should require only that the first-order characteristics correlate across the fault. The shapes of channels 1 and a were quite similar immediately upstream and downstream from the fault. In downstream exposure ne11, channel a was about 2 m deep and consisted of a deeper and a shallower channel, separated by an uneroded septum (Figure 12). The deeper channel had a nearly flat base, about 40 cm across. In upstream exposure sw13, channel 1 consisted of only one channel. However, like channel a it was about 2 m deep. Channel 1 was also asymmetric, with a steep and a shallow wall. This asymmetry would be very similar to the shape of channel a in exposure ne11, if one removed the septum between the principal and auxiliary channels in channel a. Without this septum channel a would have the same asymmetry as channel 1, steep on the northwest and shallow on the southeast.

[49] A close inspection of the internal stratigraphy of the upstream and downstream channels supports this interpretation, because it shows that the smaller channel had longitudinal continuity. Close to the fault (in exposures sw10 through sw13), this "side channel" cut to the southeast and was plastered onto the southeast wall of the older main channel (Figure 12). Downstream from the fault, the channel remained on the southeast side of the main channel from exposures ne11 through ne09, and merged into the main channel in the rest downstream exposures. The correlation of channels 1 and a is supported by other details of the stratigraphy within the channels, as well. In particular, units 12 and 30 were comparable. Unit 12 was a diagnostic thin bed of laminated fine sand to silt that mantled the underlying basal deposits of both channels (compare exposures sw05 and ne08; Figure 12). It occurred in most upstream and downstream exposures. Unit 30 was the bed immediately predated the offset event. It consisted of two well-sorted fluvial layers, which formed an inversely graded sequence; the lower bed was finer grain sized than the upper one. It was continuously correlative among most exposures.

5.3. Channel 2-b

[50] Of all our proposed correlations, the match of channels 2 and b is the strongest. The strength of the correlation lies in the similarity of their channel shapes and internal stratigraphy. Figure 13 displays the outlines of the two channels. The shapes of both channels b and 2 were about 1.5 m deep and very narrow. These two channels had, in fact, the lowest width-to-depth ratio of all the channels at the site. A side channel in the upper reach of the channel 2 merged with the main channel just upstream from the fault zone. Thus the shape of channel 2 in its lower reach was as simple as that of channel b. The strata within channels 2 and b also correlate exceptionally well. Both channels had four characteristic units, 10, 20, 30 and 40. Among these, unit 20 was the most diagnostic. This upward fining sequence comprised horizontally bedded thin layers of framework-supported pebbles and sand. Within each layer, the sediments were remarkably well sorted.

[51] Recall that from the crosscutting relationships in the upstream exposures, one cannot determine whether channel 2 was older or younger than channel 3 (Figure 11a). From the correlation between downstream channel b and channel 2, we can now say that, in fact, channel 2 was younger than channel 3.

5.4. Channels 3-c and 4-d

[52] On the basis of crosscutting relationships and the match of channel 2-b, channels 3 and 4 were the third and fourth oldest channels upstream from the fault. Similarly, channels c and d were the third and fourth oldest channels downstream from the fault.

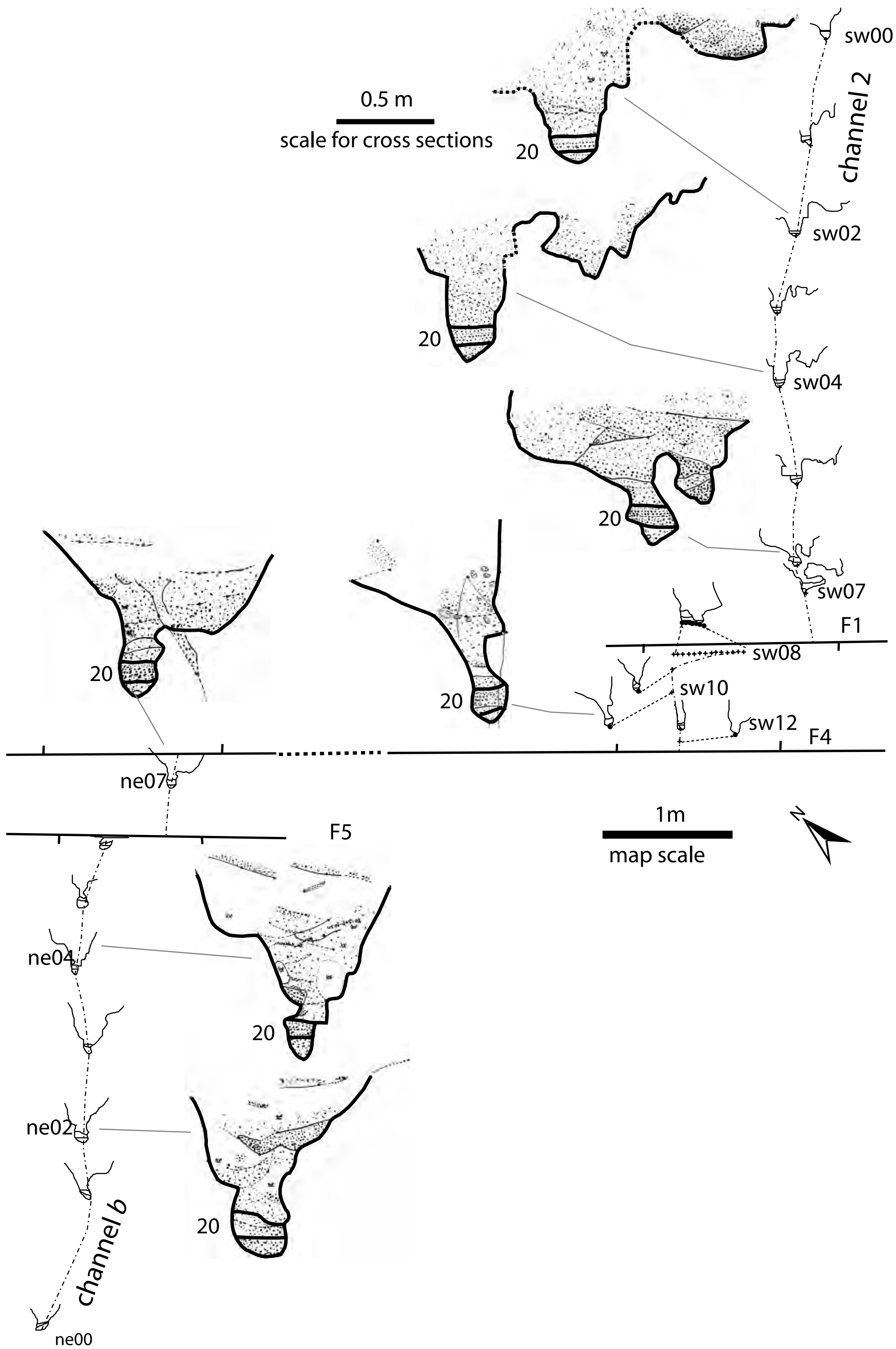

Figure 13. Correlation of channels 2 and b. The unusual narrowness of channels 2 and b and the similarity of their internal stratigraphy provide definitive evidence for their correlation. The dotted portion of the fault indicates much of the fault length between the upstream and downstream segments was removed to enable presentation of the comparison on a single page. Note the different scales for map and cross sections.

[53] The similarity of channels 4 and d strongly suggests that they are correlative (Figure 14). The morphologic features common to both channels include their W-shaped channel profile, their large width/depth ratio, their 1.2-m depth beneath the surface near the fault zone, and the fact that they both approached the fault at nearly right angles. Furthermore, both upstream and downstream channels experienced two cut-and-fill episodes. On both sides of the fault, the second down-cutting reached as deep as the first phase and widened the channels by scouring the

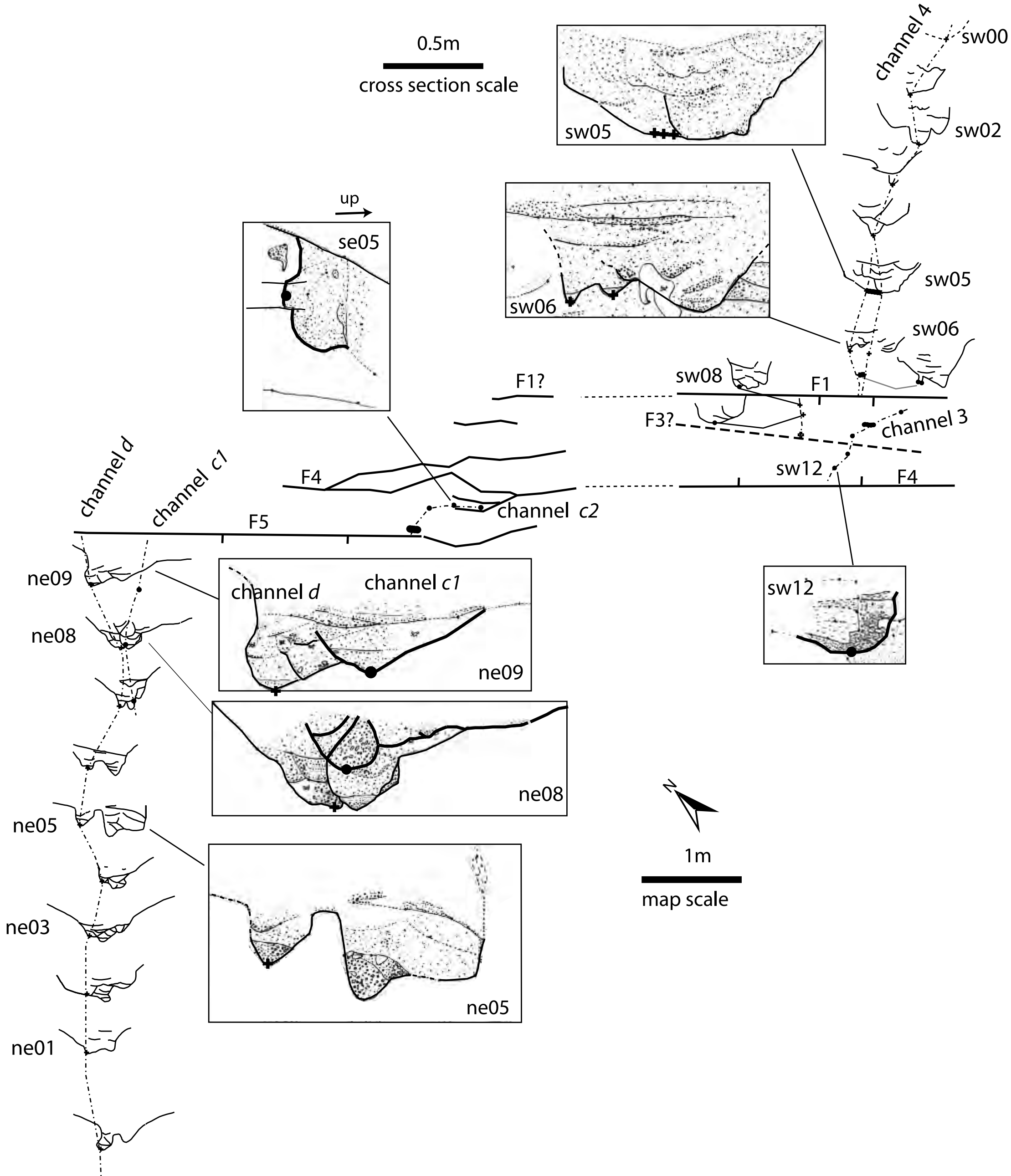

Figure 14. Map and cross sections of channels 4 and d illustrating the basis for correlation of these two channels. The correlation is strongly suggested by the W-shaped channel profiles of both upstream and downstream segments and the similarity of their stratigraphic sequences. This match is also consistent with the match of the deflected channels 3 and c.

southeastern bank. The deposits within channels 4 and d are also similar. Sediment within both channels was predominately massive, poorly sorted sandy, pebbly debris. The only fluvial units within this colluvial debris were thin basal wisps of granule- and pebble-dominated fluvial deposits above each of the basal channel scours.

[54] Having established a likely correlation between channels 4 and d, we can now consider plausible upstream correlations of channel c. Channel c consisted of two parts (section 4.1.3) Channel c1 was superimposed on channel d downstream from the fault zone but diverged eastward away from channel d near the fault (Figure 14). Channel c2 was within and parallel to the fault zone, just a few meters to the southeast. The salient question, now, is whether channel c2 is correlative with upstream channel 3. The stratigraphic position of channel 3 is proper for such a correlation, since it was demonstrably younger than channel 4 (section 4.2.2). Secondly, the fact that both channel c2 and channel 3 ran nearly parallel to the fault and within the fault zone also supports the correlation. In addition, channels 3 and c2 had similar shapes; both had a clear, circular channel profile. Strata within both channels varied greatly along profile, so we cannot martial this as strong evidence for correlation. Nonetheless, in both

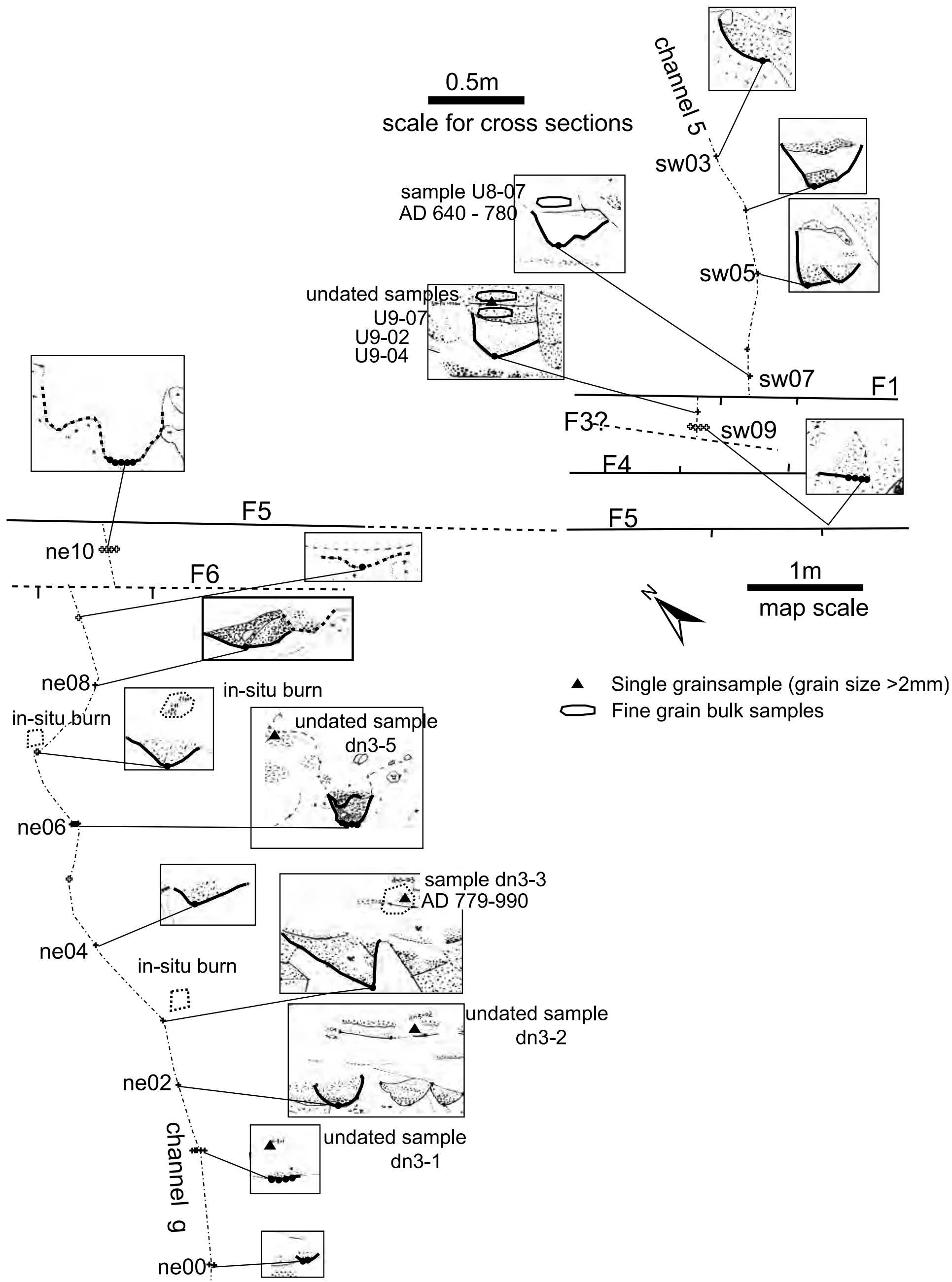

Figure 15. Summary of evidence for the correlation of channels 5 and g. Their size and stratigraphy are similar. The similar ages of two radiocarbon samples from the two channels also support the correlation. Open symbols for channel thalwegs indicate that the locations of the channel at these exposures are estimated. In particular, in exposures ne09 and ne10, the channel did not have any distinctive well-sorted coarse-grained layers and was barely recognizable by slight color contrast between channel-filling colluvium and bioturbated alluvium. Hence the positions of channel g in these two exposures were conjectural.

channels the thickness of the strata was about 30 cm in exposures near the fault.

5.5. Channel 5-g

[55] The next correlation of upstream and downstream channels is more difficult to make, because of ambiguities in the relative ages of channels both upstream and downstream from the fault. Upstream channels 5 and 6 antedated channel 4, but there were no crosscutting relationships to tell which was the younger of the two. Downstream channels e, f, g, and h were nested together (Figure 4d), with a temporal ordering of f > h > g and f > e. Channel e probably did not reach the fault, so we would not expect to be able to find a match for it across the fault. Even if channel e did reach the fault, the angle it left the fault zone is not compatible with either channel 5 or channel 6.

[56] The best match is between channel g and channel 5 (Figure 15). The basis for this proposed match is channel

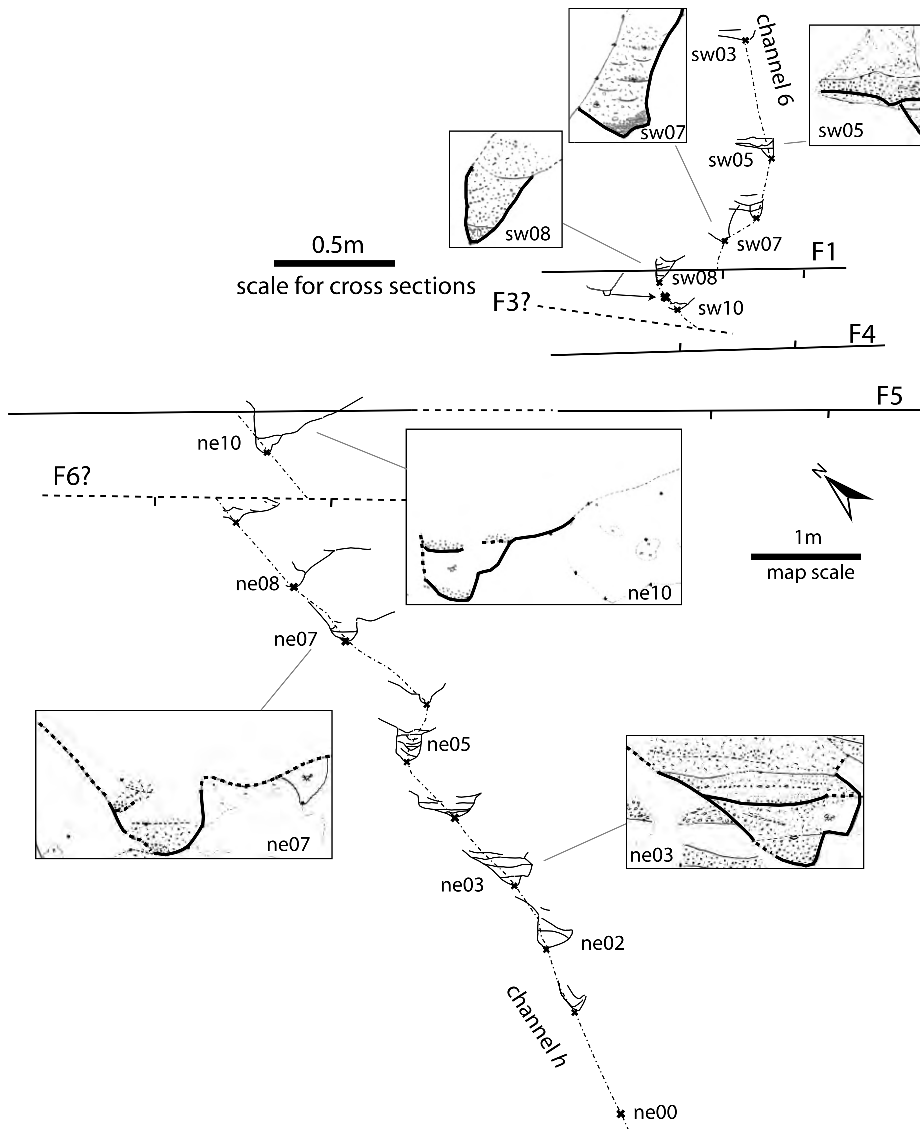

Figure 16. Correlation of channels 6 and b. The evidence includes their similar southward flow directions. Their internal stratigraphy is also similar.

geometry, stratigraphy and datable carbon in both channel segments. Both channels were narrow and shallow in mappable channel stratigraphy (≤40 cm wide and ≤40 cm deep). Unlike channel 6, both were roughly as wide as they were deep and were relatively flat bottomed. Their stratigraphy was similar: predominantly well-sorted fluvial sands with sparse pebbles, overlain by poorly sorted sandy colluvium. In neither channel was there a consistent record of multiple incisions and aggradations. Further support for the correlation of channels 5 and g is the presence of charcoal in both channels. We will discuss the radiocarbon ages of these samples in more detail later, along with ages determined for other samples at the site. For now, let it suffice to say that samples from both channels yielded similar ^{14}C ages.

5.6. Tentative Correlation of Channel 6-h

[57] Erosion of much of channel 6 by younger upstream channels makes matching of this channel a special challenge and less certain. Nonetheless, the correlation we suggest is the most plausible one. The bases for correlation are the channel size, fill and its orientation.

[58] The angle of intersection of channel 6 with the fault is the strongest basis for correlation (Figure 16). Channel 6 approached the fault zone at a distinctly acute angle. It was, in fact, the only upstream channel to trend southward as it approached the fault. We might expect, then, that its downstream equivalent would also trend southward away from the fault. Of all the downstream channels, only channels h and l had flow directions near the fault that were compatible with the deflection of channel 6. However, channel l was an unlikely match, because it was much deeper and wider than channel 6. It also had a more complex sequence of cut and fills and a more complex cross-sectional profile (Figure 4e).The general resemblance of the stratigraphy within the channels also favors correlation of channels 6 and h. Both channels had two well-sorted gravely to sandy fluvial beds near their base, separated by a

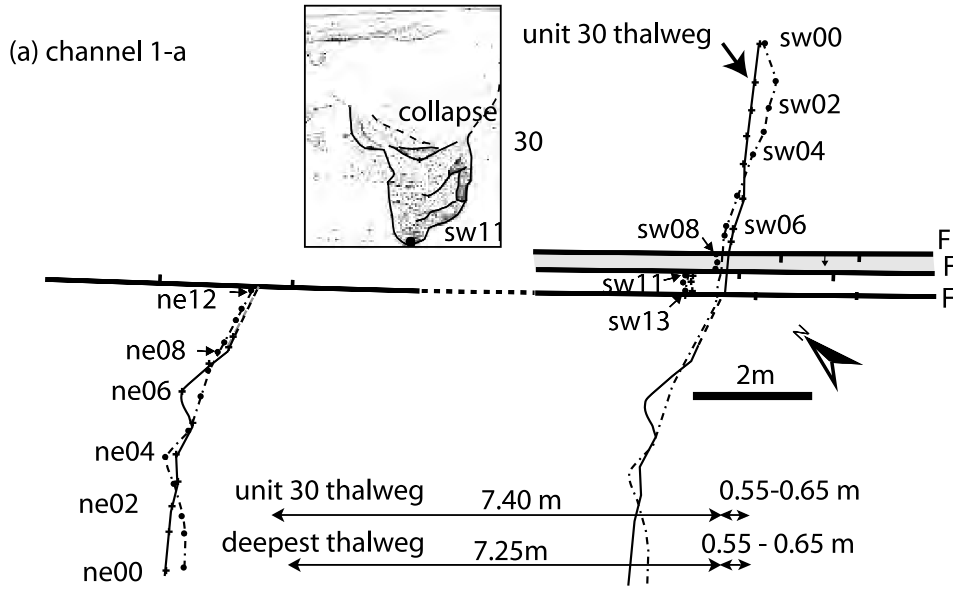

Figure 17. Horizontal and vertical offsets of the six channel pairs. (a) Offset of channel 1-a. The dextral offset of 7.8–8.0 m is indicated by the deepest thalweg and the base of unit 30. Most of this (7.25–7.42 m) is across the major strand, fault F4. (b) Total offset of channel 2-b. It is constrained to be 15.1–15.8 m by the deepest thalweg. Possible warping is confined to the reach immediately downstream from fault F5 and is about 0.4 m. (c) Restorations of channels 3-c requiring a total right-lateral offset of 20.7 ± 0.15 m. The majority of the offset is accommodated in the 0.8-m-wide zone between faults F3 and F5. (d) The 22.0 ± 0.2 m offset of channel 4-d, indicated by the average trend (dashed lines) of channel 4-d thalweg. The uncertainty is half the amplitude of channel meanders. Direct connection of channel thalweg suggests a slightly larger offset but within the uncertainty bound of that of the average trend. (e) Map showing the 30.0 ± 0.3 m offset of channel 5-g. Direct connection of data points suggests an offset larger than, but within the uncertainty bound of, that of the average trend. Open symbols for channel thalwegs indicate that the locations of the channel are uncertain at those exposures. (f) The 35.4 ± 0.3 m offset of channel 6-h, using a straight-line extrapolation. The 0.3-m uncertainty is half the maximum amplitude of channel meanders. The obliquity with which this channel intersects the fault zone suggests the offset could be substantially more than 35.4 m. (g) Vertical offsets of the six channel pairs. Longitudinal profiles of the two piercing lines of channel 1 delineate a graben within the fault zone, but the overall vertical offset across the entire fault zone is 5 cm, downstream side up. The vertical offset of channel 2 across the fault zone is 7–14 cm, downstream side down. The long profile of channel 3-c shows that the block between faults F4 and F5 is a small horst with little, if any, vertical offset across the faults. Yet, the total net vertical offset of channel 3-c should also include the offset across F1, which is 10 ± 5 cm, downstream side down. The irregularity of the long profile of channel 4-d suggests warping. However, the cumulative vertical offset across the fault since its incision is nil. Vertical offset of channel 5-g is relatively ill-constrained. If we use the trend of upstream points in the profile, the net vertical offset is 25–45 cm, with downstream side up. If we use a moderate river gradient, e.g., 3.24°, instead, the offset is 0–8 cm, downstream side down. The net vertical offset of channel 6-h is also ill-constrained. The upper bound of net vertical offset is probably about 5–30 cm, up on the downstream side. The lower bound can be 25 cm, down on the downstream side.

poorly sorted 25-cm-thick colluvial deposit (cf. exposures sw05, ne10 and ne03; Figure 16).

5.7. Uncorrelated Older Channels

[59] Thus far, we have made plausible correlations between 6 sets of upstream and downstream channels (Figure 11b). Three upstream channels, 7, 8 and 9, remain to be matched with downstream channels. Five downstream channels remain unmatched, e, f, i, j, k and l. None of these channels appear to match across the fault. The correlatives of channels 7, 8 and 9 must lie further to the northwest. The upstream correlatives of the unmatched downstream channels are slightly more complicated. They could have been eroded away by the younger channels, i.e., channels 1 through 6, or they may exist farther to the southeast, outside the bounds of the excavations.

6. Measurement of Offsets

[60] Now, we can measure the offsets of the 6 pairs of matched channels. The offset of each pair represents the cumulative displacement since the abandonment of the channel. We will mainly use the deepest thalwegs of channels as offset piercing lines. We are able to measure both horizontal and vertical offsets, because 3-D excavations and surveying by Total Station enable us to reconstruct

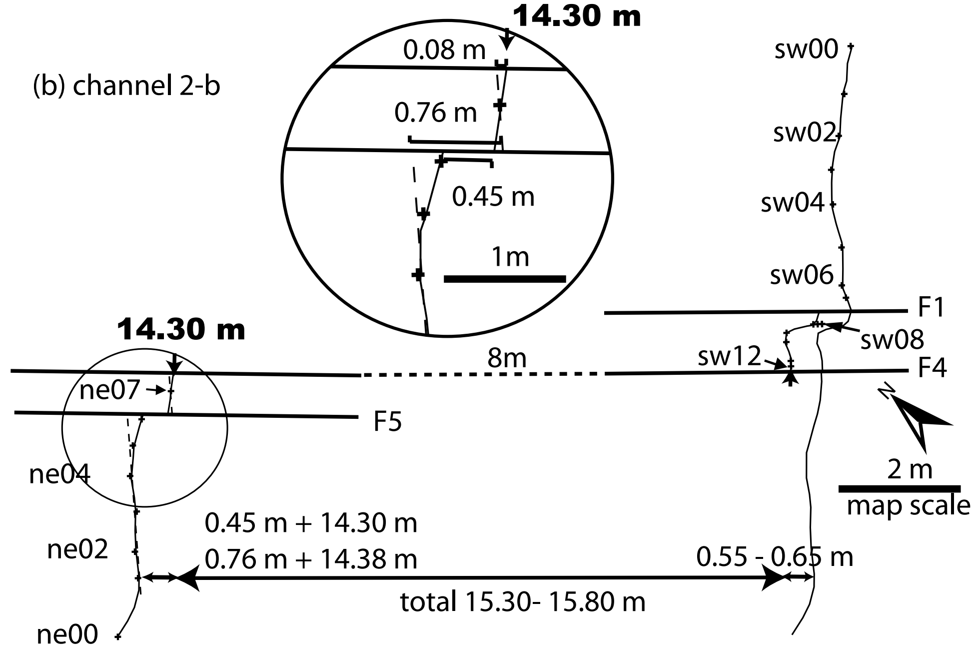

Figure 17. (continued)

the channel geometries in three dimensions. The precision of the measurements is on the order of 10 cm and is about what can be achieved measuring the offsets of a natural feature immediately after an earthquake.

[61] Faulting was concentrated in a zone just 1.5 to 2 m wide. This zone comprised six principal fault planes, fault F1 through F6 (Figure 4f). We did not find secondary traces outside this narrow zone within the channel stratigraphy. However, the total width of the fault zone in the substrate was larger than that is indicated by channels. The main fault zone in these older units was at least 4 to 5 m wide, judging from the extent of shear fabric within the substrate.

6.1. Minor Offset on Faults F1 and F2

[62] F1 was a shallow branch of F2. It was connected with F2 by a subhorizontal ramp ~1.8 m below the ground

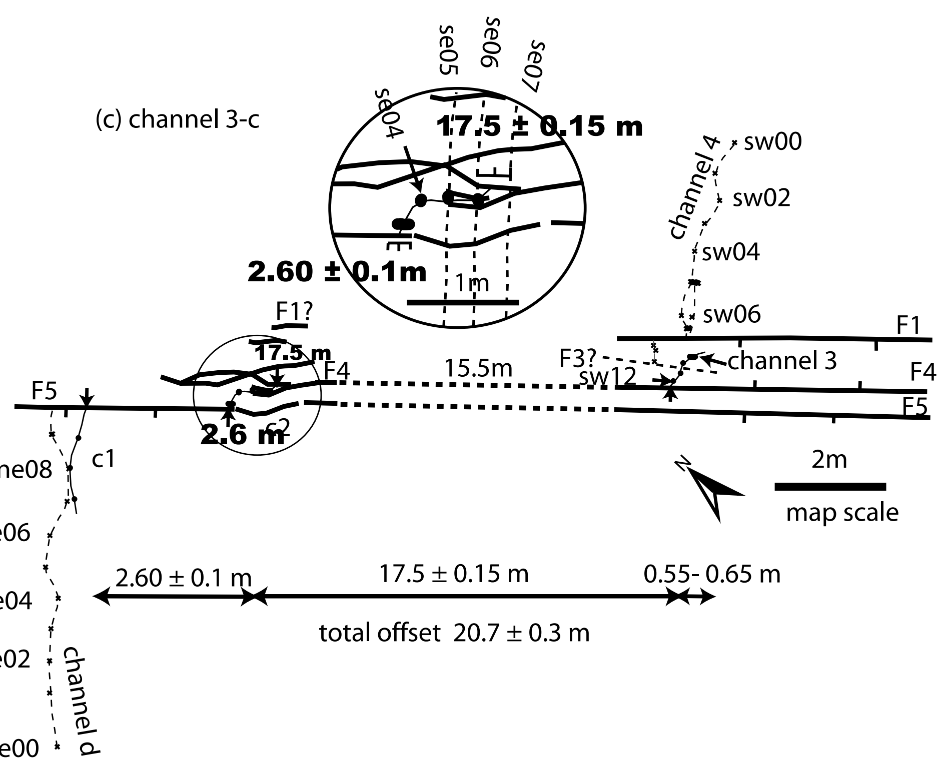

Figure 17. (continued)

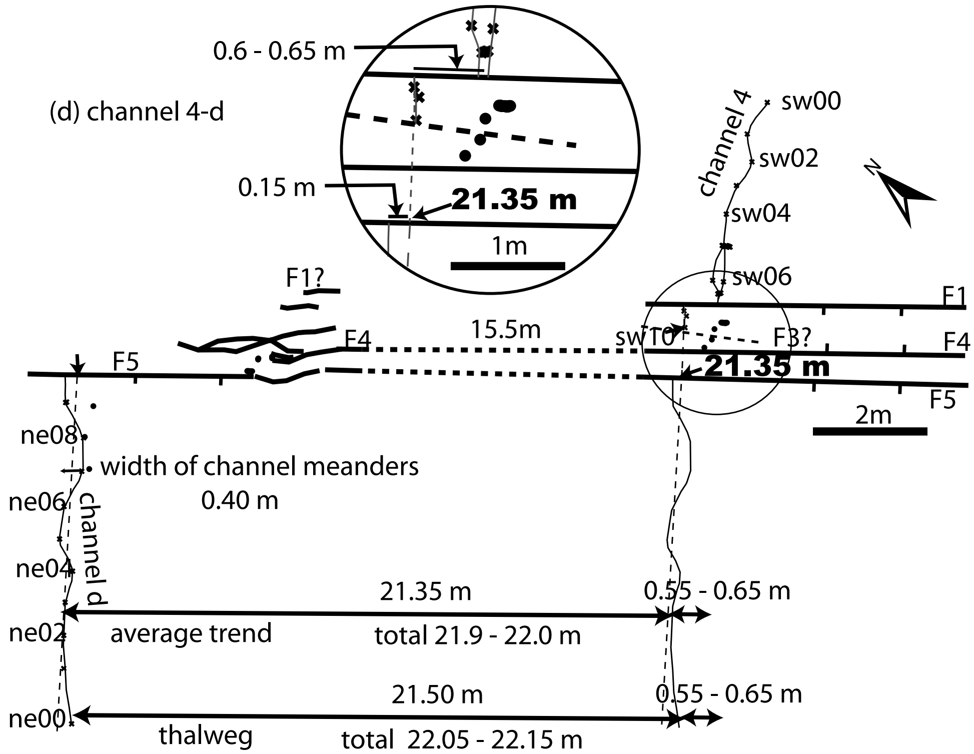

Figure 17. (continued)

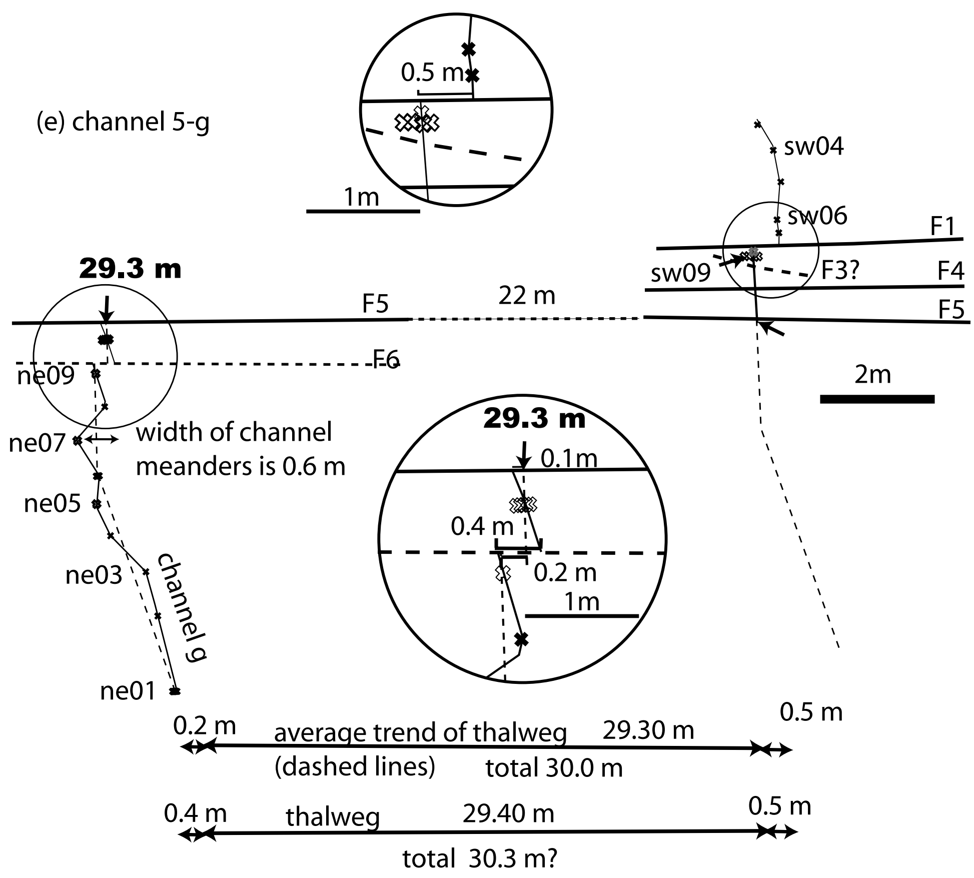

Figure 17. (continued)

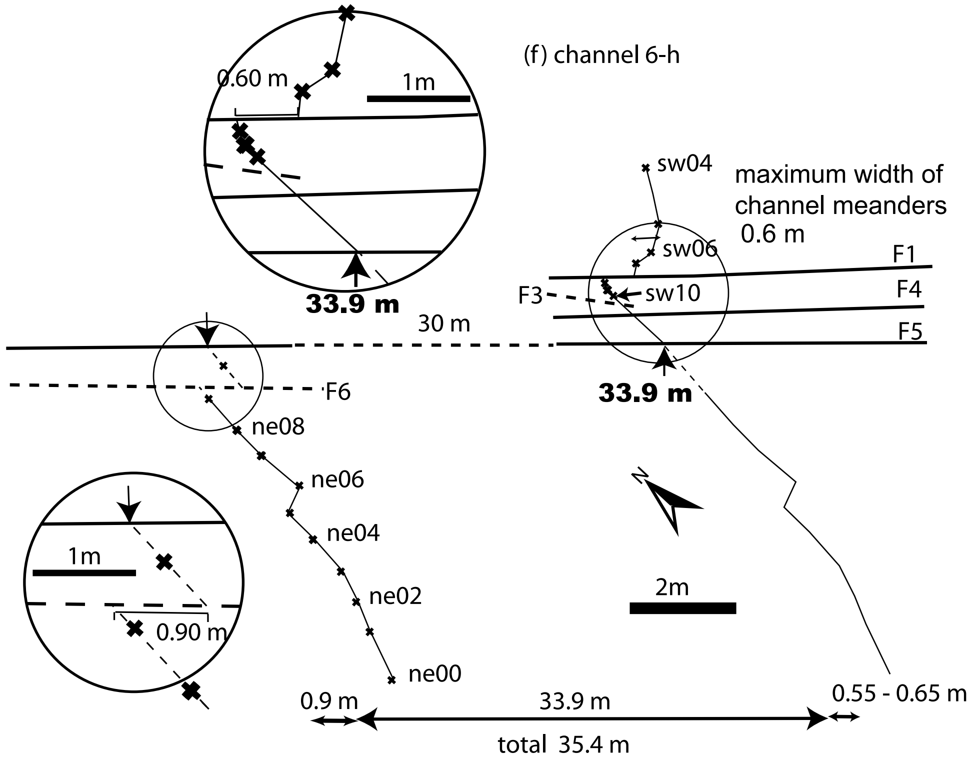

Figure 17. (continued)

surface [*Liu*, 2003, Figure 3.2]. We first discuss the offsets of channels on secondary faults F1 and F2, because these secondary faults appeared to offset channels 1 though 6 a nearly identical amount, about 60 cm (Figure 4g). The slight difference in offset measurable in Figure 4 is likely to reflect uncertainties in measurements, rather than to indicate multiple offset events. Thus F1 and F2 appeared to have slipped only once after the down-cutting of channel 6, probably during the rupture that postdated formation of channel 1. The offset of channel 2 can be ambiguous. Channel 2 was broad and had relatively ill-defined thalweg near F1. Because of this ambiguity, the dextral offset of channel 2 across F1 has a relatively large range of 20–80 cm. However, if channels both older and younger than channel 2 are offset about 60 cm, then channel 2 must also be offset this amount. The abnormal meander of channel 2 immediately downstream from fault 1 could indicate a preexisting fault scarp near fault 1.

6.2. Channel 1-a, 8-m Offset

[63] Two piercing lines constrain the offset of channel 1-a: the deepest thalweg and the basal contact of unit 30 (Figure 17a). The deepest thalweg is offset by F1 and F4 a total of 7.85 m. Our measurements of offset across all three strands have little uncertainty, since our mapping constrains the piercing lines within a couple of ten centimeters to the faults. Hence the extrapolation of piercing lines to the fault yields a trivial uncertainty of only a few cm, at most. The offset of the thalweg of unit 30 is about 8.0 m. Perhaps it is less precise because the location of unit 30 is not clear within 1m of the fault, which implies a greater extrapolation to the principal fault from the downstream segment.

6.3. Channel 2-b, 15.5-m Offset

[64] The deepest thalweg of channel 2-b, very well defined in all trench cuts, provides a superb piercing line delimiting the offset of the channel. This piercing line yields horizontal offsets of 15.30–15.80 m across three strands (Figure 17b). Two other piercing lines yield marginally different ranges of 15.10–15.75 m and 15.20–15.72 m [*Liu*, 2003]. The uncertainty is largely due to about 0.4 m of suspected near-fault warping across F5. Figure 17b shows two interpretations of the offset. If we extrapolate using the trends of the nearest data points, the total offset is at least 15.30 m. However, in the close vicinity of F5, the downstream segment of channel 2-b seemed to arch in a manner suggestive of warping. If the bending is due to warping instead of river meandering, we would have to add about 0.4 m to the offset of simple juxtaposition. Thus the total offset would be about 15.8 m.

6.4. Channel 3-c, 20.7-m Offset

[65] Interpretation of the horizontal offset of channel 3-c involves the restoration of three channel segments along F5 and F4 (Figure 17c). Measurement of offset across F4 produces most of the uncertainty for this channel, because channel c2 trends nearly parallel to the fault zone. If channel c2 turns abruptly into F4 at its southeasternmost exposure (exposure dn4-se06 in Figure 17c blowup), then it is offset 17.65 m from channel 3. If however, the channel c2 thalweg continued toward the southeast before intersecting F4, the offset would be less. A cut 25 cm southeast of exposure se06 of channel c2 constrains the southeasternmost possible extent of the channel. Thus the minimum offset of channels c2 and 3 across F4 is 17.35 m. The offset across F5 is 2.6 ± 0.1 m. To derive the total offset across the fault zone

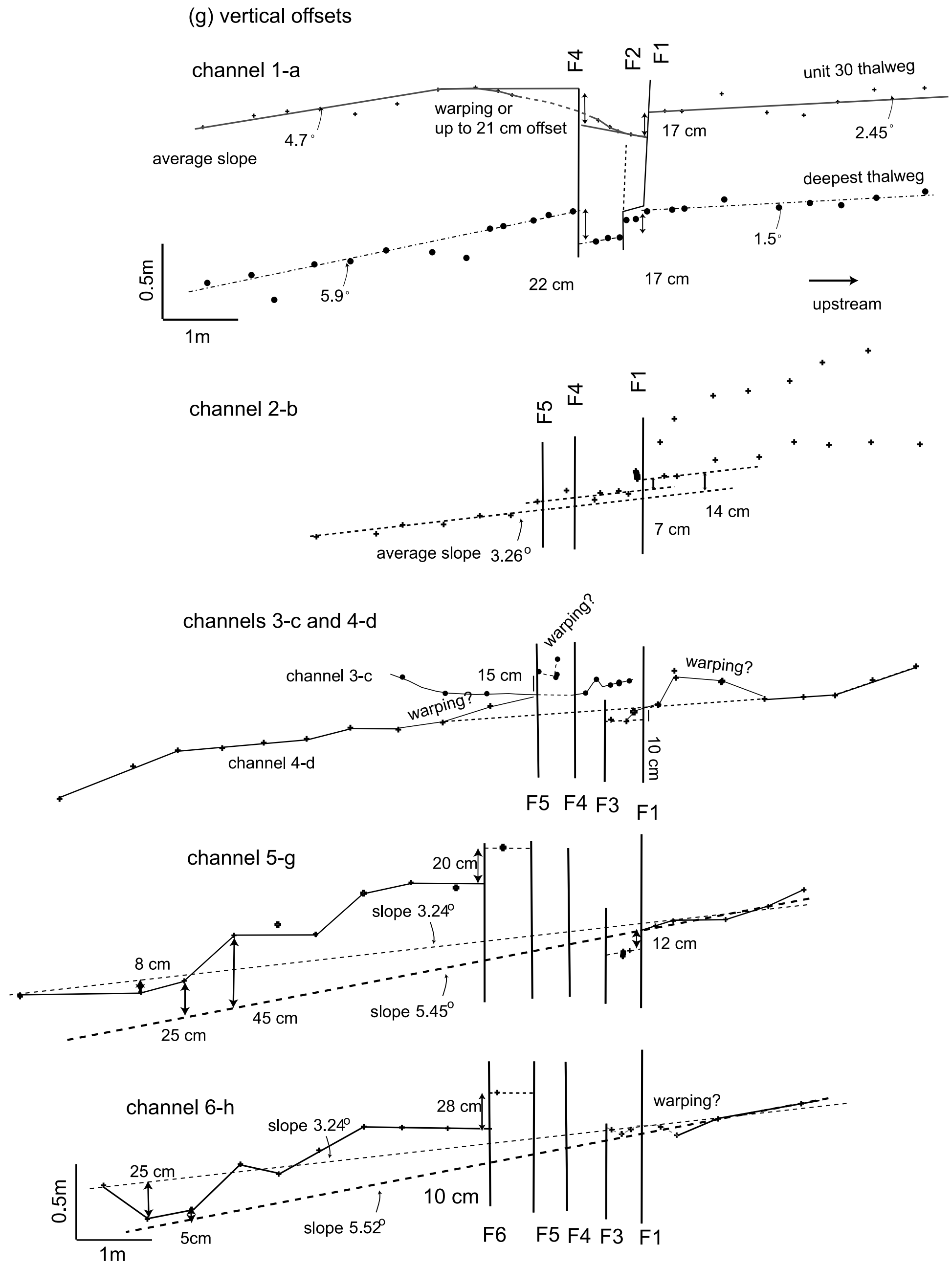

Figure 17. (continued)

since creation of channel 3-c, one must include also the 0.6-m offset of younger channels across F1. The sum of these measurements is 20.7 ± 0.3 m. The 0.2-m uncertainty that we assign to the total offset is half the amplitude of the largest channel meanders exposed in the trenches.

6.5. Channel 4-d, 22-m Offset

[66] The best estimation of the lateral offset of the channel 4-d pair is 22.05 ± 0.2 m. This is the combination of measurements using two piercing lines: the thalweg and the average trend. The thalweg suggests a total offset of about 22.1 m, if we use extrapolation between closest exposures of this channel pair (Figure 17d). If instead, we were to use the overall trend of the upstream and the downstream channel segments to extrapolate to the fault zone, the total offset would be slightly smaller, 22.0 m.

6.6. Channel 5-g, 30-m Offset

[67] Channel 5-g has accumulated about 30.0 ± 0.3 m of right-lateral offset since its creation (Figure 17e). We estimate the error of this measurement to be 0.3 m, half the largest amplitude of channel meanders observed in the excavations of channel g. A slightly larger total offset, 30.3m, is estimated if we extrapolate the thalweg between F5 and F6 using data points closest to the faults. However, this is still within the uncertainty of the previous measurement. We favor the 30.0 ± 0.3 m measurement, because

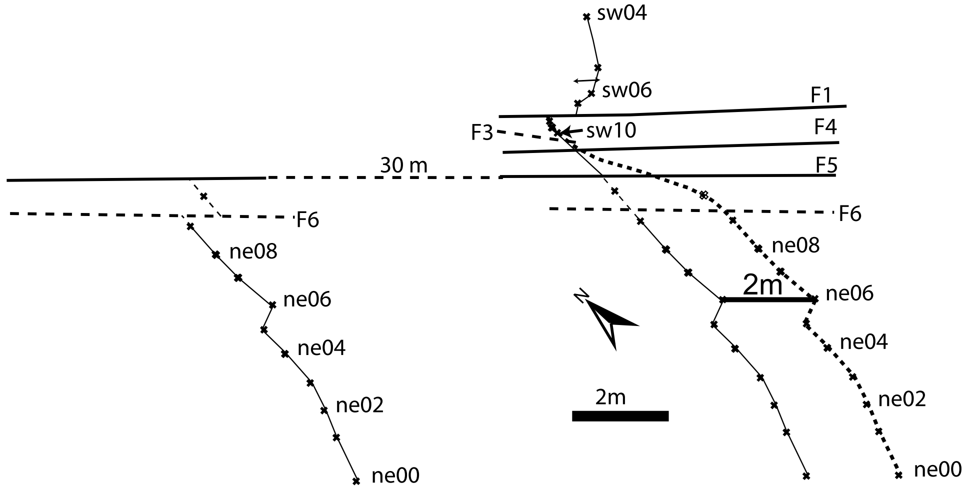

Figure 18. Uncertainty in the offset of channel 6-h. It is ambiguous because this channel intersects the fault zone at an accurate angle, compound by the lack of channel exposure in the fault zone. The solid line indicates the position of downstream channel segment after 35.4 m offset reconstruction. A more accurate intersection of channel with the fault implies larger offset. The dashed line indicates the hypothetical position of downstream segment with an additional 2-m offset.

the general trend of the thalweg provides a longer reference line, and thus a more robust estimation of the offset.

6.7. Channel 6-h, 35.5-m Offset

[68] Channel 6-h appears to record a cumulative right-lateral offset of about 35.4 ± 0.3 m (Figure 17f). However, the maximum plausible offset of this channel is subject to greater ambiguity than that of other pairs, because channel 6 had fault-subparallel deflection in the reach where the channel stratigraphy is missing and the measurement of offset is unusually sensitive to the assumption of initial channel configuration. The 35.4 ± 0.3 m offset, estimated using a straight line extrapolation, should be considered a minimum. A larger deflection of the channel through the fault zone would yield a larger offset value. Shown in Figure 18 as an example, it is not impossible to hide an additional 2m offset. This would yield an offset of 37.4 m. Thus, because of the acute intersection angle of channel 6-h with the fault, the offset is most likely to be substantially more than 35.4 m.

[69] Another source of ambiguity is the offset of channel 6 across F1. Channel 6 curved in the reach immediately upstream from F1. If the curvature were due to channel meandering, the offset across F1 would be 0.6 m. However, if the curvature indicates tectonic warping of a straight channel, then the offset across F1 could be as large as 1.5 m. In favor of the meandering hypothesis, the next older channel 7 ran straight into F1 and displayed no deflection. Furthermore, the strong asymmetry in the shape of channel 6, the southern wall being steeper than the northern wall (Figure 16), is consistent with a channel meander. On the other hand, the curvature of both channels 8 and 9 upstream from F1 suggests strongly tectonic deflection, though it is uncertain whether the event responsible for their deflection is the same as that for channel 6.

6.8. Vertical Offsets

[70] Vertical offsets for individual offsets are always less than 50 cm, but range from northeast-side-up to southwest-side-up (Figure 17g). Cumulative vertical offset is nil. This suggests that geomorphic scarp at the site might be due to juxtaposition of surfaces of different elevations [*Arrowsmith et al.*, 1998] or that earthquakes older than those in this sequence had larger vertical offset. Individual channel long profiles show also the fine structure of the fault zone. For example, channel 1-a suggests the fault zone between F4 and F1 is a graben. Channels 3-c and 4-d indicate that the narrow block between F4 and F5 is a horst. Furthermore, channel profiles are commonly irregular in the vicinity of

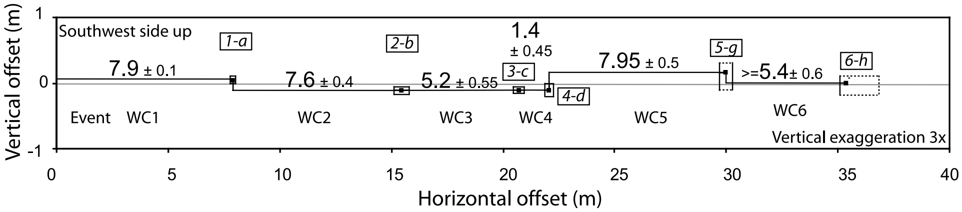

Figure 19. Plot of the offset sequence, using the six channel pairs. The horizontal and vertical offset of each pair appears as a small black rectangle, the size of which indicates the error associated with each measurement. The dextral offsets for the six discrete ruptures are shown by the numbers. The vertical component of slip is in all cases a small fraction of the dextral offset.

the fault zone, an indication of warping, or the presence of pressure ridges associated with brittle faulting.

6.9. Nonbrittle Warping

[71] Warping is prominent in a vertical plane. It is commonly indicated by the anomalous gradient in long profiles of the channels, particularly channels 3, 4, 5 and 6, within or in the vicinity of the fault zone (Figure 17g). This is consistent with the appearance of a large mole track, i.e., welts, mounds and troughs along the surface rupture of an earthquake. However, we found no significant warping in horizontal offsets within the aperture of our excavations, except a possible 0.4 m warp in channel 2-b (Figure 17b). In all other channels, there were not noticeable systematic deviations in plan view of the alignments of channel thalwegs that we can attribute to nonbrittle warping. We suspect that the warping component is probably less than half the amplitude of channel meanders within our excavation aperture. However, if warping is widely distributed away from the main fault zone [e.g., *Rockwell et al.*, 2002], then we would have underestimated the total warping. Thus, from a conservative point of view, the offset amounts we deduce from our excavation should be considered minima.

7. Derivation of a Rupture Sequence

[72] The total dextral offset of $\geq$35.4 m accumulated in six increments. They are 7.9 ± 0.1, 15.5 ± 0.3, 20.7 ± 0.2, 22.05 ± 0.2, 30 ± 0.3 and $\geq$(35.4 ± 0.3). The differences between these values yield the magnitude of the six incremental offsets. From youngest to oldest these are 7.9 ± 0.1, 7.6 ± 0.4, 5.2 ± 0.6, 1.4 ± 0.5, 8.0 ± 0.5 m and $\geq$(5.4 ± 0.6) (Figure 19). For ease of reference, the increments of offset are named WC1 (the youngest) to WC6 (the oldest). Note that at least three of the six increments are within 7.5–8 m, but two consecutive offsets, WC3 and WC4, are about 5.2 and 1.4 m.

7.1. Is Each Offset a Single Rupture Event?

[73] To determine a rupture history for this site along the San Andreas fault, we must consider how many rupture events this sequence of incremental offsets represents. Although a one-for-one correlation may exist, it must be supported by the details of the stratigraphy and geomorphology. Could it be that two separate ruptures occurred within a period during which no new channels were incised? Is it possible that one of the offsets represent two ruptures, one of which was only a few centimeters or a few tens of centimeters?

[74] The completeness of the Wallace Creek paleoseismic record is a function of the number and duration of hiatuses in the record of alluviation and channelization. Hiatuses in either deposition or erosion that occur between rupture events would result in the events not being recorded in the excavated volume. If seismic ruptures have occurred more frequently than alluviation or erosion, then some of the ruptures would not be differentiable in the geologic record. For example, between 35 and 50 m northwest of the upstream channels there are no downstream correlatives to the upstream channels. It is reasonable to propose that a hiatus in deposition and erosion occurred at the site when that 15-m section was in front of the channel. The completeness of the record is also a function of the size of ruptures relative to the size of the depositional and erosional features in the excavated volume and the spacing of our serial excavations. The width of a channel may set the limit of the offset that can be detected at the site. For example, we probably would not recognize a 10-cm offset event, if the channel is 1 m wide. However, if the offset is more than half the width of channel, and if alluviation is frequent enough, the offset event should be recognizable. We turn now to specific discussions of each of the offset channel pairs.

7.2. Offset WC1 and the 1857 Earthquake

[75] The 1857 earthquake is known to have involved rupture of this portion of the San Andreas fault [*Wood*, 1955; *Agnew and Sieh*, 1978], with 8 to 10 m offsets [*Wallace*, 1968; *Sieh*, 1978]. Three-dimensional excavations a few kilometers to the southeast of our site yielded a sharp offset of about 7 m, which has also been ascribed to the 1857 rupture [*Grant and Sieh*, 1993]. None of these geomorphic or stratigraphic offsets can include more than a few centimeters of creep in the past century, since fences constructed in 1908 a few kilometers to the northwest show no misalignments [*Brown and Wallace*, 1968]. Thus it appears that all or at least most of offset WC1 is attributable to slip in 1857.

[76] The geometry and stratigraphy of channel 1-a indicate that all but a few tens of centimeters of the 7.9-m offset must be associated with the 1857 event. Channel 1-a is offset very abruptly across the fault zone. On both sides, we have traced the channel to within 20 cm of the main fault strands. The width of channel 1, which is about 50 cm wide near the fault, also argues that events of more than 50 cm offset could not have occurred during the initial stage of the down-cutting of channel 1.

7.3. Offset WC2 and the Penultimate Rupture

[77] Several observations suggest all or nearly all of the 7.5-m offset WC2 accrued in one event. First, similar to channel 1-a, channel 2-b is offset sharply across the fault. We have traced the channel to within a couple of ten centimeters of the main fault strand. If there had been an offset of the channel greater than a 20 cm or so after initial incision and before filling of the narrow lower portion, the stratigraphy in channel 2-b would not have been continuous up to and across the fault zone. Near the fault zone, we would have expected to see collapse debris from the scarp within the sequence. Furthermore, an event in the early stages of channel filling would have led to development of a channel meander at the fault. Such a meander would be apparent in the map of the channel thalweg and walls. There is also no evidence for a second large event in the shape of the upper units of the channel fill.

7.4. Offsets WC3 and WC4

[78] The channels that define offsets WC3 and WC4 provide a good example of how multiple offsets of a channel can be discriminated if the stratigraphic and geomorphic record is adequate. The upstream channels (3 and 4) sat adjacent to each other and the downstream channels (c and d) occupied the same channel, except near the fault (Figures 4c and 4g). Whereas the older channel (d) flowed straight across the fault in a deep channel, the upper channel (c) left the fault at an angle, and merged

with the straight channel 1 m or so downstream. Channel 4-d had been offset 1–2 m when channel 3-c was incised. This small offset, WC4, is indicated by the difference in the offsets of channel 4-d and channel 3-c. The fact that channel c cut across the upper right of channel d and caused the asymmetrical cross section of d is additional evidence for a corner-cutting deflection after channel 4-d was offset a meter or two.

[79] We do not see any evidence suggesting that the 1- to 2-m offset of 4-d accumulated through multiple events. There is no asymmetric widening of the channel wall of 4-d that we can attribute to faulting, except as it relates to channel c. The double thalwegs of channel 4 and channel d appear to indicate an asymmetric widening. However, since that they are in the same direction on both sides of the fault, the widening is clearly not a response to offset. One would expect that after an offset, the upstream channel would widen in a direction opposite to that of the downstream segment.

[80] It is possible, but there is no evidence, that the 5- to 6-m offset of WC3 represents multiple events. There is only one cut-and-fill sequence within channel 3-c, so evidence of multiple offsets could be hidden in the colluvium that overlies the channel.

7.5. Offsets WC5 and WC6

[81] There is more uncertainty whether the offset WC5 represents a single event. The shallow depth and simple cut-and-fill sequence of channel 5-g may indicate that channel 5-g was incised during a period with less frequent storms. If it is the case, then the possibility of a hiatus in alluviation (and a missing rupture event) is greater for channel 5-g than other channels. Nonetheless, WC5 appears to be due to a single event. Channel 5-g ran into the fault zone at a high angle. The next younger channel, channel 4-d also crossed the fault zone at nearly a right angle. Both upstream and downstream segments were less than 1m wide near the fault.

[82] WC6 is perhaps the most uncertain case, because of the poor stratigraphy and asymmetric shape of channel 6-h. The downstream channel h was about 1m wide in the immediate vicinity of the fault zone; the cross section of channel h was asymmetric toward the south (Figure 4d). This geometry would be consistent with widening of a downstream channel after being right-laterally offset. However, poorer preservation of channel stratigraphy in the upstream reach prevents us from a more rigorous assessment of this possibility.

[83] In summary, abrupt terminations of channel walls and channel stratigraphy at the fault strongly suggest that they the channels were offset in sudden events after they had been at least partially filled. The steep channel walls and the lack of corner-cutting deflections in channel stratigraphy also suggest that most, if not all of the six offsets represent single events, rather than the multiple smaller events. Channels were narrow, about 1m or less. This indicates that events with more than 1 m can be discriminated if the stratigraphic and geomorphic record is adequate.

[84] We cannot argue, however, that hiatuses in either deposition or erosion would result in incomplete record. However, the large depth, 0.7 m or more, and multiple sets of cut-and-fill sequences within channels indicate that alluviation is frequent (once every a few tens of years?). At least, the quiescent period between rupturing events are long enough to allow these channels to stabilize. A quantitative assessment of the frequency of significant storms vs. rupture events would certainly help to resolve the issue of completeness of offset record. This depends on the abundance and quality of datable materials.

8. Radiocarbon Constraints

[85] Radiocarbon analyses of samples from the excavations allow us to place some constraints on the dates of the ruptures. Numerous tiny fragments of detrital charcoal were embedded in many strata, particularly in poorly sorted coarse debris or in well-sorted fine-grained suspended load sediments. Charcoal grains were mostly small and flaky in appearance; only a small percentage of the samples were large enough to be dated by accelerator mass spectrometry (AMS). Since few of charcoal grains were large enough to be dated individually, we also extracted and consolidated charcoal fragments from bulk samples of sediment collected from exposures where tiny charcoal grains were apparent to the naked eye. We also found several burn horizons in the excavations. These generally consisted of a concentration of tiny charcoal fragments in sediment displayed a baked, reddish color. Dates from samples from a burn horizon are generally considered to be a better approximation of the age of a stratum than detrital charcoal, because they are more likely to have burned in situ, rather than been transported to the site from a burn elsewhere.

[86] We selected 27 carbon samples from a collection of over 70 for radiogenic ^{14}C analysis. The results of dated samples are summarized in Figures 20 and S9. Only six samples were from the downstream side, including two embedded in the underlying bedrock of late Pleistocene alluvium; the majority of samples were from the upstream trench.

[87] Inheritance is a common problem in analyses of detrital charcoal. Charcoal may be transported and incorporated into a stratum long after death of the plant. The result is an age that is older than the stratum from which it comes. Inheritance is clearly demonstrated in several cases at the site. For example, U7-20(1) and U7-20(2), which are in the same suspended load layer in channel 8 and only 85 cm apart in the same trench exposure, yielded ages 500–600 years apart (calibrated ages of 2550 ± 190, 2σ range, years B.P. and 3195 ± 165 years B.P., respectively) (Figures 20 and S10). Disconcordant ages within individual strata and stratigraphic inversion of ages are common [e.g., *Rockwell et al.*, 2000; *Vaughan et al.*, 1999; *Rubin and Sieh*, 1997; *Grant and Sieh*, 1993, 1994; *Nelson*, 1992; *Blong and Gillespie*, 1978]. At the Phelan fan site, 5–6 km southeast of the Wallace Creek site, *Grant and Sieh* [1993] reported radiocarbon dates on samples from the same stratum that differed by more than 500 years. At the Bidart fan site, a 2-m-thick section that was probably deposited in 2–3 centuries, contain charcoal samples with similar or stratigraphically inverted ages [*Grant and Sieh*, 1994].

[88] Despite the clear discrepancies, our radiocarbon ages provide some constraint on the dates of the rupture events. The stratigraphic locations of each of the six rupture events appear as thick horizontal lines in Figure 20. The horizontal positioning and length of the line indicates the age range of the event. A quick glance at the relationship of the event

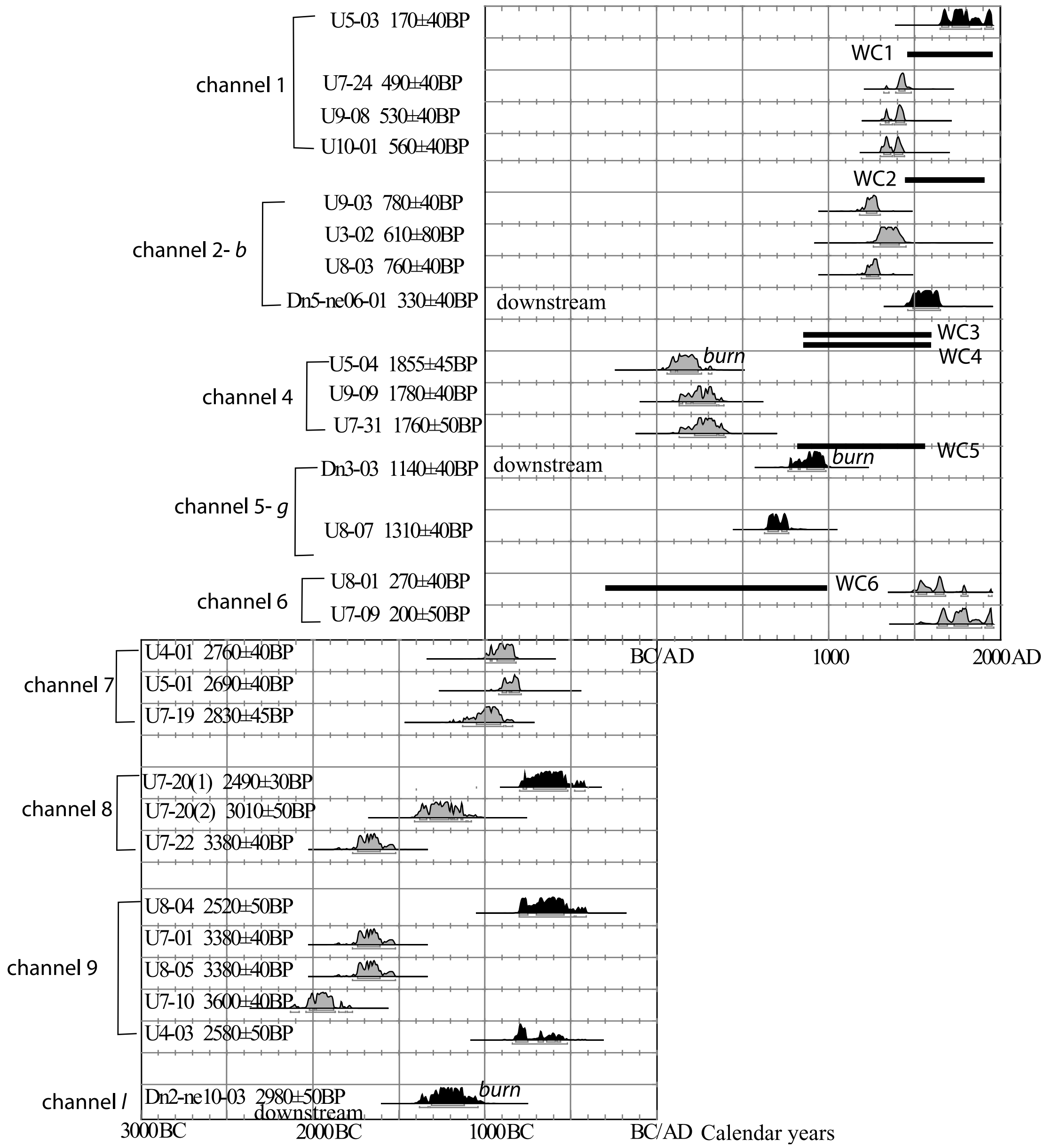

Figure 20. Radiocarbon date ranges of samples from the Wallace Creek site plotted as a function of age and stratigraphic order. The age ranges that we judge to be the most reliable and used to constrain event dates are black, whereas other ages are gray. Justification of the selection of the reliable dates and rejection of the others is given in detail by *Liu* [2003, chapter 3, section 3.6.2]. In general, one can see that the dates we consider to be reliable are the youngest ones. Bars under the age ranges are 1σ and 2σ ranges. OxCal program version 3.5 [*Ramsey*, 1995, 2000] uses atmospheric data from *Stuiver et al.* [1998]. Also shown are the stratigraphic positions of rupture events WC1 through WC6. The horizontal bars indicate their date ranges.

horizons and the black constraining date ranges shows that the ages of the events are poorly constrained. Our highly channelized and bioturbated stratigraphy provides little opportunity to refine the event dates by stratigraphic means [e.g., *Biasi et al.*, 2002] much beyond an averaging of the upper and lower bounding dates.

9. A History of the Latest Six Ruptures

[89] An offset history using dates and offset measurements at the Wallace Creek site is shown in Figure 21. The magnitude of the offsets in this history is more tightly constrained than their dates of occurrence. Constraints on the dates of the events are too poor to allow us to answer any of the important questions about recurrent behavior. Millennially averaged slip rates derived from the data range between 20 and 55 mm/yr, and we have no basis for discussing variability of recurrence within the past two millennia.

[90] Fortunately, previous paleoseismic investigations at the Phelan Creeks and Bidart fan sites, just a few kilometers to the southeast offer an opportunity to narrow the uncertainties.

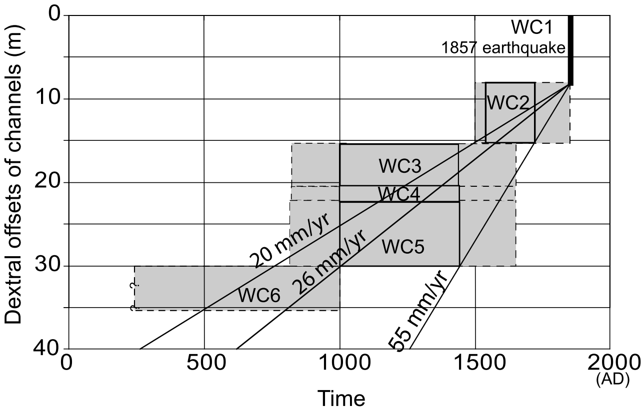

Figure 21. Tentative slip history of the Wallace Creek paleoseismic site for the last 1500 years, based solely on data from the site. The vertical dimensions of the boxes indicate the magnitude of slip in each event. Errors in slip magnitude are too small to show clearly at this scale. The horizontal dimensions of the gray boxes represent the age constraints of the events, solid lines denoting 1σ uncertainties and dashed lines indicating 2σ uncertainties. An average slip rate of 26 mm/yr is shown only for reference.

9.1. Correlation With the Phelan Creeks Site

[91] The Phelan Creeks paleoseismic site lies just 1.5 km southeast of our site (Figure 1b). It has a series of cuts and fills that may correlate with our channel cuts and fills. If so, we can benefit from the correlations, because the radiocarbon dates from the Phelan Creeks site appear to be less plagued by problems of inheritance (Figure S13; J. D. Sims et al., unpublished manuscript, 1994). The Phelan Creeks site was excavated in the 1980s [*Sims*, 1994; J. D. Sims et al., unpublished manuscript, 1994], although its sequence of offsets was first described by *Wallace* [1968]. The site encompasses two active channels, Little Phelan Creek and Large Phelan Creek. The morphology of the channels, aided by a few excavations, revealed that the Little and Large Phelan Creeks are offset 15.8 ± 0.6 m and 17.4 ± 1.6 m, respectively.

[92] A beheaded channel lies about 110 m to the northwest of Little Phelan Creek (channel HC of J. D. Sims et al. (unpublished manuscript, 1994)) [*Liu*, 2003]. Within the fault-parallel segment of the abandoned paleochannel, trenches revealed five distinct cut-and-fill episodes that occurred immediately prior to abandonment of the channel (J. D. Sims et al., unpublished manuscript, 1994). These units occurred on both sides of the fault zone. The ages of these units were comparatively well dated, but the amount of offset of each of these cuts and fills was not documented.

[93] We are intrigued by the fact that the alluvial history of the past 3000 years at Phelan Creeks is remarkably similar to the channel history at the Wallace Creek site (Figure 22). The resemblance is manifest in several aspects. First, both the timing and amount of offset of the modern Phelan Creeks are consistent with those of channel 2-b at the Wallace Creek site. Channel 2-b was incised shortly before a date within the range A.D. 1460–1600 and is offset 15.4 m. The beheaded channel at the Phelan Creeks site was abandoned at the time of incision of the Little and Large Phelan Creeks, which subsequently have been offset about 16 m, respectively. The time of the abandonment was shortly after a date within the range A.D. 1300–1440. Thus the maximum bound on the age of the 16-m offset is constrained by these youngest dates in unit HC-4 within the abandoned channel. Second, both the Phelan Creeks and at Wallace Creek sites exhibited four cuts and fills between about A.D. 500 and 1450. At Phelan Creeks, these were the 4 unconformity-bounded sedimentary units in paleochannel HC. At Wallace Creek, these were channels 3 through channel 6.

[94] A third similarity between the Phelan Creeks and Wallace Creek records is the existence of a long hiatus in erosion and deposition in the centuries before and after A.D.

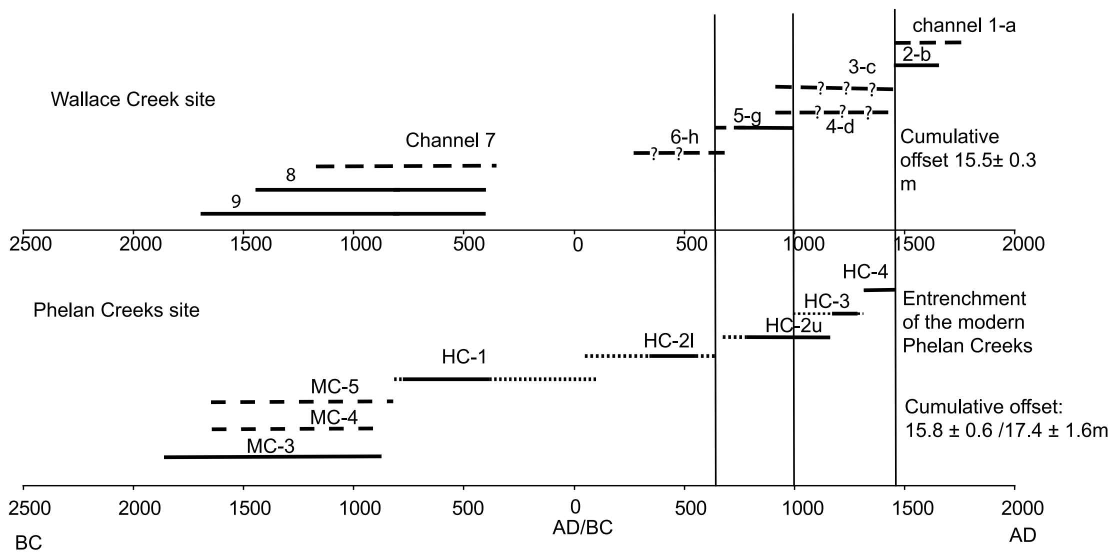

Figure 22. A proposed correlation of the alluvial history at the Wallace Creek site with that at the Phelan Creeks. Horizontal lines represent the age ranges of alluvial events, which are less certain where dashed. The six cut-and-fill events of the past 1500 years at both sites could well be correlative, as could the long hiatus in alluviation and incision centered on A.D. zero.

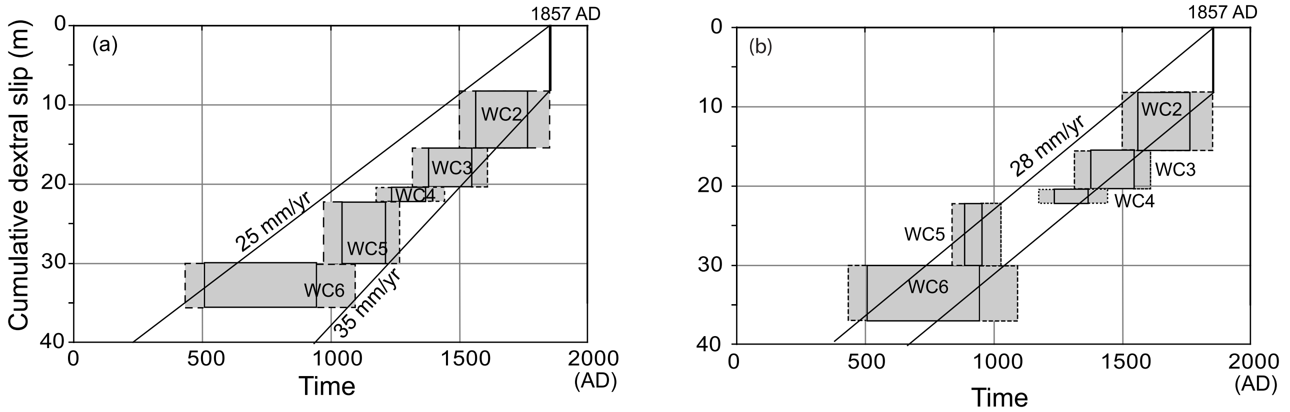

Figure 23. (a) and (b) Different scenarios of a revised slip history for the Wallace Creek site, incorporating age constraints from the nearby Phelan Creeks site. Substitution of age constraints on alluvial events at the Phelan Creeks yields tighter constraints on the dates of paleoseismic events than those derived solely from the Wallace Creek dates (Figure 21). The horizontal dimensions of the gray boxes represent the age constraints of the events; solid lines denoting 1σ uncertainties and dashed lines indicating 2σ uncertainties. Two diagonal lines represent the best estimation of average slip rate; the upper one indicates a slip-predictable idealization, and the lower one indicates a time-predictable idealization. Figures 23a and 23b are identical expect for event WC5.

zero. At Phelan Creeks, this was a 500- to 1000-year hiatus prior to HC-2l. At the Wallace Creek site, the hiatus occurred prior to incision of channel 6-h and after cutting and filling of upstream channel 7. This hiatus corresponded to the long downstream stretch that lacked downstream channels between channels h and i (Figure 4f). This hiatus appears to exist at late Holocene sites elsewhere in southern California, as well. For example, excavations across the Garlock fault, southeast of the Carrizo Plain, showed an extremely low sedimentation rate and less frequent flooding events during the same period [*McGill and Rockwell*, 1998]. Also during the same time period, Walker Lake in west Nevada became shallow and probably desiccated [*Benson et al.*, 1991]. We also find that channel incision at the Wallace Creek and Phelan Creeks sites during the last 1500 years mimic remarkably well the highstands of the Mono Lake [*Stine*, 1990] in eastern California [*Liu*, 2003]. This suggests the alluvial histories have been climatically regulated.

9.2. Revised Dates of Wallace Creek Events Using Phelan Creeks Dates

[95] We infer the ages of some channel fills at Wallace Creek to be the same as those of the sedimentary units at Phelan Creeks. Channel 3-c strata at the Wallace Creek site and correlative Phelan Creeks unit HC-4 would have been deposited about A.D. 1300–1440. Channel 4-d and correlative unit HC-3 would have formed about A.D. 1000–1300 (Figure 22).

[96] If these correlations are correct, the uncertainties in the dates of the offset events WC3, WC4 and WC5 can be narrowed by using tighter bounding ages from Phelan Creeks (Figure 23 and Figure S15). The age of the fifth event WC5, however, is still ambiguous. Figure 23a shows the offset-time plot based on surrogate dates strictly from the Phelan Creek site.

[97] In this scenario, WC5 occurred within the 2σ range of A.D. 970–1270. In the second and less favored scenario, we assume that our sample Dn03-03, an in situ burn, postdates the abandonment of channel 5, thus provides an upper bounding date for WC5. WC5 would have occurred within the 2σ range of A.D. 870–1020 (Figures 23b and S15). Although this age range overlaps with the previous estimation of A.D. 970–1270 within the 2σ uncertainty, the second estimation is significantly older than the first, particularly if one considers the corresponding 1σ age range. This ambiguity may have important implication: the second interpretation of age constraints suggests a slip time pattern more irregular than the first; it also implies a lower slip rate.

[98] The correlation in alluvial history at the Wallace Creek and the Phelan Creeks sites also supports our tentative channel match of channel 6-h: channel 6-h could have been incised about A.D. 250–540. The date of subsequent offset event WC6 still is highly uncertain; it probably occurred sometime between the 6th and 10th centuries (Figure 23).

9.3. Further Constraints From the Bidart Fan Record

[99] The Bidart fan paleoseismic site is on an alluvial fan about 5 km southeast of the Wallace Creek site (Figure 1b).

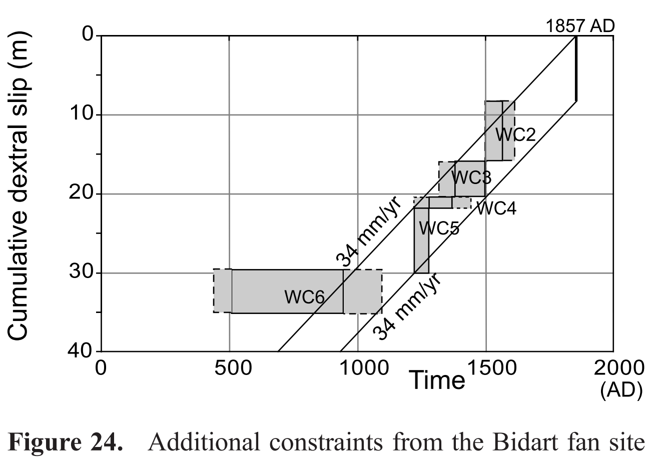

Figure 24. Additional constraints from the Bidart fan site [*Grant and Sieh*, 1994], which further improve the precision of the slip history.

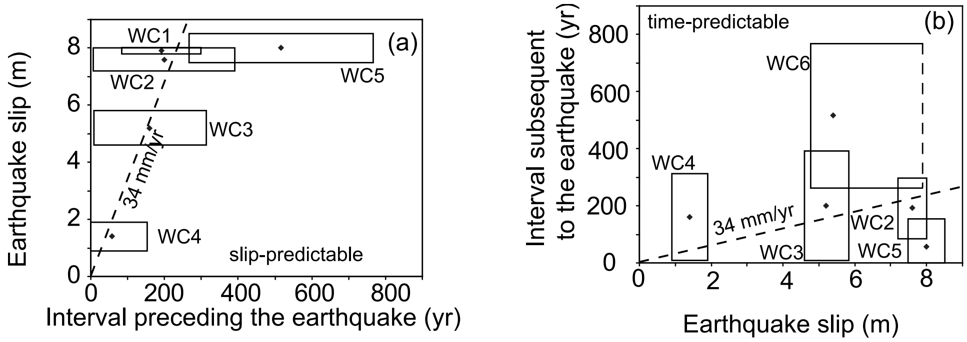

Figure 25. A test of (a) slip-predictable model and (b) time-predictable model, assuming the 4000-year average strain accumulation rate of 34 mm/yr. In Figure 25a, earthquake slip is plotted against the time since the previous earthquake. The slip-predictable model seems to be a good idealization. WC1 through WC4 appear to fall around the dashed line. The poor fit of WC5 could be due to the poorly constrained age of WC6. In Figure 25b, the time interval between two consecutive ruptures is plotted against the slip of the first event. If earthquake occurrence were time-predictable, the points should fall on the dashed line. The time intervals are calculated using 1σ range of events.

Grant and Sieh [1994] documented a sequence of 5 ruptures of the San Andreas fault there, since about A.D. 1200. The latest two events at the Bidart fan (their events A and B) occurred after a date in the range A.D. 1450–1510, and possibly within this range. *Grant and Sieh* [1994] concluded that a gully offset 15 to 18 m at the site represented the cumulative offset of these latest two events, and possibly a third event. The similar magnitude of this offset to the two-event offsets at Wallace Creek and Phelan Creeks suggests that it was the cumulative offset of two events. Radiocarbon dates constrain their other three events (C, D, and E) to have occurred within the period A.D. 1218–1510, with the oldest event (E) being tightly constrained to the period A.D. 1218–1276.

[100] The age constraints from the Bidart site may provide further limits on the date of the five events at Wallace Creek. If the record at the Bidart Fan site is complete for the past five ruptures and if the record at the Wallace Creek site is similarly complete, then their fifth event back (E) would correlate with our event WC5. We would then be able to use the date constraints for event E to bound the date of WC5. Figure 24 shows this modification to the plot of cumulative slip versus time.

10. Discussion and Conclusions

[101] We have recovered from three-dimensional excavations at the Wallace Creek site a well-constrained sequence of the six most recent offsets of the San Andreas fault. Together, they have produced the latest ≥35.5 m of dextral offset. We conclude that the dextral slips associated with the latest six events are, from oldest to youngest, ≥(5.4 ± 0.6), 7.9 ± 0.5, 1.4 ± 0.5, 5.2 ± 0.6, 7.6 ± 0.4 and 7.9 ± 0.1 m.

[102] Although it is possible that smaller events have gone unrecognized in this record, we have found no evidence for them. The resolution of the stratigraphy is such that offsets of 10 cm or so could have gone unrecognized. It is reasonable, yet conservative, to set the lower limit of detection of offsets to be about 0.5 m, about one-third the magnitude of offset WC4. However, the sharp intersections of the gully walls and internal stratigraphy with the fault planes argue against the presence of many of these. Even during long periods of dry conditions, during which gullies would not have been cut, the lack of deflection of the immediately predrought channel rules out the possibility of any of the large offsets being the cumulative result of multiple small-offset events.

[103] Constraints on the timing of the six large events from radiocarbon samples within the excavated volumes are poor. Even so, reasonable correlations with better dated depositional events and hiatuses and ruptures from the nearby Phelan Creeks and Bidart fan sites allow us to construct a useful history of rupture. The average slip rate over the span of the past five events (between A.D. 1210 and 1857) has been 34 mm/yr, a rate indistinguishable from the 3700-year average of 33.9 ± 3 mm/yr [*Sieh and Jahns*, 1984]. It is also similar to geodetically determined strain accumulation rates of 31 to 35 mm/yr over a 175 km aperture spanning the fault [e.g., *Lisowski et al.*, 1991; *Feigl et al.*, 1993].

10.1. Implications for Earthquake Recurrence Models

[104] A remarkable feature in the Wallace Creek offset series is that at least half of the offsets are in the range between 7 and 8 m and that five out of six are greater than 5 m. The asymmetry in the distribution does not prove, but certainly suggests that slips at this location do not result from a uniform random process [*Liu*, 2003]. Furthermore, data at the site do not support a power law frequency-size distribution on a smooth fault as generated by some numerical models [e.g., *Carlson and Langer*, 1989; *Ito and Matsuzaki*, 1990; *Shaw*, 1995; *Cochard and Madariaga*, 1996; *Shaw and Rice*, 2000]. For such models, one would expect that at a given location along the fault, 1- to 2-m offsets would occur far more frequently than 7- to 8-m offsets. To the contrary, our data show that large offsets are far more common than small ones.

[105] Incorporation of the dating constraints from the Phelan Creeks and Bidart fan sites allows us to evaluate the relevance of slip- and time-predictable models [*Shimazaki and Nakata*, 1980]. Assuming a 34 mm/yr strain accumulation rate, a slip-predictable model is an acceptable idealization (Figure 25a). WC5 is the only event that would not fit a slip-predictable model; the time interval preceding WC5 is too long to fit the prediction. However, since the occurrence time of WC6 is ill-con-

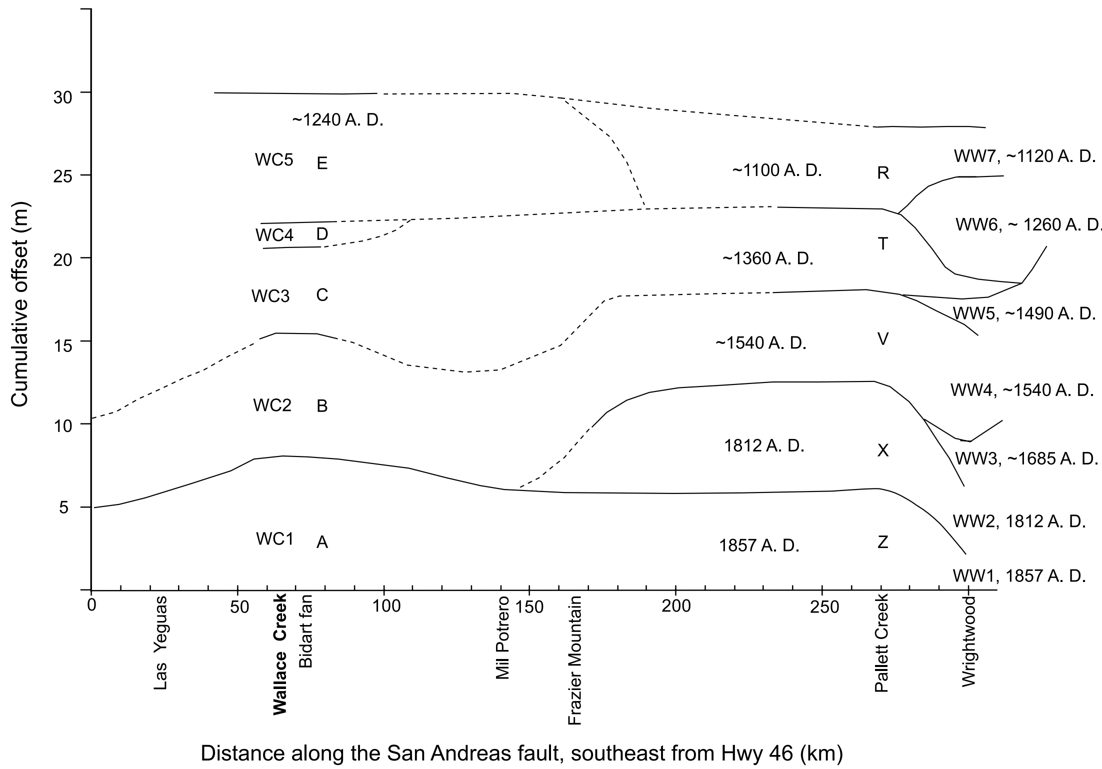

Figure 26. Speculative correlation of earthquake ruptures at the Wallace Creek, the Pallett Creek, and the Wrightwood sites, based on the information of dates of events and slip per events. Data sources for Pallett Creek site are from *Sieh* [1984] and *Salyards et al.* [1992] and for Wrightwood site are from *Weldon et al.* [2004]; slip of the 1857 earthquake is from *Sieh* [1978] and *Lienkaemper and Sturm* [1989].

strained, the time period between WC6 and WC5 could be shorter than the current estimates. A time-predictable model fits the data more poorly than the slip-predictable model (Figure 25b), because of the rapid succession of events WC5, WC4, and WC3. Others have also questioned the applicability of time-predictable models [*Murray and Segall*, 2002; *Weldon et al.*, 2004]. These assessments are important because the time-predictable model is widely used in probabilistic seismic hazard predictions.

[106] Although the dates of the Carrizo Plain events are still too loosely constrained to lend clear support to the slip-predictable model, Figure 25a does show that earthquake slip has a weak but positive correlation with the time interval preceding the earthquake. In particular, large offsets come after long intervals, and small offsets follow short intervals. This contrasts with the interpretation of the Wrightwood paleoseismic site by *Weldon et al.* [2004], 235 km to the southeast on the San Andreas fault. They found a negative correlation between offset magnitude and the period of dormancy prior to a large rupture. The disparity may simply result from different geometric settings of the fault system at the two sites. The Wallace Creek site is located on the central portion of the San Andreas fault, where the fault is geometrically simple. Motion on the San Andreas fault is taken up by a single strand, rather than multiple subparallel strands. Furthermore, 100 km to the north of our site is the Parkfield creeping section of the San Andreas fault, which may serve as a buffer to stop the propagation of ruptures from the north. Thus the Carrizo section of the San Andreas fault may be able to break relatively independently, without influence from the north and from subparallel faults. Near the Wrightwood site, however, the San Andreas fault system is more complex; interference from subparallel faults, such as the San Jacinto fault and Sierra Madre-Cucamonga fault could modulate the earthquake behavior on the San Andreas fault itself [*Palmer et al.*, 1995].

[107] The positive correlation between slip and preparation time at Wallace Creek supports the notion that most accumulated strain is relieved subsequently during large earthquakes. In this sense, the regular occurrence of similar offsets suggests that the concept of the earthquake cycle is most applicable at locations where a fault or fault segment can act independently of other faults [e.g., *Tse and Rice*, 1986; *Ben-Zion*, 1996; *Lapusta et al.*, 2000].

10.2. Correlation of Earthquakes Along the Central San Andreas Fault

[108] Unlike previous correlations along strike, we use both dating constraints on the Wallace Creek site events and the magnitude of slip (Figure 26). We rely principally on data from the Wallace Creek site and the Pallett Creek and Wrightwood sites, because these sites have the longest and best characterized records. One principal constraint on correlations is the number of ruptures that have occurred at the three principal sites since about A.D. 1100. At Wallace Creek, we have documented five events, WC 1 through WC 5. The ages of the events are constrained by history (1857) and by dates of events at the nearby Bidart Fan site. At Pallett Creek, five ruptures have occurred since

about A.D. 1100: events Z, X, V, T, and R. At Wrightwood, six ruptures appear in the record in this same period.

[109] Together, the time and slip constraints from the individual sites suggest that over the past eight centuries, slip has been about uniform along this 220-km reach of the fault (Figure 26). The amount of offset at Pallett Creek may be nearly uniform from event to event, about 6 m each time. Ruptures have been more frequent at Wrightwood, but they have been smaller on average. Furthermore, characteristic earthquakes, with similar rupture extent and slip function, are plausible but not the only form of rupture. Of the most recent five Wallace Creek events, only WC2 may be similar to the 1857 rupture. WC5, though similar in slip to the 1857 event, does not appear to have extended as far south as Pallett Creek.

[110] Some of the correlations suggested in Figure 26 are more speculative than others. For example, we suggest that WC4 propagated into the Wallace Creek site from the northwest and ended a short distance to the southeast. It is also possible that this event actually correlates with event T at Pallett Creek. In that case, it would have extended farther to the south, and later event WC3 would have terminated between Wallace Creek and Pallett Creek. As with every previous correlation chart of paleoseismic events along the San Andreas fault, this one should be viewed as just the latest attempt to make sense of a growing body of paleoseismic information. We hope that more data on both slip timing and magnitude will enable tests of our correlations and eventually lead to a more accurate picture of what has indeed actually occurred.

[111] In conclusion, we have conducted three-dimensional excavations at the Wallace Creek paleoseismic site to reconstruct the slip history at the site. We use stratigraphic evidence for correlating channels across the fault, which is more robust than geomorphologic evidence alone. Closely spaced sequential excavations allow accurate measurements of six pairs of matched channels, with uncertainty on the order of a few tens of centimeters. Evidence suggests strongly that each of the six offset increments represent one rupture event. Thus the right-lateral displacements associated with the last six events are, from youngest to oldest these are 7.9 ± 0.1, 7.6 ± 0.4, 5.2 ± 0.6, 1.4 ± 0.5, 8.0 ± 0.5 m, and > (5.4 ± 0.6). This offset series does not appear to result from a random process, nor from a simple power law process. Constraints on the timing of these events from radiocarbon samples at our site are poor. However, combination with evidence from the nearby Phelan Creeks and Bidart fan sites, allows construction of a useful rupture chronology. The average slip rate during the last millennial has been 34 mm/yr, a rate indistinguishable from the 3700-year average and geodetic rate. Despite large still uncertainty in age ranges, these events suggest earthquake slip at the site has generally a positive correlation with the time interval preceding the event. Smaller offsets coincide with shorter prior intervals and larger offset with longer prior intervals.

[112] **Acknowledgments.** We thank Brandon Maehr for continuous assistance in hand excavations and surveying and Johna Hurl and Kathy Sharum from the Bakersfield office of the Bureau of Land Management for assisting in getting permission to excavate the site. Most of the excavations were done by hand. Brandon Maehr removed at least half of the excavated 450 m^3 of sediment. Additional field assistance was provided by Jim Nye, Clay Stevens, Chris Madden, and Lingsen Zeng. Clay Stevens and O. C. Canto helped digitize the trench logs. We thank Ramon Arrowsmith and John Sims for sharing an unpublished manuscript that describes the paleoseismic investigation of the Phelan Creeks site and Lisa Grant for discussing ^{14}C dates at the Bidart fan site. Ray Weldon's thorough and critical review helped improve the manuscript. This research was partially supported by U.S. Geological Survey grant 99-HQ-GR-0043 and 01-HQ-GR-0002. The work was also partially supported by the Southern California Earthquake Center (SCEC) and private funds.

References

Agnew, D. C., and K. E. Sieh (1978), A documentary study of the felt effects of the great California earthquake of 1857, *Bull. Seismol. Soc. Am.*, *68*, 1717–1729.

Arrowsmith, R. J., D. D. Pollard, and D. D. Rhodes (1998), Morphological dating of scarps formed by repeated slip events along the San Andreas fault, Carrizo Plain, California, *J. Geophys. Res.*, *103*, 10,141–10,160.

Bak, P., and C. Tang (1989), Earthquakes as a self-organized critical phenomenon, *J. Geophys. Res.*, *94*, 15,635–15,637.

Ben-Zion, Y. (1996), Stress, slip, and earthquakes in models of complex single-fault systems incorporating brittle and creep deformations, *J. Geophys. Res.*, *101*, 5677–5706.

Benson, L. V., P. A. Meyers, and R. J. Spencer (1991), Change in the size of Walker Lake during the past 5000 years, *Palaeogeogr. Palaeoclimatol. Palaeoecol.*, *81*, 189–214.

Biasi, G. P., R. J. Weldon II, T. E. Fumal, and G. G. Seitz (2002), Paleoseismic event dating and the conditional probability of large earthquakes on the southern San Andreas fault, California, *Bull. Seismol. Soc. Am.*, *92*, 2761–2781.

Blong, R. J., and R. Gillespie (1978), Fluvially trasported charcoal gives erroneous ^{14}C ages for recent deposits, *Nature*, *271*, 739–741.

Brown, R. D., Jr., and R. E. Wallace (1968), Current and historic fault movement along the San Andreas fault between Paicines and Camp Dix, California, in *Proceedings of Conference on Geologic Problems of San Andreas Fault System*, edited by W. R. Dickinson and A. Grantz, *Stanford Univ. Publ. Geol. Sci.*, *11*, 22–41.

Carlson, J. M., and J. S. Langer (1989), Properties of earthquakes generated by fault dynamics, *Phys. Rev. Lett.*, *62*, 2632–2635.

Cochard, A., and R. Madariaga (1996), Complexity of seismicity due to highly rate-dependent friction, *J. Geophys. Res.*, *101*, 25,321–25,336.

Dibblee, T. W. (1973), Regional geologic map of the San Andreas and related faults in Carrizo Plain, Temblor, Caliente, and La Panza ranges and vicinity, California, *U.S. Geol. Surv. Misc. Geol. Invest. Map, I-757*.

Feigl, K. L. A., et al. (1993), Space geodetic measurement of crustal deformation in central and southern California, 1984–1992, *J. Geophys. Res.*, *98*, 21,677–21,712.

Gaudemer, Y., P. Tapponnier, and D. L. Turcotte (1989), River offsets across active strike-slip faults, *Ann. Tectonicae*, *3*, 55–76.

Grant, L. B., and K. Sieh (1993), Stratigraphic evidence for seven meters of dextral slip on the San Andreas fault during the 1857 earthquake in the Carrizo Plain, *Bull. Seismol. Soc. Am.*, *83*, 619–635.

Grant, L. B., and K. Sieh (1994), Paleoseismic evidence of clustered earthquakes on the San Andreas fault in the Carrizo Plain, California, *J. Geophys. Res.*, *99*, 6819–6841.

Huang, J., G. Narkounskaia, and D. L. Turcotte (1992), A cellular-automata, slider-block model for earthquakes. 2. Demonstration of self-organized criticality for a 2-D system, *Geophys. J. Int.*, *111*, 259–269.

Huang, W. (1993), Morphologic patterns of stream channels on the active Yishu fault, southern Shandong Province, eastern China: Implications for repeated great earthquakes in the Holocene, *Tectonophysics*, *219*, 283–304.

Ito, K., and M. Matsuzaki (1990), Earthquakes as self-organized critical phenomena, *J. Geophys. Res.*, *95*, 6853–6860.

Lapusta, N., J. Rice, Y. Ben-Zion, and G. Zheng (2000), Elastodynamic analysis for slow tectonic loading with spontaneous rupture episodes on faults with rate- and state-dependent friction, *J. Geophys. Res.*, *105*, 23,765–23,789.

Lienkaemper, J. J., and T. A. Sturm (1989), Reconstruction of a channel offset in 1857(?) by the San Andreas fault near Cholame, California, *Bull. Seismol. Soc. Am.*, *79*, 901–909.

Lindvall, S. C., T. K. Rockwell, K. W. Hudnut, and S. N. Ward (1989), Slip distribution of prehistorical earthquakes on the Superstition Hills Fault, San Jacinto Fault zone, southern California, based on offset geomorphic features, *Geol. Soc. Am. Abstr. Programs*, *21*, 973–974.

Lisowski, M., J. C. Savage, and W. H. Prescott (1991), The velocity field along the San Andreas fault in central and southern California, *J. Geophys. Res.*, *96*, 8369–8389.

Liu, J. (2003), Part I. Slip behavior of the San Andreas fault through several earthquake cycles. Part II. A structural interpretation of the aftershock "cloud" of the 1992 M_w 7.3 Landers earthquake, Ph.D. thesis, Calif. Inst. of Technol., Pasadena.

Liu, J., Y. Klinger, K. Sieh, and C. Rubin (2004), Six similar sequential ruptures of the San Andreas fault, Carrizo Plain, California, *Geology*, *32*, 649–652, doi:10.1130/G20478.1.

Lyakhovsky, V., Y. Ben-Zion, and A. Agnon (2001), Earthquake cycle, fault zones, and seismicity patterns in a rheologically layered lithosphere, *J. Geophys. Res.*, *106*, 4103–4120.

McCalpin, J. (Ed.) (1996), *Paleoseismology*, 588 pp., Cambridge Univ. Press, New York.

McGill, S., and T. Rockwell (1998), Ages of late Holocene earthquakes on the central Garlock fault near El Paso Peaks, California, *J. Geophys. Res.*, *103*, 7265–7279.

Murray, J., and P. Segall (2002), Testing time-predictable earthquake recurrence by direct measurement of strain accumulation and release, *Nature*, *419*, 287–291.

Nelson, A. R. (1992), Discordant ^{14}C ages from buried tidal-marsh soils in the Cascadian subduction zone, southern Oregon coast, *Quat. Res.*, *38*, 74–90.

Palmer, R., R. Weldon, E. Humphreys, and F. Saucier (1995), Earthquake recurrence on the southern San Andreas modulated by fault-normal stress, *Geophys. Res. Lett.*, *22*, 535–538.

Pantosti, D., R. Collier, G. D'Addezio, E. Masana, and D. Sakellariou (1996), Direct geological evidence for prior earthquakes on the 1981 Corinth fault (central Greece):, *Geophys. Res. Lett.*, *23*, 3795–3798.

Prentice, C. S., and K. Sieh (1989), A paleoseismic site along the Carrizo segment of the San Andreas fault, central California, *Eos Trans. AGU*, *70*, 1349.

Ramsey, C. B. (1995), Radiocarbon calibration and analysis of stratigraphy: The OxCal program, *Radiocarbon*, *37*, 425–430.

Ramsey, C. B. (2000), OxCal Program ver. 3.5, Radiocarbon Accelerator4 Unit, Univ. of Oxford, Oxford, U. K. (Available at http://www.rlaha.ox.ac.uk/O/oxcal.php)

Ran, Y., R. Duan, Q. Deng, D. Jiao, and W. Min (1997), 3-D trench excavation and paleoseismology at Gaowanzi of the Haiyuan fault (in Chinese with English abstract), *Seismol. Geol.*, *19*(2), 97–107.

Reid, H. F. (1910), The mechanics of the earthquakes, in *The California Earthquake of April 18, 1906*, *Carnegie Inst. Washington Publ.*, *87*(2), 192 pp.

Rice, J. R. (1993), Spatio-temporal complexity of slip on a fault, *J. Geophys. Res.*, *98*, 9885–9907.

Rice, J. R., and Y. Ben-Zion (1996), Slip complexity in earthquake fault models, *Proc. Natl. Acad. Sci. U. S. A.*, *93*, 3811–3818.

Rockwell, T. K., S. Lindvall, M. Herzberg, D. Murbach, T. Dawson, and G. Berger (2000), Paleoseismology of the Johnson Valley, Kickapoo, and Homestead Valley faults: Clustering of earthquakes in the eastern California shear zone, *Bull. Seismol. Soc. Am.*, *90*, 1200–1236.

Rockwell, T. K., S. Lindvall, T. E. Dawson, R. M. Langridge, W. Lettis, and Y. Klinger (2002), Lateral offsets on surveyed cultural features resulting from the 1999 Izmit and Duzce earthquakes, Turkey, *Bull. Seismol. Soc. Am.*, *92*, 79–94.

Rubin, C. M., and K. Sieh (1997), Long dormancy, low slip rate, and similar slip-per-event for the Emerson fault, eastern California shear zone, *J. Geophys. Res.*, *102*, 15,319–15,334.

Rundle, J. B. (1988), A physical model for earthquakes: 2. Application to southern California, *J. Geophys. Res.*, *93*, 6255–6274.

Salyards, S. L., K. E. Sieh, and J. L. Kirschvink (1992), Paleomagnetic measurement of nonbrittle coseismic deformation across the San Andreas fault at Pallett Creek, *J. Geophys. Res.*, *97*, 12,457–12,470.

Schumm, S. A., J. F. Dumont, and J. M. Holbrook (2000), *Active Tectonics and Alluvial Rivers*, 276 pp., Cambridge Univ. Press, New York.

Schwartz, D. P., and K. J. Coppersmith (1984), Fault behavior and characteristic earthquakes: Examples from the Wasatch and San Andreas fault zones, *J. Geophys. Res.*, *89*, 5681–5698.

Sharp, R. V., et al. (1982), Surface faulting in the central Imperial Valley, in *The Imperial Valley, California, Earthquake of October 15, 1979*, *U.S. Geol. Surv. Prof. Pap.*, *1254*, 119–143.

Shaw, B. E. (1995), Frictional weakening and slip complexity in earthquake faults, *J. Geophys. Res.*, *100*, 18,239–18,252.

Shaw, B. E., and J. R. Rice (2000), Existence of continuum complexity in the elastodynamics of repeated fault ruptures, *J. Geophys. Res.*, *105*, 23,791–23,810.

Shimazaki, K., and T. Nakata (1980), Time-predictable recurrence model for large earthquakes, *Geophys. Res. Lett.*, *7*, 279–282.

Sieh, K. E. (1978), Slip along the San Andreas fault associated with the great 1857 earthquake, *Bull. Seismol. Soc. Am.*, *68*, 1421–1448.

Sieh, K. E. (1981), A review of geological evidence for recurrence times of large earthquakes, in *Earthquake Prediction: An International Review*, *Maurice Ewing Ser.*, vol. 4, edited by D. W. Simpson and P. G. Richards, pp. 181–207, AGU, Washington, D. C.

Sieh, K. E. (1984), Lateral offsets and revised dates of large prehistoric earthquakes at Pallett Creek, southern California, *J. Geophys. Res.*, *89*, 7641–7670.

Sieh, K. (1986), Slip rate across the San Andreas fault and prehistoric earthquakes at Indio, California, *Eos Trans. AGU*, *67*(44), 1200.

Sieh, K. E. (1996), The repetition of large-earthquake ruptures, *Proc. Natl. Acad. Sci. U.S.A.*, *93*, 3764–3771.

Sieh, K. E., and R. H. Jahns (1984), Holocene activity of the San Andreas fault at Wallace Creek, California, *Geol. Soc. Am. Bull.*, *95*, 883–896.

Sims, J. D. (1994), Stream channel offset and abandonment and a 200-year average recurrence interval of earthquake on the San Andreas fault at Phelan Creeks, Carrizo Plain, California., in *Proceedings of the Workshop on Paleoseismology*, edited by C. S. Prentice, D. P. Schwartz, and R. S. Yeats, *U. S. Geol. Surv. Open File Rep.*, *94-568*, 170–172.

Stine, S. (1990), Late Holocene fluctuations of Mono Lake, eastern California, *Paleogeogr. Paleoclimatol. Paleoecol.*, *78*, 333–381.

Stuart, W. D. (1986), Forecast model for large and great earthquakes in southern California, *J. Geophys. Res.*, *91*, 13,771–13,786.

Stuiver, M., P. J. Reimer, E. Bard, J. W. Beck, G. S. Burr, K. A. Hughen, B. Kromer, G. McCormac, J. van der Plicht, and M. Spurk (1998), INTCAL98 radiocarbon age calibration, 24,000-0 cal BP, *Radiocarbon*, *40*, 1041–1083.

Tse, S. T., and J. R. Rice (1986), Crustal earthquake instability in relation to the depth variation of frictional slip properties, *J. Geophys. Res.*, *91*, 9452–9472.

Vaughan, P. R., K. M. Thorup, and T. K. Rockwell (1999), Paleoseismology of the Elsinore fault at Agua Tibia Mountain, southern California, *Bull. Seismol. Soc. Am.*, *89*, 1447–1457.

Wallace, R. E. (1968), Notes on stream channels offset by the San Andreas fault, in *Proceedings of Conference on Geologic Problems of the San Andreas Fault*, edited by W. R. Dickinson and A. Grantz, *Stanford Univ. Publ. Geol. Sci.*, *11*, 6–21.

Ward, S. N. (1997), Dogtails versus rainbows; synthetic earthquake rupture models as an aid in interpreting geological data, *Bull. Seismol. Soc. Am.*, *87*, 1422–1441.

Ward, S. N., and S. D. B. Goes (1993), How regularly do earthquakes recur? A synthetic seismicity model for the San Andreas fault, *Geophys. Res. Lett.*, *20*, 2131–2134.

Weldon, R. J., T. E. Fumal, T. J. Powers, S. K. Pezzopane, K. M. Scharer, and J. C. Hamilton (2002), Structure and earthquake offsets on the San Andreas fault at the Wrightwood, California, paleoseismic site, *Bull. Seismol. Soc. Am.*, *92*, 2704–2725.

Weldon, R., K. Scharer, T. Fumal, and G. Biasi (2004), Wrightwood and the earthquake cycles: What a long recurrence record tells us about how faults work, *GSA Today*, *14*(9), 4–10.

Wood, H. O. (1955), The 1857 earthquake in California, *Bull. Seismol. Soc. Am.*, *45*, 47–67.

Working Group of California Earthquake Probability (1988), Probabilities of large earthquakes occurring in California along the San Andreas fault, *U.S. Geol. Surv. Open File Rep., 88-398*.

Working Group of California Earthquake Probability (1995), Seismic hazards in southern California: Probable earthquakes, 1994–2024, *Bull. Seismol. Soc. Am.*, *85*, 379–439.

Yeats, R., K. Sieh, and C. Allen (1997), *The Geology of Earthquakes*, 568 pp., Oxford Univ. Press, New York.

Y. Klinger, Laboratoire de Tectonique, Institut de Physique du Globe Paris, 4 place Jussieu, F-75252 Paris cedex 05, France.

J. Liu-Zeng, Institute of Tibetan Plateau Research, Chinese Academy of Sciences, 18 Shuang Qing Road, P.O. Box 2871, Beijing 100085, China. (liu-zeng@itpcas.ac.cn)

C. Rubin, Department of Geological Sciences, Central Washington University, Ellensburg, WA 98926, USA.

G. Seitz, Department of Geological Sciences, San Diego State University, San Diego, CA 92182-1020, USA.

K. Sieh, Division of Geological and Planetary Sciences, California Institute of Technology, Pasadena, CA 91125, USA.

Bulletin of the Seismological Society of America, Vol. 95, No. 5, pp. 1970–1987, October 2005, doi: 10.1785/0120040233

High-Resolution Satellite Imagery Mapping of the Surface Rupture and Slip Distribution of the M_w ~7.8, 14 November 2001 Kokoxili Earthquake, Kunlun Fault, Northern Tibet, China

by Yann Klinger, Xiwei Xu, Paul Tapponnier, Jérome Van der Woerd, Cecile Lasserre, and Geoffrey King

Abstract The M_w 7.8 Kokoxili earthquake of 14 November 2001, which ruptured a 450-km-long stretch of the sinistral Kunlun strike-slip fault, at the northeastern edge of the Tibet plateau, China, ranks as the largest strike-slip event ever recorded instrumentally in Asia. Newly available high-resolution satellite HRS images (pixel size $\leq$1 m) acquired in the months following the earthquake proved a powerful tool to complement field investigations and to produce the most accurate map to date of the coseismic displacements along the central Kusai Hu segment of the rupture. The coseismic rupture geometry south and west of Buka Daban Feng, near the earthquake epicenter, was also investigated in detail. Along the Kusai Hu segment, slip partitioning is for the first time observed to occur simultaneously during a single event, with two parallel strands, ~2 km apart, localizing almost pure strike-slip and normal faulting. In all, 83 new HRS coseismic offset measurements, some of which calibrated by field work, show large, well-constrained variations ($\geq$100%) of the slip function over distances of only ~25 km. Tension cracks opening ahead of the shear dislocation and later offset by the upward propagating strike-slip rupture were observed, demonstrating that the rupture front propagated faster at depth than near the surface. The triple junction between the central Kusai Hu segment, the Kunlun Pass fault, where the rupture ended, and the Xidatan–Dongdatan segment, which could be the next segment to fail along the main Kunlun fault, acted as a strong barrier, implying that direct triggering of earthquake rupture on the Xidatan–Dongdatan segment by Kokoxili-type earthquakes may not be the rule.

Introduction

The M_w 7.8 Kokoxili earthquake of 14 November 2001 (also known as the Kunlun Shan earthquake [China Seismological Bureau, 2002]) was characterized by a fast eastward-propagating pulse of left-lateral slip (Bouchon and Vallée, 2003) that ruptured the Kunlun fault in northern Tibet (Figs. 1, 2) over a total distance of about 450 km (Xu *et al.*, 2002; Lin *et al.*, 2003; Antolik *et al.*, 2004). It is one of the largest continental strike-slip earthquakes ever recorded. Despite the efforts of several teams, the remoteness and high elevation of the fault and the great length of the surface break hampered exhaustive, systematic mapping of the slip along the surface rupture in the field. This rupture is often multistranded, which makes precise measurements of multiple coseismic offsets of clean piercing lines a formidable task. Hence, only partial and scattered measurements have been collected thus far. They provide a first-order shape of the slip function, but with limited detail and inconsistencies in several places (Lin *et al.*, 2002; Xu *et al.*, 2002). To document more thoroughly and quantitatively the slip and its variability along the rupture, we complemented our two field investigations by mapping the surficial breaks with recently available 1-m-resolution Ikonos and 60-cm-resolution Quickbird satellite images (later designated as high-resolution satellite [HRS] images) acquired after the earthquake. We present here the results of this work along a 100-km-long stretch of the main Kusai Hu segment of the fault (Fig. 2). Using this new tool, we are able to describe the full complexity of the surface rupture, and to obtain many measurements of coseismic displacements associated with the 14 November 2001 earthquake. The central part of the rupture was targeted for HRS image acquisition in the hours following the earthquake, since it became rapidly clear that it was the locus of the maximum amounts of coseismic slip (Kikuchi and Yamanaka, 2001; Xu *et al.*, 2002; Lin *et al.*, 2002, 2003; Antolik *et al.*, 2004). Our mapping illustrates a remarkable example of partitioning between coseismic strike-slip and

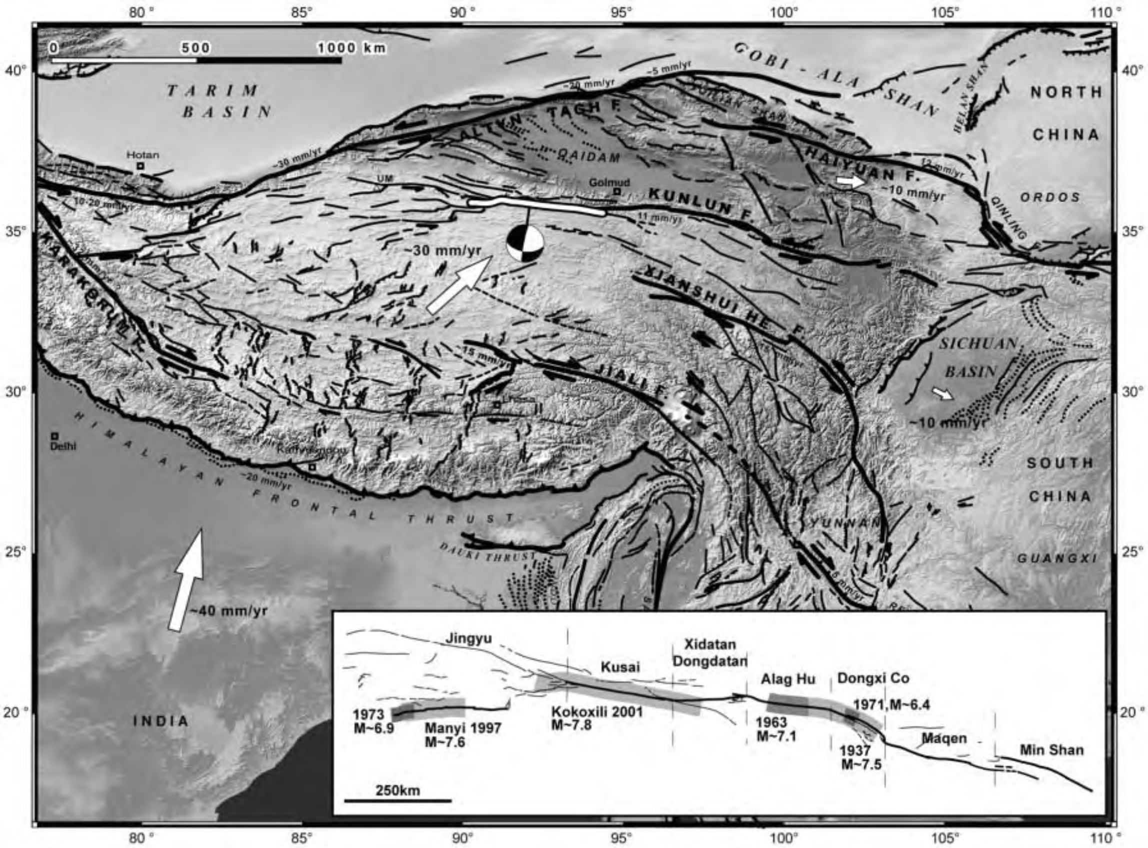

Figure 1. Main active faults of the Tibetan part of the India–Asia collision zone (modified from Tapponnier *et al.*, 2001). The 450-km-long rupture of the M_w ~7.8 Kokoxili earthquake (14 November 2001) is outlined in white, with centroid focal sphere (Harvard). The small triangle labeled UM is Ulugh Mustagh (7723 m). Inset shows earthquake dislocations along the Kunlun fault since 1930, emphasizing the very long rupture length of the 14 November 2001 earthquake and the seismic gap along the Xidatan–Dongdatan segment (different shades are used to distinguish between overlapping ruptures, modified from Van der Woerd *et al.* [2002b]).

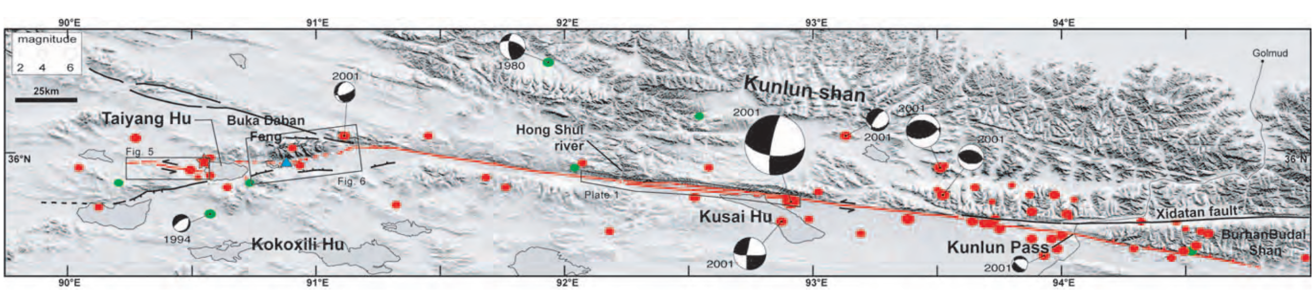

Figure 2. Rupture map of the Kokoxili earthquake. Earthquakes prior to 2001 are in green, aftershocks of the Kokoxili earthquake, in red (locations from NEIC). Focal mechanisms are from the Harvard database. For the Kokoxili main shock, the centroid moment tensor is shown. Red star, epicenter; blue triangle, hot springs. Places visited during fieldwork campaigns include areas described in Figures 5 and 6 and Plate 1, and the region east of the Plate 1 edge, as well as southeast of the Kunlun Pass. Topography is from the Space Radar Topographic Mission (SRTM) database.

normal faulting along a 70-km-long subsegment of the rupture, and affords glimpses into the time history of vertical edge-dislocation propagation (Bowman *et al.*, 2003; King *et al.*, 2005). It also provides exceptional insight into the spatial, multiscale complexity of the seismic rupture.

Seismotectonic Setting of the Kokoxili Earthquake

Together with the Haiyuan, Altyn Tagh, Xianshui He, and Karakorum faults, the Kunlun fault is one of the main faults accommodating the present-day eastward extrusion of the Tibet plateau (Fig. 1) in response to the ongoing collision between India and Asia (Tapponnier and Molnar, 1977; Tapponnier *et al.*, 2001; Wang *et al.*, 2001). Seismic tomography studies suggest that such faults extend as shear zones deep into the mantle (Wittlinger *et al.*, 1998; Vergne *et al.*, 2002; Wittlinger *et al.*, 2004), localizing a large part of the lithospheric deformation. All of them have been sites of great earthquakes ($7.5 \leq M \leq 8.5$) during the past centuries (e.g., Gu *et al.*, 1989).

The Kunlun fault is about 1600 km long, extends from 86°E to 105°E, and strikes N100°E on average. Running along the south side of the Kunlun range, it follows the north edge of the high Tibet plateau (~5000 m above sea level [asl]). Based on dated offset geomorphic markers (Van der Woerd *et al.*, 1998, 2000, 2002b) and geodetic measurements (Wang *et al.*, 2001), the Kunlun fault has been shown to slip left-laterally at about 1 cm/yr on both decadal and millennial timescales. The main stretch of the Kunlun fault may be divided into six first-order segments delimited by geometric irregularities (Van der Woerd *et al.*, 1998). The westernmost horsetail of the fault comprises two segments, the Manyi segment to the south and the Jingyu segment to the north, splaying apart at Buka Daban Feng (also named Qinxing Feng) (Fig. 1, insert, [Van der Woerd *et al.*, 2002a]). The lengths of the different segments are variable, with rather linear segments over 200 km long, and shorter 100 to 150-km-long segments, separated by large-scale jogs or secondary splays. The Kusai segment, named for the largest lake it crosses, ruptured during the 14 November 2001 earthquake and is the longest rectilinear segment of the fault (270 km) (Fig. 2). To the west, the Manyi segment (Fig. 1) ruptured 4 yr prior to 2001, during the 1997 M_w 7.6 earthquake that produced a 170-km-long surface break with maximum offsets on the order of 7 m (Peltzer *et al.*, 1999; Velasco *et al.*, 2000). Farther west, magnitude ~7.3 earthquakes in 1973 had ruptured oblique, left-lateral faults, south of Ulugh Mustagh (Tapponnier and Molnar, 1977). In the east, two other segments of the Kunlun fault have ruptured since 1930: the Dongxi Co earthquake (35.5°N–97.5°E, 1937) (Fig. 1) with an estimated magnitude M ~7.5 (Jia *et al.*, 1988) reportedly produced about 150 km of surficial ruptures. Sinistral rill offsets of 4 m corresponding to this earthquake have been measured near the eastern end of that rupture (Van der Woerd *et al.*, 2000, 2002b). In 1963 an earthquake of estimated magnitude M ~7 occurred ~100 km west of Donxi Co, along the Alag Hu segment of the fault (Fig. 1), with reported surface offsets of several meters (Li and Jia, 1981). The focal mechanism was determined to be left-lateral strike-slip (Fitch, 1970; Tapponnier and Molnar, 1977). No large earthquake had been instrumentally recorded prior to 2001 along the Kusai Hu segment of the fault. The only significant instrumental events in the region are the M ~5.8 earthquakes in 1980 and in 1994, located 50 km north and 60 km south of the western end of the Kusai Hu segment, respectively (Fig. 2). The 1980 earthquake had a left-lateral focal mechanism with a significant thrust component. The fault plane solution of the 1994 earthquake, southwest of Buka Daban Feng, within the extensional horsetail of the fault, displays clear normal faulting on northeast-trending planes, in good agreement with mapped local active faults (Fig. 2) (Van der Woerd *et al.*, 2002b). East of the Kunlun Pass, between the 2001 Kusai Hu and the 1937–1963 Dongxi Co–Alag Hu ruptures, it seems that no large earthquakes occurred in the last 300 yr, at least on the Xidatan–Dongdatan segment of the fault (Fig. 1). This singles out that segment as the last one that might be close to failure between E92° and E103° (Van der Woerd *et al.*, 2002a; Xu *et al.*, 2002).

Methods

We reached the eastern end, the central Kusai Hu segment, and the western end of the rupture during two fieldwork campaigns in May 2002 and November 2003, respectively. At several places in these areas we measured, with a total station, clearly offset geomorphic piercing lines. Such measurements are accurate to within a few centimeters, the greatest source of error being the definition of the geomorphic features themselves. Because most of the markers are of natural, not man-made, origin, the greatest difficulty is usually to make sure that the offset features (rills, risers, etc.) are young enough to have been affected by one earthquake only. Inclusion of cumulative offsets of more ancient surface markers typically leads to unrealistically large last-event offsets (see differences between Lin *et al.* [2002] and Xu *et al.* [2002]). The main value of accurate total station measurements in the field is to provide solid quantitative ground truth. The drawback is that for a 450-km-long rupture, logistical constraints and fast scarp degradation dramatically limit the number of piercing lines sites quantifiable in this way.

To complement fieldwork, we used newly available HRS images to study and quantify the details of the rupture complexity. The HRS images (Ikonos and Quickbird) have a nominal pixel resolution of 1 m and 60 cm, respectively, and are thus at least 10 times more accurate than satellite images such as Spot, Landsat TM, or ASTER, which are commonly used in neotectonic studies. They allow detection of all cracks wider than ~0.5 m and measurement of minimum horizontal offsets of the same order (≥50 cm) (Fig. 3). In fact, for the first time, they make mapping of surface

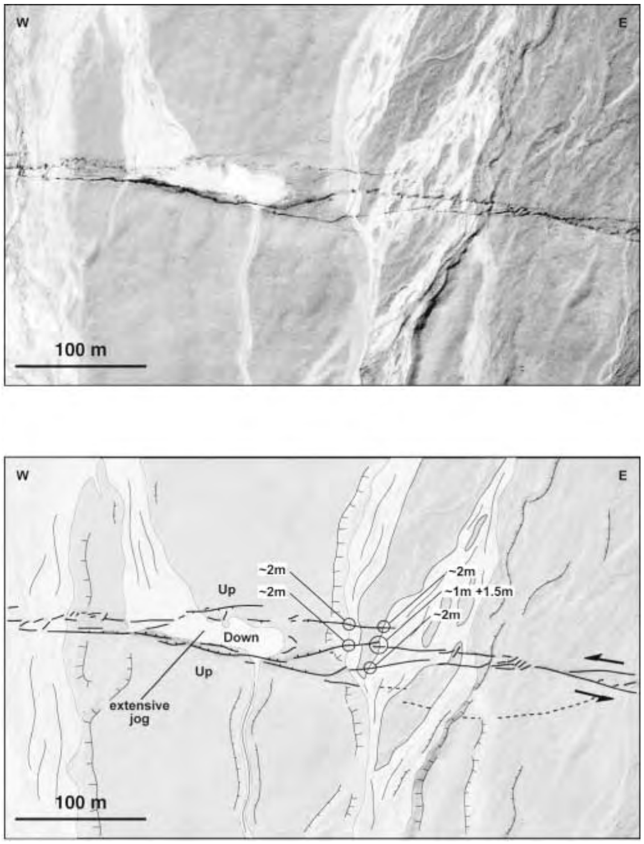

Figure 3. Example of mapping ground rupture with HRS images. Details down to ~50 cm are visible. The drainage network and terrace risers provide good piercing lines to measure sinistral offsets. Vertical throw along ruptures can only be estimated qualitatively from shading, stream capture, rupture geometry, surface deposition, erosion, and so on, as is clear for the small extensive jog. Location on Plate 1.

breaks of large earthquakes possible from optical space images. Plate 1 (unbound insert to this issue) shows the 100 × 5 km continuous swath of HRS images covering the central part of the Kusai Hu segment (Fig. 2) acquired after the 14 November 2001 earthquake. The strip map of the rupture derived from the HRS images, after georeferencing (Plate 1), shows most of the surface breaks that can be resolved on the images. Along with the detailed mapping of the rupture geometry, the HRS images are used to determine coseismic offsets associated with the November 2001 earthquake. To better assess measurement uncertainties, suitable measurement sites were cropped and resampled at 0.5 m/pixel. Stretching of the tonal response was used to increase contrast and clarity. Although we think that in most cases we can restore offsets to within 0.5 m, we conservatively take error bars on reconstructed offset measurements to be on order of ±1 pixel (±1 m). This technique not only rapidly provides a larger number of measurements compared with what can be achieved in the field, but also yields overviews of each piercing point site, limiting possibilities for erroneous mismatch (see the discussion of the Galway Lake Road offset measurements after the Landers earthquake in McGill and Rubin [1999] for a good example of this problem) and total station data projection problems due to local variation of the strike of the fault. Figure 4 illustrates the good match obtained at a site with measurements both in the field and with HRS images. Reconstruction of the beach lines on the HRS image yields an average offset of 5.5 ± 1 m (Fig. 4a and b), independently of who is performing the back-step restoration. Measuring the same features in the field leads to a comparable average horizontal offset of 5.3 m, validating the method (Fig. 4c and d). The slight difference (~10%) is due to a combination of factors: the difficulty in pinpointing the exact shape of the offset piercing line in the field, the poor definition of that line, the lack of perspective of the operator holding the staff, the variable width of the rupture zone, and the uncertainty in determining the exact angle to use to project total station profiles on the fault plane.

Outside the central Kusai Hu segment swath, other stretches of the rupture were later targeted for HRS image acquisition, but snow cover unfortunately hampered very detailed mapping and accurate offset measurements.

Geometry of the 2001 Kokoxili Earthquake Rupture

According to our observations, the November 2001 earthquake rupture appears to extend westward as far as ~90°15′E longitude. Besides rupturing the entire length of the Kusai segment of the Kunlun fault and part of the Kunlun Pass fault to the east (Figs. 1 and 2) (Lin *et al.*, 2002; 2003; Van der Woerd *et al.*, 2002a; Xu *et al.*, 2002), the earthquake dislocation broke the surface along a secondary strand of the fault, west of Taiyang Hu (Figs. 2 and 5). This is in keeping with the location of the instrumentally determined epicenter of the earthquake (National Earthquake Information Center [NEIC]), which is near the western shore of Taiyang Hu. The main dislocation then propagated eastward, reaching the Kusai segment of the fault through a series of oblique en echelon fault segments following the steep Southeast range front of the Buka Daban Feng. After fast propagation (Antolik *et al.*, 2004; Bouchon and Vallée, 2003) for about 270 km along the remarkably straight Kusai segment, the dislocation continued along the Kunlun Pass fault, leaving the Xidatan segment unbroken, to finally die off 70 km east of the Kunlun Pass (Fig. 2).

The following sections provide an overview, from west to east, of our mapping of the rupture, tied to the different styles of surface deformation we observed during our two field investigations, in May 2002 and November 2003.

West Taiyang Restraining Bend

We were able to trace the ground rupture westward to ~N35°57.6′, E90°16.2′ (Fig. 5, epicenter provided by NEIC: N35°57′, E90°32.4′), where it consists of only a few en echelon tension cracks. From that point eastward coseismic sin-

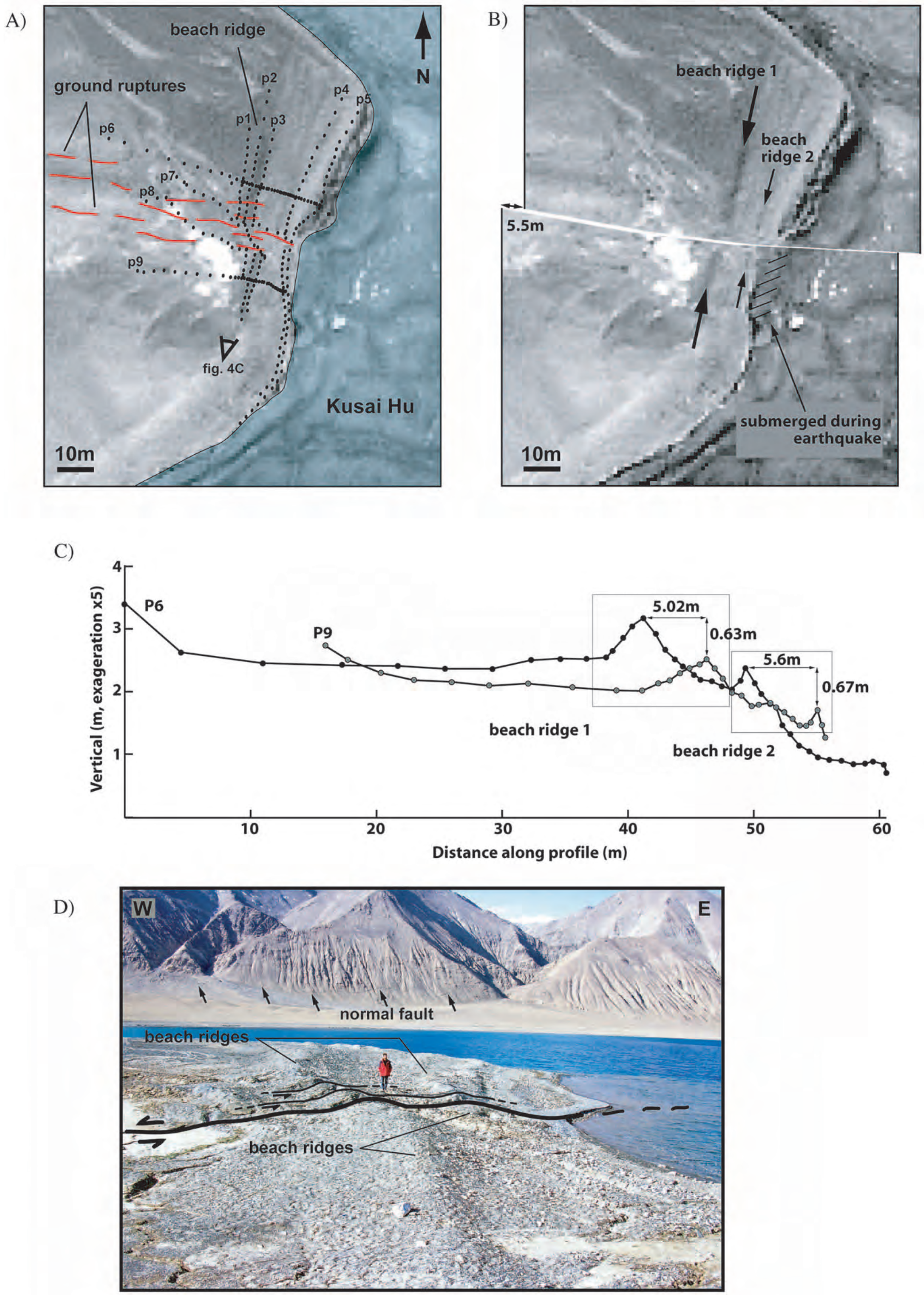
A)
beach ridge
ground ruptures
p1
p2
p3
p4
p5
p6
p7
p8
p9
N
fig. 4C
Kusai Hu
10m
B)
beach ridge 1
beach ridge 2
5.5m
submerged during earthquake
10m
C)
Vertical (m, exageration x5)
Distance along profile (m)
P6
P9
5.02m
0.63m
5.6m
0.67m
beach ridge 1
beach ridge 2
D)
W
E
normal fault
beach ridges
beach ridges

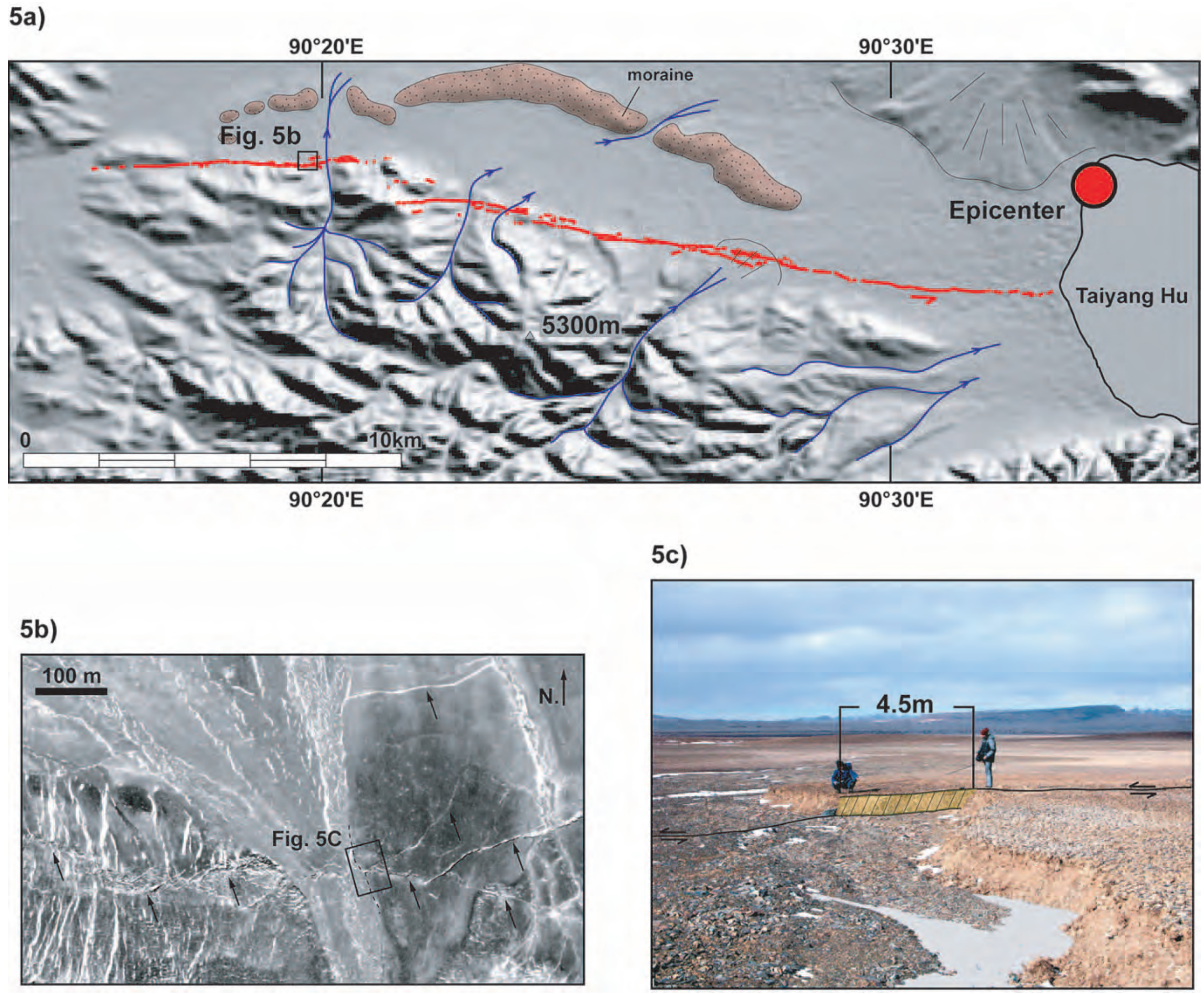

Figure 5. (a) Map of surface break west of Taiyang Hu, based on field observations and HRS images taken after the 14 November 2001 earthquake. Snow cover hampered systematic determination of accurate coseismic slip values. (b) Extract of HRS image showing ground rupture and the location of one clear 4.5-m terrace riser offset. (c) Field photograph of the 4.5-m terrace riser offset.

Figure 4. Offset of shoreline beach ridges east of large pull-part/push-up kink on the peninsula along the northern shore of Kusai Lake. (A) Profiles surveyed with the total station superimposed onto the HRS image. (B) 5.5-m retrodeformation of the shoreline to initial geometry before the Kokoxili event. (C) Projection of profiles 6 and 9 on the N102°E-striking plane, following the rupture zone. (D) Photograph, looking north, of offset beach ridges and of the range front normal fault, in background. Location on Plate 1.

istral slip increases rapidly, and the rupture takes the characteristic aspect of strike-slip surface breaks, with alternating pressure ridges and sag ponds. Few unambiguous coseismic offsets are clear in this flat area, however. We measured only one large unquestionable terrace riser offset (4.5 m at N35°57.6′, E90°19.8′, Fig. 5). At N35°57.6′, E90°21′, a 15° clockwise change of azimuth occurs, coinciding with a 1.4 km southward rupture jump and overlap. The strike of the rupture zone east of this bend is ~N110, close to the overall orientation of the Kunlun fault. The right-stepping overlap and restraining geometry of the bend suggest local shortening and folding within a 10-to 20-km long push-up (Fig. 5). East of the bend, the rupture remains within the mountainous terrain located south of the range front, and is discontinuous, with overlapping right-stepping segments typically 2 km long. The corresponding distributed deformation made unambiguous geomorphic offset measurements difficult. East of ~E90°25′, the rupture zone reaches back into the alluvial piedmont. We observed that only 2 yr after the earthquake coseismic deformation features had often already been almost completely washed out by the summer floods of seasonal streams. Elsewhere, the smoothed-out, cumulative relief of the fault scarp (down to the north, by about 1 to 2 m, much greater than that from the 2001 earthquake), however, indicates previous rupturing during the late Holocene. We could not trace the 2001 surface breaks to the Taiyang Lake shoreline in the field, but clear en echelon cracks may be followed to this shore on the HRS images (acquired earlier than our field campaign), attesting that the rupture did enter the lake. Careful inspection of the southern shoreline of the lake and of the southern edge of the sediment-filled trough south of the Buka Daban Feng show little evidence of coseismic 2001 surface rupture, with the exception of one short, completely isolated break (N35°53.4′, E90°42.6′) displaying mostly vertical throw, down to the north, over a distance of only a few hundred meters. Other well-smoothed-out scarps farther east likely correspond to older events.

Buka Daban Feng Oblique Normal Fault Corridor

The main fresh rupture zone likely comes back ashore along the northern side of Taiyang Hu. East of 35°57.4′ we mapped the 2001 break, with a down-to-the-south throw of 30 cm and a minor left-lateral strike-slip component that increases eastward. The broad alluvial fans that slope down from the range front to the small lake east of Taiyang Hu show large cracks oriented N108° on average, some with meter-wide opening. They probably formed as a result of spreading of the alluvial sediment apron toward the lake during intense seismic shaking.

The overall geometry of the earthquake rupture, which enters Taiyang Hu near its southwest corner and comes out of it near its northeast corner, indicates that the lake floods a pull-apart located within a left-stepping extensional jog of the Kunlun fault south branch. This rupture geometry, which is similar to that observed for the 1951 Damxung earthquake on either side of Beng Co Lake in southeast Tibet (Armijo *et al.*, 1989), implies that, given the location of the 14 November 2001 earthquake epicenter provided by NEIC (Fig. 2), rupture may have started within the pull-apart jog, a clear geometric asperity, and propagated eastward and westward, away from the lake (Lin *et al.*, 2003).

Below the main summit of the Buka Daban Feng range (Fig. 6), the main 2001 rupture zone is well developed, with en echelon subsegments striking N60° on average. The rupture crosses a hydrothermal field with hot springs aligned along it over a length of about 1.5 km (Fig. 7a). The rupture usually forms a dense array of en echelon fissures, with one stretch showing a prominent scarp with up to 1 m of left-lateral coseismic slip and several tens of centimeters of down-to-the-north throw. Cumulative deformation due to older events is clear. According to local eyewitnesses, hydrothermal outputs increased following the 2001 earthquake. The hydrothermal springs, already reported on geological maps, comprise many vents with surging hot or boiling water, but no H_2S. The freshly open fissures of the 2001 surface breaks also exhale water vapor. The origin of the heat cannot be assessed without heat flow measurements and subsurface investigation. While the hydrothermal vents are localized along the strike-slip surface rupture, they are also located within the extensional trough connecting the west Taiyang Hu and Kusai segments of the fault. This extensional corridor is bounded by very asymmetric range fronts, attesting to large differences in uplift rate (Figs. 2 and 6). A discontinuous front, well dissected in the east, characterizes the south side of the corridor, suggesting slow or incipient differential uplift, except west of 90.83°E. The maximum elevation is ~5500 m asl, only ~600 m above the trough floor (~4880 m asl). To the north, by contrast, steep triangular facets, more than 500 m high, bound the ice-capped Buka Daban Range (Fig. 6), which culminates at 6880 m asl, feeding eight large glaciers that pond in the trough. Large moraines and widespread till surround the toes of these glaciers. Six of them swing southwestward as they exit the range front, between the triangular facets, in a direction opposite to that of the overall, east-directed drainage of the trough. This westward swing may be due to channeling of the glaciers in a smaller graben following the range front, as suggested by the mountain-facing scarp located just east of the hot springs (Fig. 6). Sinistral offsets of the glaciers' lateral moraines are unclear, unlike those observed at glacial sites along other Tibetan strike-slip faults (Lasserre *et al.*, 2002; Meriaux *et al.*, 2004; Chevalier *et al.*, 2005). This may be due to the fact that, in the current interglacial, the glaciers still cross the range-front fault. Within the moraines at the base of Buka Daban Feng, evidence of surface rupture is unclear. Vertical motion may be distributed into numerous parallel or en echelon normal fault strands within the unconsolidated till, as suggested by the presence of multiple landslide head-scarps aligned along the moraine talus. Neither did we find unambiguous evidence for a fresh 2001 rupture at the base of the large triangular facets. Along the eastern part of the Buka Daban range front (Fig. 6), the 2001 rupture becomes more localized, with a clear south-facing normal scarp accommodating 1 to 2 m of throw, with a 1 to 1.5 m high free face (Fig. 7b). At places, a comparable amount of additional warping brings the total 2001 throw to 2 to 4 m. The horizontal slip component is not clear enough to be quantified. The area shows intense fissuring, with cracks over 30 cm wide. To the northeast, this prominent normal fault scarp meets with the Kunlun Shan range front, as the 2001 rupture bends clockwise by ~20°. It then follows this N105° striking front, resuming a predominantly strike-slip character. This sharp bend marks the western extremity of the Kusai Hu segment of the fault. That the 2001 earthquake epicenter was located in Taiyang Hu may account for

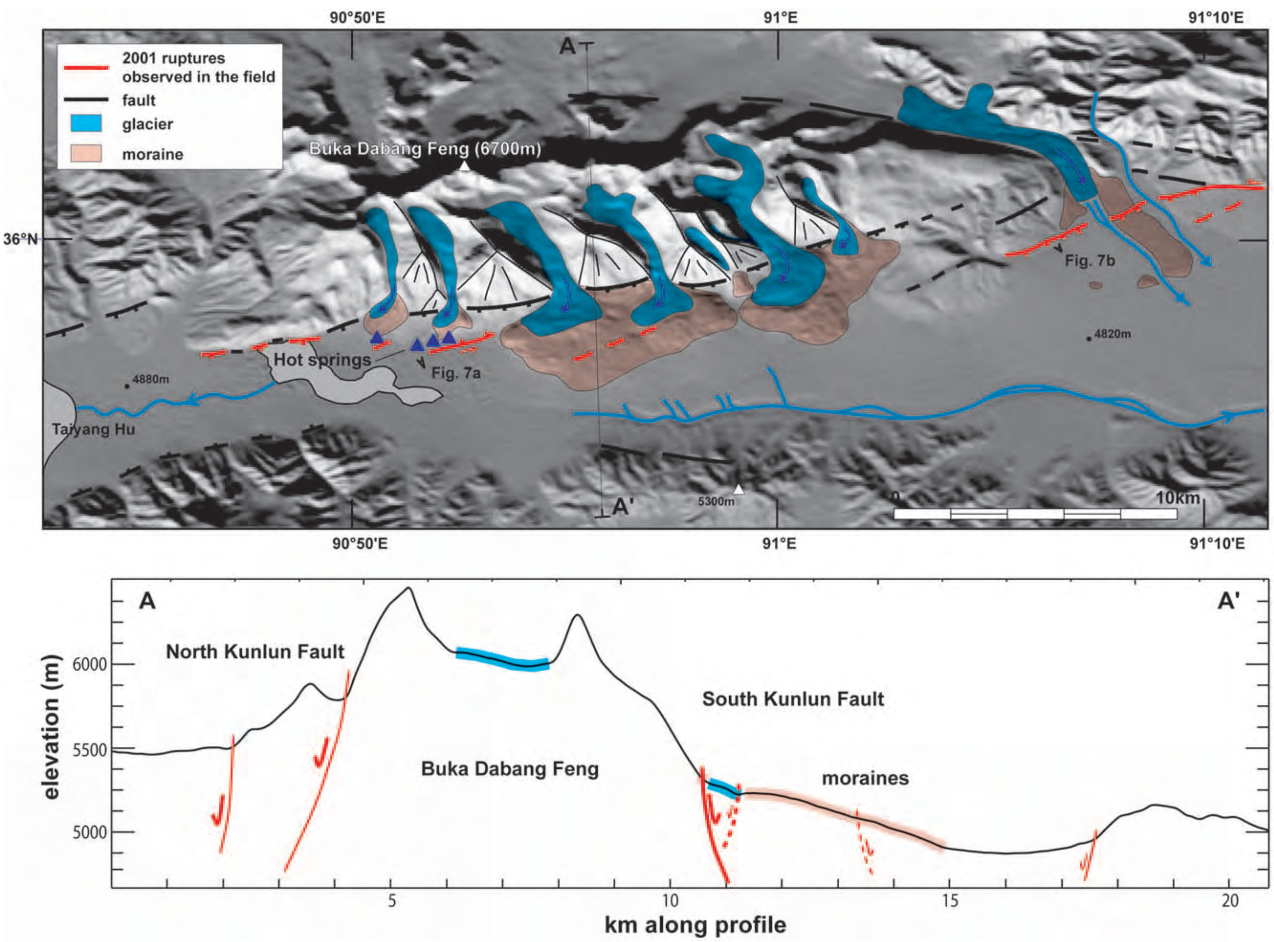

Figure 6. Map of extensional corridor south of Buka Daban Feng derived from field observations. The 14 November 2001 surface breaks are in red. Although field evidence for coseismic rupture along the range front fault was not found, or was ambiguous, overall morphology implies that it is active. Southwest deviation of glacier tongues is due to channeling in small range front graben. Hot springs (Fig. 7a) (blue triangles) are aligned along one strand that ruptured in 2001. Roughly north–south profile and cross section emphasize the asymmetry of the extensional corridor. Digital Elevation Model (DEM) is from the SRTM database.

the absence of rupture along the north branch of the western Kunlun fault, which is aligned with the Kusai Hu segment of the fault and continues to Jingyu Lake (Fig. 1 inset, Fig. 2).

Western Kusai Segment

For over 100 km eastward, the 2001 rupture zone is mostly single stranded, and exhibits nearly pure strike-slip motion. The presence of triangular facets near the western extremity of the Kusai Hu segment suggests, however, that some cumulative vertical throw is locally accommodated by the fault. This is a complex area, where the two main western branches (Jingyu and Manyi) of the Kunlun fault merge. At N35°52.8′, E92°13.8′ (Fig. 2, Plate 1) the Hong Shui River crosses the fault. It is the only drainage to breach northward across the Kunlun range to reach the Qaidam basin. West of this river, the rupture is rather simple with clear coseismic and cumulative offset of tributary fans and terrace risers. Both the fault trace and the 2001 surface break are sharp and well defined, making the area an ideal target to study the accumulation of displacement through several consecutive seismic cycles (Van der Woerd *et al.*, 2002b). Coseismic 2001 stream offsets of 3 ± 0.5m (Plate 1, Fig. 8), and cumulative offsets of 6 ± 1 m due to two successive earthquakes are measured both in the field and on the HRS images (Li *et al.*, 2005), suggestive of local characteristic slip (Klinger *et al.*, 2003; Liu *et al.*, 2004; Sieh, 1996).

Central Kusai Segment

The Hong Shui River gorge marks a second-order transition zone in the nature and style of faulting along the Kusai segment of the fault. At E92°14′, both the range front and the active fault zone slightly change azimuth, by about 3° counterclockwise, on average, and the Kunlun range front

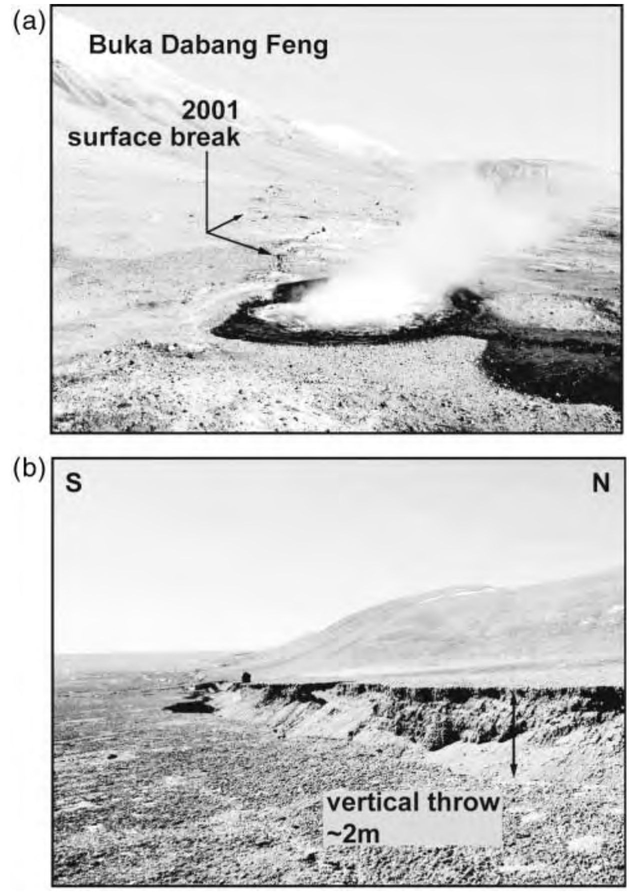

Figure 7. (a) View of boiling water in geyser pond in piedmont of Buka Daban Feng. Note hanging glacier pecten behind the moraine in the background. (b) The 2001 normal fault scarp at the eastern end of the Buka Daban Feng corridor (see location in Fig. 6).

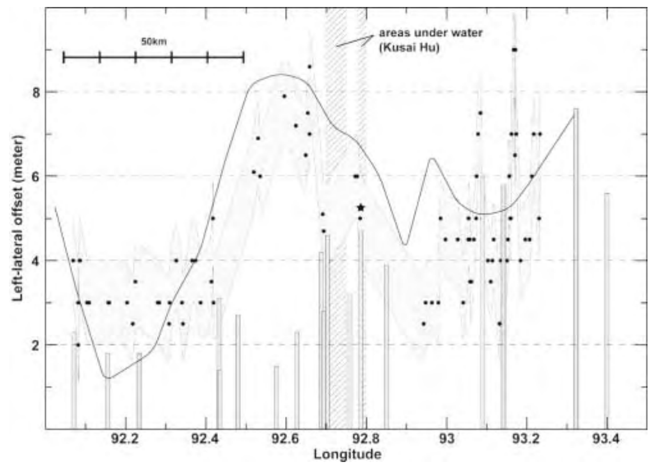

Figure 8. Horizontal slip distribution with 83 positioned offset measurements (Table 1) along the central part of the Kokoxili earthquake rupture derived from HRS images. Gray shaded envelope represents the nominal error of ± 1 m (see text for discussion). Star is shoreline measurement of Figure 4. For comparison, field data from Xu *et al.* (2002) are indicated by gray bars, and InSAR results from Lasserre *et al.* (2005) by the black line. Striped boxes locate Kusai Hu.

steps northward by about 1 km (Plate 1). This small releasing bend and step triggers partial to complete partitioning of the strike-slip and normal components of motion on two distinct, roughly parallel strands, one across the piedmont, the other along the range front, respectively, as already noted north of Kusai Hu by Van der Woerd *et al.* (2002a). The partitioned stretch of the Kusai Hu segment is about 70 km long, with a 30-km-long central part where the horizontal separation between the range front and the piedmont strands is nearly constant (2 to 2.5 km). In the west, this separation increases abruptly, in only ~2 km, to about 1–1.5 km. Then, past an abrupt kink of the parallel strands ~5 km eastward, it increases progressively over a distance of ~10 km to its maximum value of ~2.5 km. In the east, it decreases progressively, over a distance of about 20 km (Plate 1). Our field observations and detailed mapping using the HRS images (Plate 1) document the existence of fresh, coeval 2001 surface breaks along both strands, and, thus, for the first time, the occurrence of well-developed slip partitioning during a large earthquake. In related articles, we have suggested that the likely mechanical cause of such partitioning, and of the corresponding changes in near surface stresses, is the upward propagation of rupture (Bowman *et al.*, 2003; King *et al.*, 2005). The finite distance between the two strands is interpreted to reflect the depth at which the partitioning process starts and the two faults meet, likely where the oblique deep fault cuts across a rather shallow (a few kilometers deep) sediment/bedrock interface (Armijo *et al.*, 1986). Between E92°12′ and E92°56′, each ruptured strand is well defined and shows obvious signs of previous activation.

The range front, predominantly normal, fault strand follows the base of large triangular facets, several hundred meters high (Fig. 4d). The 2001 displacement due to the Kokoxili earthquake has produced free faces 1 to 2 m high, usually at the bedrock/colluvium contact. Nevertheless, parallel normal scarps cut the bedrock at places within the facet slopes. These scarps are unlikely to result from landsliding because they can be traced across several adjacent facets and alluvial fans. This leads to underestimation of the total normal throw, as measuring and integrating the throw across the upper scarps is impossible because of lack of access. Along the 70-km-long slip-partitioned stretch of the fault, the morphology of the 2001 normal escarpments varies. From the Hong Shui gorge to about 18 km eastward, these escarpments are fairly continuous. This is also the case in the east, along most of the 20-km-long stretch where the separation decreases northeast of Kusai Hu. Along much of the stretch of maximum strand separation, the normal escarpments are more discontinuous, and generally shorter. This probably reflects less efficient propagation of the normal dislocation all the way to the surface, due to the greater depth of partitioning. Indeed, there is no hint, whether on HRS images or in the field, of diffuse deformation along the range front. Concurrently, it is also in this central part of partitioned rupture (E92°36′ to E92°52′) that multiple normal fault scarps cut the fan and terrace surfaces in the intervening zone between the normal and strike-slip fault strands. Some such scarps show fresh 2001 surface breaks, particularly just north of the western extremity of Kusai Hu and at E92°26′ (Plate 1), but several others do not, even though they are large and easy to map on the HRS images. Most of these intervening scarps have a characteristic geometry in map view (Plate 1). They start close to the main strike-slip strand, with a markedly oblique azimuth (30° to 40° counterclockwise from E100°) that swings progressively northward to become parallel to the main normal strand along the range front. We interpret such a systematic azimutal swing to reflect the transition between the two superficial partitioned stress regimes in the zone where none of them is adequate to promote the formation of long-lived fault planes with steady-state kinematics (see figure 3 in King *et al.*, 2005).

The strike-slip strand is located well south of, and several tens of meters down below the range front. Along most of its length it shows little evidence of vertical motion (Plate 1). One exception is the 4-km-long stretch between E92°28′ and E92°30′, near the western end of the maximum separation zone, where a range-facing scarp developed, blocking and diverting the drainage. Although this scarp might result from apparent vertical throw due to cumulative sinistral shift of higher and older fans north of the fault to the west, shuttering younger deposits, the youthfulness of the surfaces south of the fault and very large amount of left-lateral transport required (on the order of 5 to 6 km) make this hypothesis unlikely. Vertical motion along this segment in the 2001 Kokoxili event was small enough, however, that it did not significantly dam the one large stream that continues to flow in the channel incised across the cumulative scarp.

Another area where the piedmont strand kinematics departs from pure strike-slip faulting is where it encroaches upon Lake Kusai (Fig. 2, Plate 1B). The northern shore of this lake, which lies mostly south of the fault zone and has a shape that does not suggest a simple tectonic origin, is cut four times by the fault (Plate 1). One notable pull-apart basin (Fig. 9a and b), contiguous with a push-up hill of similar size to the east, formed in the promontory near N35°49.2′, E92°46.2′. Two more pull-apart sags may be present under water on either side of this promontory. The onshore pull-apart is about 1000 m long, 200 m wide, and 20 m deep. All the normal faults bounding its floor slipped in 2001, with 1.9 m of vertical offset on the south side and about 1 m on the north side (Fig. 9a and b). One fault strand, taking up most of the 2001 strike-slip displacement, shortcuts the basin along its longest diagonal. Deformation due to the 2001 earthquake has led to upthrow and the consecutive abandonment of the pre-2001 depocenter in the lower part of the basin floor (Plate 1, Fig. 9a and b). We found no piercing line in the basin that was clear enough to constrain the horizontal 2001 coseismic offset, but several rills at the base of the push-up slope a few hundred meters eastward provided a set of consistent measurements indicating ~5 m of sinistral slip (Plate 1, Fig. 8). The offset beach ridges east of the pull-apart basin also show consistent 5 to 5.6 m lateral offsets (Fig. 4). The existence of the two other pull-aparts in the lake bays east and west of the promontory may be deduced from the fault geometry. Extensions of the rupture traces offshore show large enough misalignments that they require the presence of ~200-to 500-m-wide extensional steps beneath the lake waters. On the HRS images and in the field, we mapped dense arrays of northeast-striking cracks parallel to the lakeshore in the two areas where the rupture enters the lake from the west (Plate 1, E92°42′). Such cracks might be attributed to spreading, but because they are not as numerous elsewhere, we suspect they are due in part to the existence of the underwater extensional pull-apart jogs. The sudden counterclockwise change of azimuth of the surface rupture before it enters the lake from the east in the eastern bay, which is associated with growing vertical throw, also argues for this interpretation.

East of Kusai Lake, the strike-slip rupture zone is up to 30 m wide with parallel strands bearing clear traces of large previous events (Fig. 9c). Fresh pressure ridges, cracks, and extensional pull-aparts are superimposed on older similar features, such as extensional sag ponds still marked by grassy mats and fine, buff-colored silt deposits reflecting water stagnation prior to the 2001 earthquake, and meters-high mounds covered by shattered and weathered ground with exhumed cobbles long exposed to the harsh high-altitude climate. This indicates that the rupture localization is stable through time, and hence, that slip partitioning along the two strands is likely a permanent type of coseismic behavior that repeats itself in successive earthquakes along this stretch of the fault.

For the next 12 km eastward, between the lake and the junction of the piedmont and range front strands, the strike-slip strand is sinuous but simple. The range front strand, on the other hand, is more complex along the first half of this distance. There is also one prominent ~1200-m-long, intervening crack array in the piedmont. Outside this array, however, there is little evidence for oblique ruptures trying to connect the two strands. The eastward tapering area in between is in fact remarkably crackfree. At E92°57′ longitude, the two strands merge into a single fault zone, located at, or a few hundred meters south of, the mountain front.

Eastern Kusai Segment

From that point eastward, the rupture pattern becomes more complicated, even though full partitioning is not observed. The fault zone becomes up to 400 m wide at places. It is often composed of parallel, or oblique en echelon, kilometer-long subsegments (Plate 1). This geometry makes it more difficult than elsewhere to measure the total coseis-

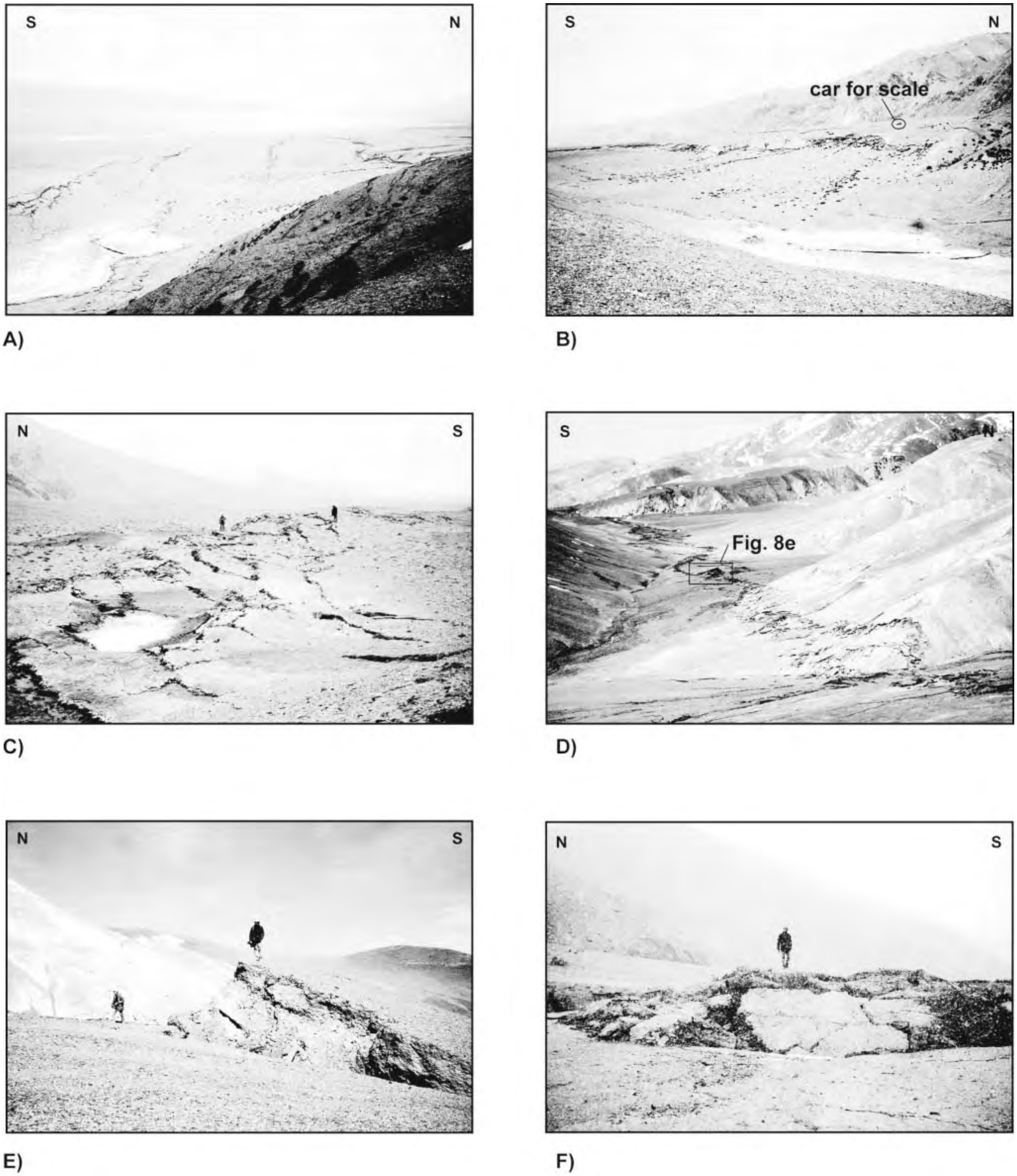

Figure 9. (A) General view of the pull-apart basin on the Kusai Hu peninsula. Normal motion is localized on the sides of the basin. The rupture in the center of the basin takes most of the strike-slip component. (B) View of the reactivated normal fault scarp on the northern side of the basin. (C) Evidence of repetitive, analogous earthquake rupture pattern along the piedmont fault trace. New sag pond created by the Kokoxili earthquake (water-filled, white on photo) formed within an ancient degraded sag created by an earlier large event (permanent, green-yellow grassy mat and fine, buff-colored silt) (D, E and F) Examples of ground rupture related to permafrost: 5-m-high pressure ridge is entirely bounded by brittle faults, including a large thrust that has tilted the intact ground surface. Location on Plate 1.

mic offset across the fault zone, which is distributed over distinct subsegments. As apparent from the disparate results of several studies of the earthquake, this is the section where the exact amount of coseismic displacement is most debated, even though it appears to be largest (Antolik *et al.*, 2004; Lasserre *et al.*, 2005; Lasserre *et al.*, 2003; Lin *et al.*, 2002, 2003; Xu *et al.*, 2002). Our total station measurements in the field and offset restorations on the HRS images confirm that the largest 2001 coseismic slip did not exceed 10 m along the section we studied in greater detail (Fig. 8). Due to the combination of multiple rupture strands, large horizontal displacements, and the presence of permafrost, this section offers some of the most spectacular surface deformation features (Fig. 9d, e, and f). At places, the frozen ground hampered surface folding, promoting instead brittle faulting and block tilting (Lin *et al.*, 2004). On Figure 8e and f, for instance, the intact upper surface of the west limb of a ~5-m-high push-up was lifted and tilted by ~30°. This implies decoupling of a rigid surface layer on a shallow thrust ramp, allowing the broken upper ground slab to rotate freely. Large plates of relatively unconsolidated, but frozen, alluvium are often observed to stand on end, in precarious equilibrium. Similar features have been documented for other large earthquakes in similarly extreme environments (Armijo *et al.*, 1989; Allen *et al.*, 1991; Haeussler *et al.*, 2004). In two deep valleys where fluvial incision exposes rocks beneath the Quaternary alluvium veneer, we observed that two parallel rupture strands followed the outer limits of a steep zone of black gouge, several hundred meters wide, separating the phyllonites and schists of the Kunlun range basement from the folded, south-dipping Tertiary red beds of the piedmont. The separation of the two strands is thus both of structural and mechanical origin. In the same area, ancient moraine ridges are offset by up to 2.5 km (Plate 1), suggesting sustained displacement since at least the late Pliocene at the current rate of ~1 cm/yr (Kidd and Molnar, 1988; Li *et al.*, 2004; Van der Woerd *et al.*, 2002b).

Kunlun Pass Fault Segment

Near N35°43.8′, E93°39′, the 2001 rupture abandons the main trace of the Kunlun fault, which follows the Xidatan and Dongdatan troughs (Fig. 2) (Van der Woerd *et al.*, 1998, 2001, 2002b). No coseismic rupture is observed along the Xidatan-Dongdatan segment of the fault, though subtle signs of ground distortion and possibly cracking are perceptible, in the west, on the HRS images and on the InSAR data (Lasserre *et al.*, 2005). Given the acquisition date of the images, such deformation traces could testify to postseismic creep. For 5 to 7 km, near E93°65′, the 2001 rupture shows short, northeast-directed splays indicating that it might have tried to jump to the Xidatan strand, without success. East of E94°, the rupture becomes linear and simple, following the trace of the Kunlun Pass fault at the foot of the Burhan Budai Shan (Kidd and Molnar, 1988; Van der Woerd *et al.*, 2002b), extending southeastward for another 70 km (Xu *et al.*, 2002). For most of its length, the Kunlun Pass fault surface break is limited to one single strand with almost pure strike-slip motion. At the Kunlun Pass, the 2001 coseismic displacement has been accurately measured by different teams to be ~4 m (Lin *et al.*, 2002; Xu *et al.*, 2002). East of the Golmud–Lhasa road (N35°40.2′, E94°3′), and south of the Burhan Budai summits (Fig. 2), a thrust component is observed locally in the field, accommodating 1–2 m of displacement in addition to the strike-slip component. Both slip components taper eastward in amplitude, to become limited to open cracks parallel to the fault near the rupture end (Xu *et al.*, 2002). This observation is hardly compatible with seismic inversion results, which require 4 m of surface slip at the eastern end of the rupture to account for the seismic waveforms (Antolik *et al.*, 2004). Rather, the surface slip decreases slowly over a long distance, which is in keeping with a dogtail type of rupture termination such as defined by Ward (1997).

Insight on Rupture Propagation from Surface Break Observations

The way seismic rupture propagates during an earthquake is an important topic of ongoing research (Bhat *et al.*, 2004; Rice *et al.*, 2005). It remains difficult to bridge theoretical models, laboratory experiments, and observations from large magnitude earthquakes owing to scaling problems. Inversion of seismic waves recorded by seismometers and accelerometers adequately images broad-scale dynamic rupture propagation along the fault plane (see, for this earthquake, Antolik *et al.*, 2004; Bouchon and Vallée, 2003; Ozacar and Beck, 2004; Rivera *et al.*, 2003 and, more generally, e.g., Peyrat *et al.*, 2001), but typical frequencies used in these studies are ill adapted to resolve details of the rupture history.

In both laboratory experiments and natural outcrops (Tchalenko, 1970), brittle faulting generally starts by an array of en echelon tensile cracks, the direction of the array being parallel to the future fault plane (e.g., Tapponnier and Brace, 1976; Scholz, 1990). Such tensile cracks are thought to ultimately coalesce into a brittle shear zone usually marked by a layer of gouge. HRS image and field mapping suggest that these two stages exist in the formation of a single earthquake rupture. Figure 10 shows two locations where the surface rupture pattern is characterized by one principal strand. The rather linear strands cross cut and offset gullies and terrace risers. At both locations, large en echelon cracks oriented northeast–southwest, in keeping with sinistral strike-slip motion, are also visible. None of them can be traced continuously across the strike-slip rupture. The opening component of the cracks must be greater than 50 cm to be visible on the images. Restoration of the offset gullies and risers by back-slipping one side of the fault relative to the other (by 7 m at one site and 4.5 m at the other), also restores the alignment of several cracks across the strike-slip rupture. Comparable observations were made along the 1968

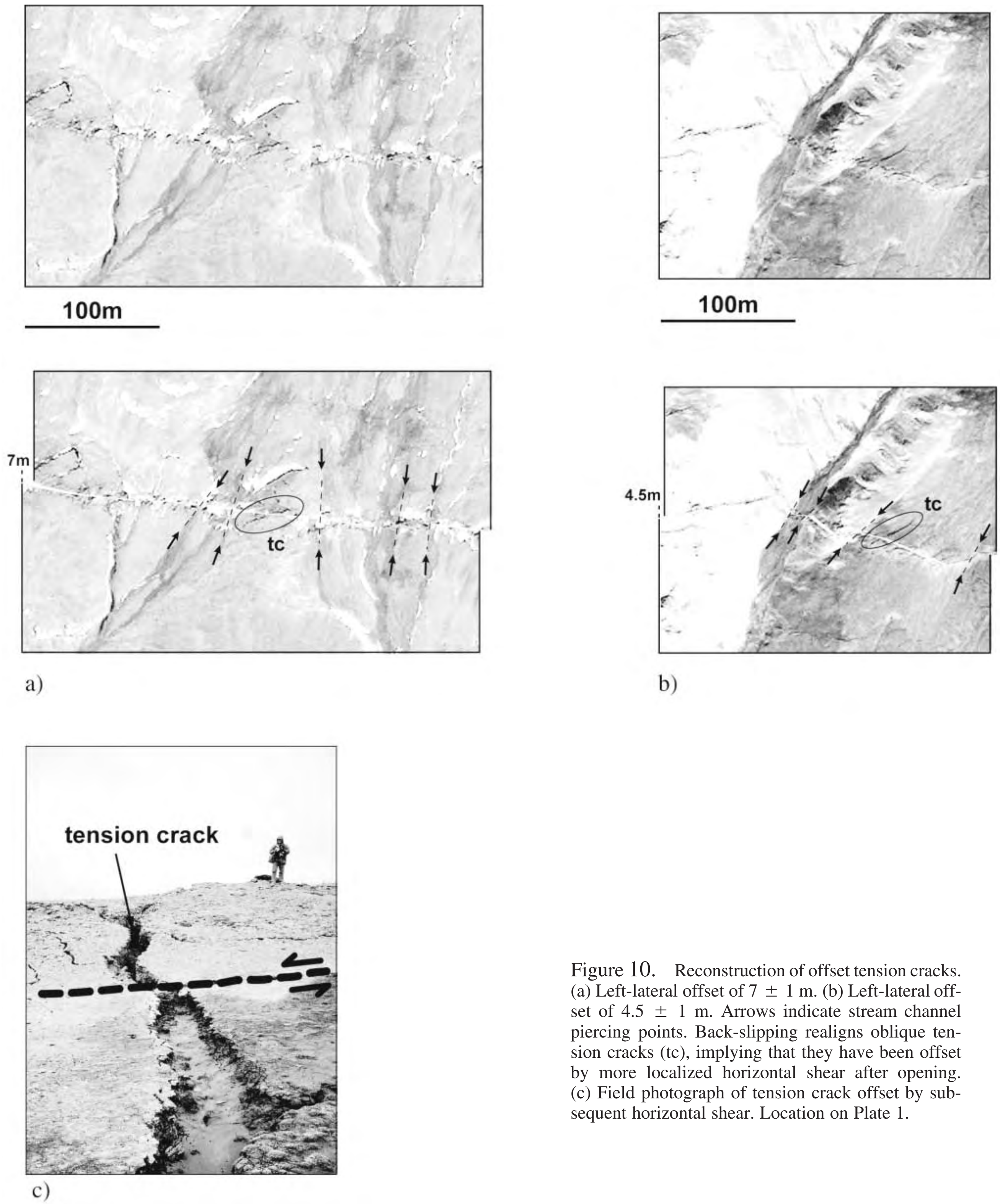

Figure 10. Reconstruction of offset tension cracks. (a) Left-lateral offset of 7 ± 1 m. (b) Left-lateral offset of 4.5 ± 1 m. Arrows indicate stream channel piercing points. Back-slipping realigns oblique tension cracks (tc), implying that they have been offset by more localized horizontal shear after opening. (c) Field photograph of tension crack offset by subsequent horizontal shear. Location on Plate 1.

Dasht-e-Bayaz earthquake surface break in Iran (Tchalenko and Ambraseys, 1970), a 24-km-long stretch of which was mapped in particularly great detail in the field and with air photos. Such examples show unambiguously that the cracks from first and are sheared only later. Such cross-cutting relationships support the inference that an en echelon crack damage zone propagates ahead of the shear rupture, whether in screw or in edge mode. This zone moves at the speed of the dynamic stress field generated by the rupture (King *et al.*, 2005), causing tensile cracks to open first, particularly at the stress-free ground surface. When the shear plane reaches the surface, it cuts and offsets the tensile cracks. In the last few meters, tensile cracking may be enhanced by the existence of unfaulted sediments deposited after the penultimate earthquake. This scenario is in keeping with a slip-partitioning mechanism involving upward propagation, with a rupture velocity much faster in the crust at depth than in the shallow, poorly consolidated sediments up above. A similar phenomenon is observed in analog experiments where a sheared clay layer is wetted at the surface by a water film (Tapponnier and Varet, 1974).

Horizontal Slip Distribution along the Central Segment of the Kokoxili Earthquake

Surface mapping of the coseismic slip distribution along the 14 November 2001 Kokoxili earthquake rupture zone is particularly challenging owing to the remoteness and great length of the surface break. Selected spots have been targeted for accurate field surveys (Li *et al.*, 2004; Lin *et al.*, 2002; Xu *et al.*, 2002), but most teams have reached different localities, which makes cross-checking of the measurements difficult. Taking advantage of the unprecedented resolution provided by the HRS sensors, we provide here additional measurements along the central stretch of the Kusai segment by systematically realigning piercing lines visible on the images (see Figs. 3, 4, and 10 for typical examples of offset restoration). One should bear in mind that telling the difference between cumulative offsets and 2001 coseismic displacements, which is not always straightforward in the field, often remains difficult on the images, even with a nominal 1 m pixel. We were able to measure a total of 239 offset features over a length of ~100 km. Among the 239 offset measurements, we eliminated all the data for which piercing points were ambiguous or for which the offset could arguably be considered as cumulative from the 2001 Kokoxili event and the penultimate event. This procedure yielded 83 reliable 2001 offset measurements (Fig. 8, Plate 1 and Table 1). The main uncertainty in the measurement is then simply related to the pixel size (~1 m). Therefore, we take the nominal error bar to be ±1 m even though it is probably smaller. The resulting slip distribution pattern can readily be compared to that obtained by other groups or with other techniques. In the west, over a length of ~30 km, surface slip is nearly constant, with an average value of ~3 m. This value is validated in the field at Hongshui Gou (Li *et al.*, 2005). Between E92°24′ and the western shore of Kusai Hu, even though data is more limited, in part due to the north-facing scarp damming the drainage (Plate 1), the slip increases regularly to a maximum value of ~8 m around E92°42′. This is a stretch with well-established partitioning and no significant extensional jog. The few onshore data points farther east, which include our total station field measurements, confirm that the slip decreases back to 4-5 m. East of E92°54′, the slip increases again to a maximum value of 9 ± 1 m, accurately measured on two nearby offset geomorphic features at E93°6′. The whole data set reveals two relative maxima in the surface slip function, one at ~8 m, the other at 9 m, about 30 km apart. Field studies (Xu *et al.*, 2002) and InSAR data (Lasserre *et al.*, 2005) suggest that the largest amount of coseismic slip along the entire rupture, ~10 m, is located 10–20 km east of the area targeted with the HRS images, a region covered with snow at the time of image acquisition. Thus, the eastern slip function maximum in Figure 8 should in fact be seen as part of an increasing ramp toward the actual maximum. But the comparison with other data sets (Fig. 8) shows that our HRS measurements are generally in keeping with slip functions found with alternative techniques, particularly with InSAR. The field measurements of Xu *et al.* (2002), which tend to underestimate the total slip and should thus be regarded as lower bounds, nevertheless fit adequately with the HRS data in the west and east. The slip peak of ~8 m centered at ~E92°36′, on the other hand, does not show up in the field data of Xu *et al.* (2002), while it is quite clear in the InSAR results derived from the study of Lasserre *et al.* (2005). Since the slip function derived from seismic-wave inversion (Antolik *et al.*, 2004) was forced to be consistent with the data of Xu *et al.* (2002), where available, it is not surprising that it also misses the E92°36′ slip peak. The fit between the InSAR results and the HRS data set, which is quite good on average, indicates that most of the surface deformation is localized. Otherwise displacements measured by InSAR would be systematically larger than the surficial offset data. Such localized, shallow slip is confirmed by seismic inversions, which locates the largest slip patches above 5 km depth (Antolik *et al.*, 2004; Ozacar and Beck, 2004; Rivera *et al.*, 2003). All the data sets also show that coseismic slip increased eastward, in keeping with east-directed rupture propagation (Bouchon and Vallée, 2003; Le Pichon *et al.*, 2003; Rivera *et al.*, 2003; Antolik *et al.*, 2004).

Discussion

As one of the largest shallow continental earthquakes ever recorded, the 14 November 2001 Kokoxili earthquake provides a unique opportunity to study rupture processes in the continental crust. Using new metric-resolution satellite images, with local fieldwork calibration, we have been able to produce accurate maps of the surface break of this earth-

Table 1
Measures of Displacements from HRS Images (See Also Plate 1)

Longitude	Offset (m)	Longitude	Offset (m)	Longitude	Offset (m)	Longitude	Offset (m)
92°4′8.04	4	92°23′11.76	3	92°59′5.28	5	93°9′2.16	4
92°4′51.96	3	92°24′48.6	3.5	92°59′49.92	4.5	93°9′10.8	4.5
92°4′53.76	2	92°25′3	5	93°1′40.08	4.5	93°9′21.96	6
92°5′5.64	4	92°25′8.4	3	93°2′28.68	3	93°9′30.96	5
92°5′9.96	4	92°31′10.2	6.1	93°3′14.4	4.5	93°9′35.64	5
92°6′12.96	3	92°31′48	6.9	93°3′17.64	5	93°9′42.12	7
92°6′32.04	3	92°32′6.36	6	93°3′26.64	4.5	93°10′0.48	9
92°9′23.4	3	92°35′43.8	7.9	93°3′31.68	3.5	93°10′13.08	6.5
92°9′30.96	3	92°37′27.12	7.2	93°3′41.4	3.5	93°10′17.4	9
92°12′11.88	3	92°38′55.68	6.5	93°4′4.8	4.5	93°10′24.6	7
92°13′3	2.5	92°39′14.04	7.5	93°4′24.96	5	93°10′26.76	7
92°13′26.04	3.5	92°39′28.8	7	93°4′28.56	6	93°11′3.48	4
92°16′46.92	3	92°39′29.88	8.6	93°4′42.24	7	93°11′46.68	4.5
92°17′0.96	3	92°41′28.68	5.1	93°5′3.48	7.5	93°12′25.2	4.5
92°18′29.16	2.5	92°41′36.24	4.7	93°5′17.88	5	93°12′45	6
92°18′32.76	3	92°46′20.28	6.0	93°6′10.44	4	93°13′3	7
92°19′33.6	4	92°46′37.56	6.0	93°6′35.64	3.5	93°13′49.44	5
92°20′24	3	92°47′3.48	5.0	93°6′50.76	4	93°13′57.72	7
92°20′33.36	2.5	92°56′33.72	2.5	93°7′2.64	4.5		
92°21′56.16	4	92°56′51	3	93°7′54.48	2.5		
92°22′2748	4	92°57′47.16	3	93°8′5.64	4		
92°58′45.48	3	93°8′21.48	4				

quake and an overview of the different rupture styles from west to east. Our mapping of the rupture documents a unique example of large scale coseismic slip partitioning along the central stretch of the Kusai segment of the Kunlun fault. Evidence for previous events on both the normal and strike-slip strands suggests that such partitioning behavior maybe stable rather than transient. A slight 3° counterclockwise swing in the strike of the fault suffices to cause such partitioning (King *et al.*, 2005). The kilometer-size displacements of ancient moraines confirm that, from Buka Daban Feng to the Kunlun Pass, and probably since at least the end of the penultimate glacial maximum (~140 ka), the Kusai segment may have slipped at a rate similar to that constrained for the Holocene (Kidd and Molnar, 1988; Li *et al.*, 2005; Van der Woerd *et al.*, 2002b). A novel set of coseismic surface offset measurements has been obtained from the restoration of geomorphic piercing lines on the HRS images. Although this data set is restricted to the central part of the Kusai segment of the fault, it shows clear fluctuations, by a factor of ~3, of the slip function over distances on the order of 30 km that correlate well with InSAR results. From ~3 m in the west, slip increases to 8 m around E92°36′ along a linear stretch of the fault where partitioning is well established. Farther eastward, smaller sinistral slip amounts of 4 to 5 m, near E92°42′, characterize a fault stretch marked by the succession of three pull-apart basins located in left-stepping jogs of a less linear fault zone. Seismic inversion (Antolik *et al.*, 2004) shows that this relative minimum lies in between the sources of two high-energy pulses, probably owing to the greater complexity of the fault surface at depth. Superficial slip increases again eastward as the fault becomes more linear. This suggests that variations of the slip function at scales of tens of kilometers actually reflect first-order changes in fault geometry at the surface and at depth. Slip fluctuations of this kind, which reach up to 100% (see also over a shorter rupture length, McGill and Rubin, 1999), thus not only provide important information on the internal subsegmentation of the fault but should also be taken into account when considering slip-per-event estimates derived from paleoseismic studies. Clearly, matching trench results with surface offsets measured tens of kilometers away should be regarded as hazardous.

For most of its length, the main rupture of the Kokoxili earthquake follows a long-lived tectonic feature (Kidd and Molnar, 1988; Meyer *et al.*, 1998; Van der Woerd *et al.*, 2002b) but the onset and termination of the rupture veer into somewhat unexpected paths. In the west, the rupture appears to have started on a hitherto poorly mapped fault in the west Tayang Hu basin, rather than on faults southwest of this lake that show more prominent active topographic and geomorphic signatures (Fig. 2), and are in more direct connection with the Manyi earthquake fault (1997). Our field survey nevertheless demonstrates that the west Tayang restraining bend broke several times during the Holocene prior to the 2001 event. This illustrates the complexity of the west Kunlun fault horsetail between the Manyi and Jingyu faults (Fig. 1). In the east, the rupture also follows a surprising path, running parallel to the main Xidatan segment of the Kunlun fault for few kilometers without triggering rupture of this segment. Instead it continues unabated south of the Burhan Budai range, propagating along the Kunlun Pass fault, with a minor thrust component. Careful inspection of

HRS and Spot (pixel, 10 m) images (acquired after the earthquake) of the region immediately west of the Kunlun Pass shows that the Kusai and Xidatan segments have no clear connection but remain separated at the surface by a still significant, probably long-lived step. The main south-directed drainages that cross the Kunlun Pass fault east of the Golmud–Lhasa road show rapidly decreasing sinistral cumulative offsets toward the east. Immediately south of the Burhan Budai ice cap, much of the long-term geomorphic evidence suggests predominant thrusting in contrast with the mostly sinistral motion observed during the 2001 earthquake. This implies that the east-propagating sinistral rupture triggered by the 2001 Kusai Hu earthquake east of the Kunlun Pass may not reflect the most common type of event on the Kunlun Pass fault. Ruptures of this style alone cannot generate the steep topographic gradient and prominent thrust throw that characterize the south flank of the Burhan Budai range. Smaller Kusai Hu earthquake ruptures may generally end at the eastern extremity of the Kusai Hu segment. One reason the 2001 Kusai Hu segment rupture did not continue along the Xidatan segment of the Kunlun fault may be related to the supershear rupture velocity (Bouchon and Vallée, 2003). In such a circumstance, the dynamic stress field ahead of the rupture front is strongly asymmetric (Poliakov *et al.*, 2002; Kame *et al.*, 2003) with a stress shadow north of the fault and a stress increase south of it promoting easier rupture along the Kunlun Pass fault. The lack of an established surface connection between the Kusai Hu and Xidatan segments of the fault suggests that rupture of the Kusai segment rarely continues along Xidatan in the same event. The Xidatan–Dongdatan segment is currently one of the last ones not to have ruptured along the western part of the Kunlun fault in the last few hundred years and is probably very close to failure (Li *et al.*, 2005; Van der Woerd *et al.*, 2002b). The region just west of the Kunlun Pass is the place where the Kunlun fault penetrates into the Kunlun range instead of following its southern edge, as farther west. It would seem that a place where the rupture has to break across metamorphic rock (Li *et al.*, 2005) is likely to form a particularly deep and strong structural asperity capable of surviving scores of great earthquake seismic cycles.

Acknowledgments

This work was supported in France by the Institut National des Sciences de l'Univers/Centre National de la Recherche Scientifique (INSU-CNRS) and the Association Franco-Chinoise pour la Recherche Scientifique et Technique (AFCRST) and in China by the Chinese Earthquake Administration (CEA) Institute of Geology for the fieldwork. We are very indebted to Z. Chang from the CEA, Bureau of Golmud City, for his constant help to solve logistic issues. D. Bowman and W. Ma provided help and insight during the field operation. We thank G. Hilley and an anonymous reviewer for helpful reviews. The acquisition of the HRS images was possible due to support from Action Concertée Incitative (ACI) "Observation de la Terre" of INSU and the data purchase program of NASA. This article is IPGP contribution number 2062 and INSU contribution number 385.

References

Allen, C. R., L. Zhuoli, Q. Hong, W. Xueze, Z. Huawei, and H. Weishi (1991). Field study of a highly active fault zone: the Xianshuihe fault of southwestern China, *Geol. Soc. Am. Bull.* **103,** 1178–1199.

Antolik, M., R. E. Abercrombie, and G. Ekstrom (2004). The 14 November 2001 Kokoxili (Kunlunshan), Tibet, earthquake: rupture transfer through a large extensional step-over, *Bull. Seism. Soc. Am.* **94,** no. 4, 1173–1194.

Armijo, R., P. Tapponnier, J. L. Mercier, and H. Tong-Lin (1986). Quaternary extension in southern Tibet: field observations and tectonic implications, *J. Geophys. Res.* **91,** no. B14, 13,803–13,872.

Armijo, R., P. Tapponnier, and H. Tong-Lin (1989). Late Cenozoic right-lateral faulting in southern China, *J. Geophys. Res.* **94,** no. B3, 2787–2838.

Bhat, H., R. Dmowska, J. Rice, and N. Kame (2004). Dynamic slip transfer fromthe Denali to Totschunda faults, Alaska: testing theory for fault branching, *Bull. Seism. Soc. Am.* **94,** no. 6B, S202–S213.

Bouchon, M., and M. Vallée (2003). Observation of long supershear rupture during the $M_s = 8.1$ Kunlunshan earthquake, *Science* **301,** no. 5634, 824–826.

Bowman, D., G. King, and P. Tapponnier (2003). Slip partitioning by elastoplastic propagation of oblique slip at depth, *Science* **300,** 1121–1123.

Chevalier, M. L., F. J. Ryerson, P. Tapponnier, R. C. Finkel, J. Van der Woerd, H. B. Li, and Q. Liu (2005). Slip-rate measurements on the Karakorum fault may imply secular variations in fault motion, *Science* **307,** no. 5708, 411–414.

China Seismological Bureau (2002). *Album of the Kunlun Pass W. Ms = 8.1 Earthquake, China*, Seismological Press, Beijing China.

Fitch, T. J. (1970). Earthquake mechanisms in the Himalayan, Burmese, and Adaman regions and continental tectonics in central Asia, *J. Geophys. Res.* **75,** 2699–2709.

Gu, G., L. Tinghuang, and S. Zhenliang (1989). *Catalogue of Chinese Earthquakes (1831 BC–1969 AD)*, Science Press, Beijing, China.

Haeussler, P. J., D. P. Schwartz, T. E. Dawson, H. D. Stenner, J. J. Lienkaemper, B. Sherrod, F. R. Cinti, P. Montone, P. A. Craw, A. J. Crone, and S. F. Personius (2004). Surface rupture and slip distribution of the Denali and Totschunda faults in the 3 November 2002 *M* 7.9 earthquake, Alaska, *Bull. Seism. Soc. Am.* **94,** no. 6, S23–S52.

Jia, Y., H. Dai, and X. Su (1988). Tuosuo Lake earthquake fault in Qinghai Province, in *Research on Earthquake Faults in China*, X. S. Bureau (Editor), Xinjiang Press, Wurumuqi, 66–77.

Kame, N., J. R. Rice, and R. Dmowska (2003). Effects of prestress state and rupture velocity on dynamic fault branching, *J. Geophys. Res. Solid Earth* **108,** no. B5, 2265, doi 10.1029/2002JB002189, 2003.

Kidd, W. S. F., and P. Molnar (1988). Quaternary and active faulting observed on the 1985 Academia Sinica–Royal Society Geotraverse of Tibet, *Phil. Trans. R. Soc. London* **A327,** 337–363.

Kikuchi, M., and Y. Yamanaka (2001). *Special Event Page, 2001/11/14 Qinghai Xinjiang Border, China*, wwweic.eri.u-tokyo.ac.jp/topics/200111140926, Earthquake Information Center, ERI, Univ. Tokyo, Japan.

King, G., Y. Klinger, D. Bowman, and P. Tapponnier (2005). Slip partitioned surface breaks for the 2001 Kokoxili earthquake, China (M_w 7.8), *Bull. Seism. Soc. Am.* **95,** no. 2, 731–738.

Klinger, Y., K. Sieh, E. Altunel, A. Akoglu, A. Barka, T. Dawson, T. Gonzales, A. Meltzner, and T. Rockwell (2003). Paleoseismic evidence of characteristic slip on the western segment of the North Anatolian fault, Turkey, *Bull. Seism. Soc. Am.* **93,** no. 6, 2317–2332.

Lasserre, C., Y. Gaudemer, P. Tapponnier, A. S. Meriaux, J. Van der Woerd, D. Y. Yuan, F. J. Ryerson, R. C. Finkel, and M. W. Caffee (2002). Fast late Pleistocene slip rate on the Leng Long Ling segment of the Haiyuan fault, Qinghai, China, *J. Geophys. Res. Solid Earth* **107,** no. B11, 2276, doi 10.1029/2000JB000060, 2002.

Lasserre, C., G. Peltzer, Y. Klinger, J. Van der Woerd, and P. Tapponnier (2005). Coseismic deformation of the 2001 $M_w = 7.8$ Kokoxili earthquake in Tibet, measured by SAR interferometry, *J. Geophys. Res.* (in press).

Lasserre, C., G. Peltzer, J. Van der Woerd, Y. Klinger, and P. Tapponnier (2003). Coseismic deformation from the $M_w = 7.8$ Kokoxili, Tibet earthquake, from ERS InSAR data, *EGS EUG meeting (abstract)*, Nice, France, April 2003.

Le Pichon, A., J. Guilbert, M. Vallee, J. X. Dessa, and M. Ulziibat (2003). Infrasonic imaging of the Kunlun Mountains for the great 2001 China earthquake, *Geophys. Res. Lett.* **30,** no. 15, 1814, doi 10.1029/2003GL017581, 2003.

Li, H., J. Van Der Woerd, P. Tapponnier, Y. Klinger, X. Qi, J. Yang, and Y. Zhu (2005). Slip rate on the Kunlun Fault at Hongshui Gou, and recurrence time of great events comparable to the 14/11/2001, M_w ~7.9 Kokoxili earthquake, *Earth Planet. Sci. Lett.* (in press).

Li, L., and Y. Jia (1981). Characteristic of deformation band of the 1937 Tuosuohu earthquake ($M = 7.5$) in Qinghai, *Northwest. Seis. J.* **3,** 61–65.

Lin, A., B. Fu, J. Guo, Q. Zeng, G. Dang, W. He, and Y. Zhao (2002). Co-seismic strike-slip and rupture length produced by the 2001 M_s 8.1 central Kunlun earthquake, *Science* **296,** 2015–2017.

Lin, A. M., J. M. Guo, and B. H. Fu (2004). Co-seismic mole track structures produced by the 2001 M_s 8.1 Central Kunlun earthquake, China, *J. Struct. Geol.* **26,** no. 8, 1511–1519.

Lin, A. M., M. Kikuchi, and B. H. Fu (2003). Rupture segmentation and process of the 2001 M_w 7.8 central Kunlun, China, earthquake, *Bull. Seism. Soc. Am.* **93,** no. 6, 2477–2492.

Liu, J., Y. Klinger, K. Sieh, and C. Rubin (2004). Six similar sequential ruptures of the San Andreas fault, Carrizo Plain, California, *Geology* **32,** no. 8, 649–652.

McGill, S., and C. Rubin (1999). Surficial slip distribution on the central Emerson fault during the June 28, 1992, Landers earthquake, *J. Geophys. Res.* **104,** no. B3, 4811–4834.

Meriaux, A. S., F. J. Ryerson, P. Tapponnier, J. Van der Woerd, R. C. Finkel, X. W. Xu, Z. Q. Xu, and M. W. Caffee (2004). Rapid slip along the central Altyn Tagh Fault: morphochronologic evidence from Cherchen He and Sulamu Tagh, *J. Geophys. Res. Solid Earth* **109,** no. B06401, doi 10.1029/2003JB002558, 2004.

Meyer, B., P. Tapponnier, L. Bourjot, F. Metivier, Y. Gaudemer, G. Peltzer, G. Shunmin, and C. Zhitai (1998). Crustal thickening in Gansu-Qinghai, lithospheric mantle subduction, and oblique, strike-slip controlled growth of the Tibet plateau, *Geophys. J. Int.* **135,** 1–47.

Ozacar, A. A., and S. Beck (2004). The 2002 Denali fault and 2001 Kunlun fault earthquakes: complex rupture processes of two large strike-slip events, *Bull. Seism. Soc. Am.* **94,** no. 6B, S278–S292.

Peltzer, G., F. Crampe, and G. King (1999). Evidence of nonlinear elasticity of the crust from the M_w 7.6 Manyi (Tibet) earthquake, *Science* **286,** 272–276.

Peyrat, S., K. Olsen, and R. Madariaga (2001). Dynamic modeling of the 1992 Landers earthquake, *J. Geophys. Res. Solid Earth* **106,** no. B11, 26,467–26,482.

Poliakov, A. N., R. Dmowska, and J. R. Rice (2002). Dynamic shear rupture interactions with fault bends and off-axis secondary faulting, *J. Geophys. Res.* **107,** no. B11, 6-1–6-18, doi 10.1029/2001JB000572.

Rice, J., C. G. Sammis, and R. Parsons (2005). Off-fault secondary failure induced by a dynamic slip-pulse, *Bull. Seism. Soc. Am.* **95,** 109–134.

Rivera, L., J. Van Der Woerd, A. Topechort, Y. Klinger, and C. Lasserre (2003). The Kokoxili, November 14, 2001, earthquake: history and geometry of the rupture from teleseismic data and field observations, *EGS-AGU-EUG Joint Assembly*, Nice, France, April 2003.

Scholz, C. (1990). *The Mechanics of Earthquakes and Faulting*, Cambridge University Press, New York.

Sieh, K. (1996). The repetition of large-earthquake ruptures, *Proc. Natl. Acad. Sci. U.S.A.* **93,** 3764–3771.

Tapponnier, P., and W. F. Brace (1976). Development of stress induced microcracks in Westerly granite, *Int. J. Rock. Mech. Min. Sci.* **13,** 103–112.

Tapponnier, P., and P. Molnar (1977). Active faulting and tectonics in China, *J. Geophys. Res.* **82,** 2905–2930.

Tapponnier, P., and J. Varet (1974). La zone de Mak'Arrosou en Afar: un equivalent émergé des failles transformantes océaniques, *CR Acad. Sci.* **278,** 209–212.

Tapponnier, P., X. Zhiqin, F. Roger, B. Meyer, N. Arnaud, G. Wittlinger, and Y. Jingsui (2001). Oblique stepwise rise and growth of the Tibet plateau, *Science* **294,** 1671–1677.

Tchalenko, J. S. (1970). Similarities between shear zones of different magnitudes, *Geol. Soc. Am. Bull.* **81,** 1625–1640.

Tchalenko, J. S., and N. Ambraseys (1970). Structural analysis of the Dasht-e Bayaz (Iran) earthquake fractures, *Geol. Soc. Am. Bull.* **81,** 41–60.

Van der Woerd, J., A. S. Meriaux, Y. Klinger, F. J. Ryerson, Y. Gaudemer, and P. Tapponnier (2002a). The 14 November 2001, $M_w = 7.8$ Kokoxili earthquake in northern Tibet (Qinghai Province, China), *Seism. Res. Lett.* **73,** no. 2, 125–135.

Van der Woerd, J., F. J. Ryerson, P. Tapponnier, Y. Gaudemer, R. Finkel, A. S. Meriaux, M. Caffee, G. Zao, and Q. He (1998). Holocene left slip-rate determined by cosmogenic surface dating on the Xidatan segment of the Kunlun fault (Qinghai, China), *Geology* **26,** 695–698.

Van der Woerd, J., F. J. Ryerson, P. Tapponnier, A. S. Meriaux, Y. Gaudemer, B. Meyer, R. Finkel, M. Caffee, G. Zhao, and Z. Xu (2000). Uniform slip-rate along the Kunlun fault: implication for seimic behaviour and large-scale tectonics, *Geophys. Res. Lett.* **27,** 2353–2356.

Van der Woerd, J., P. Tapponnier, F. J. Ryerson, A. S. Meriaux, B. Meyer, Y. Gaudemer, R. C. Finkel, M. W. Caffee, G. G. Zhao, and Z. Q. Xu, (2002b). Uniform postglacial slip-rate along the central 600 km of the Kunlun Fault (Tibet), from Al-26, Be-10, and C-14 dating of riser offsets, and climatic origin of the regional morphology, *Geophys. J. Int.* **148,** no. 3, 356–388.

Van der Woerd, J., X. W. Xu, H. B. Li, P. Tapponnier, B. Meyer, F. J. Ryerson, A. S. Meriaux, and Z. Q. Xu (2001). Rapid active thrusting along the northwestern range front of the Tanghe Nan Shan (western Gansu, China), *J. Geophys. Res. Solid Earth* **106,** no. B12, 30,475–30,504.

Velasco, A. A., C. J. Ammon, and S. Beck (2000). Broadband source modeling of the November 8, 1997 Tibet ($M_w = 7.5$) earthquake and its source implications, *J. Geophys. Res.* **105,** 28,065–28,028.

Vergne, J., G. Wittlinger, Q. Hui, P. Tapponnier, G. Poupinet, J. Mei, G. Herquel, and A. Paul (2002). Seismic evidence for stepwise thickening of the crust across the NE Tibatan plateau, *Earth Planet. Sci. Lett.* **203,** 25–33.

Wang, Q., P. Zhang, J. T. Freymueller, R. Bilham, K. M. Larson, X. Lai, X. You, Z. Niu, J. Wu, Y. Li, J. Liu, Z. Yang, and Q. Chen (2001). Present-day crustal deformation in China constrained by global positioning system measurements, *Science* **294,** 574–577.

Ward, S. (1997). Dogtails versus rainbows: synthetic earthquake rupture models as an aid in interpreting geological data, *Bull. Seism. Soc. Am.* **87,** 1422–1441.

Wittlinger, G., P. Tapponnier, G. Poupinet, J. Mei, S. Danian, G. Herquel, and F. Masson (1998). Tomographic evidence for localized lithospheric shear along the Altyn Tagh fault, *Science* **282,** 74–76.

Wittlinger, G., J. Vergne, P. Tapponnier, V. Farra, G. Poupinet, M. Jiang, H. Su, G. Herquel, and A. Paul (2004). Teleseismic imaging of subducting lithosphere and Moho offsets beneath western Tibet, *Earth Planet. Sci. Lett.* **221,** no. 1-4, 117–130.

Xu, X., W. Chen, W. Ma, G. Yu, and G. Chen (2002). Surface rupture of the Kunlunshan earthquake (M_s 8.1), northern Tibetan plateau, China, *Seism. Res. Lett.* **73,** no. 6, 884–892.

Laboratoire de Tectonique – UMR7578
Institut de Physique du Globe
4 place Jussieu
75005 Paris, France
klinger@ipgp.jussieu.fr
tappon@ipgp.jussieu.fr
king@ipgpjussieu.fr
(Y.K., P.T., G.K.)

Institut of Geology, CEA
Beijing 100029, China
xiweixu@vip.sina.com
(X.X.)

UMR7516, EOST, 5 r. Descartes
67000 Strasbourg, France
jeromev@eost.u-strasbg.fr
(J.V.)

Department of Earth and Space Sciences, UCLA
Los Angeles, California
lasserre@geologie.ens.fr
(C.L.)

Manuscript received 12 March 2004.

Bulletin of the Seismological Society of America, Vol. 95, No. 5, "High-resolution Satellite Imagery Mapping of the Surface Rupture and Slip Distribution of the M_W ~7.8, 14 November 2001 Kokoxili Earthquake, Kunlun Fault, Northern Tibet, China," Klinger et al., pp. 1970–1987

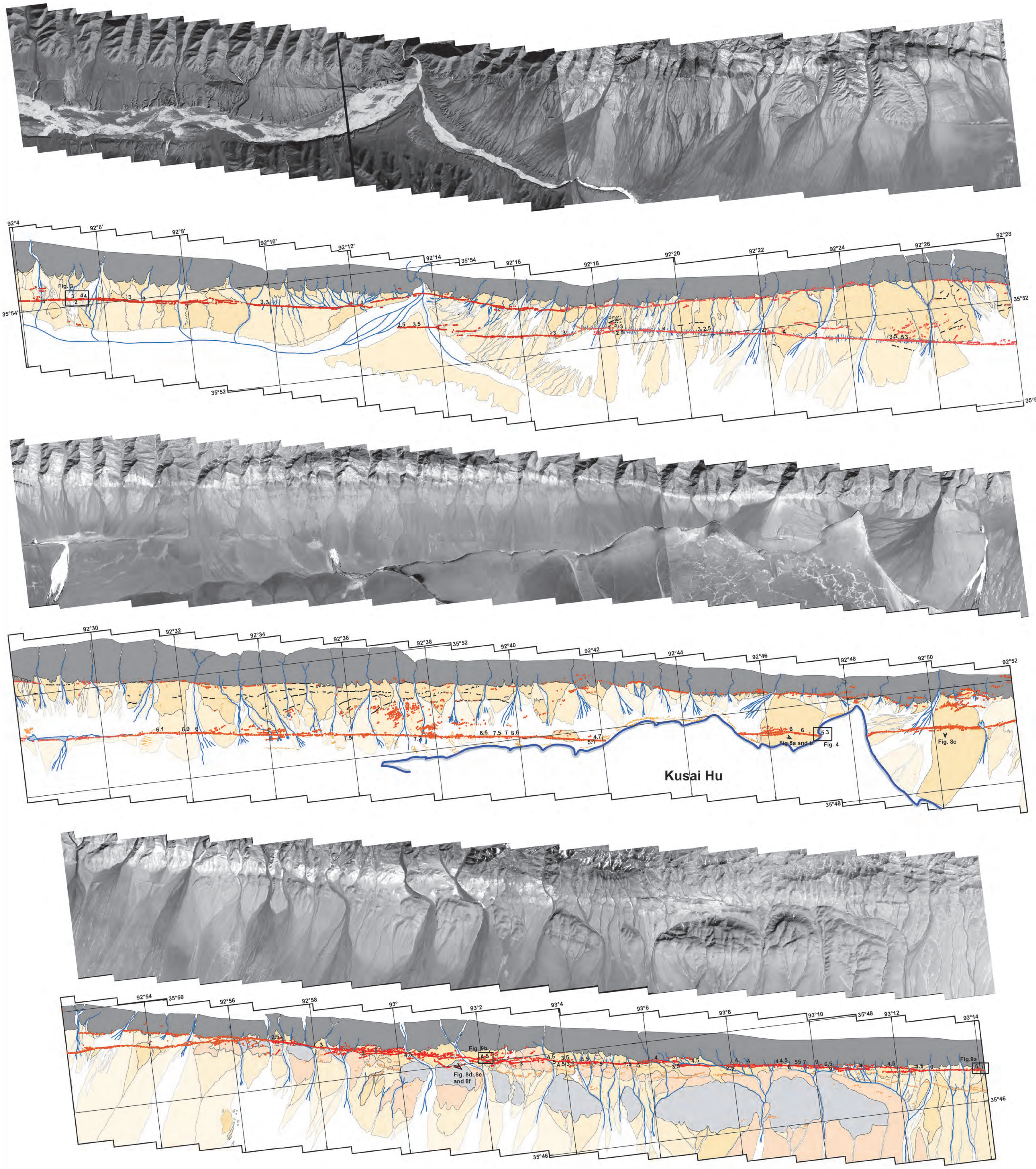

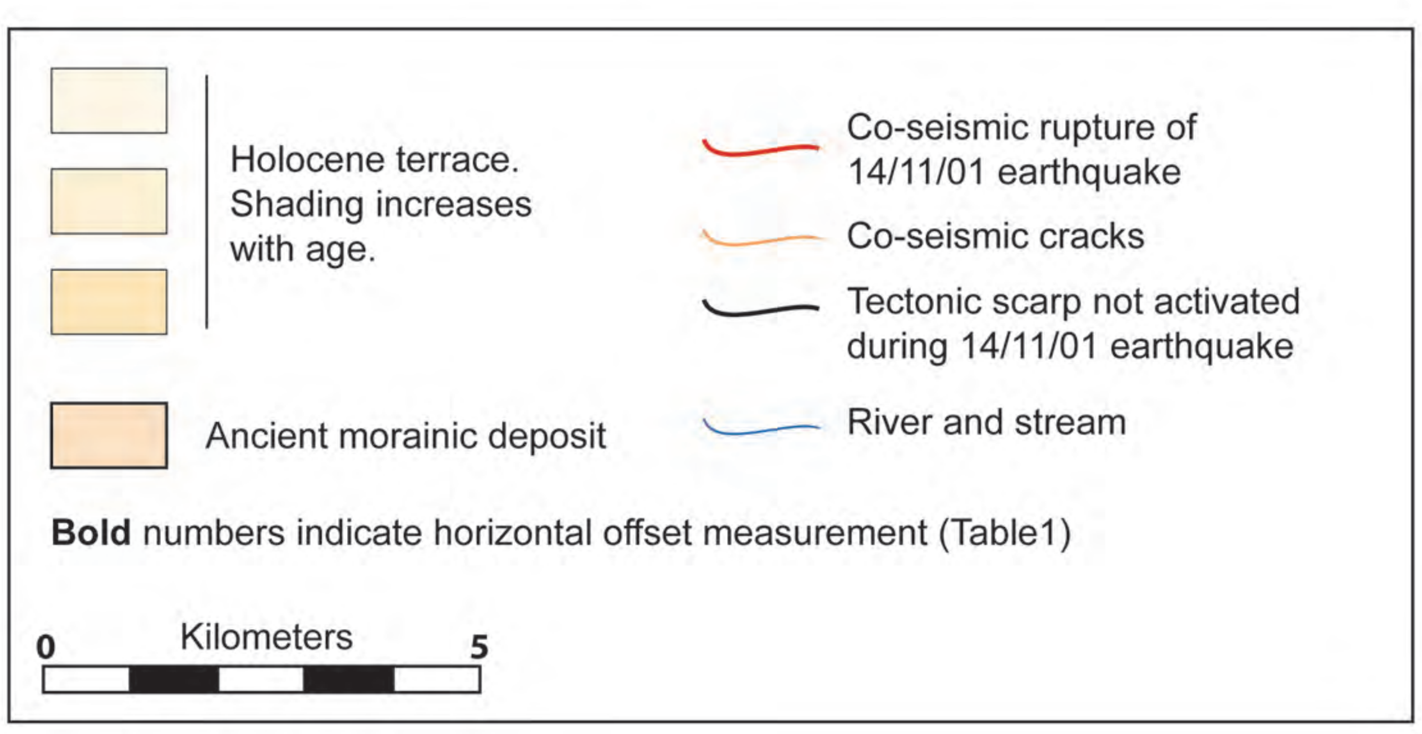

Plate 1. Map of the central part of the 2001 Kokoxili earthquake rupture. The upper swath displays assembled HRS images (pixels 1 m, acquisition date 29 March 2002). Lower panel is a map of surface breaks derived from the georeferenced HRS swath. Numbers indicate horizontal offsets restored with the HRS images (in meters). A 1/50000 scale version of this map is available at www.ipgp.jussieu.fr/~klinger

Bulletin of the Seismological Society of America, Vol. 95, No. 2, pp. 731–738, April 2005, doi: 10.1785/0120040101

Slip-Partitioned Surface Breaks for the M_w 7.8 2001 Kokoxili Earthquake, China

by Geoffrey King, Yann Klinger, David Bowman, and Paul Tapponnier

Abstract Slip-partitioned fault breaks have been mapped for a 70-km stretch of the 450-km surface rupture of the 14 November 2001 Kokoxili earthquake. Simultaneous dip-slip and strike-slip motion on parallel faults has been proposed before, but the new observations demonstrate unequivocally that it can occur in a single earthquake and allows the mechanical processes to be scrutinized. Observed normal fault offsets were between 0.5 and 1 m and strike-slip offsets were 3–5 m. The partitioned stretch of faulting has a strike that differs by 2–3° from the pure strike-slip faulting to the east and west. This allows a horizontal opening vector of 0.25 m to be determined for the partitioned region. The distance between the two faults is greatest (~2 km) at the center of the partitioned portion and diminishes toward the ends.

The faulting is modeled to result from strains due to a buried oblique slip-fault dipping at 80° to the south. The depth to the top of the buried fault is shown to vary commensurately with the separation of the surface faults. Clear surface rupture is observed where the predicted model mechanisms are colinear and where substantial faults can develop into a kinematically stable partitioned system. In a few interesting examples fragmentary, oblique surface ruptures occur where the predicted mechanisms are not colinear, but they are not associated with long-term surface faulting.

The proposed mechanism for slip partitioning requires that rupture propagates upward from depth. For the Kokoxili surface breaks this is a consequence of coseismic, dynamic rupture traveling faster at depth than near the surface, leaving the surface deformation to catch up. While the mechanism we propose requires slip weakening and localization to create faults or shear zones, it does not require that faults with different mechanisms have different frictional behavior.

Introduction

On 14 November 2001, a major earthquake (M_w 7.8) occurred in the Kokoxili region of the Kunlun fault along the North side of the Tibetan Plateau (Fig. 1a). The surface breaks extended for more than 400 km making it one of the largest strike-slip events known (Van der Woerd *et al.*, 2002a; Xu *et al.*, 2002; Lin *et al.*, 2002). The desert conditions resulted in clear surface breaks being formed and preserved. Mapping of these breaks has been undertaken by field mapping combined with analysis of Ikonos satellite images (Klinger *et al.*, unpublished manuscript, 2004). The latter have a pixel size of 1 m, which allows even small surface features with sufficient intensity contrast to be seen. In practice, this means that fissures with widths as small as 30 cm can be mapped. At present 100 km of the fault rupture has been mapped in detail. Here we discuss a stretch that shows clear slip partitioning. The major displacement is ~ 5 m of left-lateral strike slip, although at up to 2 km away and parallel to the strike slip are pure normal surface breaks with throws of up to 1 m. Although slip partitioning at this scale has been documented elsewhere (Allen *et al.*, 1984; Armijo *et al.*, 1986, 1989), this is the first time that such faults are known to have moved simultaneously in a single earthquake.

Recently Bowman *et al.* (2003) have shown that a process of upward propagation of deformation from a buried oblique-slip fault can explain fault distribution and mechanisms on the scale of tens of kilometers. In this article we show that the same process can explain the smaller-scale Kokoxili observations and suggest how it relates to the processes of dynamic rupture propagation.

The Origin of Slip Partitioning

The term "slip partitioning" is used to describe oblique motion along a fault system that is accommodated on two or more faults with different mechanisms (Fitch, 1972). Nu-

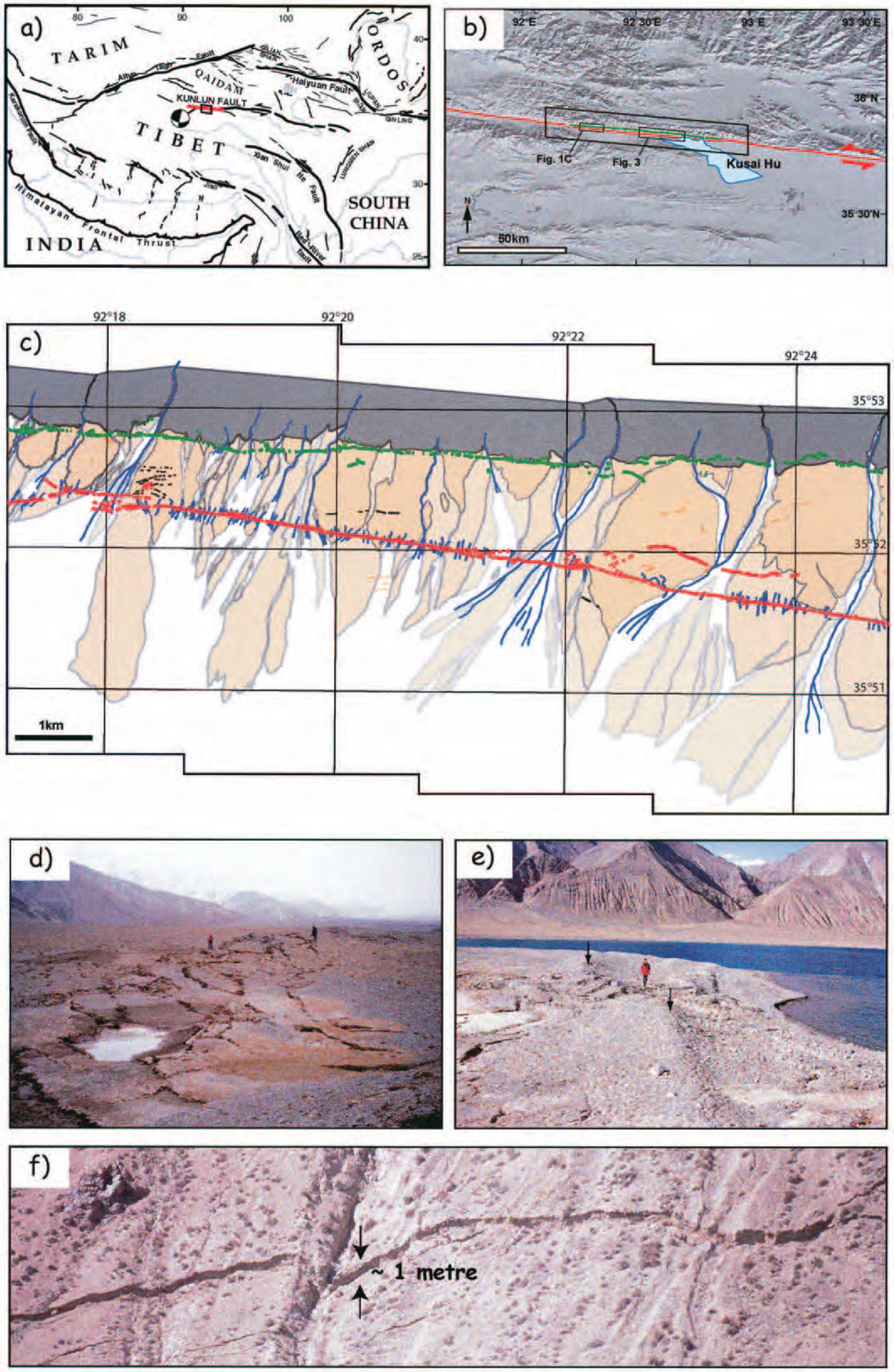
a)
TARIM
QAIDAM
KUNLUN FAULT
TIBET
ORDOS
Haiyuan Fault
QIN LING
Xian Shui He Fault
Himalayan Frontal Thrust
INDIA
SOUTH CHINA
Red River Fault
b)
92°E
92°30'E
93°E
93°30'E
36°N
35°30'N
Fig. 1C
Fig. 3
Kusai Hu
N
50km
c)
92°18
92°20
92°22
92°24
35°53
35°52
35°51
1km
d)
e)
f)
~ 1 metre

Figure 1. (a) The location and overall focal mechanism (Harvard moment tensor) of the 14 November 2001 (M_w 7.8) earthquake. The section that ruptured is marked in red. (b) 200 km of the mapped faulting near Kusai Hu (Lake). The central sector exhibits strike-slip and normal surface breaks (enclosed in a box). Strike-slip breaks are shown in red and dip-slip in green. There is a difference in strike between the central section and the fault to the east and west of 3–4°. (c) A 12-km part of the detailed fault map. Strike-slip surface breaks are identified in red and dip-slip in green. In many places the November 2001 earthquake broke along features from previous events: Older scarps not reactivated in the recent event are shown in black. Rivers are shown in blue and older terraces in shades of yellow. Bedrock is indicated by dark gray. The locations of Figure 1c and Figure 3 are shown. (d) Strike-slip faulting surface breaks to the east of Kusai Hu. The remains of a sag pond from a previous event can be seen in the foreground. (e) Strike-slip surface breaks cutting the shore of Kusai Hu (Lake) with an offset of ~5 m. Arrows indicate an offset beach strand. The normal fault surface breaks occur near the base of the approximately 500-m-high escarpment in the background. The faceted spurs and wine-glass valleys indicate substantial late Quaternary normal faulting. (f) Normal surface breaks near the base of the escarpment shown in d.

merous examples are reviewed by Molnar (1992). The mechanics of slip partitioning has long been controversial because of the complex stress fields implied by the geometry and kinematics of partitioned systems. Michael (1990) and Wesnousky and Jones (1994) have suggested that slip partitioning might represent a minimum energy condition. However, because faults do not form closed thermodynamic systems there is no reason why such a condition should prevail. Another common explanation of partitioning is that major strike-slip faults evolve to have very low friction and thus are able to move in an overall stress field that favors dip-slip faulting. This has also been proposed as a solution to the low-heat-flow paradox along the San Andreas Fault (Henyey and Wasserburg, 1971). However, neither a widely accepted mechanism for producing low friction nor the reliability of the heat-flow measurements has been established (Scholz, 2000).

Jackson and McKenzie (1983) and Molnar (1992) have proposed models where a solid upper crust is deformed by viscous flow in the lower crust and upper mantle. These models might produce features similar to slip partitioning, but specific examples of partitioned faults in the crust have never been modeled in this way. Their view is also compromised by geological evidence (Wallace, 1984; Tapponnier *et al.*, 1990; Leloup *et al.*, 1995; Meyer *et al.*, 1998; Tapponnier *et al.*, 2001; Hubert-Ferrari *et al.*, 2003) and Global Positioning System (GPS) data (Meade *et al.*, 2002; Flerit *et al.*, 2004) showing that the deformation in the lower crust and upper mantle of continents is localized on shear zones. Seismic imaging of Moho offsets and lower crust and upper mantle features are also inconsistent with modeling deformation of the lower crust and upper mantle as a viscous fluid (Wittlinger *et al.*, 1998, 2004; Vergnes *et al.*, 2002).

Simple kinematic models for slip partitioning have been suggested, with a number of authors proposing that many examples of partitioned systems in Asia are an upper crustal response to oblique slip on deep-seated faults or shear zones (Armijo *et al.*, 1986, 1989; Gaudemer *et al.*, 1995; Tapponnier *et al.*, 2001). These models provide kinematic explanations of the observed surface deformation. The kinematic models, however, do not explain the origin and evolution of the stress fields that initiate and maintain partitioned systems, although, as we discuss below, specific kinematic conditions must be satisfied for partitioned faults to become long-lived features.

Bowman *et al.* (2003) recently proposed that slip partitioning can be explained as a result of upward propagation of oblique shear at depth. If the lower crust and upper mantle are not a viscous fluid then a slip-weakening, elasto-plastic rheology is the best approximation to their behavior (McClintock, 1971; Peltzer and Tapponnier, 1988; Cowie and Scholz, 1992a,b; Lawn and Wilshaw, 1975; Hubert-Ferarri *et al.*, 2003). As discussed by Bowman *et al.* (2003), the upper crust responds to stress from buried shear zones in a process of upward crack propagation that can be modeled with elastic fracture mechanics. Their approach is similar to that used to explain the creation and maintenance of en echelon midocean ridge structures (Abelson and Agnon, 1997; Hubert-Ferarri *et al.*, 2003).

Standard fracture mechanics models describe a zone of permanent deformation that extends around a crack or fault tip. The deformation within this "process or damage zone" can be modeled using an elastic approximation. In the process zone, stress amplitudes are poorly determined and much lower than an elastic model predicts, but strains and the principal axes of strain are more or less correct (Hubert-Ferrari *et al.*, 2003). The form of the strain tensor can consequently be used together with a simple Coulomb-like failure criterion (King and Cocco, 2000) to define the orientations and mechanism of predicted faulting.

In the process zone the material loses strength before being traversed by the propagating fault. Under simple shear conditions a mode II or III crack (Lawn and Wilshaw, 1975) can propagate through the process zone. However, the complex strain boundary conditions associated with an oblique fault beneath the Earth's surface prevent it from extending through the process zone as a single structure. The strain field around the fault tip is not simple, and hence, deformation distributes over several planes with different orientations and slip directions. Nearer to the surface and further from the fault tip the strains over substantial regions are more homogeneous, allowing new faults to form. These faults have mechanisms that are different from each other and from the buried fault, however. This explanation of the origin of slip partitioning (Bowman *et al.*, 2003) and can be used to create simple numerical models of partitioned systems that closely imitate observations.

Field Observations

The 14 November 2001 earthquake ruptured part of the Kunlun fault in northeast Tibet (Fig. 1a). This fault has long been recognized as one of the major strike-slip faults in Tibet, allowing eastward escape of the Tibetan plateau in response to the India/Eurasia collision (Tapponnier *et al.*, 2001). With a slip-rate of $\sim$1 cm/yr (Van der Woerd *et al.*, 1998, 2000, 2002b), the Kunlun fault is known to have hosted several large earthquakes with magnitude > 7 (Tapponnier and Molnar, 1977; Peltzer *et al.*, 1999; Van der Woerd *et al.*, 2002a). The ground rupture associated with the 14 November 2001 events is more than 400 km long and mainly follows the southern flank of the Kunlun range (Lin *et al.*, 2002; Van der Woerd *et al.*, 2002b; Xu *et al.*, 2002) with the exception of the two extremities where the rupture branches onto secondary faults. This study focuses on the central segment of the rupture, the Kusai Hu segment, named after the largest lake in the region (Fig. 1b). This includes a 70-km stretch of slip partitioning with parallel normal and strike-slip surface breaks separated by up to 2 km. These partitioned faults strike at an angle of 3–4° to the pure strike-slip faulting observed to the east and west. The average horizontal slip along the stretch of faulting shown in Figure 1b is about 5 m. This change of strike allows the opening due to partitioning to be estimated to be $\sim$0.25 m.

A part of the mapped fault is shown in Figure 1c with strike-slip surface breaks shown in red and normal slip breaks shown in green. Photographs of the strike-slip fault are shown in Figure 1d and e. In Figure 1e a sag pond formed by a previous earthquake can be seen, and Figure 1d shows where the fault offsets the shore of the Kusai Hu (lake) by about 5 m. Normal faults occur near the base of the escarpment shown in Figure 1e and f. The faceted spurs and wineglass canyons (Fig. 1e) indicate that normal faulting has been taking place for tens of thousands of years.

Modeling Slip Partitioning

The mechanics of slip partitioning can be understood by regarding the buried oblique fault to be a dislocation. The resulting strain field and fault mechanisms are calculated with Almond 7.05 software (www.ipgp.jussieu.fr/$\sim$king) based on the program developed by Okada (1982) to calculate displacements and strains around a rectangular dislocation in a homogeneous half-space. Figure 2a shows that the strain between the dislocation and the surface exhibits a range of different fault mechanisms (for more examples, see Bowman *et al.*, 2003 supplementary material). Two regions occur that have either predominantly strike-slip or predominantly normal mechanisms. These are outlined in red and green, respectively. Although deformation occurs throughout the zone of high strain, it is only within these regions that coherent and colinear strike-slip or normal faults can form. Where the predicted mechanisms vary spatially, no single simple through-going fault can form, instead incoherent multiple fracturing is to be expected (Bowman *et al.*, 2003).

The mathematical modeling treats the top of the dislocation as an edge dislocation. As discussed earlier, the region is in reality a large damage zone with no such abrupt boundary. Consequently, the term "top of the buried fault" that we use later should be interpreted as the center of the damage zone rather than as an abrupt feature.

The surface breaks in map view are modeled assuming that the strike-slip component of displacement on the buried fault is 5 m and the horizontal component of opening is 0.25 m (Fig. 2b). The depth to the top of the fault and its dip are adjusted to fit the observations (Fig. 2c). The dip-slip component of motion is calculated from the horizontal motion and the chosen dip. There are consequently two variables that can be adjusted to fit the observations, dip and depth. The best fit is found by forward modeling. This is straightforward because of the limited sensitivity to parameters discussed by Bowman *et al.* (2003) (see supplementary material www.sciencemag.org/cgi/content/full/300/5622/1121/DC1) and below. Models can be found that fit the location of the observed faulting over a range of dips from 65° to 85°. The amount of dip-slip motion on the main fault is determined by its dip to give the 0.25 m of horizontal motion. This in turn determines the vertical component. Thus, shallower dips require a smaller vertical component of displacement on the main fault. A dip of 80° on the buried fault requires a dip-slip component of 1.5 m. Resolving this onto a near-surface normal fault with a nominal dip of 45° permits the observed 1-m displacements. Shallower dips predict smaller displacements and consequently seem less likely.

The distance between the zones of normal and strike-slip faulting is relatively insensitive to the dip of the oblique fault. The separation between the normal and strike-slip faulting, however, is sensitive to the depth to the top of the oblique driving fault. The depth to the top of the driving fault that produces the best fit is shown in Figure 2d.

The fit of the model to the main through-going strike-slip and normal surface breaks is very close. These occur where the predicted mechanisms are colinear and thus allow a through-going fault to form for the same reason considered when discussing the cross section. Deformation is mainly localized on two structures; however, some deformation does occur elsewhere as shown in Figure 3. Although the strike-slip surface break forms a narrow feature, normal faulting may consist of many small ruptures oblique to the overall trend of the faulting. This is consistent with the model, which correctly predicts such a distribution of faulting. Unlike faults evolving where colinear faulting is predicted, these scattered oblique surface breaks cannot link to form long-lived features. Many older breaks (black in Fig. 3) that did not move in the last event attest to the transitory nature of this oblique faulting.

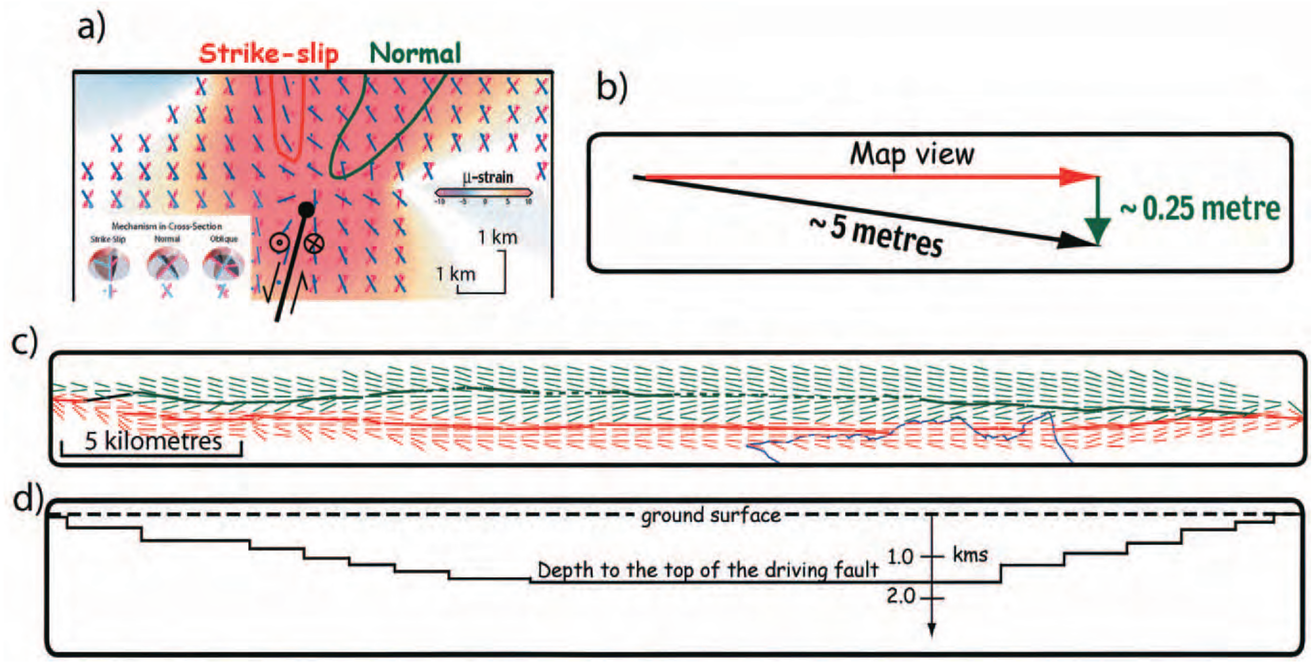

Figure 2. (a) Cross section of the distribution of strain resulting from a dipping buried strike-slip, normal-slip fault. The mechanism of faults that can relieve the strain is indicated by lines and dots. (See the inset for interpretation and Bowman *et al.*, 2003.) Two areas are identified where strike-slip and dip-slip mechanisms predominate. The separation between these zones at the surface is slightly less than the depth to the top of the dislocation. (b) The faulting to the east and west of the partitioned section is pure strike slip with and average offset of 5 m. The 3–4° strike difference suggests that the opening component is about 0.25 m. (c) A simplified surface break map of the region shown in the box in Figure 1b. Strike-slip surface breaks are shown in red and normal fault in green. Predicted fault strikes using the same color code are shown by short lines. The predicted slip directions are calculated for an 80° dipping fault with 5 m of strike-slip motion and 1.5 m of dip-slip motion (corresponding to 0.25 m of opening). The continuous strike-slip and normal breaks occur where the model predicts colinear faulting. (d) A cross section showing the depth to the top of the dislocation that produces the model shown in c.

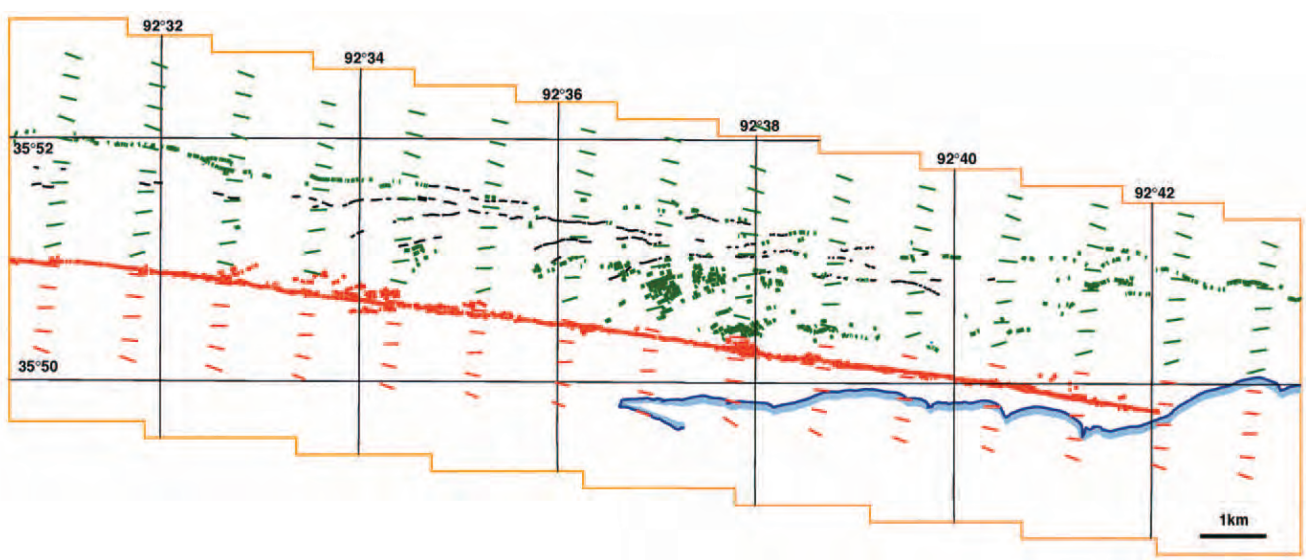

Figure 3. In some places the normal faulting does not form a continuous trace. Both old and new breaks correspond to predicted directions that are not colinear.

Discussion

Slip partitioning is a consequence of propagation of rupture. Should all parts of a fault move together, partitioning would not occur. It is consequently appropriate to ask why some parts of a fault should move before other parts. This problem is analogous to the question of how edge dislocations can be repeatedly created within the body of a crystal. This was solved by the recognition of the Frank-Reid source from which dislocations are born and spread along crystal planes (Nabarro, 1967).

No such single explanation seems available for faults. For the crustal scale examples discussed by Bowman *et al.* (2003) it was noted that faults or shear zones in lower crust or mantle must slip prior to those in the upper crust. King and Bowman (2003) discuss why stable sliding at depth should drive slip in the seismogenic upper crust and why slip at seismogenic depths lags slip at greater depth, catching up only at the time of an earthquake. Although this provides a possible explanation, their models for the Transverse Ranges and North Tibet require that the top of the driving fault is at 40–50 km (Bowman *et al.*, 2003). This is too deep to correlate with the stick-slip/stable sliding transition. For the even larger-scale slip partitioning associated with subduction systems (Fitch, 1972) no unequivocal explanation seems to be immediately available.

Unlike the larger-scale examples, the small-scale partitioning associated with the Kokoxili earthquake can be explained in terms of dynamic propagation. The rupture in the November 2001 earthquake propagated from west to east (Xu *et al.*, 2002; Antolik *et al.*, 2004; Bouchon and Vallée, 2003). Figure 4 indicates the generalized form of the rupture front. Seismic velocities almost invariably increase with depth. Thus, the rupture advances faster at depth than near to the surface and, consequently, the top kilometer or two experience nearly upward propagation.

The reduction of seismic velocity near to the surface can be due to several effects. Surface, poorly consolidated sediments exhibit low velocities and low velocity also appears in basement rocks as a result of cracks and fissures that remain open under the low confining pressures (Scholz, 2002). A further effect is the relaxation of stress over a similar depth range due to stress corrosion cracking (Scholz, 2002). This latter process has been discussed by King and Vita-Finzi (1981) and Vita-Finzi and King (1985) in the context of surface folding, a process that also involves upward propagation.

For the Kokoxili earthquake partitioning, the top of the driving oblique fault could coincide with the bottom of surface sediments with the low seismic velocity in the sediments being largely responsible for upward propagation as proposed by Armijo *et al.* (1986, 1989). For the Kokoxili earthquake slip partitioning is only observed where the strike-slip fault cuts sediment; elsewhere, the strike-slip fault appears at the base of the mountain front. This is consistent with the partitioning being a result of the surface sediments. However, because of the differences of strike, only the partitioned Kusai segment is associated with opening. Thus no normal faulting is expected elsewhere. The sediments can also be the consequence rather than the cause of slip partitioning. Sediments deposited on the hanging wall of normal faults will, over time, cover the strike-slip fault, causing the system to evolve toward that observed.

No shallow focal mechanism data are available to support the field observations of slip partitioning near Kusai Hu because no local stations exist in the region. However, the mechanisms of small earthquakes along the central Denali Fault, Alaska, after the 2002 earthquake (Ratchkovski, 2003) could be explained by the propagation processes that we invoke.

Conclusions

Coseismic slip partitioning between pure strike-slip and pure normal faulting is observed along the Kusai Hu segment of the Kunlun fault. Both the strike-slip and the normal faulting have been active through the Quaternary and both rebroke during the 14 November 2001 Kokoxili earthquake. By combining field studies with analysis of Ikonos high-resolution satellite images, the faulting has been mapped in

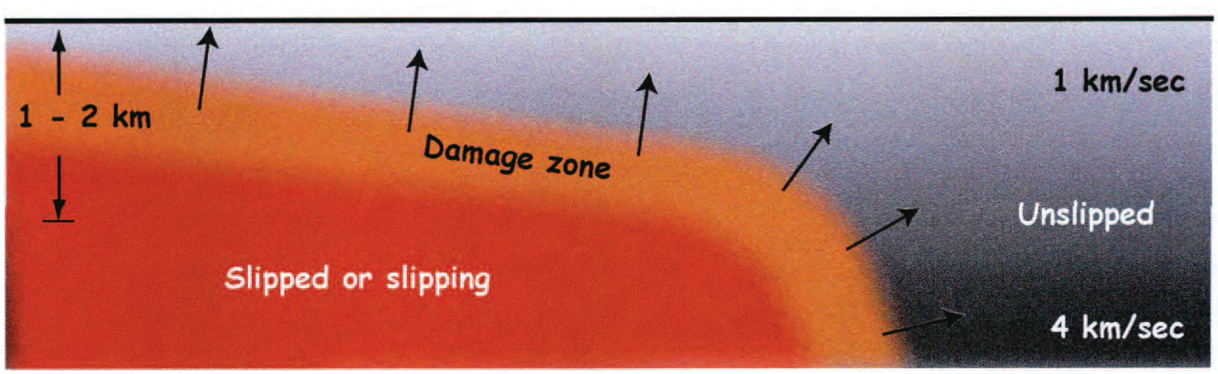

Figure 4. Seismic velocity increases with depth. Thus, deep rupture propagates faster than rupture near to the surface, resulting in upward rupture propagation.

detail. Following earlier work by Bowman *et al.* (2003), we have modeled the surface ruptures on the assumption that they result from upward propagation from a dipping oblique-slip fault at depth. We follow their assumption that a plastic (or damage zone) develops ahead of the propagating fault and that distinct faults form where the strain is coherent over a sufficient distance to be relieved by a fault of significant dimensions.

The modeling has only two adjustable parameters—the dip of the buried fault and its depth—and is consequently robust. The model that most closely fits the observations has a dip of 80° and a maximum depth to the top of the buried fault of 2 km. Through-going rupture occurs only where the model mechanisms are colinear, allowing coherent faults to form. The resulting geometry is similar to that described kinematically by Armijo *et al.* (1986, 1989). It is unlikely, however, that the faults join at a simple triple junction at depth. It is more likely to be a region of a complex of small faults with a range of mechanisms as predicted by the modeling. In a few places scattered oblique faults occur at the surface in places where the predicted mechanisms are not colinear. These include both new rupture and features from previous events that were not reactivated. The foregoing adds further support to the view proposed by Bowman *et al.* (2003) that significant faults can only evolve where the strain field is homogeneous over a significant distance.

The mechanism for slip partitioning that we adopt requires that rupture propagates upward from depth. For the Kokoxili surface breaks this is a consequence of coseismic, dynamic rupture traveling faster at depth than near the surface, leaving the surface deformation to catch up. Although the mechanism we propose requires slip weakening and localization to create faults or shear zones, it does not require different values of friction for faults with different mechanisms.

Acknowledgments

We thank Jerome Van der Woerd and Xu Xiwei who participated in field work and made early versions of their publications available to us. We thank José Hurtado for a very helpful review. This article is INSU contribution number 369 and IPGP number 2910. This research was supported by the Southern California Earthquake Center (SCEC) funded by NSF Cooperative Agreement EAR-0106924 and USGS Cooperative Agreement 02HQAG0008.

References

Abelson, M., and A. Agnon (1997). Mechanics of oblique spreading and ridge segmentation, *Earth Planet. Sci. Lett.* **148,** 405–421.

Allen, C., A. Gillespie, H. Yuan, K. Sieh, Z. Buchun, and Z. Chengnan (1984). Red River and associated faults, Yunnan Province, China: quaternary geology, slip rate and seismic hazard, *Geol. Soc. Am. Bull.* **95,** 686–700.

Antolik, M., R. E. Abercrombie, and G. Ekström (2004). The 14 November, 2001 Kokoxili (Kunlunshan), Tibet, earthquake: rupture transfer through a large extensional step-over, *Bull. Seism. Soc. Am.* **94,** no. 4, 1173–1194.

Armijo, R., P. Tapponnier, and T. Han (1989). Late Cenozoic right-lateral strike-slip faulting in southern Tibet, *J. Geophys. Res.* **94,** no. 3, 2787–2838.

Armijo, R., P. Tapponnier, J. L. Mercier, and H. Tong-Lin (1986). Quaternary extension in Southern Tibet: field observations and tectonic implications, *J. Geophys. Res.* **91,** no. B14, 13,803–13,872.

Bouchon, M., and M. Vallée (2003). Observation of long supershear rupture during the magnitude 8.1 Kunlunshan earthquake, *Science* **301,** 824–826.

Bowman, D., G. King, and P. Tapponnier (2003). Slip partinioning by elastoplastic propagation of oblique slip at depth, *Science* **300,** 1121–1123.

Cowie, P. A., and C. H. Scholz (1992a). Physical explanation for the displacement-length relationship of faults using a post-yield fracture mechanics model, *J. Struct. Geol.* **14,** 1133–1148.

Cowie, P. A., and C. H. Scholz (1992b). Growth of faults by accumulation of seismic slip, *J. Geophys. Res.* **97,** 11,085–11,095.

Fitch, T. (1972). Plate convergence, transcurrent faults, and internal deformation adjacent to southeast Asia and the western Pacific, *J. Geophys. Res.* **77,** 4432–4462.

Flerit, F., G. C. P. King, R. Armijo, and B. Meyer (2004). The mechanical interaction between the propagating North Anatolian Fault and the back-arc extension in the Aegean. *Earth Planet. Sci. Lett.* **224,** 347–362.

Gaudemer, Y., P. Tapponnier, B. Meyer, G. Peltzer, G. Shunmin, C. Zhitai, D. Huangung, and I. Cifuentes (1995). Partitioning of crustal slip between linked active faults in the eastern Qilian Shan, and evidence for a major seismic gap, the 'Tianzhu Gap', on the western Haiyuan fault, Gansu (China), *Geophys. J. Int.* **120,** no. 3, 599–645.

Henyey, T. L., and G. J. Wasserburg (1971). Heat flow near major strike-slip faults in California, *J. Geophys. Res.* **76,** no. 32, 7924–7946.

Hubert-Ferrari, A., G. C. P. King, I. Manighetti, R. Armijo, B. Meyer, and P. Tapponnier (2003). Long-term elasticity in the continental lithosphere; modelling the Aden Ridge propagation and the Anatolian extrusion process, *Geophys. J. Int.* **153,** 111–132.

Jackson, J., and D. McKenzie (1983). The geometrical evolution of normal fault systems, *J. Struct. Geol.* **5,** no. 5, 471–482.

King, G. C. P., and D. Bowman (2003). The evolution of regional seismicity between large earthquakes. *J. Geophys. Res.* **108,** no. B2, 2096, doi 10.1029/2001JB000783.

King, G. C. P., and M. Cocco (2000). Fault interaction by elastic stress changes: new clues from earthquake sequences, *Adv. Geophys.* **44,** 1–38.

King, G. C. P., and C. Vita-Finzi (1981). Active folding in the Algerian earthquake of 10 October 1980, *Nature* **292,** no. 5818, 22–26.

Lawn, B. R., and T. R. Wilshaw (1975). *Fracture of Brittle Solids*, Cambridge U. Press, New York.

Leloup, P. H., R. Lacassin, P. Tapponnier, U. Schärer, D. Zhong, X.-H. Liu, L.-S. Zhang, S.-C. Ji, and T. T. Phan (1995). The Ailao Shan-Red River shear zone (Yunnan, China), tertiary transform boundary of Indochina, *Tectonophysics* **251,** 3–84.

Lin, A., B. Fu, J. Guo, Q. Zeng, G. Dang, W. He, and Y. Zhao (2002). Co-seismic strike-slip and rupture length produced by the 2001 Ms 8.1 central Kunlun earthquake, *Science* **296,** 2015–2017.

McClintock, F. A. (1971). Plasticity aspects of fracture, in *Fracture. An Advanced Treatise*, H. Liebowitz (Editor), Vol. III. Engineering Fundamentals Band Environment Effects, Academic Press. New York.

Meade, B. J., B. H. Hager, S. McClusky, R. Reilinger, S. Ergintav, O. Lenk, A. Barka, and H. Ozener (2002). Estimates of seismic potential in the Marmara Sea Region from block models of secular deformation constrained by global positioning system measurements, *Bull. Seism. Soc. Am.* **92,** 208–215.

Meyer, B., P. Tapponnier, L. Bourjot, F. Metivier, Y. Gaudemer, G. Peltzer, G. Shunmin, and C. Zhitai (1998). Crustal thickening in Gansu-Qinghai, litospherique mantle subduction, and oblique, strike-slip controlled growth of the Tibet plateau, *Geophys. J. Int.* **135,** 1–47.

Michael, A. J. (1990). Energy constraints on kinematic models of oblique faulting; Loma Prieta versus Parkfield-Coalinga, *Geophys. Res. Lett.* **17,** 1453–1456.

Molnar, P. (1992). Brace-Goetze strength profiles, the partitioning of strike-slip and thrust faulting at zones of oblique convergence, and the stress-heat flow paradox of the San Andreas Fault, in *Fault Mechanics and Transport Properties of Rocks*, B. Evans and T.-f. Wong (Editors), Academic Press, New York, 436–459.

Nabarro, F. R. N. (1967). *Theory of Crystal Dislocations*, Clarendon Press, Oxford.

Okada, Y. (1982). Internal deformation due to shear and tensile fault in a half-space, *Bull. Seism. Soc. Am.* **82,** 1018–1040.

Peltzer, G., and P. Tapponnier (1988). Formation and evolution of strike-slip fauls, rift, and basins during the India-Asia collision: an experimental approach, *J. Geophys. Res.* **93,** no. B12, 15,085–15,117.

Peltzer, G., F. Crampe, and G. King (1999). Evidence of nonlinear elasticity of the crust from the Mw7.6 Manyi (Tibet) earthquake, *Science* **286,** 272–276.

Ratchkovski, N. A. (2003). Change in stress directions along the central Denali fault, Alaska, after the 2002 earthquake sequence, *Geophys. Res. Lett.* **30,** no. 19, 2017, doi 10.1029/2003GL01795.

Scholz, C. H. (2000). Evidence for a strong San Andreas fault, *Geology* **28,** 163–166.

Scholz, C. H. (2002). *The mechanics of Earthquakes and Faulting*, Cambridge U. Press, New York.

Tapponnier, P., and P. Molnar (1977). Active faulting and tectonics in China, *J. Geophys. Res.* **82,** 2905–2930.

Tapponnier, P., R. Lacassin, Ph. H. Leloup, U. Schärer, D. Zhong, H.-W. Wu, X.-H. Liu, S.-C. Ji, L.-S. Zhang, and J.-Y. Zhong (1990). The Ailoa Shan/River metamorphic belt: tertiary left-lateral shear between Indochina and South China, *Nature* **343,** 431–437.

Tapponnier, P., X. Zhiqin, F. Roger, B. Meyer, N. Arnaud, G. Wittlinger, and Y. Jingsui (2001). Oblique stepwise rise and growth of the Tibet plateau, *Science* **294,** 1671–1677.

Van der Woerd, J., A. S. Meriaux, Y. Klinger, F. J. Ryerson, Y. Gaudemer, and P. Tapponnier (2002a). The 14 November 2001, Mw = 7.8 Kokoxili earthquake in northern Tibet (Qinghai Province, China), *Seism. Res. Lett.* **73,** no. 2, 125–135.

Van der Woerd, J., F. J. Ryerson, P. Tapponnier, Y. Gaudemer, R. Finkel, A.-S. Mériaux, M. W. Caffee, G. Zhao, and Q. He (1998). Holocene left-slip rate determined by cosmogenic surface dating on the Xidatan segment of the Kunlun fault (Qinghai, China), *Geology* **26,** 695–698.

Van der Woerd, J., F. J. Ryerson, P. Tapponnier, A. S. Meriaux, Y. Gaudemer, B. Meyer, R. Finkel, M. Caffee, G. Zhao, and Z. Xu (2000). Uniform slip-rate along the Kunlun fault: Implication for seimic behaviour and large-scale tectonics, *Geophys. Res. Lett.* **27,** 2353–2356.

Van der Woerd, J., P. Tapponnier, F. J. Ryerson, A.-S. Mériaux, B. Meyer, Y. Gaudemer, R. C. Finkel, M. W. Caffee, G. Zhao, and Z. Xu (2002b). Uniform post-glacial slip-rate along the central 600 km of the Kunlun Fault (Tibet), from ^{26}Al, ^{10}Be and ^{14}C dating of riser offsets, and climatic origin of the regional morphology, *Geophys. J. Int.* **148,** 356–388.

Vergne, J., G. Wittlinger, Q. Hui, P. Tapponnier, G. Poupinet, J. Mei, G. Herquel, and A. Paul (2002). Seismic evidence for stepwise thickening of the crust across the NE Tibetan plateau, *Earth Planet. Sci. Lett.* **203,** 25–33.

Vita-Finzi, C., and G. C. P. King (1985). The seismicity, geomorphology and structural evolution of the Corinth area of Greece, *Philos. Trans. R. Soc. London A* **314,** 379–407.

Wallace, R. E. (1984). Patterns and timing of late Quaternary faulting in the Great Basin province and relation to some regional tectonic features, *J. Geophys. Res.* **89,** no. B7, 5763–5769.

Wesnousky, S. G., and C. H. Jones (1994). Oblique slip, slip partitioning, spatial and temporal changes in the regional stress field, and the relative strength of active faults in the Basin and Range, Western United States, *Geology* **22,** 1031–1034.

Wittlinger, G., P. Tapponnier, G. Poupinet, J. Mei, S. Danian, G. Herquel, and F. Masson (1998). Tomographic evidence for localized lithospheric shear along the Altyn Tagh fault, *Science* **28.**

Wittlinger, G., J. Vergne, P. Tapponnier, V. Farra, G. Poupinet, M. Jiang, H. Su, G. Herquel, and A. Paul (2004). Teleseismic imaging of subducting lithosphere and Moho offsets beneath western Tibet, *Earth Planet. Sci. Lett.* **221,** 117–130.

Xu, X., W. Chen, W. Ma, G. Yu, and G. Chen (2002). Surface rupture of the Kunlunshan earthquake (Ms 8.1), northern Tibetan plateau, China, *Seism. Res. Lett.* **73,** no. 6, 884–892.

Laboratoire Tectonique
Institut de Physique du Globe de Paris
4 place Jussieu
75252, Paris, France
(G.K., Y.K., P.T.)

Department of Geological Sciences
California State University, Fullerton
800 N. State College Blvd.
Fullerton, California 92834-6850
(D.B.)

Manuscript received 3 June 2004.

Available online at www.sciencedirect.com
SCIENCE DIRECT
ELSEVIER
Earth and Planetary Science Letters 242 (2006) 354 – 364
EPSL
www.elsevier.com/locate/epsl

Evidence for an earthquake barrier model from Mw ~ 7.8 Kokoxili (Tibet) earthquake slip-distribution

Y. Klinger [a,*], R. Michel [b], G.C.P. King [a]

[a] *Tectonique, Institut Physique du Globe de Paris, BP89, 4 place Jussieu, 75005 Paris, France*
[b] *Lab. Détection et de Géophysique, CEA, BP12, 91680 Bruyères-le-Châtel, France*

Received 8 September 2005; received in revised form 30 November 2005; accepted 2 December 2005
Available online 18 January 2006
Editor: V. Courtillot

Abstract

The slip distribution of the Mw ~ 7.8 Kokoxili (Tibet, 2001) earthquake has been measured at high resolution using optical correlation of satellite images and provides both the parallel and perpendicular components of the horizontal co-seismic slip. This reveals a variation of the horizontal slip at a scale of ~ 20 km along-strike. Anti-correlation of slip parallel and perpendicular to the fault indicates transfer of slip from the horizontal to the vertical component at the ends of segments. These features suggest a rupture model with segments separated by strong persistent geometric barriers. The unexpected ending of the rupture south of the main fault can be explain by such a structure but bears important implications for the initiation and rupture directivity of the next earthquake.

Keywords: earthquake rupture; fault mechanics; Kunlun fault

1. Introduction

Dynamic rupture studies of earthquakes adopt different views of the relation between the propagating rupture and fault geometry. On one hand, the asperity concept [1] where the rupturing part of fault plane is described as the “stronger” or more stressed part of the fault, and on the other hand the barrier concept [2] where tough [3] and hence stressed regions delimit the parts of the fault that ruptures. In this view, the ruptured fault segment is regarded as less “strong”. The barriers arrest rupture and, in extreme cases, stop it [4]. In the asperity model, large earthquakes form when several neighbouring asperities rupture consecutively. There is little reason why the slip-distribution associated with this model should reflect observed fault segmentation. In the barrier model, the rupture initiates on one segment and propagates to the neighboring segments, either unilaterally or bilaterally, having to pass barriers between each segment. In this case, barriers are associated with identifiable fault features such as bends or offsets and the signature of the barrier should be visible in the slip-distribution associated with the earthquake [5].

Although such features have been identified from mapping surface rupture [6], seismic, Insar and GPS data lack the resolution to distinguish between the models [7]. Most field measurements of rupture carried out after large earthquakes are either spatially too

* Corresponding author.
E-mail addresses: klinger@ipgp.jussieu.fr (Y. Klinger), remi.michel@cea.fr (R. Michel).

0012-821X/$ - see front matter © 2006 Elsevier B.V. All rights reserved.
doi:10.1016/j.epsl.2005.12.003

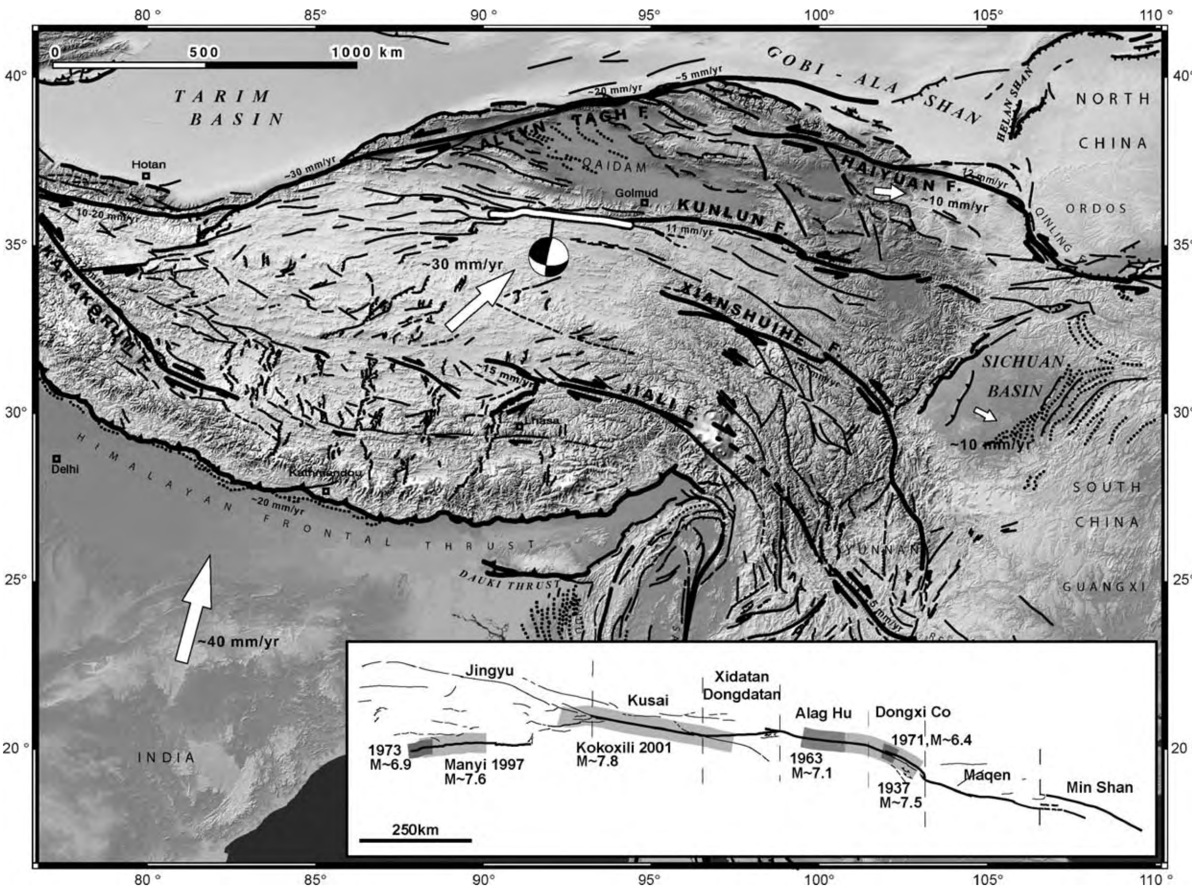

Fig. 1. Main active faults of the Tibetan part of the India–Asia collision zone (modified from [10]). The 450-km-long rupture of the Mw ~7.8 Kokoxili earthquake (14 November 2001) is outlined in white, with centroid focal sphere (Harvard). Inset shows earthquake dislocations along the Kunlun fault since 1930, emphasizing the very long rupture length of the 14 November 2001 earthquake and the seismic gap along the Xidatan-Dongdatan segment (different shades are used to distinguish between overlapping ruptures).

limited [8] or too sparse along strike [9], preventing the relation between slip-variations and segmentation (10–30 km) to be clearly identified. Here, we correlate optical images to study the surface rupture of the Mw ~ 7.8 Kokoxili (Tibet) event (Fig. 1), and provide observations that support the barrier model for earthquake rupture.

2. Kokoxili earthquake ruptures

The Kokoxili event triggered a flurry of studies because it provided a unique opportunity to study a giant continental earthquake in an arid environment where surface features are not masked by vegetation. This earthquake occurred along the western end of the Kunlun fault (Fig. 1). This fault is one of the major left-lateral strike-slip faults that allow extrusion of the Tibet plateau eastward [10]. The slip-rate along the Kunlun fault has been estimated to be about 1 cm/yr based on independent geologic [11] and GPS [12] studies. A detailed description of the rupture and the geodynamic context has already been published (see [13] and references herein) and only salient features are summarized below.

The rupture initiated in a pull-apart basin (N35°57′/E90°32.4′, Fig. 2), and propagated ~50 km along the western section and for ~400 km to the east along the extensional corridor, the Kusai section and the Kunlun Pass section. The rupture, in the extensional corridor was oriented about 20° CCW relative to the Kusai section. Surface expression of the rupture is not well developed along this part. From the point where the rupture joined the Kusai section (N36°01.35′/E90°14.32′), it propagated eastward for ~270 km without any major change in strike. At the end of the Kusai section (N35°43.8′/E93°39′) instead of following the Xidatan fault, generally regarded as the main strand of the Kunlun fault eastward [11] the rupture continued on the Kunlun Pass section where it propagated for a

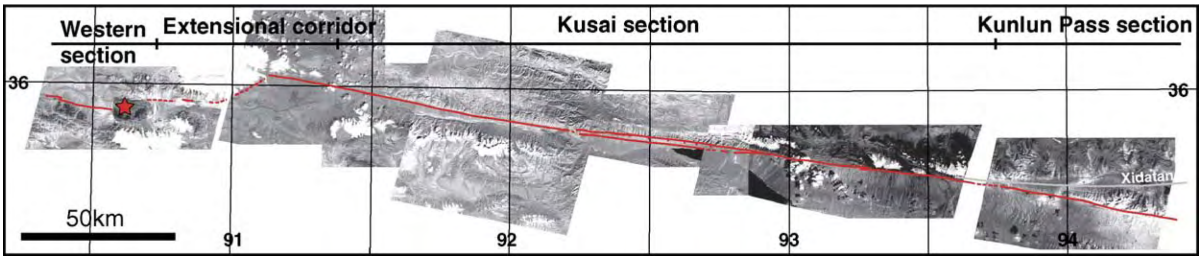

Fig. 2. Spot mosaic covering the entire 2001 earthquake rupture. Epicentre and surface ruptures are indicated.

further ~70 km. This last section displays a modest thrust component in addition to the strike-slip component. The average co-seismic slip associated with the 2001 earthquake is 2 to 3 m with a maximum slip of ~10 m.

3. Optical image correlation

Maps of ground displacement and associated uncertainties are computed from subpixel correlation of optical images acquired by the SPOT satellites before and after the earthquake [14–16]. This technique yields robust estimates of the rupture geometry and of the two components of horizontal displacement near the fault, parallel and perpendicular to the co-seismic rupture. It complements SAR interferometry that often fails near the fault due to excessive temporal decorrelation of the images and signal saturation. Furthermore, SAR data only provide the satellite to ground component of the deformation [15]. Thus, the study in this paper, which shows the relation between the two horizontal components, cannot be accomplished using SAR.

We processed 8 pairs (Table 1) of Spot images covering ~400 km of rupture and measured the displacements with an accuracy of ~1 m, every 320 m. Fig. 3A, B and C show, respectively, the degree of correlation and the map of horizontal offset along x- and y-axes. Loss of coherence within the western and extensional sections, characterized by a snowy pattern in the correlation image, prevents reliable offset measurements there. In the western section, the co-seismic rupture lies on the northern front of the mountain range (Fig. 2). The fault trace is hardly discernable from the limit between the coherent patch, to the south, which corresponds to the mountain range, and the zone of low coherence, to the north, which is associated with unstable alluvial surfaces (alluvial fan, river bed, etc.). This prevents useful offset measurement, although fieldwork has shown that offset can locally reach 4 m [13]. The corridor section, affected by several active drainages, does not display a coherent signal either. From the western end of the Kusai section eastward, the trace of the co-seismic rupture is very sharp. Changes in azimuth (A on Fig. 3B) and relay zones (B on Figs. 3B and 4) can be identified. The Kunlun Pass fault section is characterized by a higher decorrelation probably due to larger snow coverage and glaciers. Nevertheless, the trace of the rupture (C on Fig. 3B and boxes indicating location of Fig. 8) is clearly visible just north of the range front, which is responsible for a small residual topographic signal. The trace of the co-seismic rupture along the y-axis is subdued (Fig. 3C), in keeping with the dominant strike-slip behavior of the East–West oriented Kunlun fault. Any significant signal observed along the y-axis corresponds to the projection of some vertical motion on the horizontal plane, in the case of extensional or compressional jogs for example. Such deformation, ubiquitous along the whole rupture, is responsible for the faint co-seismic trace visible in Fig. 3C.

Offsets maps include bias induced by instrumental uncertainties (view parameters, optics and detection) and by the correlation procedure [14]. For SPOT

Table 1
List of spot images used to compute correlation maps

Platform	Date (DD.MM.YYYY)	Reference (K–J)	Incidence (Left/Right degree)
SPOT–3	3.8.1996	230–278	L 8.30
SPOT–4	7.4.2004	230– 277	R 5.00
SPOT–3	5.11.1996	231–278	R 2.30
SPOT–4	22.7.2003	231–277	R 0.30
SPOT–3	5.11.1996	232–278	L 2.30
SPOT–4	8.10.2003	232–278	L 2.50
SPOT–1	29.10.1989	233–278	L 4.60
SPOT–4	30.11.2002	233–278	L 4.50
SPOT–1	12.6.1988	234–278	R 4.60
SPOT–4	24.10.2003	234–277	R 5.70
SPOT–4	22.1.2003	235–278	R 20.30
SPOT–1	15.5.1998	235–278	R 21.60
SPOT–4	28.8.2002	236–278	L 25.40
SPOT–2	31.8.1992	236–278	L 26.20
SPOT–4	17.6.2002	238–278	L 6.90
SPOT–2	2.10.1992	237–278	L 5.90

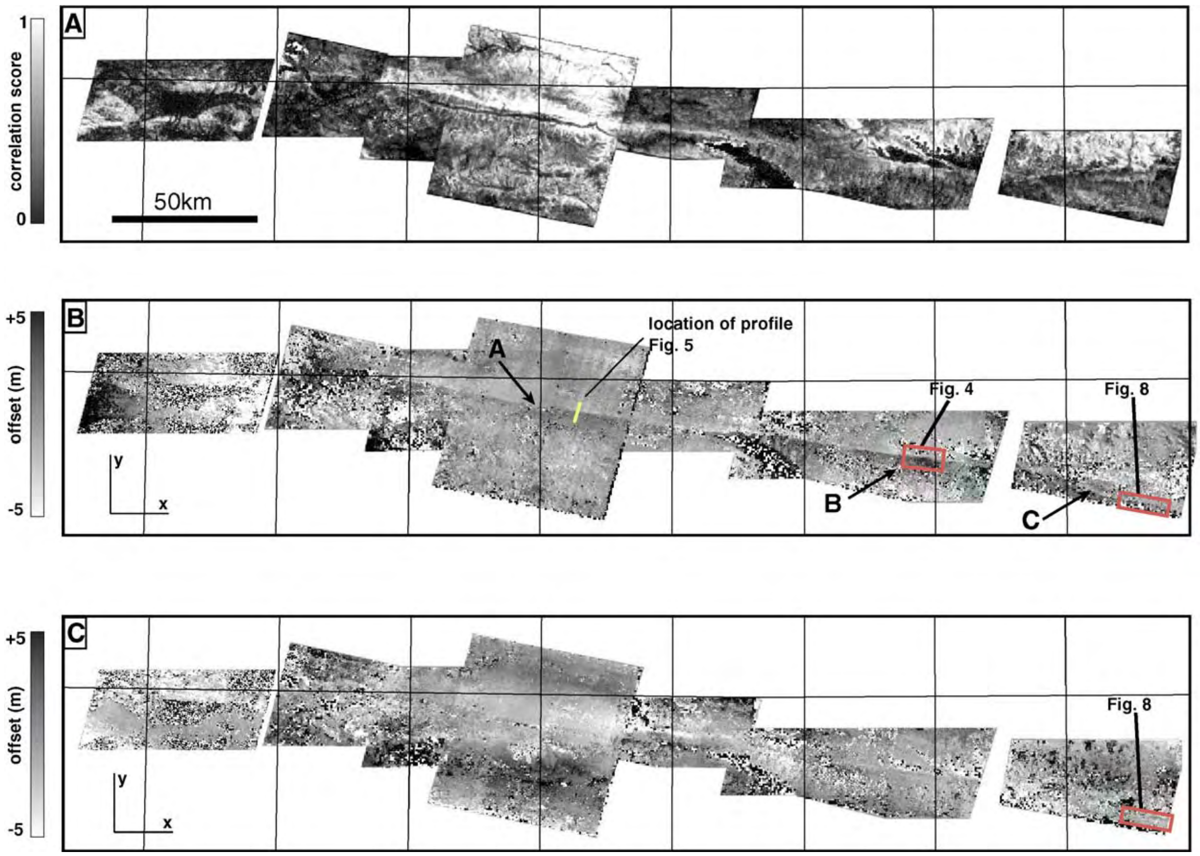

Fig. 3. (A) Map of the correlation score. Loss of coherence within the western and extensional sections, characterized by a snowy pattern in the correlation image, prevents reliable offset measurements there. (B) Map of offset along the *x*-axis direction. Motion eastward is positive. (C) Map of offset along the *y*-axis direction. Motion southward is negative.

imagery, it has been demonstrated that bias is scale dependant, yielding pluri-metric errors at the 5 km^{-1} scale or below and error of few tens of centimetres at the 100 m^{-1} scale or above [14]. This prevents estimates of low spatial frequency patterns of ground deformation, but has no influence on slip estimates from profiles across the fault [17] (Fig. 5). Offsets may also suffer from residual topographic errors resulting from uncertainties in Digital Elevation Models and on stereoscopic angles. Using SRTM DEM and SPOT imagery and the procedure describe by [14], this source of uncertainty is estimated to be as high as 107 cm (rms) for correlation windows 640 m × 640 m in size in a highly mountainous area. Fortunately, this noise is reduced to about 21 cm within the relatively flat area (alluvial fans and bajada) ruptured by the earthquake.

Fault offsets are then estimated every kilometre from the amplitude of the discontinuity on stacked profiles, weighted by correlation score, perpendicular to the fault (Fig. 5). Accuracy of offset is limited by this local correlation score (Fig. 3A).

Slip estimated from profiles mainly includes noise from temporal decorrelation of the images and offset gradients within the correlation window. Calibrated uncertainties on measurement are derived from the correlation score [14]. Uncertainty of slip from a raw profile is typically slightly below 1/10th of the pixel size (1 m on the ground) for correlation windows 640 m × 640 m in size, but may increase to 1 pixel within highly decorrelated area (Fig. 3A). The resulting uncertainty in slip decreases with the resolution in a near square-root-n form down to about 34.4 cm (rms) for slip estimated with independent measurement every 5 km (Fig. 6).

4. Discussion

Fig. 6 shows the slip-curve projected parallel and perpendicular to the local strike of the fault. Acknowledging that the Kunlun fault accommodates almost pure strike-slip displacement, the component of slip measured perpendicular to the fault corresponds to

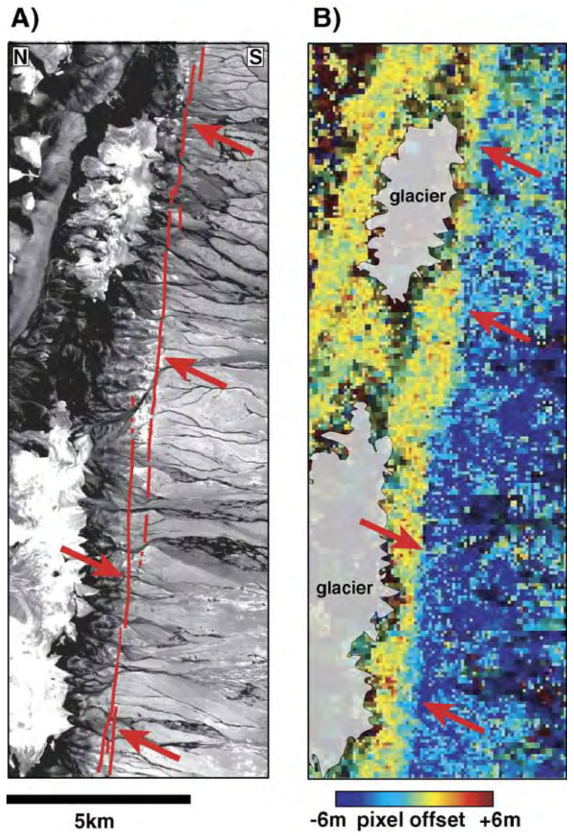

Fig. 4. Close-up views of measurements showing details of the co-seismic rupture in a relay zone. (A) Extract of post-earthquake Spot image. The surface rupture is outlined in red. (B) Corresponding correlation image measured in the direction parallel to the rupture. Red arrows point to the co-seismic rupture.

projection onto the horizontal direction of vertical motion (up or down) on dipping faults (Fig. 7). The average slip along strike (Fig. 6A) is 2.7 m with 2 maximum peaks reaching ~8 m with, on average, no slip perpendicular to the fault (Fig. 6B), although locally it can reach large positive or negative values, reflecting local geometric complexities. The Kunlun Pass section is characterized by a lower slip, ~0.6 m. Interestingly, the eastern part of the Kulun Pass section shows a more coherent pattern with a systematic motion southward (Fig. 8). The average horizontal motion is ~1.7 m. This could result from 1.96 m slip occurring on a 30° dipping fault. This is consistent with the thrust component of the Kunlun Pass section reported from field observation [18]. Our results show overall good agreement with the slip-curve extrapolated from InSar data [19]. Comparison with offset data measured in the field [20] also shows general good agreement. Interestingly, places where field data clearly are larger than offsets we measured from optical correlation, are places where larger dispersion of the field data is observed. The western end of the Kusai section provides a good example where offsets from optical correlation yield values between 2 m and 3 m, in good agreement with Insar data [19]. At the same place, field data range from 2 m to 6 m. It seems very probable to us that some cumulative offsets have been misinterpreted to be 2001 offsets as in some cases it could be tricky to distinguish between single and cumulative offset due to earthquake [13]. This interpretation is supported by the fact that the largest values measured in such place are almost twice as large of the lower values collected in the same place, in good agreement with characteristic-slip models [21,22].

The moment magnitude Mw corresponding to the slip-distribution we measured was computed using a crust 15 km thick [19,23] and slip-values from correlation data where reliable data exist and an average horizontal slip of 2 m for the western section, based on field observations [13]. The shear modulus was assumed to be 3×10^{11} dyn/cm^2. The extensional corridor was not included because no surface slip distribution is available. This gives a Mw ~ 7.7, in good agreement with the magnitude estimated from other methods. This suggests that the slip distribution at the surface is compatible with the actual motion on the fault plane and that no major slip occurred at depth that did not reach the surface, unlike for smaller earthquakes [24,25].

The slip-curves presented here allow us to discuss the relation between segmentation of the fault and surface rupture. Although these relations were already

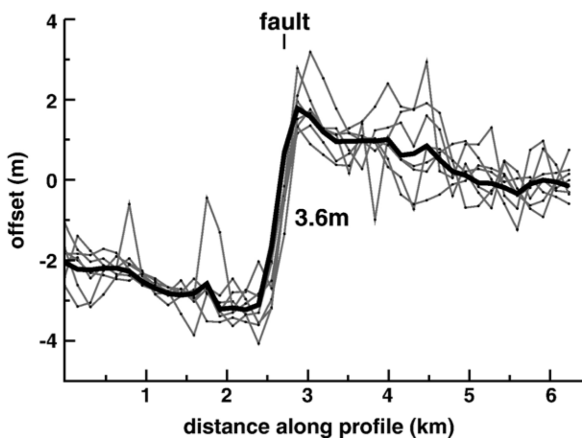

Fig. 5. Raw profiles (gray) extracted from the parallel component offset map (see Fig. 3B for location). Profiles are measured each 160 m along fault for 1 km and stacked (bold line) to reduce noise. Seismic offset is measured from the stacked profile.

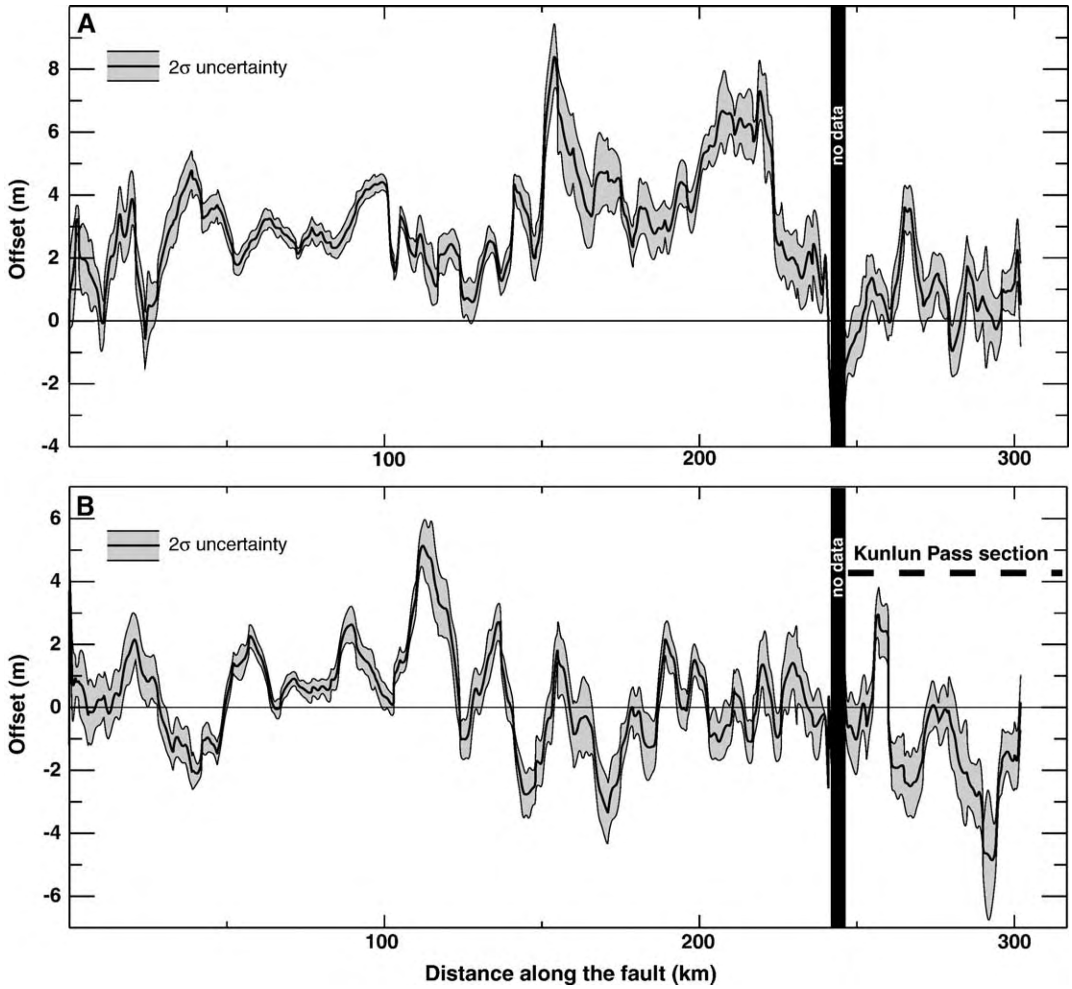

Fig. 6. (A) Displacement parallel, along *x*-axis, (A) and normal, along *y*-axis, (B) to the fault measured from stacked profiles averaged over 5 km along fault. Left-lateral and northward motion is positive. Local azimuth of the rupture is measured directly from Spot images acquired after the event.

suggested from seismic data (e.g. [4]) and field observations (e.g. [6]), measurements of slip, both parallel and perpendicular to the rupture were not possible. Fig. 9 shows the slip distribution in the direction parallel to the rupture. The slip-distribution consists of short segments, 15 to 25 km long (average length 14.9 km), that display bumps of larger slip. The edges of the sections are marked by low points in the slip curve. Although spatial resolution is lower, inversion based on Insar data shows that variations of slip are not only due to surficial effect but could be extended at depth [19]. Fig. 9 shows the map of the rupture associated with the Kokoxili earthquake, derived from field exploration and satellite image interpretation. The location of the jogs (compressional and extensional) that were activated during the event are indicated in red. Side faults that connect to the main rupturing fault are in light grey. Almost without exception low slip zones match the location of jogs, bends or a junction with side faults. The slip-distribution is clearly related to the geometrical structure of the fault. Field investigation has shown that most of these features

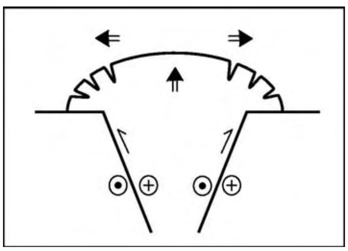

Fig. 7. In compressional or extensional jogs vertical motion generates displacement perpendicular to the fault.

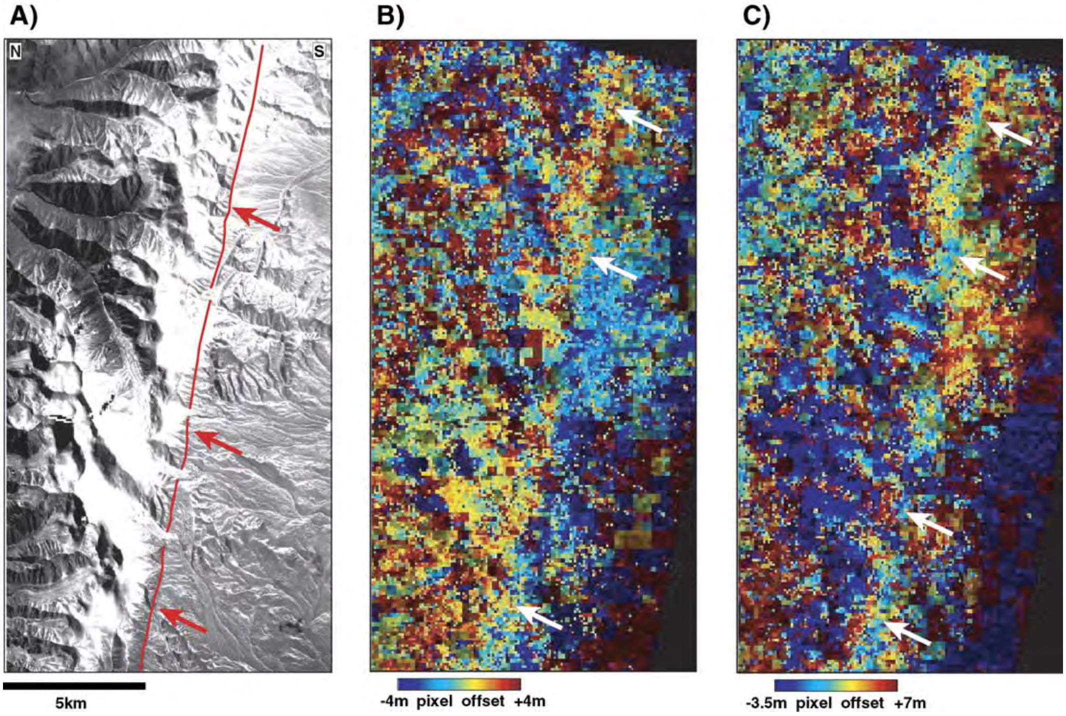

Fig. 8. Close-up views of measurements showing details of the co-seismic rupture along the Kunlun Pass section where thrust has been observed in addition to strike-slip motion. (A) Extract of post-earthquake Spot image. The surface rupture is outlined in red. (B) Correlation image measured in the direction parallel to the fault. White arrows point to the trace of the strike-slip motion. (C) Correlation image measured in the direction perpendicular to the fault. Systematic motion southward indicated by white arrows corresponds to the projection of the thrust component of the motion onto the horizontal plane, detectable by optical correlation.

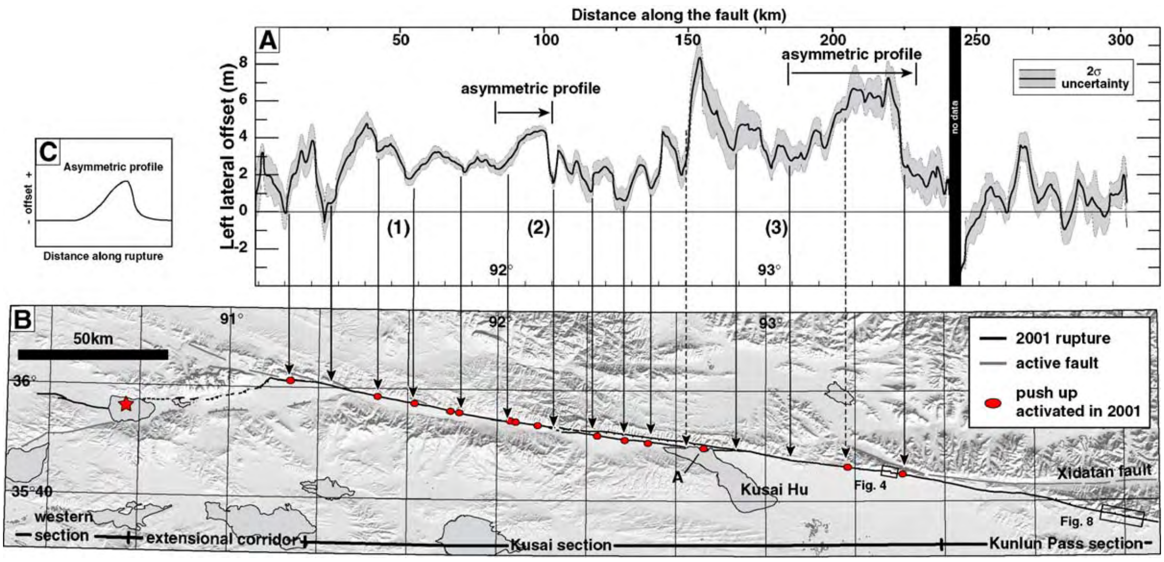

Fig. 9. (A) Slip measured parallel to the fault (left-lateral motion is positive). The slip is derived from correlation of Spot images averaged over 5 km along rupture. (B) Map of the 2001 event surface ruptures. Red star locates earthquake epicenter. (C) Asymmetric profile is characterized by slow rising of the slip value followed by a sharp drop. Local minima of the slip-curve correspond (black arrows), with two exceptions (dashed arrows), to geometric barriers like push-ups (1), fault branching (2) or changes of fault azimuth (3) identified along the fault. At least two asymmetric slip profiles can be identified that are unambiguously associated to split of the fault trace.

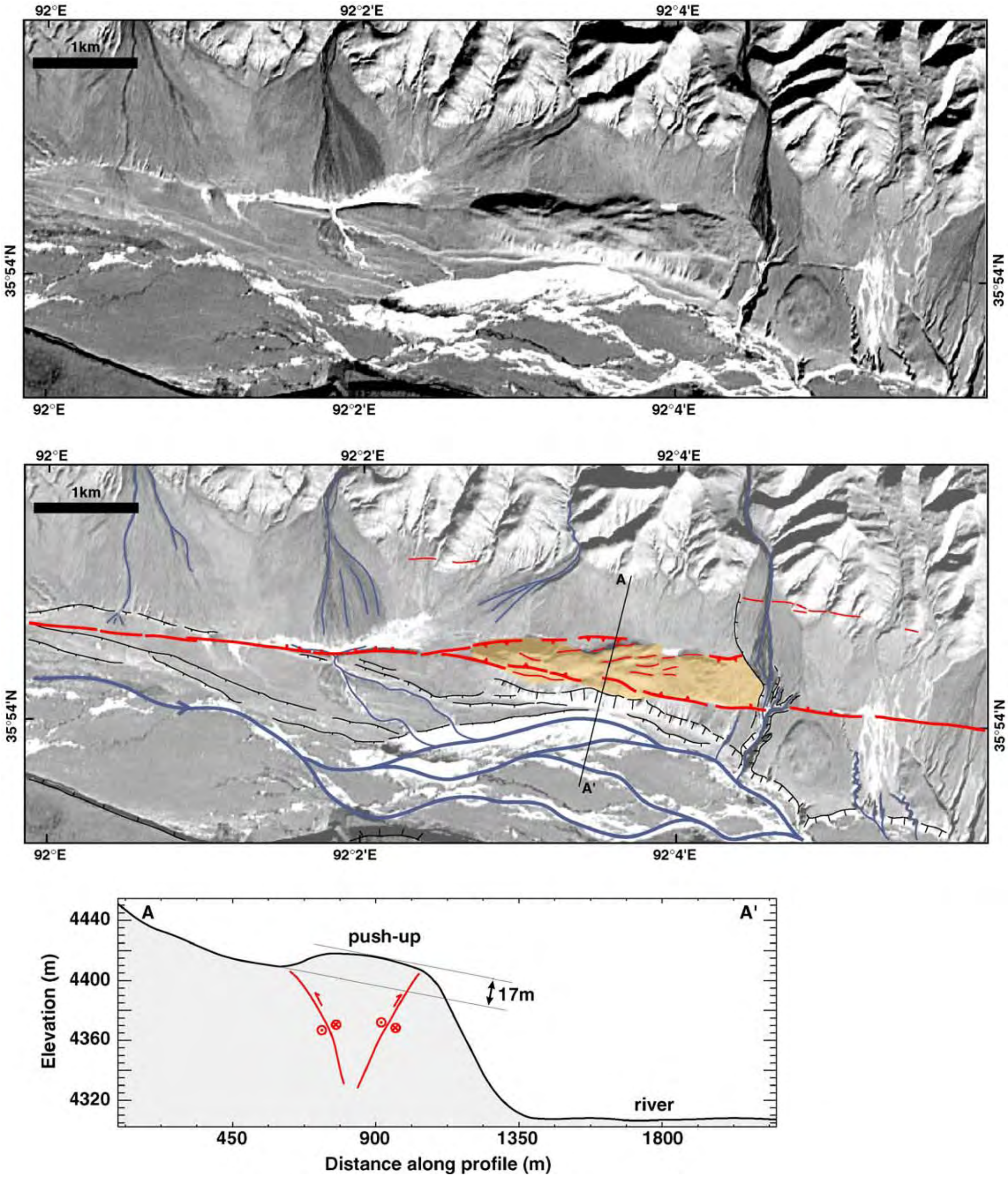

Fig. 10. Satellite image of a typical push-up along the Kusai section activated during the 2001 earthquake. The horizontal motion transfers to vertical in the relay zone. The size of this ridge shows that it has been active for several seismic cycles.

have been activated and apparently played a similar role in many previous earthquakes (Fig. 10). It is worth noting that the pull-apart basin on the northern shore of the Kusai Hu (A in Fig. 9) does not affect the slip-distribution in a visible way. The slip seems to be most affected by compressive jogs or side faults connecting to the rupturing fault [26]. Fig. 11 shows the coefficient of cross-correlation between the slip measured parallel to and perpendicular to the fault, computed for a lag of ±50 km. For lag values close to zero, the coefficient is significant [27] and negative indicating anti-correlation between the motion on the two components.

This behaviour is to be expected for a geometric barrier where the slip is accommodated on a multitude of small faults distributed through a wide range of scales and orientations that differ from that of the main fault

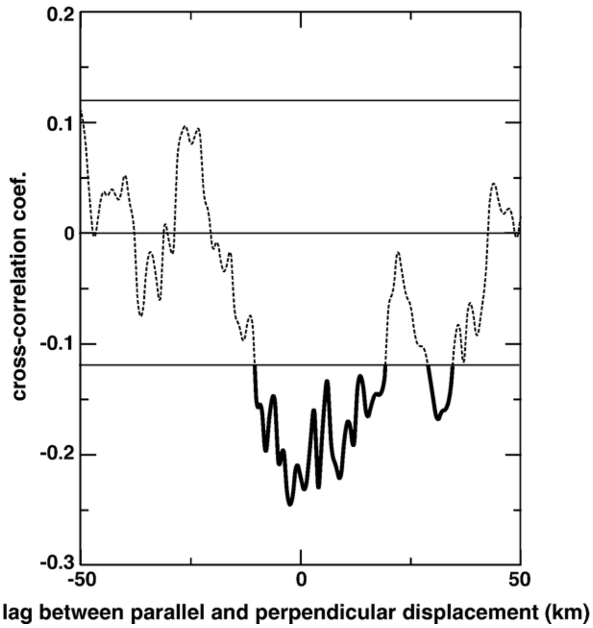

Fig. 11. Cross-correlation between displacement measured parallel and perpendicular to the fault along the Kusai section. The bold line indicates where the coefficient is significantly different from zero. The minimum around zero indicates anti-correlation of the two components of motion.

[28]. Such barrier geometry favours the transfer of horizontal motion to vertical motion that is visible on the component perpendicular to the fault (Figs. 3C and 8). Compressive jogs and junctions between different fault segments are most favourable places for such behaviour.

Some barriers are tough enough to stop the rupture propagation and force the fault system to activate other segments to allow further propagation of the rupture. In a normal faulting context, cumulative slip-curves with linear increase ending in a sharp drop have been identified as specific signature of such barriers [29]. A similar signature has also been suggested for the 1979 Imperial fault strike-slip earthquake [30]. Such patterns can be recognized in at least two places along the Kokoxili rupture (Fig. 9). In both cases, the slip distribution is highly asymmetrical. In the western case, slip rises smoothly from 2 m to 4 m in about 15 km and drops abruptly to less than 2 m in few km. The decrease is associated (Fig. 9) with the onset of the slip-partitioning section [31] where the rupture splits into two parallel branches. In the eastern case, slip increases progressively eastward from 2 m to 7 m over ~50 km, to drop abruptly to 2 m in ~10 km (Fig. 9). This rapid decrease is associated with the triple junction where the rupturing fault meets with the, as yet, unbroken Xidatan segment and an additional side fault connecting from the north. At this point, the rupture propagated southward along the Kunlun Pass fault instead of the Xidatan section. We suggest that the junction between the eastern termination of the Kusai section and the western part of the Xidatan section forms a tough barrier. This barrier stopped the rupture abruptly. Some short discontinuous cracks located in the first kilometre of the Xidatan fault perhaps indicate an aborted attempt to trigger rupture along the Xidatan fault. As no clear connection between the Kusai section and the Xidatan fault exists, it was apparently easier for the rupture to transfer to the better oriented Kunlun Pass fault, although it is only a secondary feature at regional scale [11]. Once the rupture started along the Kunlun Pass fault, the western end of the Xidatan fault was immediately affected by the stress shadow of the

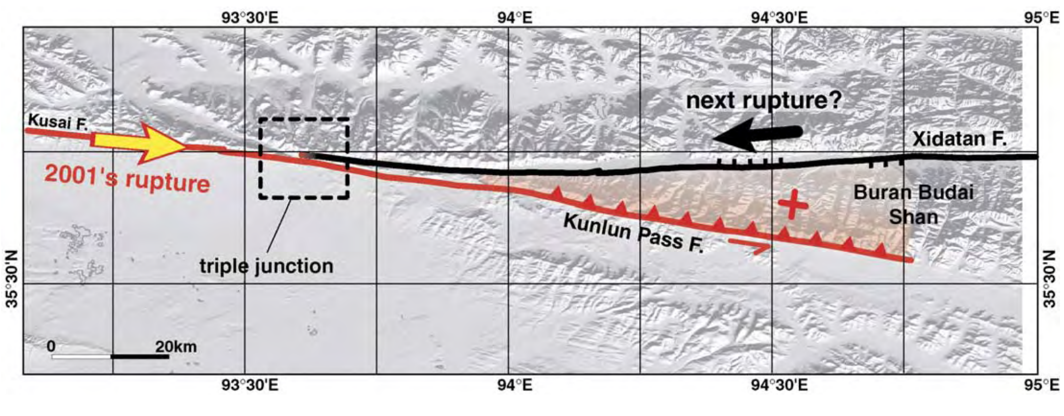

Fig. 12. Field observation shows no clear connection between Kusai and Xidatan Faults. Earthquake rupture propagated preferably along the Kunlun Pass Fault, whose azimuth requires a thrust component to explain the growth of the Buran Budai Shan. A stress shadow due to the 2001 rupture minimises chances for future earthquake to initiate at the western end of the Xidatan Fault, and favours propagation from the east and ending at the triple junction.

current rupture [32], impeding any further triggering along the Xidatan fault. The thrust component along the Kunlun Pass fault partially reduced the normal stress along the Xidatan fault and brought it closer to failure. However, the absence of a real connection between Kusai section and Xidatan fault and the stress shadow due to the 2001 rupture at this barrier make the next earthquake along the Xidatan fault unlikely to start at this barrier and suggests that the next rupture along Xidatan fault will initiate farther east and propagate westward (Fig. 12).

With few exceptions, the barriers identified along the 2001 Kokoxili rupture correspond to compressive jogs or changes in azimuth of the fault trace. The average length of the segments delimited by the barriers is 14.9 km. Almost no very large continental strike-slip earthquake has been documented in a similar way to the Kokoxili earthquake. However, reasonable maps and offset data have been published for the Haiyuan Mw ∼ 8 earthquake in 1920 [33] and the Luzon Mw ∼ 7.8 earthquake in 1990 [34], with rupture lengths of ∼ 120 km and ≥ 120 km, respectively, and maximum horizontal slip larger than 5 m in both cases. Study of the segmentation reveals that these two cases again show average segment lengths of 15–20 km. Morphological mapping of the southern San Andreas fault, also exhibits similar segment scaling [35] although not directly correlated to specific events. Finally, indirect evidences from seismology support these observations. A signature visible in the power spectrum of accelerograms recorded for large earthquakes corresponds to breaking segments with lengths of the order of 10 to 30 km [36].

5. Conclusion

Based on the new high resolution and unambiguous observations from the Kokoxili earthquake, we propose, following earlier suggestions, that the length of the seismic segments is limited by barriers, which are geometric in nature. Although faults have a broadly self-similar geometry [37] segment regularity appears at scales of 15–20 km which we speculate is related to the thickness of the seismogenic crust. The clear support that our observations provide to the Aki model has major implications for modelling the dynamics of earthquake rupture [38].

Acknowledgments

This paper benefits from fruitful discussions with P. Tapponnier. We thank S. Dominguez and an anonymous reviewer for constructive comments. Spot data were acquired through ISIS Program of CNES. This is IPGP contribution number 2109 and INSU contribution number 389.

References

[1] H. Kanamori, G. Stewart, Seismological aspects of the Guatemala Earthquake of February 4, 1976, Journal of Geophysical Research 83 (B7) (1978) 3427–3434.
[2] S. Das, K. Aki, Fault plane with barriers: a versatile earthquake model, Journal of Geophysical Research 82 (1977) 5658–5669.
[3] C. Scholz, The Mechanics of Earthquakes and Faulting, Cambridge University Press, New York, 1990. 439 pp.
[4] K. Aki, Characterization of barriers on an earthquake fault, Journal of Geophysical Research 84 (1979) 6140–6148.
[5] E.M. Dunham, P. Favreau, J.M. Carlson, A supershear transition mechanism for cracks, Science 299 (2003) 1557–1559.
[6] G.C.P. King, G. Yielding, The evolution of a thrust fault system: processes of rupture initiation, propagation and termination in the 1980 El Asnam (Algeria) earthquake, Geophysical Journal Royal Astronomic Society 77 (1984) 915–933.
[7] S. Peyrat, R. Madariaga, K. Olsen, La dynamique des tremblements de terre vue à travers le séisme de Landers du 28 juin 1992, Comptes Rendus de l'Academie des Sciences, Mecanique 330 (2002) 1–14.
[8] S. McGill, C. Rubin, Surficial slip distribution on the central Emerson fault during the June 28, 1992, Landers earthquake, Journal of Geophysical Research 104 (B3) (1999) 4811–4834.
[9] P.J. Haeussler, D.P. Schwartz, T.E. Dawson, H.D. Stenner, J.J. Lienkaemper, B. Sherrod, F.R. Cinti, P. Montone, P.A. Craw, A.J. Crone, S.F. Personius, Surface rupture and slip distribution of the Denali and Totschunda faults in the 3 November 2002 M 7.9 earthquake, Alaska, Bulletin of the Seismological Society of America 94 (6) (2004) S23–S52.
[10] P. Tapponnier, X. Zhiqin, F. Roger, B. Meyer, N. Arnaud, G. Wittlinger, Y. Jingsui, Oblique stepwise rise and growth of the Tibet plateau, Science 294 (2001) 1671–1677.
[11] J. Van Der Woerd, P. Tapponnier, F.J. Ryerson, A.S. Meriaux, B. Meyer, Y. Gaudemer, R.C. Finkel, M.W. Caffee, G.G. Zhao, Z.Q. Xu, Uniform postglacial slip-rate along the central 600 km of the Kunlun Fault (Tibet), from Al-26, Be-10, and C-14 dating of riser offsets, and climatic origin of the regional morphology, Geophysical Journal International 148 (3) (2002) 356–388.
[12] Q. Wang, P. Zhang, J.T. Freymueller, R. Bilham, K.M. Larson, X. Lai, X. You, Z. Niu, J. Wu, Y. Li, J. Liu, Z. Yang, Q. Chen, Present-day crustal deformation in China constrained by global positioning system measurements, Science 294 (2001) 574–577.
[13] Y. Klinger, X. Xu, P. Tapponnier, J. Van Der Woerd, C. Lasserre, G.C.P. King, High-resolution satellite imagery mapping of the surface rupture and slip distribution of the Mw 7.8, November 14, 2001 Kokoxili earthquake (Kunlun fault, northern Tibet, China), Bulletin of the Seismological Society of America 95 (5) (2005) 1970–1987.
[14] N. Van Puymbroeck, R. Michel, R. Binet, J.P. Avouac, J. Taboury, Measuring earthquakes from optical satellite images, Applied Optics 39 (20) (2000) 3486–3494.
[15] R. Michel, J.P. Avouac, Deformation due to the 17 August 1999 Izmit, Turkey, earthquake measured from Spot images, Journal of Geophysical Research 107 (B4) (2002).

[16] S. Dominguez, J.P. Avouac, R. Michel, Horizontal coseismic deformation of the 1999 Chi-Chi earthquake measured from Spot satellite images: implications for the seismic cycle along the western foothills of central Taiwan, Journal of Geophysical Research 108 (B2) (2003), doi:10.1029/2001JB000951.
[17] R. Michel, J.P. Avouac, Imaging co-seismic fault zone deformation from air photos: the Kickapoo stepover along the surface ruptures of the 1992 Landers earthquake, Journal of Geophysical Research (in press).
[18] X. Xu, W. Chen, W. Ma, G. Yu, G. Chen, Surface rupture of the Kunlunshan earthquake (Ms 8.1), northern Tibetan plateau, China, Seismological Research Letters 73 (6) (2002) 884–892.
[19] C. Lasserre, G. Peltzer, F. Crampe, Y. Klinger, J. Van Der Woerd, P. Tapponnier, Coseismic deformation of the 2001 Mw = 7.8 Kokoxili earthquake in Tibet, measured by SAR interferometry, Journal of Geophysical Research 110 (B12408) (2005), doi:10.1029/2004JB003500.
[20] J. Chen, Y. Chen, G. Ding, Z. Wang, Q. Tian, G. Yin, X. Shan, Z. Wang, Surficial slip distribution and segmentation of the 426-km-long surface rupture of the 14 November, 2001, Ms8.1 earthquake on the east Kunlun fault, northern Tibetan plateau, China, Seismology and Geology 26 (3) (2004) 378–392 (in Chinese with English abstract).
[21] J. Liu, Y. Klinger, K. Sieh, C. Rubin, Six similar sequential ruptures of the San Andreas fault, Carrizo Plain, California, Geology 32 (8) (2004) 649–652.
[22] K. Sieh, The repetition of large-earthquake ruptures, Proceedings of the National Academy of Sciences 93 (1996) 3764–3771.
[23] M. Antolik, R.E. Abercrombie, G. Ekstrom, The 14 November 2001 Kokoxili (Kunlunshan), Tibet, earthquake: rupture transfer through a large extensional step-over, Bulletin of the Seismological Society of America 94 (4) (2004) 1173–1194.
[24] G.C.P. King, C. Vita-Finzi, Active folding in the Algerian earthquake of 10 October 1980, Nature 292 (5818) (1981) 22–26.
[25] Y. Fialko, D. Sandwell, M. Simons, P. Rosen, Three-dimensional deformation caused by the Bam, Iran, earthquake and the origin of shallow slip deficit, Nature 435 (19) (2005) 295–299.
[26] G.C.P. King, Speculations on the geometry of the initiation and termination processes of earthquake rupture and its relation to morphology and geological structures, Pure and Applied Geophysics 124 (3) (1986) 567–585.
[27] C. Chatfield, The Analysis of Time Series, Chapman and Hall, London, 1989.
[28] G.C. King, J. Nabelek, The role of fault bends in faults in the initiation and termination of earthquake rupture, Science 283 (1985) 984–987.
[29] I. Manighetti, G.C.P. King, C.G. Sammis, The role of off-fault damage in the evolution of normal faults, Earth and Planetary Science Letters 217 (2004) 399–408.
[30] S. Ward, Dogtails versus rainbows: synthetic earthquake rupture models as an aid in interpreting geological data, Bulletin of the Seismological Society of America 87 (1997) 1422–1441.
[31] G. King, Y. Klinger, D. Bowman, P. Tapponnier, Slip partitioned surface breaks for the 2001 Kokoxili earthquake, China (Mw 7.8), Bulletin Seismological Society America 95 (2) (2005) 731–738.
[32] G.C.P. King, M. Cocco, Fault interaction by elastic stress changes: new clues from earthquake sequences, Advances in Geophysics 44 (2001) 1–38.
[33] Institut of Geology and Ninxia Bureau of seismology, Active Haiyuan fault Zone Monograph, Seismological Publishing House, Beijing, China, 1990 286 pp.
[34] T. Nakata, H. Tsutsumi, R.S. Punongbayan, R.E. Rimando, J. Daligdig, A. Daag, G.M. Besana, Surface Fault Ruptures of the 1990 Luzon Earthquake, Philippines, Hiroshima University Special Pub, Hiroshima, Japan, 1996.
[35] R. Bilham, P. Williams, Sawtooth segmentation and deformation processes on the southern San Andreas fault, California, Geophysical Research Letters 12 (1985) 557–560.
[36] A.A. Gusev, Descriptive statistical model of earthquake source radiation and its application to an estimation of short-period strong motion, Geophysical Journal Royal Astronomic Society 74 (1983) 787–808.
[37] G.C.P. King, The accommodation of large strains in the upper lithosphere of the Earth and other solids by self-similar fault systems: the geometrical origin of b-value, Pure and Applied Geophysics 121 (1983) 761–1093.
[38] M.R. Handy, G. Hirth, N. Hovius, The dynamic of fault zones, in: M.R. Handy, G. Hirth, N. Hovius (Eds.), Dahlem Workshop 95, MIT Press, Berlin, 2005.